PREDICTING THE IGNITION AND BURNING RATE OF WOOD IN THE CONE CALORIMETER USING AN INTEGRAL MODEL

Michael John Spearpoint

NIST

PREDICTING THE IGNITION AND BURNING RATE OF WOOD IN THE CONE CALORIMETER USING AN INTEGRAL MODEL

Prepared for
U.S. Department of Commerce
Building and Fire Research Laboratory
National Institute of Standards and Technology
Gaithersburg, MD 20899

By
Michael John Spearpoint
University of Maryland
College Park, MD 20742

May 1999

Notice

This report was prepared for the Building and Fire Research Laboratory of the National Institute of Standards and Technology under grant 60NANB2D1266 number. The statement and conclusions contained in this report are those of the authors and do not necessarily reflect the views of the National Institute of Standards and Technology or the Building and Fire Research Laboratory.

ACKNOWLEDGEMENTS

ABSTRACT

Title of Thesis: Predicting the ignition and burning rate of wood in the Cone Calorimeter using an integral model.

Name of degree candidate: Michael John Spearpoint

Degree and Year: Master of Science in Fire Protection Engineering, 1999.

Thesis directed by: Dr. James G. Quintiere, Professor, Department of Fire Protection Engineering

This study compares ignition and burning rate measurements of wood in the Cone Calorimeter with a one-dimensional integral model that describes the transient pyrolysis of a semi-infinite charring solid subject to a constant radiant heat flux.

Four species of wood were exposed to a range of incident heat fluxes both with their grain parallel and perpendicular to the incident heat flux. The time to ignition and burning rate measurements obtained from the Cone Calorimeter were used to derive characteristic properties of the materials. These properties were used as input to the integral model to compare its predictions with the experimental data.

Thermocouples were embedded as various depths in the samples. Temperature measurements were used to determine the progress of the thermal penetration wave and char depth through the material. The measurements were compared to predictions from the integral model.

TABLE OF CONTENTS

LIST OF TABLES

iv

LIST OF FIGURES

NOMENCLATURE

a pre-exponential factor for char fraction relationship [-]

α thermal diffusivity, [m²/s], absorptivity [-]

A area, [m²]

β Ratio of convective gain and radiative loss with incident heat flux, [-]

c specific heat [J/kg.K]

C ignition constant, [-]

D diameter (of cylindrical flame), [m]

δ depth [m]

Δ dimensionless depth, [-]

ε flame emissivity, [-]

ϕ, ϕ' char fraction, [-]

f grain orientation coefficient, [-]

ΔH_c heat of combustion [J/kg]

ΔH_v heat of vaporisation or heat of pyrolysis [J/kg]

η height, [m]

h heat transfer coefficient [W/m².K], enthalpy [J]

I thermal inertia, $k\rho c$, [J².m⁻⁴.K⁻².s⁻¹]

k thermal conductivity, [W/m.K]

κ absorption coefficient, [m⁻¹]

L heat of gasification, [J/kg]

L_{fl} mean beam length of flame, [m]

m mass, [kg]

M dimensionless mass loss rate, [-]

n power factor for char fraction relationship [-]

p pressure, [Pa]

π pi, [3.141]

Π peak mass loss rate ratio [-]

Q power output, [W]

q heat flux, [W/m^2]

ρ density, [kg/m^3]

s specific gravity, [-]

T temperature, [°C] or [K]

t time, [s]

θ dimensionless temperature, [-]

τ dimensionless time, [-]

σ Stefan-Boltzmann constant [W/m^2.K]

ω shrinkage factor, [%]

u moisture content, [%], internal energy [J]

v velocity, [m/s]

V volume, [m^3]

Z constant used in pure convective loss ignition analysis, [-]

Subscripts

0	initial, ambient
b	back
calc	calculated
conv	convection
cr	critical
ϕ	char
f	final
fl	flame
g	gas
i	incident
ig	ignition
meas	measured
p	constant pressure
peak	peak
rad	radiation
s	surface, steady (when subscripted to δ)
steady	steady-state
tc	thermocouple
v	vaporisation, constant volume
w	virgin wood
X	*across* grain
L	*along* grain

tr   transitional

Superscripts

( )″   per unit area

(˙)   per unit time

1. INTRODUCTION

"We are not beginners
we will not be fooled
the times have been our teachers & they
teach an iron rule, we do our
best work in the dark, we do our
thinking on the run"
A Fire is Burning, Oysterband (Holy Bandits, 1993)

1.1 Background

Ever since prehistoric times humans have known that wood burns. The ability of wood to

burn has been both a benefit and a problem for humans. The capability to predict the

burning rate of wood in modern times has become increasingly important as fire safety

engineering moves toward a performance-based approach to building design. Computer

based fire and hazard models require the burning rate of materials to be specified as

input.

The pyrolysis behaviour of solid materials can be divided into two types: non-charring

and charring. Non-charring materials burn away completely leaving no residue and can

be modelled using theory similar to flammable liquids. In contrast, charring materials

leave relatively significant amounts of residue when they burn. The pyrolysis of charring

materials such as wood is a complex interplay of chemistry, heat and mass transfer.

Charring materials must be modelled in terms of a pyrolysis front penetrating into the

material with an increasing surface temperature and without a well-defined steady state.

The purpose of this study is to examine a one-dimensional integral model for charring materials (in this case wood) by comparing the model with data obtained from an ignition and burning rate apparatus (the Cone Calorimeter). This study will show how we might predict the ignition and burning characteristics of a charring material using a limited number of experimental measurements to obtain properties that are required by the model. Although some material properties can be obtained from the literature, several properties are derived from the time to ignition measurements and through an iterative process of comparing the model predictions from the integral model with experimental test data. This study demonstrates a methodology for obtaining these properties.

1.2 Structure and thermal decomposition of wood

1.2.1 Growth and structure

There are many species of wood and they are used by society for a wide range of construction, utensil and decorative purposes. Woods are subdivided into two botanical categories: softwoods and hardwoods and the physical structure as well as the chemical composition is considerably different between these two.

Janssens [1] in his thesis gives an excellent overview of the composition of wood and its thermal decomposition. Much of the description given is this section is taken from his work supplemented by information from Drysdale [2] and Cholin [3].

The macroscopic structure of softwood and hardwood stems is very similar. The stems consist of a core of wood *(xylem)* covered by a protective layer of bark. The *xylem*

consists of long fibre-like cells that are oriented preferentially in one direction (vertical) referred to as the grain. Water, minerals and nutrients are taken up by the roots and are transported through the outer part of the *xylem* to the leaves. Photosynthesis in the leaves uses the water and CO_2 (from the atmosphere) to form various sugars. A solution of the sugars into water (also referred to as sap) is moved to various parts of the tree through the inner layer of the bark (*phloem*). The growth process is limited to a thin layer between the *xylem* and the *phloem*, called the *cambium*. New cells are created on either side of the *cambium* through division of existing cells. Thus, both the *phloem* and the *xylem* are growing. The *cambium* forms a ring with a continuously increasing diameter.

After a number of years, the cells in the inner part of the *xylem* die. The wood in this part of the *xylem* is referred to as heartwood. The remaining (outer) part of the *xylem* is called sapwood. From the moment the first heartwood is formed, it expands together with the *cambial* layer. Therefore, commercial lumber usually consists of a mixture of primarily heartwood and some sapwood. The mechanical properties of heartwood and sapwood of the same stem are very similar. However, heartwood is often denser than sapwood. In addition, heartwood contains a variety of products of sugar decomposition originating in the *cambium*. These products can be removed by physical or chemical extraction processes and are therefore commonly referred to as extractives. The extractives clog tiny passages in the cell walls. Consequently they significantly reduce the permeability of wood. The chemical composition of some extractives is very different from that of the main components of wood; cellulose, hemicellulose and lignin. Thus, because of the aforementioned physical and chemical phenomena associated with the presence of

3

extractives, the fire behaviour of heartwood may be somewhat different from that of sapwood.

The elemental composition of dry wood consists of about 50% carbon, 6% hydrogen, 44% oxygen and small amounts of nitrogen and some inorganic compounds. The principal elemental constituents are combined into a number of natural polymers; cellulose, hemicellulose and lignin. Cellulose consists of a large number of glucose molecules joined together in a chain-like polymer. The molecules align themselves into bundles (microfibrils) which provide structural strength and rigidity to the cell wall. Glucose, $(C_6H_{12}O_6)$, is the principal sugar generated by photosynthesis. The chemical formula of cellulose is $(C_6H_{10}O_5)_n$ i.e. one molecule of water is generated for every pair of glucose molecules linked together. The degree of polymerisation, n, may be as high as 30,000. Various other sugars produced in the leaves are combined to branched-chain polymers called hemicellulose. The degree of polymerisation is generally only a few hundred. Lignin is a stable high molecular weight polymer that is phenolic in nature. It acts as a binding agent within and between cell walls. The lignin content, in general, is significantly higher in softwoods as illustrated in Table 1.

Type	Cellulose	Hemicellulose	Lignin
Hardwood	40-44	23-40	18-25
Softwood	40-44	20-32	25-35

Table 1. Chemical composition of dry wood in percent mass.

Wood normally contains a quantity of moisture present by different physical mechanisms. Much of the space in a live tree is occupied by water, called "free water".

4

When a tree is cut, the free water is gradually replaced by air. Wood also contains water that is hygroscopically bound to the cellulose molecules through a weak chemical bond. This "bound water" will leave the wood at a rate determined by the temperature and relative humidity. The moisture content of wood below the range of 5 to 7 per cent is called the "moisture of constitution". This water forms the bonds between the adjacent cellulose molecules and cannot be removed without the physical destruction of the wood. Thus, even "dry" wood always contains some moisture.

Due to its grain, wood is an anisotropic material i.e. it does not have the same structure in its orthogonal directions. Thus the structure of wood can be considered parallel to the grain, tangential to the grain and radial to the grain. As will be discussed later in more detail, the properties and burning characteristics vary with the grain orientation.

1.2.2 Burning characteristics

As a result of the complex chemical and physical structure of wood, its ignition and burning characteristics are also complex. Consequently, only a simplified description of these mechanisms is given here.

Consider a slab of wood with one surface uniformly exposed to a constant external incident heat flux and a source of ignition (a pilot) close by. The homogeneity of the incident heat flux to the exposed surface allows the heat and mass transfer through the slab to be considered one-dimensional. The incident flux pyrolyses the surface of the wood thus releasing volatile fuel gases. The mass flow rate of the volatiles is a function

5

of several factors including the intensity of the incident energy and the orientation of the grain. If the mass flow rate of the volatiles is sufficient to reach the lower flammable limit of the fuel/air mixture then ignition occurs. At this instant the heat flux to the surface of the wood is a combination of the external flux plus the flux from the flame. The rate of heat release rapidly rises to a maximum then a char layer gradually builds up as the pyrolysis front moves inward. The char layer forms an increasing thermal resistance between the exposed surface and the pyrolysis front resulting in a continuously decreasing rate of heat release after the first peak. Experimental data are available showing that if the slab is sufficiently thick, its rate of heat release eventually reaches a more or less steady value.

The char layer begins to break down rapidly at temperatures above 300 °C. The char layer also shrinks and pressure gradients (i.e. stresses) are set-up within the material. Small cracks appear on the surface, perpendicular to the grain, and these cracks allow volatiles to escape more easily. The cracks gradually widen as the char layer deepens leading to the characteristic 'alligatoring' patterns that are frequently observed.

After the volatiles have been exhausted, flaming ceases and a solid char residue remains. The char continues to burn in a smouldering mode. Prior to that, char oxidation is usually minimal since the flame prevents diffusion of O_2 to the surface. Therefore, heat release rate and related quantities measured during the flaming phase are predominantly those of the volatiles. The main constituent of wood char is carbon, so that its net heat of combustion is around 32 MJ/kg. It has been found for various species of dry wood that

the char yield is 33% ± 3% of the original mass of wood. With an average net heat of combustion of wood of 17 MJ/kg, the mean heat of combustion measured in the Cone Calorimeter during the flaming mode should then be about 10 MJ/kg. The values (§ 4.4.1) actually measured are somewhat different due to variations in the char yield and moisture in the conditioned samples.

The three main components of wood have quite different thermal degradation characteristics. This is illustrated by thermogravimetric analysis, showing that the constituents decompose to release volatiles over different temperature ranges [2], typically:

Cellulose   240-350 °C

Hemicellulose   200-260 °C

Lignin   280-500 °C

Consequently, the thermal degradation characteristics of wood shift towards higher temperatures with increasing lignin content. This explains why the surface temperature at ignition is significantly higher for softwoods than for hardwoods (see § 3.2.3). In addition, at temperatures in excess of 400-450 °C lignin decomposes to volatiles for about 50% of its mass and is therefore responsible for most of the char. In contrast, α-cellulose leaves only 5% char after prolonged heating at 300 °C. The charring rate of wood is also very sensitive to the presence of inorganic impurities, such as fire retardants, because they affect the chemical kinetics of the pyrolysis process.

The heat of combustion of wood measured in an oxygen bomb, which includes the heat released by the char, increases with lignin content. This may not be relevant to real fire situations of interest for this work, since the heat released under such conditions is primarily that of the volatiles. However, the net heat of combustion of the volatiles is also slightly higher for lignin than for the other constituents. Parker [4] measured 14.7 MJ/kg for lignin, 13.8 MJ/kg for cellulose and even lower values for some hemicelluloses of Douglas fir. Still, since more energy is required to generate the volatiles, it is expected that fire performance of wood improves with increasing lignin content.

As a result of the grain structure of wood, not only do the material properties vary but also the mechanisms by which the volatiles are able to exit the surface of the wood and thus the ignition and burning characteristics. Consider the xylem cells as long "tubes" and two scenarios where the incident heat flux is either parallel or perpendicular to these tubes (Figure 1)

(a) Incident flux parallel to grain.   (b) Incident flux perpendicular to grain.
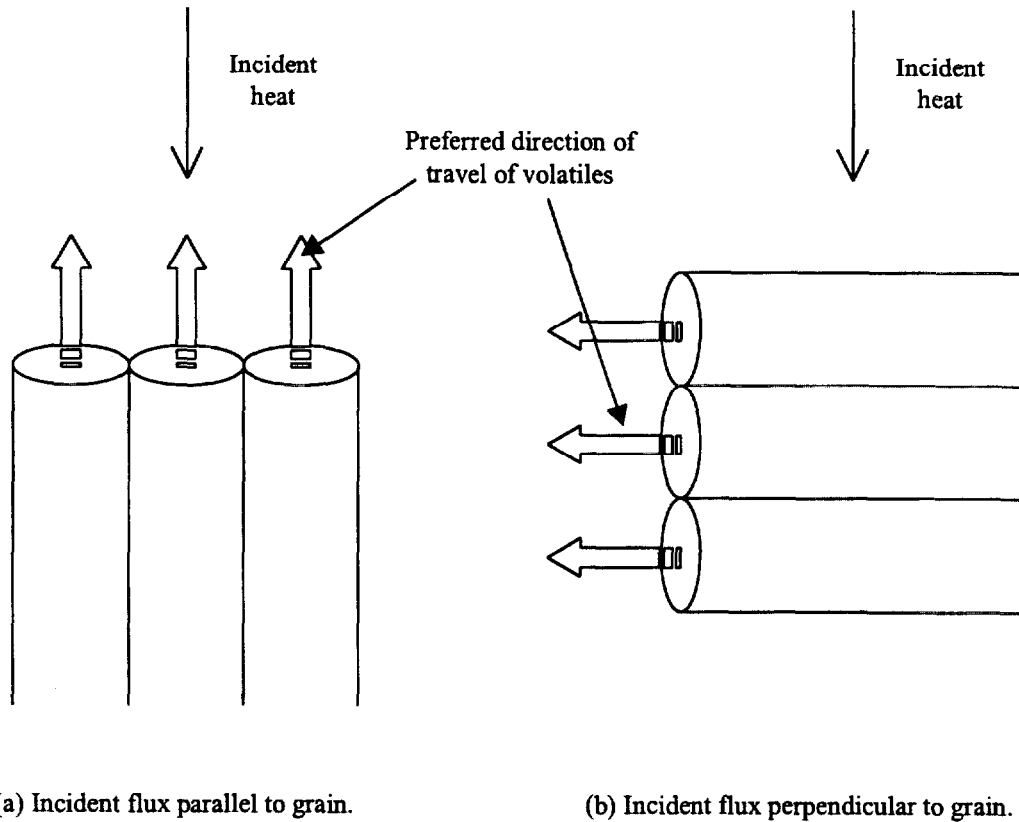
Figure 1. Incident flux and grain orientation scenarios.

Volatiles generated just below the surface of the unaffected wood can travel more easily along the grain compared to at right-angles. The appearance of jets of volatiles and flames at the ends of a burning log is evidence for this. In case (b), the cell wall impede the flow of volatiles to the exposed surface and thus the walls have to decompose to allow a sufficient mass flux of fuel to achieve the lower flammable limit. This decomposition process requires additional energy and thus we might expect (and this study demonstrates, at least for low heat fluxes) that the ignition of wood is more easily achieved when the wood is exposed with its grain end-on i.e. case (a).

1.3 The Cone Calorimeter

1.3.1 Background

The Cone Calorimeter [5] is a standard apparatus for measuring the ignition and burning characteristics of materials. The apparatus was developed during the 1980's at the National Institute of Standards and Technology (NIST) formerly the National Bureau of Standards (NBS). The Cone Calorimeter at the University of Maryland was installed and tested by Woodford [6]. It is not the intention of this study to provide details of the theory and operation of the apparatus as this can be readily found in the literature. For example, the construction and operation of the apparatus is detailed in NFPA 264 [7] and ASTM 1354 [8]. The University of Maryland Cone Calorimeter and its accompanying software was designed and built during or prior to 1988 and thus meets earlier versions of the relevant standards than those currently in use. Figure 2 shows a schematic diagram of the Cone Calorimeter taken from reference 8. The University of Maryland Cone Calorimeter includes the chamber.
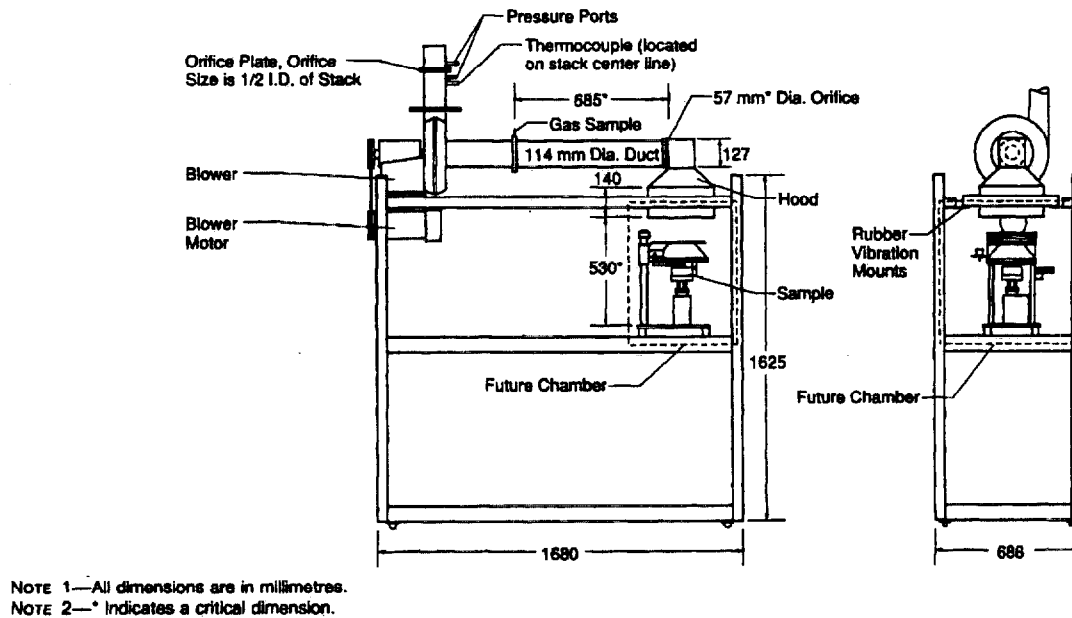
Figure 2. Schematic of the Cone Calorimeter (from ASTM 1354, 1995).

Samples are mounted in a retainer frame. A truncated cone shaped electric heater is used

to impose an external incident heat flux onto the surface of the sample. An electric spark

igniter can be used to initiate piloted ignition. The time to ignition t_{ig} is recorded by the

operator. The apparatus uses a load cell to measure mass loss rate per unit area $\dot{m}''$.

Oxygen consumption calorimetry is used to obtain the rate of energy release per unit area

$\dot{Q}''$. The combustion products from the burning sample are collected in the hood and

passed along the duct. The relative decrease in the oxygen concentration in the

combustion gases compared with normal ambient is recorded. The mass flow of the

combustion gases is obtained from the measurements of the temperature and pressure

difference across an orifice plate located in the stack. A thermocouple is used to measure

the gas temperature and a pressure transducer is used to obtain the pressure difference.

Thus, the amount of oxygen consumed per unit mass of combustion gas can be found. By

using the fact that the energy release of a burning material per unit mass of oxygen consumed is almost a constant for most materials [9], the energy release rate can be obtained. The instantaneous heat of combustion ΔH_c can be obtained from

$$\Delta H_c = \frac{\dot{Q}''}{\dot{m}''}$$

<div align="right">*Equation 1*</div>

and it has been observed that the heat of combustion is generally constant for a material undergoing flaming combustion. In addition, the smoke density across the duct is determined by using a receiver to measure the obscuration of a laser as smoke passes through its optical path.

The mass loss rate, rate of heat release (rate of energy release or also referred to as the burning rate), instantaneous heat of combustion, smoke obscuration and other data were all automatically recorded as functions of time by a commercial data acquisition system connected to the Cone Calorimeter. For the majority of the tests, the scanning rate of the data acquisition system was 5 s. However, smaller scan rates of 2 s and 1 s were used in a limited number of the experimental tests. Note that the current (1995) version of the NFPA standard [7] requires a scan rate of 2 seconds or less as opposed to 5 s or less in earlier versions. In addition, the definition of sustained flaming is 4 seconds rather than the earlier definition of 10 seconds which is used in this study.

The data collected by the Cone Calorimeter data acquisition system was post-processed using a program provided with the system. Finally, this processed data was imported into a commercial spreadsheet package for analysis.

1.3.2 Calibration and set-up

In preparation for the study, a retainer frame was modified to allow thermocouples to be located inside the test sample. The heat flux from the cone heater was calibrated against a calibrated total heat flux gauge. A second standard reference total heat flux gauge was used to verify the calibration. Thus the temperature of the cone heater was selected to provide a known incident heat flux (Figure 3).
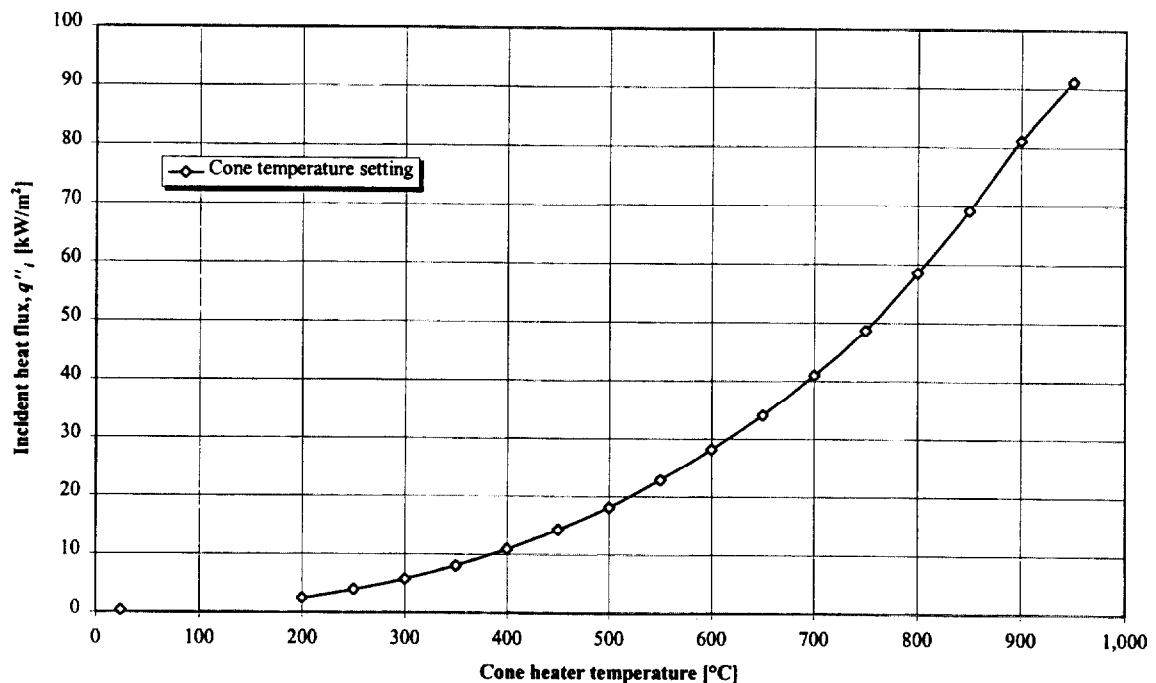
Figure 3. Comparison between the temperature setting on the Cone Calorimeter and the calibrated total heat flux gauge.

Prior to each day of testing the Cone Calorimeter was calibrated according to the procedure laid down by Woodford [6]. The load cell was calibrated between 0 g and 250 g in increments of 50 g using standard weights. The pressure transducer in the duct

was zeroed. The oxygen analyser was calibrated with nitrogen (i.e. 0% oxygen) and ambient (i.e. 20.95 % oxygen). The smoke extinction laser system was calibrated using 0.3 OD/m and 0.8 OD/m neutral density filters. A 5 kW methane burner flame was used to obtain the calibration factor. The heater was positioned such that the exposed surface of the material under test was 25 mm away. Finally, the system was checked for consistency by burning a 25 mm thick sample of black PMMA.

Each time the incident heat flux was changed, the output from the heater was verified with one of the calibrated total heat flux gauges.

1.4 Burning rate and ignition tests

1.4.1 General

The wood samples were provided such that the grain was parallel to the incident heat flux (i.e. cut *across* the grain) and perpendicular to the incident heat flux (i.e. cut *along* the grain) as shown in Figure 4.
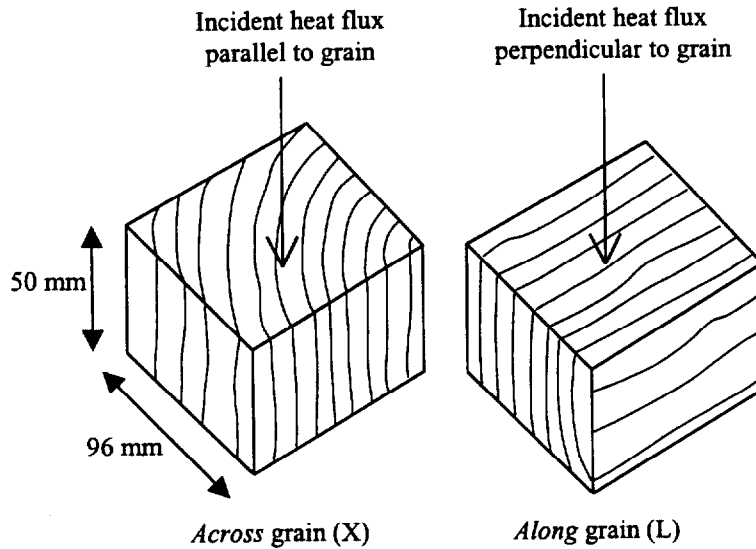
Figure 4. Sample grain configurations.

Four species of wood were tested in the study: Douglas fir, Redwood, Red oak and

Maple. Douglas fir and Redwood are both softwoods whereas Red oak and Maple are

both hardwoods. The samples were all cut from the sapwood portion of sections of

lumber. The test numbering system used in this study was as follows

$n\,ss\,o\,t$ [i]   e.g. 1DFL2

where

n	denotes the test series; 1 or 2
ss	denotes the species; Douglas fir (DF), Redwood (R), Red oak (O), Maple (M),
o	denotes the grain orientation; L is *along* or X is *across* (Figure 4),
t	is the test number for that species and orientation; 1 ... n,

and the optional post-fix letter 'i' indicates an 'ignition only' test.

Samples were stored in a desiccator at nominally 50 % relative humidity and 20 °C. The moisture content of each sample was measured with a hand-held moisture meter prior to exposure. In many cases, it was found that the moisture content of the samples was below the sensitivity of the meter. The minimum sensitivity value was recorded in such instances.

All samples were tested in the horizontal orientation. Samples were wrapped in a single layer of aluminium foil, placed into the sample holder and backed by non-combustible ceramic fibre insulation material. In most tests the layer of ceramic fibre blanket was necessarily thin since the maximum height of the sample retainer frame is 50 mm and the nominal height of the samples was also 50 mm.

The doors to the chamber were closed during the experiments and air was provided by a vent in the base of the chamber below the load cell. The spark igniter was located ~10 mm above the surface of the sample. Sustained ignition is defined as when the sample continues to flame for an uninterrupted period of at least 10 s.

The majority of the experimental tests used in this study were conducted at the University of Maryland by the author on behalf of Schroeder [10] as part of his analysis of the change in the structure of materials when exposed to an external heat flux for relatively prolonged durations. The test materials and experimental protocol were thus primarily selected by the requirements of Schroeder's analysis. As it will be described in § 4.2, these requirements presented certain problems and limitations on the results obtained.

16

The experimental series' were supplemented by a small number of additional tests that were not part of Schroeder's study. The small number of extra samples available to the author limited these tests. The experiments described in this study were conducted in two series as described below.

1.4.2 Burning rate tests

The main 'burning rate' series of 54 tests included the complete measurement of time to ignition, mass loss, rate of heat release and smoke extinction data. Incident heat fluxes of 25 kW/m^2, 35 kW/m^2, 50 kW/m^2 and 75 kW/m^2 were selected for these experiments. These heat fluxes are typical of values used by other researchers. For the majority of the burning rate tests, exposure times t_f of 25 minutes were used, however, in a few cases the exposure time was extended to 75 minutes. A summary of the exposure conditions for each species of wood in the two grain orientations is given in Table 2.

Incident heat flux q''_i [kW/m²]	Douglas fir Duration t_f [mins]		Redwood Duration t_f [mins]		Red oak Duration t_f [mins]		Maple Duration t_f [mins]		Total	
	25	75	25	75	25	75	25	75	25	75
25	2 (1L, 1X)	-	3 (1L, 2X)	1X	2 (1L, 1X)	2 (1L, 1X)	2 (1L, 1X)	2 (1L, 1X)	9 (4L, 5X)	5 (2L, 3X)
35	1 (1L)	-	2 (1L, 1X)	-	-	-	-	-	3 (2L, 1X)	-
50	5 (3L, 2X)	-	6 (3L, 3X)	-	-	-	-	-	11 (6L, 5X)	-
75	7 (3L, 4X)	1 (1X)	6 (3L, 3X)	-	6 (3L, 3X)	-	6 (3L, 3X)	-	25 (12L, 13X)	1 (1X)
Total	15 (8L, 7X)	1 (1X)	17 (8L, 9X)	1 (1X)	8 (4L, 4X)	2 (1L, 1X)	8 (4L, 4X)	2 (1L, 1X)	48 (24L, 24X)	6 (2L, 4X)

Table 2. Main 'burning rate' series test exposure conditions for each species of wood in the two grain orientations.

Each sample was nominally 50 mm thick and 96 mm square (measured to the nearest millimetre). For the majority of the 'burning rate' tests, 0.813 mm (0.032") diameter

sheathed Type K thermocouples were inserted into the samples through holes at heights

of 4 mm, 12 mm, 24 mm and 36 mm below the top surface (Figure 5). A thermocouple

was located between the back of the sample and the retainer frame and a thermocouple

was used to record the ambient temperature outside the Cone Calorimeter. The

thermocouple measurements were recorded by a data logging system separate from the

Cone Calorimeter data acquisition system.
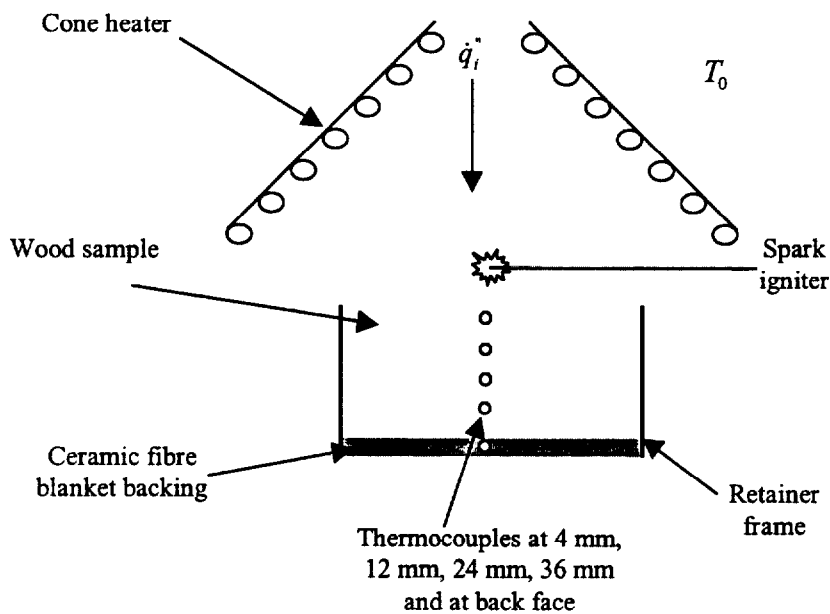
Figure 5. Cone Calorimeter sample configuration in main 'burning rate' tests.

Although the post-processing program provided with the Cone Calorimeter provided an

average heat of combustion, in this study the value was obtained manually from the

instantaneous data. This was necessary for several reasons. Firstly, at the end of each test

the Cone Calorimeter normally requires that the sample remain on the load cell for

approximately one minute while the data collected is completed. However, since the

requirement of Schroeder's work was to have exact exposure times, the sample was

necessarily removed immediately after the end of the test was declared. This resulted in the output from the load cell being affected and thus the final automatic average heat of combustion calculation. Secondly, the wood samples were exposed for long periods of time during which burning did not occur. As will be described in § 4.7, during these long test periods the instantaneous heat of combustion would shift as the wood charred and this char oxidised. Finally, as will be discussed later in § 4.2, a meaningful measurement of the instantaneous heat of combustion was not always achieved.

Thus, where applicable, the average heat of combustion was found by obtaining the mean of the instantaneous heat of combustion data over the portion of the test between ignition and before any fluctuations at the end of the test (Figure 6). Where char oxidation effects were observed, a separate average heat of combustion for the char was obtained.
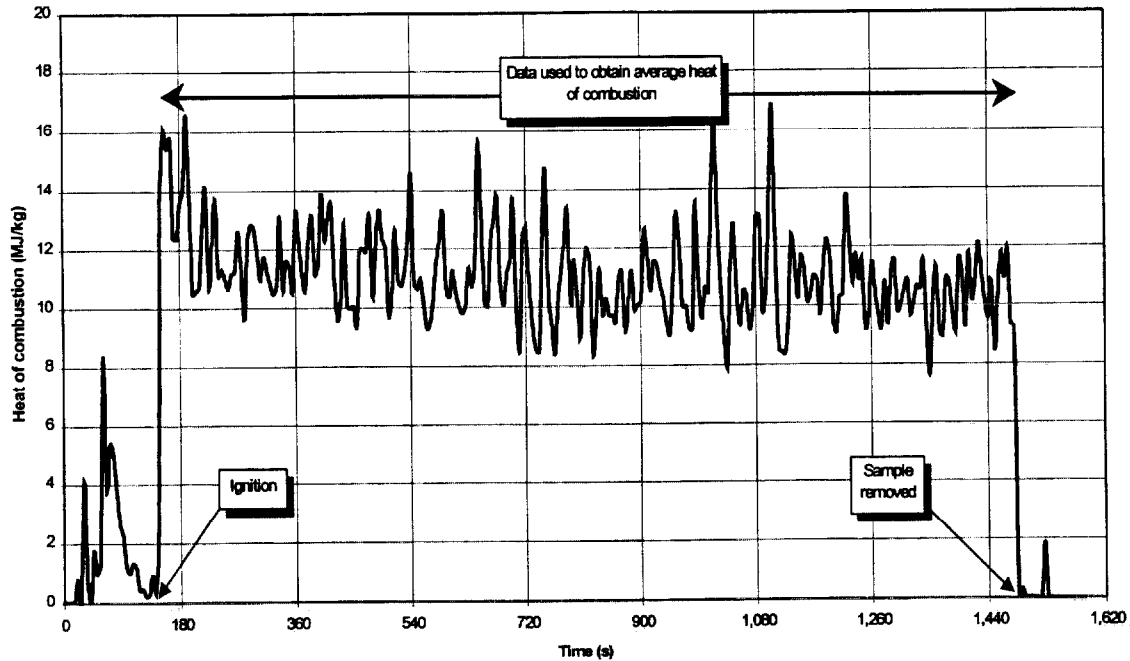
Figure 6. Obtaining the average heat of combustion (Test 1RL3).

Observations were made prior to and during the burning of the sample. It was noted that as the samples burned, the flames would initially be at their tallest (Figure 7 {a}), then reduce in size over time and would sometimes disappear completely leaving the char layer to glow (Figure 7 {b}). Figure 8 shows an example of a normalised flame height for Test 2DFX9i (Douglas fir at 35 kW/m^2)

Figure 7. Sample burning in the Cone Calorimeter; {a} 1:40 after ignition; {b} 25:00 after ignition (Test 2DFX9i).
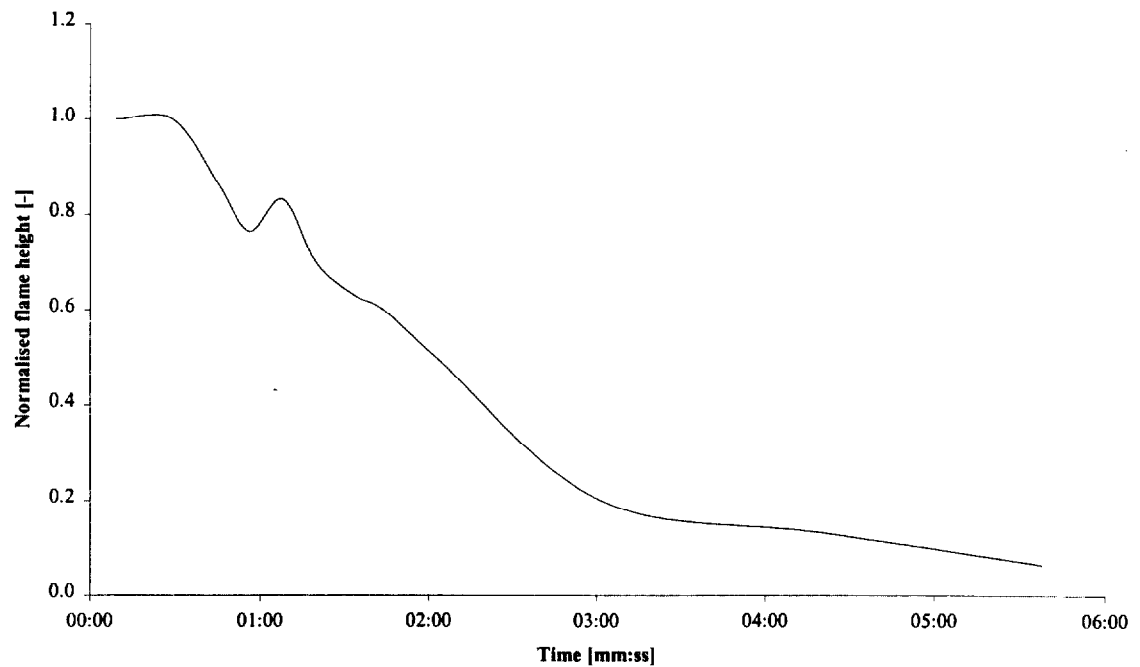
Figure 8. Normalised flame height (Test 2DFX9i).

21

The flames were more likely to cease at the lower incident heat fluxes but that was not always the case. In some cases, after the majority of the exposed surface had ceased flaming, some smaller flames could be seen around the edges of the sample. This was due to shrinkage and volatile gases escaping from the vertical edges of the sample.

1.4.3 Ignition tests

A total of 41 additional 'ignition only' tests at lower heat fluxes were conducted where only time to ignition was measured. These tests were conducted between heat fluxes below 25 kW/m^2 down to heat fluxes in the region of the critical heat flux for ignition for a particular species of wood at a particular grain orientation. The critical heat flux is defined as the minimum external heat flux required to achieve piloted ignition of an exposed sample. In these 'ignition only' tests, the sample was exposed to the external heat flux until sustained ignition occurred or until it was determined by observation that ignition was unlikely to take place. If ignition occurred, the sample was extinguished immediately.

The selection of a 'failure to ignite' criterion is somewhat subject to operator interpretation and patience. The ASTM standard for the Cone Calorimeter [7] suggests in paragraph 11.2.8

> *If the specimen does not ignite in 10min, remove and discard, unless the specimen is showing signs of heat evolution.*

Similarly, the ASTM standard for the Lateral Ignition and Flame Test (LIFT) apparatus [11] suggests in its paragraph 11.2.8

> *The test is considered complete if ignition does not occur within 20 min. However, this is an arbitrary cut-off, and longer times can be considered.*

Clearly both of these test methods leave the ultimate decision as to when ignition has not (or will not occur) to the operator and the requirements of the particular experiment. In this study the decision as to when to terminate a test was of particular importance in determining the critical heat flux for ignition (§ 3.2.2).

In the 'ignition only' tests single 50 mm thick samples of wood were cut into four equal thickness slices. For each test, the four slices were stacked in the sample holder to mimic the full thickness samples used in the main test series. The arrangement of samples in the Cone Calorimeter was thus similar to Figure 5 with the exclusion of the thermocouples. Critical heat flux measurements were not conducted for Red oak since all samples were used in the main 'burning rate' experiments.

In retrospect the use of the stack of samples may have been unnecessary and also may have influenced the results somewhat. Where the stacked samples were subject to incident heat flux for a considerable period of time, the moisture and volatile content in the lower samples may have been altered so that when those samples were repositioned at the exposure surface in subsequent tests they were no longer effectively 'virgin' wood.

On the other hand, since samples were exposed for several tens of minutes before ignition, the moisture and volatile content would have undergone charges regardless of any effects.

Prior to ignition it was noted that some samples would warp either away from or towards the cone heater. The warping was seen to 'self-correct' (i.e. return to almost level) in some instances. In addition, coupled with shrinkage, there were cases of the sample warping out of the retainer frame at one corner or along an edge. These factors may have introduced some margin of error into the ignition results since the sample may have ignited sooner or later than if it had remained level.

In the tests conducted in this study it was found that the wood continued to ignite even at very low incident heat fluxes i.e. below 10 kW/m^2, which is considerably lower than values quoted in the literature (see § 3.2.2). It was observed that at these low heat fluxes, a localised glowing could be seen on the surface of the wood prior to ignition. In such cases, ignition would eventually occur with the flames initially limited to the region of glowing but gradually spreading over the exposed surface of the sample. In contrast, at higher heat fluxes the sample would immediately ignite over the complete surface of the sample. It is likely that this localised glowing contributed an additional source of energy to that provided by the heater to the surface of the wood eventually leading to ignition.

For example, Figure 9 shows the glowing on the surface of a sample of *along* grain

Maple exposed to an incident heat flux of 12 kW/m^2 (Test 2ML4i). The glowing

appeared approximately 1 hr into the test followed by ignition at 1 hr and 10 minutes.
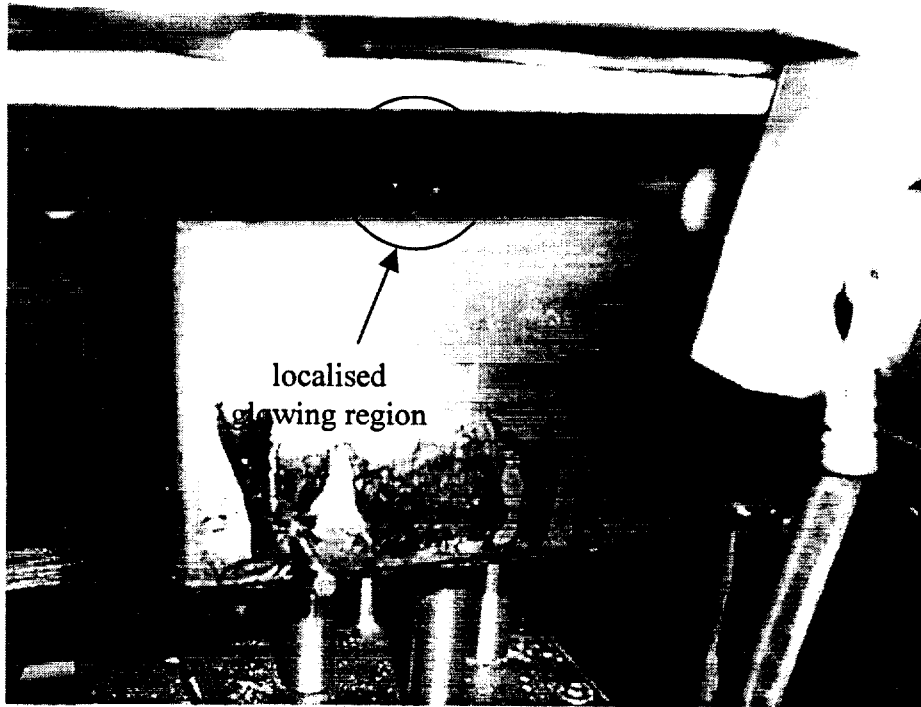
Figure 9. Localised glowing region observed on sample 2ML4i.

Martin [12] alludes to this change in the ignition mechanism at low heat fluxes. He

suggests that the ignition behaviour of cellulose can be split into three regions;

convection-controlled, diffusion-controlled and ablation-controlled. He further notes that

cellulose exhibits basically two kinds of ignition phenomena without the presence of a

pilot flame - spontaneous flaming and glowing ignition.

The glowing ignition typically occurs under conditions of slow heating and therefore is

not the usual response to the diffusion-controlled region. Its occurrence is dependent on

the mineral content of the specimen and size of the irradiated area. Finally, the glowing ignition, almost without exception, sustains itself once started whereas the flaming ignition may be either transient or persistent.

1.5 Literature review

1.5.1 General

There is a substantial volume of work in the literature regarding the pyrolysis, burning and charring behaviour of wood (and cellulosic materials). It is not within the scope of this work to be able to reference and review every study conducted. The exclusion of a particular piece of work does not neglect its importance to this field of study but simply highlights the inability of the author to cover every contribution. However, several of the more directly relevant studies have been selected as sources of material property data, modelling techniques and for comparison purposes.

Kanury [13] gives a general overview of the ignition of solids by thermal radiation or convection. Roberts [14] reviewed the role of kinetics for the pyrolysis of wood and related materials. Simms [15] examined the role of thermal radiation on the damage to cellulosic solids by considering the chemical and thermal histories of the material. Work on char rate in wood includes studies by Kanury [16] who examined the phenomenon using Arrhenius pyrolysis kinetics. Schaffer [17] also investigated the charring rates of various species of wood.

26

Atreya and co-workers have done extensive work on the ignition and burning of wood. Included in this was the initial work by Atreya [18] that included experimental observations for the piloted ignition of wood and identified several important factors. A detailed finite difference ignition model was developed by Tzeng & Atreya [19] in an attempt to quantify the experimental observations. Abu-Zaid & Atreya [20] considered the effect of moisture on the ignition of cellulosic materials. Further work by Atreya, Carpentier & Harkleroad [21] examined the effect of sample orientation on piloted ignition and flame spread on wood.

A detailed study of the pyrolysis kinetics of cellulose has been conducted by Suuberg, Milosavljevic & Lilly [22]. Cellulose was chosen because it is relatively well characterised material and, as described in § 1.2.1, cellulose forms a major component in the structure of wood.

1.5.2   Ignition and burning rate models

Several models for the burning rate of solid materials, both charring and non-charring, have been developed. Examples include the studies by Delichatsios & de Ris [23]; Chen *et al.* [24]; Wichman & Atreya [25]; Yuen *et al.* [26] and Parker [4]. These models range from simple treatments of the ignition and burning process, integral model approaches through to an analysis of the complex chemical kinetics involved in the burning of a charring material. Many of the models consist of complex computational codes that require a relatively large number of property values to complete their predictions. These factors can (at least at present) limit the use of such models since many of the properties

27

are difficult to obtain and the codes may not be suitable for incorporation into more general fire hazard models.

In this study, we examine the integral model initially developed by Quintiere [27]. A one-dimensional pyrolysis model which includes the processes of charring, vaporisation, flame and heat conduction effects was proposed. This model was further developed by Quintiere & Iqbal [28] to solve the one-dimensional unsteady heat transfer equations during the pre-heating and gasification periods using an integral method. Anderson [29] studied the integral solution to Quintiere's [27] model and compared the integral solution with the exact solution. Finally, in the study conducted by Hopkins [30], the model developed by Quintere [27] was compared against experimental data for non-charring thermoplastics tested in the Cone Calorimeter.

The integral model approach to the burning of a charring material has been successfully demonstrated by Moghtaderi, Novozhilov, Fletcher & Kent [31] using a computational fluid dynamics model. Simulation times of about eight hours are quoted by the authors.

1.5.3 Experimental data

Experimental data for the ignition and burning rate of several species of wood have been presented in the literature. Studies of particular reference are outlined below.

Janssens [1], [32], [33] tested several species of wood in the Cone Calorimeter of which Douglas fir and Redwood will be of particular interest to this study. In all cases the

samples were tested in the vertical orientation with the grain perpendicular to the incident

heat flux (i.e. equivalent to the *along* grain orientation used in this study). Parameters

obtained included critical heat fluxes, ignition temperatures and energy release rates.

Measurements of the burning rate of wood have been made by Tran & White [34] using

the Ohio State University (OSU) apparatus. Four types of wood, namely Redwood,

Southern pine, Red oak and Basswood were tested at a range of incident heat fluxes

between around 17 and 56 kW/m^2. Parameters including times to ignition, average

burning rates, charring rates were obtained. The study also obtained properties for the

char residue for each type of material tested.

Other experimental data have been reported by Parker [35] for Douglas fir and

Dietenberger [36] for Redwood in both the LIFT and Cone Calorimeter. The study by

Hopkins [30] also includes data for two charring materials, namely Redwood and Red

Oak, but no detailed analysis or comparison with the integral model was conducted with

these data.

2. THERMO-PHYSICAL MATERIAL PROPERTIES

The ignition and burning rate integral model used in this study requires a number of properties to be obtained for the material. A few of the properties can be easily measured, others can be obtained from experimental data and the remainder may be obtained from the literature.

The determination of fundamental material properties can be a complex process. For the pyrolysis of wood we require the thermal conductivity k, density ρ and specific heat capacity c and the related properties of thermal inertia $k\rho c$ and thermal diffusivity $k/\rho c$. These properties may change as the material undergoes thermal and/or mechanical changes.

In addition we may also need to obtain estimates of the heat of gasification of the pyrolysis gases L and heat flux of the flame $\dot{q}''_{fl}$ as the material burns. Anderson & Quintiere [37] suggest that an iterative procedure of choosing a heat of gasification and comparing the predictions of the model with experimental data be used. The guess is refined until there is good agreement. This approach is used in this study as the way in which to obtain reasonable values for the heat of gasification and flame heat flux.

2.1 Density

The density of wood is primarily dependent on the species but it will also vary by individual tree and within that individual tree. Any moisture in the wood will also affect

the density. In this study, the average bulk density of each sample was calculated from its

mass and volume such that

$$\rho_w = \frac{m_{w,0}}{A_0 \cdot \eta_{w,0}}$$

where A_0 is the surface area of the exposed face of the sample and $\eta_{w,0}$ is the initial height

of the sample. In this study, the mass and volume were recorded prior to testing in the

Cone Calorimeter and the density simply obtained from Equation 2. The calculated

density for each individual sample is shown in Figure 10.
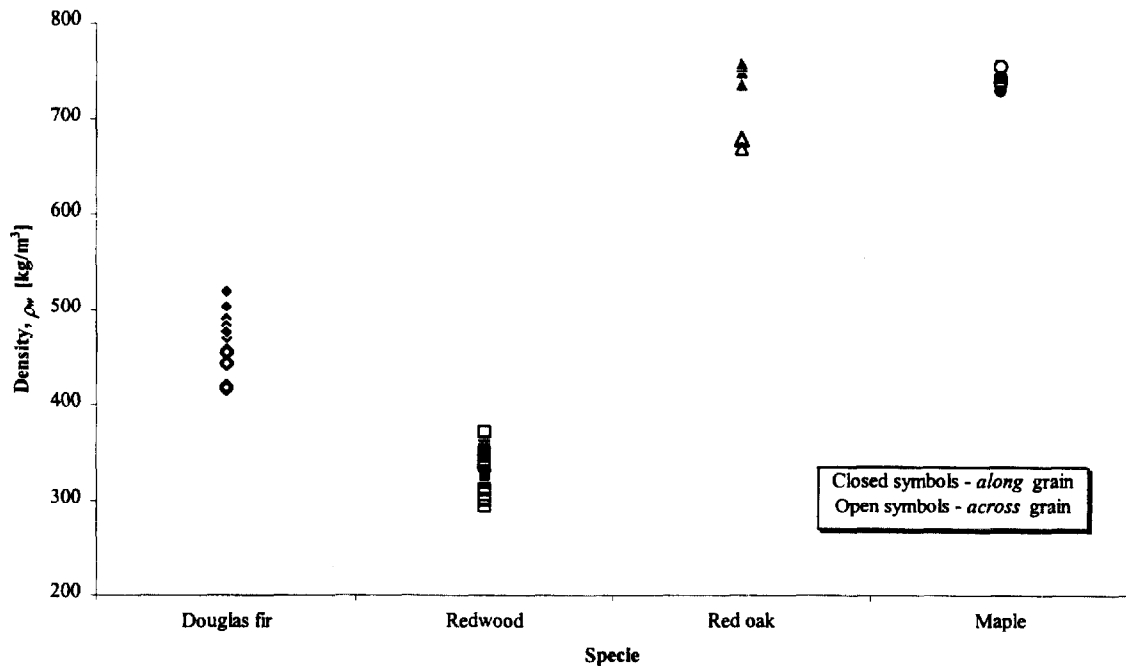
Figure 10. Sample density variation.

The sample densities for Douglas fir exhibit a spread with the *along* and *across* grain

samples clustered into two distinct groups. Similarly for the Red oak samples. The

Redwood samples also show a spread of values but no apparent clustering. The densities

of the Maple samples show less variation than found for the other three specie. Table 3 shows the average density of the wood species tested with a comparison of some values quoted in the literature.

Species	Grain orientation	Average density ρ_w [kg/m^3]	Values quoted in the literature [kg/m^3]
Redwood	along	354	430 [1], 312 [34]
	across	328	
Red oak	along	753	660 [34]
	across	678	
Douglas fir	along	502	465 [1], 500 [35], 450 [2], 512 [40]
	across	455	
Maple	along	741	
	across	742	

Table 3. Average density of virgin wood samples.

2.2 Specific gravity

The specific gravity s of wood is based on its weight when oven dry and volume at 6% moisture content [38]. The relationship between density and specific gravity, using values for the specific gravity quoted in the Wood Engineering Handbook [38] for the species tested in this study and the average densities given in Table 3, is shown in Figure 11.
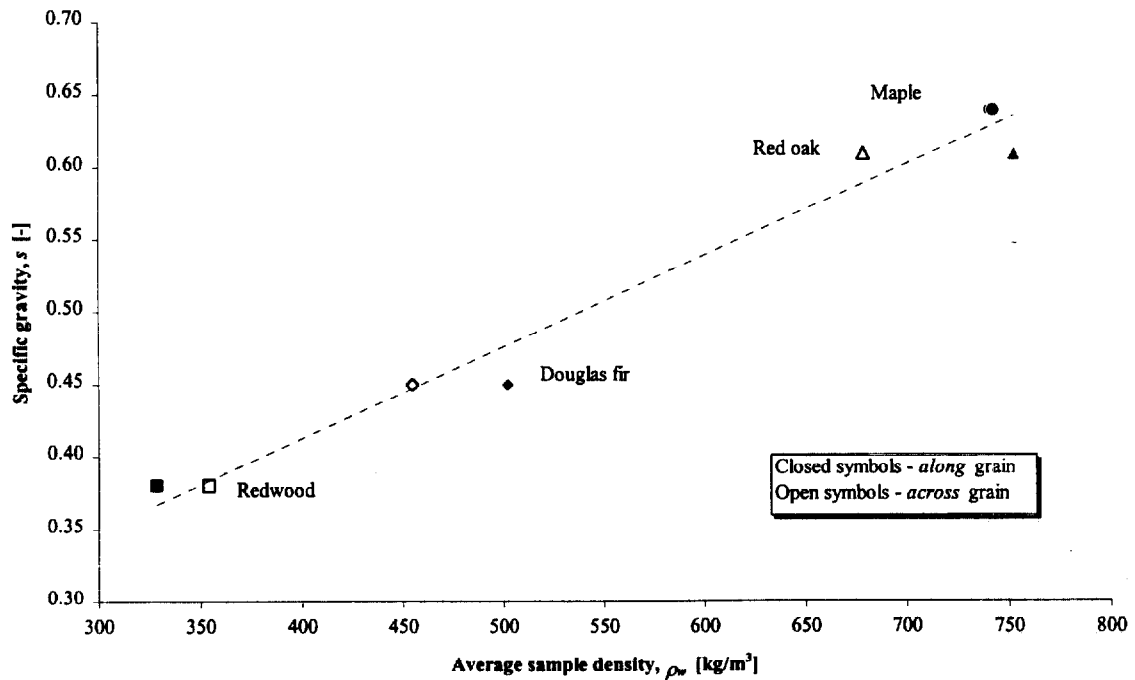
Figure 11. Relationship between density and specific gravity.

It is clear from Figure 11 that the measured average densities of the samples are consistent with the average specific gravity values.

2.3 Moisture content

The moisture content of wood may be assumed to be a pseudo-property of the material and, as described in § 2.4 and § 2.5, it can have an influence on the thermal conductivity and specific heat capacity and thus the ignition and burning rate characteristics of wood. The moisture content is a function of the species of wood and the conditions in which it is stored (§ 1.2.1). For example, Cholin [3] shows that the moisture content of wood is affected by the relative humidity of the atmosphere. The study by the Fire Officers Committee quoted by Cholin [3] demonstrates how the increase in the moisture content of wood increases the time to ignition for a given incident heat flux.

The measured moisture content of the samples tested is shown in Figure 12. The minimum sensitivity limit of the moisture meter (see § 1.4.1) for each species is also shown. Thus where the moisture meter indicated that the moisture content was below the minimum sensitivity it was no possible to determine the exact moisture content but only determine the maximum limit.
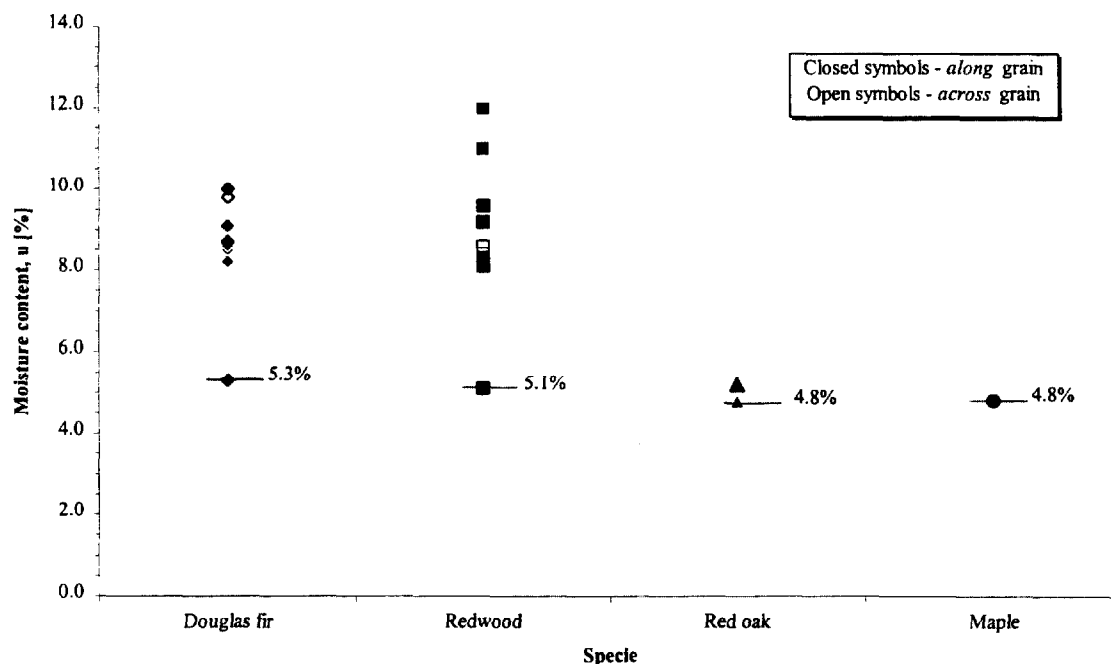
Figure 12. Measured moisture content of wood samples used in 'burning rate' tests.

For the Red oak and Maple samples, the moisture content was at or just above the sensitivity limit of the meter. The majority of the Douglas fir and Redwood samples had moisture contents above the sensitivity limit of the meter with the Redwood exhibiting the widest variation in moisture content.

2.4 Thermal conductivity

The study by Fredlund [39] showed how the thermal conductivity varies in wood with emittance, density, moisture content, temperature and the type of gas enclosed in the material. Thermal conductivity increases markedly with increasing moisture content, being about twice as high at 100 per cent moisture content as it is at 10 per cent.

The thermal conductivity also depends on the orientation of the grain of the wood. According to the Wood Engineering Handbook [38], the thermal conductivity of wood is approximately 2.0 to 2.8 greater along the grain than perpendicular to the grain. Fredlund [39] quotes a study that gives the range of ratios as between 1.75 and 2.25 (though he appears to use a weighting factor of $\frac{1}{0.58} = 1.72$ in his calculations). Desch & Dinwoodie [40] quote values for the thermal conductivity of Spruce and European oak for the various grain orientations (parallel or tangential/radial). The ratios of the values give 2.10 and 1.75 for Spruce and European oak respectively. From these literature data it is assumed that the increase in the thermal conductivity for the samples tested *across* the grain is typically 2.1 times greater than *along* the grain for any species of wood.

Janssens [41] provides equations that allow the thermal conductivity to be calculated. The equations include the effect of moisture, density, the thermal conductivity contributions due to the air and radiation effects. Figure 13 shows typically how the thermal conductivity for dry and wet wood varies with temperature and density using Janssens equations.

35
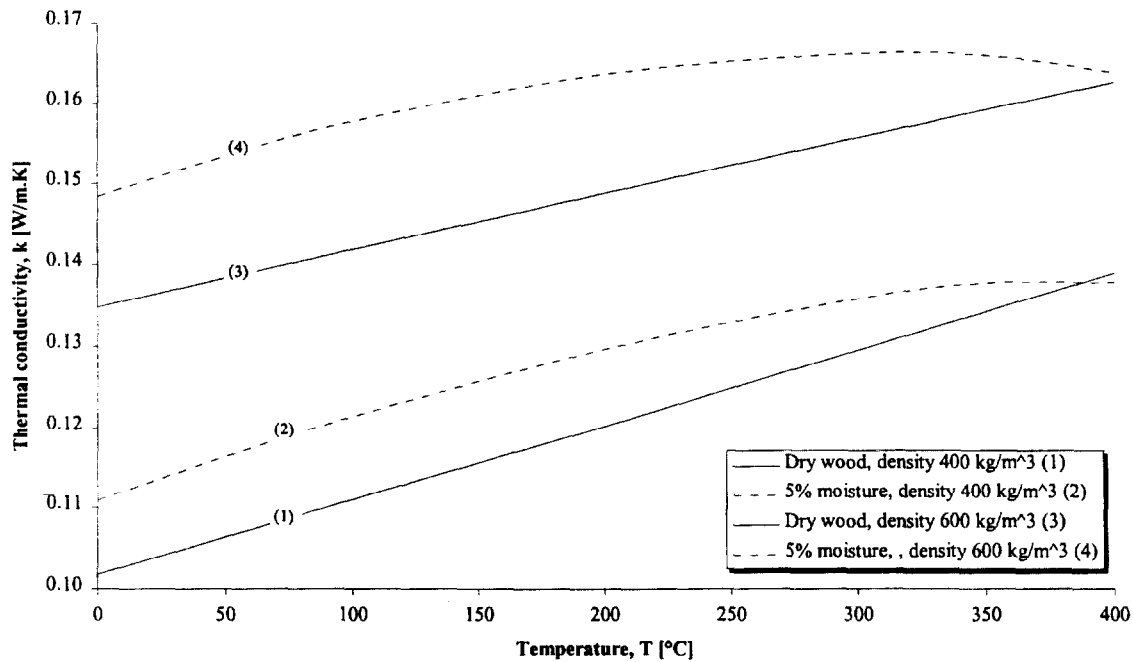
Figure 13. Variation of thermal conductivity with temperature for typical wood densities.

Many investigators have suggested that the thermal conductivity of dry wood varies as a linear relationship with temperature and Figure 13 shows this relationship. Figure 13 indicates that the inclusion of moisture results in a non-linear relationship although it is not clear over what range of temperatures Janssens equations are valid. Finally, using Janssens equations, the thermal conductivity for wood with a density of 500 kg/m^3 at 50 °C was calculated to be 0.13 W/m.K with 10% moisture and 0.36 W/m.K with 100% moisture. This result is comparable with the increases suggested by Fredlund [39].

2.5 Specific heat capacity

The specific heat capacity of wood depends on temperature but is practically independent of density or species. For oven-dry wood, Desch & Dinwoodie [40] give the specific heat

capacity as 1,360 J/kg.K. When wood contains water, the specific heat is greater than dry wood because of the larger specific heat of water. The apparent specific heat of moist wood is larger than the simple sum of the separate effects of wood and the water. This is due to the thermal energy absorbed by the wood-water bonds. The specific capacity of wood will also increase with increasing temperature.

2.6 Char fraction

As described in § 1.2.2, the burning of a charring material consists of a pyrolysis front moving through the unburned material leaving behind the char residue. Figure 14 shows a schematic of the form of a wood sample prior to testing and after exposure to the incident heat flux. Down to a certain depth below the exposed surface of the sample becomes char and the top surface of this char layer η_f is lower than the original sample height η_0. In practice, the top surface of the char layer and the interface between the char layer and the virgin wood below were not necessarily horizontal and the interface not necessarily as distinct as suggested in the schematic (see § 4.5.2). Thus the determination of the final height of the sample and the char depth were open to a certain degree of interpretation.

At the termination of a test in the Cone Calorimeter, the remainder of the sample was weighed and its dimensions recorded. An average final height and char layer depth were reported by Schroeder [10] and those values are used in this study to obtain the char fraction as follows:
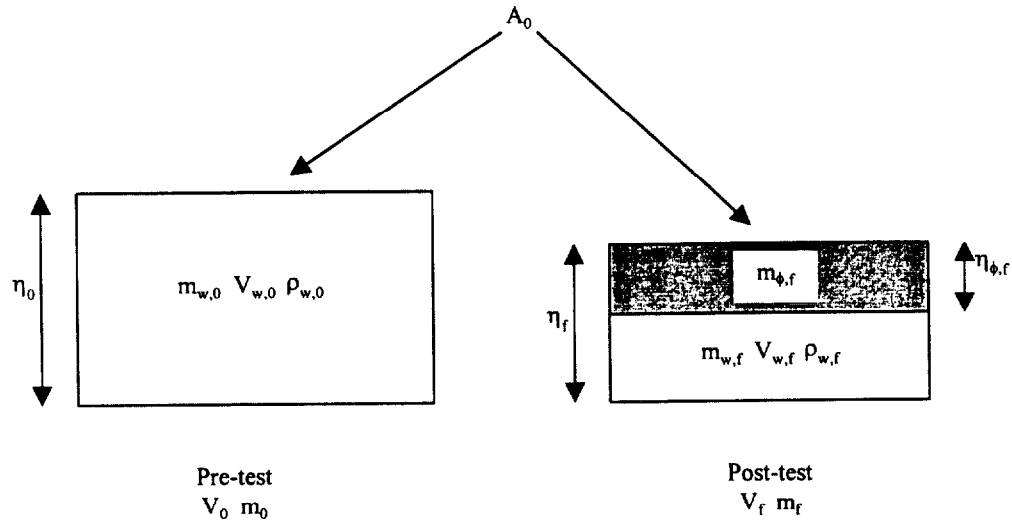
Figure 14. Pre-test and post-test char fraction determination.

Post-test, the mass of the whole sample is

$$m_f = m_{w,f} + m_{\phi,f}$$

thus the mass of the char is

$$m_{\phi,f} = m_f - m_{w,f}$$

Equation 3

The mass and volume of the post-test virgin wood can be found from

$$m_{w,f} = \rho_{w,f} . V_{w,f}$$

$$V_{w,f} = A_0(\eta_f - \eta_{\phi,f})$$

thus

$$m_{w,f} = \rho_{w,f} A_0(\eta_f - \eta_{\phi,f})$$

Substituting into Equation 3 gives

38

$$m_\phi = m_f - \rho_{w,f} A_0 (\eta_f - \eta_{\phi,f})$$

hence

$$V_{\phi,f} \, \rho_\phi = m_f - \rho_{w,f} A_0 (\eta_f - \eta_{\phi,f})$$

<div align="right">*Equation 4*</div>

The volume of the char portion is

$$V_{\phi,f} = A_0 \eta_{\phi,f}$$

thus the density of the char, from Equation 4

$$\rho_\phi = \frac{m_f - \rho_{w,f} A_0 (\eta_f - \eta_{\phi,f})}{A_0 \eta_{\phi,f}}$$

The char fraction is defined as

$$\phi' \equiv \frac{\rho_\phi}{\rho_w}$$

thus

$$\phi' = \frac{1}{\rho_w} \left(\frac{m_f - \rho_{w,f} A_0 (\eta_f - \eta_{\phi,f})}{A_0 \eta_{\phi,f}} \right)$$

<div align="right">*Equation 5*</div>

and it is assumed that $\rho_{w,f} = \rho_{w,0}$, i.e. the density of the post-test virgin wood is the same

is the initial density of the sample.

At temperatures exceeding 200 °C, the thermal degradation process results in a decrease

in the volume and the amount of shrinkage is different parallel or perpendicular to the

grain. Janssens [41] provides methods to obtain the shrinkage as a function of

temperature and wood type. Analysis of the post-test samples by Schroeder [10]

identified varying amounts of shrinkage compared to the original sample. The shrinkage

factor ω was used to obtain a modified char fraction such that

$$\phi = \omega \phi'$$

Tran & White [34] suggest a similar relationship between the char contraction factor and

the char yield in their analysis. Thus the char fraction can be obtained from

$$\phi = \frac{\omega}{\rho_w} \left(\frac{m_f - \rho_w A(\eta_f - \eta_{\phi,f})}{A\eta_{\phi,f}} \right)$$

The char fractions obtained from the test samples are detailed in § 4.5.
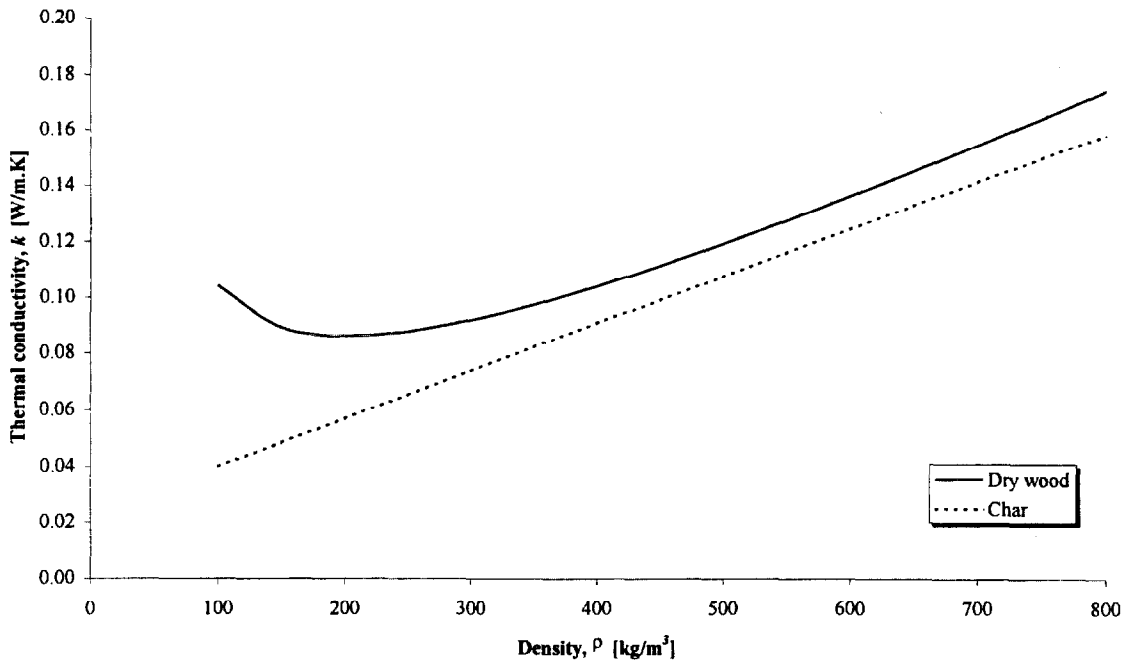
Figure 15. Thermal conductivity of dry wood and char with density.

Figure 15 shows the variation in the thermal conductivity of a typical dry wood at given

densities as given by Janssens [41] (§ 2.4) and the variation in the thermal conductivity of

40

char [41]. Figure 15 shows that the change in thermal conductivities is almost equivalent over a wide range of densities. As discussed in § 2.1, the average density of the samples tested in this study ranged from around 330 kg/m³ up to around 750 kg/m³. Thus, it can be assumed that the ratio of the thermal conductivity of the virgin wood with the thermal conductivity of the char can be approximated to the ratio of the virgin wood density to the char density such that

$$\frac{k_\phi}{k_w} \approx \frac{\rho_\phi}{\rho_w}$$

Equation 8

Figure 16 confirms that Equation 8 holds for a range of virgin wood densities with the approximation better at the higher virgin wood density of 800 kg/m³ compared to 300 kg/m³.
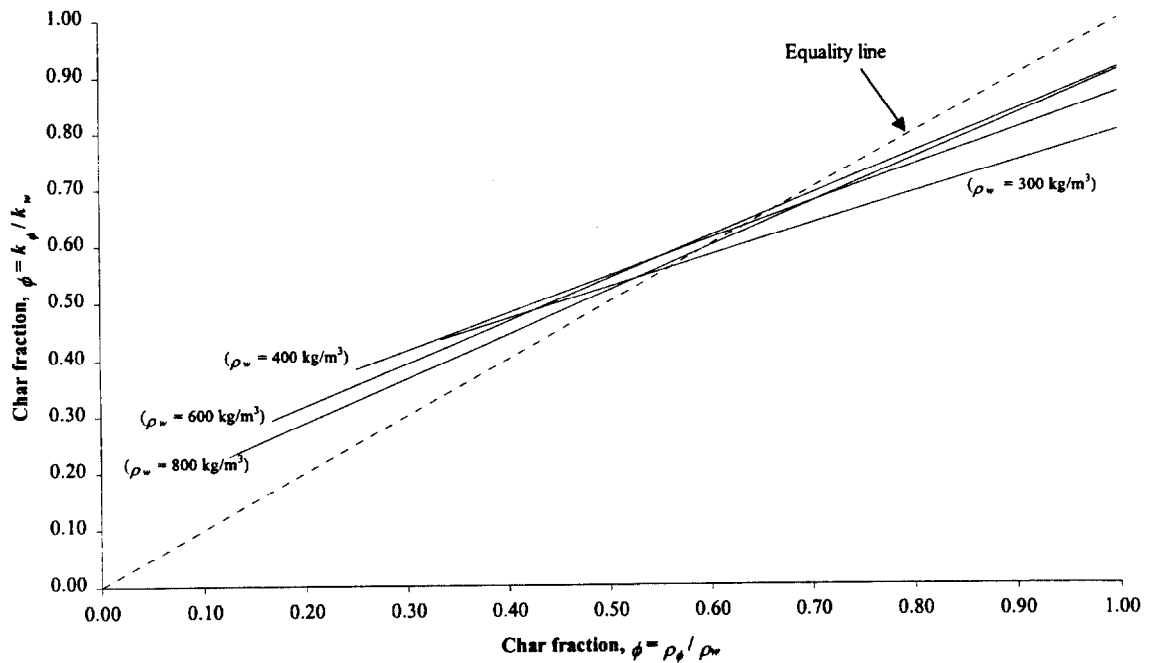
Figure 16. Thermal conductivity and density ratio approximation.

2.7 Thermal inertia and thermal diffusivity

The thermal inertia I is defined as the product of the thermal conductivity, density and specific heat capacity such that

$$I = k\rho c$$

and the thermal diffusivity α is defined as

$$\alpha = \frac{k}{\rho c}$$

The integral model described in this study requires values for the thermal conductivity k and the specific heat capacity c at elevated temperatures. It is clear from § 2.4 and § 2.5 that, since the thermal inertia and the specific heat capacity are temperature dependent, the thermal inertia at ignition is not that what would be obtained at ambient conditions. Instead the thermal inertia at ignition is an 'apparent' value and it will be shown in § 3.2.4 that this apparent thermal inertia can be obtained from ignition data.

In the study by Parker [35] it was shown that the thermal diffusivity of Douglas fir remained at an almost constant value of 2.1×10^{-7} m^2/s up to temperatures of around 250 °C. Similarly, Suuberg et al. [22] found that the thermal diffusivity of raw cellulose remained constant at 0.86×10^{-7} m^2/s ±22% between 116 °C and 289 °C. Janssens [41] also quotes work in which it is suggested that the thermal diffusivity is independent of temperature. Thus, in this study it is assumed that the thermal diffusivity is constant for each given species of wood.

The values of the thermal diffusivities perpendicular to the grain used in this study are given in Table 4. The value for Douglas fir is taken from Parker [35] and the value for Redwood taken from Dietenberger [36].

Species	Thermal diffusivity α [m^2/s]
Redwood	1.65E-07
Red oak	1.88E-07
Douglas fir	2.10E-07
Maple	1.88E-07

Table 4. Thermal diffusivity values.

Values for Maple and Red oak were not found in the literature and so these had to be estimated by simply taking the average of the two known values quoted. Taking an average value was justified by the fact that according to the Wood Engineering Handbook [38] the typical value for the thermal diffusivity of wood is 1.61×10^{-7} m^2/s and this value varies with specific gravity s over the range of 0.35 to 0.60 by 6.45×10^{-8} m^2/s. Assuming that the typical quoted value in the Wood Engineering Handbook for the thermal diffusivity is at the mid-range of the specific gravity (i.e. for a specific gravity of 0.48), the variation of thermal diffusivity with specific gravity can be compared with the values quoted by Parker and Dietenberger assuming similar moisture contents for each species (Figure 17).
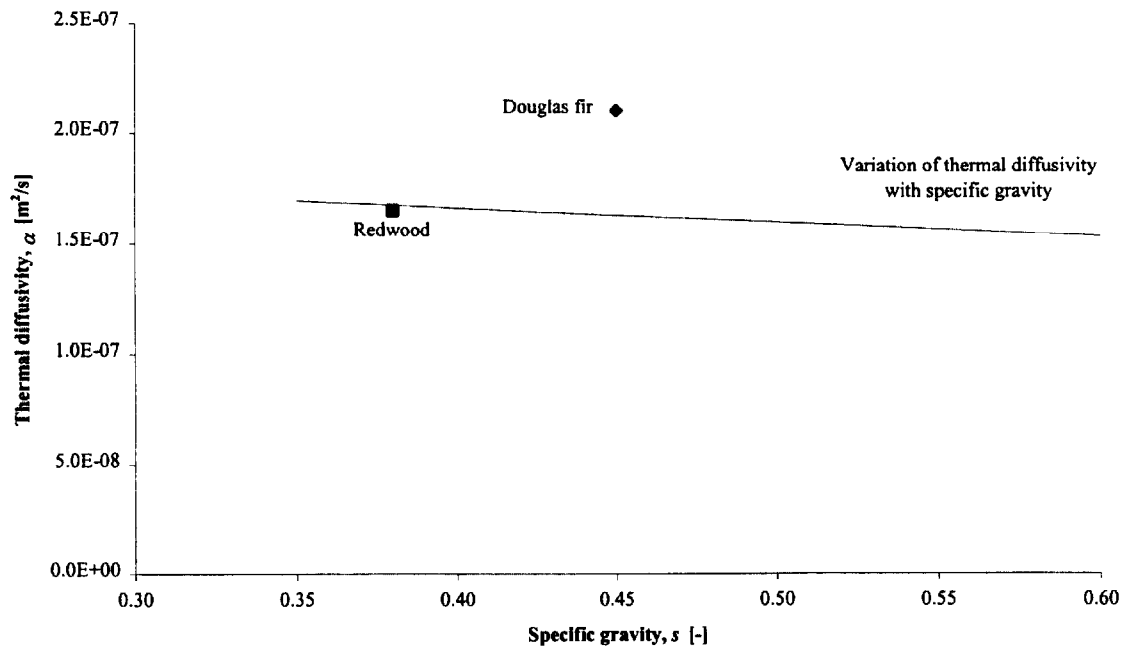
Figure 17. Variation of thermal diffusivity with specific gravity.

It is clear that the data quoted by Parker and Dientenberger closely match the relationship

given in the Wood Engineering Handbook. Furthermore, there is almost negligible

change in the thermal diffusivity over the specified range of specific gravities. Thus,

given the relationship between the density and specific gravity discussed in § 2.2 (Figure

11), using an average value for the thermal diffusivity for the Maple and Red oak appears

reasonable.

It is interesting to note that the thermal diffusivity of 6.6×10^{-7} m^2/s used for White pine

by Moghtaderi *et al.* [31] was considerably greater than the values quoted above.

Using Equation 9 and Equation 10, apparent values for the thermal conductivity and the

specific heat capacity can be obtained. However, as discussed in § 2.4, the thermal

44

conductivity of wood increases by a factor of around 2.1 along the grain compared to perpendicular to the grain. Hence a factor f of 2.1 is introduced for the *across* grain orientation thermal diffusivity. Thus, from Equation 9

$$\rho c = \frac{I}{k}$$

<div align="right">*Equation 11*</div>

substituting into Equation 10 and including f where $f = 1$ for the *along* grain samples and $f = 2.1$ for the *across* grain orientation,

$$f\alpha = \frac{k}{I/k}$$

<div align="right">*Equation 12*</div>

rearranging to solve for k we get

$$\alpha = \frac{k^2}{fI}$$

<div align="right">*Equation 13*</div>

$$k = \sqrt{f\alpha I}$$

<div align="right">*Equation 14*</div>

and we can find c from

$$c = \frac{I}{k\rho}$$

<div align="right">*Equation 15*</div>

2.8 Emissivity

In this study the emissivity of the surface of the wood is assumed to be unity. Janssens [1] quotes several sources regarding the emissivity and absorptivity of wood that suggest the absorptivity of virgin wood is on average 0.76, independent of species. After thermal

exposure begins, this value changes due to the darkening of the surface as it chars. The

emissivity of oven dry wood varies between 0.60 and 0.72 depending on species. Finally,

the assumption that Kirchoff's law ($\alpha = \varepsilon$) holds is reasonable for most analyses. Thus we

might expect the emissivity to be around 0.72 prior to exposure and this value to

approach 1 as the surface chars due to the external heat flux.

3. IGNITION MODELLING AND EXPERIMENTS

3.1 Theory

3.1.1 The integral model

The integral analysis for ignition was developed by Quintiere [27] assuming radiative

ignition of the surface of the material due to an incident radiative heat flux.
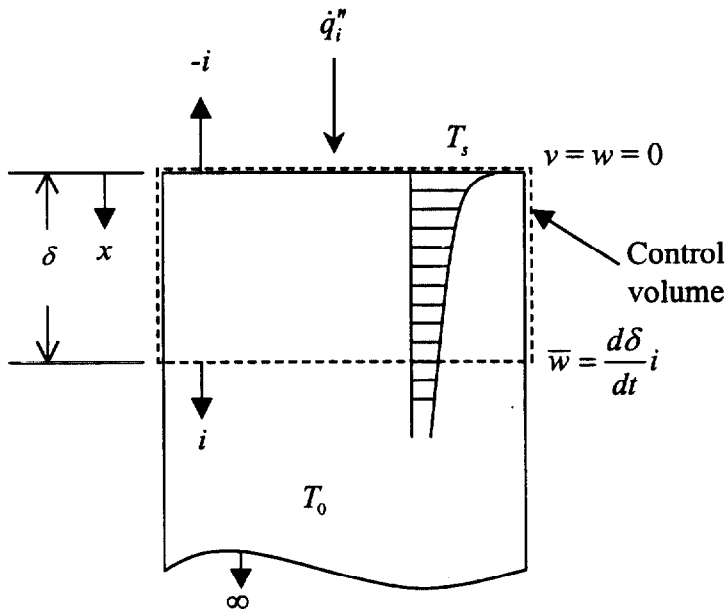
Figure 18. Integral model ignition scenario.

The following assumptions are made for the ignition model:

(a)   Ignition occurs when the surface temperature achieves a critical value, T_{ig}

(b)   Solid is inert up to ignition and

(c)   Solid is infinitely thick

The thermal heating of the solid is depicted by a thermal penetration layer of depth $\delta(t)$ as shown in Figure 18. By considering the incident heat flux and the losses due to radiation and convection, the net heat flux at a given time t is given by

$$\dot{q}''(t) = \alpha \dot{q}''_i - \varepsilon \sigma (T_s^4 - T_0^4) - h_c(T_s - T_0)$$

where the emissivity ε and the absorptivity α are assumed to be 1 as discussed in § 2.8, thus $\dot{q}''_i(t)$ becomes

$$\dot{q}''(t) = \dot{q}''_i - \sigma (T_s^4 - T_0^4) - h_c(T_s - T_0)$$

Equation 16

The control volume form of conservation of energy

$$\frac{d}{dt} \iiint_{CV} \rho u dV + \iint_{CS} \rho h (\overline{v} - \overline{w}).\overline{n} dS = \dot{Q}_{added} + \dot{W}_{shaft} - \iint p \overline{w}.\overline{n} dS$$

Equation 17

gives

$$\rho c \frac{d}{dt} \int_0^\delta T(x)dx + \rho c T_0 \left(-\frac{d\delta}{dt} \right) = \dot{q}''(t)$$

$$\rho c \left[\frac{d}{dt} \int_0^\delta T(x)dx - T_0 \frac{d\delta}{dt} \right] = \dot{q}''(t)$$

Equation 18

Where c is the specific capacity of the wood at ignition i.e. $c \equiv c_{w,ig}$ and ρ is the density of

wood at ignition i.e. $\rho \equiv \rho_{w,ig} \equiv \rho_w$ since we assume the density remains constant.

Consider

$$\frac{d}{dt} \int_0^\delta (T - T_0) dx$$

$$= \frac{d}{dt} \int_0^\delta T \, dx - \frac{d}{dt} \int_0^\delta T_0 \, dx$$

$$= \frac{d}{dt} \int_0^\delta T \, dx - T_0 \frac{d}{dt} [x]_0^\delta$$

$$= \frac{d}{dt} \int_0^\delta T \, dx - T_0 \frac{d\delta}{dt}$$

Thus, from Equation 18 and Equation 19

$$\rho c \frac{d}{dt} \int_0^\delta (T - T_0) dx = \dot{q}''(t)$$

We need to select a temperature profile through the region δ such that the boundary

conditions are

(i)   when $x = 0$, $\dot{q}''(t) = -k \frac{\partial T}{\partial x}$

(ii)   when $x = \delta$, $T = T_0$

(iii)   when $x = \delta$, $k \frac{\partial T}{\partial x} = 0$ *i.e.* no heat loss

where k is the thermal conductivity of the wood at ignition i.e. $k \equiv k_{w,ig}$. Consider a

profile such that

$$T - T_0 = \frac{\dot{q}''(t)\delta}{2k}\left(1 - \frac{x}{\delta}\right)^2$$

Equation 21

when $x = \delta$

$$T - T_0 = \underbrace{\frac{\dot{q}''(t)\delta}{2k}\left(1 - \frac{\delta}{\delta}\right)^2}_{0}$$

$$T = T_0$$

which satisfies boundary condition (ii); by expansion of Equation 21

$$T - T_0 = \frac{\dot{q}''(t)\delta}{2k}\left(1 - \frac{2x}{\delta} + \frac{x^2}{\delta^2}\right)$$

and differentiating both sides with respect to x

$$\frac{\partial}{\partial x}\left(T - T_0\right) = \frac{\dot{q}''(t)\delta}{2k}\frac{\partial}{\partial x}\left(1 - \frac{2x}{\delta} + \frac{x^2}{\delta^2}\right)$$

$$\frac{\partial T}{\partial x} - \underbrace{\frac{\partial T_0}{\partial x}}_{0} = \frac{\dot{q}''(t)\delta}{2k}\left(-\frac{2}{\delta} + \frac{2x}{\delta^2}\right)$$

$$\frac{\partial T}{\partial x} = -\frac{\dot{q}''(t)}{k} + \frac{\dot{q}''(t)x}{k\delta}$$

when $x = 0$

$$\frac{\partial T}{\partial x} = -\frac{\dot{q}''(t)}{k}$$

$$-k\frac{\partial T}{\partial x} = \dot{q}''(t)$$

which satisfies boundary condition (i); when $x = \delta$ then

$$\frac{\partial T}{\partial x} = -\frac{\dot{q}''(t)}{k} + \frac{\dot{q}''(t)\delta}{k\delta}$$

$$\frac{\partial T}{\partial x} = 0$$

which satisfies boundary condition (iii). Substituting Equation 21 into Equation 20 gives

$$\rho c \frac{d}{dt} \int_0^\delta \frac{\dot{q}''(t)\delta}{2k} \left(1 - \frac{x}{\delta^2}\right)^2 dx = \dot{q}''(t)$$

$$\rho c \frac{d}{dt} \int_0^\delta \frac{\dot{q}''(t)}{2k} \delta \left(1 - \frac{2x}{\delta} + \frac{x^2}{\delta^2}\right) dx = \dot{q}''(t)$$

$$\rho c \frac{d}{dt} \frac{\dot{q}''(t)}{2k} \left[\delta x - x^2 + \frac{x^3}{3\delta}\right]_0^\delta = \dot{q}''(t)$$

$$\rho c \frac{d}{dt} \frac{\dot{q}''(t)}{2k} \left[\underbrace{\delta.\delta - \delta^2}_{0} + \frac{\delta^3}{3\delta}\right] = \dot{q}''(t)$$

$$\rho c \frac{d}{dt} \frac{\dot{q}''(t)\delta^2}{6k} = \dot{q}''(t)$$

$$\frac{d}{dt} \dot{q}''(t)\delta^2 = 6\frac{k}{\rho c}\dot{q}''(t)$$

Integrating

$$\dot{q}''\delta^2 = 6\frac{k}{\rho c} \int_0^t \dot{q}''(t)\,dt$$

51
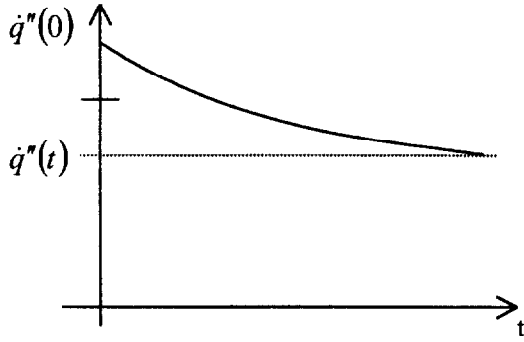
Figure 19. Assumed heat flux profile.

From Figure 19, we assume that the incident heat flux is the average of the heat flux at

time = 0, i.e. $\dot{q}''(0)$ and at time = t, i.e. $\dot{q}''(t)$

$$\int_0^t \dot{q}''(t)\,dt = \left[\frac{\dot{q}''(t)+\dot{q}''(0)}{2}\right]t$$

thus

$$\dot{q}''(t)\delta^2 = 6\frac{k}{\rho c}\left[\frac{\dot{q}''(t)+\dot{q}''(0)}{2}\right]t$$

Equation 22

From Equation 16, at time $t = 0$, the surface temperature is at ambient i.e. $T_s = T_0$ thus

$$\dot{q}''(0) = \dot{q}_i''$$

Equation 23

and at time $t = t_{ig}$, we assume that the surface temperature is at the ignition temperature,

$T_s = T_{ig}$ thus

52

$$\dot{q}''(t_{ig}) = \dot{q}_i'' - \sigma(T_{ig}^4 - T_0^4) - h_c(T_{ig} - T_0)$$

From Equation 16, multiplying through by -1

$$-\dot{q}''(t) = -\dot{q}_i'' + \sigma(T_s^4 - T_0^4) + h_c(T_s - T_0)$$

and then dividing through by $-\dot{q}_i''$

$$\frac{\dot{q}''(t)}{\dot{q}_i''} = 1 - \frac{\sigma(T_s^4 - T_0^4) + h_c(T_s - T_0)}{\dot{q}_i''}$$

Let

$$\beta \equiv \frac{\sigma(T_s^4 - T_0^4) + h_c(T_s - T_0)}{\dot{q}_i''}$$

$$\frac{\dot{q}''(t)}{\dot{q}_i''} = 1 - \beta$$

$$\dot{q}''(t) = \dot{q}_i''(1 - \beta)$$

The parameter β characterises the magnitude of radiation and convective losses relative to the incident heat flux. Substituting Equation 23 and Equation 26 into Equation 22 we obtain

$$\dot{q}_i''(1 - \beta)\delta^2 = 6\frac{k}{\rho c}\left[\frac{\dot{q}_i''(1 - \beta) + \dot{q}_i''}{2}\right]t$$

$$\delta^2 = 3\frac{k}{\rho c}\left[\frac{2\dot{q}_i'' - \dot{q}_i''\beta}{\dot{q}_i''(1 - \beta)}\right]t$$

$$\therefore \quad \delta^2 = 3\frac{k}{\rho c}\left[\frac{2-\beta}{1-\beta}\right]t$$

If we consider the surface at the time of ignition and assume that the surface temperature

is at the ignition temperature $t = t_{ig}$, $T_s = T_{ig}$, $x = 0$, then from Equation 21

$$T_{ig} - T_0 = \frac{\dot{q}''(t_{ig})\delta}{2k}\underbrace{\left(1-\frac{x}{\delta}\right)^2}_{0}$$

$$\therefore \quad \left(T_{ig} - T_0\right)^2 = \frac{[\dot{q}''(t_{ig})]^2\delta^2}{4k^2}$$

Substituting Equation 27

$$\frac{\left(T_{ig} - T_0\right)^2}{[\dot{q}''(t_{ig})]^2} = \frac{3}{4k^2}\frac{k}{\rho c}\left[\frac{2-\beta_{ig}}{1-\beta_{ig}}\right]t_{ig}$$

$$\boxed{t_{ig} = \frac{4}{3}k\rho c\left[\frac{1-\beta_{ig}}{2-\beta_{ig}}\right]\frac{\left(T_{ig}-T_0\right)^2}{[\dot{q}''(t_{ig})]^2}}$$

where from Equation 26

$$\dot{q}''(t_{ig}) = \dot{q}_i''(1-\beta_{ig})$$

and from Equation 25

$$\beta_{ig} \equiv \frac{\sigma(T_{ig}^4 - T_0^4) + h_c(T_{ig} - T_0)}{\dot{q}_i''}$$

When $\dot{q}_i''$ is large, from Equation 25, $\beta_{ig} \to 0$, thus from Equation 28

$$t_{ig} \approx \frac{4}{3}k\rho c \left[\frac{1-0}{2-0}\right] \frac{(T_{ig}-T_0)^2}{[\dot{q}_i''(1-0)]^2}$$

$$t_{ig} \approx \frac{2}{3}k\rho c \frac{(T_{ig}-T_0)^2}{(\dot{q}_i'')^2}$$

The 2/3 coefficient has been found to be $\pi/4$ in the more exact (pure convective loss) solution of this problem (see § 3.1.2). Substituting Equation 29 into Equation 28 we obtain

$$t_{ig} = \frac{4}{3}k\rho c \left[\frac{1-\beta_{ig}}{2-\beta_{ig}}\right] \frac{(T_{ig}-T_0)^2}{\dot{q}_i''^2 (1-\beta_{ig})^2}$$

$$t_{ig} = \frac{4}{3}k\rho c \left[\frac{1}{(2-\beta_{ig})(1-\beta_{ig})}\right] \frac{(T_{ig}-T_0)^2}{\dot{q}_i''^2}$$

Or alternatively

$$t_{ig} = C_{ig}k\rho c \frac{(T_{ig}-T_0)^2}{\dot{q}_i''^2}$$

where

$$C_{ig} = \frac{4}{3}\left[\frac{1}{(2-\beta_{ig})(1-\beta_{ig})}\right]$$

As $\beta_{ig} \rightarrow 1$, Equation 34 approaches ∞ and thus from Equation 33, $t_{ig} \rightarrow \infty$ also. As the time to ignition increases we are approaching the critical heat flux for ignition. From Equation 30 with $\beta_{ig} \rightarrow 1$

$$1 \approx \frac{\sigma(T_{ig}^4 - T_0^4) + h_c(T_{ig} - T_0)}{\dot{q}_i''}$$

or alternatively, with $\dot{q}_{cr}'' \equiv \dot{q}_i''$ as $t \to \infty$

$$\boxed{\dot{q}_{cr}'' = \sigma(T_{ig}^4 - T_0^4) + h_c(T_{ig} - T_0)}$$

Equation 35

Thus from Equation 30

$$\beta_{ig} \equiv \frac{\dot{q}_{cr}''}{\dot{q}_i''}$$

Equation 36

3.1.2   Comparison of approximate solutions for ignition

a) Quintiere [42] compared the approximate solution for ignition from the integral model with the exact solution for convective heat loss only and the approximate solutions by Delichatsios *et al.* [43]. For the exact solution for convective heat loss only, Drysdale [2] states that

$$\frac{T - T_0}{T_\infty - T_0} = 1 - \exp\left(\frac{\alpha t}{(k/h_c)^2}\right).\mathrm{erfc}\left(\frac{\sqrt{\alpha t}}{k/h_c}\right)$$

Given, from Equation 16, for convection only

$$\dot{q}_i'' = h_c(T_\infty - T_0)$$

56

thus

$$\frac{T_{ig} - T_0}{\left(\dot{q}_i'' \middle/ h_c\right)} = 1 - e^{\gamma^2} \operatorname{erfc}(\gamma)$$

where

$$\gamma \equiv h_c \sqrt{\frac{t_{ig}}{k\rho c}}$$

From Carslaw & Jaeger [44], when $\gamma \to \infty$

$$\frac{\sqrt{\pi}}{2} \operatorname{erfc}(\gamma) \approx \frac{e^{-\gamma^2}}{2\gamma}$$

or rearranging Equation 39

$$\operatorname{erfc}(\gamma) \approx \frac{e^{-\gamma^2}}{\sqrt{\pi}\gamma}$$

Then, from Equation 37 and Equation 40

$$\lim_{\gamma \to \infty}\left(1 - e^{\gamma^2} \operatorname{erfc}(\gamma)\right) = 1 - e^{\gamma^2} \cdot \frac{e^{-\gamma^2}}{\sqrt{\pi}\gamma}$$

$$= 1 - \frac{1}{\sqrt{\pi}\gamma} \to 1$$

From Equation 35, neglecting radiation heat losses, as $t_{ig} \to \infty$

$$\dot{q}_i'' = h_c(T_{ig} - T_0) \equiv \dot{q}_{cr}''$$

When $t_{ig} \to 0$ or $\gamma \to 0$, from Carslaw & Jaeger [44],

$$\text{erf}(\gamma) \approx \frac{2}{\sqrt{\pi}}\gamma$$

and

$$\text{erfc}(\gamma) = 1 - \text{erf}(\gamma)$$

By expansion of the right-hand side of Equation 37

$$1 - e^{\gamma^2}\,\text{erfc}(\gamma) \approx 1 - \left(1 + \gamma^2 + ...\right)\left(1 - \frac{2}{\sqrt{\pi}}\gamma + ...\right)$$

$$\approx 1 - 1 + \frac{2}{\sqrt{\pi}}\gamma$$

$$= \frac{2}{\sqrt{\pi}}\gamma$$

Thus substituting Equation 44 and Equation 38 into Equation 37

$$\frac{T_{ig} - T_0}{\left(\dot{q}_i'' / h_c\right)} = \frac{2}{\sqrt{\pi}} h_c \sqrt{\frac{t_{ig}}{k\rho c}}$$

therefore, the time to ignition is

$$t_{ig} = \frac{\pi}{4} k\rho c \left(\frac{T_{ig} - T_0}{\dot{q}_i''} \right)^2$$

To make the approximate integral solution given in Equation 32 fit the limit of the exact

(pure convective loss) solution, let

$$\frac{Z}{(2 - \beta_{ig})(1 - \beta_{ig})} = \frac{\pi}{4}$$

where Z is a new constant in place of the 4/3 given in Equation 32. At high incident heat

fluxes, $t_{ig} \rightarrow 0$ and $\beta_{ig} \rightarrow 0$, thus

$$\frac{Z}{2} = \frac{\pi}{4} \qquad \text{or} \qquad Z = \frac{\pi}{2}$$

therefore, substituting for Z the 4/3 in Equation 32 we obtain

$$t_{ig} = \frac{\pi}{2} k\rho c \left[\frac{1}{(2 - \beta_{ig})(1 - \beta_{ig})} \right] \frac{(T_{ig} - T_0)^2}{\dot{q}_i''^2}$$

or

$$\frac{1}{\sqrt{t_{ig}}} = \frac{1}{\sqrt{\pi k\rho c}} \sqrt{2(2 - \beta_{ig})(1 - \beta_{ig})} \frac{\dot{q}_i''}{(T_{ig} - T_0)}$$

b) In the study by Delichatsios, Panagiotou & Kiley [43], the authors suggest that when

the incident heat flux is greater than about three times the critical heat flux (i.e. $\dot{q}_i'' > 3\dot{q}_{cr}''$)

then

$$\frac{1}{\sqrt{t_{ig}}} = \frac{2}{\sqrt{\pi k \rho c}} \frac{1}{(T_p - T_0)} [\dot{q}_i'' - 0.64 \dot{q}_{cr}'']$$

Equation 49

and when the incident heat flux is less than 1.1 times the critical heat flux (i.e.

$\dot{q}_i'' < 1.1 \dot{q}_{cr}''$) then

$$\frac{1}{\sqrt{t_{ig}}} = \frac{\pi}{\sqrt{\pi k \rho c}} \frac{\dot{q}_i'' - \dot{q}_{cr}''}{(T_p - T_0)}$$

Equation 50

where T_p is the pyrolysis temperature and the critical heat flux ignores convective heat

fluxes which are considered by Delichatsios *et al.* to be negligible, that is

$$\dot{q}_{cr}'' = \sigma(T_{ig}^4 - T_0^4)$$

Equation 51

Defining the following dimensionless heat flux (from Equation 30) and time variables as

$$\frac{1}{\beta_{ig}} \equiv \frac{\dot{q}_i''}{\dot{q}_{cr}''} \qquad \text{and} \qquad \tau_{ig} \equiv \frac{\dot{q}_{cr}''^2 t_{ig}}{(T_{ig} - T_0)^2 k \rho c} \qquad \text{respectively, we can write Equation 48 as}$$

$$\tau_{ig} = \frac{\pi}{2(2 - \beta_{ig})(1 - \beta_{ig})} \beta_{ig}^2$$

Equation 52

60

or by rearranging

$$\frac{1}{\sqrt{\tau_{ig}}} = \left[\frac{2(2-\beta_{ig})(1-\beta_{ig})}{\pi}\right]^{1/2} \frac{1}{\beta_{ig}}$$

<div align="right">Equation 53</div>

plus the Delichatsios high and low heat flux equations (Equation 49 and Equation 50) as

$$\frac{1}{\sqrt{\tau_{ig}}} = \frac{2}{\sqrt{\pi}}\left(\frac{1}{\beta_{ig}} - 0.64\right), \qquad \frac{1}{\beta_{ig}} > 3$$

<div align="right">Equation 54</div>

$$\frac{1}{\sqrt{\tau_{ig}}} = \sqrt{\pi}\left(\frac{1}{\beta_{ig}} - 1\right), \qquad \frac{1}{\beta_{ig}} < 1.1$$

<div align="right">Equation 55</div>

Figure 20 shows a comparison between the integral model and the Delichatsios high and

low heat flux equations. The solutions to the two models run parallel at high heat fluxes

and both models terminate at the same point at the intercept to the x-axis. The

Delichatsios solutions are given for specified limits $\frac{1}{\beta_{ig}}$ (Equation 54 and Equation 55).

By extending the two solutions for the region between the specified limits such that they

overlap we find that they cross at around $\frac{1}{\beta_{ig}} = 1.6$.
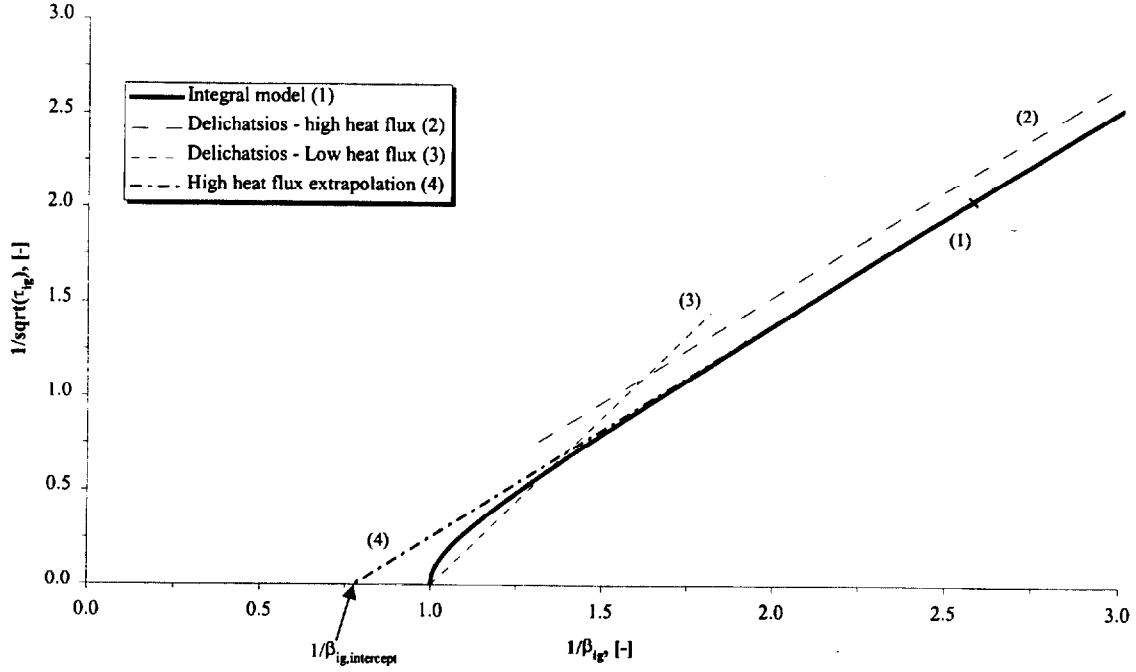
Figure 20. Comparison of the integral model and the Delichatsios *et al.* equations.

Figure 20 also includes the extrapolation of the high heat flux portion of the integral

model which shows that there is an error in using such an extrapolation compared with

the integral model solution for the determination of the intercept along the x-axis. Let

$\dfrac{1}{\beta_{ig,intercept}}$ be the intercept of the linear extrapolation of a graph of $\dfrac{1}{\sqrt{\tau_{ig}}}$ plotted against

$\dfrac{1}{\beta_{ig}}$. From the integral solution given in Equation 53, choosing values of $\dfrac{1}{\beta_{ig}}$ for two

typical high heat flux cases we get

$$\text{when } \frac{1}{\beta_{ig}} = 5, \qquad \frac{1}{\sqrt{\tau_{ig}}} = 4.787$$

when $\dfrac{1}{\beta_{ig}} = 2.5,$ $\qquad \dfrac{1}{\sqrt{\tau_{ig}}} = 1.954$

At high heat fluxes, $\beta_{ig} \rightarrow 0$ and therefore we can reduce Equation 53 to

$$\frac{1}{\sqrt{\tau_{ig}}} = \frac{2}{\sqrt{\pi}} \cdot \frac{1}{\beta_{ig}}$$

<div align="right">*Equation 56*</div>

By assuming that the difference between the exact solution and the extrapolated solution

is $\left(\dfrac{1}{\beta_{ig}} - \dfrac{1}{\beta_{ig,intercept}} \right)$, we can write Equation 53 as

$$\frac{1}{\sqrt{\tau_{ig}}} = \frac{2}{\sqrt{\pi}} \cdot \left(\frac{1}{\beta_{ig}} - \frac{1}{\beta_{ig,intercept}} \right)$$

<div align="right">*Equation 57*</div>

Substituting in for our approximate values we obtain

$$4.787 = \frac{2}{\sqrt{\pi}} \left(5.0 - \frac{1}{\beta_{ig,intercept}} \right) \qquad \rightarrow \qquad \frac{1}{\beta_{ig,intercept}} = 0.758$$

$$1.954 = \frac{2}{\sqrt{\pi}} \left(2.5 - \frac{1}{\beta_{ig,intercept}} \right) \qquad \rightarrow \qquad \frac{1}{\beta_{ig,intercept}} = 0.768$$

Hence the extrapolated intercept is $\dfrac{\dot{q}_i''}{\dot{q}_{cr}''} \approx 0.76$, thus the critical heat flux is found from

$$\boxed{\dot{q}_{cr}'' = \frac{\dot{q}_i''}{0.76}}$$

<div align="right">*Equation 58*</div>

In comparison, from Equation 53 (which is equivalent to Equation 57), Delichatsios *et al.*

obtain a correction factor of 0.64 for the determination of the critical heat flux using high

incident flux data.

3.1.3   Analysis of the C_{ig} parameter

A qualitative comparison of the C_{ig} parameter between the integral model and other

solutions can be conducted. Equating the Delichatsios *et al.* [43] low heat flux equation

(Equation 50) with the integral theory presented in this study (Equation 28) and assuming

the pyrolysis temperature used by Delichatsios *et al.* is equivalent to the ignition

temperature $T_p = T_{ig}$ we obtain

$$\frac{\pi}{\sqrt{\pi k \rho c}} = \frac{1}{\sqrt{\frac{4}{3} k \rho c \left[\frac{1 - \beta_{ig}}{2 - \beta_{ig}} \right]}}$$

Equation 59

thus

$$\left[\frac{1 - \beta_{ig}}{2 - \beta_{ig}} \right] = \frac{3}{4\pi}$$

Equation 60

Solving for β_{ig} numerically we obtain a value of 0.67. Similarly, equating the

Delichatsios *et al.* [43] high heat flux equation (Equation 49) with the integral model

(Equation 28) we obtain

$$\left(\dot{q}_i'' - \dot{q}_{cr}''\right) \cfrac{1}{\sqrt{\cfrac{4}{3}kpc\left[\cfrac{1-\beta_{ig}}{2-\beta_{ig}}\right]}} \cfrac{1}{\left(T_{ig}-T_\infty\right)} = \cfrac{2}{\sqrt{\pi kpc}} \cfrac{1}{\left(T_p-T_0\right)}\left[\dot{q}_i'' - 0.64\dot{q}_{cr}''\right]$$

thus

$$\dot{q}_i''\left(\cfrac{2}{\sqrt{\pi kpc}} - \cfrac{1}{\sqrt{\cfrac{4}{3}kpc\left[\cfrac{1-\beta_{ig}}{2-\beta_{ig}}\right]}}\right) = \dot{q}_{cr}''\left(-\cfrac{1}{\sqrt{\cfrac{4}{3}kpc\left[\cfrac{1-\beta_{ig}}{2-\beta_{ig}}\right]}} + 0.64\cfrac{2}{\sqrt{\pi kpc}}\right)$$

At high heat fluxes $\dot{q}_i'' \gg \dot{q}_{cr}''$ thus $\cfrac{\dot{q}_{cr}''}{\dot{q}_i''} \rightarrow 0$ and therefore

$$\cfrac{2}{\sqrt{\pi kpc}} = \cfrac{1}{\sqrt{\cfrac{4}{3}kpc\left[\cfrac{1-\beta_{ig}}{2-\beta_{ig}}\right]}}$$

or

$$\left[\cfrac{1-\beta_{ig}}{2-\beta_{ig}}\right] = \cfrac{3\pi}{16}$$

However, this time solving for β_{ig} numerically, we obtain a value of -0.433. Using the

definition of C_{ig} given in Equation 34 such that

$$C_{ig} = \cfrac{4}{3}\left[\cfrac{1}{\left(2-\beta_{ig}\right)\left(1-\beta_{ig}\right)}\right]$$

65

we obtain values for C_{ig} of 3.24 and 0.38 for the low heat flux and high heat flux cases respectively.

Abu-Zaid & Atreya [20] found experimentally that C_{ig} depends on $\dot{q}_i''$ with values from 0.5 to 0.62 obtained for heat fluxes of 10 to 60 kW/m^2. Figure 21 shows the qualitative comparison between Abu-Zaid's results, the analysis of Delichatsios *et al.* [43] equations and the theoretical values for C_{ig} using the integral model with a critical heat flux selected to be a typical value of 12 kW/m^2.

Best fit lines are shown through Abu-Zaid's measurements and the Delichatsios values to examine the trends in the relationships. At high incident heat fluxes, the integral model compares well with Abu-Zaid's data and Delichatsios equations. At low incident heat fluxes there is a significant difference between the Abu-Zaid's data value and the integral theory. The Delichatsios equations fall somewhere between the integral model and Abu-Zaid but with the trend at least similar to the integral model.
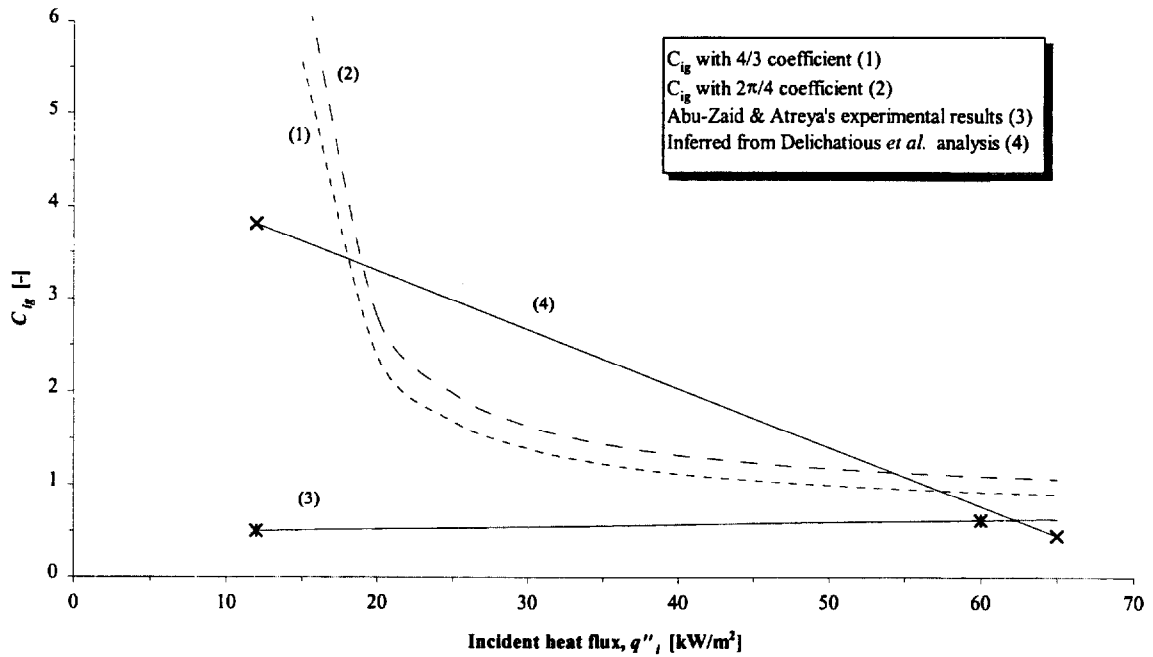
Figure 21. Form of C_{ig} parameter with incident heat flux.

3.2 Analysis

3.2.1 Times to ignition

Time to ignition data for each wood specie in the *across* grain and *along* grain

configurations are given in Table 5 to Table 8 and plots of ignition time against incident

heat flux were made (Figure 22 to Figure 25). The plots include a 'best-fit' trend lines (in

the form of a power curve, ax^b, where a and b are different constants for each set of data)

through the data to indicate the form of the data. The data and 'best-fit' curves confirm

that, from Equation 28, as $\dot{q}_i'' \rightarrow \dot{q}_{cr}''$ then $t_{ig} \rightarrow \infty$ and when $\dot{q}_i'' \gg \dot{q}_{cr}''$ then $t_{ig} \rightarrow 0$.

Along grain			
ID	Heat flux q''_i [kW/m²]	Ignition time t_{ig} [s]	$1/\sqrt{t_{ig}}$ [s$^{-1/2}$]
1DFL1	75	5.6	0.1788
1DFL2	75	5.6	0.1785
1DFL3	25	90.7	0.0110
1DFL4	75	5.6	0.1770
1DFL6	50	13.8	0.0722
1DFL7	50	14.3	0.0700
1DFL8	50	18.6	0.0539
1DFL9	35	45.6	0.0219
2DFL1i	20	684.0	0.0015
2DFL2i	18	851.0	0.0012
2DFL3i	16	1205.0	0.0008
2DFL4i	14	2045.0	0.0005
2DFL5i	13	3330.0	0.0003
2DFL6i	12	5580.0	0.0002

Across grain			
ID	Heat flux q''_i [kW/m²]	Ignition time t_{ig} [s]	$1/\sqrt{t_{ig}}$ [s$^{-1/2}$]
1DFX1	75	13.5	0.0743
1DFX2	75	10.6	0.0943
1DFX3	75	12.0	0.0835
1DFX4	25	147.5	0.0068
1DFX5	75	11.5	0.0867
1DFX6	50	22.0	0.0455
1DFX7	50	31.0	0.0322
2DFX1i	20	370.0	0.0027
2DFX2i	18	493.0	0.0020
2DFX3i	16	564.0	0.0018
2DFX4i	14	752.0	0.0013
2DFX5i	13	806.0	0.0012
2DFX6i	11	1685.0	0.0006
2DFX7i	10	1465.0	0.0007
2DFX8i	9	2395.0	0.0004
2DFX9i	35	73.0	0.0137

Table 5. Ignition data for Douglas fir.
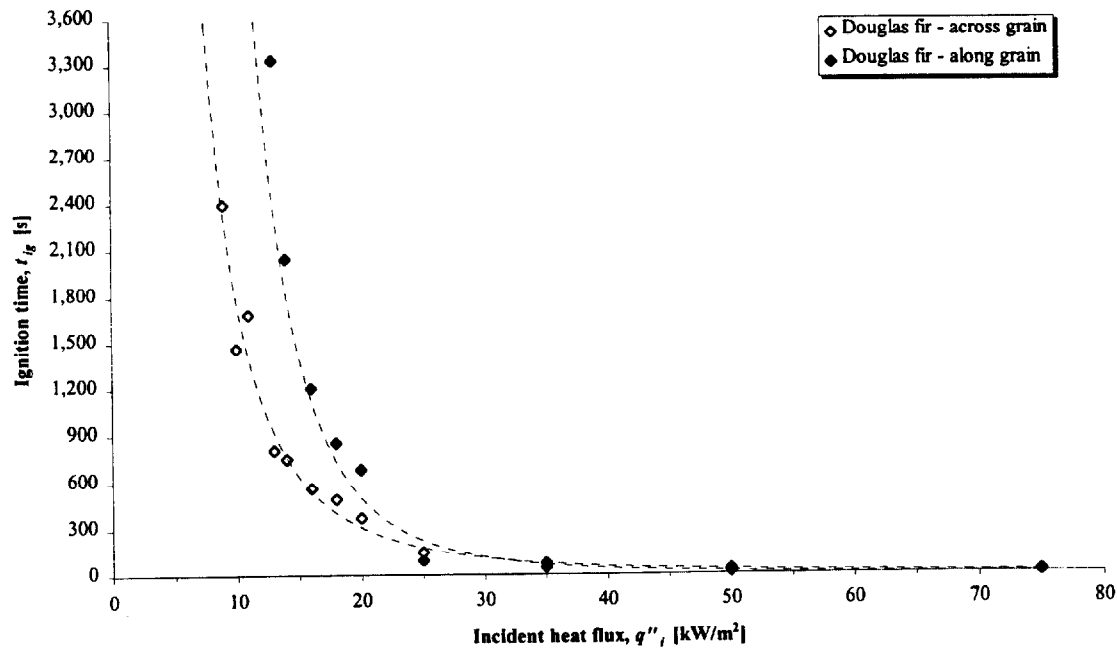
Figure 22. Ignition time against incident heat flux for Douglas fir.

68

ID	Heat flux q''_i [kW/m²]	Ignition time t_{ig} [s]	$1/\sqrt{t_{ig}}$ [s$^{-1/2}$]
1RL1	75	4.8	0.2092
1RL2	75	4.8	0.2095
1RL3	25	150.6	0.0066
1RL4	75	4.7	0.2114
1RL6	50	11.0	0.0910
1RL7	50	10.6	0.0943
1RL8	50	11.1	0.0902
1RL9	35	35.6	0.0281
2RL1i	20	362.0	0.0028
2RL2i	18	746.0	0.0013
2RL3i	16	927.0	0.0011
2RL4i	14	1388.0	0.0007
2RL5i	13	2170.0	0.0005
2RL6i	12	No ignition	-

Along grain

ID	Heat flux q''_i [kW/m²]	Ignition time t_{ig} [s]	$1/\sqrt{t_{ig}}$ [s$^{-1/2}$]
1RX1	75	17.8	0.0562
1RX2	75	7.9	0.1264
1RX3	25	105.9	0.0094
1RX4	75	6.6	0.1517
1RX6	25	112.8	0.0089
1RX7	50	n/a	n/a
1RX8	50	25.7	0.0390
1RX9	50	20.7	0.0484
1RX10	35	48.6	0.0206
2RX1i	20	201.0	0.0050
2RX2i	18	248.0	0.0040
2RX3i	16	308.0	0.0032
2RX4i	14	320.0	0.0031
2RX5i	13	290.0	0.0034
2RX6i	11	570.0	0.0018
2RX7i	10	567.0	0.0018
2RX8i	9	1416.0	0.0007

Across grain

Table 6. Ignition data for Redwood.
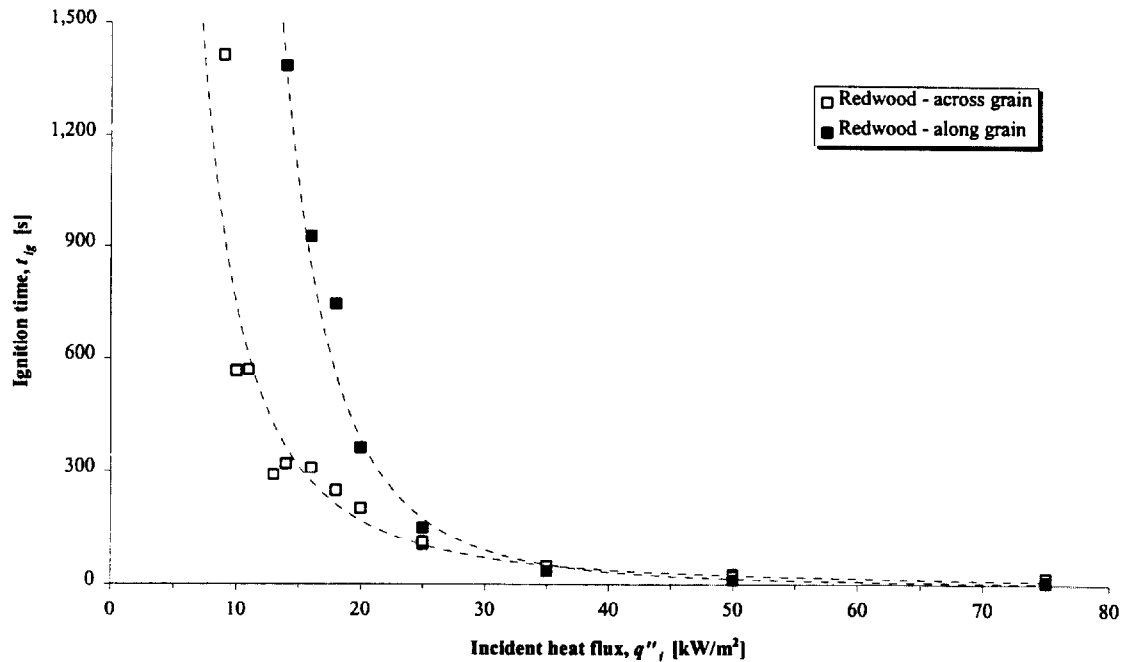
Figure 23. Ignition time against incident heat flux for Redwood.

Along grain			
ID	Heat flux q''_i [kW/m^2]	Ignition time t_{ig} [s]	1/sqrt(t_{ig}) [s$^{-1/2}$]
1OL1	25	192.7	0.0052
1OL2	25	192.7	0.0052
1OL3	75	12.7	0.0788
1OL4	75	11.3	0.0884
1OL5	75	12.6	0.0792

Across grain			
ID	Heat flux q''_i [kW/m^2]	Ignition time t_{ig} [s]	1/sqrt(t_{ig}) [s$^{-1/2}$]
1OX1	25	248.2	0.0040
1OX2	25	250.6	0.0040
1OX3	75	17.8	0.0560
1OX4	75	16.3	0.0613
1OX5	75	18.5	0.0542

Table 7. Ignition data for Red oak.
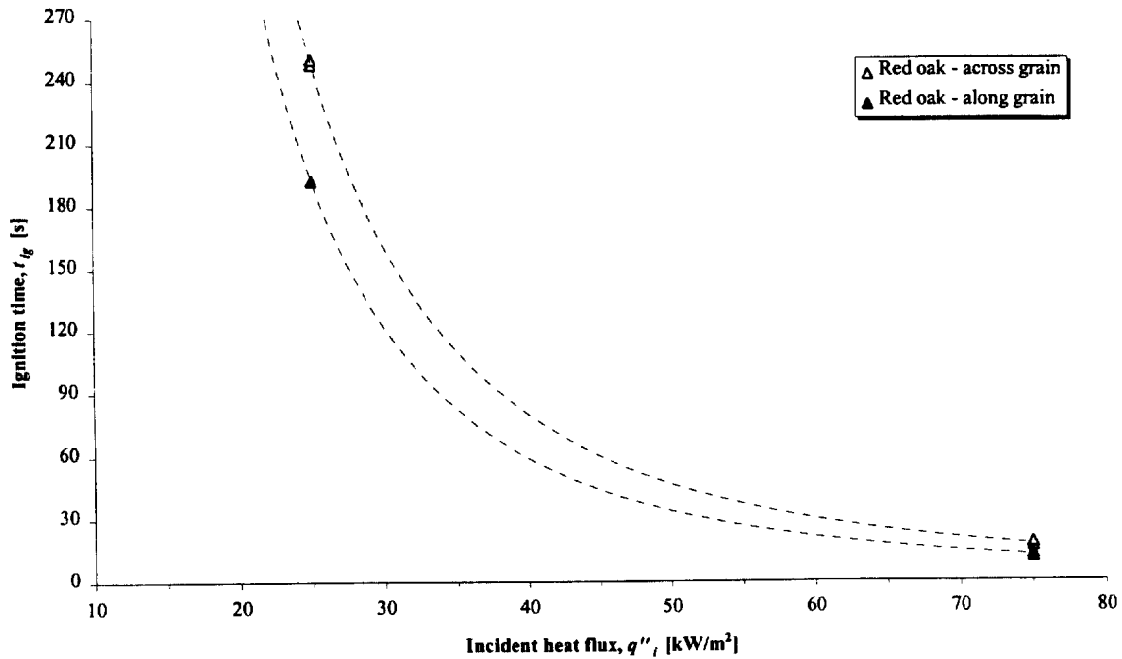
Figure 24. Ignition time against incident heat flux for Red oak.

70

Table 8. Ignition data for Maple.

Long grain

ID	Heat flux q''_i [kW/m²]	Ignition time t_{ig} [s]	$1/\sqrt{t_{ig}}$ [s$^{-1/2}$]
1ML1	75	11.4	0.0879
1ML2	75	12.5	0.0802
1ML3	75	12.0	0.0831
1ML4	25	185.7	0.0054
1ML5	25	346.0	0.0029
2ML1i	20	659.0	0.0015
2ML2i	16	1157.0	0.0009
2ML3i	14	1274.0	0.0008
2ML4i	12	4200.0	0.0002
2ML5i	50	32.0	0.0313

Across grain

ID	Heat flux q''_i [kW/m²]	Ignition time t_{ig} [s]	$1/\sqrt{t_{ig}}$ [s$^{-1/2}$]
1MX1	25	229.6	0.0044
1MX2	25	251.6	0.0040
1MX3	75	23.8	0.0419
1MX4	75	23.6	0.0423
1MX5	75	23.1	0.0433
2MX1i	20	461.0	0.0022
2MX2i	16	593.0	0.0017
2MX3i	14	650.0	0.0015
2MX4i	12	987.0	0.0010
2MX5i	10	1471.0	0.0007
2MX6i	9	1585.0	0.0006
2MX7i	8	2680.0	0.0004
2MX8i	No ignition		-
2MX9i	50	48.0	0.0208

o Maple - across grain
● Maple - along grain

Figure 25. Ignition time against incident heat flux for Maple.

With the exception of the Red oak, it is noted that the *across* grain orientation samples ignited sooner at the lower incident heat fluxes (~20 kW/m^2 or below). Yet at the high heat fluxes the *along* grain samples ignited quicker. Further analysis of this observation is given in § 3.4.

3.2.2   Critical heat flux

As described in § 1.4.3 the critical heat flux is taken to be the minimum incident heat flux required to obtain sustained piloted ignition of a material. The critical heat flux can be obtained experimentally by successively exposing samples of the material at decreasing incident heat fluxes until ignition no longer occurs. Thus the critical heat flux is somewhere between the lowest incident heat flux at which ignition occurred and the highest incident heat flux where ignition did not occur. Clearly this approach can be a time consuming process as it may require several tests to find the bounds of critical heat flux depending on the resolution required. In addition, as the critical heat flux is approached, then times to ignition become increasingly longer. Finally, there is the question as to how long one should wait before deciding that ignition will not occur. As it will be demonstrated in this study, ignition may not occur until anything between several tens of minutes and up to one and a half hours have elapsed.

Species	Grain orientation	Critical heat flux for ignition q''_{cr} [kW/m^2]
Redwood	along	13.00
	across	9.00 *
Douglas fir	along	12.00 *
	across	9.00 *
Maple	along	12.00 *
	across	8.00

(*) no ignition case not achieved

Table 9. Critical heat fluxes obtained from experiments.

Table 9 shows the critical heat fluxes obtained from the ignition experiments. It should be noted that in some cases the final experimental critical heat might not have been achieved simply due to the lack of test samples. In some cases, the sample at the lowest measured incident heat flux achieved ignition and thus the case in which no ignition was ever obtained was not found. Thus ignition may still have been possible at even lower incident fluxes. Such data are indicated in Table 9. The glowing ignition process at low heat fluxes was somewhat unexpected and had this been identified earlier in the study then the ignition testing protocol would have been modified accordingly in an attempt to gain further insights into the mechanism.

As an alternative to directly obtaining the critical heat flux from an experimental procedure, the critical heat flux can be obtained from time to ignition data. By rearranging Equation 28, we obtain

$$\frac{1}{\sqrt{t_{ig}}} = \dot{q}''(t_{ig}) \frac{1}{\sqrt{\frac{4}{3}k\rho c \left[\frac{1-\beta_{ig}}{2-\beta_{ig}}\right]}} \frac{1}{(T_{ig}-T_0)}$$

Equation 65

From Equation 24 and Equation 35

$$\dot{q}''(t_{ig}) = \dot{q}''_i - \dot{q}''_{cr}$$

thus

$$\frac{1}{\sqrt{t_{ig}}} = (\dot{q}''_i - \dot{q}''_{cr}) \frac{1}{\sqrt{\frac{4}{3}k\rho c \left[\frac{1-\beta_{ig}}{2-\beta_{ig}}\right]}} \frac{1}{(T_{ig}-T_0)}$$

Equation 66

The critical heat flux can be found from the plot of $1/\sqrt{t_{ig}}$ against incident heat flux. By

plotting a best-fit straight line through the data, the intercept yields a low estimate critical

heat flux where, from Equation 66

$$slope = \frac{1}{\sqrt{\frac{4}{3}k\rho c \left[\frac{1-\beta_{ig}}{2-\beta_{ig}}\right]}} \frac{1}{(T_{ig}-T_0)}$$

and

$$intercept = -slope.\dot{q}''_{cr}$$

This follows because by the above theory the slope of the curve becomes vertical when

$1/\sqrt{t_{ig}} \rightarrow 0$ or $\beta_{ig} = 1$, while for higher heat fluxes the curve has a distinct positive finite

slope as given by Equation 31 (see Figure 20).

74

In the study of non-charring materials by Hopkins [30], it was suggested that a linear

regression through data below 40 kW/m^2 gives a better measure for the critical heat flux

since at lower heat fluxes ignition takes longer. However, examination of the plot of

$1/\sqrt{t_{ig}}$ against incident heat flux show that at low heat fluxes the data tends to exhibit a

secondary upward trend towards a very low critical heat flux. This was as a result of the

localised glowing ignition discussed in § 1.4.3.

Thus, it was decided that the critical heat flux without the effect of the localised heating

could be obtained from a linear regression through only the 'high' heat flux

measurements and the low heat flux data was not utilised in the determination of the final

critical heat flux. In this case, the 'high' heat flux data was taken to be where the incident

heat flux was around 20 kW/m^2 or above. The selection of the lower limit of the 'high'

heat flux data was based on experimental observations, the shapes of the $1/\sqrt{t_{ig}}$ curves

and from the theory shown in Figure 20. In this case 'high' heat fluxes are taken to be

where $\dot{q}_i'' > \dot{q}_{cr}''$ and Figure 20 suggests that the integral model gives an approximately

straight line when $\dfrac{1}{\beta_{ig}} \geq 1.5$ i.e. $\dot{q}_i'' \geq 1.5\,\dot{q}_{cr}''$, in order to be consistent with the theory.

Since values for the critical heat fluxes were found to be at most around 12 kW/m^2 (and

1.5 x 12 = 18) then a 'high' heat flux threshold of 20 kW/m^2 is reasonable.

Figure 26 to Figure 29 show the $1/\sqrt{t_{ig}}$ against incident heat flux data for the four wood

specie with a linear regression through the 'high' heat flux points shown by large symbols.

The figures also show the theoretical curves obtained from Equation 28 and the critical

heat fluxes obtained by the linear regression and theoretical curves. Table 10 shows the

critical heat fluxes obtained from the intercept of the linear regression line.
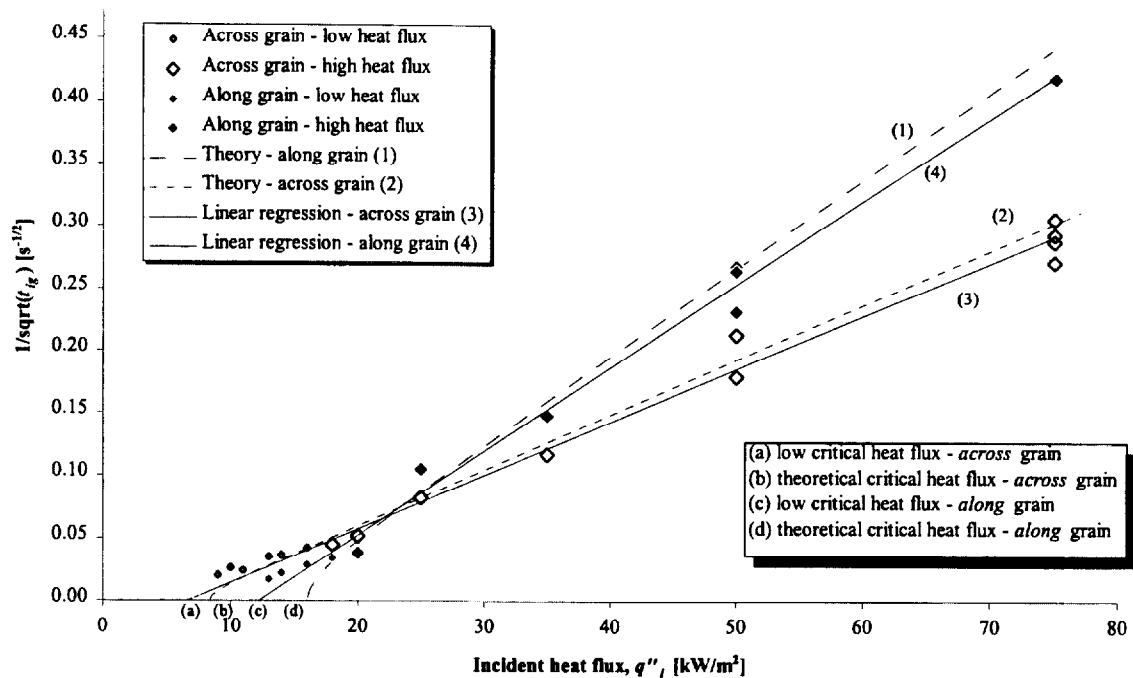
Figure 26. Determination of the critical heat flux for ignition for Douglas fir.
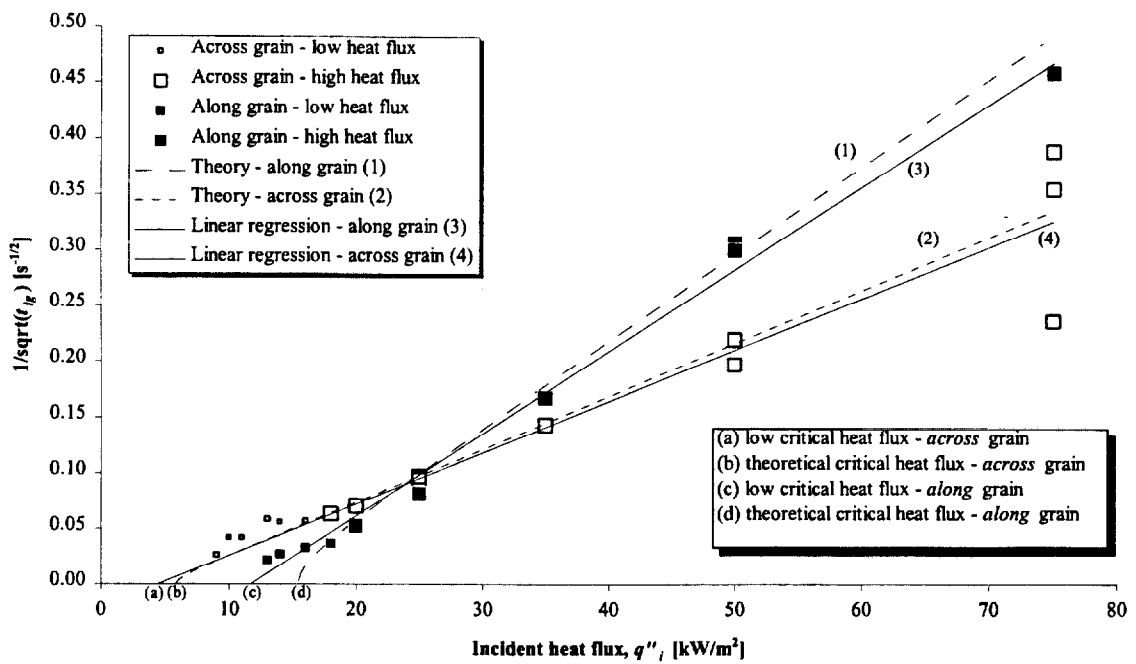
Figure 27. Determination of the critical heat flux for ignition for Redwood.
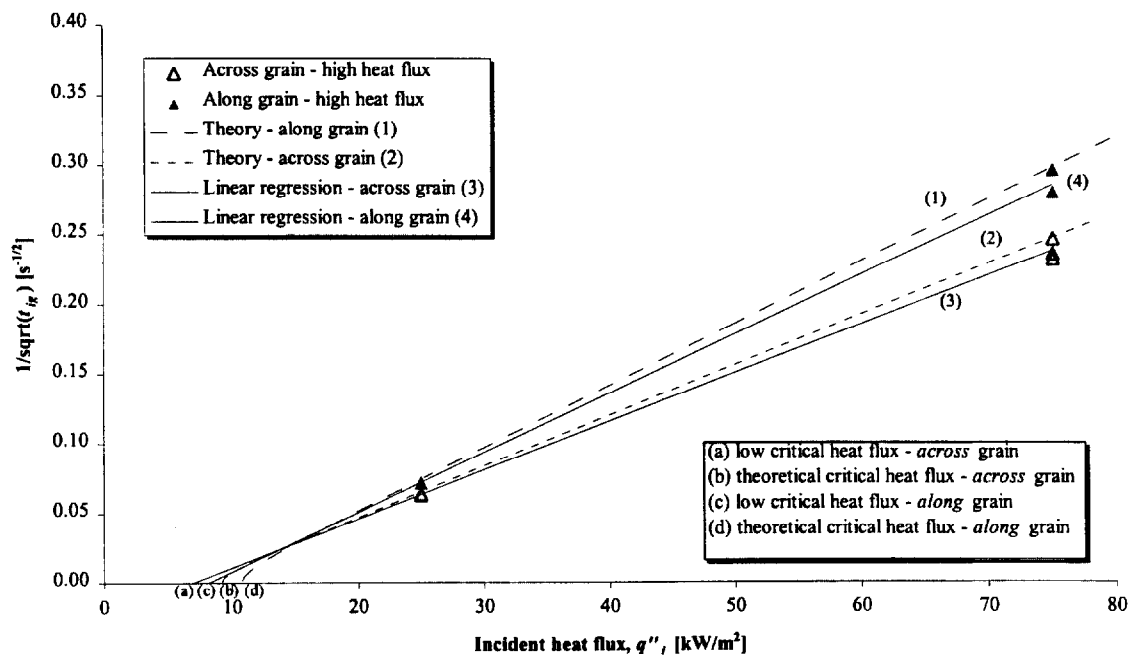
Figure 28. Determination of the critical heat flux for ignition for Red oak.
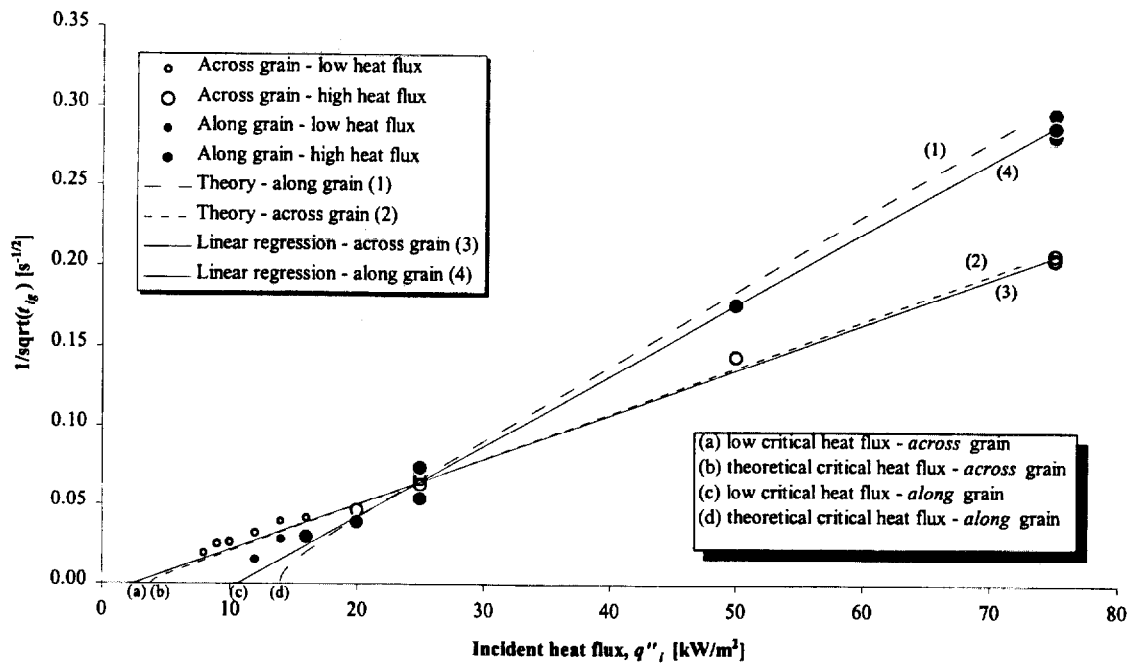
Figure 29. Determination of the critical heat flux for ignition for Maple.

In order to investigate the difference between using only the 'high' heat flux data and all of the data linear regression fits were also made through all of the time to ignition data obtained for the Douglas fir, Redwood and Maple species and the critical heat flux determined. These data are compared with the 'high' heat flux data critical heat flux values in Table 10. In general, the *along* grain orientations show little difference. However, the *across* grain orientations for the Maple and Redwood show significant differences with the 'high' incident flux data giving critical heat fluxes approximately twice are large. There is no difference between the data for the Red oak since no low incident heat flux measurements were made in the experiments.

Species	Grain orientation	Critical heat flux for ignition $-q''_{cr}$	
		'High' heat flux [kW/m²]	**All data [kW/m²]**
Redwood	*along*	11.74	11.67
	across	4.48	2.55
Red oak	*along*	8.20	8.20
	across	6.98	6.98
Douglas fir	*along*	12.19	11.64
	across	6.36	5.74
Maple	*along*	10.58	9.54
	across	2.91	1.07

Table 10. Comparison of critical heat fluxes for ignition using 'high' and all incident heat flux data.

Table 11 shows the final critical heat fluxes for ignition for each specie using the 'high' heat flux data modified by the 0.76 factor given in Equation 58 (§ 3.1.2). Hereafter, in this study, these data were taken to be the critical heat flux for ignition for each specie in the two grain orientations.

Species	Grain orientation	Critical heat flux for ignition q''_{cr} [kW/m^2]
Redwood	*along*	15.45
	across	5.89
Red oak	*along*	10.79
	across	9.18
Douglas fir	*along*	16.04
	across	8.37
Maple	*along*	13.92
	across	3.83

Table 11. Final critical heat fluxes for ignition used in this study obtained by the analysis of the time to ignition data.

For Redwood, Janssens [33] quotes a critical heat flux of 14 kW/m^2 whilst Tran & White [34] give a value of 12.42 kW/m^2. In this study, the critical heat flux for ignition of the Redwood along the grain was found to be 11.74 kW/m^2. Janssens [33] gives a critical heat for ignition for Douglas fir of 13 kW/m^2 compared to 12.19 kW/m^2 in this study for the along the grain samples. Tran & White [34] quote a critical heat flux for ignition of 10.53 kW/m^2 for Red oak compared to the value of 8.20 kW/m^2 for the along the grain orientation samples tested in this study.

An overall comparison of the critical heat flux values obtained in this study compared with literature values show slightly lower values for the along grain orientation and significantly lower values for the across grain orientations.
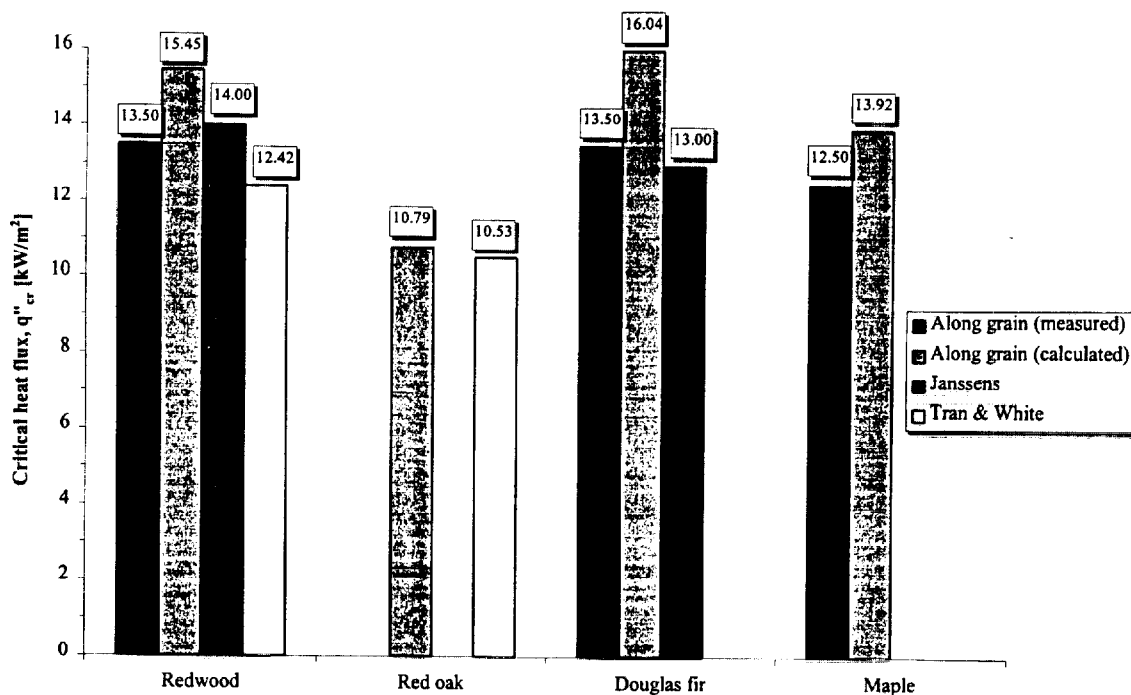
Figure 30. Comparison of calculated and measured critical heat fluxes with data given by Janssens and Tran & White.

The differences in the values may be partly explained by natural variation in the wood species but also by the fact that Tran & White's tests were conducted in the OSU and that Janssens [33] tested his samples in the Cone Calorimeter in the vertical orientation. However, in the study by Atreya *et al.* [21] it was found that the critical heat flux only varied by about 10% between horizontal and vertical samples and the critical heat flux was greater in the vertical case. Thus we might expect Janssens critical heat flux data to be somewhat less if his samples had been tested horizontally.

Finally, the critical heat fluxes obtained in the experiments (Table 9) were compared with those derived from the analysis of the ignition data (Table 11). Figure 31 shows a plot of the experimental critical heat fluxes and derived critical heat fluxes. It is clear that

81

although the two do not match there appears to be a relationship between the two as shown by the linear regression fit. The difference between the derived and experimental critical heat fluxes may be as a result of neglecting the glowing ignition data for the low heat fluxes. However, since in only two cases were the no ignition incident heat flux found (Table 9), this comparison is not conclusive and further tests should be conducted to verify these findings.
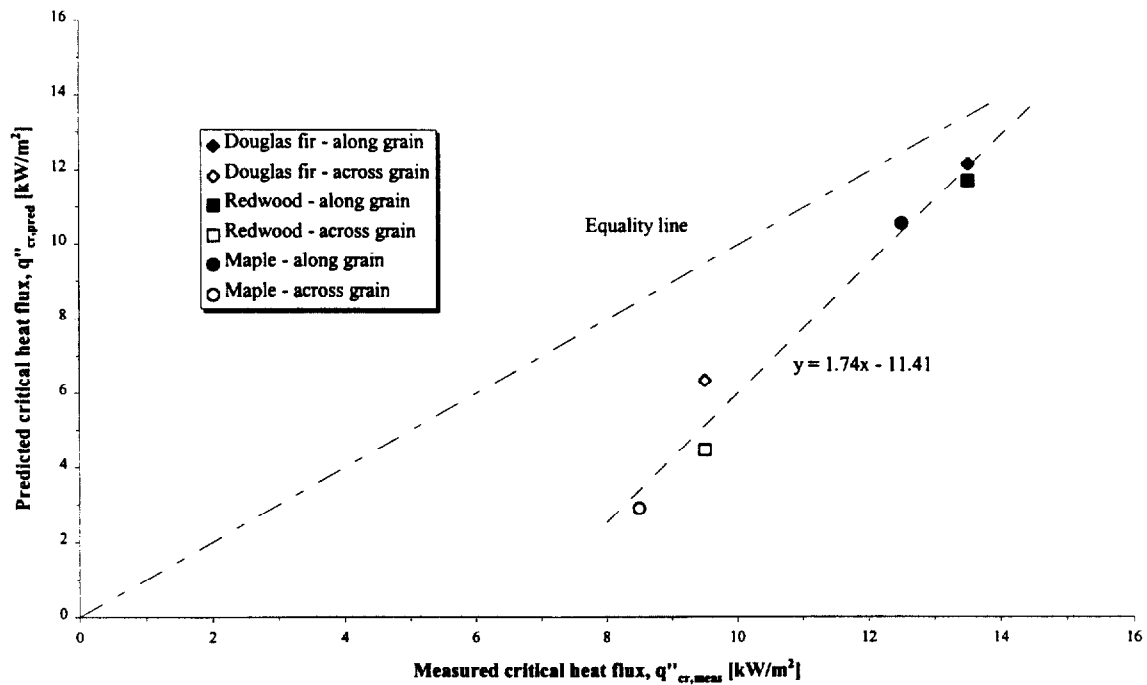
Figure 31. Comparison of measured and calculated critical heat fluxes.

3.2.3 Ignition temperature

a) Average ignition temperature

By obtaining the critical heat flux for ignition for each species in the *along* and *across* orientations, Equation 35 can be used to solve for the average ignition temperature. Since Equation 35 assumes a long ignition time, i.e. a low heat flux, the value for the

convective heat transfer to the surface of the sample in the Cone Calorimeter was taken

as that at the critical heat flux using a correlation provided by Spearpoint [45] such that

$$h_c = -2.04\dot{q}_i'' + 19.58$$

Equation 67

Equation 35 was then solved numerically by an iterative process for the critical heat flux

to obtain a value for the average ignition temperature. Table 12 shows the calculated

ignition temperatures obtained for the various species in the *across* and *along* grain

configurations.

Species	Grain orientation	Ignition temperature T_{ig} [°C]
Redwood	*along*	375
	across	204
Red oak	*along*	304
	across	275
Douglas fir	*along*	384
	across	258
Maple	*along*	354
	across	150

Table 12. Calculated average ignition temperatures.

The average ignition temperatures for Redwood and Douglas fir (softwoods) are

generally greater than those for Red oak and Maple (hardwoods) in the two grain

orientations which agrees with the findings discussed in § 1.2.2.

83

The average ignition temperatures obtained in this study were compared with data quoted in the literature. Tran & White [34] measured the ignition temperature of their samples with a thermocouple on the exposed surface of the samples. They quote an average ignition temperature for Redwood as 364 °C. Janssens [33] gives an average ignition temperature from Redwood as 363 °C. Dietenberger [36] gives ignition temperatures of 353 °C in the Cone Calorimeter and values between 290 °C and 356 °C (depending on the moisture content of the samples) in the LIFT [11]. All of these values compare reasonably well with the average temperature calculated in this study for the *along* grain oriented Redwood with the value given here being slightly above those quoted by the other researchers.

Janssens [33] quotes an ignition temperature of 350 °C for Douglas fir which is lower than the temperature of 384 °C calculated in this study for the *along* grain orientation.

Tran & White [34] obtained an ignition temperature of 315 °C for Red oak and Atreya *et al.* [18] quotes 365 °C. Both of these values are greater than the ignition temperatures obtained in this study for the *along* and *across* grain orientations. The data from the literature and this study demonstrate that there is a fair degree of variability in the ignition temperatures of wood. As discussed earlier, there are many factors that influence the ignition properties of wood. However, the average ignition temperatures obtained in this study are comparable with the data quoted by other researchers and an average

ignition temperature of somewhere between 300 °C and 380 °C for *along* grain oriented wood is typical.

b) Ignition temperature as a function of incident heat flux

By rearranging Equation 33 we obtain

$$T_{ig} = T_0 + \sqrt{\frac{t_{ig}\left(\dot{q}_i''\right)^2}{C_{ig}k\rho c}}$$

Using the measured times to ignition and the apparent thermal inertia obtained in 3.2.4, the ignition temperature at a given incident heat flux can be calculated with Equation 68. Since C_{ig} also includes T_{ig}, Equation 68 cannot be solved analytically but has to be solved iteratively.

In the study by Hopkins [30], thermocouples were also located on the exposed surface of the samples tested so as to obtain the ignition temperatures at given incident heat fluxes. Figure 32 compares these calculated ignition temperatures obtained from Equation 68 for Redwood with those measured by Hopkins [30] and quoted by Tran & White [34] and Janssens [33].
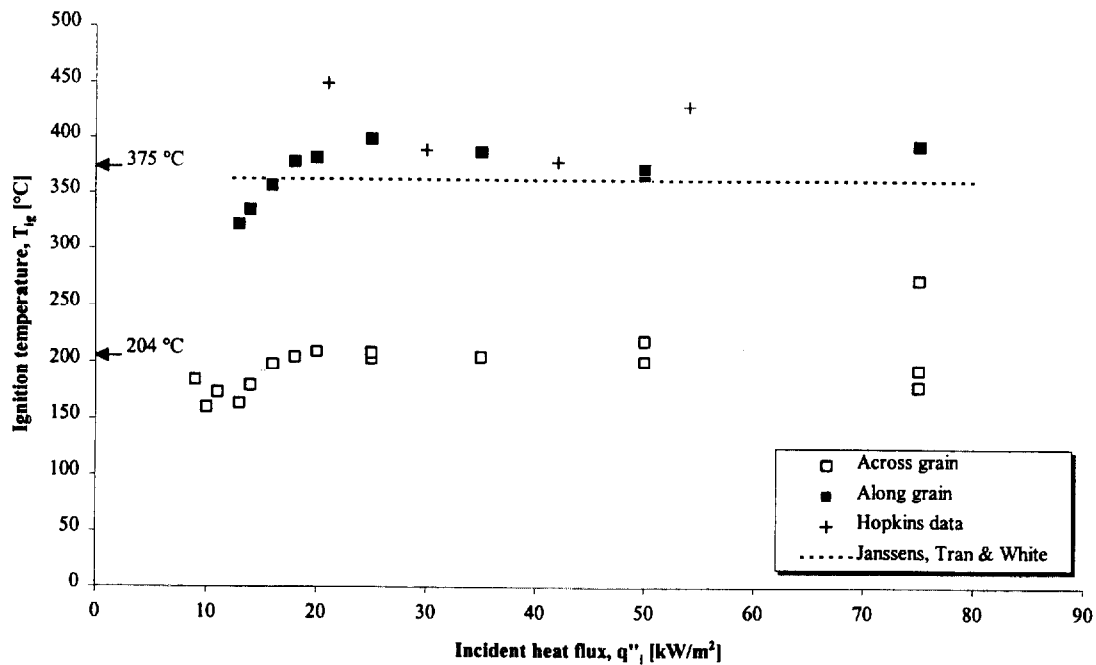
Figure 32. Predicted ignition temperatures for given incident heat fluxes for Redwood

The calculated ignition temperatures, particularly for the *along* grain configuration, compare well with the other literature data at heat fluxes above around 20 kW/m². The ignition temperature quoted by Hopkins at 21 kW/m² is greater than those found elsewhere. Below 20 kW/m² the calculated ignition temperatures show a downward trend with a limiting value of around 200 °C for the *across* grain configuration.

Similarly, for Douglas fir, the calculated ignition temperatures at given incident heat fluxes are shown in Figure 33. As for Redwood, the calculated temperatures compare well with the data quoted by Janssens [33] at heat fluxes above 20 kW/m². Again, below 20 kW/m² the temperatures decrease to values around 200 °C for the *across* grain configuration.
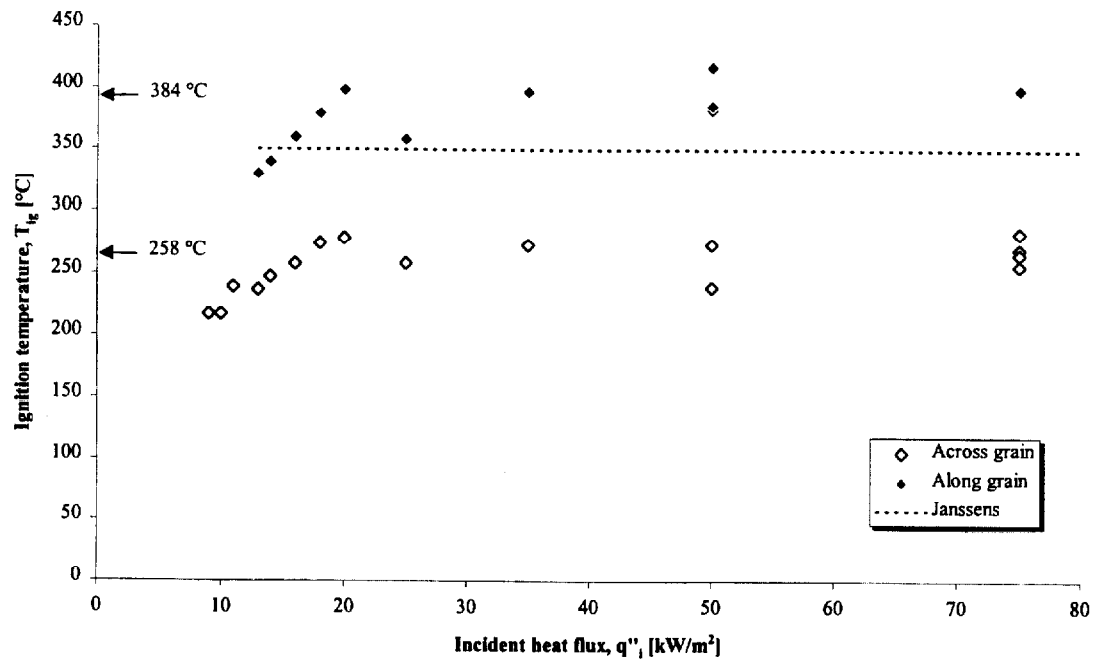
Figure 33. Predicted ignition temperatures for given incident heat fluxes for Douglas fir.
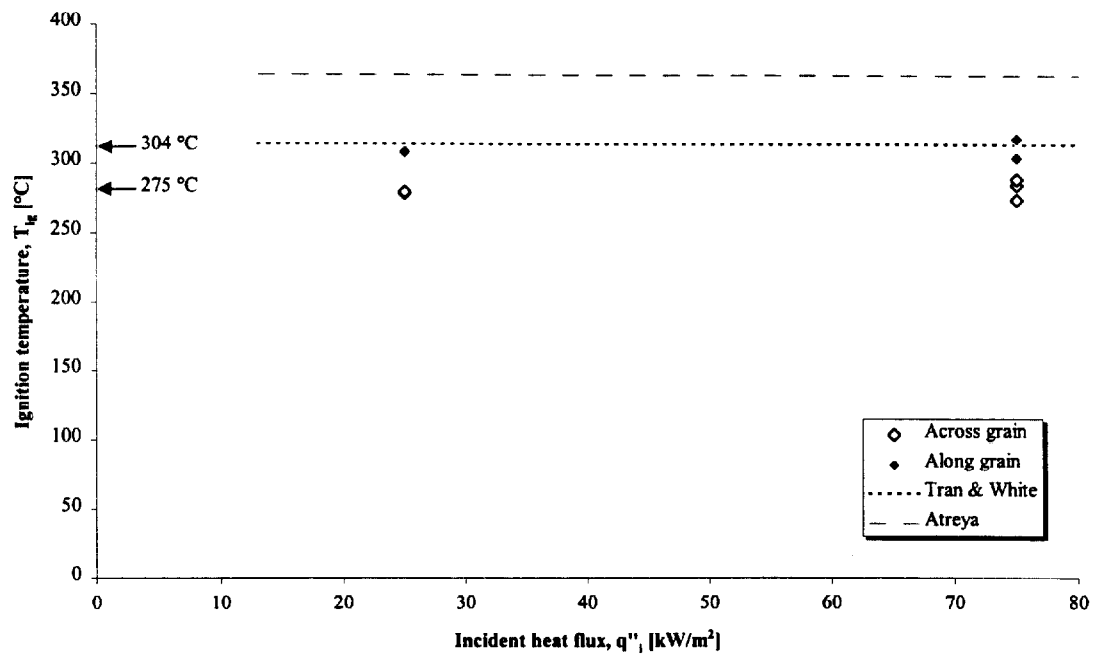
Figure 34. Predicted ignition temperatures for given incident heat fluxes for Red oak.

87
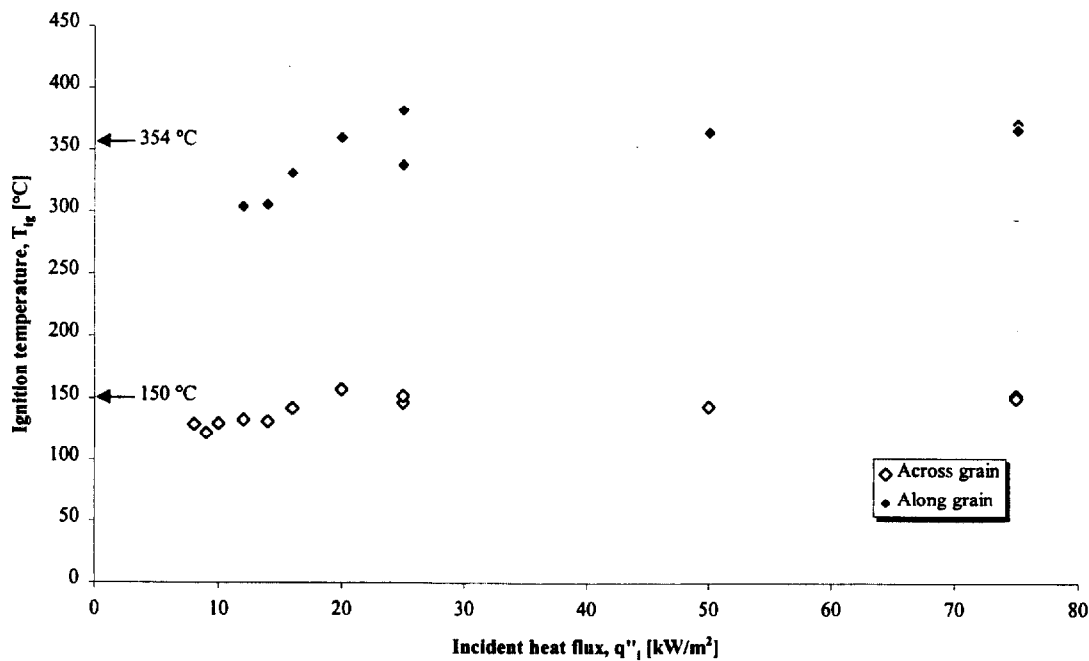
Figure 35. Predicted ignition temperatures for given incident heat fluxes for Maple.

The calculated ignition temperatures for Red oak and Maple at given incident heat fluxes are shown in Figure 34 and Figure 35.

In all four cases the ignition temperatures are almost constant at incident heat fluxes above around 20 kW/m^2. Simms [15] quotes work by Bamford, Crank & Malan in which it is suggested that at high incident fluxes the energy required for surface ignition appeared to tend to a constant value. The results from this study agree with these findings. Except for Red oak, below 20 kW/m^2, the ignition temperatures fall to values lower than the constant values found above 20 kW/m^2. These results appear to confirm that the ignition mechanism is different at low incident heat fluxes as observed in the experiments (§ 1.4.3). A similar decrease in the measured ignition temperature of PMMA with decreasing incident heat flux was obtained by Rhodes & Quintiere [46]

The fact that the ignition temperature falls as the incident heat flux is reduced initially appears to conflict with Atreya *et al.* [21] in which they found that the ignition temperature rises as the incident heat flux decreases. However on close examination of their data (for Mahogany) it was found that the minimum incident heat flux used in their experiments was ~18 kW/m². The data obtained in this study for Douglas fir, Redwood and Maple shows that around this same flux region the ignition temperatures also shows a slight rise (Figure 32 and Figure 33) before decreasing again as the incident flux is further reduced. The ignition temperatures obtained by Hopkins [30] for Redwood also shows a rise at 21 kW/m² compared with 30 kW/m² and 42 kW/m².

It is interesting to note that the ignition temperatures of around 200 °C in this study at low incident heat fluxes is similar to those given for self-ignition temperatures of wood. For example, Cholin quotes [3] self-ignition temperatures of small samples of wood are quoted as being between 192 °C and 220 °C.

3.2.4 Thermal inertia

The apparent thermal inertia can also be obtained from the slope of the best-fit line of the plot of $1/\sqrt{t_{ig}}$ against incident heat flux. From Equation 31, at 'high' heat fluxes (as defined in § 3.2.2),

$$\dot{q}_i'' = \frac{1}{\sqrt{t_{ig}}} \sqrt{\frac{2}{3} k\rho c} \left(T_{ig} - T_0\right)$$

thus

$$slope = \left[\frac{1}{\sqrt{\frac{2}{3} k\rho c} \left(T_{ig} - T_0\right)}\right]$$

$$k\rho c = \frac{3}{2} \left[\frac{1}{slope\left(T_{ig} - T_0\right)}\right]^2$$

Table 13 shows the apparent thermal inertia values calculated for the various wood species tested using the average ignition temperatures from 3.2.3.

Species	Grain orientation	Apparent thermal inertia $k\rho c$ [kJ^2.m^{-4}K^{-2}s^{-1}]
Redwood	*along*	0.22
	across	2.07
Red oak	*along*	1.01
	across	1.88
Douglas fir	*along*	0.25
	across	1.44
Maple	*along*	0.67
	across	10.91

Table 13. Calculated apparent thermal inertia for wood species tested.

Equation 14 states that

$$I \sim k^2$$

where the thermal conductivity k varies by a factor of around 2.1 due to grain orientation. § 2.4 shows that k is also a function of temperature (and moisture), thus Equation 70 can be rewritten as

$$I \sim [f\,k(T)]^2$$

Consider a typical *along* grain wood with $f = 1$ and normalised thermal inertia and thermal conductivity $k(T_{ig})$ of 1 each. For the equivalent *across* grain orientation $f = 2.1$ and assuming the ignition temperature is twice that for the along grain case then, from Figure 13, the normalised $k(T_{ig})$ may be typically $\dfrac{0.13}{0.12} \approx 1.01$. Thus the normalised thermal inertia would be from Equation 71, $(2.1 \times 1.01)^2 = 5.2$ times that of the *along* grain case.

The data obtained in this study shows increased values for the thermal inertia of the *across* grain orientations although the ratios between the *across* and *along* grains vary considerably (Table 14). Only Douglas fir exhibits a ratio approximately equivalent to the 5.2 suggested above.

Species	Thermal inertia ratio I_X / I_L
Redwood	9.5
Red oak	1.9
Douglas fir	5.8
Maple	16.3

Table 14. Ratio of *across* to *along* grain thermal inertia.

The *along* grain orientation values for the thermal inertia obtained in this study are

greater than those quoted by Janssens [33]. For Douglas fir and Redwood, Janssens gives

$0.154 \text{ kJ}^2.\text{m}^{-4}.\text{K}^{-2}.\text{s}^{-1}$ and $0.138 \text{ kJ}^2.\text{m}^{-4}.\text{K}^{-2}.\text{s}^{-1}$ respectively. Tran & White [34] obtained

the apparent thermal inertia of Redwood and Red oak as $0.073 \text{ kJ}^2.\text{m}^{-4}.\text{K}^{-2}.\text{s}^{-1}$ and

$0.360 \text{ kJ}^2.\text{m}^{-4}.\text{K}^{-2}.\text{s}^{-1}$ respectively. Again there is a noticeable difference between these

data and those obtained in this study. Tran & White's data for Redwood is also only

approximately one half that obtained by Janssens. As for the critical heat flux and

ignition temperature comparisons, these differences may be due to several factors;

previous samples were tested oven dry whereas the samples tested in this study included

higher levels of moisture; previous samples were tested in the vertical orientation in

different apparatuses; the natural variation of wood.

3.3 Dimensionless ignition analysis

The time to ignition against incident heat flux data can be plotted in a dimensionless

form. From Equation 69 we can define dimensionless irradiance and dimensionless time

as

$$\frac{1}{\beta_{ig}} \equiv \frac{\dot{q}_i''}{\dot{q}_{cr}''} \qquad \text{and} \qquad \tau_{ig} \equiv \frac{\dot{q}_{cr}''^2 \, t_{ig}}{(T_{ig} - T_0)^2 \, k\rho c} \qquad \text{respectively.}$$

Rearranging Equation 33 we obtain

$$\dot{q}_i''^2 = \frac{1}{t_{ig}} C_{ig} k\rho c (T_{ig} - T_0)^2$$

Equation 72

dividing through by $\dot{q}_{cr}''^2$

$$\frac{\dot{q}_i''^2}{\dot{q}_{cr}''^2} = \frac{1}{\dot{q}_{cr}''^2 \, t_{ig}} C_{ig} k\rho c (T_{ig} - T_0)^2$$

Equation 73

thus, substituting the dimensionless forms

$$\left(\frac{1}{\beta_{ig}}\right)^2 = C_{ig} \frac{1}{\tau_{ig}}$$

or

$$\frac{1}{\beta_{ig}} = \sqrt{C_{ig}} \frac{1}{\sqrt{\tau_{ig}}}$$

Equation 74

A dimensionless plot of all the ignition data is shown in Figure 36. The plot also shows

the theoretical curves with C_{ig} having either the *4/3* or *2π/4* factors. The plot shows that

scatter of the data is within the bounds of either the *4/3* or *2π/4* factor used in the theory.

'4/3'

'2π/4'

1/sqrt(τ_{ig})

Linear regression

• Douglas fir - along grain
○ Douglas fir - across grain
■ Redwood - along grain
□ Redwood - across grain
▲ Red oak - along grain
△ Red oak - across grain
● Maple - along grain
○ Maple - across grain

Dimensionless irradiance, 1/β_{ig} [-]
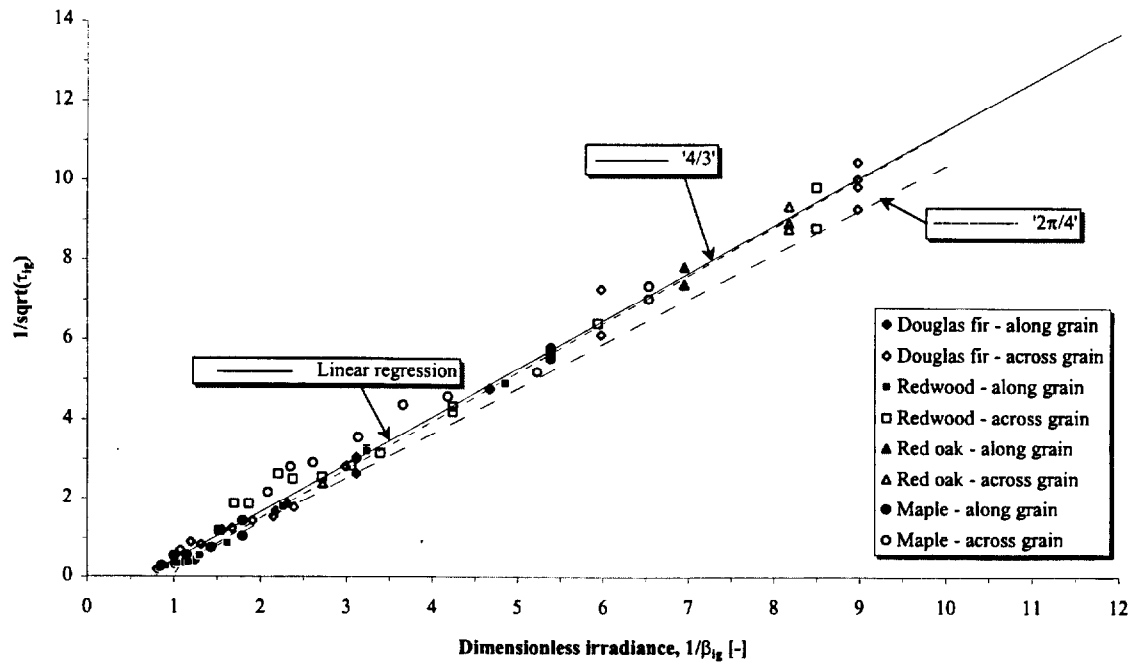
Figure 36. Dimensionless ignition plot on linear scales for all species tested showing comparison between measured ignition times and theoretical values.

The data shown in Figure 36 was plotted on log scales to show the low incident heat flux data more clearly (Figure 37). It can be seen that the experimental data at low heat fluxes does not match the theory. The data does not curve as sharply to $\frac{1}{\beta_{ig}} = 1$ as the integral model solution suggests. This discrepancy between the data and theory is a result of the localised ignition mechanism observed in the experiments as described in § 1.4.3. In the theory we only account for the external heat flux and not any additional energy from the glowing process.
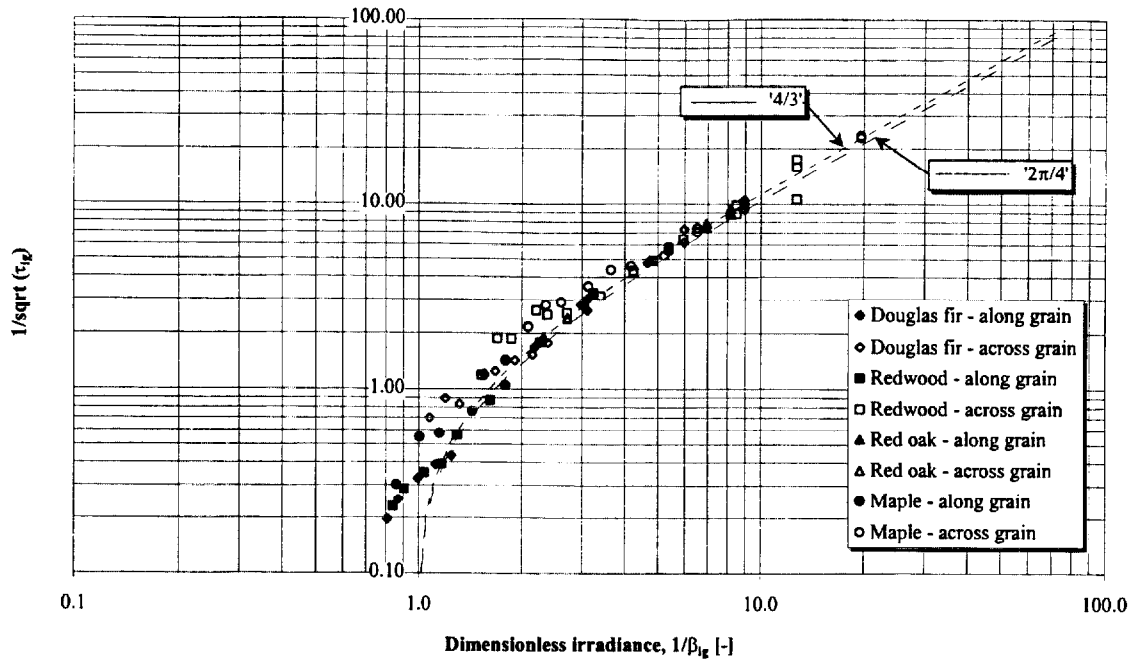
Figure 37. Dimensionless ignition plot on logarithmic scales for all species tested showing comparison between measured ignition times and theoretical values.

From Equation 74 the gradient of the dimensionless plot gives

$$C_{ig} = \left(\frac{1}{gradient}\right)^2$$

<div align="right">*Equation 75*</div>

By plotting a best-fit line through the data shown in Figure 36, a gradient of 1.21 is

obtained. Thus, from Equation 75, C_{ig} is found to be 0.68. The value for C_{ig} compares

well to the 0.62 quoted by Abu-zaid & Atreya [20] and the gradient of 1.21 is close to the

4/3 (= 1.333) value predicted by the integral solution.

3.4 Transitional critical heat flux

As noted in § 3.2.1, the difference between times to ignition for the *along* and *across* grain samples for a given wood exhibited a distinct pattern. The *across* grain orientation samples ignited sooner at the lower incident heat fluxes (~20 kW/m^2 or below). Yet at the high heat fluxes the *along* grain samples ignited quicker. This pattern can also be seen in the plots for $1/\sqrt{t_{ig}}$ against incident heat flux where the linear regression and theoretical lines intersect at some 'transitional' incident heat flux (i.e. the heat flux at which the *along* and *across* grain ignition times are the same).

To find this transitional heat flux from the plots of $1/\sqrt{t_{ig}}$ against incident heat flux we note that,

$$1/\sqrt{t_{ig,L}} = gradient_L \cdot \dot{q}''_{i,L} + intercept_L$$

Equation 76

$$1/\sqrt{t_{ig,X}} = gradient_X \cdot \dot{q}''_{i,X} + intercept_X$$

Equation 77

Thus, at the transitional heat flux, $1/\sqrt{t_{ig,L}} = 1/\sqrt{t_{ig,X}}$ and $\dot{q}''_{tr} = \dot{q}''_{i,L} = \dot{q}''_{i,X}$ and so substituting and rearranging Equation 76 and Equation 77

$$\dot{q}''_{tr} = \frac{intercept_X - intercept_L}{gradient_L - gradient_X}$$

The transitional critical heat fluxes were determined as 21.7 kW/m^2 for Douglas fir, 25.7 kW/m^2 for Redwood, 24.0 kW/m^2 for Maple but only 13.75 kW/m^2 for Red oak. It interesting to note that for Douglas fir, Maple and Redwood the values for the transitional heat flux are similar. These values also correspond to the suggested boundary between the 'high' and 'low' incident heat flux values given in § 3.2.2.

4. BURNING RATE

4.1 Integral model theory

4.1.1 Assumptions

The ignition process described in the previous chapter determines the initial conditions

for the burning rate model. The assumptions used in the ignition model are carried

forward to the burning rate model with the additional assumptions specified. Thus, for the

decomposition model (Figure 38) it is assumed that

(a) The fuel decomposes to gaseous fuel (volatiles) and char in an infinitesimal

pyrolysis front at a fixed vaporisation temperature,

(b) The solid is infinitely thick,

(c) The virgin wood is inert up to ignition and decomposition,

(d) The char material is also inert,

(e) The flame heat flux remains constant,

(f) The density of the volatiles is much less than the density of the virgin wood

and the char.

(g) Material properties are constant over the range of temperatures considered,

(h) The volatiles do not accumulate within the char layer but are produced and

exit immediately.

For simplicity in assumption (a), we assume that the vaporisation temperature and the

ignition temperature are the same though in reality these differ as compared to a liquid

fuel's flash point and boiling point. Suuberg *et al.* [22] indicate that chemical kinetics are important, but also two separate kinetic regimes that must be included. They also find that the assumption of an infinitesimal pyrolysis zone is valid for an incident heat flux greater than 40 kW/m^2.

Assumption (c) tells us that it is presumed that there is no mass loss prior to ignition as a result of the pyrolysis of the wood due to the incident heat flux. The mass loss only occurs after ignition due to the flame heat flux.

Assumption (d) implies that the exposed char layer is not affected by the incident heat flux. However, as discussed in § 1.2.2, the char layer will crack due to pressure gradients within the material. The char will also undergo oxidation that will contribute to the mass loss rate of the sample and will reduce the dimensions of the char layer.
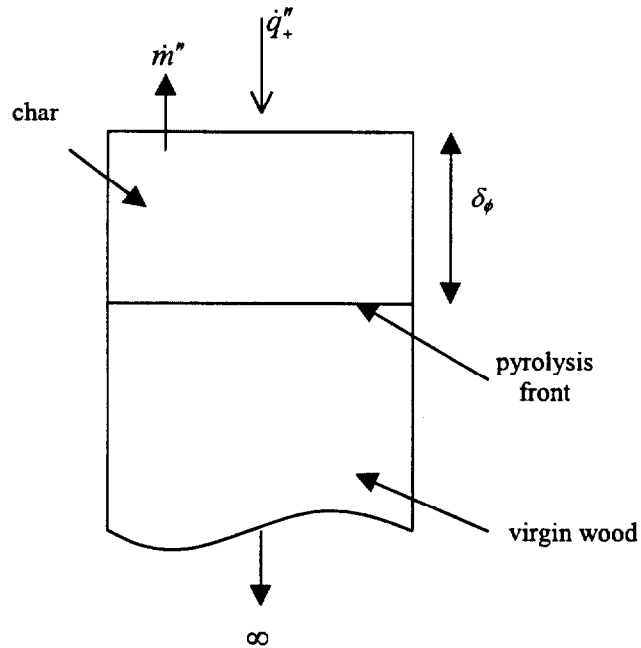
Figure 38. Schematic of model for decomposition.

4.1.2 Flame boundary condition

The heat flux from the flame by radiation and convection can be intimately coupled to the

burning rate of the mass supply rate of the fuel. In the Cone Calorimeter it is assumed

here that the flame radiant flux to its base is constant for a given material provided the

flame is tall i.e. its height H is greater than its diameter D (Figure 39).
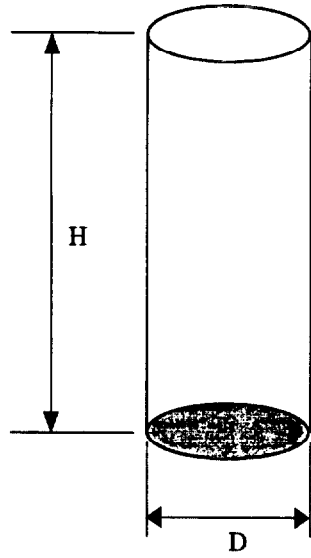
Figure 39. Assumed cylindrical flame.

The emissivity of a cylindrical flame ε_{fl} can be given as

$$\varepsilon_{fl} = 1 - e^{-\kappa L_{fl}}$$

<div align="right">Equation 78</div>

where κ is the absorption coefficient which depends on the fuel and L_{fl} is the mean beam

length [46]. Thus, as L_{fl} increases, ε_{fl} approaches a constant value.
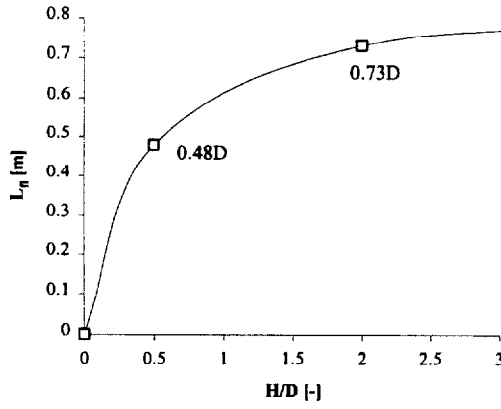
Figure 40. Relationship between flame height, diameter and mean beam length (from reference 47).

From Seigel & Howell [47] and shown in Figure 40, $\dfrac{L_{fl}}{D} \to 0.81$ for $\dfrac{H}{D} > 3$. Since, as

discussed by Rhodes & Quintiere [46], $\dot{q}''_{fl,rad} = \varepsilon_{fl}\sigma T_{fl}^4$ and $\dot{q}''_{fl,conv} \approx$ constant, it follows

that for $\dfrac{H}{D} > 3$, L_{fl} becomes constant, thus from Equation 78, ε_{fl} becomes constant and

hence $\dot{q}''_{fl,rad}$ is constant. As an approximation we assume that the flame heat flux $\dot{q}''_{fl,rad}$ is

always constant even during the growth or decay of the flame though it is recognised that

the flame heat flux is coupled to the fuel supply rate which affects the flame height,

thickness and surface convection.

Just after ignition the net surface heat flux is the sum of the external incident flux and the

flame heat flux minus radiation losses

$$\dot{q}''_+(T_s) = \dot{q}''_i + \dot{q}''_{fl} - \sigma\left(T_s^4 - T_0^4\right), \qquad x = 0$$

Equation 79

102

The absorption of the incident heat flux due to the presence of the flame is not considered. Rhodes and Quintiere [46] showed that the flame from a sample of black PMMA tested in the Cone Calorimeter is almost transparent (>90%) to the incident flux.

Thus just before ignition when $t = t_{ig}^-$, from Equation 16

$$\dot{q}'' = \dot{q}''_- = \dot{q}''_i - \sigma\left(T_{ig}^4 - T_0^4\right) - h_c\left(T_{ig} - T_0\right)$$

<div align="right">

Equation 80

</div>

and when $t = t_{ig}^+$, from Equation 79

$$\dot{q}'' = \dot{q}''_+\left(T_{ig}\right) = \dot{q}''_{fl} + \dot{q}''_i - \sigma\left(T_{ig}^4 - T_0^4\right)$$

<div align="right">

Equation 81

</div>

Hence there is a step-discontinuous change in the surface heat flux at ignition.

4.1.3 Conservation equations

The decomposition of the charring material is split into three regions; the char layer, the pyrolysis front and the virgin material (Figure 41). Each zone is considered in control volume form.

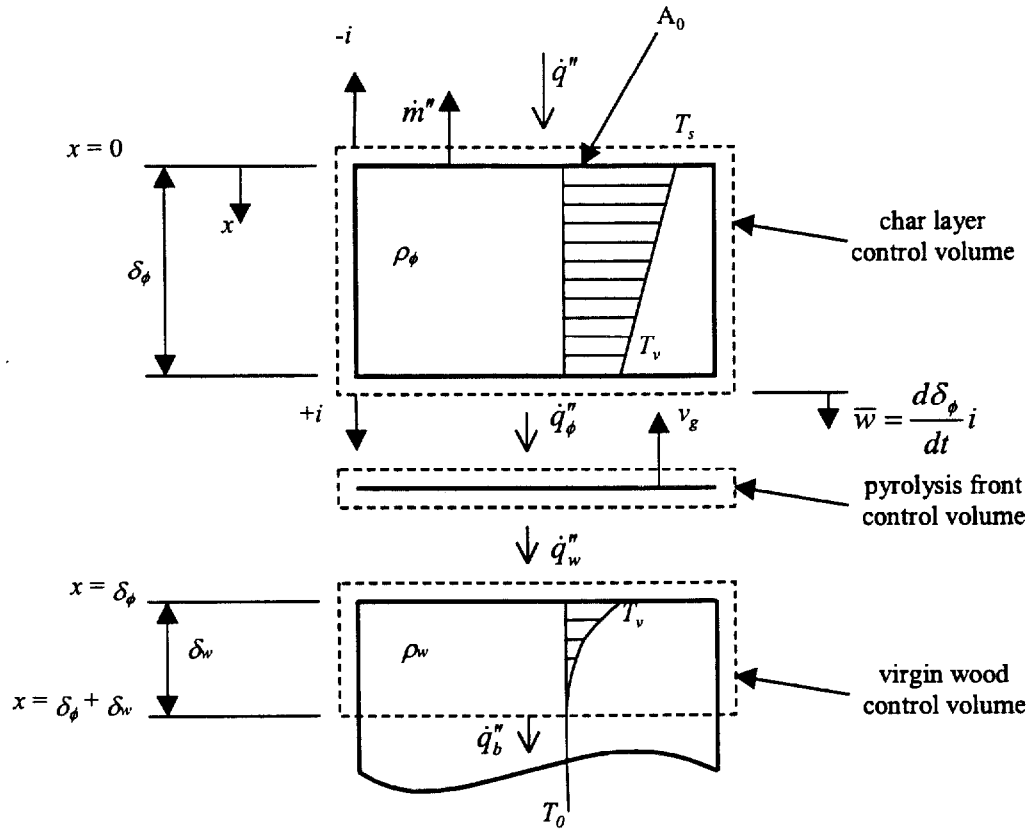**Figure 41.** Burning rate model control volumes.

a) Char layer

The char matrix contains solid char and fuel gases. These are described in terms of bulk

properties based on the volume V of the char-gas matrix such that

$$m_g = V \cdot \rho_g$$

Equation 82

where m_g and ρ_g are the mass and density of the gas respectively, and

$$m_\phi = V \cdot \rho_\phi$$

Equation 83

104

where m_ϕ and ρ_ϕ are the mass and density of the char respectively, and

$$m = m_g + m_\phi$$

thus

$$\rho = \rho_g + \rho_\phi$$

Using conservation of mass on the char layer control volume we obtain

$$\frac{d}{dt}\int_0^{\delta_\phi} A_0\,\rho\,dx - \dot{m}'' A_0.(-i) + A_0\,\rho_g\left(v_g.(-i) - \frac{d\delta_\phi}{dt}.i\right).(+i)$$

$$+ A_0\,\rho_\phi\left(\underbrace{v_\phi.(i)}_{=0} - \frac{d\delta_\phi}{dt}.i\right).(+i) = 0$$

Substituting Equation 84 into Equation 85 and dividing through by A_0

$$\frac{d\delta_\phi}{dt}\left(\rho_g + \rho_\phi\right) + \dot{m}'' - \rho_g v_g - \rho_g\frac{d\delta_\phi}{dt} - \rho_\phi\frac{d\delta_\phi}{dt} = 0$$

thus, cancelling through we obtain

$$\boxed{\dot{m}'' = \rho_g v_g}$$

Consider conservation of energy for the char layer

105

$$\frac{d}{dt}\int_0^{\delta_\phi}\left(\rho_g u_g + \rho_\phi u_\phi\right)dx - \dot{m}'' h_g(T_s)(-i)$$

$$+\rho_g h_g(T_v)\left[-v_g.(i)-\frac{d\delta_\phi}{dt}.(i)\right].(+i)$$

$$+\rho_\phi h_\phi(T_v)\left[0-\frac{d\delta_\phi}{dt}.(i)\right].(+i)$$

$$+\rho_\phi h_\phi(T_s)[0-0](-i)$$

$$=\dot{q}_+''(T_s)-\dot{q}_\phi''-p(T_v)\frac{d\delta_\phi}{dt}i.i$$

<div align="right">*Equation 88*</div>

where $\dot{q}_\phi''$ is the heat flux from the char to the pyrolysis front and from Equation 79,

$\dot{q}_+''(T_s)$ is the net surface heat flux at the temperature T_s. Rearranging we obtain

$$\frac{d}{dt}\int_0^{\delta_\phi}\left(\rho_g u_g + \rho_\phi u_\phi\right)dx + \dot{m}'' h_g(T_s)-\overbrace{\rho_g v_g}^{=\dot{m}''} h_g(T_v)$$

$$+\left[-\rho_g h_g(T_v)-\rho_\phi h_\phi(T_v)+p(T_v)\right]\frac{d\delta_\phi}{dt}$$

$$=\dot{q}_+''(T_s)-\dot{q}_\phi''$$

<div align="right">*Equation 89*</div>

Given that

$$h = u + \frac{p}{\rho}$$

<div align="right">*Equation 90*</div>

we can express

$$h_g(T_v)=u_g(T_v)+\frac{p(T_v)}{\rho_g}$$

<div align="right">*Equation 91*</div>

and

<div align="center">106</div>

$$h_\phi(T_v) = u_\phi(T_v) + \frac{p(T_v)}{\rho_\phi}$$

We can use Equation 91 and Equation 92 to write from Equation 89

$$-\rho_g h_g(T_v) - \rho_\phi h_\phi(T_v) + p(T_v) = -\rho_g\left[u_g(T_v) + \frac{p(T_v)}{\rho_g}\right] - \rho_\phi\left[u_\phi(T_v) + \frac{p(T_v)}{\rho_\phi}\right] + p(T_v)$$

$$= -\rho_g u_g(T_v) - \rho_g\frac{p(T_v)}{\rho_g} - \rho_\phi u_\phi(T_v) - \rho_\phi \cdot \frac{p(T_v)}{\rho_\phi} + p(T_v)$$

$$= -\rho_g u_g(T_v) - \rho_\phi u_\phi(T_v) - p(T_v)$$

Thus substituting back into Equation 89

$$\frac{d}{dt}\int_0^{\delta_\phi}\left(\rho_g u_g + \rho_\phi u_\phi\right)dx + \dot{m}'' h_g(T_s) - \dot{m}'' h_g(T_v)$$

$$+\left[-\rho_g u_g(T_v) - \rho_\phi u_\phi(T_v)\right]\frac{d\delta_\phi}{dt} = \dot{q}''_+(T_s) - \dot{q}''_\phi - p(T_v)$$

From thermodynamics, let $u_g = c_{v,g}T$, $u_\phi = c_\phi T$ and take $h_g = c_{p,g}T$. Assuming that

$c_{v,g} = c_{p,g} \equiv c_g$ then Equation 93 can be written as

$$\frac{d}{dt}\int_0^{\delta_\phi}\left(\rho_g c_g T + \rho_\phi c_\phi T\right)dx + \dot{m}'' c_g T_s - \dot{m}'' c_g T_v$$

$$+\left[-\rho_g c_g T_v - \rho_\phi c_\phi T_v\right]\frac{d\delta_\phi}{dt} = \dot{q}''_+ - \dot{q}''_\phi$$

Since

$$\left[-\rho_g c_g T_v - \rho_\phi c_\phi T_v\right]\frac{d\delta_\phi}{dt} \equiv \frac{d}{dt}\int_0^{\delta_\phi}\left(-\rho_g c_g T_v - \rho_\phi c_\phi T_v\right)dx$$

we can rearrange and write Equation 94 as

$$\frac{d}{dt}\int_0^{\delta_\phi}\left(\rho_g\,c_g\,T+\rho_\phi\,c_\phi\,T-\rho_g\,c_g\,T_v-\rho_\phi\,c_\phi\,T_v\right)dx+\dot{m}''c_g\left(T_s-T_v\right)$$

$$=\dot{q}''_+(T_s)-\dot{q}''_\phi+p(T_v)\frac{d\delta_\phi}{dt}$$

Equation 95

$$\frac{d}{dt}\int_0^{\delta_\phi}\left[\left(\rho_g\,c_g+\rho_\phi\,c_\phi\right)T-\left(\rho_g\,c_g+\rho_\phi\,c_\phi\right)T_v\right]dx+\dot{m}''c_g\left(T_s-T_v\right)$$

$$=\dot{q}''_+(T_s)-\dot{q}''_\phi+p(T_v)\frac{d\delta_\phi}{dt}$$

Equation 96

$$\left(\rho_g\,c_g+\rho_\phi\,c_\phi\right)\frac{d}{dt}\int_0^{\delta_\phi}(T-T_v)dx+\dot{m}''c_g\left(T_s-T_v\right)=\dot{q}''_+(T_s)-\dot{q}''_\phi+p(T_v)\frac{d\delta_\phi}{dt}$$

Equation 97

Typically $\rho_g\,c_g\ll\rho_\phi\,c_\phi$ since $\rho_g\approx1$ kg/m^3 and $c_g\approx1$ kJ/kg.K while $\rho_\phi\approx200$ kg/m^3

and $c_\phi\approx3$ kJ/kg.K. In addition, $\rho_\phi\,c_\phi\left(T-T_v\right)\gg p(T_v)$ since $\left(T-T_v\right)\approx100$ K and

$p\approx10^5$ N/m^2, thus $\rho_\phi\,c_\phi\left(T-T_v\right)\approx6\times10^4$ kJ/m^3 or 6×10^7 N/m^2. Thus Equation 97 can be

written as

$$\rho_\phi\,c_\phi\frac{d}{dt}\int_0^{\delta_\phi}(T-T_v)dx+\dot{m}''c_g\left(T_s-T_v\right)=\dot{q}''_+(T_s)-\dot{q}''_\phi$$

Equation 98

b) Pyrolysis front

Using conservation of mass on the pyrolysis front control volume we obtain

$$\underbrace{\frac{d}{dt}\int_{\delta_\phi}^{\delta_\phi} A_0\, \rho_w\, dx}_{=0} + A_0\, \rho_g\left[v_g.(-i)-\frac{d\delta_\phi}{dt}.(i)\right].(-i)+A_0\, \rho_\phi\left[0-\frac{d\delta_\phi}{dt}.(i)\right].(-i)$$

$$+A_0\, \rho_w\left[0-\frac{d\delta_\phi}{dt}.(i)\right].(+i)=0$$

Equation 99

Thus, dividing through by A_0

$$\rho_g\, v_g + \rho_g\frac{d\delta_\phi}{dt}+\rho_\phi\frac{d\delta_\phi}{dt}-\rho_w\frac{d\delta_\phi}{dt}=0$$

$$\left(\rho_w-\rho_\phi-\rho_g\right)\frac{d\delta_\phi}{dt}=\rho_g\, v_g$$

Equation 100

Substituting Equation 87 from the char layer analysis into Equation 100

$$\left(\rho_w-\rho_\phi-\rho_g\right)\frac{d\delta_\phi}{dt}=\dot{m}''$$

Equation 101

and assuming the density of the gas is small,

$$\boxed{\left(\rho_w-\rho_\phi\right)\frac{d\delta_\phi}{dt}=\dot{m}''}$$

Equation 102

Consider conservation of energy for the pyrolysis front

109

$$\underbrace{\frac{d}{dt}\int_{\delta_\phi}^{\delta_\phi}\rho_w u_w\, dx}_{=0} + \rho_g\, h_g(T_v)\left[v_g(-i)-\frac{d\delta_\phi}{dt}.(i)\right].(-i)$$

$$+\rho_\phi\, h_\phi(T_v)\left[0-\frac{d\delta_\phi}{dt}.(i)\right].(-i)$$

$$+\rho_w\, h_w(T_v)\left[0-\frac{d\delta_\phi}{dt}.(i)\right].(+i)$$

$$=\dot{q}_\phi'' - \dot{q}_w'' - \underbrace{p(T_v)\left(\frac{d\delta_\phi}{dt}.(i)\right).(-i)-p(T_v)\left(\frac{d\delta_\phi}{dt}.(i)\right).(+i)}_{=0}$$

<div align="right">Equation 103</div>

$$\underbrace{\rho_g v_g}_{=\dot{m}''}\, h_g(T_v)+\rho_g\, h_g(T_v)\frac{d\delta_\phi}{dt}+\rho_\phi\, h_\phi(T_v)\frac{d\delta_\phi}{dt}-\rho_w\, h_w(T_v)\frac{d\delta_\phi}{dt}=\dot{q}_\phi''-\dot{q}_w''$$

<div align="right">Equation 104</div>

$$\dot{m}''\, h_g(T_v)+\frac{d\delta_\phi}{dt}\left[\rho_g\, h_g(T_v)+\rho_\phi\, h_\phi(T_v)-\rho_w\, h_w(T_v)\right]=\dot{q}_\phi''-\dot{q}_w''$$

<div align="right">Equation 105</div>

Substituting Equation 101 into Equation 105

$$\left(\rho_w-\rho_\phi-\rho_g\right)\frac{d\delta_\phi}{dt}h_g(T_v)+\frac{d\delta_\phi}{dt}\left[\rho_g\, h_g(T_v)+\rho_\phi\, h_\phi(T_v)-\rho_w\, h_w(T_v)\right]=\dot{q}_\phi''-\dot{q}_w''$$

$$\frac{d\delta_\phi}{dt}\left[\rho_w\, h_g(T_v)-\rho_\phi\, h_g(T_v)-\underbrace{\rho_g\, h_g(T_v)+\rho_g\, h_g(T_v)}_{=0}+\rho_\phi\, h_\phi(T_v)-\rho_w\, h_w(T_v)\right]=\dot{q}_\phi''-\dot{q}_w''$$

thus

$$\rho_w\frac{d\delta_\phi}{dt}\left[\left\{h_g(T_v)-h_w(T_v)\right\}-\frac{\rho_\phi}{\rho_w}\left\{h_g(T_v)-h_\phi(T_v)\right\}\right]=\dot{q}_\phi''-\dot{q}_w''$$

<div align="right">Equation 106</div>

110

Based on the mass of the virgin wood, we define the heat of vaporisation or heat of pyrolysis as

$$\Delta H_v \equiv \{h_g(T_v) - h_w(T_v)\} - \frac{\rho_\phi}{\rho_w}\{h_g(T_v) - h_\phi(T_v)\}$$

then Equation 106 becomes

$$\boxed{\rho_w \frac{d\delta_\phi}{dt}[\Delta H_v] = \dot{q}''_\phi - \dot{q}''_w}$$

c) Virgin wood

Consider conservation of energy for the virgin wood control volume

$$\frac{d}{dt}\int_{\delta_\phi}^{\delta_\phi+\delta_w}\rho_w \, u_w \, dx + \rho_w \, h_w(T_v)\left[0 - \frac{d\delta_\phi}{dt}.(i)\right].(-i) + \rho_w \, h_w(T_0)\left[0 - \frac{d(\delta_\phi+\delta_w)}{dt}.(i)\right].(i)$$

$$= \dot{q}''_w - \dot{q}''_b - p(T_v)\frac{d\delta_\phi}{dt}.i.i - p(T_0)\frac{d(\delta_\phi+\delta_w)}{dt}.i.i$$

Let $u_w = c_w T$ and assume negligible heat loss to the back i.e. $\dot{q}''_b = 0$

$$\frac{d}{dt}\int_{\delta_\phi}^{\delta_\phi+\delta_w}\rho_w \, c_w \, T(x)dx + \rho_w \, h_w(T_v).\frac{d\delta_\phi}{dt} - \rho_w \, h_w(T_0).\frac{d(\delta_\phi+\delta_w)}{dt}$$

$$= \dot{q}''_w + p(T_v)\frac{d\delta_\phi}{dt} - p(T_0)\frac{d(\delta_\phi+\delta_w)}{dt}$$

Expanding for $h_w(T_v)$ using Equation 90, then

$$\frac{d}{dt}\int_{\delta_\phi}^{\delta_\phi+\delta_w} \rho_w\, c_w\, T(x)dx + \rho_w\left[u_w(T_v)+\frac{p(T_v)}{\rho_w}\right]\frac{d\delta_\phi}{dt} - \rho_w\left[u_w(T_0)+\frac{p(T_0)}{\rho_w}\right]\frac{d(\delta_\phi+\delta_w)}{dt}$$

$$= \dot{q}_w'' + p(T_v)\frac{d\delta_\phi}{dt} - p(T_0)\frac{d(\delta_\phi+\delta_w)}{dt}$$

Equation 111

Since $u_w = c_w\, T$ and the $p(T)$ terms cancel then Equation 111 can be written as

$$\frac{d}{dt}\int_{\delta_\phi}^{\delta_\phi+\delta_w} \rho_w\, c_w\, T(x)dx + \rho_w\, c_w\, T_v\cdot\frac{d\delta_\phi}{dt} - \rho_w\, c_w\, T_0\cdot\frac{d(\delta_\phi+\delta_w)}{dt} = \dot{q}_w''$$

$$\therefore \qquad \frac{d}{dt}\int_{\delta_\phi}^{\delta_\phi+\delta_w} \rho_w\, c_w\, T(x)dx + \rho_w\, c_w\, T_v\cdot\frac{d\delta_\phi}{dt} - \rho_w\, c_w\, T_0\cdot\frac{d\delta_\phi}{dt} - \rho_w\, c_w\, T_0\cdot\frac{d\delta_w}{dt} = \dot{q}_w''$$

$$\therefore \qquad \frac{d}{dt}\int_{\delta_\phi}^{\delta_\phi+\delta_w} \rho_w\, c_w\, T(x)dx + \rho_w\, c_w\frac{d\delta_\phi}{dt}(T_v-T_0) - \rho_w\, c_w\frac{d}{dt}\int_{\delta_\phi}^{\delta_\phi+\delta_w} T_0\, dx = \dot{q}_w''$$

Equation 112

Let $x = x'+\delta_\phi$ then Equation 112 becomes

$$\boxed{\rho_w\, c_w\frac{d}{dt}\int_{0}^{\delta_w}[T(x',t)-T_0]dx' + \rho_w\, c_w\frac{d\delta_\phi}{dt}(T_v-T_0) = \dot{q}_w''}$$

Equation 113

4.1.4 Temperature profiles

Taken from the analysis by Anderson [29], temperature profiles for the char layer and virgin wood are selected that satisfy the specified boundary conditions.

112

a) Char layer

The temperature profile in the char layer is assumed to be linear function with depth with boundary conditions such that

(i) when $x = 0$, $T = T_s$

(ii) when $x = \delta_\phi$, $T = T_v$

Consider a profile such that

$$T - T_v = (T_s - T_v)\left(1 - \frac{x}{\delta_\phi}\right)$$

Equation 114

When $x = 0$

$$T - T_v = (T_s - T_v)\underbrace{\left(1 - \frac{0}{\delta_\phi}\right)}_{=1}$$

thus

$$T = T_s$$

and boundary condition (i) is satisfied. When $x = \delta_\phi$

$$T - T_v = (T_s - T_v)\underbrace{\left(1 - \frac{\delta_\phi}{\delta_\phi}\right)}_{=0}$$

thus

$$T = T_v$$

and boundary condition (ii) is satisfied.

113

b) Virgin wood

The temperature profile in the virgin wood is assumed to be some function of depth with boundary conditions such that

(i)   when $x' = 0$, $T = T_v$

(ii)   when $x' = \delta_w$, $T = T_0$

(iii)   when $x' = \delta_w$, $\dfrac{\partial T}{\partial x} = 0$

Consider a profile such that

$$T - T_0 = (T_v - T_0)\left(1 - \frac{x'}{\delta_w}\right)^2$$

When $x' = 0$

$$T - T_0 = (T_v - T_0)\underbrace{\left(1 - \frac{0}{\delta_w}\right)^2}_{=1}$$

thus

$$T - T_0 = T_v - T_0$$

$$T = T_v$$

hence boundary condition (i) is satisfied. When $x' = \delta_w$

$$T - T_0 = (T_v - T_0)\underbrace{\left(1 - \frac{\delta_w}{\delta_w}\right)^2}_{=0}$$

114

thus

$$T = T_0$$

hence boundary condition (ii) is satisfied. By expanding Equation 115 we obtain

$$T - T_0 = (T_v - T_0)\left(1 - \frac{2x'}{\delta_w} + \frac{x'^2}{\delta_w^2}\right)$$

and differentiating with respect to x'

$$\frac{\partial}{\partial x'}(T - T_0) = \frac{\partial}{\partial x'}\left(T_v - \frac{2T_v x'}{\delta_w} + \frac{T_v x'^2}{\delta_w^2} + T_0 - \frac{2T_0 x'}{\delta_w} - \frac{2T_0 x'}{\delta_w} + \frac{T_0 x'^2}{\delta_w^2}\right)$$

$$\frac{\partial T}{\partial x'} - \frac{\partial T_0}{\partial x'} = \frac{\partial T_v}{\partial x'} - 2\frac{\partial T_v}{\partial x'}\cdot\left(\frac{1}{\delta_w}\right) + \frac{\partial T_v}{\partial x'}\cdot\left(\frac{2x'}{\delta_w^2}\right) - \frac{\partial T_0}{\partial x'} + 2\frac{\partial T_0}{\partial x'}\cdot\left(\frac{1}{\delta_w}\right) - \frac{\partial T_0}{\partial x'}\cdot\left(\frac{2x'}{\delta_w^2}\right)$$

since $x' = \delta_w$, by substitution

$$\frac{\partial T}{\partial x'} - \frac{\partial T_0}{\partial x'} = \frac{\partial T_v}{\partial x'} \underbrace{- 2\frac{\partial T_v}{\partial x'}\cdot\left(\frac{1}{\delta_w}\right) + \frac{\partial T_v}{\partial x'}\cdot\left(\frac{2\delta_w}{\delta_w^2}\right)}_{=0} - \frac{\partial T_0}{\partial x'} \underbrace{+ 2\frac{\partial T_0}{\partial x'}\cdot\left(\frac{1}{\delta_w}\right) - \frac{\partial T_0}{\partial x'}\cdot\left(\frac{2\delta_w}{\delta_w^2}\right)}_{=0}$$

thus

$$\frac{\partial T}{\partial x'} - \frac{\partial T_0}{\partial x'} = \frac{\partial T_v}{\partial x'} - \frac{\partial T_0}{\partial x'}$$

$$\frac{\partial T}{\partial x'} = \frac{\partial T_v}{\partial x'}$$

and since T_v is a constant then

$$\frac{\partial T}{\partial x'} = 0$$

which satisfies boundary condition (iii).

4.1.5 Governing equations

Now that we have considered the conservation of mass, conservation of energy and temperature profiles for the char layer, pyrolysis front and virgin wood we need to develop our governing equations.

Given that

$$\dot{q}_\phi'' = -\left(k_\phi \frac{\partial T}{\partial x}\right)_{x=\delta_\phi}$$

<div align="right">*Equation 117*</div>

Differentiating Equation 114

$$\frac{\partial T}{dx} = (T_s - T_v)\left(-\frac{1}{\delta_\phi}\right)$$

<div align="right">*Equation 118*</div>

and substituting into Equation 117

$$\boxed{\dot{q}_\phi'' = \frac{k_\phi(T_s - T_v)}{\delta_\phi}}$$

<div align="right">*Equation 119*</div>

and similarly

$$\dot{q}_w'' = -\left(k_w \frac{\partial T}{\partial x'}\right)_{x'=0}$$

<div align="right">*Equation 120*</div>

Differentiating Equation 116

$$\frac{\partial T}{\partial x'} = (T_v - T_0)\left(-\frac{2}{\delta_w} + \frac{2x'}{\delta_w^2}\right)$$

116

thus when $x' = 0$

$$\frac{\partial T}{\partial x'} = (T_v - T_0)\left(-\frac{2}{\delta_w}\right)$$

substituting Equation 121 into Equation 120

$$\dot{q}_w'' = \frac{2k_w(T_v - T_0)}{\delta_w}$$

From the analysis of the char layer, Equation 98 states

$$\rho_\phi c_\phi \int_0^{\delta_\phi}(T - T_v)dx + \dot{m}''c_g(T_s - T_v) = \dot{q}_+''(T_s) - \dot{q}_\phi''$$

and from the temperature profile in the char layer given in Equation 114, at time t

$$T - T_v = (T_s - T_v)\left(1 - \frac{x}{\delta_\phi}\right)$$

thus

$$\int_0^{\delta_\phi}(T - T_v)\,dx = \int_0^{\delta_\phi}(T_s - T_v)\left(1 - \frac{x}{\delta_\phi}\right)dx$$

$$= (T_s - T_v)\left[1 - \frac{1}{2}\frac{x^2}{\delta_\phi}\right]_0^{\delta_\phi}$$

$$= (T_s - T_v)\left[1 - \frac{\delta_\phi^2}{2\delta_\phi}\right] - \left[1 - \frac{0}{2\delta_\phi}\right]$$

$$= \frac{1}{2}(T_s - T_v)\delta_\phi$$

substituting Equation 123 and Equation 119 into Equation 98 we obtain

117

$$\boxed{\frac{\rho_\phi c_\phi}{2} \frac{d}{dt}(T_s - T_v)\delta_\phi + \dot{m}'' c_g (T_s - T_v) = \dot{q}''_+(T_s) - \frac{k_\phi(T_s - T_v)}{\delta_\phi}}$$

<div align="right">Equation 124</div>

From the analysis of the pyrolysis front Equation 102 states

$$(\rho_w - \rho_\phi)\frac{d\delta_\phi}{dt} = \dot{m}''$$

substituting for the char fraction, $\phi \equiv \dfrac{\rho_\phi}{\rho_w}$

$$\dot{m}'' = \rho_w (1 - \phi)\frac{d\delta_\phi}{dt}$$

$$\boxed{\frac{\dot{m}''}{(1 - \phi)} = \rho_w \frac{d\delta_\phi}{dt}}$$

<div align="right">Equation 125</div>

Equation 108 states

$$\rho_w \frac{d\delta_\phi}{dt} \Delta H_v = \dot{q}''_\phi - \dot{q}''_w$$

substituting Equation 108 with Equation 119 and Equation 122

$$\rho_w \frac{d\delta_\phi}{dt} \Delta H_v = \frac{k_\phi(T_s - T_v)}{\delta_\phi} - \frac{2k_w(T_v - T_0)}{\delta_w}$$

<div align="right">Equation 126</div>

substituting Equation 125 gives

$$\boxed{\frac{\dot{m}''}{(1 - \phi)} \Delta H_v = \frac{k_\phi(T_s - T_v)}{\delta_\phi} - \frac{2k_w(T_v - T_0)}{\delta_w}}$$

<div align="right">Equation 127</div>

From the analysis of the virgin wood, Equation 113 states

<div align="center">118</div>

$$\rho_w c_w \frac{d}{dt} \int_0^{\delta_w} [T(x',t) - T_0] dx' + \rho_w \frac{d\delta_\phi}{dt} c_w (T_v - T_0) = \dot{q}_w''$$

from the temperature profile in the virgin wood given in Equation 115, at time t and x'

$$T - T_0 = (T_v - T_0)\left(1 - \frac{x'}{\delta_w}\right)^2$$

thus

$$\int_0^{\delta_w} [T(x',t) - T_0] dx' = \int_0^{\delta_w} (T_v - T_0)\left(1 - \frac{x'}{\delta_w}\right)^2 dx'$$

$$= (T_v - T_0) \int_0^{\delta_w} 1 - \frac{2x'}{\delta_w} + \frac{x'^2}{\delta_w^2} dx'$$

$$= (T_v - T_0)\left[x' - \frac{2}{\delta_w}\frac{1}{2}x'^2 + \frac{1}{\delta_w^2}\frac{1}{3}x'^3\right]_0^{\delta_w}$$

$$= (T_v - T_0)\left[\delta_w - \frac{\delta_w^2}{\delta_w} + \frac{\delta_w^3}{3\delta_w^2}\right]$$

$$= \frac{(T_v - T_0)}{3}\delta_w$$

Equation 128

substituting Equation 120, Equation 125 and Equation 128 into Equation 113

$$\rho_w c_w \frac{(T_v - T_\infty)}{3}\frac{d\delta_w}{dt} + \frac{\dot{m}''}{(1-\phi)} c_w (T_v - T_0) = \frac{2k_w(T_v - T_0)}{\delta_w}$$

dividing through by $\rho_w c_w (T_v - T_0)$

$$\boxed{\frac{1}{3}\frac{d\delta_w}{dt} + \frac{\dot{m}''}{\rho_w(1-\phi)} = \frac{2\left(k_w / \rho_w c_w\right)}{\delta_w}}$$

Equation 129

119

Adding Equation 124 and Equation 127 we obtain

$$\frac{\rho_\phi c_\phi}{2}\frac{d}{dt}(T_s - T_v)\delta_\phi + \dot{m}''c_g(T_s - T_v) + \frac{\dot{m}''}{(1-\phi)}[\Delta H_v]$$

$$= \dot{q}''_+(T_s) - \frac{k_\phi(T_s - T_v)}{\delta_\phi} + \frac{k_\phi(T_s - T_v)}{\delta_\phi} - \frac{2k_w(T_v - T_0)}{\delta_w}$$

$$\frac{\rho_\phi c_\phi}{2}\frac{d}{dt}(T_s - T_v)\delta_\phi + \dot{m}''c_g(T_s - T_v) + \frac{\dot{m}''}{(1-\phi)}[\Delta H_v] = \dot{q}''_+(T_s) - \frac{2k_w(T_v - T_0)}{\delta_w}$$

Equation 130

$$\frac{\rho_\phi c_\phi}{2}\left(\frac{d}{dt}T_s - \frac{d}{dt}T_v\right)\delta_\phi + \dot{m}''c_g(T_s - T_v) + \frac{\dot{m}''}{(1-\phi)}[\Delta H_v] = \dot{q}''_+(T_s) - \frac{2k_w(T_v - T_0)}{\delta_w}$$

Equation 131

If the time just after ignition is considered then $t = t_{ig}^+$ with $T_s = T_v = T_{ig}$, $\dot{m}'' = \dot{m}''_{ig}$ and

$\delta_w = \delta_{ig}$. Thus, from Equation 131

$$\underbrace{\frac{\rho_\phi c_\phi}{2}\left(\frac{d}{dt}T_s - \frac{d}{dt}T_v\right)\delta_\phi}_{=0} + \underbrace{\dot{m}''c_g(T_s - T_v)}_{=0} + \frac{\dot{m}''}{(1-\phi)}[\Delta H_v] = \dot{q}''_+(T_s) - \frac{2k_w(T_v - T_0)}{\delta_w}$$

hence

$$\dot{m}''_{ig} = \frac{(1-\phi)}{\Delta H_v}\left[\dot{q}''_+ - \frac{2k_w(T_{ig} - T_0)}{\delta_{ig}}\right]$$

Equation 132

Assuming that at ignition $T_v = T_{ig}$, $\delta_w = \delta_{ig}$ and $\dot{q}''_w = \dot{q}''_-$ then from Equation 122

$$\delta_{ig} = \frac{2k_w(T_v - T_0)}{\dot{q}''_-}$$

Equation 133

Substituting for δ_{ig} in Equation 132

120

$$\dot{m}''_{ig} = \frac{(1-\phi)}{\Delta H_v}\left[\dot{q}''_+(T_s) - 2k_w(T_{ig} - T_0)\frac{\dot{q}''_-}{2k_w(T_{ig} - T_0)}\right]$$

thus

$$\dot{m}''_{ig} = \frac{(1-\phi)}{\Delta H_v}[\dot{q}''_+(T_s) - \dot{q}''_-]$$

from the ignition analysis, Equation 16 can be used to approximate $\dot{q}''_-$ such that

$$\dot{q}''_- = \dot{q}''\!\left(t_{ig}^{\ -}\right) = \dot{q}''_i - \sigma(T_{ig}^4 - T_0^4) - h_c(T_{ig} - T_0)$$

and from Equation 81

$$\dot{q}''_+ = \dot{q}''\!\left(t_{ig}^{\ +}\right) = \dot{q}''_{fl} + \dot{q}''_i - \sigma T_{ig}^4$$

Thus substituting into Equation 134 we obtain

$$\dot{m}''_{ig} = \frac{(1-\phi)}{\Delta H_v}[\dot{q}''_{fl} + \dot{q}''_i - \sigma(T_{ig}^4 - T_0^4) - \{\dot{q}''_i - \sigma(T_{ig}^4 - T_0^4) - h_c(T_{ig} - T_0)\}]$$

hence

$$\dot{m}''_{ig} = \frac{(1-\phi)}{\Delta H_v}[\dot{q}''_{fl} + h_c(T_{ig} - T_0)]$$

It is interesting to note that Equation 135 suggests that the mass loss at ignition does not explicitly depend on the incident heat flux but only on the flame heat flux $\dot{q}''_{fl}$. This fits with the assumption (c) given in § 4.1.1. However, it will be shown later that the char fraction ϕ and the convective heat transfer coffeicient h_c can be considered to be functions of the incident heat flux.

4.1.6 Dimensionless analysis

Finally we make the governing equations dimensionless by defining the following dimensionless variables specified by Anderson [29]

$$M \equiv \frac{\dot{m}'' L}{(1-\phi)\dot{q}_+''(T_s)}; \qquad M_{ig} \equiv \frac{\dot{m}_{ig}'' L}{(1-\phi)\dot{q}_+''(T_s)}$$

$$\Delta \equiv \frac{\delta_w}{\delta_s}; \qquad \Delta_\phi \equiv \frac{\delta_\phi}{\delta_s}; \qquad \Delta_{ig} \equiv \frac{\delta_{ig}}{\delta_s}$$

$$\theta \equiv \frac{T}{T_v}; \qquad \theta_s \equiv \frac{T_s}{T_v}; \qquad \theta_0 \equiv \frac{T_0}{T_v}$$

$$\tau \equiv \frac{\alpha t}{\delta_s^2}; \qquad \phi \equiv \frac{\rho_\phi}{\rho_w}$$

$$\delta_s \equiv \frac{2 k_w L}{c_w \dot{q}_+''(T_v)}$$

plus the dimensional variable

$$L \equiv \Delta H_v + c_w (T_v - T_0)$$

where L is the heat of gasification per unit mass of virgin wood.

From Equation 130

$$\frac{\rho_\phi c_\phi}{2}\frac{d}{dt}(T_s - T_v)\delta_\phi + \dot{m}'' c_g (T_s - T_v) + \frac{\dot{m}''}{(1-\phi)}[\Delta H_v] = \dot{q}_+''(T_s) - \frac{2 k_w (T_v - T_0)}{\delta_w}$$

Substituting for the dimensionless variables M, τ, θ_s, θ_0, Δ and Δ_ϕ

$$\frac{\rho_\phi c_\phi}{2}\frac{d}{d\left(\tau \delta_s^2 / \alpha\right)}\left[T_v (\theta_s - 1)\Delta_\phi \, \delta_s\right] + \frac{M(1-\phi)}{L}\dot{q}_+''(T_s) c_g T_v (\theta_s - 1)$$

$$+ \frac{M(1-\phi)}{L}\dot{q}_+''(T_s)\frac{\Delta H_v}{(1-\phi)} = \dot{q}_+''(T_s) - \frac{2 k_w T_v (1-\theta_0)}{\Delta \delta_s}$$

122

Multiply through by $\dfrac{\delta_s}{k_w T_v}$ to obtain

$$\frac{\delta_s}{k_w T_v} \cdot \frac{\rho_\phi c_\phi}{2} \frac{k_w}{\rho_w c_w \delta_s} \frac{d}{d\tau}\left[T_v (\theta_s - 1)\Delta_\phi\right] + \frac{\delta_s}{k_w T_v} \cdot \frac{M(1-\phi)}{L} \dot{q}''_+(T_s) c_g T_v (\theta_s - 1)$$

$$+ \frac{\delta_s}{k_w T_v} \cdot \frac{M \Delta H_v}{L} \dot{q}''_+(T_s) = \frac{\delta_s}{k_w T_v} \cdot \dot{q}''_+(T_s) - \frac{\delta_s}{k_w T_v} \cdot \frac{2 k_w T_v (1-\theta_0)}{\Delta \delta_s}$$

Since $\delta_s \equiv \dfrac{2 k_w L}{c_w \dot{q}''_+(T_v)}$

$$\frac{1}{2}\left(\frac{\rho_\phi c_\phi}{\rho_w c_w}\right)\frac{d}{d\tau}\left[(\theta_s - 1)\Delta_\phi\right] + \frac{2 k_w L}{c_w \dot{q}''_+(T_v)} \cdot \frac{M(1-\phi)}{k_w L} \dot{q}''_+(T_s) c_g (\theta_s - 1)$$

$$+ \frac{2 k_w L}{c_w \dot{q}''_+(T_v)} \cdot \frac{1}{k_w T_v} \cdot \frac{M \Delta H_v}{L} \dot{q}''_+(T_s) = \frac{2 k_w L}{c_w \dot{q}''_+(T_v)} \cdot \frac{1}{k_w T_v} \cdot \dot{q}''_+(T_s) - \frac{2(1-\theta_0)}{\Delta}$$

$$\therefore \quad \frac{1}{2}\left(\frac{\rho_\phi c_\phi}{\rho_w c_w}\right)\frac{d}{d\tau}\left[(\theta_s - 1)\Delta_\phi\right] + 2\left(\frac{c_g}{c_w}\right)(\theta_s - 1)(1-\phi)M$$

$$+ 2\left(\frac{\Delta H_v}{c_w T_v}\right)M = \frac{2L}{c_w T_v} \cdot \frac{\dot{q}''_+(T_s)}{\dot{q}''_+(T_v)} - \frac{2(1-\theta_0)}{\Delta}$$

Thus substituting for $\phi \equiv \dfrac{\rho_\phi}{\rho_w}$ and rearranging,

$$\boxed{\frac{1}{4}\phi\left(\frac{c_\phi}{c_w}\right)\frac{d}{d\tau}\left[(\theta_s - 1)\Delta_\phi\right] + \left[(1-\phi)\left(\frac{c_g}{c_w}\right)(\theta_s - 1) + \frac{\Delta H_v}{c_w T_v}\right]M = \frac{L}{c_w T_v}\frac{\dot{q}''_+(T_s)}{\dot{q}''_+(T_v)} - \frac{(1-\theta_0)}{\Delta}}$$

Equation 136

From Equation 127

$$\frac{\dot{m}''}{(1-\phi)}\Delta H_v = \frac{k_\phi(T_s - T_v)}{\delta_\phi} - \frac{2 k_w(T_v - T_0)}{\delta_w}$$

substituting for M, Δ_ϕ, Δ, θ_s, θ, and θ_0

123

$$\frac{M(1-\phi)\dot{q}''_+(T_s)}{L}\frac{\Delta H_v}{(1-\phi)} = k_\phi \frac{1}{\delta_s \Delta_\phi}(\theta_s - 1)T_v - 2k_w \frac{1}{\delta_s \Delta}(1-\theta_0)T_v$$

and then substituting for δ_s

$$\frac{M\dot{q}''_+(T_s)\Delta H_v}{L} = k_\phi \frac{c_w \dot{q}''_+(T_v)}{2k_w L}\frac{1}{\Delta_\phi}(\theta_s - 1)T_v - 2k_w \frac{c_w \dot{q}''_+(T_v)}{2k_w L}\frac{1}{\Delta}(1-\theta_0)T_v$$

thus

$$M = \frac{\dot{q}''_+(T_v)}{\dot{q}''_+(T_s)}\frac{T_v c_w}{\Delta H_v}\left[\left(\frac{k_\phi}{k_w}\right)\frac{1}{2}\frac{(\theta_s - 1)}{\Delta_\phi} - \frac{(1-\theta_0)}{\Delta}\right]$$

Equation 137

From Equation 129

$$\frac{1}{3}\frac{d\delta_w}{dt} + \frac{\dot{m}''}{\rho_w(1-\phi)} = \frac{2\left(k_w \middle/ \rho_w c_w\right)}{\delta_w}$$

substituting for M, Δ and τ

$$\frac{1}{3}\frac{d(\Delta\delta_s)}{d\left(\dfrac{\tau\delta_s^2}{\alpha}\right)} + \frac{M(1-\phi)\dot{q}''_+(T_s)}{L}\cdot\frac{1}{\rho_w(1-\phi)} = \frac{2k_w}{\rho_w c_w}\cdot\frac{1}{\Delta\delta_s}$$

$$\therefore \quad \frac{1}{3}\frac{d\Delta}{d\tau}\frac{\alpha}{\delta_s} + \frac{M\dot{q}''_+(T_s)}{\rho_w L} = \frac{2k_w}{\rho_w c_w}\cdot\frac{1}{\Delta\delta_s}$$

$$\therefore \quad \frac{1}{3}\frac{d\Delta}{d\tau} + \frac{\delta_s \rho_w c_w M\dot{q}''_+(T_s)}{k_w \rho_w L} = \frac{2k_w}{\rho_w c_w}\cdot\frac{\rho_w c_w}{k_w}\frac{1}{\Delta}$$

$$\therefore \quad \frac{1}{3}\frac{d\Delta}{d\tau} + \frac{2k_w L}{c_w \dot{q}''_+(T_v)}\frac{c_w M\dot{q}''_+(T_s)}{k_w L} = \frac{2}{\Delta}$$

thus

$$\frac{1}{3}\frac{d\Delta}{d\tau} + 2M = \frac{2}{\Delta}$$

a) At ignition, from Equation 134

$$\dot{m}_{ig}'' = \frac{(1-\phi)}{\Delta H_v}[\dot{q}_+''(T_s) - \dot{q}_-'']$$

Substituting for the dimensionless variable M_{ig}

$$M_{ig} = \frac{L}{(1-\phi)\dot{q}_+''}\frac{(1-\phi)}{\Delta H_v}[\dot{q}_+''(T_s) - \dot{q}_-'']$$

thus

$$M_{ig} = \left(\frac{L}{\Delta H_v}\right)\left[1 - \frac{\dot{q}_-''}{\dot{q}_+''(T_s)}\right]$$

From Equation 27

$$\delta = \sqrt{3\frac{k_w}{\rho_w c_w}\left[\frac{2-\beta}{1-\beta}\right]t}$$

Since $\Delta_{ig} \equiv \frac{\delta_{ig}}{\delta_s}$, at ignition $t = t_{ig}$ and $\dot{q}_+''(T_s) = \dot{q}_+''(T_{ig})$, thus

$$\Delta_{ig} = \frac{\sqrt{3\frac{k_w}{\rho_w c_w}\left[\frac{2-\beta_{ig}}{1-\beta_{ig}}\right]t_{ig}}}{\frac{2k_w L}{c_w \dot{q}_+''(T_{ig})}}$$

From Equation 28

$$t_{ig} = \frac{4}{3}k_w \rho_w c_w\left[\frac{1-\beta_{ig}}{2-\beta_{ig}}\right]\frac{(T_{ig}-T_0)^2}{[\dot{q}''(t_{ig})]^2}$$

125

substituting into Equation 140 and cancelling common terms

$$\Delta_{ig} = \left[\frac{c_w \left(T_{ig} - T_0 \right)}{L} \right] \left[\frac{\dot{q}_+''\left(T_{ig} \right)}{\dot{q}_i''\left(t_{ig} \right)} \right]$$

b) Consider times just after ignition (i.e. small-time). From Equation 125

$$\frac{\dot{m}''}{(1 - \phi)} = \rho_w \frac{d\delta_\phi}{dt}$$

Substituting for the dimensionless variables M, τ and Δ_ϕ

$$\frac{M \dot{q}_+''\left(T_s \right)}{L} = \rho_w \frac{d\left(\Delta_\phi \delta_s \right)}{d\left(\tau \delta_s^2 / \alpha \right)}$$

$$\frac{M \dot{q}_+''\left(T_s \right)}{L} = \frac{k_w}{c_w \delta_s} \frac{d\Delta_\phi}{d\tau}$$

Substituting for δ_s

$$M = \frac{L}{\dot{q}_+''\left(T_s \right)} \cdot \frac{k_w}{c_w} \cdot \frac{c_w \dot{q}_+''\left(T_v \right)}{2 k_w L} \cdot \frac{d\Delta_\phi}{d\tau}$$

$$M = \frac{1}{2} \cdot \frac{d\Delta_\phi}{d\tau}$$

At time τ_{ig}, char depth $\Delta_\phi = 0$ and at time τ, char depth is Δ_ϕ. Integrating Equation 142

$$\int_{\tau_{ig}}^{\tau} M \, d\tau = \int_0^{\Delta_\phi} \frac{1}{2} \, d\Delta_\phi$$

126

$$M\left(\tau - \tau_{ig}\right) = \frac{1}{2}\Delta_\phi$$

since $M \approx M_{ig}$ at τ_{ig} then

$$\boxed{\Delta_\phi \approx 2M_{ig}\left(\tau - \tau_{ig}\right)}$$

From Equation 136, with no char $\Delta_\phi = 0$ and assuming $T_s = T_v$ thus $\theta_s = 1$ and

$$\dot{q}''_+(T_s) \rightarrow \dot{q}''_+(T_v)$$

$$\underbrace{\frac{1}{4}\phi\left(\frac{c_\phi}{c_w}\right)\frac{d}{d\tau}[(\theta_s - 1)\Delta_\phi]}_{=0} + \left[\underbrace{(1-\phi)\left(\frac{c_g}{c_w}\right)(\theta_s - 1)}_{=0} + \left(\frac{\Delta H_v}{c_w T_v}\right)\right]M = \left(\frac{L}{c_w T_v}\right)\underbrace{\frac{\dot{q}''_+(T_s)}{\dot{q}''_+(T_v)}}_{\approx 1} - \frac{(1-\theta_0)}{\Delta}$$

$$\therefore \quad \left(\frac{\Delta H_v}{c_w T_v}\right)M = \frac{L}{c_w T_v} - \frac{(1-\theta_0)}{\Delta}$$

$$\therefore \quad M = \frac{L}{\Delta H_v} - \frac{c_w T_v}{\Delta H_v}\cdot\frac{(1-\theta_0)}{\Delta}$$

Since $\theta_0 \equiv \frac{T_0}{T_v}$ then

$$c_w T_v(1-\theta_0) = c_w T_v\left(1 - \frac{T_0}{T_v}\right) = c_w(T_v - T_0)$$

substituting back into Equation 144

$$M = \frac{L}{\Delta H_v} - \frac{c_w(T_v - T_0)}{\Delta H_v}\cdot\frac{1}{\Delta}$$

alternatively

127

$$M = \frac{L}{\Delta H_v}\left[1 - \frac{c_w\left(T_v - T_0\right)}{L} \cdot \frac{1}{\Delta}\right]$$

<div align="right">*Equation 146*</div>

From Equation 138

$$\frac{1}{3}\frac{d\Delta}{d\tau} + 2M = \frac{2}{\Delta}$$

substituting for M using Equation 145 and rearranging

$$\frac{1}{3}\frac{d\Delta}{d\tau} + 2\left[\frac{L}{\Delta H_v} - \frac{c_w\left(T_v - T_0\right)}{\Delta H_v} \cdot \frac{1}{\Delta} - \frac{1}{\Delta}\right] = 0$$

<div align="right">*Equation 147*</div>

Since, from our definition of L

$$c_w\left(T_v - T_0\right) = L - \Delta H_v$$

Equation 147 becomes

$$\frac{1}{3}\frac{d\Delta}{d\tau} + 2\left[\frac{L}{\Delta H_v} - \frac{\left(L - \Delta H_v\right)}{\Delta H_v} \cdot \frac{1}{\Delta} - \frac{1}{\Delta}\right] = 0$$

$$\frac{1}{3}\frac{d\Delta}{d\tau} + 2\left[\frac{L}{\Delta H_v} - \frac{L}{\Delta H_v} \cdot \frac{1}{\Delta} + \underbrace{\frac{\Delta H_v}{\Delta H_v} \cdot \frac{1}{\Delta} - \frac{1}{\Delta}}_{=0}\right] = 0$$

$$\frac{d\Delta}{d\tau} = -6\left(\frac{L}{\Delta H_v}\right)\left[1 - \frac{1}{\Delta}\right]$$

$$\frac{d\Delta}{d\tau} = 6\left(\frac{L}{\Delta H_v}\right)\left[\frac{1 - \Delta}{\Delta}\right]$$

<div align="right">*Equation 148*</div>

Let $\psi = 1 - \Delta$

<div align="center">128</div>

$$\frac{d(1-\psi)}{d\tau} = 6\left(\frac{L}{\Delta H_v}\right)\left[\frac{\psi}{1-\psi}\right]$$

$$\therefore \quad \frac{\frac{d\psi}{d\tau}(1-\psi)}{\psi} = -6\left(\frac{L}{\Delta H_v}\right)$$

by integration of Equation 149

$$\int_{\tau_{ig}}^{\tau}\left[\frac{1}{\psi}\frac{d\psi}{d\tau} - \frac{d\psi}{d\tau}\right] = -6\left(\frac{L}{\Delta H_v}\right)$$

$$\therefore \quad \ln\left(\frac{\psi}{\psi_{ig}}\right) - (\psi - \psi_{ig}) = -6\left(\frac{L}{\Delta H_v}\right)(\tau - \tau_{ig})$$

$$\therefore \quad \frac{1-\Delta}{1-\Delta_{ig}} = \exp\left[(\Delta_{ig} - \Delta) - 6\left(\frac{L}{\Delta H_v}\right)(\tau - \tau_{ig})\right]$$

Since at early times $\Delta - \Delta_{ig}$ is small, $\tau - \tau_{ig}$ is small and $e^x \approx 1 + x$ for small x, Equation

150 can be approximated as

$$\frac{1-\Delta}{1-\Delta_{ig}} \approx 1 - (\Delta - \Delta_{ig}) + 6\left(\frac{L}{\Delta H_v}\right)(\tau - \tau_{ig})$$

by rearranging

$$\Delta \approx 1 - (1 - \Delta_{ig}) + \underbrace{(1 - \Delta_{ig})(\Delta - \Delta_{ig})}_{\approx 0} + 6\left(\frac{L}{\Delta H_v}\right)(1 - \Delta_{ig})(\tau - \tau_{ig})$$

$$\boxed{\Delta \approx \Delta_{ig} + 6\left(\frac{L}{\Delta H_v}\right)(1 - \Delta_{ig})(\tau - \tau_{ig})}$$

c) Finally consider times much later than the ignition time (i.e. long-time)

Let the char depth rate approach zero, $\dfrac{d\Delta_\phi}{d\tau} \to 0$, the surface temperature approach a

constant, $\dfrac{d\theta_s}{d\tau} \to 0$, and the burning rate tend to zero, $M \to 0$. From Equation 138

$$\frac{1}{3}\frac{d\Delta}{d\tau} + 2M = \frac{2}{\Delta}$$

$$\therefore \qquad \frac{1}{3}\frac{d\Delta}{d\tau} \approx \frac{2}{\Delta}$$

By integration between ignition and time τ

$$\int_{\Delta_{ig}}^{\Delta} \Delta \, d\Delta = \int_{\tau_{ig}}^{\tau} 6 \, d\tau$$

$$\frac{\Delta^2 - \Delta_{ig}^2}{2} = 6\left(\tau - \tau_{ig}\right)$$

thus

$$\boxed{\Delta \approx \sqrt{\Delta_{ig}^2 + 12\left(\tau - \tau_{ig}\right)}}$$

Equation 152

From Equation 136

$$\frac{1}{4}\phi\left(\frac{c_\phi}{c_w}\right)\frac{d}{d\tau}\left[(\theta_s - 1)\Delta_\phi\right] + \left[(1-\phi)\left(\frac{c_g}{c_w}\right)(\theta_s - 1) + \frac{\Delta H_v}{c_w T_v}\right]M = \frac{L}{c_w T_v}\frac{\dot{q}_+''(T_s)}{\dot{q}_+''(T_v)} - \frac{(1-\theta_0)}{\Delta}$$

since $\dfrac{d\theta_s}{d\tau} \to 0$ and $M \to 0$

$$\frac{\dot{q}_+''(T_s)}{\dot{q}_+''(T_v)} \approx \frac{c_w T_v}{L}\frac{(1-\theta_0)}{\Delta}$$

From Equation 79

130

$$\dot{q}''_+(T_s) = \dot{q}''_i + \dot{q}''_{fl} - \sigma\left(T_s^4 - T_0^4\right)$$

thus by substituting, rearranging and dividing by T_v^4

$$\frac{\sigma\left(T_s^4 - T_0^4\right)}{T_v^4} = \frac{\dot{q}''_{fl} + \dot{q}''_i}{T_v^4} - \frac{\dot{q}''_+(T_v)}{T_v^4}\left(\frac{c_w T_v}{4}\right)\left(\frac{1-\theta_0}{\Delta}\right)$$

As $\Delta \to \infty$ then

$$\frac{\sigma\left(T_s^4 - T_0^4\right)}{T_v^4} \approx \frac{\dot{q}''_{fl} + \dot{q}''_i}{T_v^4}$$

substituting for θ_s and θ_0

$$\theta_s^4 - \theta_0^4 \approx \frac{\dot{q}''_{fl} + \dot{q}''_i}{\sigma T_v^4}$$

$$\therefore \qquad \theta_s \approx \left[\frac{\dot{q}''_{fl} + \dot{q}''_i}{\sigma T_v^4} + \theta_0^4\right]^{1/4}$$

assuming θ_0^4 is small then

$$\boxed{\theta_s \approx \left[\frac{\dot{q}''_{fl} + \dot{q}''_i}{\sigma T_v^4}\right]^{1/4}}$$

Equation 153

Equating M's in Equation 137 and Equation 142

$$\frac{1}{2}\frac{d\Delta_\phi}{d\tau} = \frac{\dot{q}''_+(T_v)}{\dot{q}''_+(T_s)}\frac{T_v c_w}{\Delta H_v}\left[\left(\frac{k_\phi}{k_w}\right)\frac{1}{2}\frac{(\theta_s - 1)}{\Delta_\phi} - \frac{(1-\theta_0)}{\Delta}\right]$$

assuming $T_s = T_v$ thus $\dot{q}''_+(T_s) \to \dot{q}''_+(T_v)$

$$\frac{1}{2}\frac{d\Delta_\phi}{d\tau} = \frac{T_v c_w}{\Delta H_v}\left[\left(\frac{k_\phi}{k_w}\right)\frac{1}{2}\frac{(\theta_s - 1)}{\Delta_\phi} - \frac{(1-\theta_0)}{\Delta}\right]$$

131

further assume θ_s is constant, the thermal penetration depth approaches infinity, $\Delta \rightarrow \infty$,

as time tends to infinity, $\tau \rightarrow \infty$ and finally at time τ_{ig} the char depth $\Delta_\phi = 0$

$$\int_0^{\Delta_\phi} \Delta_\phi \, d\Delta_\phi \approx \int_{\tau_{ig}}^{\tau} \left(\frac{c_w T_v}{\Delta H_v} \right) \left(\frac{k_\phi}{k_w} \right) (\theta_s - 1) \, d\tau$$

thus

$$\frac{\Delta_\phi^2}{2} \approx \left(\frac{c_w T_v}{\Delta H_v} \right) \left(\frac{k_\phi}{k_w} \right) (\theta_s - 1)(\tau - \tau_{ig})$$

Since, from § 2.6, $\phi \approx \dfrac{k_\phi}{k_w}$ then

$$\Delta_\phi \approx \sqrt{2 \left(\frac{c_w T_v}{\Delta H_v} \right) \phi (\theta_s - 1)(\tau - \tau_{ig})}$$

Equation 154

From Equation 142

$$M = \frac{1}{2} \cdot \frac{d\Delta_\phi}{d\tau}$$

substituting Equation 154

$$M \approx \frac{1}{2} \frac{d}{d\tau} \left[\sqrt{2 \left(\frac{c_w T_v}{\Delta H_v} \right) \phi (\theta_s - 1)(\tau - \tau_{ig})} \right]$$

thus

$$M \approx \sqrt{\frac{\left(\dfrac{c_w T_v}{\Delta H_v} \right) \phi (\theta_s - 1)}{8(\tau - \tau_{ig})}}$$

Equation 155

132

Thus the dimensionless groups of relevance are as follows -

Ignition:

$$M_{ig} = \left(\frac{L}{\Delta H_v}\right)\left[1 - \frac{\dot{q}_-''}{\dot{q}_+''(T_s)}\right]$$

(Equation 139)

$$\Delta_{ig} = \left[\frac{c_w(T_{ig} - T_0)}{L}\right]\left[\frac{\dot{q}_+''(T_{ig})}{\dot{q}_i''(t_{ig})}\right]$$

(Equation 141)

Small-time burning rate solutions:

$$M = \left(\frac{L}{\Delta H_v}\right)\left[1 - \frac{c_w(T_v - T_0)/L}{\Delta}\right]$$

(Equation 146)

$$\Delta \approx \Delta_{ig} + 6\left(\frac{L}{\Delta H_v}\right)(1 - \Delta_{ig})(\tau - \tau_{ig})$$

(Equation 151)

$$\Delta_\phi \approx 2M_{ig}(\tau - \tau_{ig})$$

(Equation 143)

Long-time burning rate solutions:

$$\Delta_\phi \approx \sqrt{\frac{2\phi c_w(T_s - T_v)(\tau - \tau_{ig})}{\Delta H_v}}$$

(from Equation 154)

$$M \approx \sqrt{\frac{\phi c_w(T_s - T_v)}{8\Delta H_v(\tau - \tau_{ig})}}$$

(from Equation 155)

$$\Delta \approx \sqrt{\Delta_{ig}^2 + 12(\tau - \tau_{ig})}$$

(Equation 152)

$$T_s \approx \left(\frac{\dot{q}_{fl}'' + \dot{q}_i''}{\sigma}\right)^{1/4}$$

(from Equation 153)

As discussed in § 2.6, we can replace the ratio of the thermal conductivity of char and the thermal conductivity of wood k_ϕ / k_w with the char fraction ϕ.

4.1.7 Solutions of the integral model

The general form of the dimensionless equations is shown in Figure 42 and the equivalent dimensional variables in Figure 43. The small-time burning rate solution is equivalent to what would be obtained by a non-charring material as detailed by Hopkins [30]. At ignition the small-time burning rate starts at a given point after which it increases to a maximum steady-state value, where it remains. A real burning material would of course eventually consume all its fuel and the burning rate would drop to zero.

The long-time solution effectively starts from an infinite burning rate from where it decays towards zero. There is a transition point at which the small-time and long-time solutions cross (marked by the diamond-shaped symbol in Figure 42). This point marks the peak burning rate and it is less than the steady-state non-charring material burning rate. Thus for a charring material the burning rate follows the small-time solution up to the transition point (the peak burning rate) and thereafter follows the long-time solution.
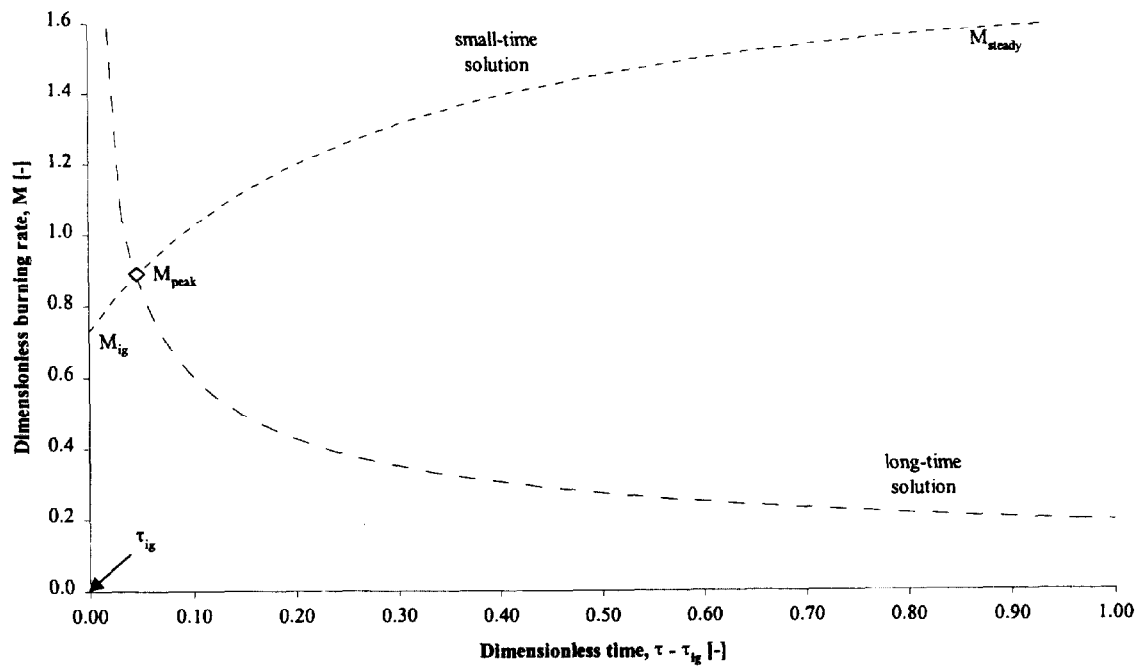
Figure 42. Dimensionless burning rate solutions.
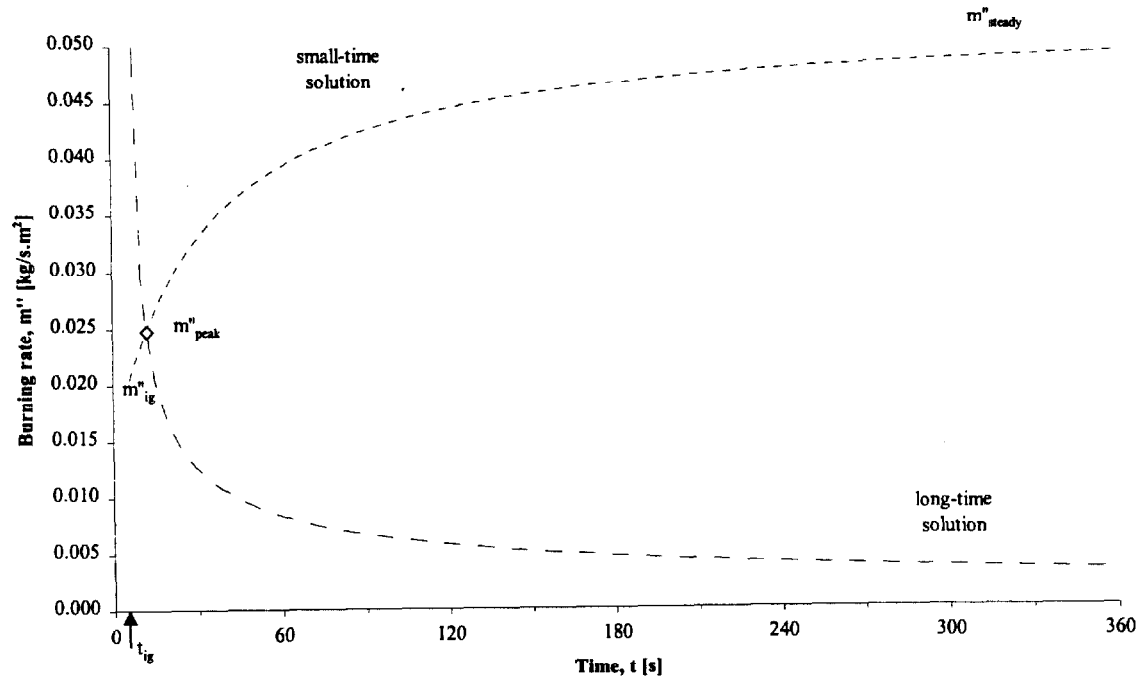
Figure 43. Dimensional burning rate solutions.

135

Other parameters such as the char depth and thermal penetration depth exhibit a similar

behaviour. For the thermal penetration depth we can also include the period prior to

ignition. Figure 44 shows the thermal penetration in dimensionless form and Figure 45

shows the thermal penetration in dimensional form. Figure 45 has been re-plotted in

Figure 46 to show more clearly the transition between the pre-ignition, small-time and

long-time solutions by removing the non-applicable portions of the curves. The

dimensionless and dimensional char depth solutions are shown in Figure 47 and Figure

48.
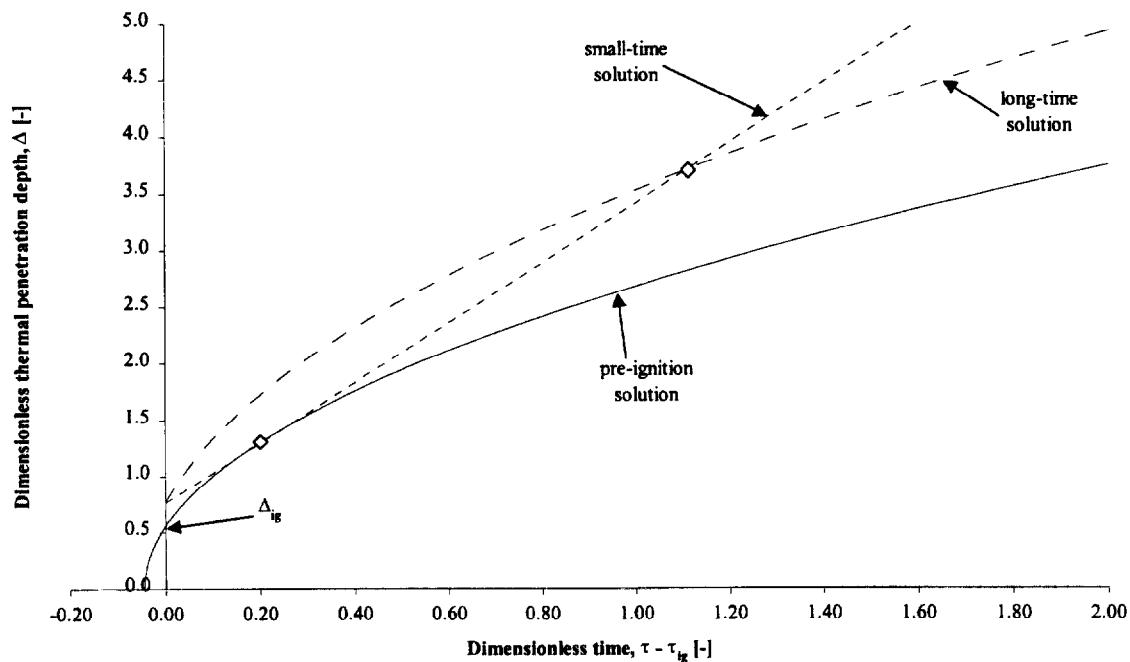
Figure 44. Dimensionless thermal penetration depth solutions.
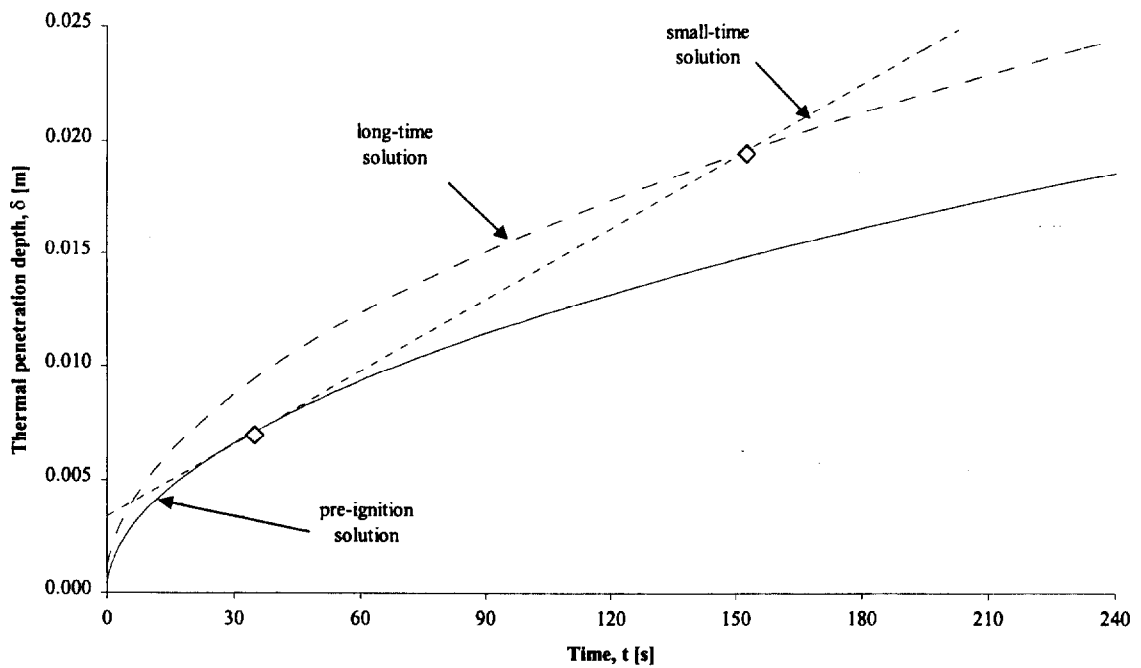
Figure 45. Dimensional thermal penetration depth solutions.
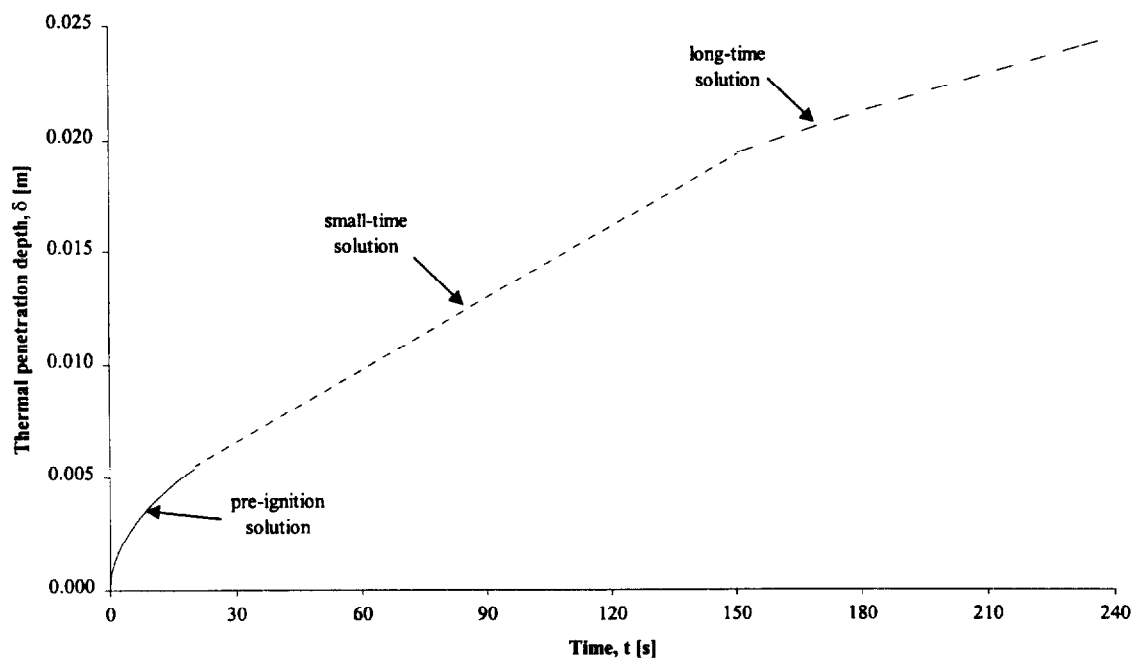
Figure 46. Dimensional thermal penetration depth solutions re-plotted for clarity.

137
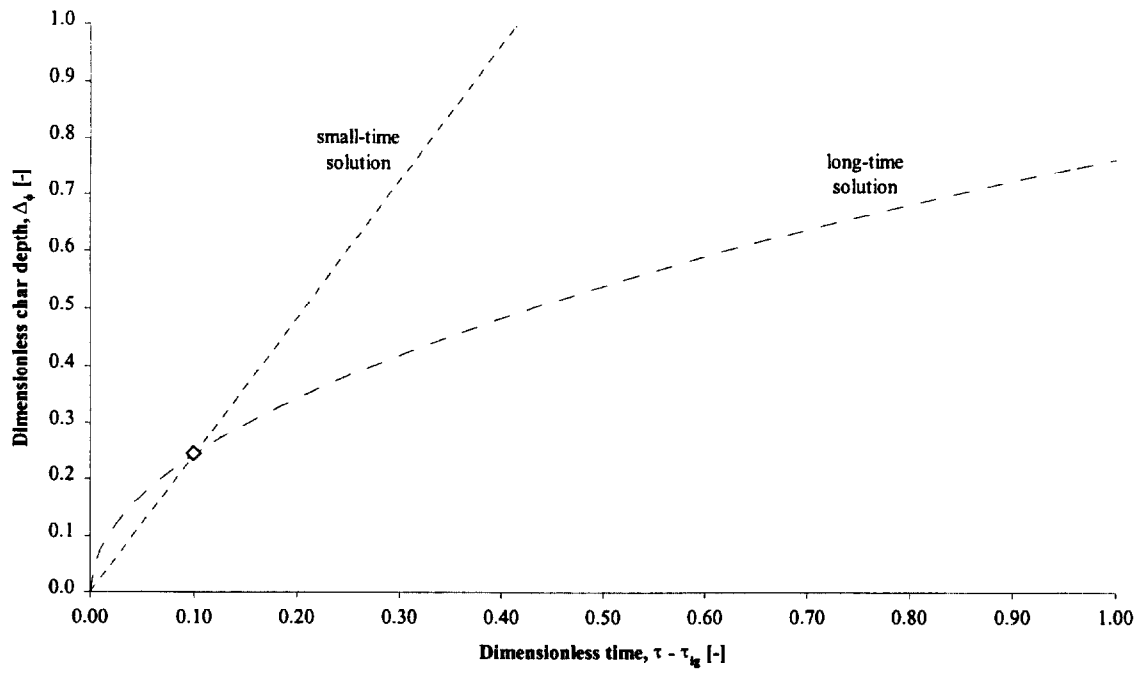
Figure 47. Dimensionless char depth solutions.
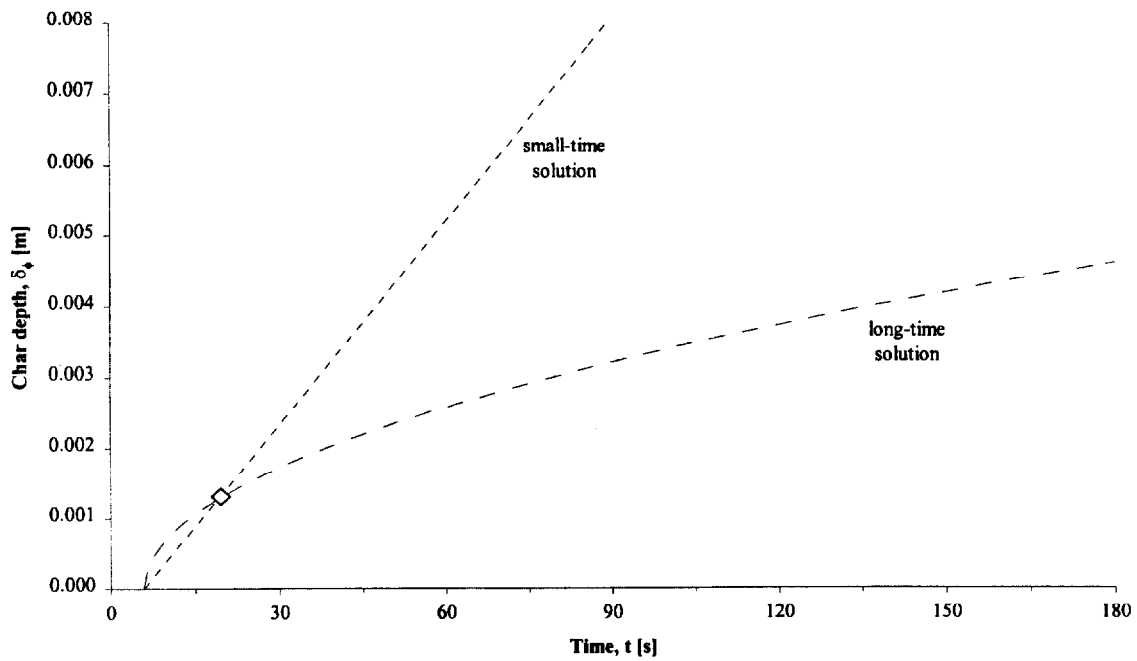
Figure 48. Dimensional char depth solutions.

We can now examine these dimensionless groups to investigate the form of the small and long time solutions. Each dimensionless group is a relatively complex function of many variables. In order to examine how each variable contributes to the behaviour of the model, we will select a set of typical values for these variables and then vary one at a time. The values were chosen on the basis of properties measured for a typical wood (§ 2) and those obtained by the analysis of the experimental data (§ 4.6.1) and are presented in Table 15.

Incident heat flux	q''_i	[W/m²]	50,000
Flame heat flux	q''_{fl}	[W/m²]	20,000
Critical heat flux	q''_{cr}	[W/m²]	15,500
q plus	$q''_+ = q''_{fl} + q''_i - \sigma(T_v^4 - T_0^4)$	[W/m²]	60,297
q minus	$q''_- = q''_i - h_c(T_v - T_0) - \sigma(T_v^4 - T_0^4)$	[W/m²]	36,949
Beta	$\beta = q''_{cr} / q''_i$	[-]	0.310
Thermal diffusivity	α	[m²/s]	0.00000021
Heat of gasification	L	[J/kg]	1,500,000
Heat of vaporisation	$\Delta H_v = L - c_w(T_{ig} - T_0)$	[J/kg]	803,207
Average heat of combustion	ΔH_c	[J/kg]	12,000,000
Ignition temperature	T_{ig}	[K]	650
Ambient temperature	T_0	[K]	293
Vaporisation temperature	$T_v = T_{ig}$	[K]	650
Surface temperature (long time solution)	$T_s = [(q''_{fl} + q''_i)/\sigma]^{1/4}$	[K]	1054
Convective heat transfer coefficient	h_c	[W/m²]	9.38
Specific heat capacity	c_w	[J.kg⁻¹.K⁻¹]	1,952
Char fraction function	a	[-]	0.74
Char fraction function	n	[-]	-0.64
Char fraction	ϕ	[-]	0.35
Density	ρ_w	[kg/m³]	500
Thermal conductivity	k_w	[W/m².K]	0.20
Stefan-Boltzmann constant	σ	[W/m²K⁴]	5.67E-08
Time to ignition	t_{ig}	[s]	20
Thermal inertia	I	[J².m⁻⁴K⁻²s⁻¹]	200,000

Table 15. Typical values used for variable analysis.

140

The effect on the predicted burning rate and the predicted char depth are considered. In each case, the small-time and long-time solutions have been varied above and below the typical value. Plots using the dimensionless variables are presented, however, these can be difficult to relate to real world measurements and thus the plots are also shown in terms of dimensional values. Common x-axis and y-axis scales have been used for each plot to allow for direct comparisons to be made between the relative effect of each variable. In addition, each plot shows the transition point (marked by the diamond-shaped symbol) between the small-time and long-time solutions.

These dimensionless plots present an idealised view of the effect of each variable. As already discussed, wood is a complex material in which its properties vary between species and between individual samples. Therefore it may not be so obvious which properties are having the greatest influence on the burning rate of a particular sample when tested experimentally.

a)   Incident heat flux, $\dot{q}_i''$

Plots for the variation in the incident heat flux (Figure 49 to Figure 52) are shown at the values used in the main experimental test series, namely 25 kW/m², 35 kW/m², 50 kW/m² and 75 kW/m². Since the char fraction was found to be a function of the incident heat flux (§ 4.5.1), this varies as labelled.

The analysis shows that as the incident heat flux is increased so is the burning rate and the small-time solution is more sensitive to the influence of the incident flux. The analysis agrees with the findings of the work conducted at the Joint Fire Research Organisation (JFRO) [48] which also concluded that the burning rate increases with incident flux.

The char depth solutions show that at low incident heat fluxes the small-time solution predominates over the long-time solution. In Figure 51 and Figure 52 the long-time solution for $\dot{q}_i'' = 25\,\text{kW/m}^2$ does not appear in the time scale shown.
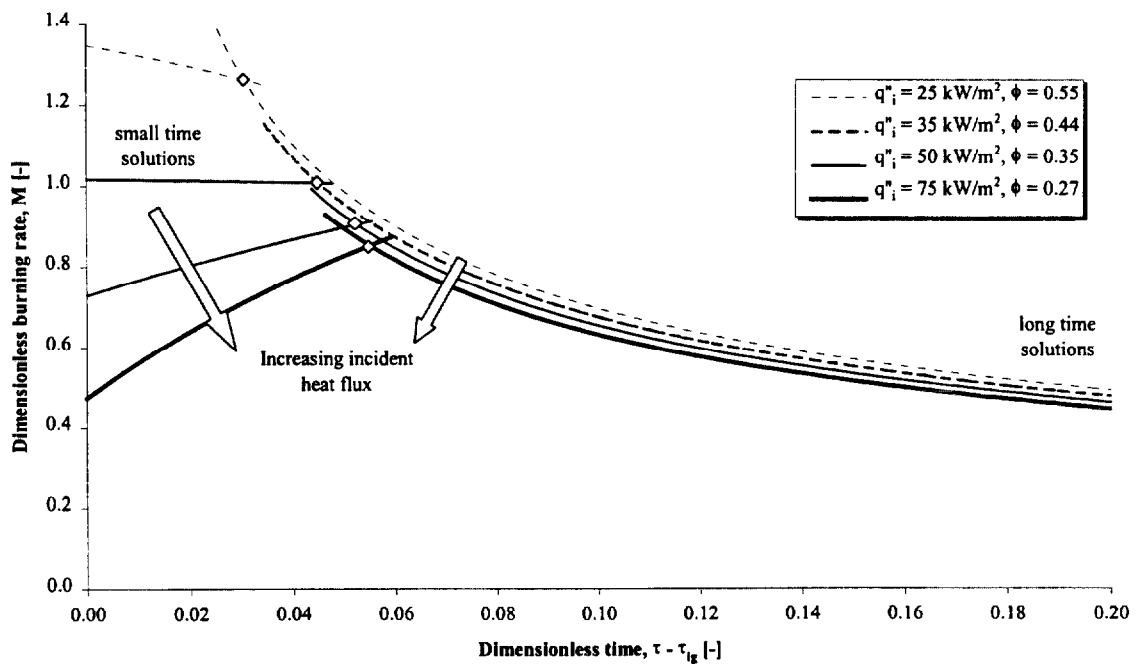
Figure 49. Effect of incident heat flux on burning rate, dimensionless plot.
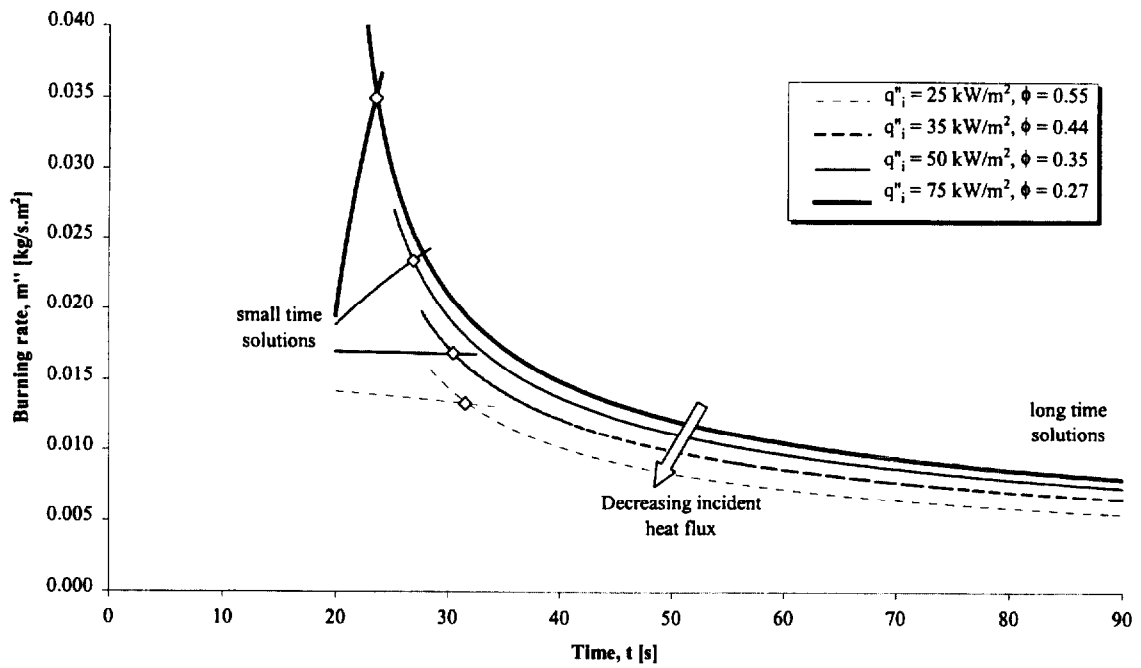
Figure 50. Effect of incident heat flux on burning rate, dimensional plot.
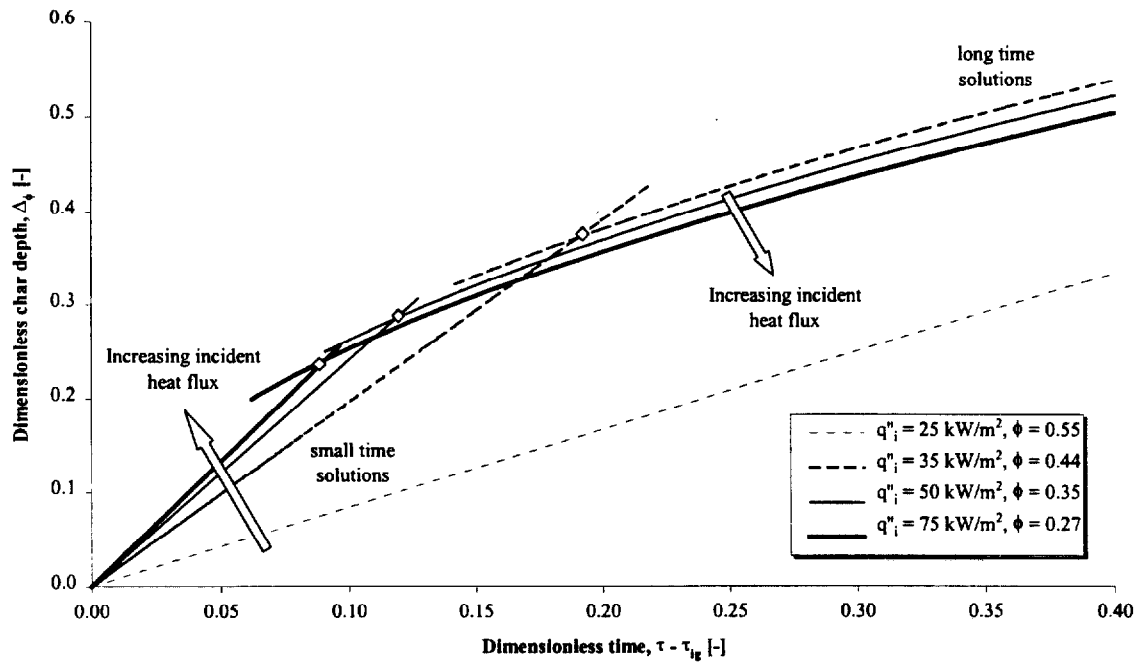
Figure 51. Effect of incident heat flux on char depth, dimensionless plot.
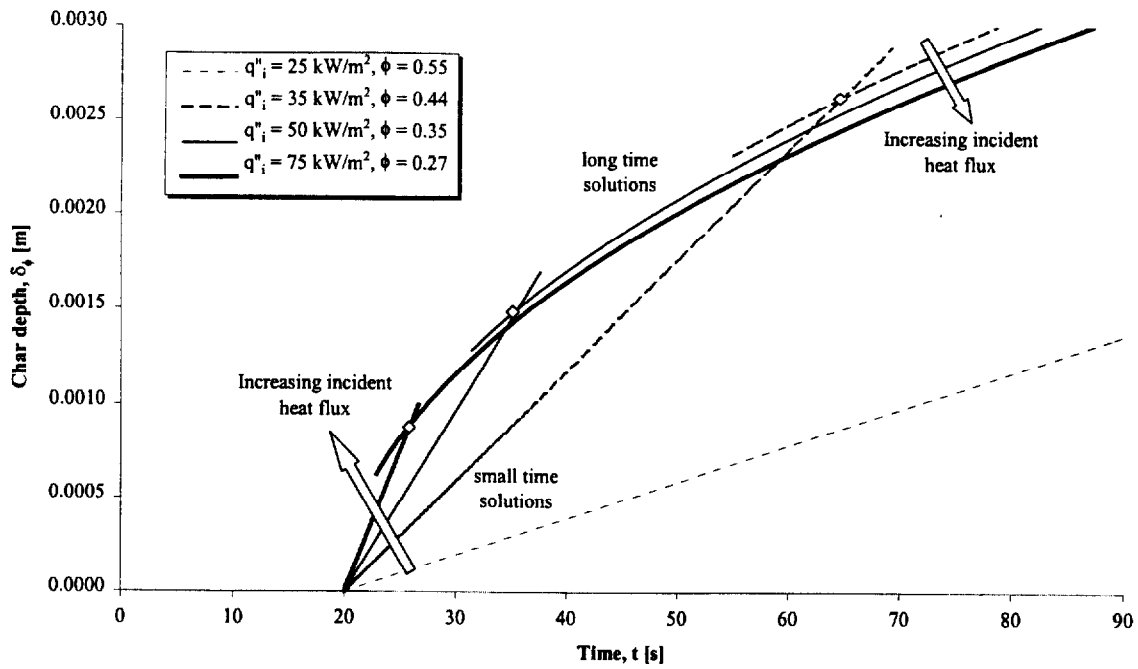
Figure 52. Effect of incident heat flux on char depth, dimensional plot.

b)   Flame heat flux, $\dot{q}''_{fl}$

The flame heat flux was taken to be values of 15 kW/m^2, 20 kW/m^2, 25 kW/m^2 and

30 kW/m^2 and the results are shown in Figure 53 to Figure 56.
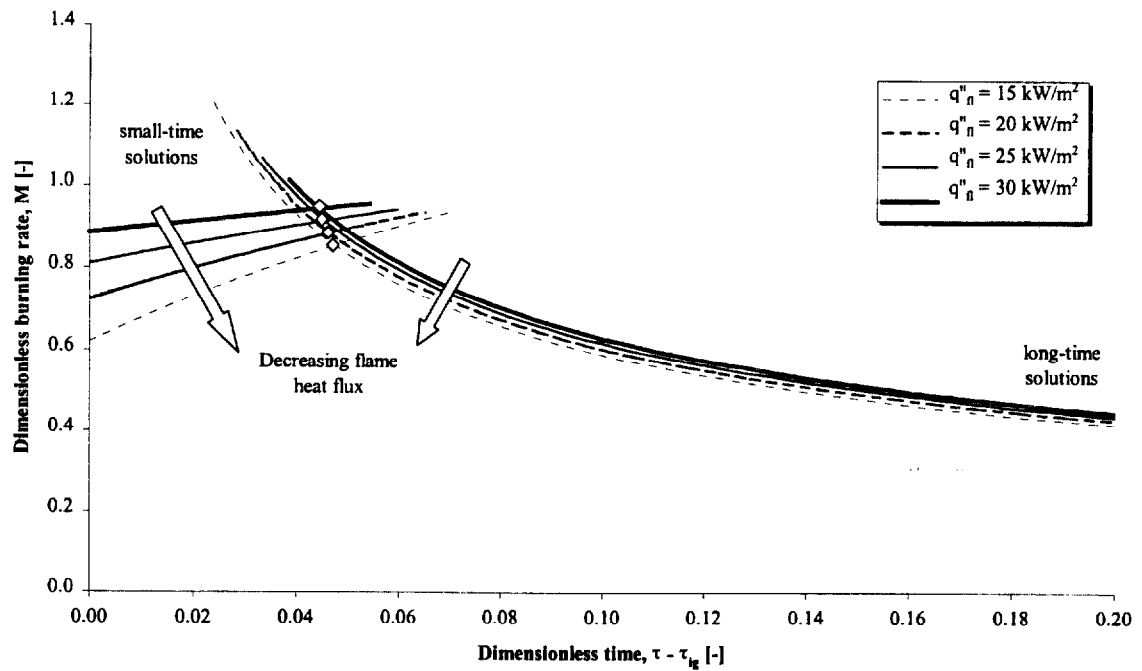
Figure 53. Effect of flame heat flux on burning rate, dimensionless plot.
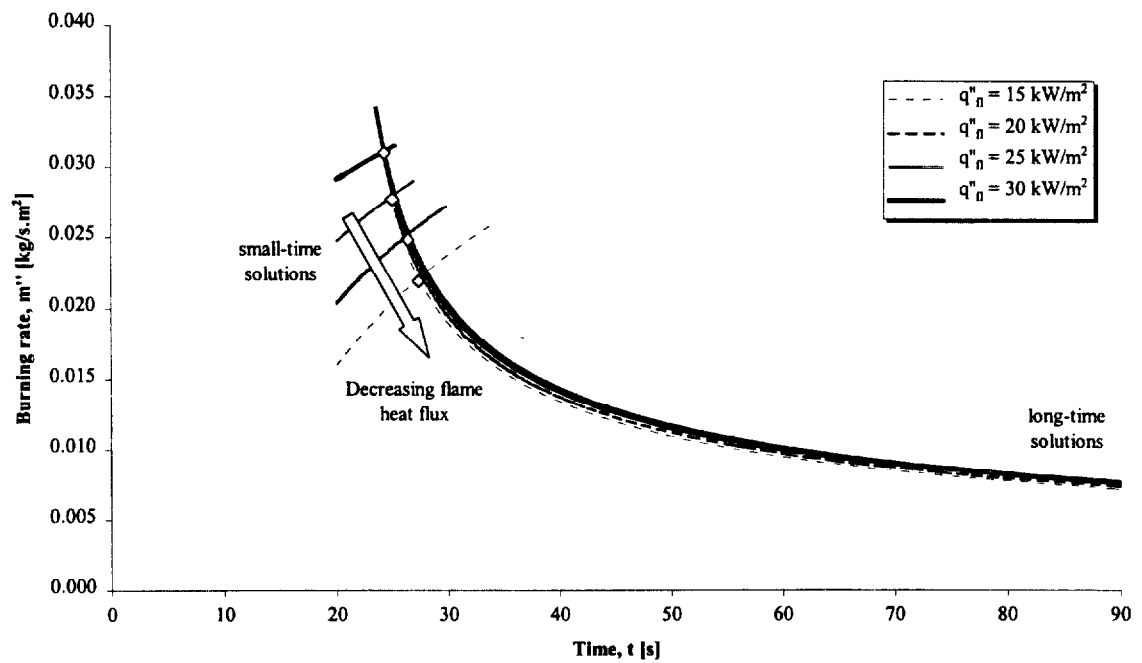
Figure 54. Effect of flame heat flux on burning rate, dimensional plot.

145
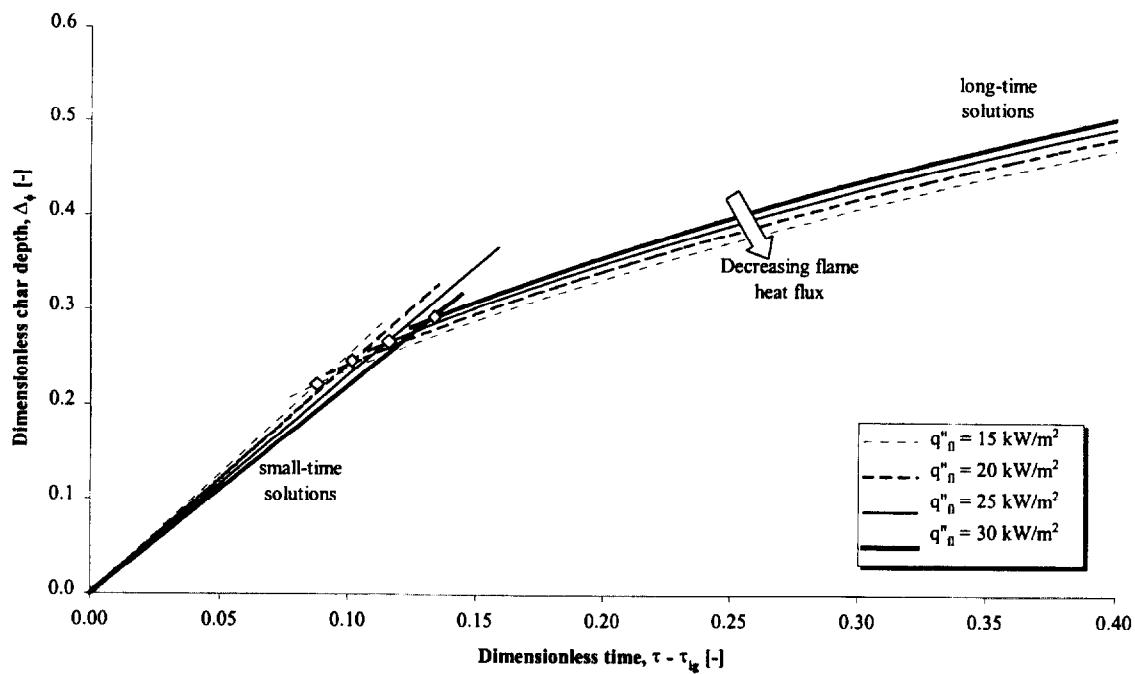
Figure 55. Effect of flame heat flux on char depth, dimensionless plot.
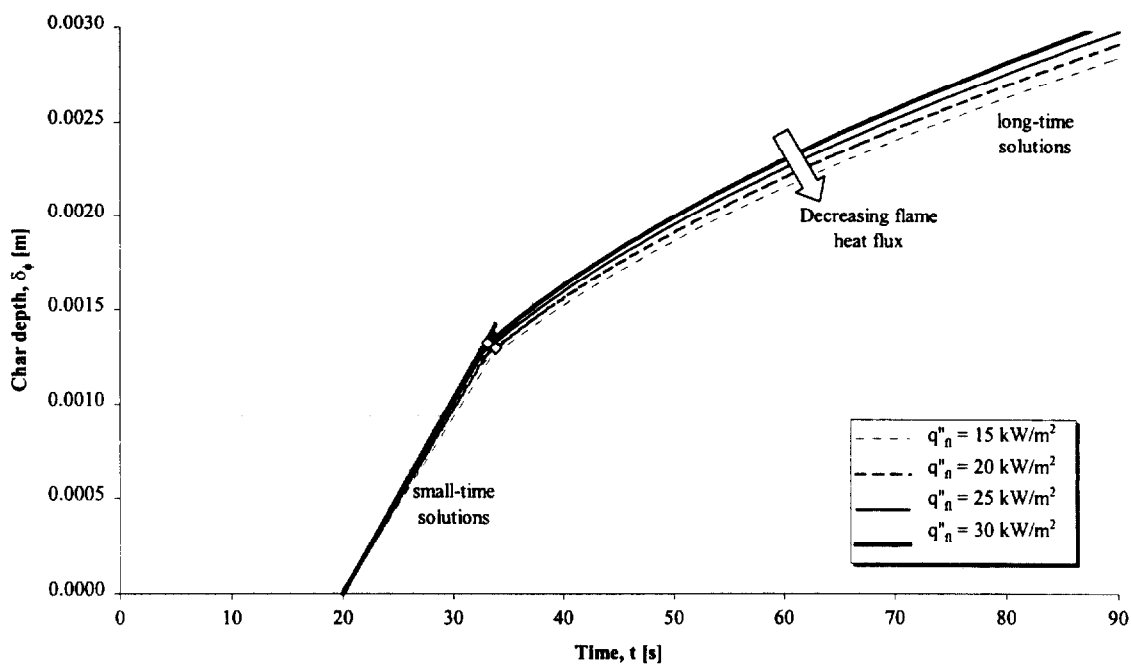
Figure 56. Effect of flame heat flux on char depth, dimensional plot.

146

c)   Critical heat flux, $\dot{q}''_{cr}$

Plots for the variation in the critical heat flux (Figure 57 to Figure 60) are shown at

values of 15.5 kW/m², 14 kW/m², 12.5 kW/m² and 11 kW/m². As discussed in § 3.2.3,

the ignition temperature of the material is a function of the critical heat flux and thus the

calculated values for the ignition temperature are indicated on each plot. As with the

incident heat flux, the char fraction also varies with critical heat flux.
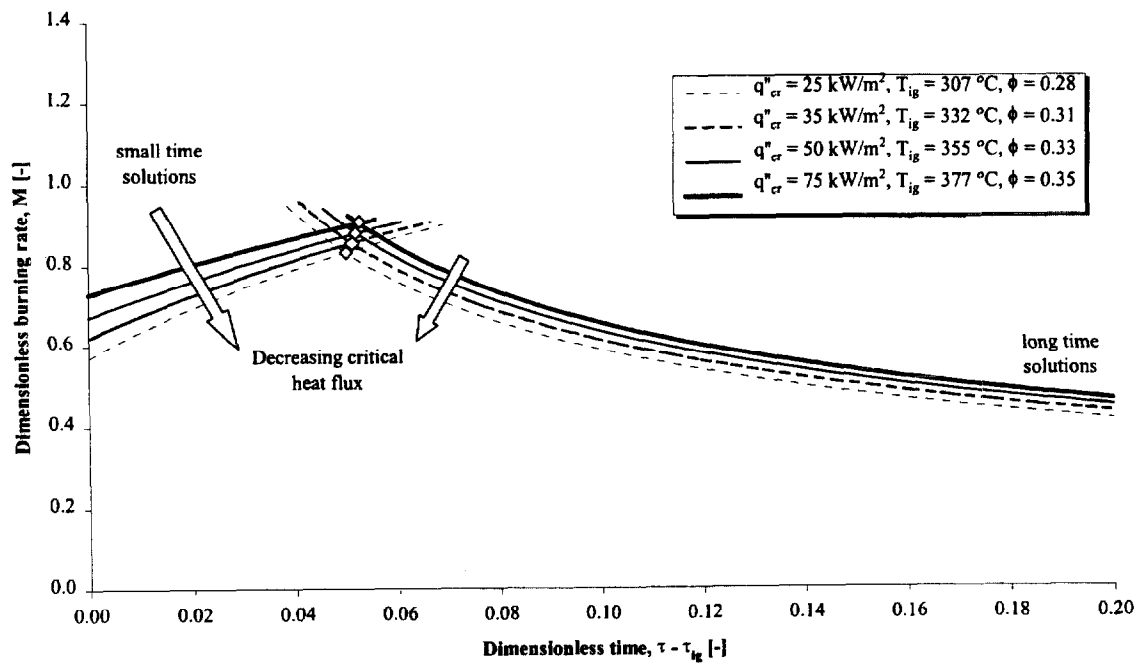
Figure 57. Effect of critical heat flux on burning rate, dimensionless plot.
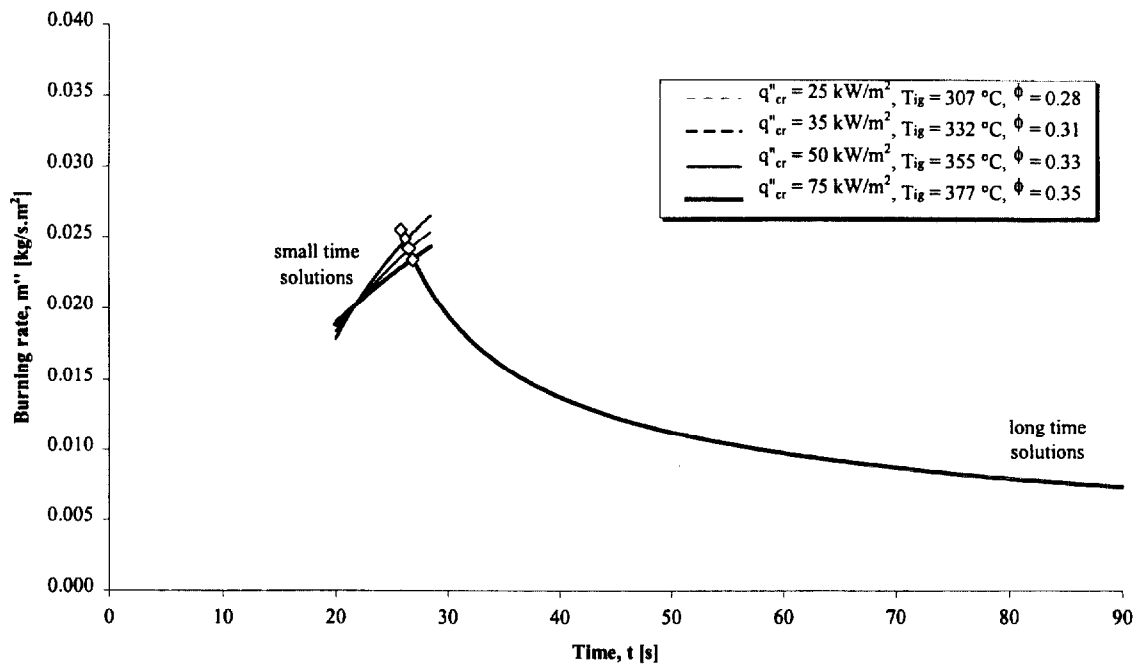
Figure 58. Effect of critical heat flux on burning rate, dimensional plot.
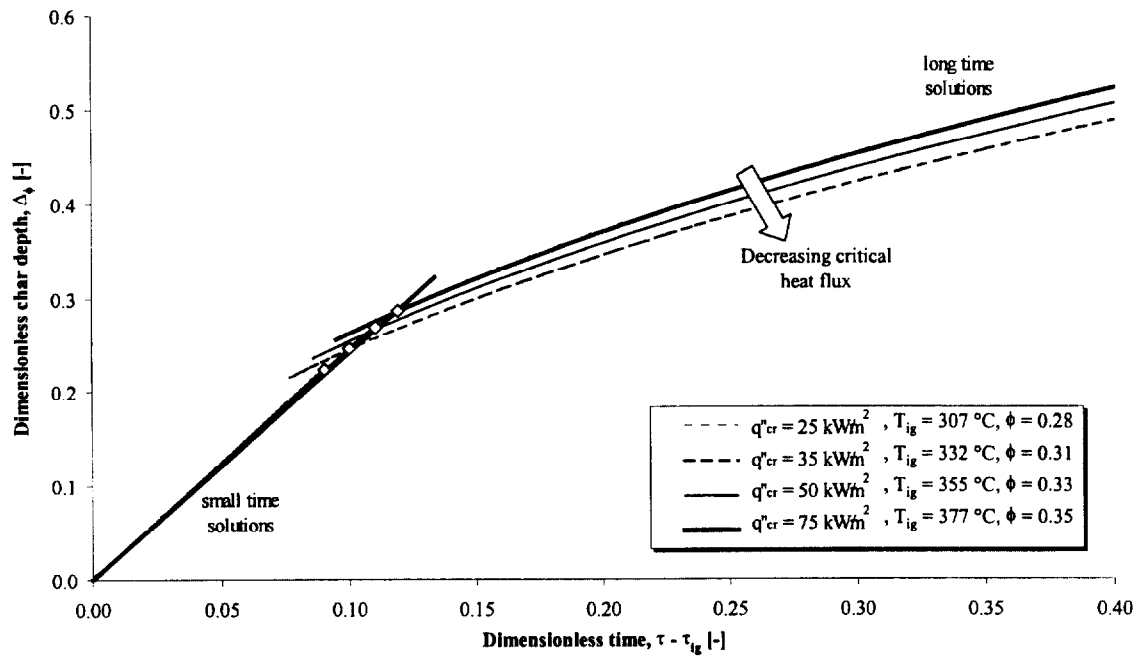
Figure 59. Effect of critical heat flux on char depth, dimensionless plot.

148
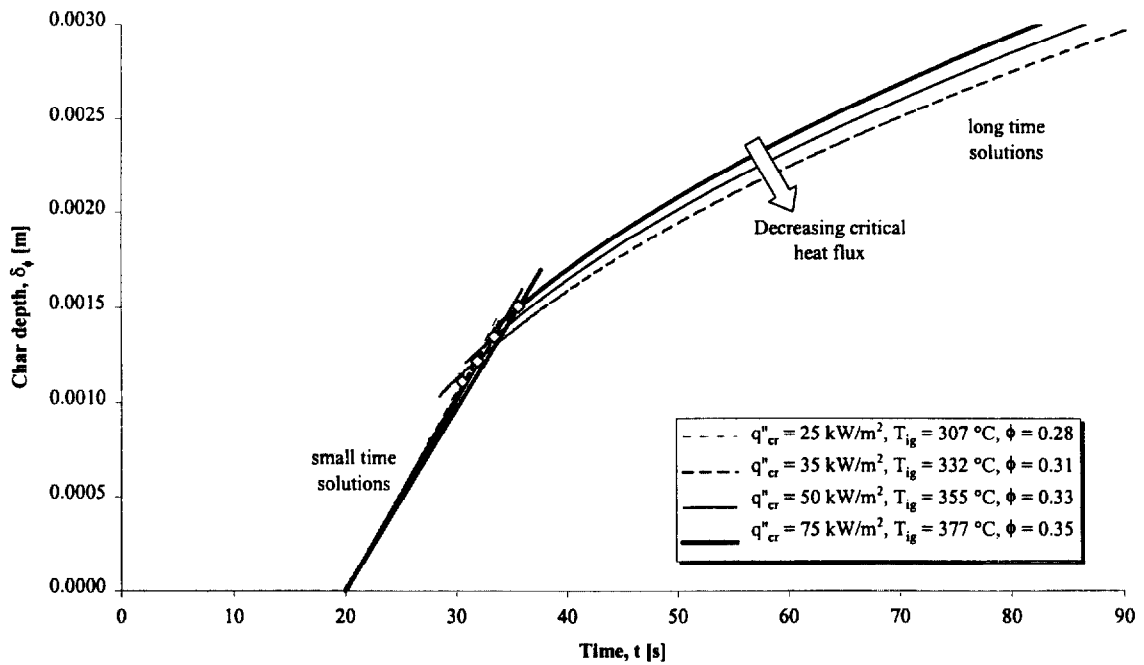
Figure 60 Effect of critical heat flux on char depth, dimensional plot.

d)   Heat of gasification, L

Values for the heat of gasification of 100,000 J/kg, 1,500,000 J/kg, 2,000,000 J/kg and 2,500,000 J/kg were selected in order to investigate its contribution to the burning rate and char depth (Figure 61 to Figure 65). Since the heat of gasification is the amount of energy required to vaporise the virgin wood, it would be expected that as it increases so the burning rate would decrease as shown in this analysis. However, the analysis also shows that as the heat of gasification is reduced, the small-time solution reaches a point where the burning rate begins at a higher value and immediately starts to decrease. Once this occurs, the small-time and long-time solutions for both the burning rate and char depth no longer intersect.

149
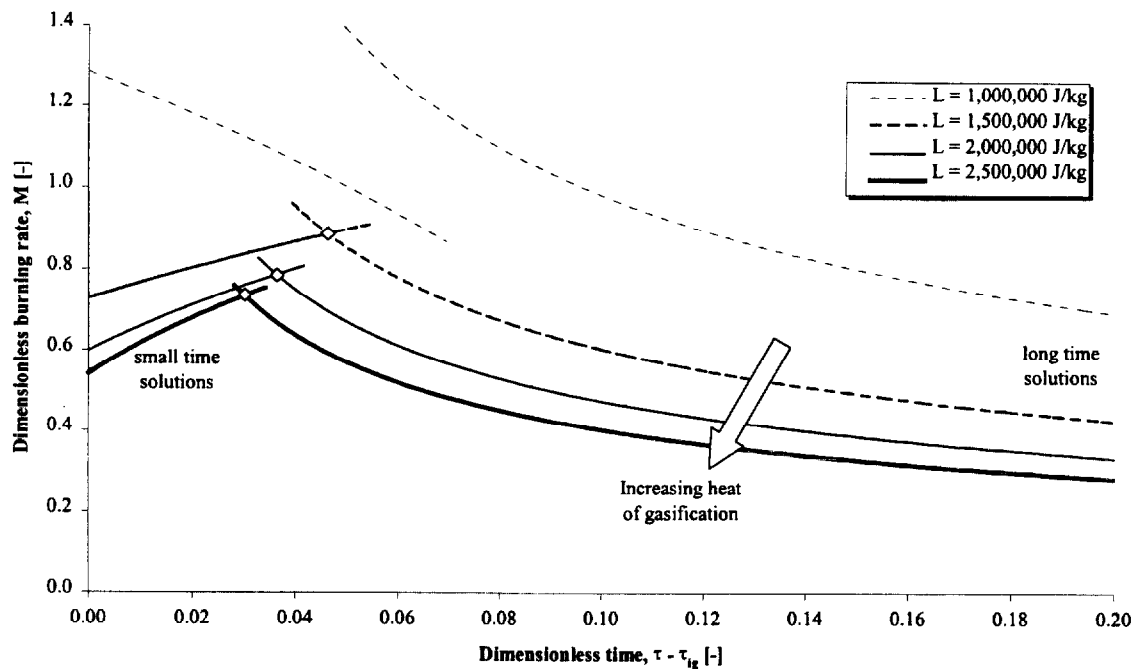
Figure 61. Effect of heat of gasification on burning rate, dimensionless plot.
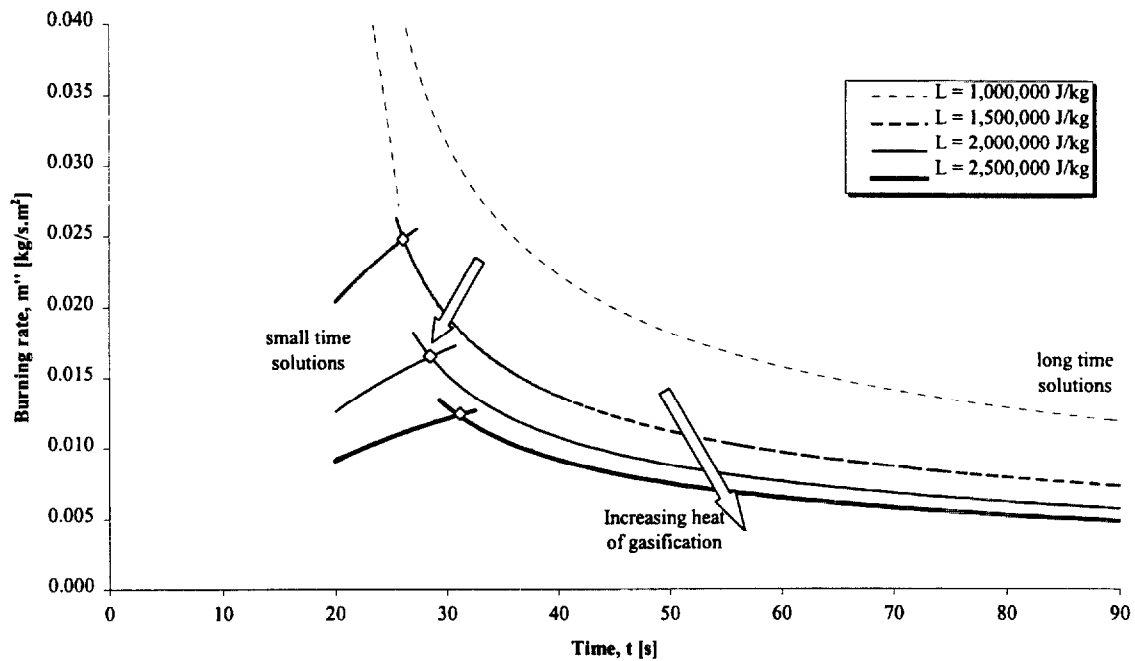
Figure 62. Effect of heat of gasification on burning rate, dimensional plot.
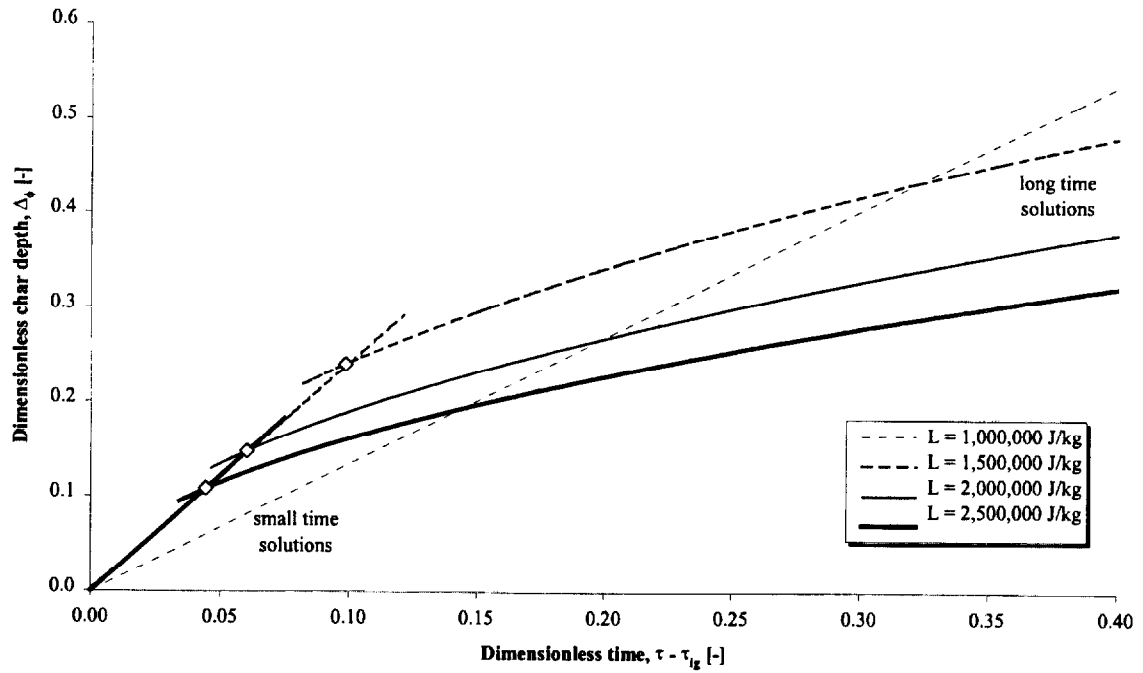
Figure 63. Effect of heat of gasification on char depth, dimensionless plot.
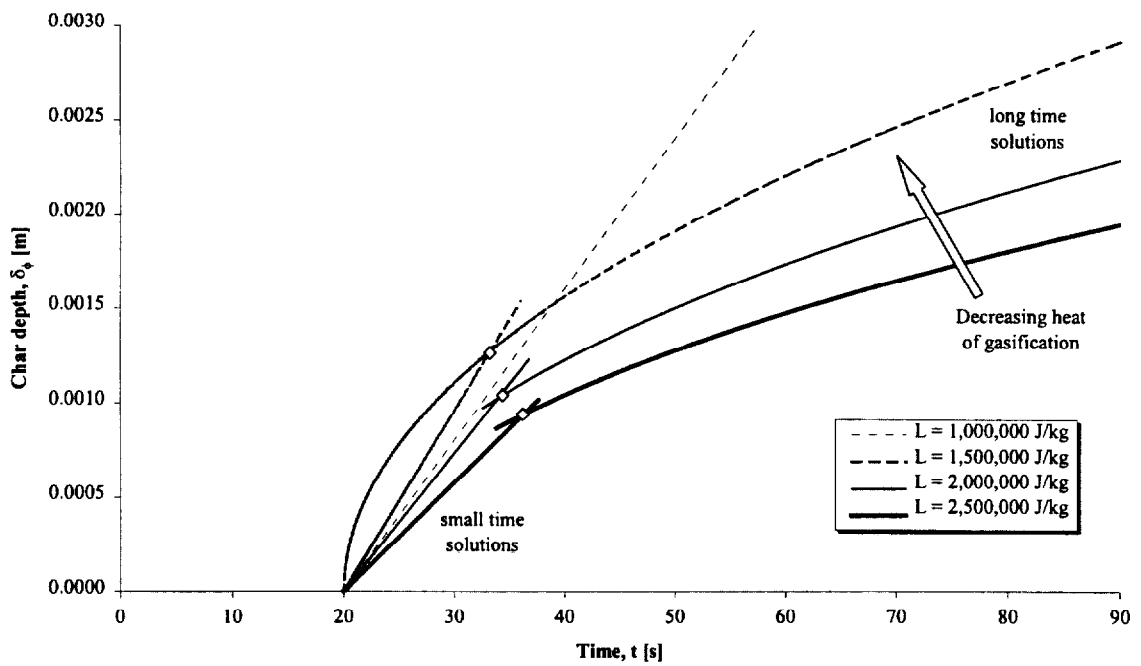
Figure 64. Effect of heat of gasification on char depth, dimensional plot.

151
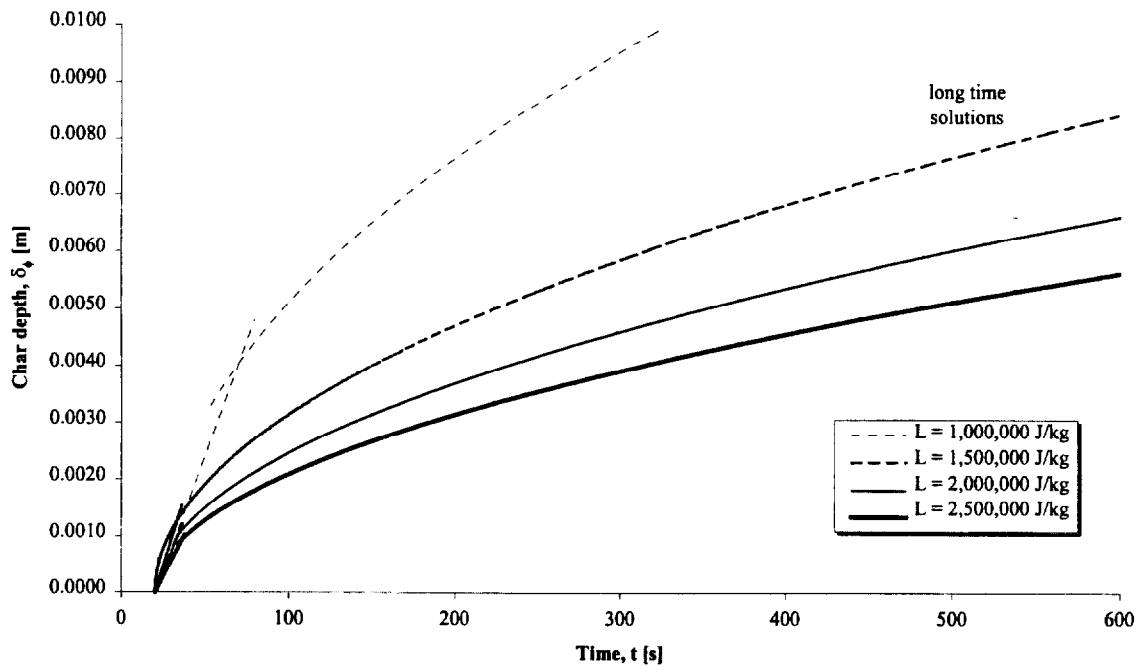
Figure 65. Effect of heat of gasification on char depth, dimensional plot with extended axes.

e)   Apparent thermal inertia, $k\rho c$

In Figure 66 to Figure 69 the apparent thermal inertia was selected to be

$100,000 \ J^2.m^{-4}K^{-2}s^{-1}$, $200,000 \ J^2.m^{-4}K^{-2}s^{-1}$, $300,000 \ J^2.m^{-4}K^{-2}s^{-1}$ and $400,000 \ J^2.m^{-4}K^{-2}s^{-1}$.

In the analysis of the experimental data, the apparent thermal inertia was found to vary widely depending on the wood species and grain orientation. Since the specific heat capacity and thermal conductivity were calculated as a function of the thermal inertia (§ 2.7), they also varied as indicated. The analysis shows that as the thermal inertia increases, the model reaches a situation in which the small and long time burning rate solutions do not cross.

152
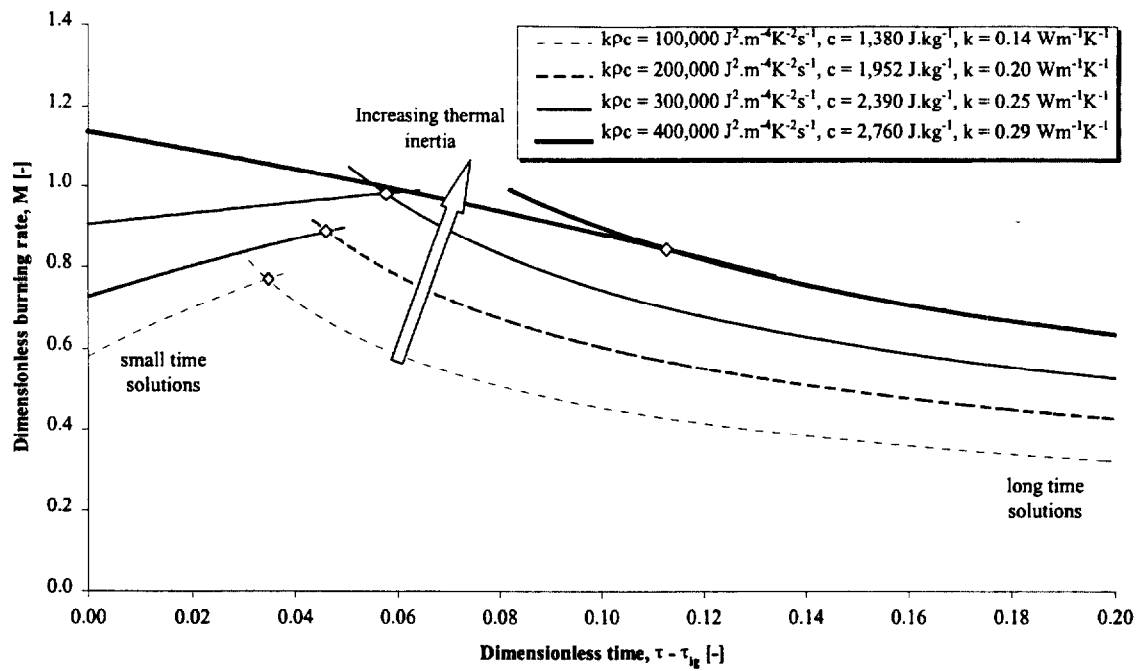
Figure 66. Effect of thermal inertia on burning rate, dimensionless plot.
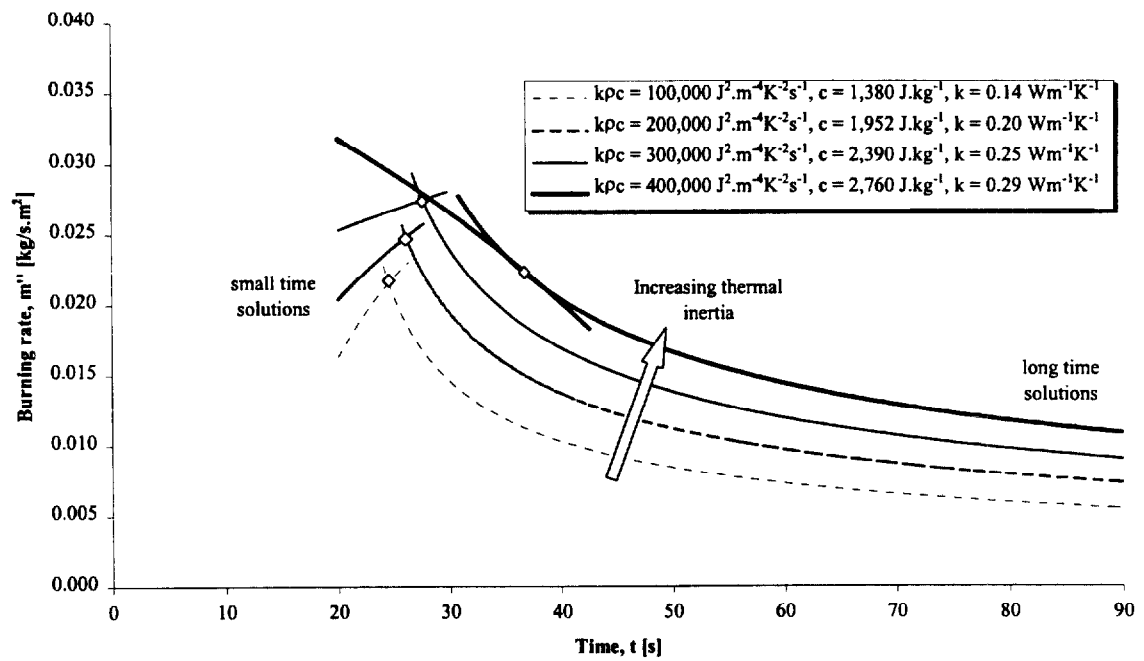
Figure 67. Effect of thermal inertia on burning rate, dimensional plot.

Figure 68 chart:

Dimensionless char depth, Δ_ϕ [-] (y-axis, 0.0 to 0.6)

Dimensionless time, $\tau - \tau_{ig}$ [-] (x-axis, 0.00 to 0.50)

long-time solutions

Increasing thermal inertia

small-time solutions

$k\rho c = 100{,}000 \ J^2.m^{-4}K^{-2}s^{-1}$, $c = 1{,}380 \ J.kg^{-1}$, $k = 0.14 \ Wm^{-1}K^{-1}$
$k\rho c = 200{,}000 \ J^2.m^{-4}K^{-2}s^{-1}$, $c = 1{,}952 \ J.kg^{-1}$, $k = 0.20 \ Wm^{-1}K^{-1}$
$k\rho c = 300{,}000 \ J^2.m^{-4}K^{-2}s^{-1}$, $c = 2{,}390 \ J.kg^{-1}$, $k = 0.25 \ Wm^{-1}K^{-1}$
$k\rho c = 400{,}000 \ J^2.m^{-4}K^{-2}s^{-1}$, $c = 2{,}760 \ J.kg^{-1}$, $k = 0.29 \ Wm^{-1}K^{-1}$
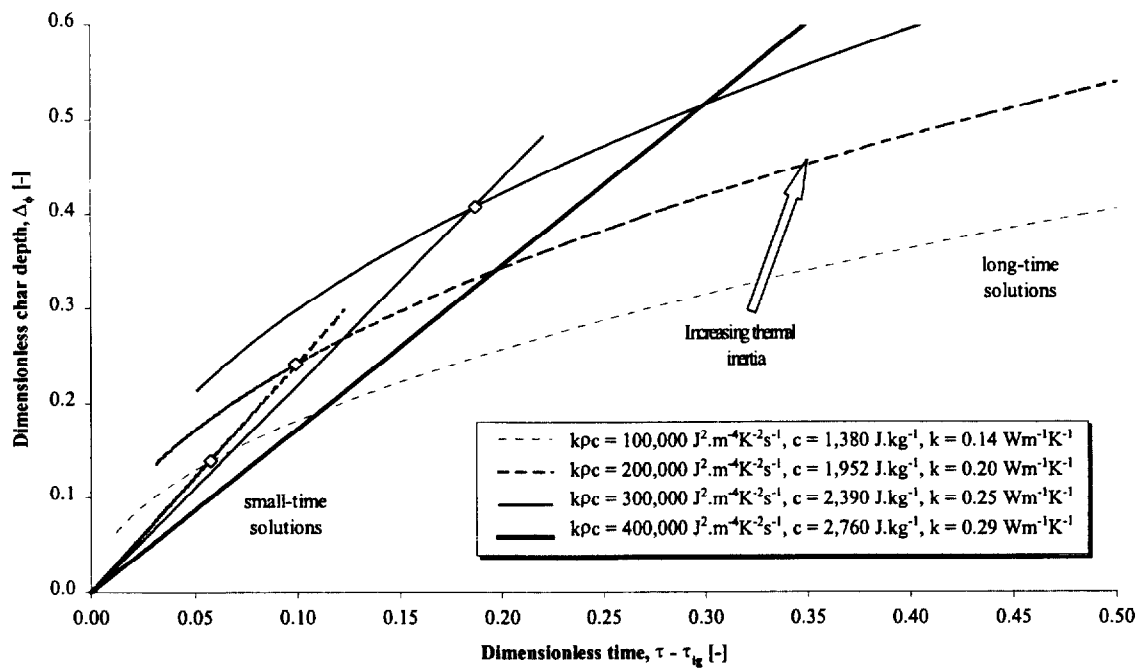
Figure 68. Effect of thermal inertia on char depth, dimensionless plot.

Figure 69 chart:

Char depth, δ_ϕ [m] (y-axis, 0.0000 to 0.0030)

Time, t [s] (x-axis, 0 to 90)

long time solutions

Increasing thermal inertia

small time solutions

$k\rho c = 100{,}000 \ J^2.m^{-4}K^{-2}s^{-1}$, $c = 1{,}380 \ J.kg^{-1}$, $k = 0.14 \ Wm^{-1}K^{-1}$
$k\rho c = 200{,}000 \ J^2.m^{-4}K^{-2}s^{-1}$, $c = 1{,}952 \ J.kg^{-1}$, $k = 0.20 \ Wm^{-1}K^{-1}$
$k\rho c = 300{,}000 \ J^2.m^{-4}K^{-2}s^{-1}$, $c = 2{,}390 \ J.kg^{-1}$, $k = 0.25 \ Wm^{-1}K^{-1}$
$k\rho c = 400{,}000 \ J^2.m^{-4}K^{-2}s^{-1}$, $c = 2{,}760 \ J.kg^{-1}$, $k = 0.29 \ Wm^{-1}K^{-1}$
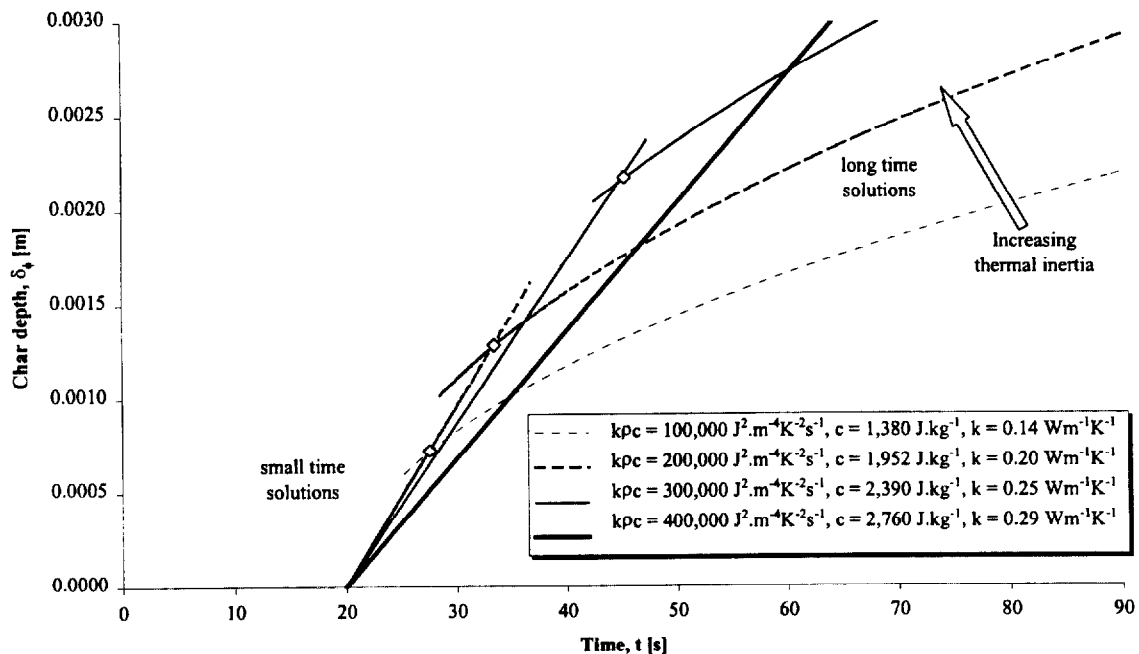
Figure 69. Effect of thermal inertia on char depth, dimensional plot.

154

f) Thermal diffusivity, α

Although, as described in § 2.7, the thermal diffusivity is assumed to be constant, the dimensionless equations allow us to investigate its contribution to the model. Values of 1.0×10^{-7} m²/s, 2.1×10^{-7} m²/s, 3.2×10^{-7} m²/s and 4.3×10^{-7} m²/s were graphed as shown in Figure 70 to Figure 73. Since the thermal diffusivity along with the thermal inertia are used to calculate the specific heat capacity and the thermal conductivity, the form of the curves are similar to those in which different thermal inertias are graphed as shown in part e) of this section. However, in this case, a decrease in the thermal diffusivity rather than an increase in the thermal inertia eventually leads to a situation where the small and long time burning rate solutions do not cross.
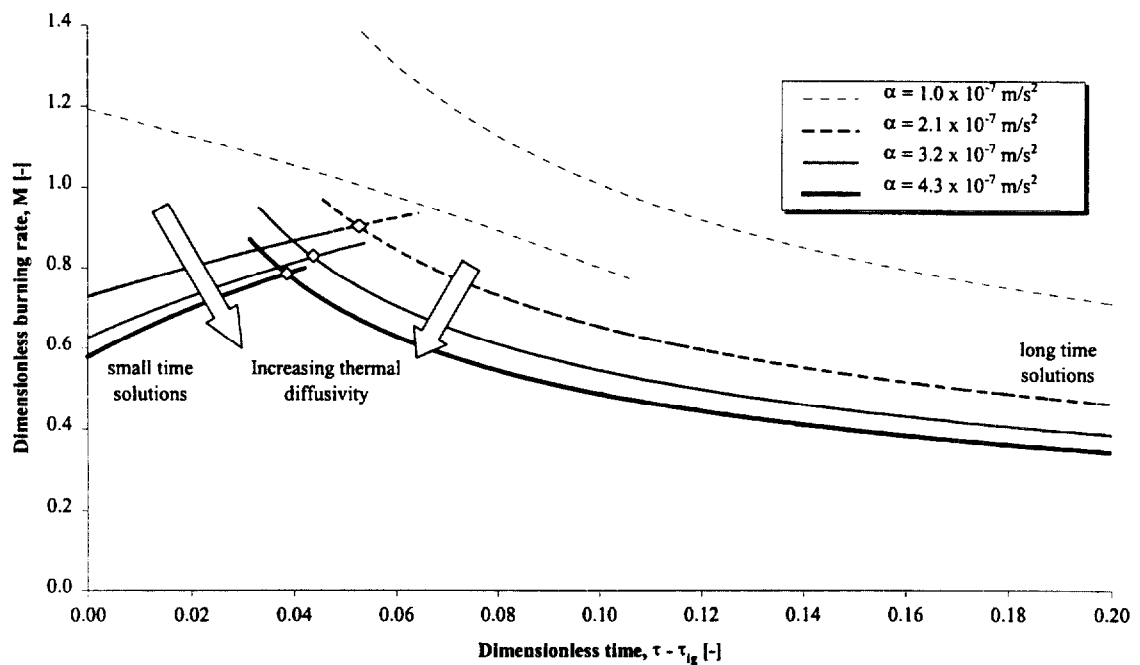
Figure 70. Effect of thermal diffusivity on burning rate, dimensionless plot.
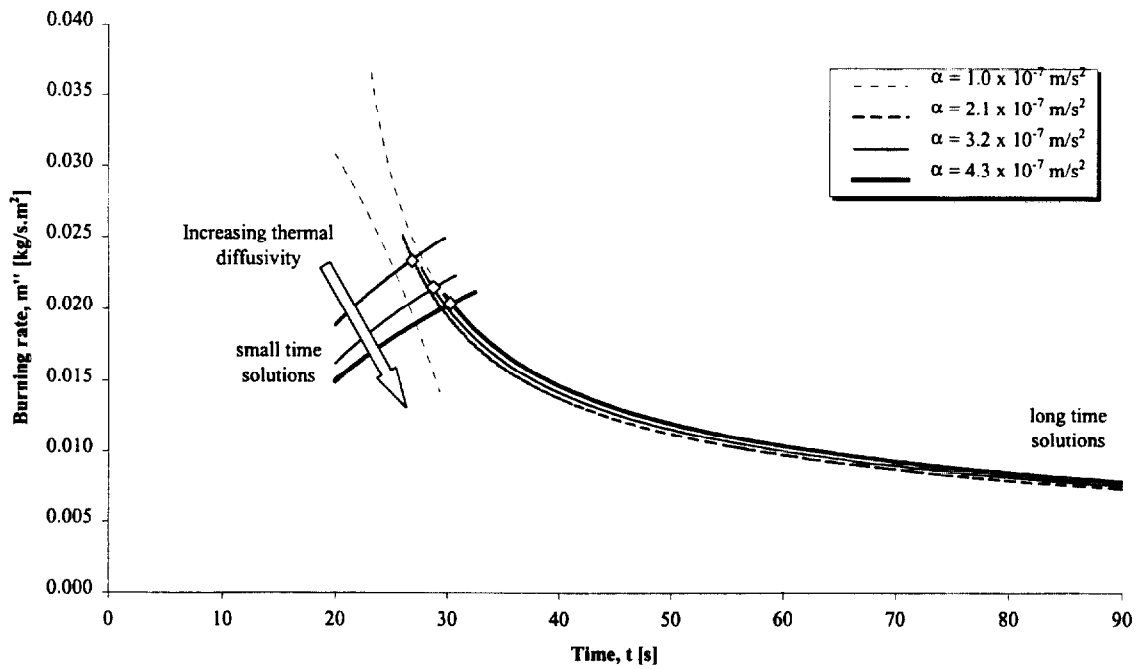
Figure 71. Effect of thermal diffusivity on burning rate, dimensional plot.
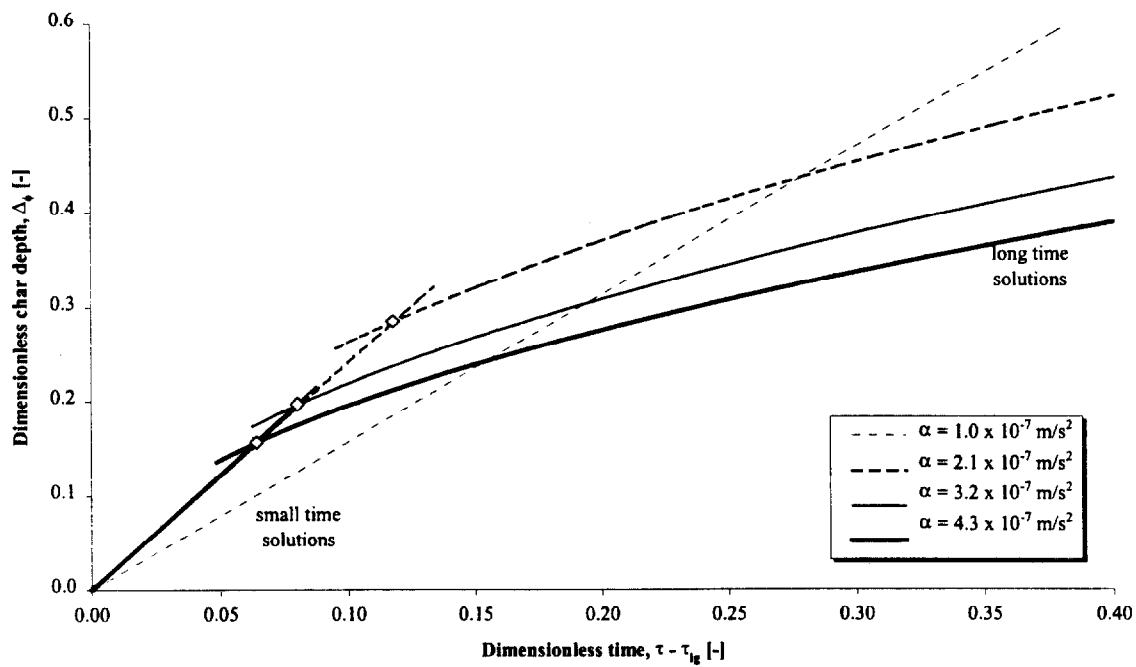
Figure 72. Effect of thermal diffusivity on char depth, dimensionless plot.

156
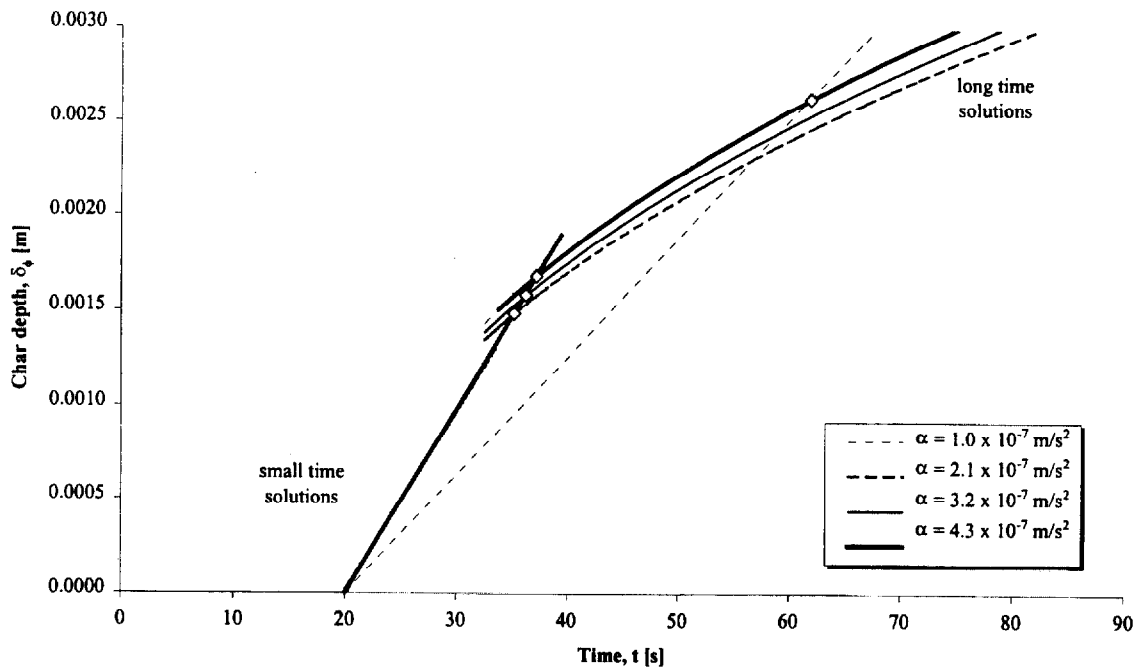
Figure 73. Effect of thermal diffusivity on char depth, dimensional plot.

g)   Density, ρ

The effect of density on the burning rate and char depth was investigated by choosing

values of 400 kg/m^3, 500 kg/m^3, 600 kg/m^3 and 700 kg/m^3 (Figure 74 to Figure 77). The

small-time burning rate solution is more sensitive to density and the long-time solution

shows relatively little variation. In the work conducted by JFRO [48] it was found that

the burning rate increased as the density decreased. The solutions to the integral model do

not show this result but instead indicates that, although the peak burning rate is higher for

lower densities, for long-times the burning rate is slightly higher for higher densities.

In contrast to the burning rate, the variation of density has a greater effect on the long-

time char depth solution with less dense materials charring quicker than more dense

materials. It is interesting to note that the transition between the small-time and long-time

solutions is almost constant (Figure 77).
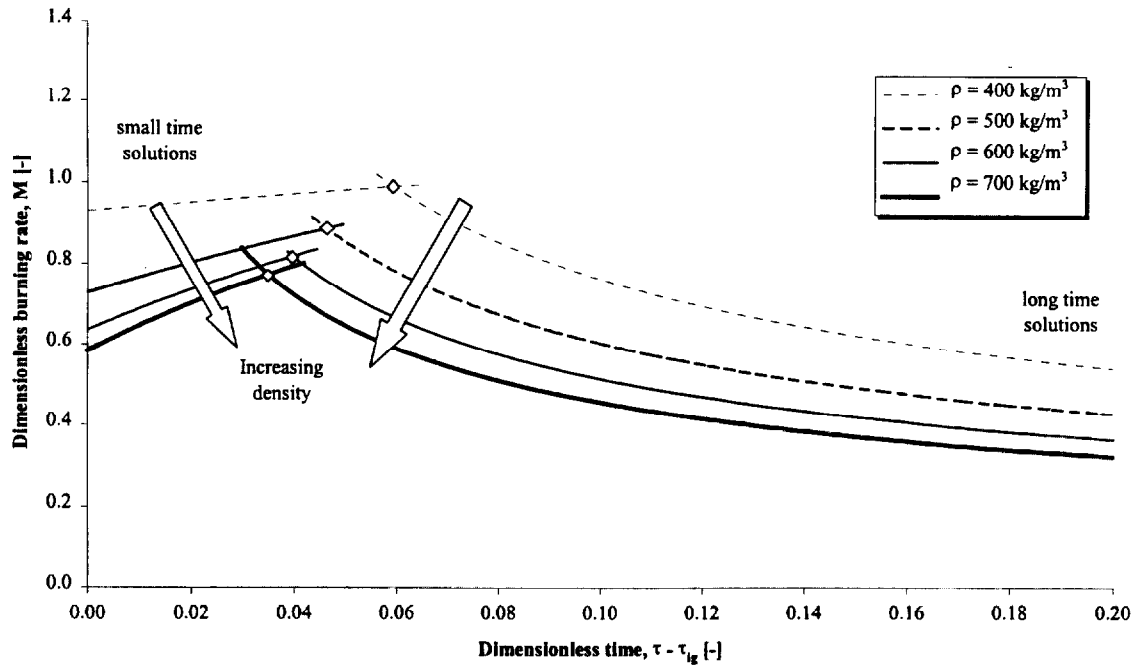
Figure 74. Effect of density on burning rate, dimensionless plot.
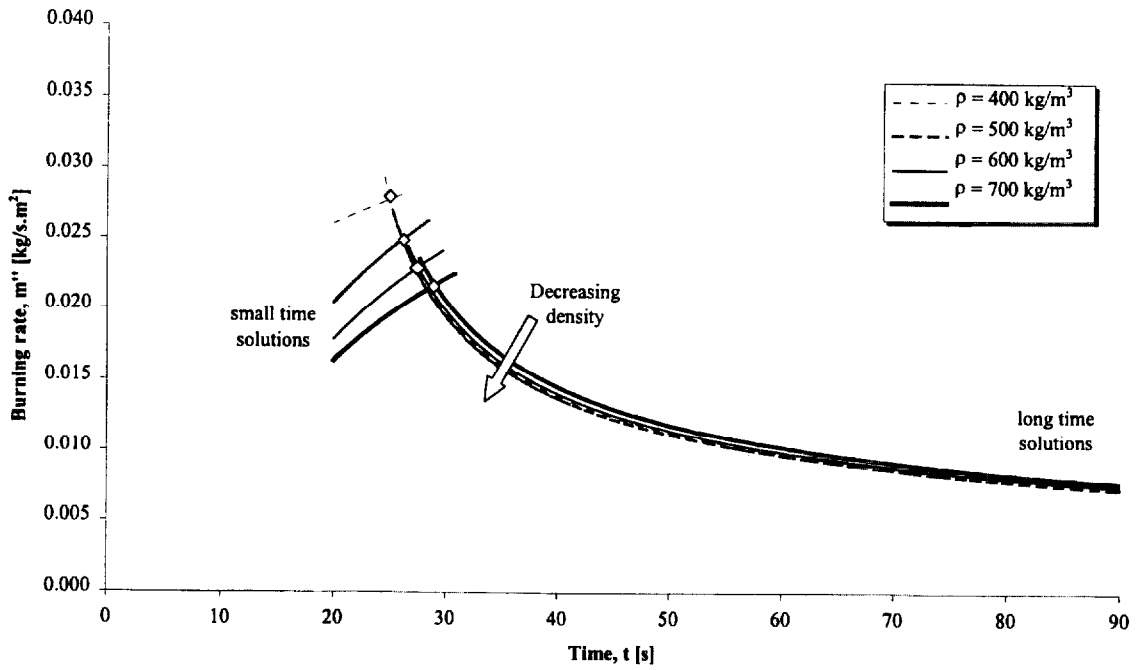
Figure 75. Effect of density on burning rate, dimensional plot.
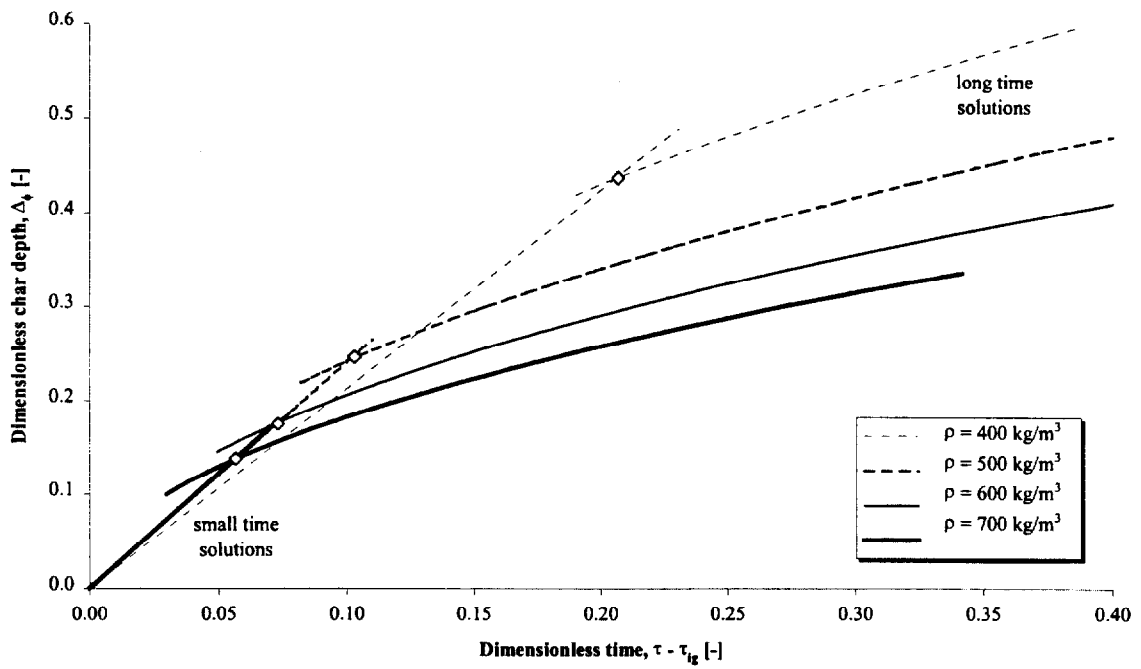
Figure 76. Effect of density on char depth, dimensionless plot.

159
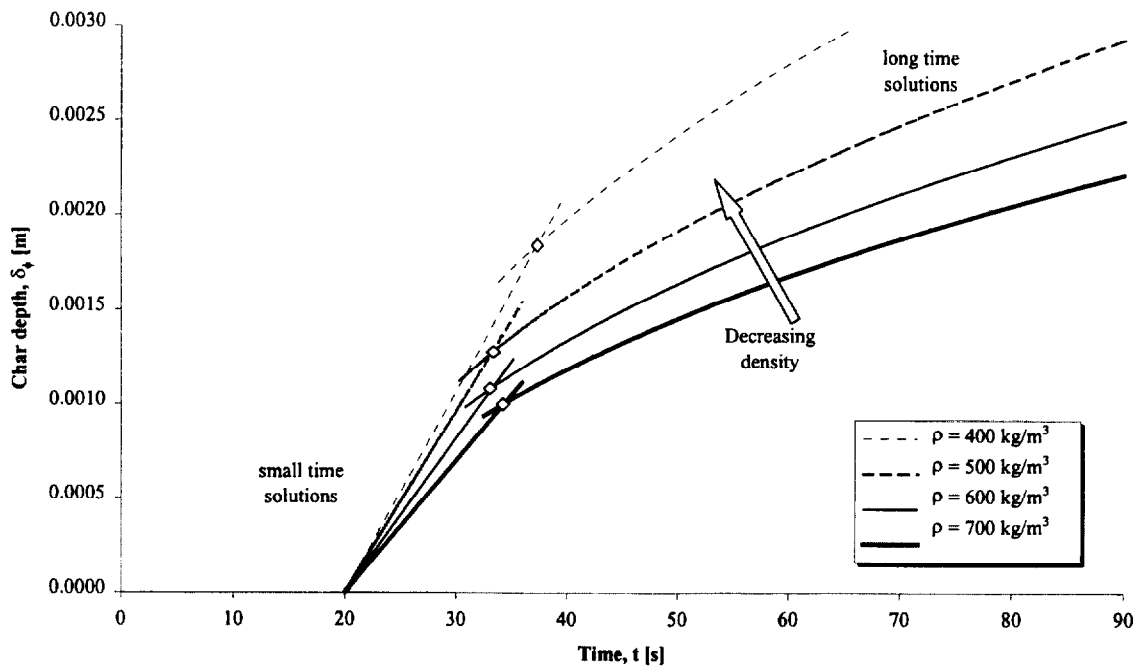
Figure 77. Effect of density on char depth, dimensional plot.

h)   Ignition time, t_{ig}

Ignition times of 10 s, 20 s, 30 s and 40 s were selected to examine their contribution to

the predicted burning rate and char depth (Figure 79 to Figure 81). In the dimensionless

plots the curves fall on top of one another. The dimensional plot clearly shows how the

effect of increasing the ignition time shifts the burning rate curve along the x-axis but

does not change the magnitude of the intersection point.
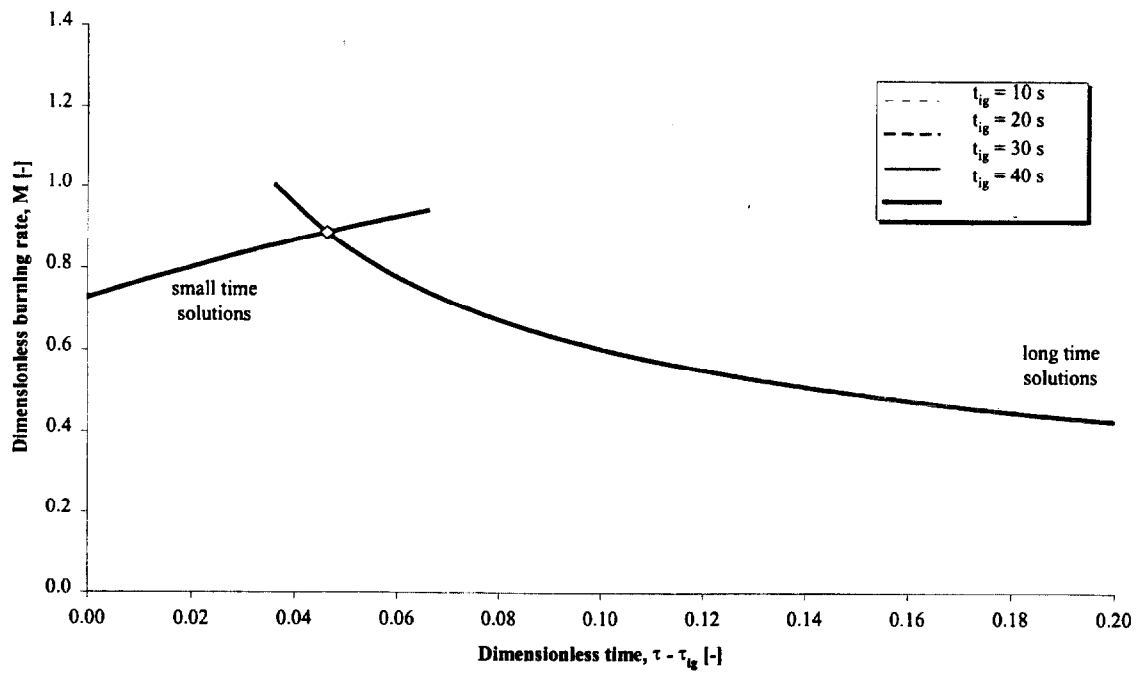
Figure 78. Effect of ignition time on burning rate, dimensionless plot.
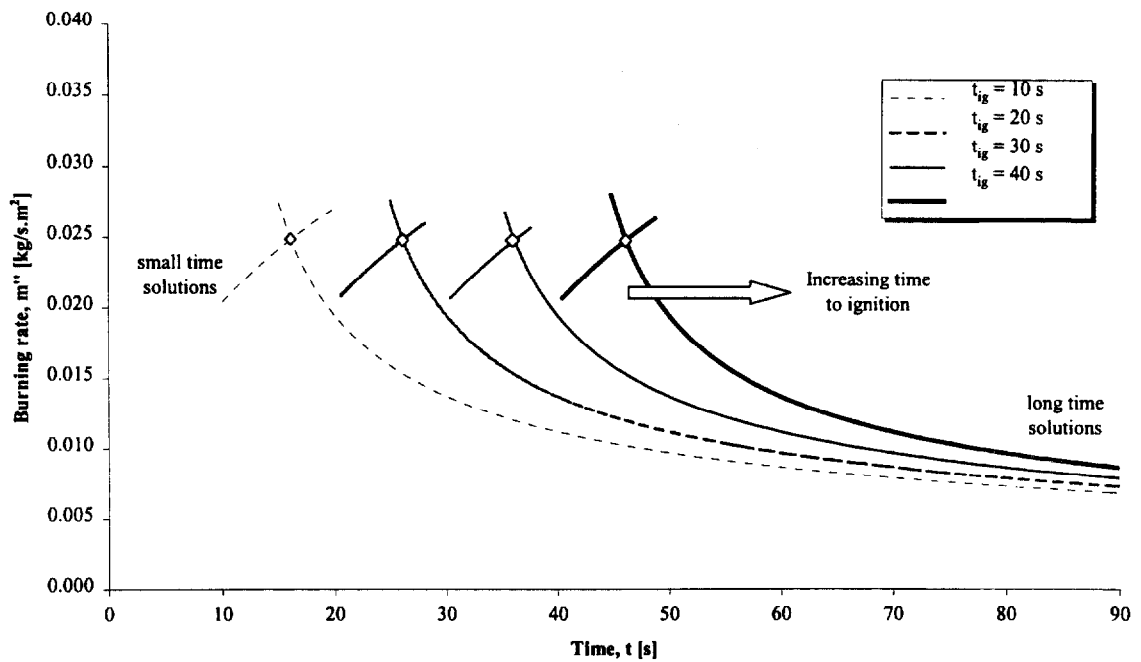
Figure 79. Effect of ignition time on burning rate, dimensional plot.

161
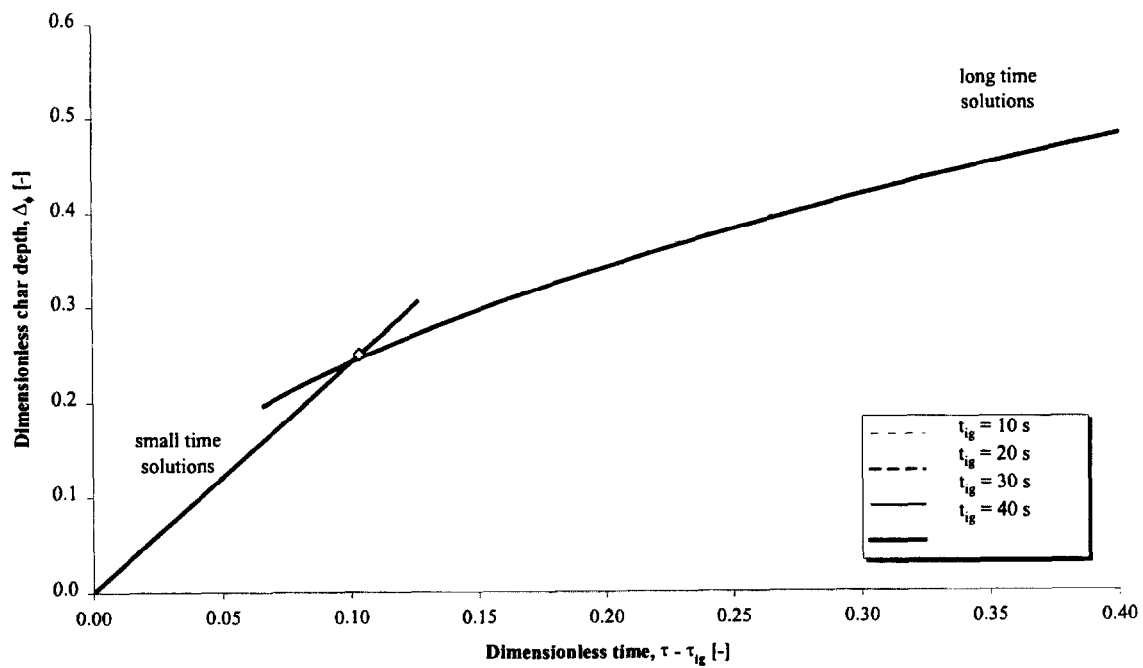
Figure 80. Effect of ignition time on char depth, dimensionless plot.
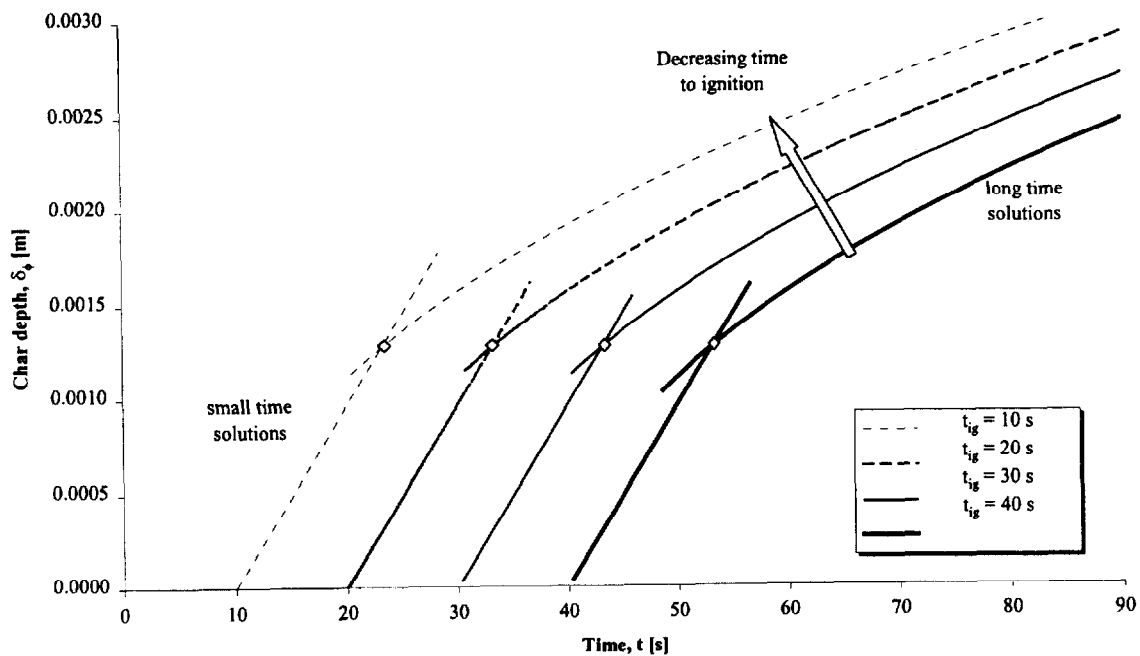
Figure 81. Effect of ignition time on char depth, dimensional plot.

162

i)   Char fraction , ϕ

The dimensionless analysis (§ 4.1.6) shows that the char fraction only contributes to the long-time solution and this is shown in Figure 82. However, since the definition of the dimensionless burning rate M includes the char fraction, when the small-time dimensional burning rate is plotted, the char fraction makes a significant difference. As the char fraction approaches zero, the peak burning rate approaches that what would be given by a non-charring material
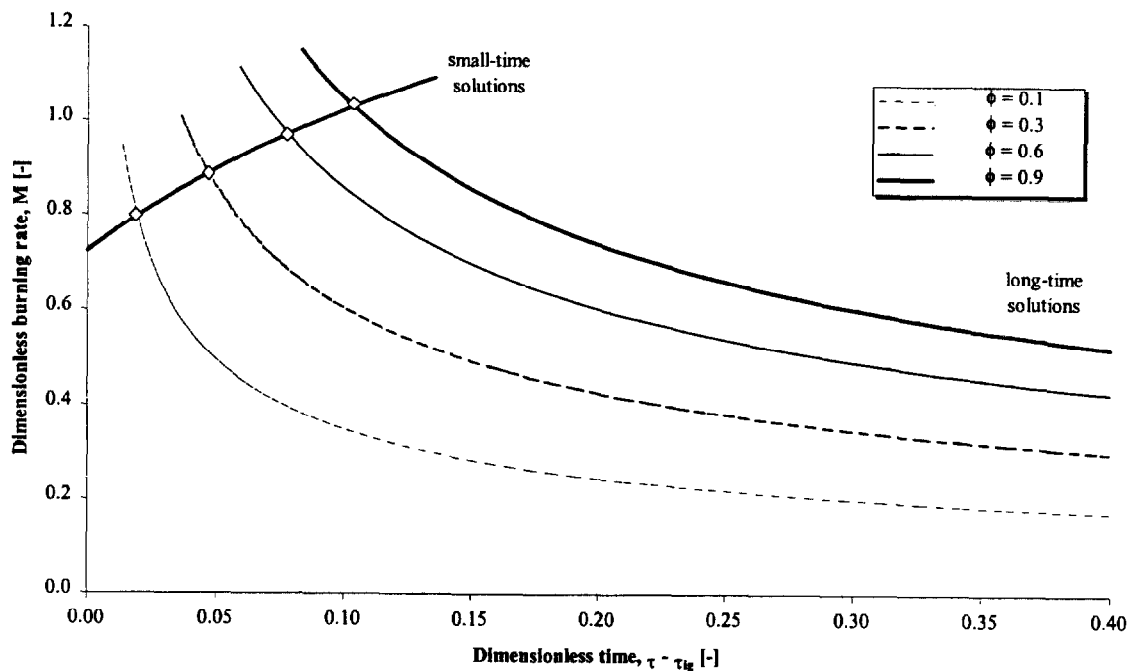
Figure 82. Effect of char fraction on burning rate, dimensional plot.
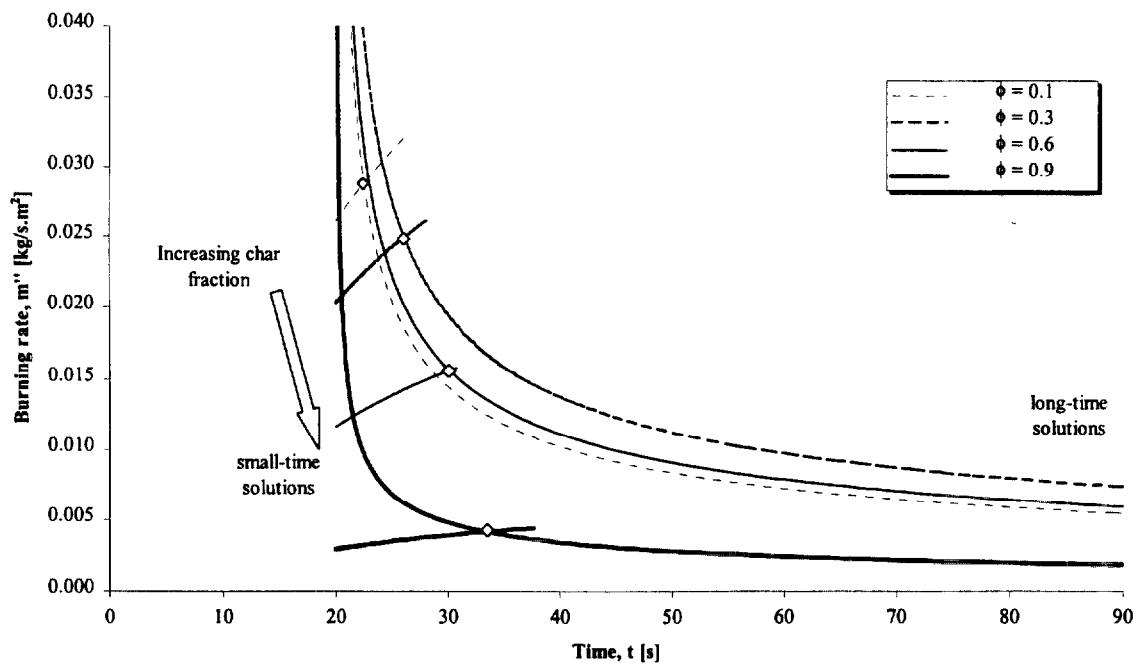
Figure 83. Effect of char fraction on burning rate, dimensionless plot.
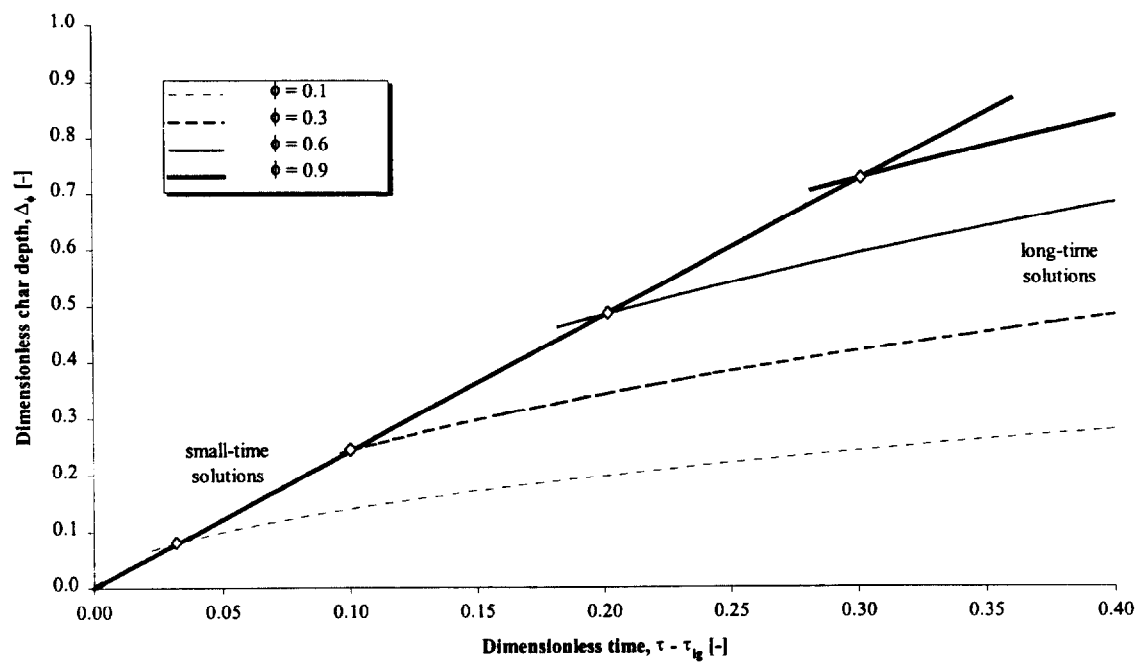
Figure 84. Effect of char fraction on char depth, dimensionless plot.
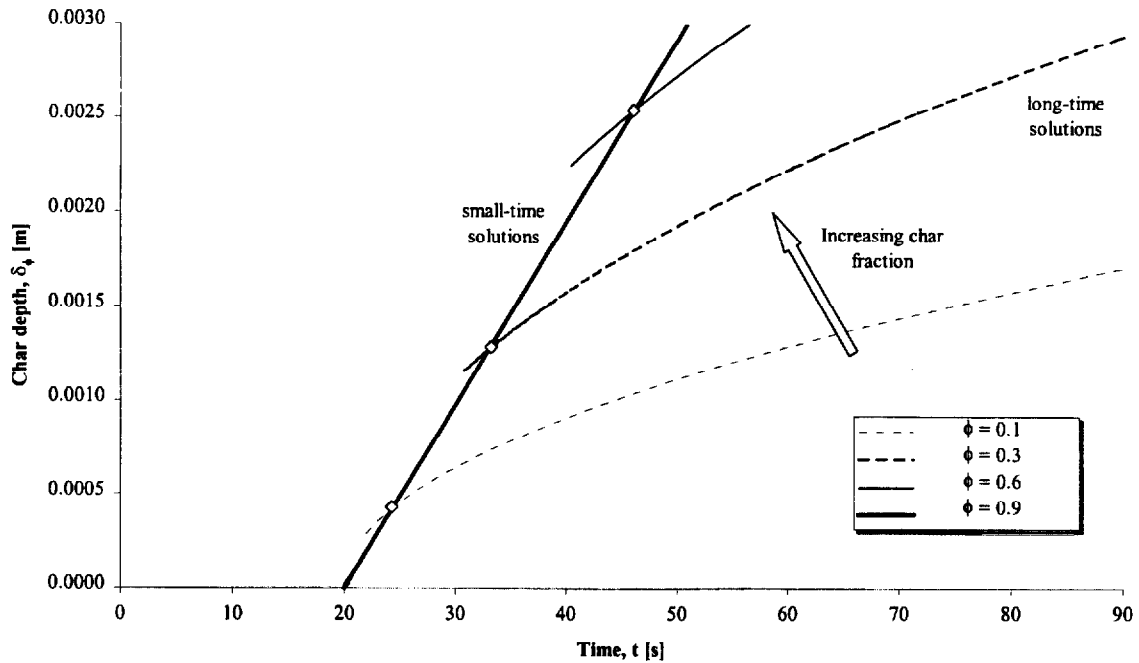
Figure 85. Effect of char fraction on char depth, dimensional plot.

4.2   Experimental limitations and difficulties

A number of limitations and difficulties were encountered during the course of the

experimental programme.

a)   Scan rate

The relatively slow scan rate used by the Cone Calorimeter may have resulted in aliasing

problems particularly for obtaining the peak mass loss rate data. Unlike for a non-

charring material, the peak mass loss rate of a charring material only occurs for a very

short (almost instantaneous) time. If the peak mass loss occurred in-between scans then

the actual value was not recorded rather a lower value may have been recorded (Figure

86).

165
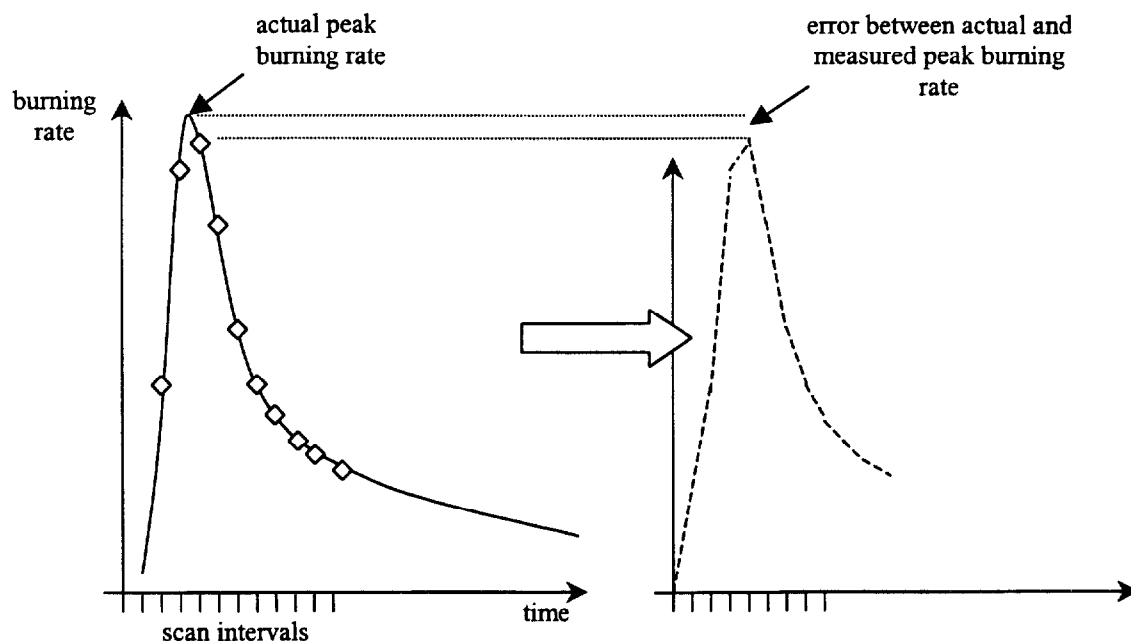
Figure 86. Error between actual and measured peak burning rate.

In a few selected experiments the scan rate was increased to 1 or 2 scans per second to investigate whether this would enable a more accurate peak burning rate to be obtained although the results of this procedure were inconclusive.

b) Thermocouples

It was found that the use of thermocouples inserted into the sample could affect the mass loss rate measurements. The weight of the probes and the associated wires may have introduced an error and it was found that vibrations in the probes could result in very noisy mass loss data. For this reason, tests conducted later in the main 'burning rate' series were completed without any thermocouples inserted into the samples. As a result of the noisy mass loss rate measurements, the effective mass loss rate (or the effective burning rate) of the sample was obtained from **Equation 1**, using the measured rate of

166

heat release at each time interval and the average heat of combustion over the duration of the test. Since the instantaneous heat of combustion is obtained from the rate of heat release and the mass loss rate, the effect of the noisy mass loss rate data resulted also in noisy heat of combustion data and thus no average heat of combustion for a given test. In these cases the average heat of combustion calculated for all similar species of wood at a given orientation was used to obtain the effective mass loss rate.

b) Back effects

The integral model described in this study assumes that the sample is semi-infinite. As described in § 1.4.2, the samples necessarily had a finite thickness. For long duration exposures the thermal wave would effectively be 'reflected' at the back thus affecting the burning characteristics of the sample. Figure 83 shows an analysis for the predicted depth of the thermal penetration wave depth as a function of time using the long-time solution to the integral model (Equation 152) and the typical wood properties given in § 4.1.7.
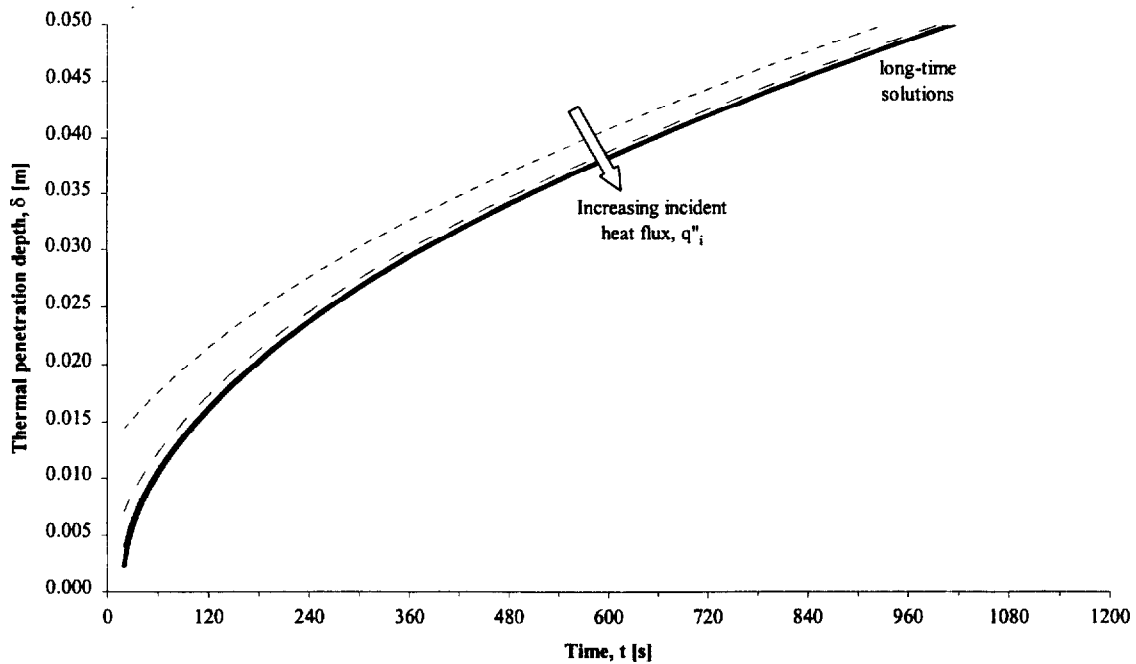
Figure 87. Predicted depth of the thermal penetration wave using the long-term integral model solution.

The integral model suggests that the thermal penetration wave reaches the back of the sample (i.e. a depth of 50 mm) in around 960 seconds (16 min). Thus, back effects may not be important up to this time. It should be note that the integral model developed by Moghtaderi *et al.* [31] successfully predicts the finite thickness effects.

The finite thickness of the sample and the experimentally configuration also affected the thermocouple measurements. As the retainer frame was heated by the incident flux, it would transfer heat into the sides and back of the sample. This heat would penetrate into the sample and thus affect the internal temperature profiles. This effect was particularly noticeable with the thermocouple mounted at the back of the sample. The output of this thermocouple would often be higher than the thermocouple at 36 mm for the initial stages

168

of a test. Eventually, as the heat from the exposed surface penetrated through the sample, the 36 mm thermocouple would record temperatures above the back thermocouple.

4.3 Data analysis and presentation

A significant volume of data was recorded in this study for the burning rate of the samples and the accompanying temperature data. In addition the analysis of this data also generated a significant volume of information. In order not to present the reader with large numbers of plots in the main text, the complete set data are provided in the Appendix. For each sample tested, plots of the energy release rate; heat of combustion; temperature profiles; measured and predicted burning rate; derived and predicted thermal penetration depth and derived and predicted char depth are given where available.

4.4 Cone Calorimeter data

The energy release rate and instantaneous heat of combustion data for each sample tested are shown in the Appendix.

4.4.1 Effective heat of combustion

The average effective heat of combustion for an individual test was found as described in § 1.4.2 and the overall average heat of combustion calculated for each species and grain orientation (Table 16).

Douglas fir		Redwood		Red oak		Maple	
along [kJ/g]	across [kJ/g]	along [kJ/g]	across [kJ/g]	along [kJ/g]	across [kJ/g]	along [kJ/g]	across [kJ/g]
10.97	9.08	11.85	8.96	12.25	12.10	13.03	12.10

Table 16. Average effective heats of combustion for each species and grain orientation.

169

In comparison Tran & White [34] obtained values of between 10.5 kJ/g and 14.5 kJ/g for Redwood and between 9.0 kJ/g and 11.9 kJ/g for Red oak.

4.4.2 Energy release

In order to verify that the measurements recorded in this study were consistent, the average and peak energy release rates obtained from the oxygen calorimetry measurements were compared with data reported by Tran & White [34], Janssens [1] and Hopkins [30].

a) Douglas fir

The peak energy release from the *along* grain samples compare well with Janssens [1] data (which were also tested in the same grain orientation) and the general trend in all three sets of data are similar.
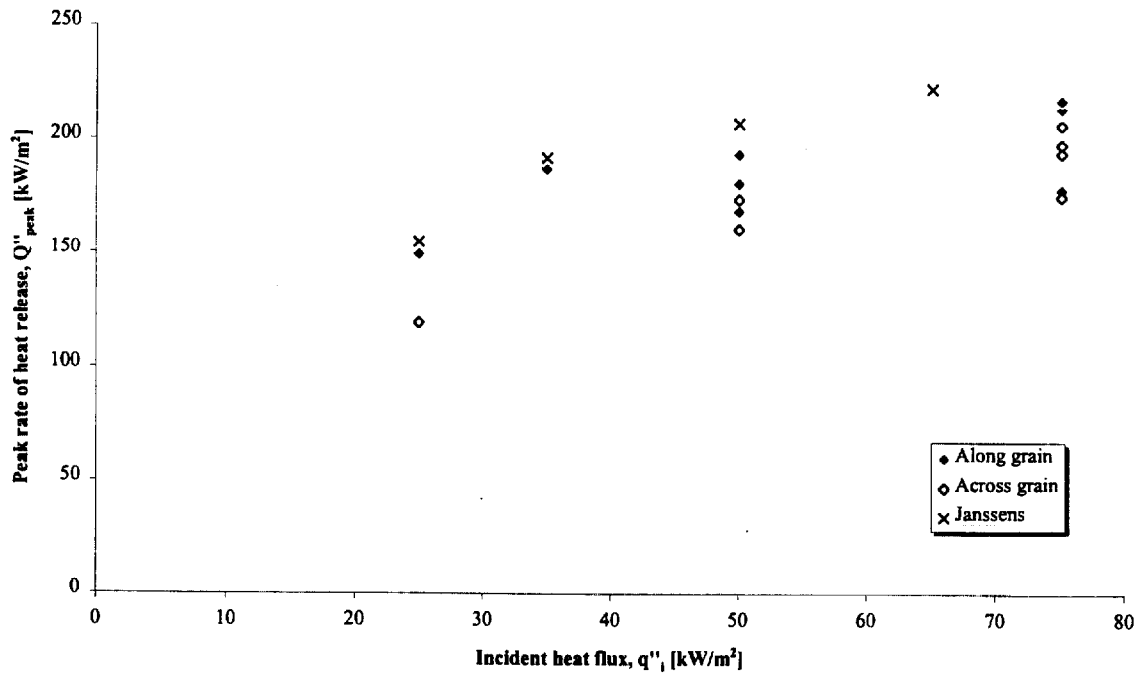
Figure 88. Comparison of peak energy release rates from Douglas fir.

b) Redwood

Figure 89 shows that Janssens [1] obtained generally higher average energy release rates

for Redwood compared to those obtained in this study. The peak energy release rates

measured by Janssens fall in-between the *along* and *across* grain measurements recorded

here (Figure 90).

171
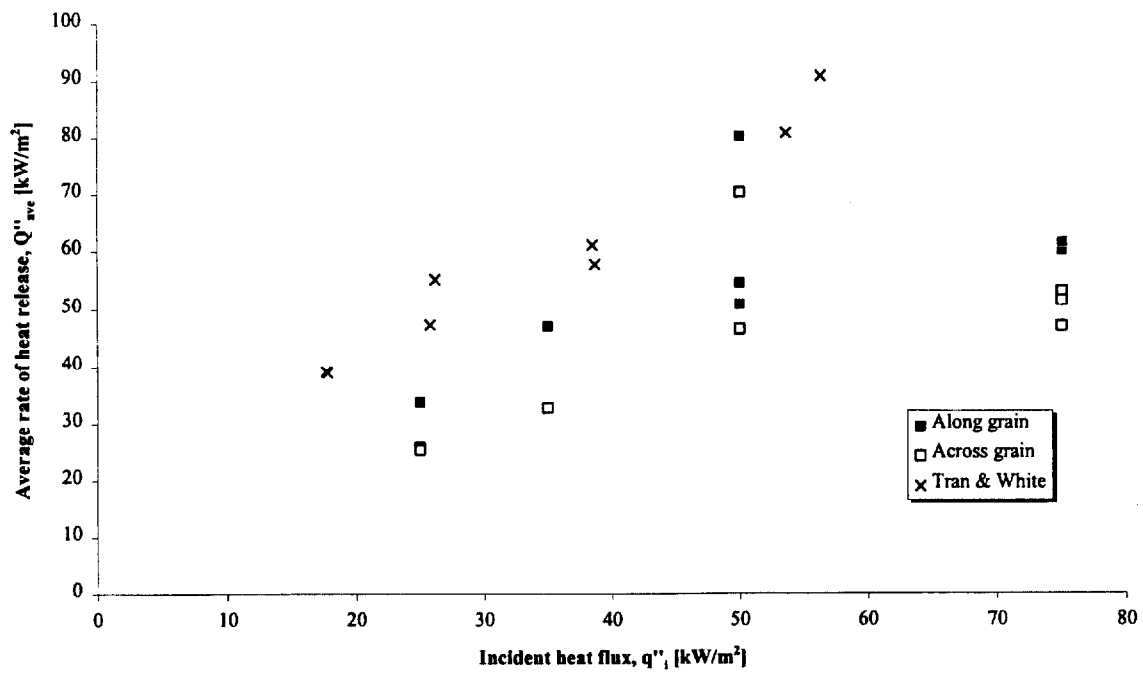
Figure 89. Comparison of average energy release rates from Redwood.
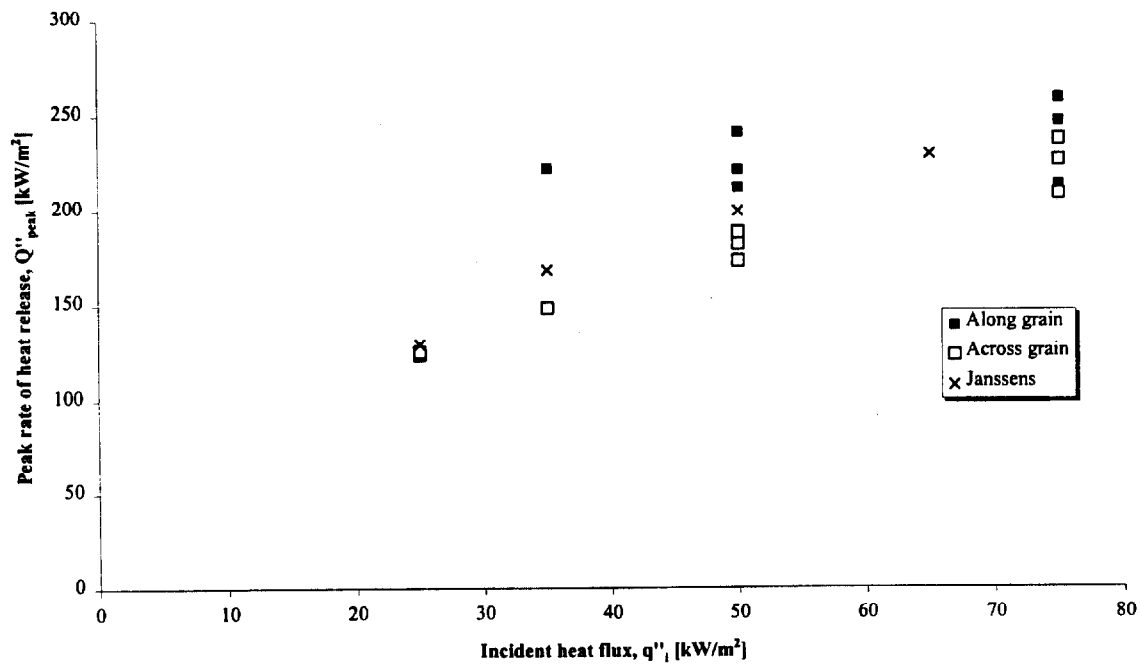
Figure 90. Comparison of peak energy release rates from Redwood.

172

c) Red oak

Figure 91 compares the average energy release from the Red oak samples with those quoted by Tran & White [34]. The along grain sample tested at 25 kW/m^2 is comparable with Tran & White's data but further comparisons cannot be made since Tran & White did not measure the energy release rates at 75 kW/m^2.
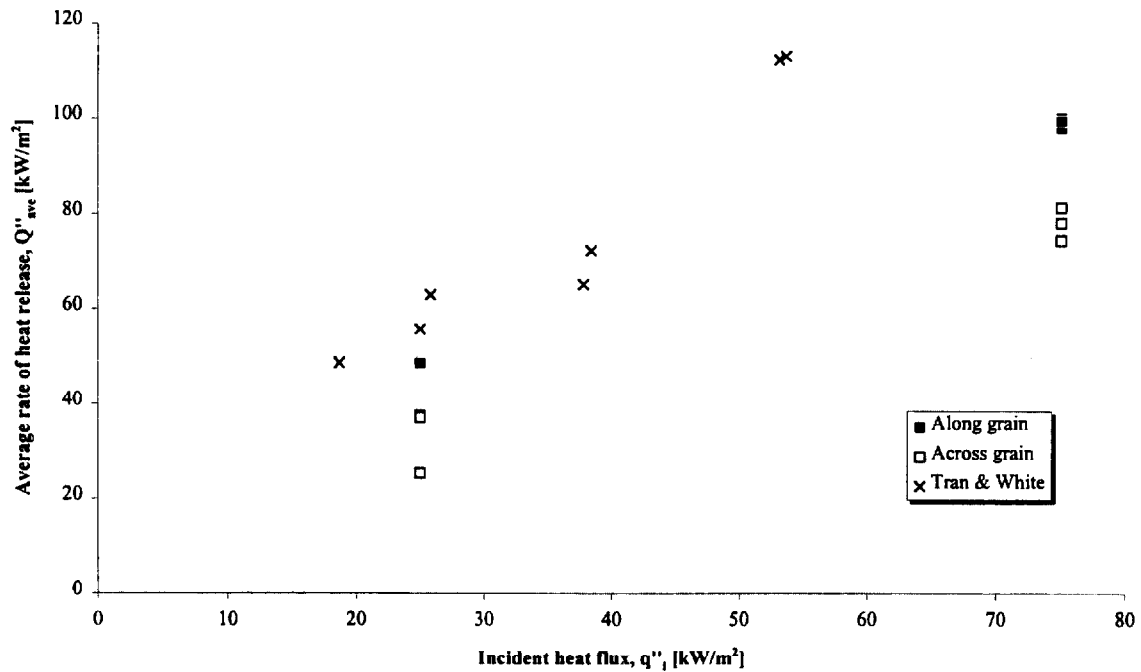
Figure 91. Comparison of average energy releases from Red oak.

d) Maple

Figure 92 shows the average energy release data for Maple. At an incident heat flux of 75 kW/m^2 the average values are almost identical for the two grain orientations. At 25 kW/m^2, there is a wider variation in the average energy release rate for the two tests conducted on the across grain samples.
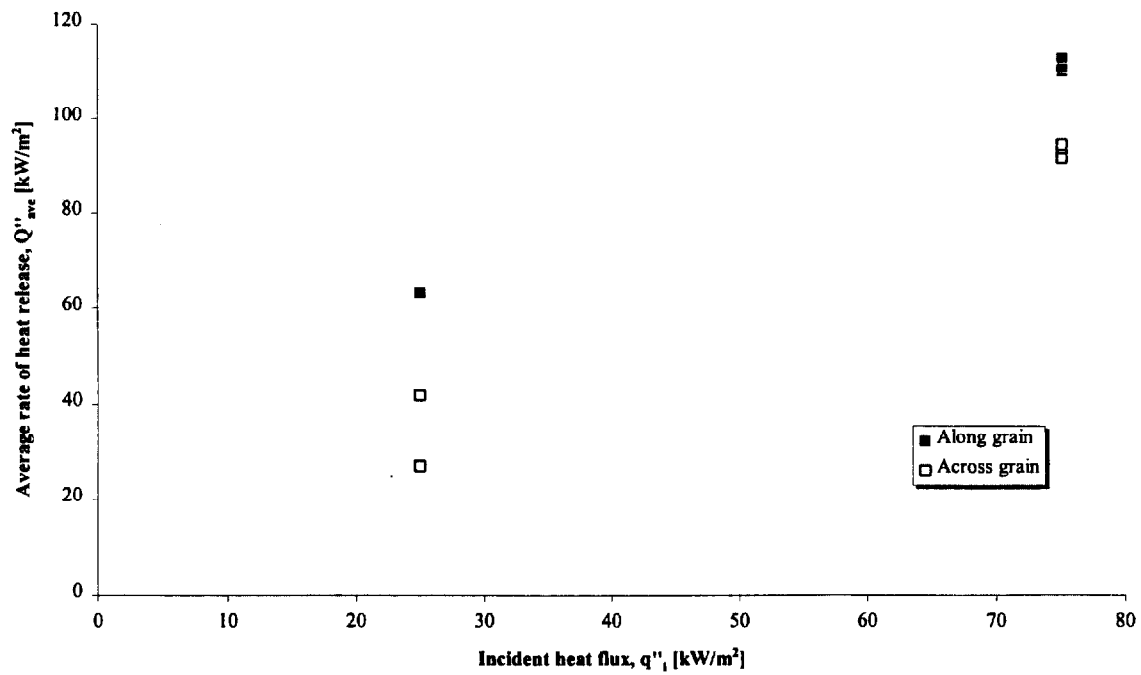
Figure 92. Average energy releases from Maple.

4.5 Char fraction

4.5.1 Analysis

In order to use the model to predict the burning rate of wood the char fraction needs to be calculated or measured. The char fraction for each sample tested in the experiments was found using Equation 5. Table 17 to Table 20 show the values used to obtain the char fractions for each specie.

174

ID	Heat flux q''_i [kW/m²]	Duration t_f [mins]	Surface area A_0 [m²]	Initial height η_0 [m]	Density ρ_w [kg/m³]	Final height η_f [m]	Char depth $\eta_{\phi,r}$ [m]	Shrinkage ω [%]	Char fraction ϕ [-]
1DFL1	75	25	0.0094	0.049	505	0.043	0.024	12%	0.27
1DFL2	75	25	0.0096	0.049	520	0.044	0.023	10%	0.34
1DFL3	25	25	0.0096	0.049	481	0.041	0.018	16%	0.62
1DFL4	75	25	0.0095	0.049	504	0.043	0.024	12%	0.32
1DFL6	50	25	0.0096	0.050	478	0.043	0.022	14%	0.40
1DFL7	50	25	0.0096	0.050	490	0.043	0.022	14%	0.40
1DFL8	50	25	0.0096	0.050	470	0.044	0.022	12%	0.36
1DFL9	35	25	0.0096	0.050	483	0.043	0.021	14%	0.52
1DFX1	75	25	0.0093	0.050	477	0.046	0.022	8%	0.19
1DFX2	75	25	0.0096	0.049	442	0.046	0.023	6%	0.16
1DFX3	75	75	0.0096	0.049	454	0.028	0.050	43%	0.34
1DFX4	25	25	0.0095	0.049	457	0.044	0.016	10%	0.42
1DFX5	75	25	0.0095	0.049	444	0.046	0.025	6%	0.24
1DFX6	50	25	0.0096	0.050	416	0.045	0.023	10%	0.25
1DFX7	50	25	0.0096	0.050	419	0.044	0.022	12%	0.37

Table 17. Sample dimensions used to obtain char fraction of Douglas fir.

ID	Heat flux q''_i [kW/m²]	Duration t_f [mins]	Surface area A_0 [m²]	Initial height η_0 [m]	Density ρ_w [kg/m³]	Final height η_f [m]	Char depth $\eta_{\phi,r}$ [m]	Shrinkage ω [%]	Char fraction ϕ [-]
1RL1	75	25	0.0095	0.048	344	0.043	0.031	10%	0.27
1RL2	75	25	0.0093	0.049	362	0.048	0.026	2%	0.12
1RL3	25	25	0.0095	0.049	357	0.045	0.019	8%	0.34
1RL4	75	25	0.0094	0.049	353	0.046	0.028	6%	0.21
1RL6	50	25	0.0096	0.050	321	0.046	0.027	8%	0.23
1RL7	50	25	0.0096	0.050	332	0.041	0.026	18%	0.41
1RL8	50	25	0.0096	0.050	319	0.043	0.027	14%	0.40
1RL9	35	25	0.0096	0.050	327	0.047	0.023	6%	0.30
1RX1	75	25	0.0090	0.050	350	0.049	0.030	2%	0.17
1RX2	75	25	0.0091	0.049	337	0.042	0.032	14%	0.29
1RX3	25	25	0.0090	0.049	339	0.042	0.022	14%	0.45
1RX4	75	25	0.0092	0.050	348	0.047	0.028	6%	0.20
1RX6	25	75	0.0096	0.050	312	0.022	0.032	56%	0.31
1RX7	50	25	0.0096	0.050	303	-	-	-	-
1RX8	50	25	0.0096	0.050	372	-	-	-	-
1RX9	50	25	0.0096	0.050	295	0.043	0.033	14%	0.39
1RX10	35	25	0.0096	0.050	300	0.042	0.025	16%	0.40

Table 18. Sample dimensions used to obtain char fraction of Redwood.

ID	Heat flux q''_i [kW/m²]	Duration t_r [mins]	Surface area A_0 [m²]	Initial height η_0 [m]	Density ρ_w [kg/m³]	Final height η_f [m]	Char depth $\eta_{\phi,r}$ [m]	Shrinkage ω [%]	Char fraction ϕ [-]
1OL1	25	25	0.0096	0.05	738	0.046	0.013	8%	0.49
1OL2	25	75	0.0096	0.05	757	0.034	0.038	32%	0.43
1OL3	75	25	0.0096	0.05	751	0.045	0.022	10%	0.31
1OL4	75	25	0.0096	0.05	757	0.047	0.022	6%	0.21
1OL5	75	25	0.0096	0.050	759	0.046	0.022	8%	0.26
1OX1	25	25	0.0096	0.050	681	0.047	0.012	6%	0.39
1OX2	25	75	0.0096	0.050	681	0.039	0.018	22%	-0.07
1OX3	75	25	0.0096	0.050	670	0.046	0.018	8%	0.06
1OX4	75	25	0.0096	0.050	680	0.047	0.018	6%	0.00
1OX5	75	25	0.0096	0.050	680	0.046	0.018	8%	0.10

Table 19. Sample dimensions used to obtain char fraction of Red oak.

ID	Heat flux q''_i [kW/m²]	Duration t_r [mins]	Surface area A_0 [m²]	Initial height η_0 [m]	Density ρ_w [kg/m³]	Final height η_f [m]	Char depth $\eta_{\phi,r}$ [m]	Shrinkage ω [%]	Char fraction ϕ [-]
1ML1	75	25	0.0096	0.05	746	0.038	0.028	24%	0.49
1ML2	75	25	0.0096	0.05	741	0.038	0.026	24%	0.47
1ML3	75	25	0.0096	0.05	743	0.039	0.027	22%	0.44
1ML4	25	25	0.0096	0.05	743	0.039	0.018	22%	0.71
1ML5	25	75	0.0096	0.050	730	0.026	0.043	48%	0.41
1MX1	25	25	0.0096	0.050	744	0.047	0.013	6%	0.39
1MX2	25	75	0.0096	0.050	731	0.005	0.050	90%	0.13
1MX3	75	25	0.0096	0.050	756	0.046	0.020	8%	0.08
1MX4	75	25	0.0096	0.050	740	0.045	0.028	10%	0.31
1MX5	75	25	0.0096	0.050	739	0.046	0.020	8%	0.06

Table 20. Sample dimensions used to obtain char fraction of Maple.
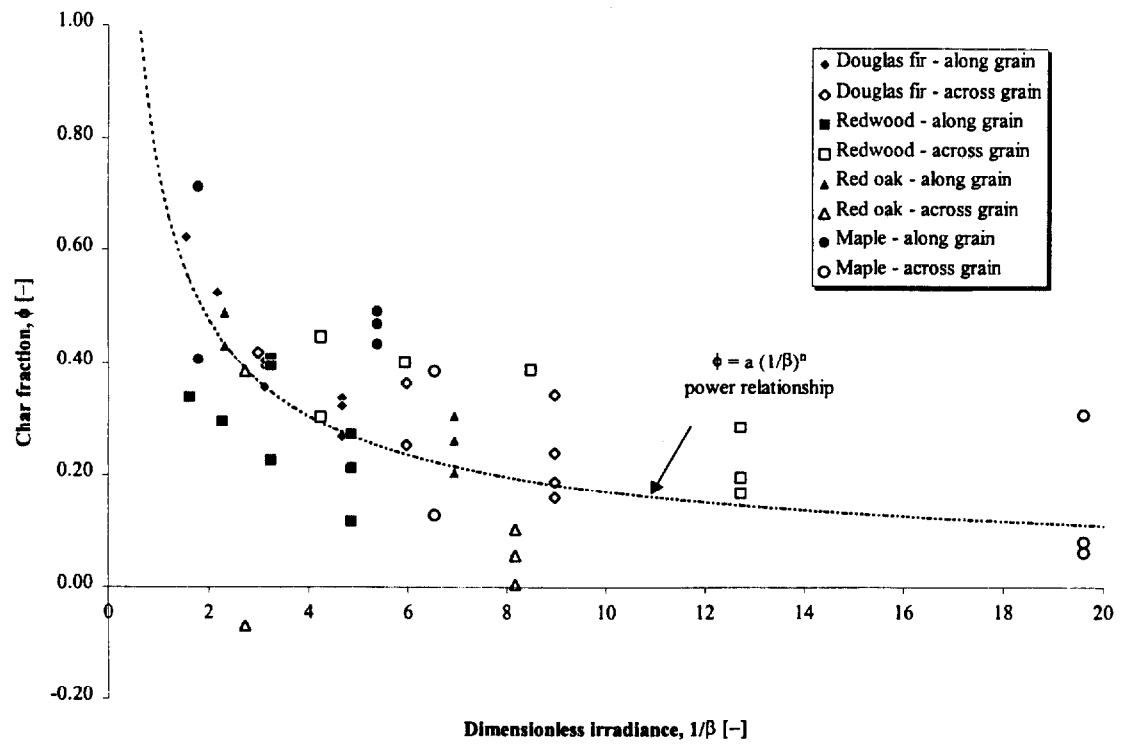
Figure 93. Char fraction against dimensionless irradiance.

A plot of char fraction against dimensionless irradiance is shown in Figure 93. Assuming that the char fraction is related to the dimensionless irradiance such that

$$\phi = a\left(\frac{1}{\beta}\right)^n$$

where a and n are constants. By taking logs of both sides

$$\ln\phi = \ln\left[a\left(\frac{1}{\beta}\right)^n\right]$$

$$= n\ln\left(\frac{1}{\beta}\right) + \ln a$$

177

By plotting $\ln\phi$ against $\ln\left(\dfrac{1}{\beta}\right)$ the values for a and n can be obtained from the gradient

and intercept of the best-fit line. Figure 94 shows the ln-ln plot with a best-fit line.
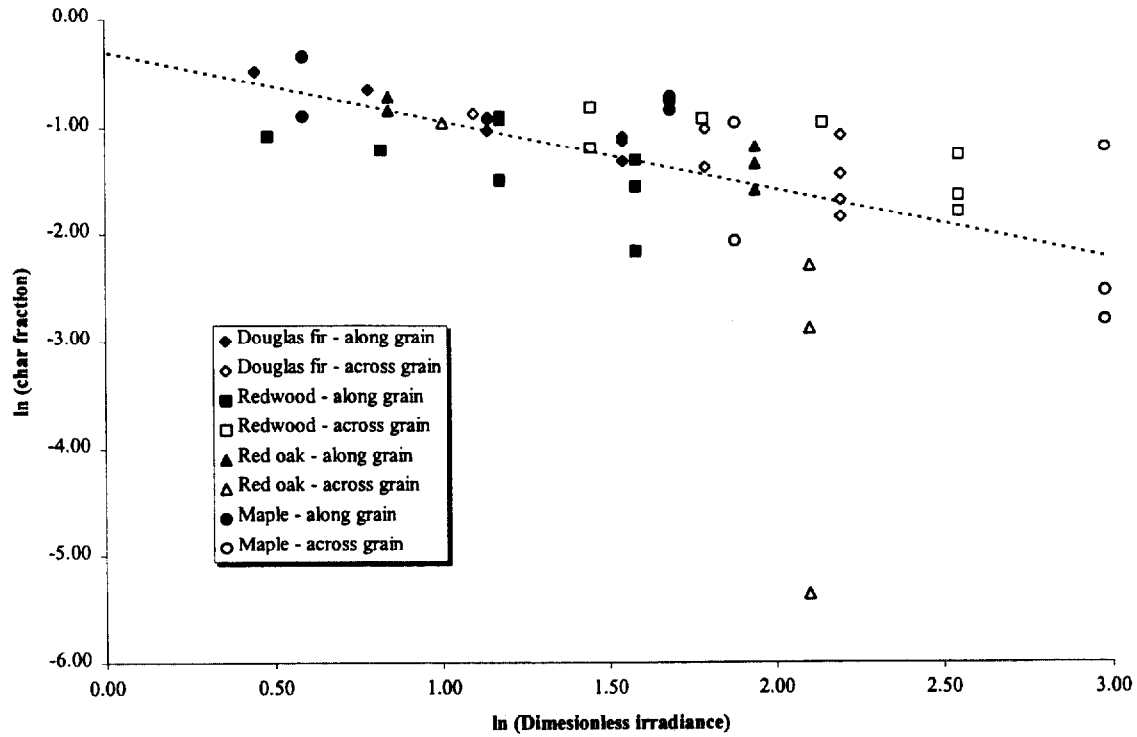
Figure 94. ln (char fraction) against ln (dimensionless irradiance).

Thus, the values for a and n were 0.74 and -0.64 respectively and the relationship

between the char fraction and the dimensionless irradiance is

$$\phi = 0.74\left(\frac{1}{\beta}\right)^{-0.64}$$

Equation 156

This relationship is plotted back on Figure 93 to show how it compares to the data. There

is a fair degree of scatter of the data which may partly be due to the difficulties of

measuring the char depth. Clearly, this relationship may not be universal for all charring materials or even all species of wood but is applicable to this study.

4.5.2 Measurements

Three samples, all exposed for 75 minutes, were carefully examined and the actual char fraction obtained by measuring the mass of the char and the mass of the virgin wood. Figure 95 {a} shows sample 1ML5 prior to separating the char from the virgin wood. Note how it is not easy to determine the exact transition between the char layer and the virgin wood, which made the estimation of the volume difficult.
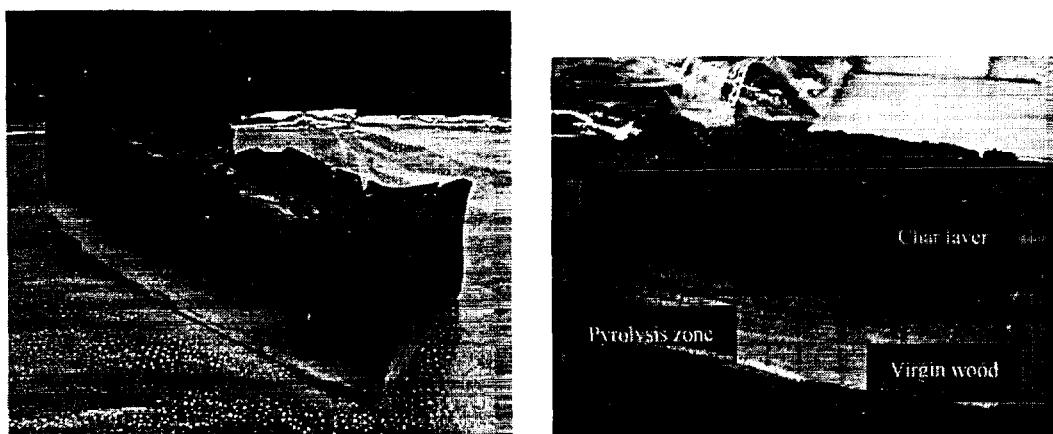
Figure 95. Half of samples of {a} 1ML5 and {b} 2DFX9i showing char layer and virgin wood.

		Sample ID		
		1ML5	1MX2	1OL2
Char volume	[m³]	0.000152	0.000095	0.000128
Virgin wood volume	[m³]	0.000050	0.000034	0.000055
Char mass	[kg]	0.0331	0.0217	0.0346
Virgin wood mass	[kg]	0.0407	0.0204	0.0318
Char density	[kg/m³]	217	228	299
Virgin wood density	[kg/m³]	837	606	576
Measured char fraction	[-]	0.26	0.38	0.52
Char fraction from analysis	[-]	0.41	0.13	0.43

Table 21. Comparison of measured and calculated char fraction.

Table 21 shows a comparison of the measured and calculated char fraction. Only with the 1OL2 sample is the comparison relatively close. It would have been desirable to have continued this comparison with additional samples, however, the samples were required by Schroeder [10] as part of his study and so were not available to the author.

4.6 Burning rate

4.6.1 Determination of flame heat flux and heat of gasification

a) Burning rate analysis

Equation 79 suggests that the net surface heat flux just after ignition is given by

$$\dot{q}''_+ = \dot{q}''_{fl} + \dot{q}''_i - \sigma\left(T_s^4 - T_0^4\right)$$

by neglecting the ambient temperature contribution which is small, this equation becomes

$$\dot{q}''_+ = \dot{q}''_{fl} + \dot{q}''_i - \sigma T_s^4$$

Equation 157

Consider the case of a material with a steady state burning rate $\dot{m}''_{steady}$. From Equation 131,

$$\frac{\rho_\phi c_\phi}{2}\left(\frac{d}{dt}T_s - \frac{d}{dt}T_v\right)\delta_\phi + \dot{m}'' c_g(T_s - T_v) + \frac{\dot{m}''}{(1-\phi)}[\Delta H_v] = \dot{q}''_+(T_s) - \frac{2k_w(T_v - T_0)}{\delta_w}$$

assuming that the surface temperature T_s of the burning material is at T_v, the thermal

penetration depth δ_w is δ_s and the burning rate $\dot{m}''$ is $\dot{m}''_{steady}$, then

$$\underbrace{\frac{\rho_\phi c_\phi}{2}\left(\frac{d}{dt}T_s - \frac{d}{dt}T_v\right)\delta_\phi}_{=0} + \underbrace{\dot{m}''_{steady} c_g(T_s - T_v)}_{=0} + \frac{\dot{m}''_{steady}}{(1-\phi)}[\Delta H_v] = \dot{q}''_+(T_v) - \frac{2k_w(T_v - T_0)}{\delta_s}$$

$$\therefore \quad \frac{\dot{m}''_{steady}}{(1-\phi)}[\Delta H_v] = \dot{q}''_+(T_v) - \frac{2k_w(T_v - T_0)}{\delta_s}$$

Equation 158

Multiplying Equation 158 through by c_w

$$c_w \frac{\dot{m}''_{steady}}{(1-\phi)}[\Delta H_v] = c_w \dot{q}''_+(T_v) - \frac{2k_w c_w(T_v - T_0)}{\delta_s}$$

Equation 159

From the definition of L, Equation 159 can be written as

$$c_w \frac{\dot{m}''_{steady}}{(1-\phi)}[\Delta H_v] = c_w \dot{q}''_+(T_v) - \frac{2k_w(L - \Delta H_v)}{\delta_s}$$

$$\frac{\dot{m}''_{steady}}{(1-\phi)} = \frac{\dot{q}''_+(T_v)}{\Delta H_v} - \frac{2k_w L}{\delta_s c_w \Delta H_v} + \frac{2k_w}{\delta_s c_w}$$

substituting for δ_s (§ 4.1.6)

$$\frac{\dot{m}''_{steady}}{(1-\phi)} = \frac{\dot{q}''_+(T_v)}{\Delta H_v} - \frac{2k_w L}{c_w \Delta H_v} \cdot \frac{c_w \dot{q}''_+(T_v)}{2k_w L} + \frac{2k_w}{c_w} \cdot \frac{c_w \dot{q}''_+(T_v)}{2k_w L}$$

$$\frac{\dot{m}''_{steady}}{(1-\phi)} = \frac{\dot{q}''_+(T_v)}{\Delta H_v} - \frac{\dot{q}''_+(T_v)}{\Delta H_v} + \frac{\dot{q}''_+(T_v)}{L}$$

thus, recalling that $T_v = T_s$, the steady mass loss rate is given by

$$\dot{m}''_{steady} = \frac{(1-\phi)\dot{q}''_+(T_s)}{L}$$

Equation 160

Combining Equation 157 with Equation 160 gives

$$\frac{\dot{m}''_{steady}}{(1-\phi)} = \frac{\dot{q}''_{fl} + \dot{q}''_i - \sigma T_s^4}{L}_+ = \frac{\dot{q}''_{fl}}{L} + \frac{\dot{q}''_i}{L} - \frac{\sigma T_s^4}{L}$$

Equation 161

Using a linear regression line through the a plot of steady mass loss rate against incident

heat flux, the slope can be expressed with the following equation

$$slope = \frac{(1-\phi)}{L} = \frac{\Delta \dot{m}''_{steady}}{\Delta \dot{q}''_i}$$

Equation 162

Thus

$$L = \frac{slope}{(1-\phi)}$$

Equation 163

In addition, the value for the intercept of the best fit-line is where the incident heat flux

$\dot{q}''_i$ equals zero. Therefore, Equation 161 can be rewritten as

$$\dot{m}''_{steady} = intercept = \frac{(1-\phi)}{L}(\dot{q}''_{fl} - \sigma T_s^4)$$

Equation 164

182

By rearranging, we can calculate the flame heat flux $\dot{q}''_{fl}$ with

$$\dot{q}''_{fl} = \frac{\text{intercept} \cdot L}{(1-\phi)} + \sigma T_s^4$$

Equation 165

assuming that the surface temperature T_s is at the ignition temperature T_{ig}.

The theory described above in Equation 164 and Equation 165 is similar to those developed for a non-charring material but with addition of the char fraction. For a charring material the mass loss rate does not reach a steady value at ignition but reaches a peak and then decays over time (§ 1.2.2). Thus, by plotting the peak mass loss rate against incident heat flux, an (over-)estimate of the heat of gasification and flame heat flux at the peak burning rate can be obtained from Equation 162 and Equation 165.

Figure 96 to Figure 99 shows the graphs of the measured peak burning rate against incident heat flux for each species tested in the Cone Calorimeter. The heat of gasification and flame heat flux obtained from these in the *along* grain and *across* grain configurations are shown in Table 22 and Table 23.
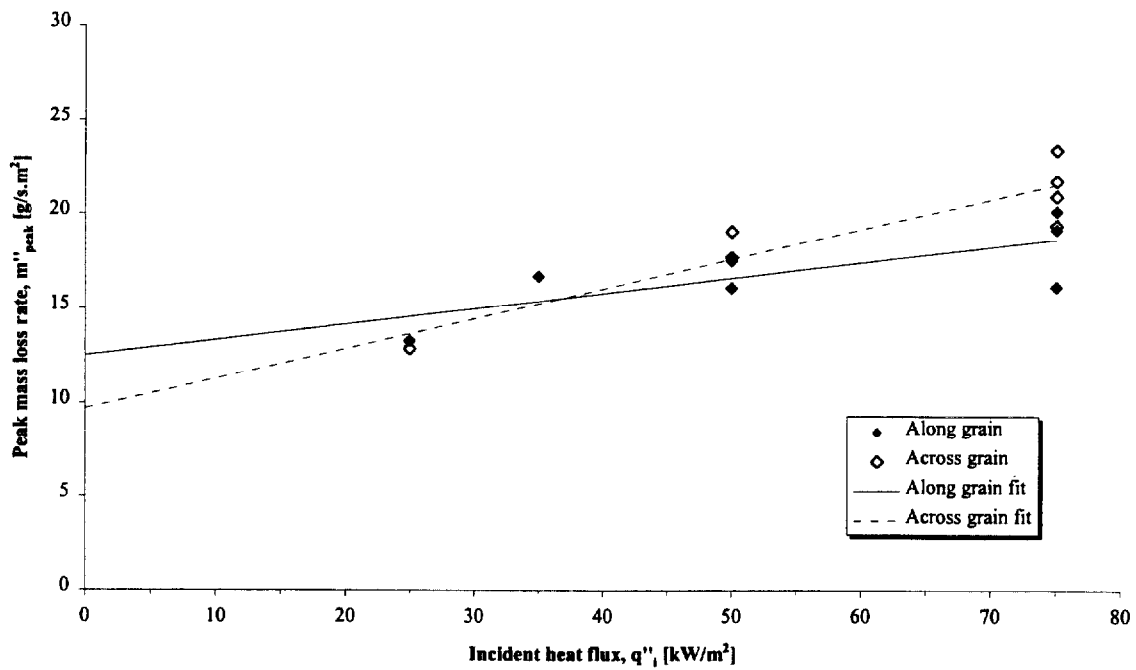
Figure 96. Peak burning rate as a function of incident heat flux for Douglas fir.
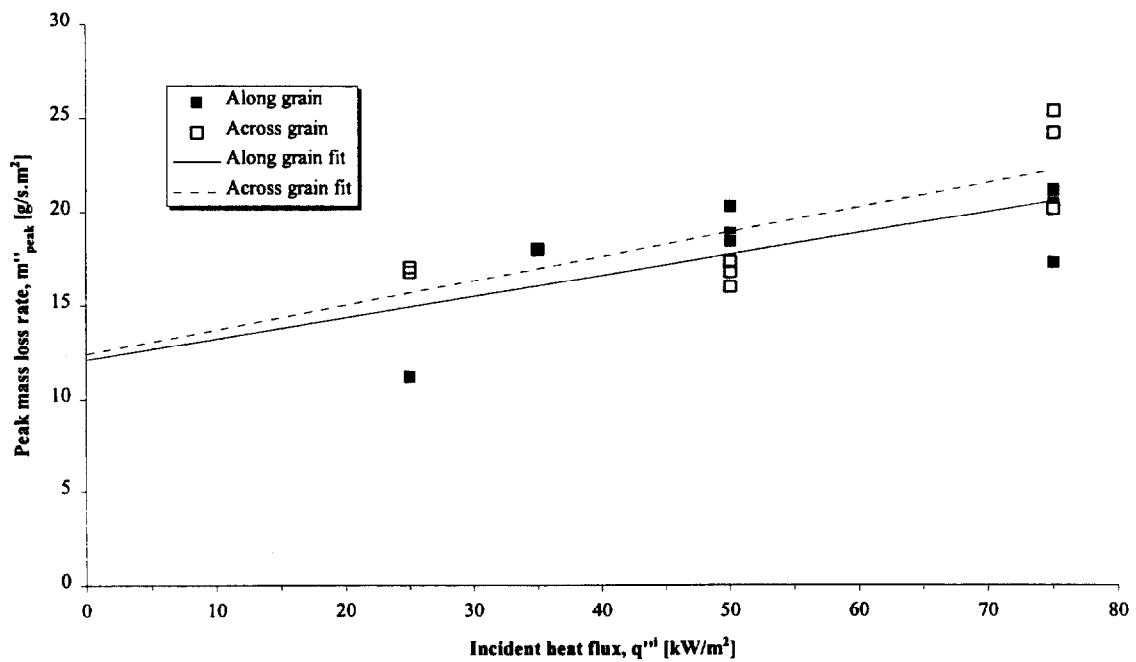
Figure 97. Peak burning rate as a function of incident heat flux for Redwood.

184
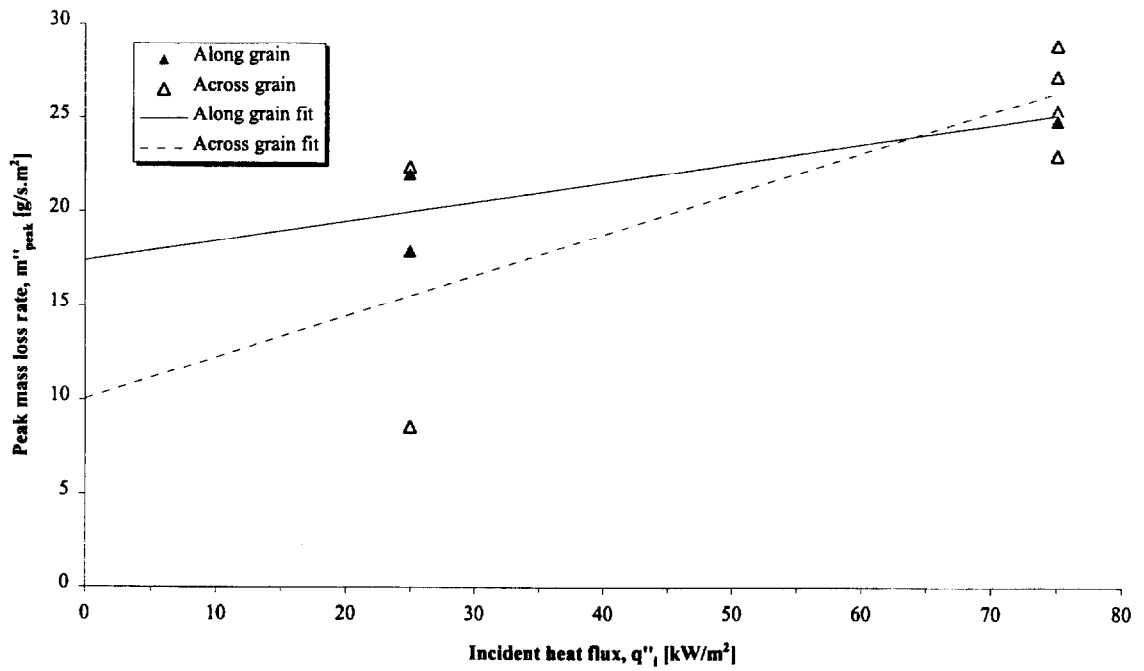
Figure 98. Peak burning rate as a function of incident heat flux for Red oak.
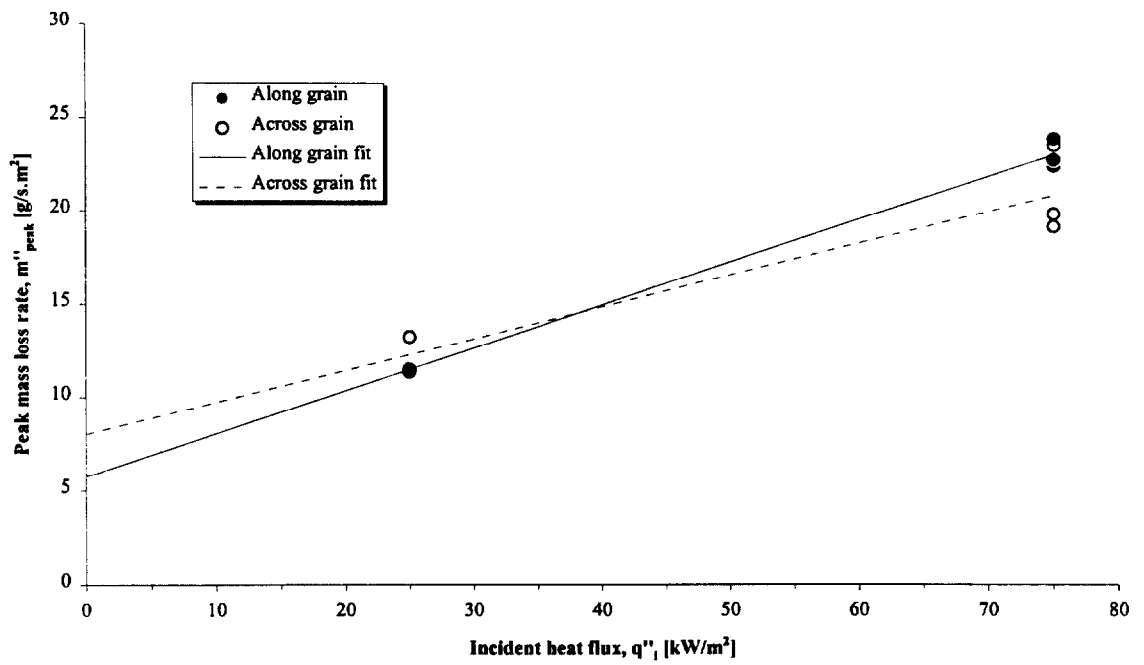
Figure 99. Peak burning rate as a function of incident heat flux for Maple.

185

Incident heat flux [kW/m²]	Douglas fir along [kJ/g]	Douglas fir across [kJ/g]	Redwood along [kJ/g]	Redwood across [kJ/g]	Red oak along [kJ/g]	Red oak across [kJ/g]	Maple along [kJ/g]	Maple across [kJ/g]
25	4.59	3.65	5.73	4.16	5.14	4.29	1.90	4.33
35	5.77	6.28	6.10	4.50	9.54	4.55	4.32	5.83
50	7.44	4.34	5.69	4.60	9.54	4.55	4.32	5.83
75	8.36	5.06	6.94	5.90	7.07	4.30	2.31	4.95

Table 22. Calculated heats of gasification from peak burning rate data.

Douglas fir along [kW/m²]	Douglas fir across [kW/m²]	Redwood along [kW/m²]	Redwood across [kW/m²]	Red oak along [kW/m²]	Red oak across [kW/m²]	Maple along [kW/m²]	Maple across [kW/m²]
162	65	115	96	172	51	34	49

Table 23. Calculated flame heat fluxes from peak burning rate data.

b)   Iterative approach

An iterative approach, as suggested by Quintiere & Anderson [37], was used to adjust the flame heat flux and heat of gasification such that there was an overall best agreement between the model predictions and the experimental data.

For each wood at a given orientation, the effective burning rate obtained from the Cone Calorimeter experiments were plotted in dimensionless terms and each individual dimensionless burning rate curve was plotted on a single set of axes (for e.g. Figure 96, similar results were obtained for the other woods). Since the definition of the dimensionless burning rate M is

$$M \equiv \frac{\dot{m}'' L}{(1-\phi)\dot{q}''_+(T_s)}$$

186

initial values of the heat of gasification L and the flame heat flux $\dot{q}_{fl}''$ (used to find $\dot{q}_+''(T_s)$ from Equation 81) were taken from the effective steady state burning rate analysis described above.

Using the examination of the contribution of the flame heat flux and heat of gasification (§ 4.1.7) to the small-time and long-time solutions to the integral model as a guide, single values for these two variables were selected such that the following were achieved:

i. The small-time solution gave a reasonable match with the initial mass loss rate at ignition,

ii. The intersection of the small-time and long-time solutions was comparable with the peak experimental burning rate,

iii. The long-time solution followed the decay portion of the experimental burning rate.

It was found that adjusting the flame heat flux and heat of gasification to exactly match any one of the three criteria resulted in a poor comparison with the remaining two. Thus the selection of the flame heat flux and heat of gasification was based on obtaining a reasonable match with each of the three criteria.

Clearly the values of the flame heat flux and heat of gasification obtained in this study are not intended to be exact for a particular species of wood at a given orientation. As already discussed in § 1.2.1, wood by its very nature varies from tree to tree and within any one

187

tree. In addition, the iterative process and the need to arbitrarily decide what constituted a

good match means that the values given here are only representative.

Legend:
- DFL1 : 75 kW/m^2 (1)
- DFL2 : 75 kW/m^2 (2)
- DFL3 : 25 kW/m^2 (3)
- DFL4 : 75 kW/m^2 (4)
- DFL6 : 50 kW/m^2 (6)
- DFL7 : 50 kW/m^2 (7)
- DFL8 : 50 kW/m^2 (8)
- DFL9 : 35 kW/m^2 (9)
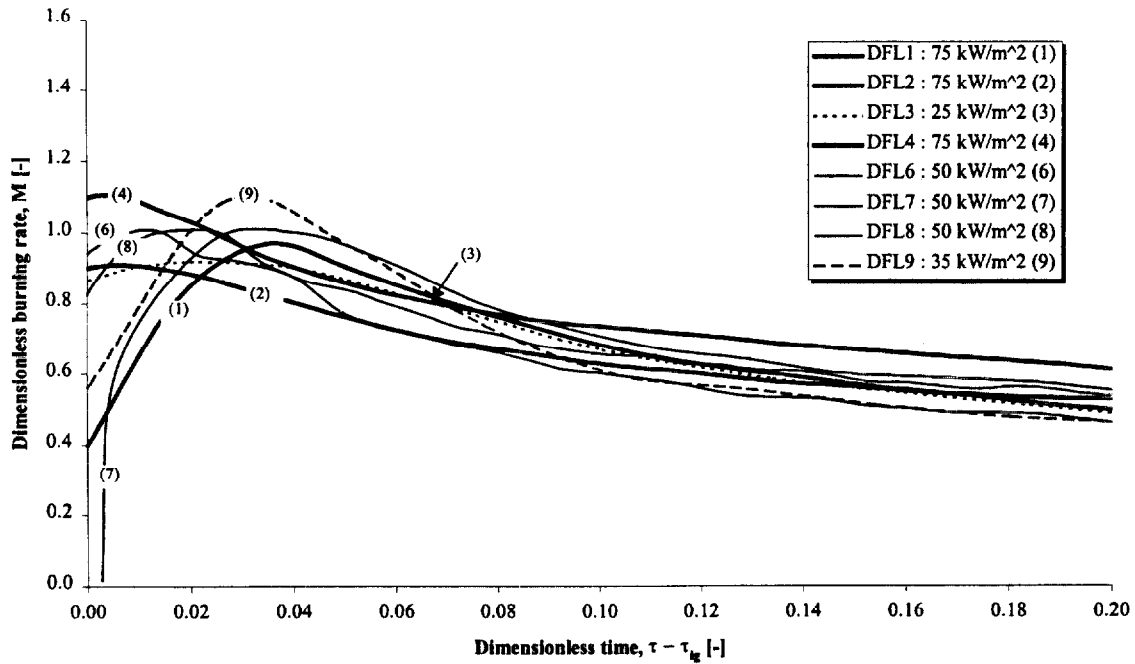
Figure 100. Dimensionless burning rates of Douglas fir in the *along* grain orientation
using properties calculated in each individual test.

Table 24 and Table 25 show the final derived values for the heat of gasification and flame

heat flux for each wood in the two grain configurations.

Douglas fir		Redwood		Red oak		Maple	
along [kJ/g]	*across* [kJ/g]	*along* [kJ/g]	*across* [kJ/g]	*along* [kJ/g]	*across* [kJ/g]	*along* [kJ/g]	*across* [kJ/g]
1.57	2.93	2.83	3.18	2.34	2.33	1.70	3.53

Table 24. Final derived heats of gasification from iterative analysis.

Douglas fir		Redwood		Red oak		Maple	
along [kW/m^2]	across [kW/m^2]	along [kW/m^2]	across [kW/m^2]	along [kW/m^2]	across [kW/m^2]	along [kW/m^2]	across [kW/m^2]
17	46	35	33	35	33	16	36

Table 25. Final derived flame heat fluxes from iterative analysis.

In the study by Rhodes & Quintiere [46] and also by Hopkins [30] it was found that the flame heat flux for burning PMMA was approximately constant at 37 kW/m^2. Hopkins also measured the flame heat flux as a function of time for Redwood and Red oak. For Redwood, peak flame heat fluxes between 32 kW/m^2 and 53 kW/m^2 with an average of 44 kW/m^2 were recorded by Hopkins compared to an average of 34 kW/m^2 obtained in this study. For Red oak, Hopkins recorded values between 32 kW/m^2 and 52 kW/m^2 with an average of 42 kW/m^2 compared to an average of again 34 kW/m^2 obtained in this study. In comparison, for thermoplastics, Hopkins obtained values between 14 kW/m^2 and 37 kW/m^2. The peak flame heat fluxes obtained by Hopkins are on average higher than those obtained using the iterative approach. However, it should be noted that in many of the experiments conducted by Hopkins, the flame heat flux would reduce over time presumably because, as observed in § 1.4.2, the flames became smaller as the char layer formed. We might conclude that the flame heat fluxes derived here are more akin to the average flame heat flux over the duration of the test and thus would be expected to be less than the peak value.

Figure 101 shows the dimensionless burning rate for Douglas fir, *along* grain, for the four incident heat fluxes using the final heat of gasification and flame heat flux given in Table 24 and Table 25. The chart is a combination of the individual burning rates for each

189

sample, averaged and smoothed so as to obtain the general form of the experimental data. Comparison with Figure 49 shows how the experimental data compares with the integral model solutions. The peak dimensionless burning rate at low heat fluxes is greater than at high heat fluxes in both cases. The relative offset in the peaks as a function of time is more difficult to identify in the experimental data. At long-times the burning rates at the various heat fluxes run parallel although there is some minor fluctuation in the experimental data. Similar results were obtained for the other species.
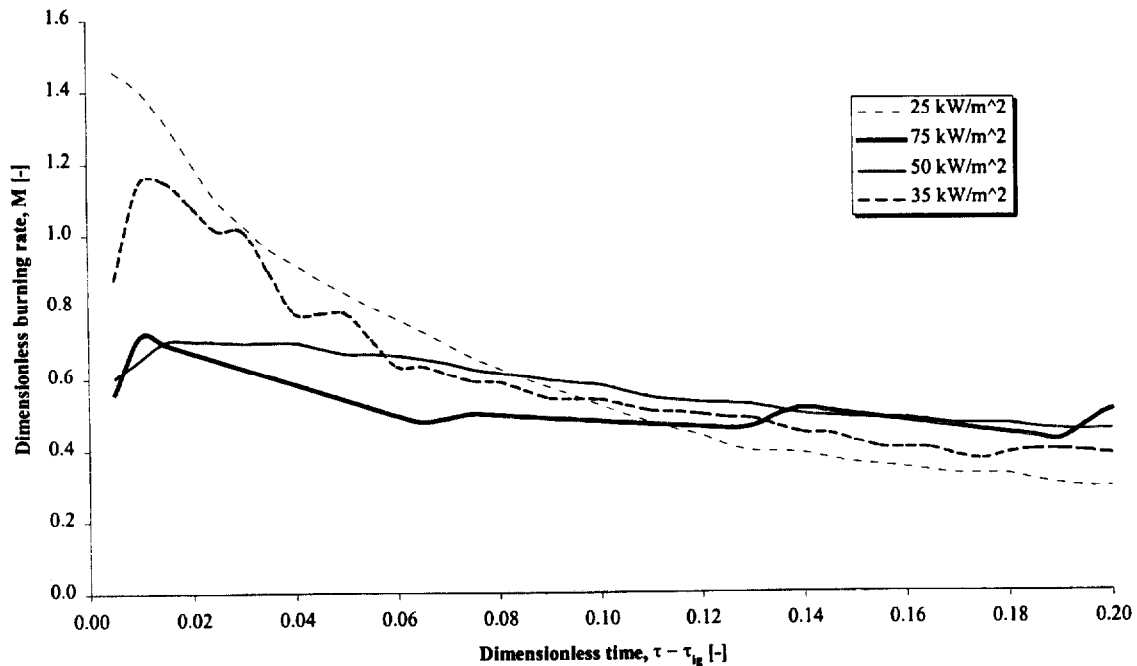
Figure 101. Combined dimensionless burning rates of Douglas fire in the *along* grain orientation using derived properties.

Figure 102 shows the dimensionless char depths for Douglas fir, *along* grain. Comparison with Figure 51 shows similarities between the experimental data and integral model solutions. In general, the char depths run parallel leading to an inflection point at around

$\tau = 0.1$ where the gradient of the lines decrease but continue to run parallel. The relative order of the experimental data does not compare as well with the integral model solutions. For example, Test 1DF3 (25 kW/m^2) shows a higher dimensionless char depth than the other tests whereas the integral model predicts lower dimensionless char depths for lower incident heat fluxes.
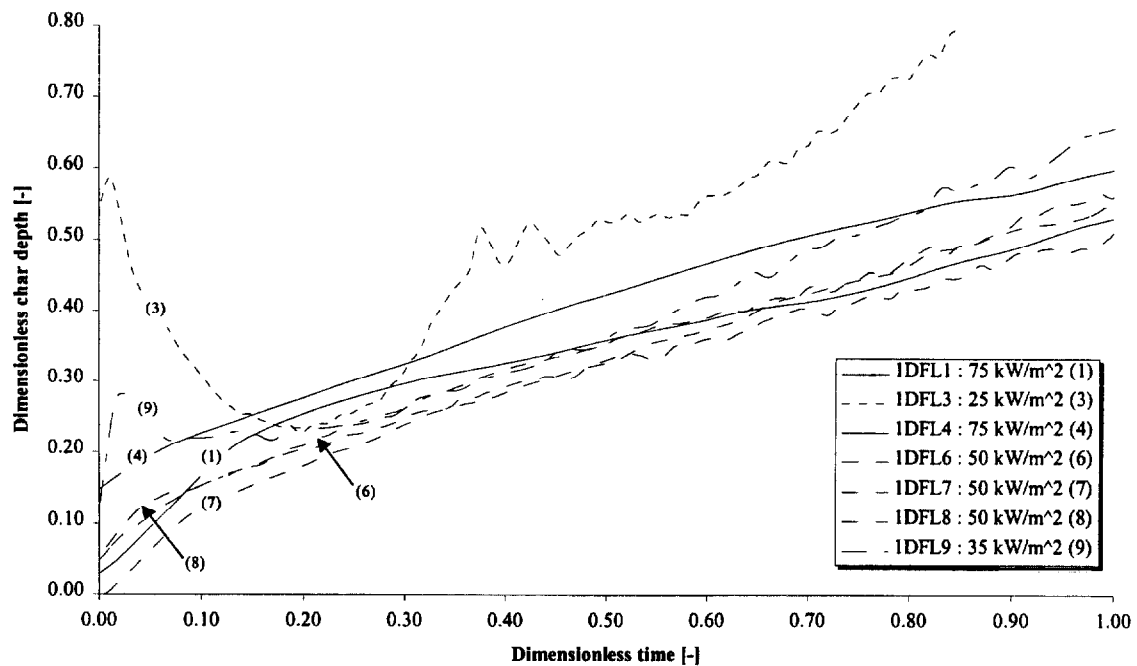
Figure 102. Dimensionless char depths of Douglas fire in the *along* grain orientation using derived properties.

4.6.2 Comparisons with model predictions

The Appendix shows the comparison between the measured effective mass loss rate (as discussed in § 4.2) and the small-time and long-time integral model solutions. To obtain the solutions, the analysis used the following properties and relationships:

191

i)   the heat of gasification and flame heat flux derived from the iterative approach

(Table 24 and Table 25),

ii)   the critical heat flux (Table 11), ignition temperature (Table 12) and thermal

inertia (Table 13) obtained from the ignition analysis,

iii)   the average density (Table 3) and thermal diffusivity (Table 4),

iv)   the convective heat transfer relationship (Equation 67) and

v)   the char fraction relationship (Equation 156)

For each sample, the burning rate is shown in both dimensionless and dimensional forms

with common scales for the x-axis and y-axis to allow for easy comparison. Examination

of the burning rate curves found the following points of note:

a) Douglas fir

The peak burning rate obtained by the intersection of the small-time and long-time

solutions is greater than the measured data at high incident heat fluxes. For the *along*

grain samples the long-time burning rate is lower than the measured data however a

better match is achieved for the *across* grain samples. As discussed in § 4.6.1, by

changing the properties we could get a better match between the long-time solution and

the experimental data but at the expense of the match between the peak burning rates.

Thus the results shown for this and the other woods is a compromise between these

conflicting requirements. The results from Test 1DFX3 are discussed in more detail in

§ 4.7.

b) Redwood

For reasons not determined, the energy release data from Test 1RL1 shows an offset. For *along* grain samples the long-time burning rate is lower than the measured data but, as for Douglas fir, the *across* grain results compare well.

c) Red oak

Both grain orientations exhibit a reasonable general match between the measured burning rate and the integral model.

d) Maple

The *across* grain samples show a good match between the measured and predicted burning rate. The *along* grain samples again have a lower burning rate from the integral model compared with the measured data. Only limited data was available for Test 1ML5 as the Cone Calorimeter's data acquisition system crashed 3:50 after the start of the test. The system was restarted at 5:45 by which point the sample had just started to burn. Processing the data files for this test was problematic and thus some of the analysis has not been completed for this sample.

In several cases, it appeared that the long-time solution for the burning rate using the derived properties gave an under-estimate compared to the measured data. As shown in § 4.1.7, by decreasing the heat of gasification, the long-time burning rate can be shifted upwards. However if the heat of gasification is decreased sufficiently, it is found that the small-time and long-time solutions no longer intersect thus providing a solution that

departs from what is actually measured. Again, this demonstrates the difficulty in determining the properties whilst maintaining an overall reasonable match with reality.

4.6.3 Peak burning rate

As discussed in § 4.1.7, the small-time solution of the integral model eventually reaches a steady-state level equivalent to what would be expected from a non-charring material (Figure 42). The peak burning rate from a charring material, whether measured or obtained from the intersection of the small-time and long-time solutions, is always less than the small-time steady-state level as shown in § 4.1.7.

By calculating the small-time steady-state value and obtaining the peak burning rate either from experiments or the integral model, the ratio

$$\Pi = \frac{\dot{m}''_{peak}}{\dot{m}''_{steady}}$$

Equation 166

can be found for each sample at its incident heat flux exposure condition. Figure 103 and Figure 104 show the average ratios for each wood species at the given orientations and incident heat fluxes. The general form of the curves is similar with the ratio higher at the low incident heat fluxes and decreasing as the heat flux increases. In general, the curves obtained from the integral model compare well. For *across* grain Maple the ratio remains almost constant and for *along* grain Douglas fir and Redwood the ratio increases at 35 kW/m^2 compared to all species apart from the *across* grain Maple.
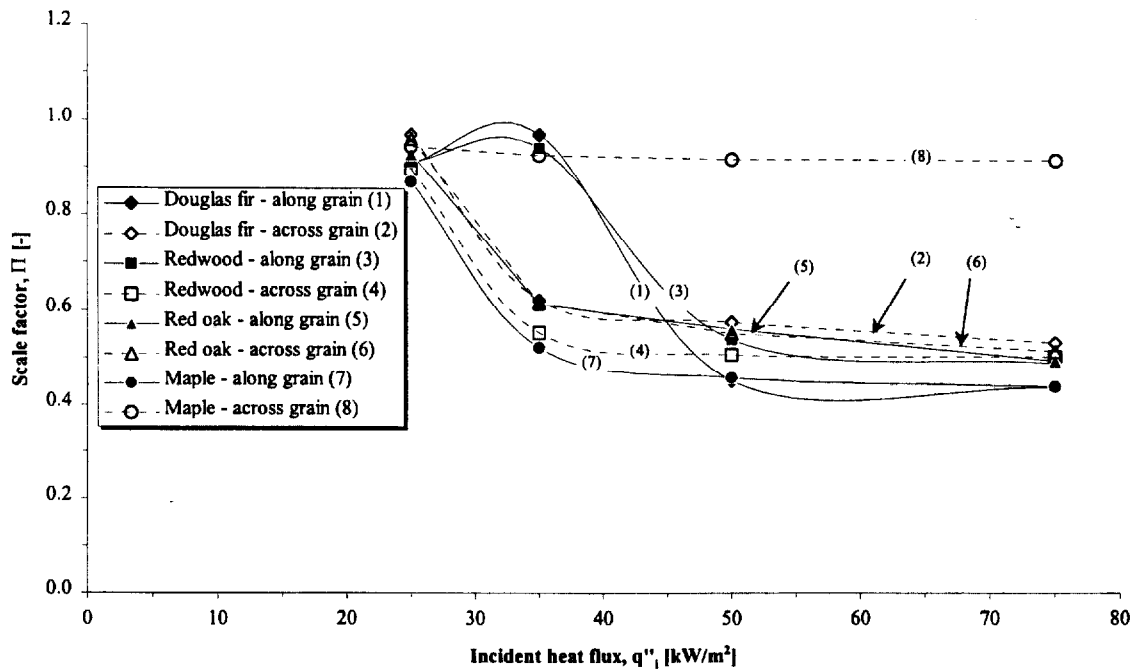
Figure 103. Ratio of charring peak burning rate with non-charring steady-state burning rate from integral model solutions.
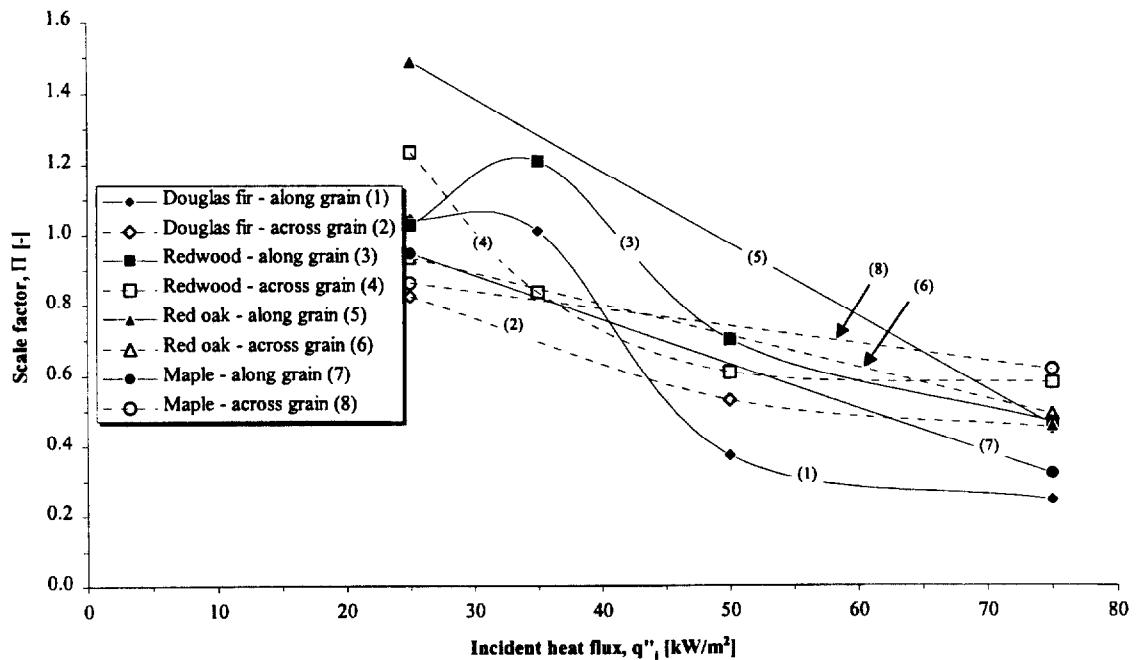
Figure 104. Ratio of charring peak burning rate with non-charring steady-state burning rate from experimental data.

An overall set of average values can be obtained from the results of the above analysis of the charring peak burning rate with non-charring peak burning rate (Figure 105). In this case, where no ratio for the experimental data exists for a particular wood (e.g. Maple, across grain at 35 kW/m^2 etc.) then the ratio is found by interpolation. The chart indicates the reasonable comparison between the integral model and the experimental data over the range of incident heat fluxes.
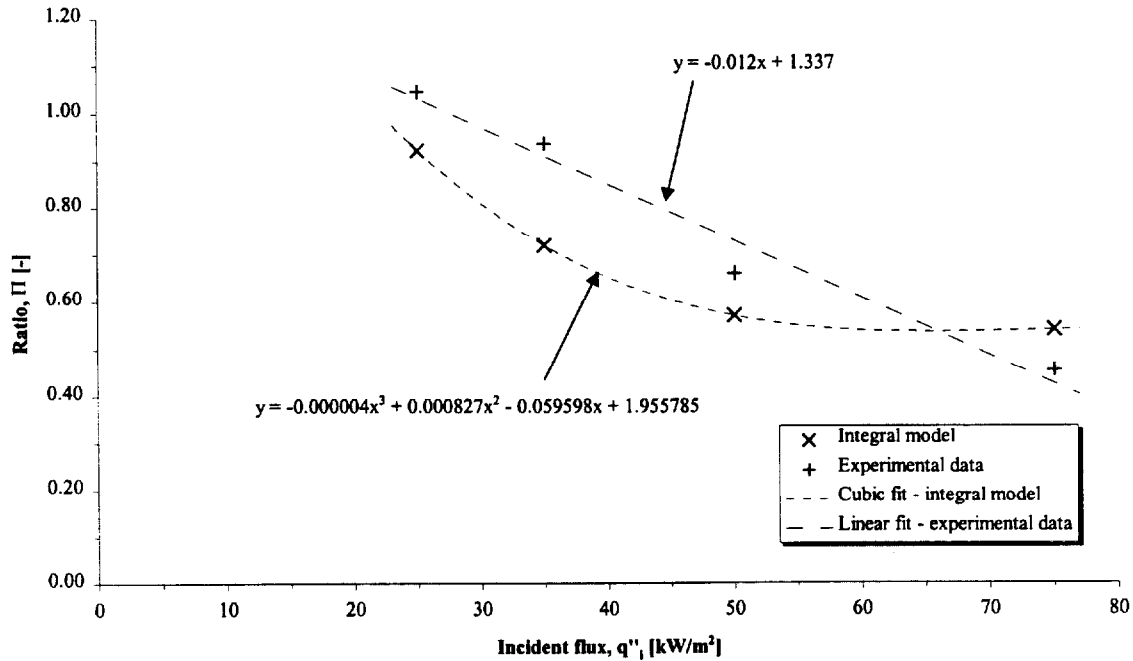
Figure 105. Average ratios of charring peak burning rate with non-charring peak burning rate from integral model solutions and experimental data.

Thus, an empirical relationship can be obtained for estimating the peak burning rate from the integral model solution. From Equation 160, the steady burning rate is given by

$$\dot{m}''_{steady} = \frac{(1-\phi)\dot{q}''_+(T_s)}{L}$$

Using a cubic polynomial fit to the integral model ratios as shown in Figure 105, the peak burning rate factor Π is given by

$$\Pi = -0.000004[\dot{q}_i'']^3 + 0.00083[\dot{q}_i'']^2 - 0.06\dot{q}_i'' + 1.96$$

Equation 167

thus, from Equation 166, the peak burning rate is simply

$$\dot{m}_{peak}'' = \Pi.\dot{m}_{steady}''$$

Equation 168

Figure 106 shows a comparison between the calculated peak burning rate using Equation 167 and Equation 168 with the experimentally measured peak burning rates. The values for $\dot{m}_{steady}''$ were obtained using the values for the heat of gasification and flame heat flux given in § 4.6.1 (Table 24 and Table 25). The char fraction ϕ was found from Equation 156.
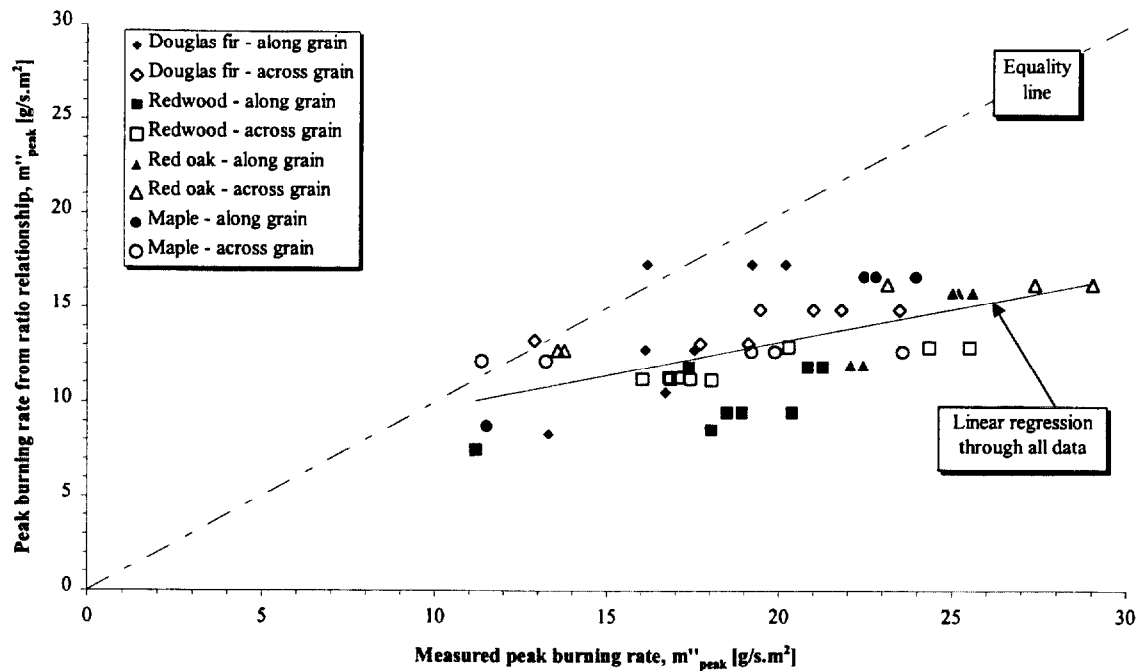
Figure 106. Comparison of measured peak burning rate and calculated burning rate using the ratio of peak to steady burning rate relationship.

The empirical relationship for the prediction of the peak burning rate shows that, although the trend is consistent, for higher measured values the relationship underestimates the peak burning rate.

4.7 Burning rate of char

During the tests conducted in this study it was observed that flaming would eventually cease and instead the char at the surface of the material would be oxidised away by the incident heat flux. The best example of this was in Test 1DFX3 (Douglas fir, 75 minutes at 75 kW/m^2) where the rate of heat release and heat of combustion data clearly shows the transition from wood burning to char oxidation (Figure 107).

250

Rate of heat release
Heat of combustion

Peak burning
rate

200

Back effect starts to
influence burning rate

Char oxidation
phase

80

70

60

50

Rate of heat release [kW/m²]

150

100

50

0

40

30

20

Heat of combustion [MJ/kg]

10

0

0   480   960   1,440   1,920   2,400   2,880   3,360   3,840   4,320

Time [s]
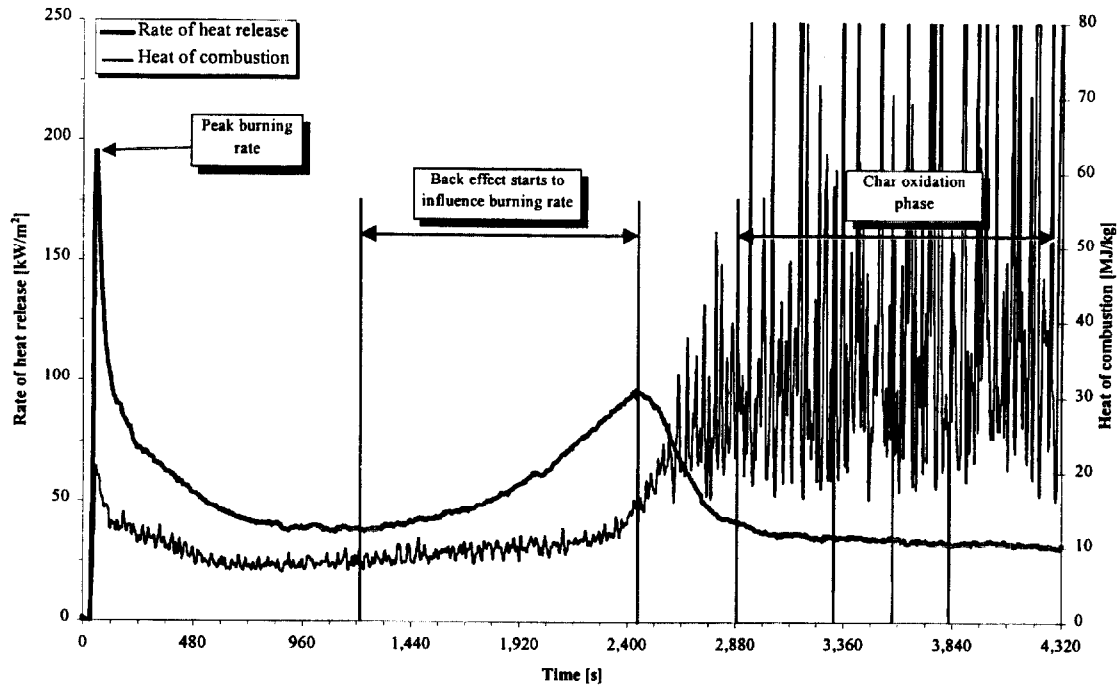
Figure 107. Rate of heat release and heat of combustion for Test 1DFX3 showing back effect and char oxidation phases.

The heat of combustion data exhibits a higher degree of fluctuation during the char oxidation phase due to the relatively low instantaneous mass loss rates. From Equation 1 it can be seen that small values for the instantaneous mass loss have a significant effect on the calculated instantaneous heat of combustion. By taking an average of the heat of combustion during the char oxidation stage of the test and neglecting the high and low peaks, the heat of combustion of the char was found to be 35.5 MJ/kg. This value compares well with the average heat of combustion for char of 34.3 MJ/kg quoted by Drysdale [2]. By using the average heat of combustion for char and the measured rates of heat release the average 'burning' rate of the char was found to be 0.0015 $kg/s.m^2$.

Figure 107 also clearly shows the back effect (§ 4.2) where the burning rate of the sample

increases as the thermal wave is reflected at the rear of the sample. It is interesting to note

that the increase in burning rate appears to begin at around 20 minutes. This result is

comparable to the value of around 16 minutes for the thermal wave to reach a depth of

50 mm found in the analysis of the long-time solution for the integral model (§ 4.2).

4.8   Charring rate and char depth

4.8.1   Background

In this section the char depth is analysed using the integral model solutions, the

thermocouple measurements, the mass loss data and the measured char depth at the end

of the test. These aspects are discussed and compared below.

4.8.2   Mass loss rate data

From the derivation of governing equations, Equation 125 states that

$$\frac{\dot{m}''}{(1-\phi)} = \rho_w \frac{d\delta_\phi}{dt}$$

thus rearranging

$$\frac{d\delta_\phi}{dt} = \frac{\dot{m}''}{\rho_w (1-\phi)}$$

Equation 169

and integrating over time t we obtain

$$\delta_\phi = \frac{\dot{m}''}{\rho(1-\phi)} t$$

Equation 170

200

Since the experimental data provides the char depth at the end of each test, we can

compare the measured char depth and the calculated char depth from Equation 170 using

the average mass loss rate measured in the Cone Calorimeter and t equal to the duration

of the test t_f. Figure 108 shows a plot of calculated char depth against measured char

depth. At earlier times (25 minutes), the calculated and measured data match fairly well

though the mass loss rate relationship appears to over-predict slightly. However, at later

times (75 minutes) the integral model fails to successfully predict the char depth

compared with the measured data. It is likely that this is due to a back face effect where

in the experiments heat is lost through the back face and/or the sample is completely

charred whereas the integral model treats the sample as having an infinite depth that can

continue to char indefinitely.
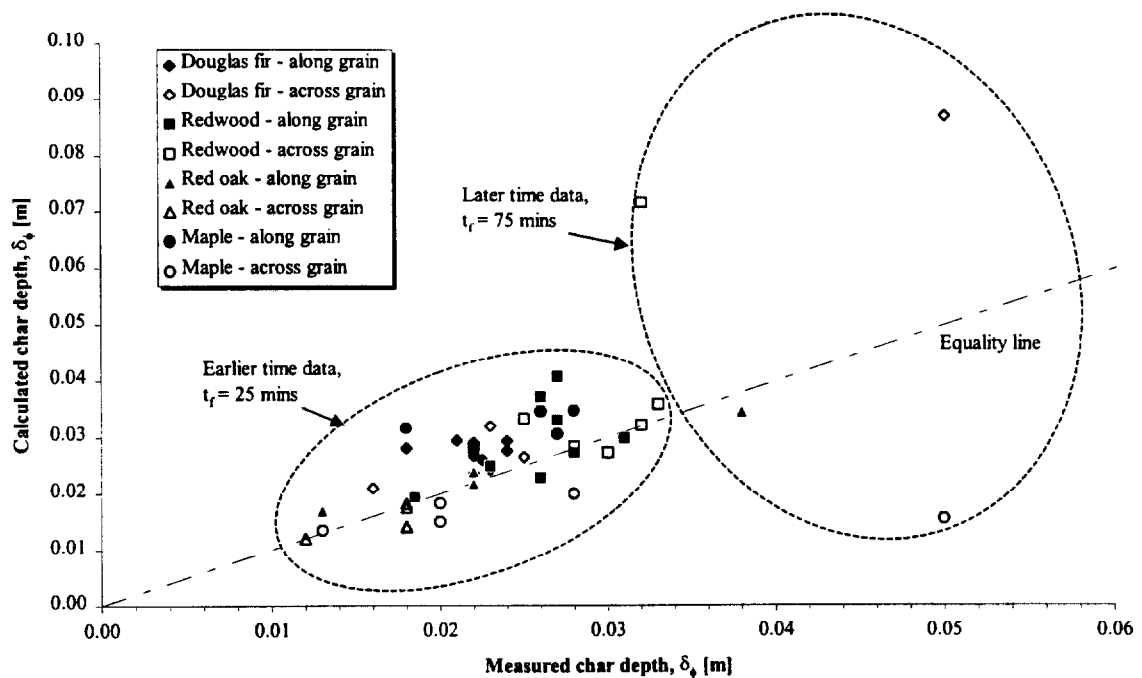
Figure 108. Comparison of measured and calculated char depth.

201

It is interesting to note that Tran & White [34] suggest that the charring rate can be found from

$$\frac{d\delta_\phi}{dt} = \frac{\dot{m}''}{\rho_w}$$

assuming that the mass of the char is negligible and ignoring the mass loss in advance of the char front. Equation 171 is equivalent to the charring rate equation, Equation 169, obtained from the integral model with the difference being that the integral model includes the effect of the char fraction. In § 4.5.1 we show that as $\dot{q}_i'' >> \dot{q}_{cr}''$ the $\phi \to 0$, thus Equation 169 and Equation 171 would give the same result.

4.8.3 Final char depth from integral model solutions

A similar analysis as that shown in § 4.8.2 can be performed using the predicted char depth from the long-time solution given by the integral model. The dimensionless char depth is given by Equation 154. From $\tau \equiv \frac{\alpha t}{\delta_s^2}$, the equivalent dimensionless time τ for 25 minutes can be obtained and hence the char depth calculated. Similarly the measured char depth and the char depth from the mass loss data can be made dimensionless since

$$\Delta_\phi \equiv \frac{\delta_\phi}{\delta_s}$$

Thus a comparison can be made by plotting the dimensionless char depths from the integral model, the measured data and the mass loss data against each other (Figure 109 to Figure 112). In each figure, three plots are shown; the measured depths versus the

integral model solution (line 1, using + symbols), the mass loss versus integral model

solution (line 2, using - symbols) and mass loss versus measured depths (line 3, using x

symbols).
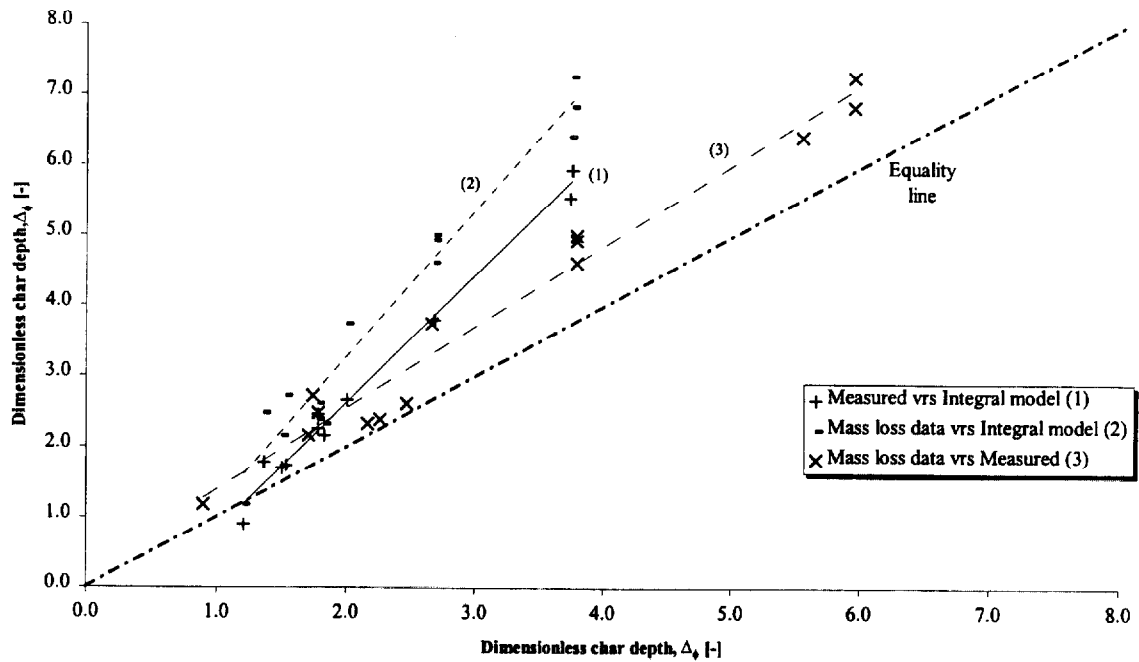
Figure 109. Comparison of char depths at 25 minutes for Douglas fir.
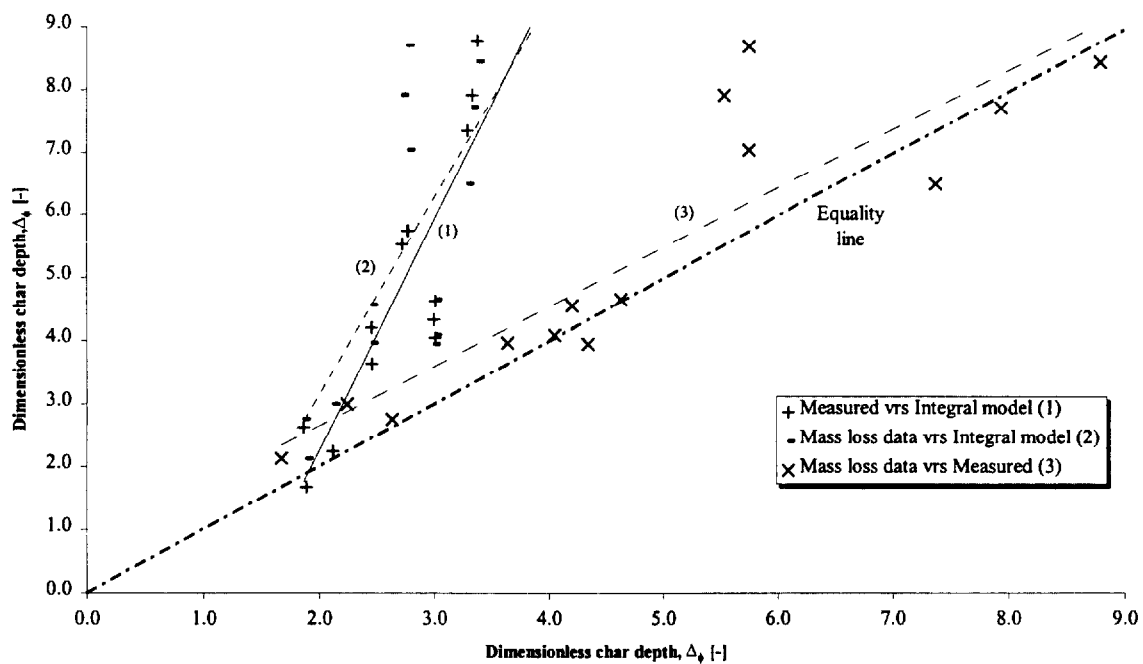
Figure 110. Comparison of char depths at 25 minutes for Redwood.
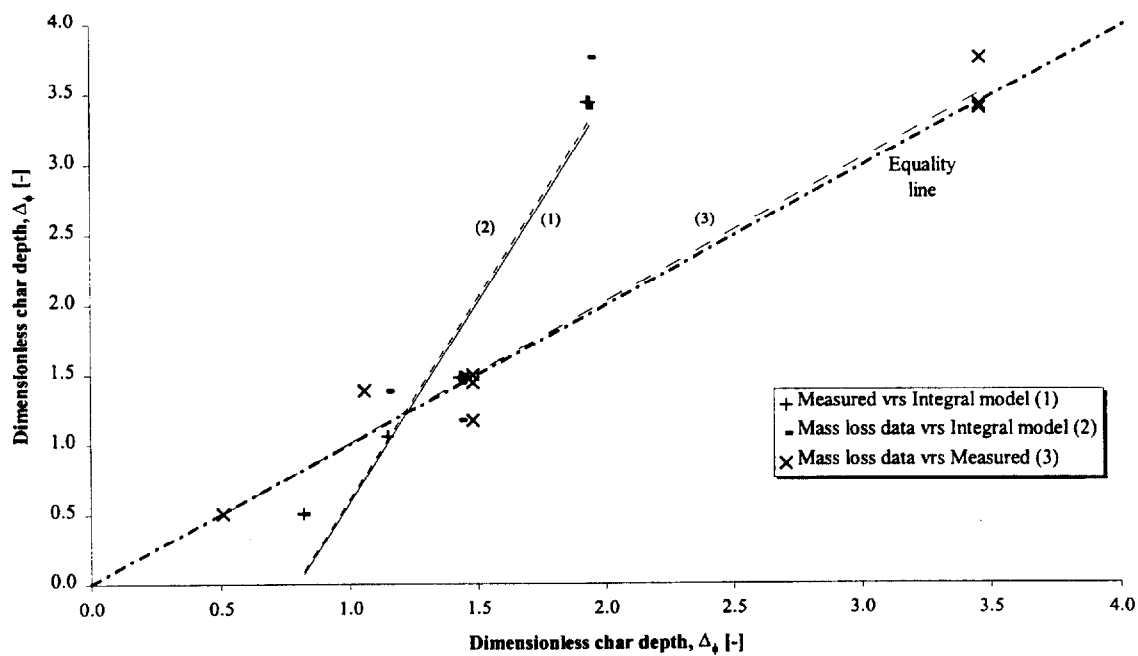
Figure 111. Comparison of char depths at 25 minutes for Red oak.

204
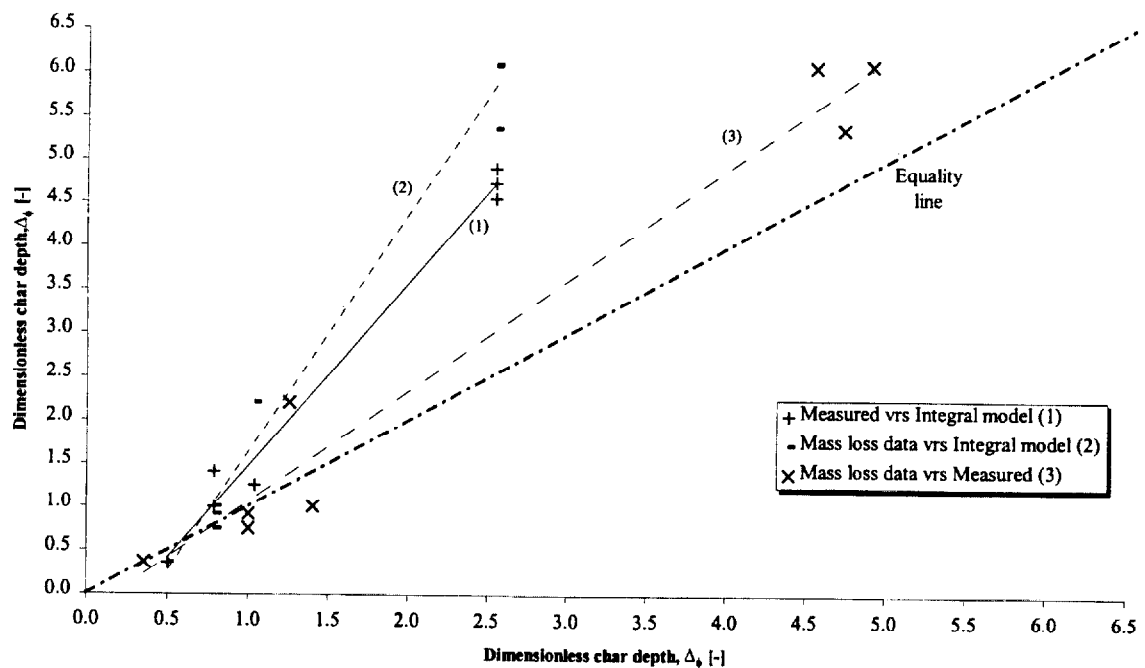
Figure 112. Comparison of char depths at 25 minutes for Maple.

The analysis shows, as found in § 4.8.2, the mass loss and measured depths compare well. The data (line 3) lie close to the equality line and follow the equality line over the range of depths obtained.

The comparison between the integral model and the measured data (line 1) shows that at low dimensionless char depths (between 1.0 and 2.0) the two compare well but as the depth increases the integral model predicts shallower depths than measured.

4.8.4 Char depth using thermocouple data

In addition to using the thermocouple data to obtain the thermal penetration wave (§ 4.9.1), the measurements were used to map the travel of the pyrolysis front (i.e. char depth) as it moved through the samples.

205

In § 4.1.1 it is assumed that the vaporisation temperature of the volatiles T_v in the pyrolysis zone is equivalent to the ignition temperature T_{ig}. Thus, if the time at which the thermocouples first record a temperature at the calculated ignition temperature for a species of wood at a given orientation (Table 12) then the char depth can be obtained. In the studies by Schaffer [17] it was found that the transition temperature for wood to become char is around 288 °C regardless of species. Therefore, in this study, the char depth using the thermocouple measurements has also been obtained by using a critical temperature of T_{char} = 288 °C in addition to the calculated ignition temperatures. Figure 113 shows an example of the method used to obtain the char depths.
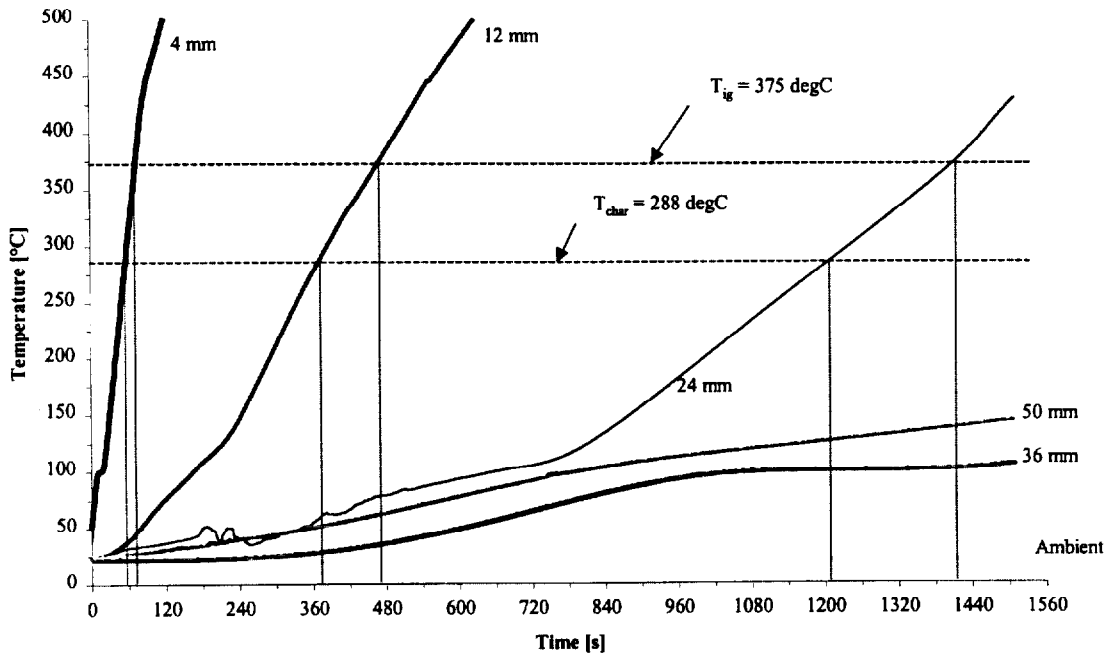
Figure 113. Determination of char depth using wood ignition temperature or char ignition temperature (Test 1RL2).

The char depth can be examined in terms of dimensionless variables for each species of wood at given incident heat fluxes. The dimensionless depth of each thermocouple probe can be obtained from

$$\Delta_{tc} = \frac{\delta_{tc}}{\delta_s}$$

where δ_{tc} is the depth of the thermocouple and the time at which it reaches the ignition temperature $t(T_{ig})$ from

$$\tau_\phi = \frac{\alpha t(T_{ig})}{\delta_s^2}$$

The integral model gives Equation 143 for the small-time char depth,

$$\Delta_\phi \approx 2M_{ig}(\tau - \tau_{ig})$$

and Equation 154 for the long-time char depth,

$$\Delta_\phi \approx \sqrt{2\left(\frac{c_w T_v}{\Delta H_v}\right)\phi(\theta_s - 1)(\tau - \tau_{ig})}$$

Plots for the char depth using the thermocouple data are compared with the theoretical predictions from the integral model are presented below. In each plot a trend line is drawn through the thermocouple data as a means to compare the experimental data with the theoretical curves.

a) Douglas fir
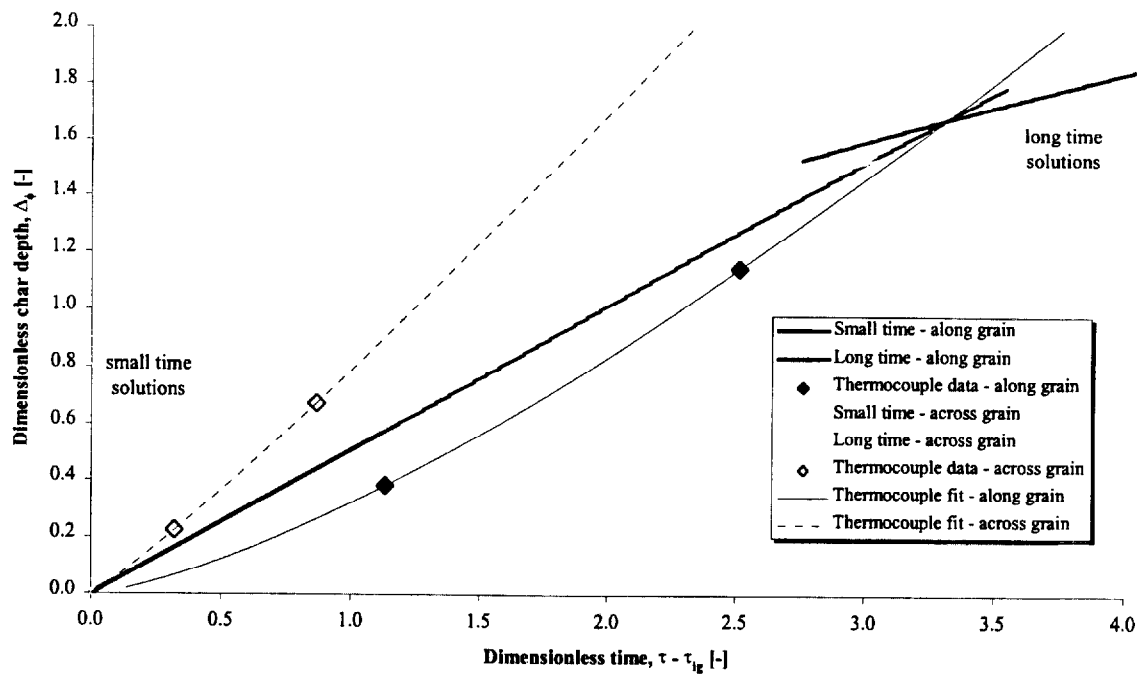
Figure 114. Dimensionless char depth using thermocouple measurements for Douglas fir at 25 kW/m^2.
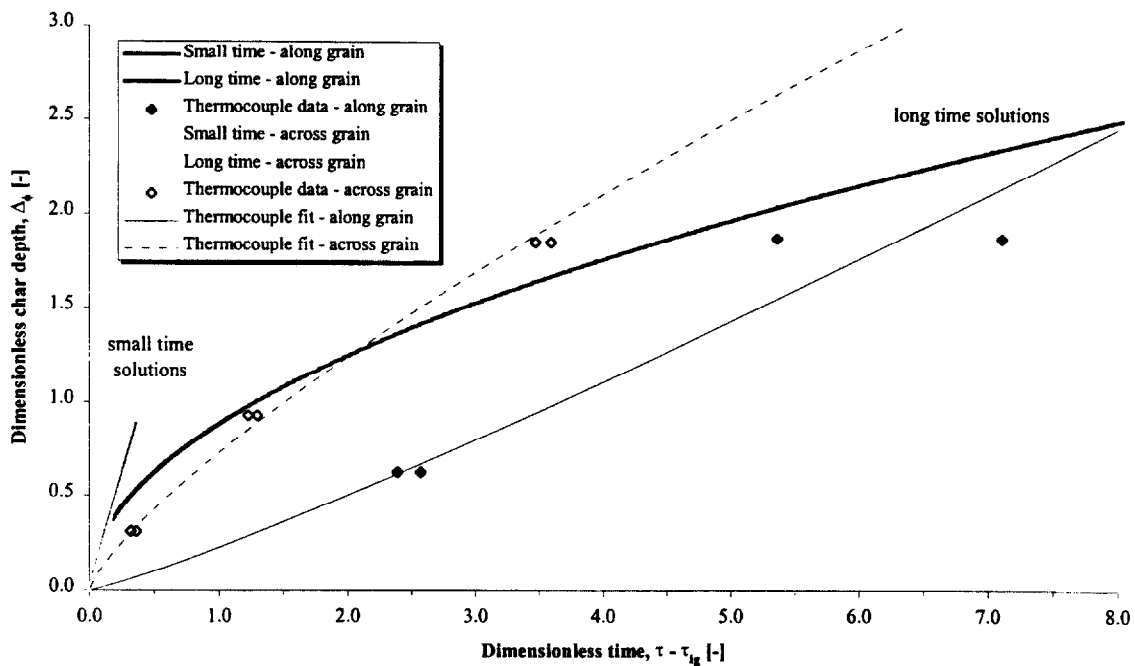
Figure 115. Dimensionless char depth using thermocouple measurements for Douglas fir at 50 kW/m^2.

208
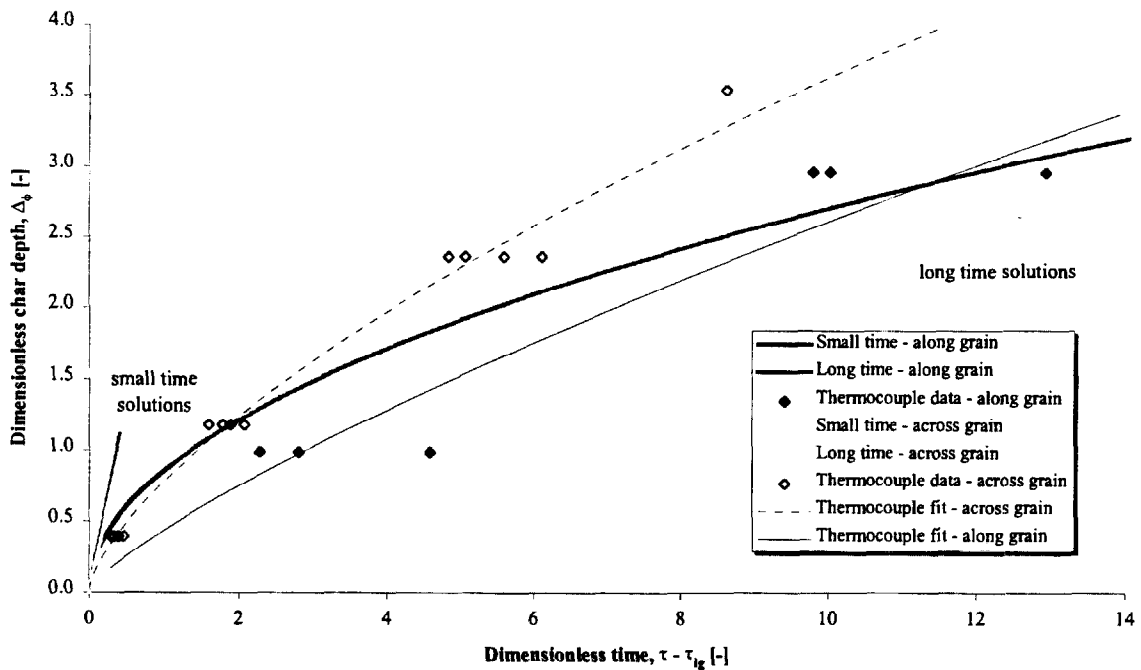
Figure 116. Dimensionless char depth using thermocouple measurements for Douglas fir at 75 kW/m^2.

Figure 114 to Figure 116 show the dimensionless char depth plots for Douglas fir. The trend for the thermocouple data at 25 kW/m^2 differs from the theory simply because only two depths were obtained from the temperature data. The plots for 50 kW/m^2 and 75 kW/m^2 thermocouple data show reasonable consistency between tests particularly for the *across* grain configuration. Comparison of the thermocouple data with the theoretical predictions show a fair qualitative match.

b)   Redwood
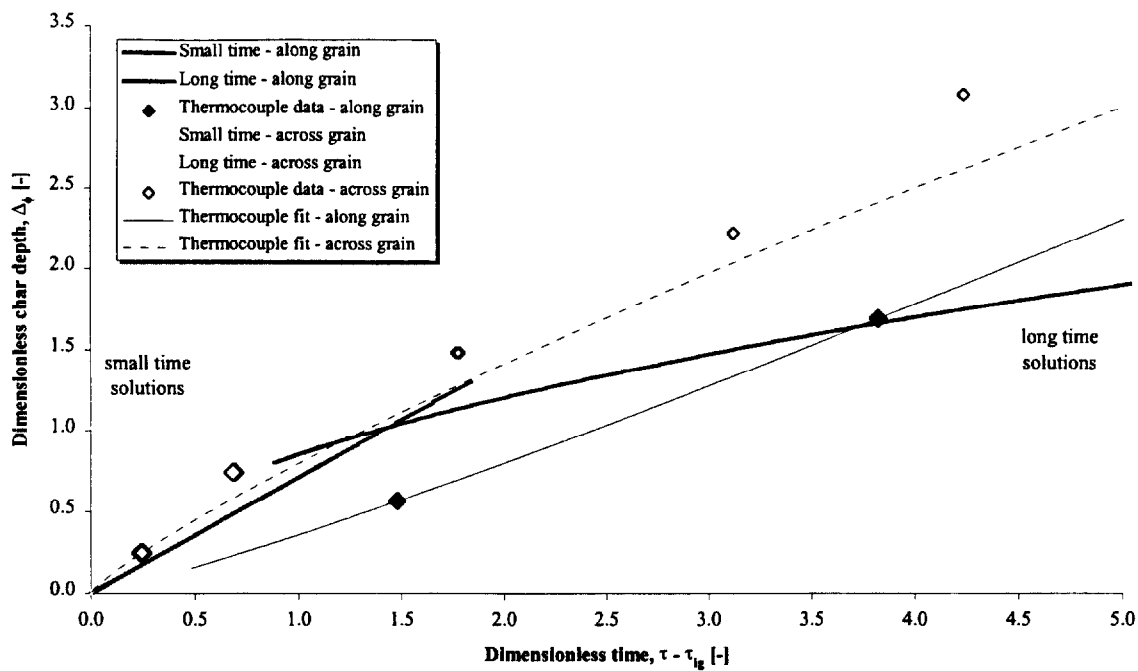
Figure 117. Dimensionless char depth using thermocouple measurements for Redwood at 25 kW/m².
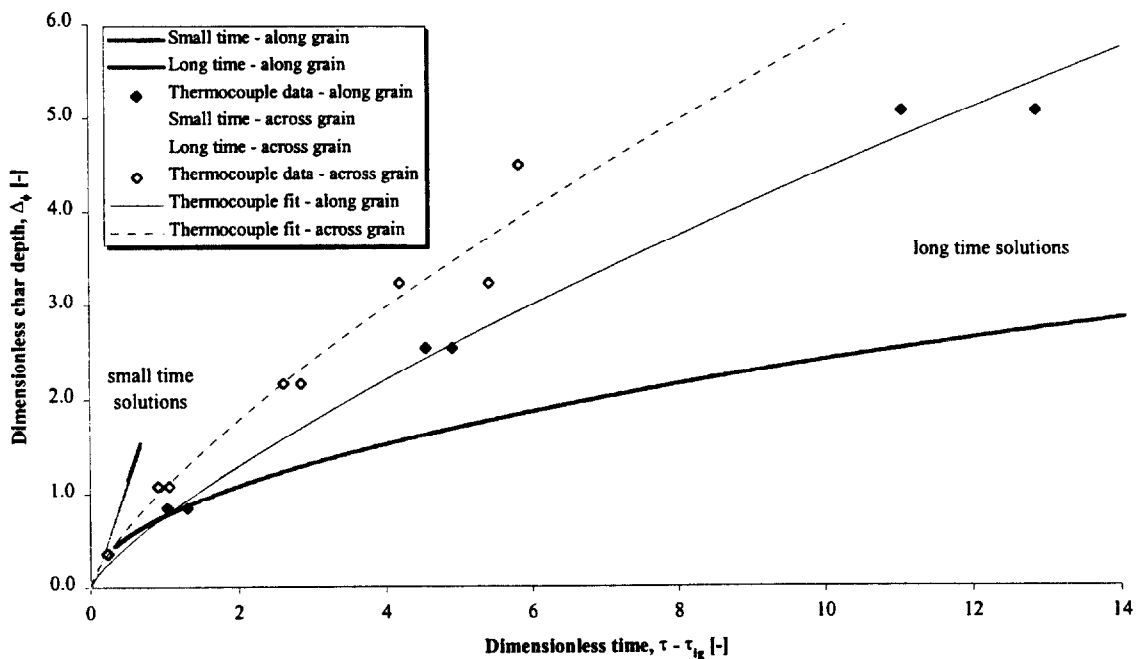
Figure 118. Dimensionless char depth using thermocouple measurements for Redwood at 50 kW/m².
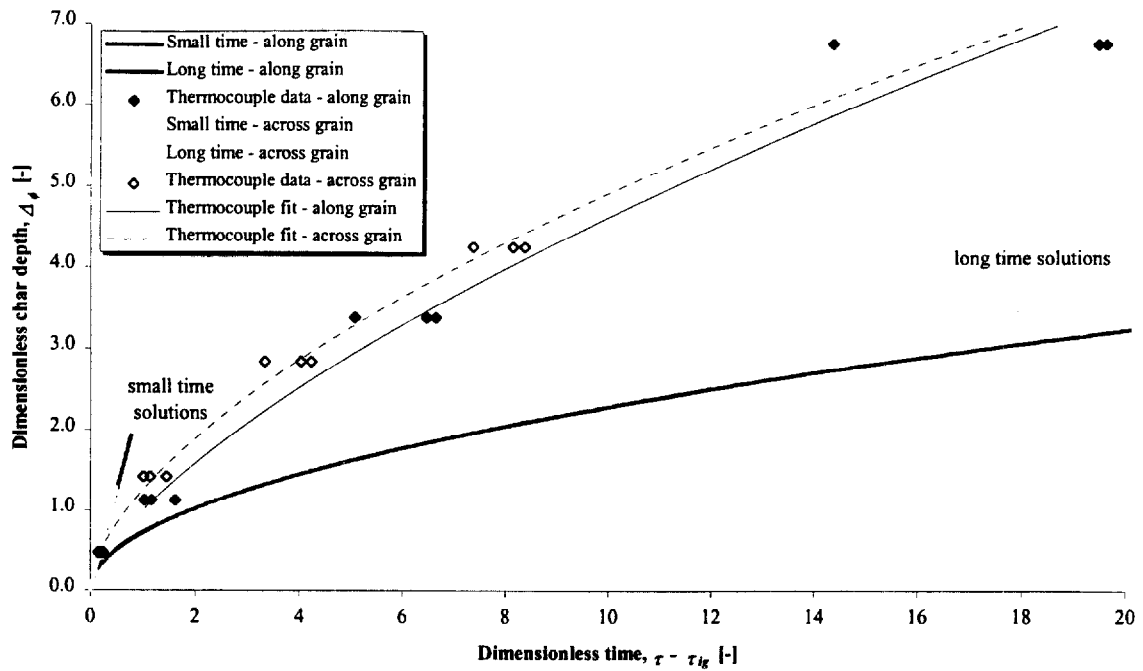
Figure 119. Dimensionless char depth using thermocouple measurements for Redwood at 75 kW/m².

Figure 117 to Figure 119 show the dimensionless char depth plots for Redwood. The plots for the thermocouple data show good consistency in both grain configuration. Comparison of the thermocouple data with the theoretical predictions show a good qualitative match compared with the Douglas fir. In all three cases the dimensionless char depth for the *across* grain configuration is greater than the *along* grain configuration for both the thermocouple data and the integral model predictions. The general trend for the thermocouple data follows the model predictions albeit the thermocouple data gives generally higher dimensionless char depths compared with the theoretical values.

Similarly, dimensionless plots could be made for Red oak and Maple and also plots using the critical char temperature of 288 °C.

4.8.5 Overall results

The char depth obtained from the mass loss data, the integral model solutions and the thermocouple data for each wood sample tested is shown in the Appendix. Concluding observations regarding the results for each wood species are given here:

a) Douglas fir

For the *along* grain samples, with the exception of Test 1DFL3 (25 kW/m^2 for 25 minutes), the integral model follows the mass loss data up to around 8-10 minutes at which point the two curves intersect. Thereafter, the integral model predicts shallower char depths than given by the mass loss data. This result agrees with the findings discussed in § 4.8.3. For Test 1DFL3 the short-time solution prevails for almost the whole test. In general, the thermocouple data compares reasonable well with the mass loss and integral solutions with the T_{ig} analysis comparing better in some cases and the T_{char} analysis in others.

For the *across* grain samples the integral model and mass loss data show similar trends with the long-time solution and mass loss data almost coinciding at the termination of each test. The T_{ig} thermocouple measurement analysis matches the integral model reasonably well. In Test 1DFX3 the thermocouple data follows the mass loss data remarkably well (Figure 187) as the end effects become significant.

b) Redwood

For the *along* grain samples the long-time solution and mass loss data only compare well for the first few minutes and thereafter the integral model predicts shallower char depths. With the exception of Test 1RL1, the T_{ig} thermocouple data closely follows the mass loss data. In Test 1RL1 (25 minutes at 75 kW/m^2), there appeared to an offset with the measured mass loss data that affect the analysis.

The integral model and char depth from mass loss rate measurements compare well for across grain samples. The thermocouple data follows the same trends with the T_{char} analysis performing better than the T_{ig} analysis.

c) Red oak

There is a good match between the integral model and the mass loss analysis of the char depth. The match between the char depth and the thermocouple data is fair. Similar to Test 1DFX3, in Test 1OL2 the thermocouple measurements again follow the mass loss rate at long times. There was only limited data for Test 1OL3 as the 12 mm and 24 mm deep thermocouples failed early in the test.

d) Maple

The *along* grain integral model predictions and mass loss rate char depths compare well however the thermocouple data gives deeper char depths in comparison. For across grain, the T_{char} temperatures match the integral model for an incident heat flux of 25 kW/m^2 whereas the T_{ig} data gives deeper char depths. For an incident heat flux of 75 kW/m^2 the

integral model is comparable to the mass loss data but the thermocouple data does not compare well.

4.9 Temperature measurements

4.9.1 Thermal penetration depth

From the integral model we can determine the depth of the thermal penetration wave prior to ignition from Equation 27

$$\delta^2 = 3\frac{k}{\rho c}\left[\frac{2-\beta}{1-\beta}\right]t$$

Once ignition has occurred, the thermal penetration wave follows Equation 151 from the small-time solution,

$$\Delta \approx \Delta_{ig} + 6\left(\frac{L}{\Delta H_v}\right)\left(1 - \Delta_{ig}\right)\left(\tau - \tau_{ig}\right)$$

and Equation 152 from the long-time solution,

$$\Delta \approx \sqrt{\Delta_{ig}^2 + 12\left(\tau - \tau_{ig}\right)}$$

The measurements from the thermocouples inserted into the samples were used to map the thermal penetration wave and Figure 120 shows the analysis method. A temperature difference ΔT between ambient and a given temperature rise was selected. The thermocouple measurements at each depth were examined and the first time at which the measured value reached or exceeded ΔT was noted. Thus the time for the thermal wave to penetrate through the depth of the sample could be obtained as a function of the depth of each thermocouple.

214
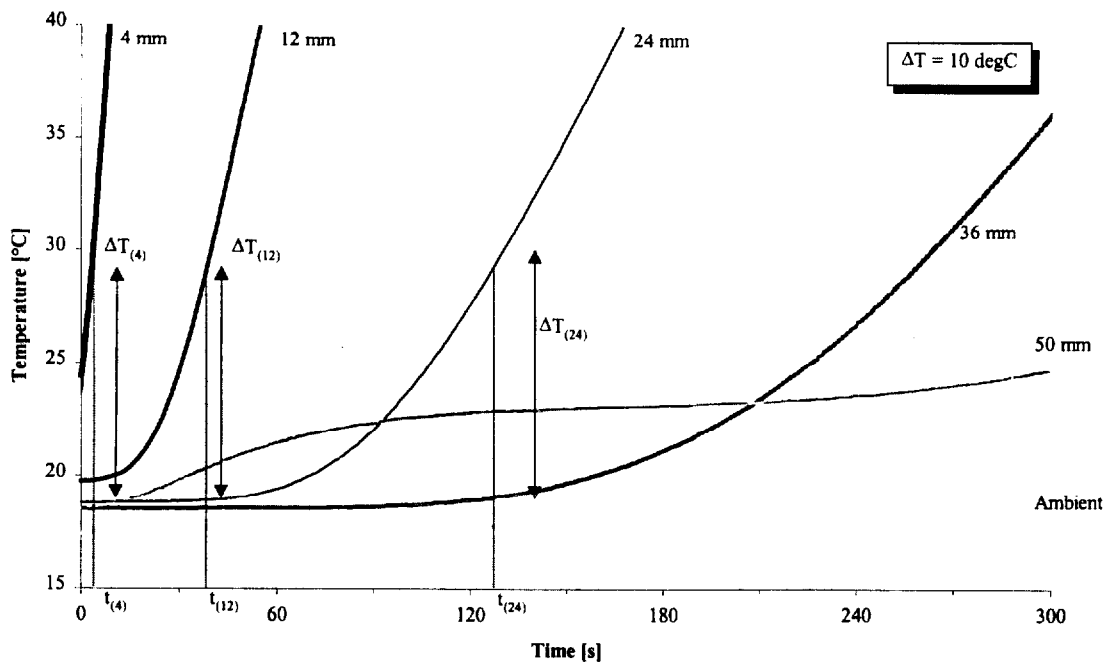
Figure 120. Detail of temperature measurements for Test 1DFX4.

It must be recalled that, as described in § 4.2, at greater depths and longer times the temperature measurements are influenced by the heat penetrating through the rear of the sample from the hot sample retainer. Figure 120 also shows how the 50 mm (back) thermocouple would record higher temperatures during the initial stages of a test due to the hot retainer frame. As the test progresses, the temperature from the 36 mm thermocouple continues to rise and eventually overtakes the back thermocouple.

In theory, the moment the top surface of the sample is exposed to the incident heat flux, the rise in temperature is transmitted through the complete depth of the material. In practice this is not the case and even if this were true it would not be possible to measure the minute temperature changes at the locations remote from the exposed surface. Thus a temperature rise was selected that was relatively small so that the progress of the thermal

215

penetration wave through the sample was measured, but not so small that the inherent measurement error from the thermocouples and other factors became important.

Figure 121 shows the measured thermal penetration depth using four temperature rises of 2 °C, 5 °C, 10 °C and 15 °C and the theoretical values for Test 1DFX4 (25 kW/m^2). It clearly shows how the results for the back thermocouple give erroneous results for the time for the thermal penetration wave to reach a depth of 50 mm. For a ΔT of 2 °C the time is only 42 s which is considerably sooner than the time of 170 s for the thermal wave to reach 36 mm. As ΔT is increased, the back thermocouple begins to give results that are more appropriate and by a ΔT of 15 °C the result is closer to what would be expected. Because of this problem with the back thermocouple, it was normally neglected from the analysis of the thermal penetration wave.
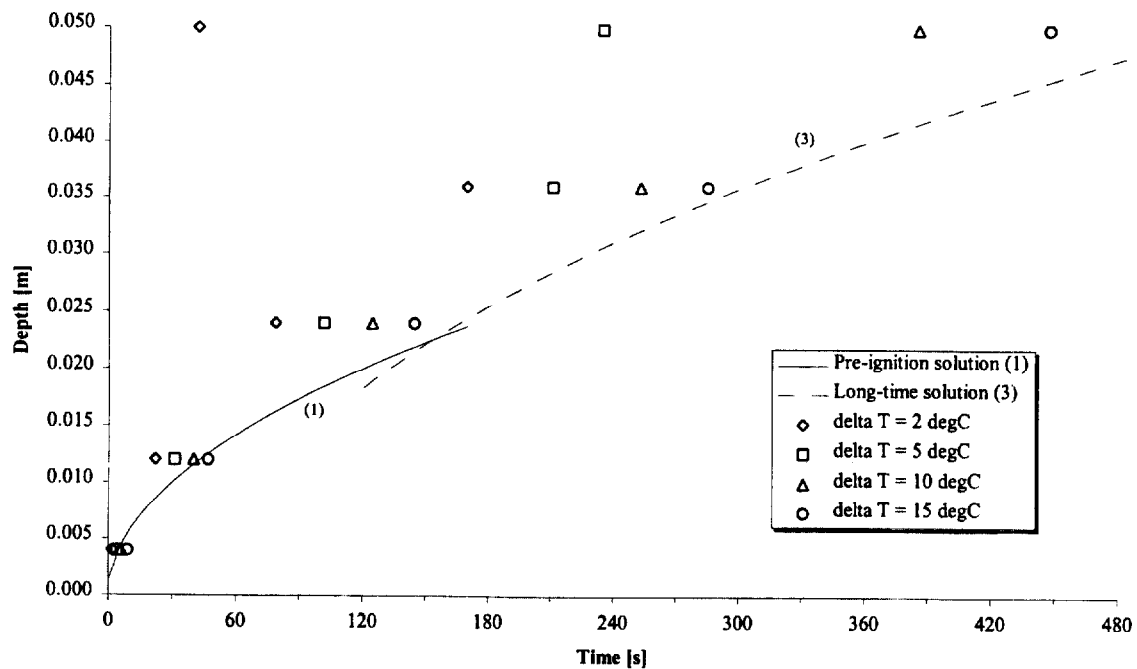
Figure 121. Determination of thermal penetration depth using temperature rises (ΔT) measured by the thermocouples (1DFX4).

Figure 122 shows a similar analysis for Test 1DFL1 (75 kW/m^2). At small times, i.e. at the top-most thermocouple, there is little difference between the four temperature rises and the theory. As the thermal wave penetrates the sample, using the different temperature differences begins to have a greater effect on the match between the measurements and the theory. At 24 mm the 2 °C temperature difference shows the best match with the theory whereas at 36 mm the 15 °C temperature difference shows the best match with the theory.
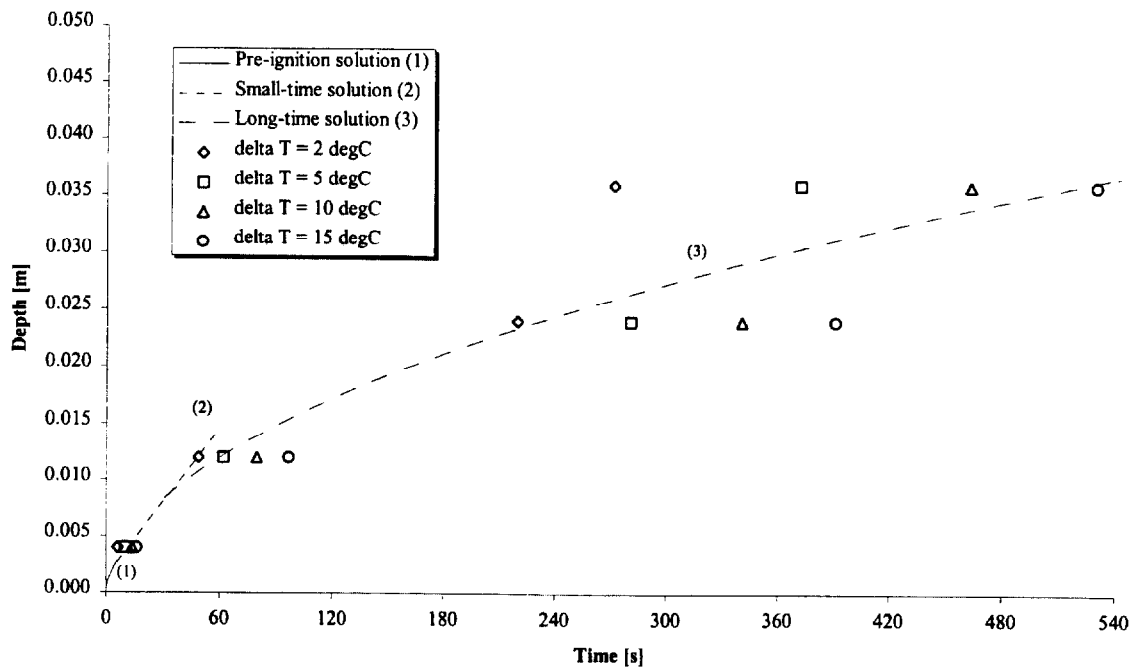
Figure 122. Determination of thermal penetration depth using temperature rises (ΔT) measured by the thermocouples (1DFL1).

Furthermore, the theory does not account for the effects of moisture in the sample. Which is evident in Figure 123. Some heat is required to vaporise the moisture which results in the plateaus that can be seen in the temperature measurements at 100 °C. This process effectively slows the thermal penetration wave as it moves through the sample.
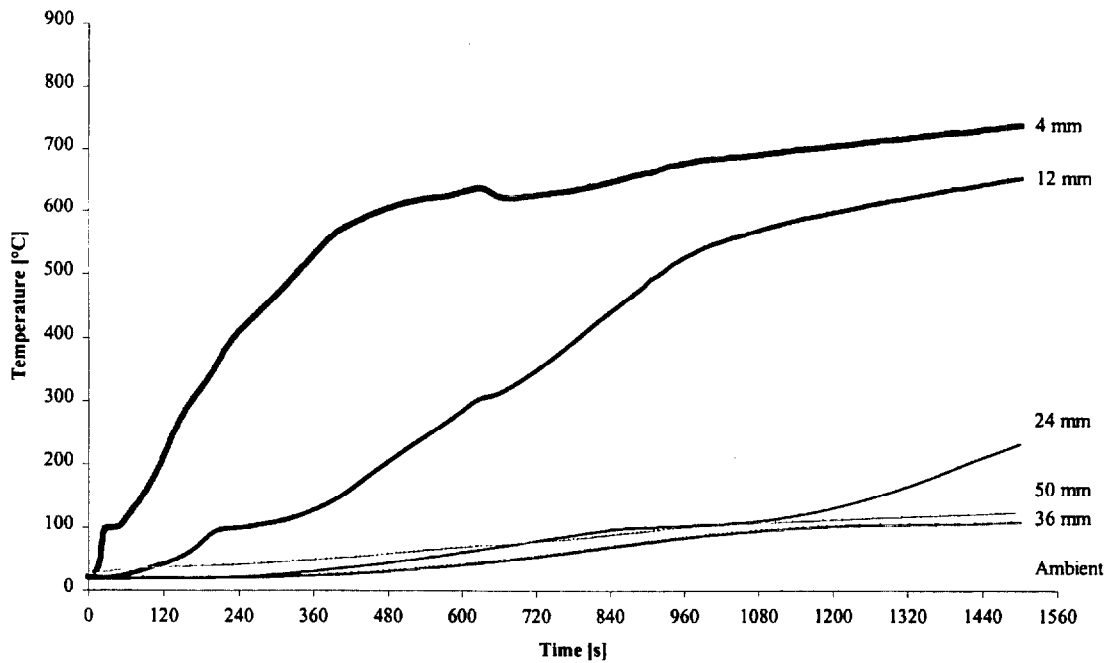
Figure 123. Temperature profiles for Test 1DFL1 showing plateaus at 100 °C.

As a result of this analysis and in order to obtain an appropriate approximation of the thermal penetration wave a temperature difference of 5 °C was selected for the comparison between the measured and theoretical temperature profiles.

Plots for the thermal penetration depths in each sample in which thermocouples were utilised are shown in the Appendix. For all of the tests in which thermocouples were used the match between the measured data and integral model solutions is excellent to a depth of 36 mm. Only for the *across* grain Redwood samples do the thermocouples and integral model not compare so well.

219

4.9.2 Surface temperature

Equation 153 gives the temperature of the exposed surface after a 'long' time where

$$T_s \approx \left(\frac{\dot{q}''_{fl} + \dot{q}''_i}{\sigma} \right)^{1/4}$$

If it is assumed that the maximum temperature recorded by the top-most thermocouple is

equivalent to the surface temperature (i.e. the wood surface and the wood or char at a

depth of 4 mm are at equilibrium) then the measurements and Equation 153 can be

compared. As discussed in § 1.4.2 and 4.6.1, the flame on the burning surface of the

sample would not remain constant but would gradually reduce and eventually extinguish.

Thus Equation 153 gives an estimate of the maximum long time surface temperature. If

it assumed that the flame heat flux at long time is negligible i.e. $\dot{q}''_{fl} \approx 0$, then Equation

153 becomes

$$T_s \approx \left(\frac{\dot{q}''_i}{\sigma} \right)^{1/4}$$

Equation 174

and thus this is an estimate of the minimum long time surface temperature. The

maximum temperature was obtained from each test in which thermocouples were utilised

and plotted against incident heat flux (Figure 124 and Figure 125). The figures also show

the theoretical maximum and minimum long time surface temperatures given by

Equation 153 and Equation 174 using the flame heat fluxes derived in § 4.6.1 (Table 25).
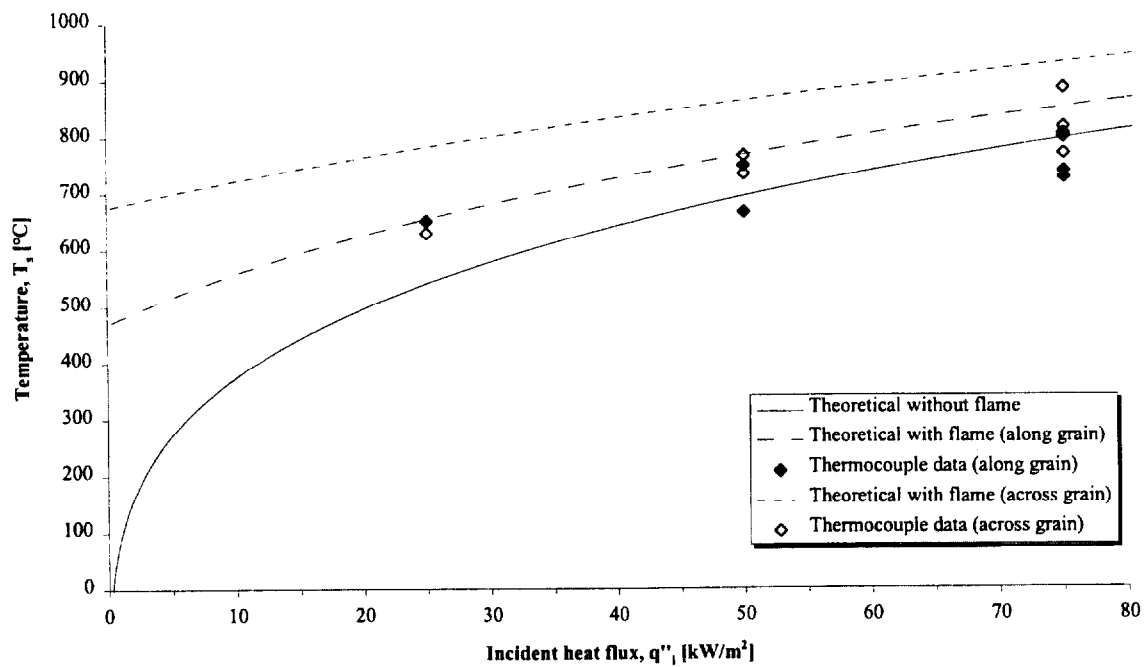
Figure 124. Measured and theoretical long time surface temperatures for Douglas fir.
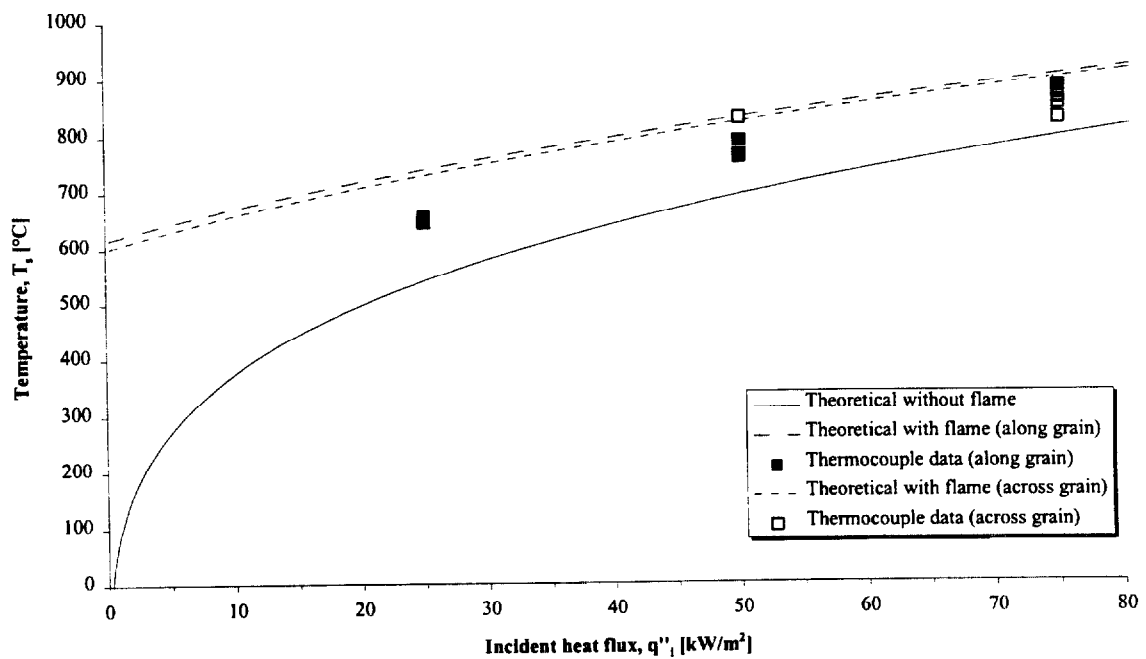
Figure 125. Measured and theoretical long time surface temperatures for Redwood.

221
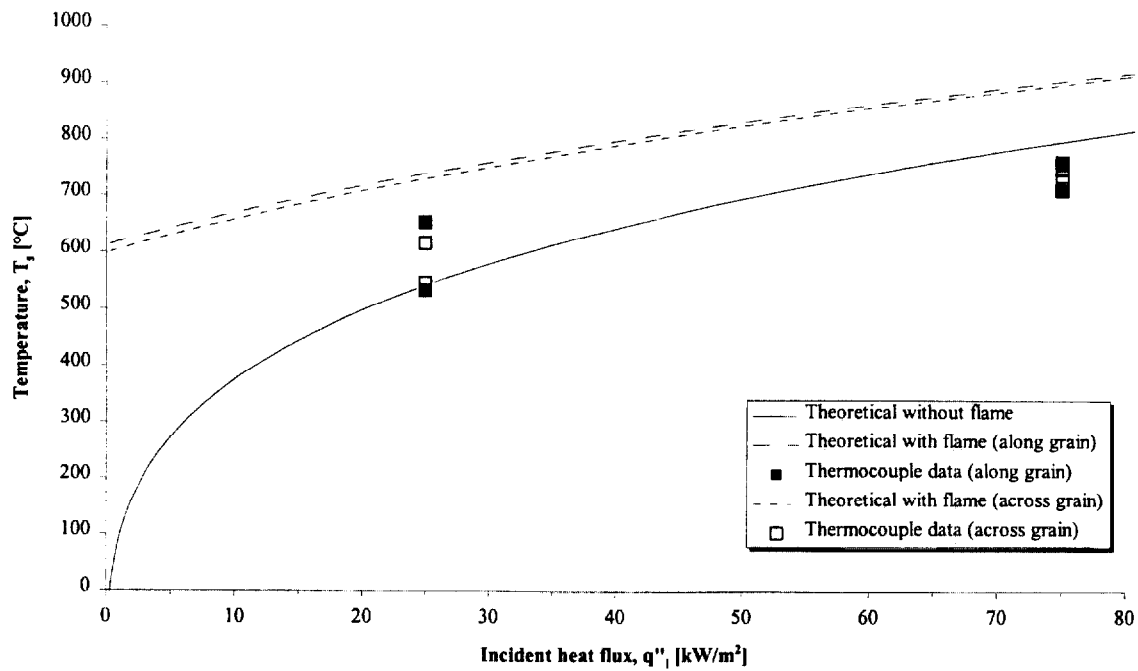
Figure 126. Measured and theoretical long time surface temperatures for Red oak.
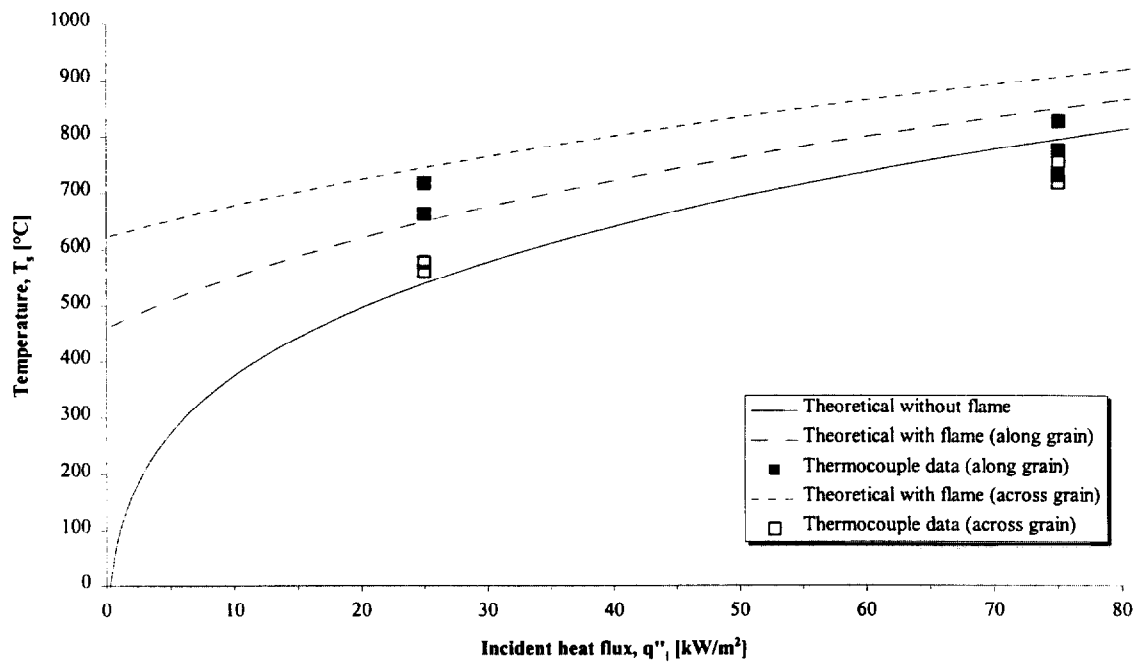
Figure 127. Measured and theoretical long time surface temperatures for Maple.

For Douglas fir and Redwood it can be seen that the thermocouple measurements generally fall in-between the two theoretical curves. For the Douglas fir *along* grain surface temperatures at high heat fluxes the thermocouple measurements fall below the theoretical minimum temperature curve. Similarly for Red oak and Maple, the thermocouple measurements generally fall in-between the two theoretical curves at 25 kW/m^2 but lie below the theoretical curves at 75 kW/m^2.

5. FURTHER WORK

This study presents a relatively simple model describing the ignition and burning characteristics of charring materials and methods to obtain the properties required to use the model. Suggested further work is given here although some of these may have only a minor effect on the theoretical predictions.

a) The current integral model assumes that the char layer remains in place throughout the burning duration. As shown in this study, the exposed surface of the char layer recedes as it is oxidised by the incident heat flux. Thus the model could be modified to account for the oxidation in terms of an additional mass loss rate from the sample and thus a reduction in the overall height of the sample

b) The integral model does not explicitly include the effect of any free moisture in the sample. As discussed in § 2.3, the moisture content of wood will influence the ignition properties. However, this moisture effect is effectively accounted for in the apparent thermal inertia obtained from the time to ignition data. Moisture also plays a part in the burning rate of wood and, as discussed in § 4.9.1, the thermal penetration into the material. Again the effect of the moisture is, at least partly, accounted for by the derivation of the effective heat of gasification of the material.

c) The processes involved in the ignition of wood at lower incident heat fluxes clearly warrants further investigation. The results from this study have shown that the mechanism for ignition appears to change from a 'bulk' surface ignition to a localised glowing ignition. The ignition temperature of wood is almost constant at high incident heat fluxes but appears to initially rise as the flux is reduced before falling to considerably lower values as the glowing ignition process becomes predominant.

Finally, there appears to be an almost constant transitional incident flux at which the ignition of wood as a function of grain exhibits a cross-over between the relative times to ignition.

d) As observed in § 1.4.2 and measured by Hopkins [30] (§ 4.6.1), the flame from a burning charring material such as wood does not remain constant as assumed in the integral model. The size of the flame, its heat flux back to the surface of the material and thus the mass flow rate of the volatiles are all interdependent. We might therefore want to consider modification of the model to account for this process.

6. CONCLUSIONS

- The integral model for the time to ignition gives good agreement with experimental data at high incident heat fluxes (greater than ~20 kW/m^2)

- A low estimate of the critical heat flux for piloted ignition can be obtained from the time to ignition data using the intercept along the x-axis of a linear extrapolation of a plot of $1/\sqrt{t_{ig}}$ against incident heat flux. Comparison with the integral model theory shows that this intercept value needs to be modified by a constant factor to obtain a better estimate of the critical heat flux.

- An estimate for the ignition temperature of wood can be obtained from the critical heat flux derived from the ignition time measurements.

- The apparent thermal inertia of a material can be obtained from the slope of a linear extrapolation of a plot of $1/\sqrt{t_{ig}}$ against incident heat flux.

- The ignition and burning rate of wood depends on many factors including the species, grain orientation, moisture content, exposure conditions and the inherent variability of wood as a natural material.

- The integral model for the burning rate of a charring material combines a small-time and a long-time solution. It may be possible to use the transition between the two solutions to obtain an estimate of the peak burning rate of the material although the results obtained do not compare particularly well with the measurements.

- The effective heat of gasification and flame heat flux can be obtained from burning rate experiments conducted in the Cone Calorimeter. An iterative approach is necessary to obtain appropriate values of the heat of gasification and flame heat flux which best match the measured data. The choice of the properties is a balance between conflicting requirements so as to match the small-time solution, the peak burning rate and the long-time solution and is therefore based on a certain degree of interpretation.

- The char fraction of wood has been found to be a function of the ratio of the incident heat flux and the critical heat flux. The function may not be universal for all charring materials or even all species of wood.

- Once suitable properties have been derived, the integral model's solutions for the burning rate qualitatively compares well with the measured data. The model predicts both the initial growth and the subsequent decay.

- Thermocouples embedded into a burning sample can be used to estimate the thermal penetration depth, char depth and the surface temperature after a long time. Comparison between the thermocouple data and the integral model shows reasonable

agreement particularly for the thermal penetration depth and the long-time surface temperatures. Prediction of the char depth using the thermocouple data is not particularly reliable.

- Prediction of the char depth can be made using the average burning rate. The predictions of char depth based on the measured mass loss rate and the measured char depth after an exposure of 25 minutes compare well. For an exposure of 75 minutes, the match is poor and this may be due to the finite thickness of the samples.

- The mechanism for the ignition of wood at low heat fluxes close to the critical heat flux appears to be different from that at high heat fluxes. At low heat fluxes, localised smouldering of the wood may increase the energy input at that point and thus lead to a localised ignition.

"Science is not the easy road to simple answers, but a torturous path to more complex questions."

"And this thumping in our chest said ... there is no rest.
We would hang together
or they'd hang us one by one"
    A Fire is Burning, Oysterband (Holy Bandits, 1993)

7. APPENDIX

Test (1DFL1), Douglas Fir, along grain at 75 kW/m^2 for 25 minutes.
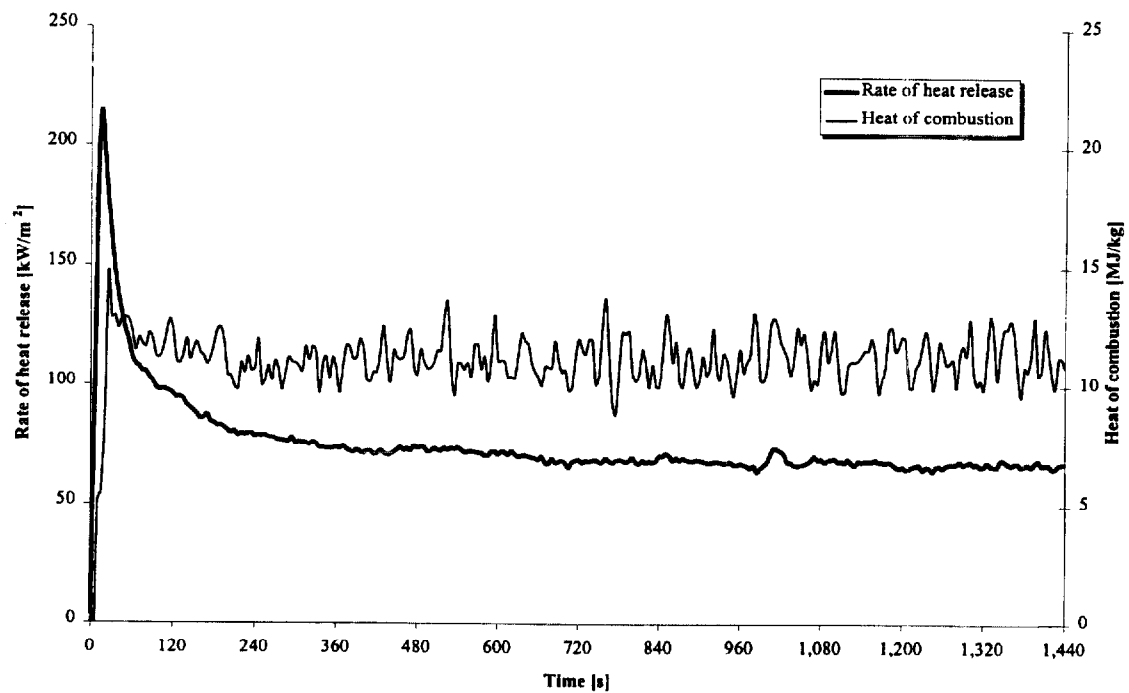
Figure 128. Rate of heat release and heat of combustion (1DFL1).
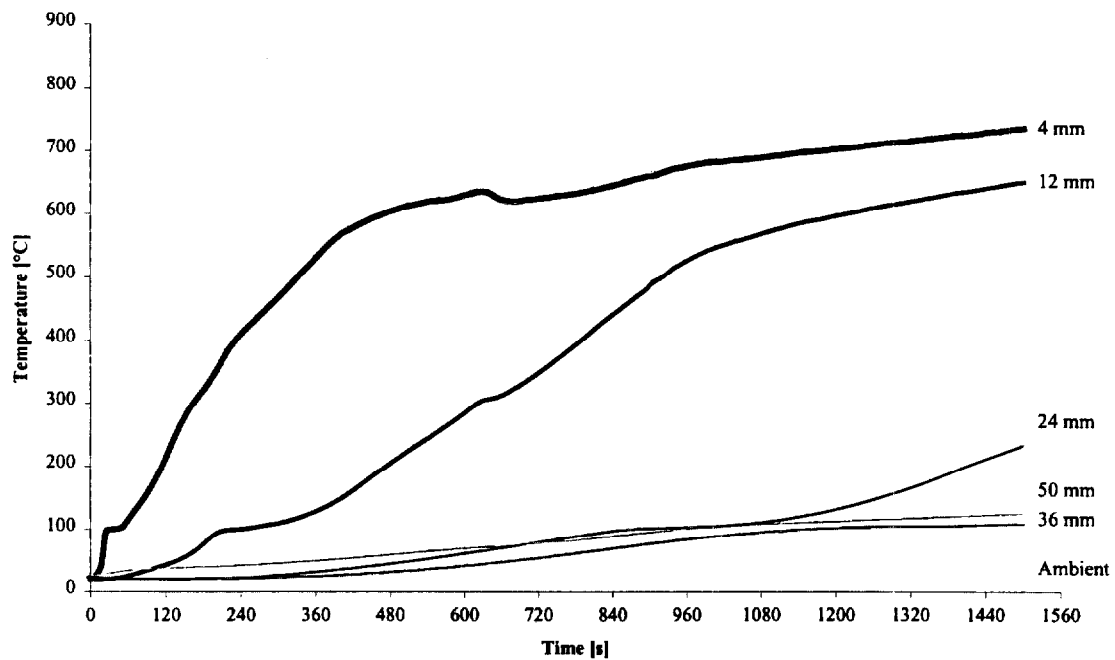
Figure 129. Temperatures measured in sample (1DFL1).

229
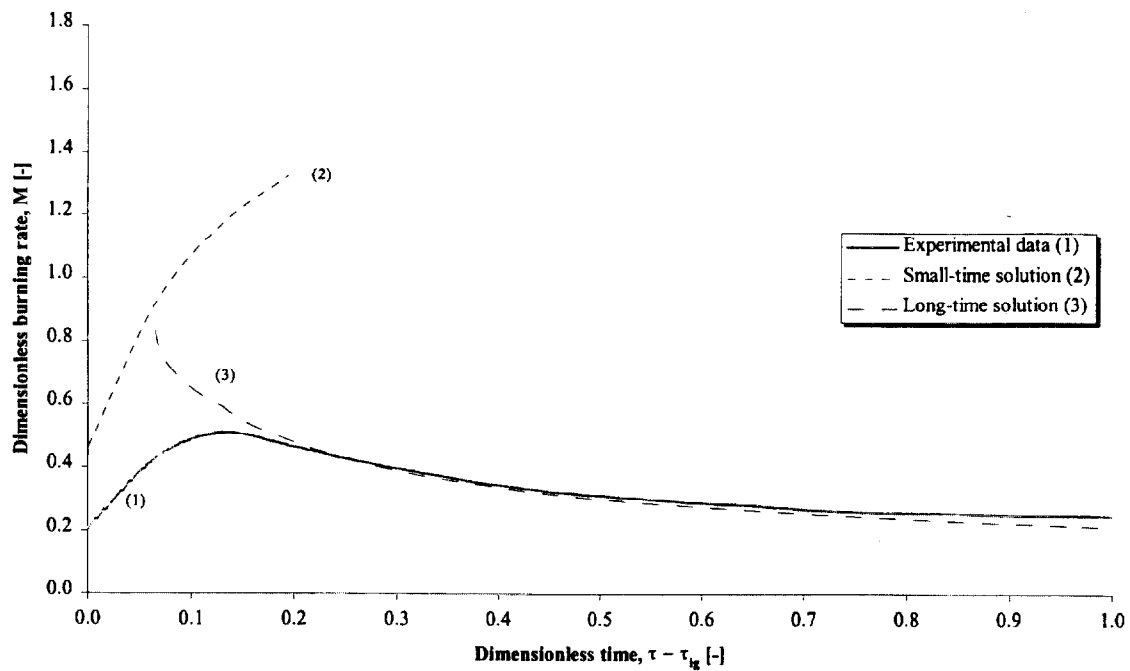
Figure 130. Comparison of dimensionless burning rate using derived properties for species and orientation (1DFL1).
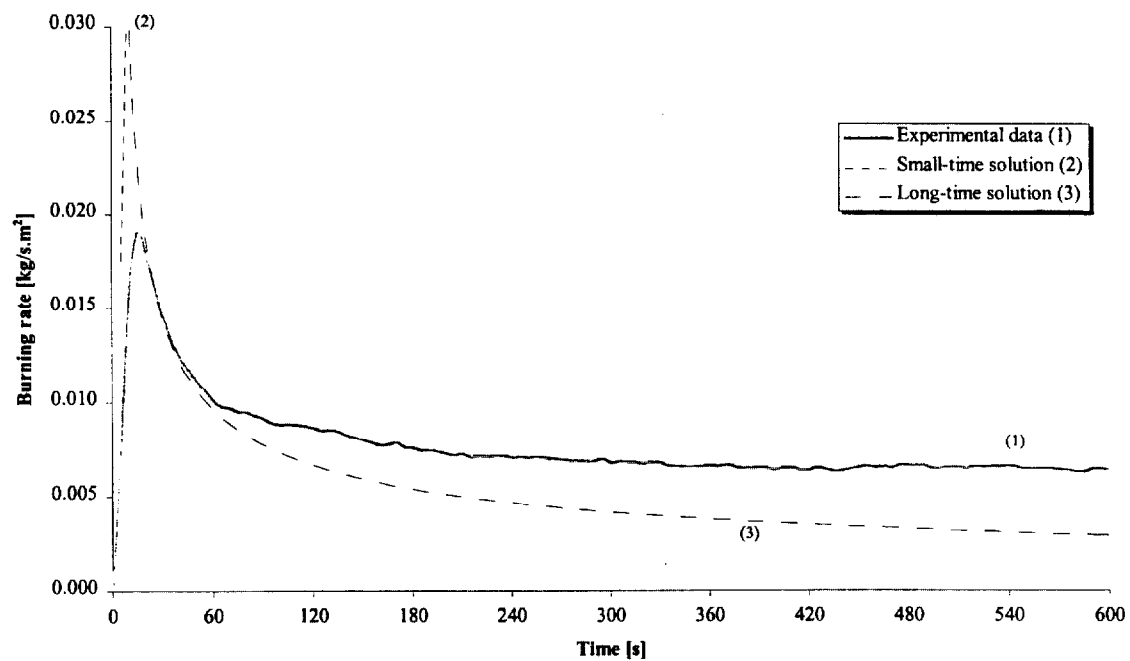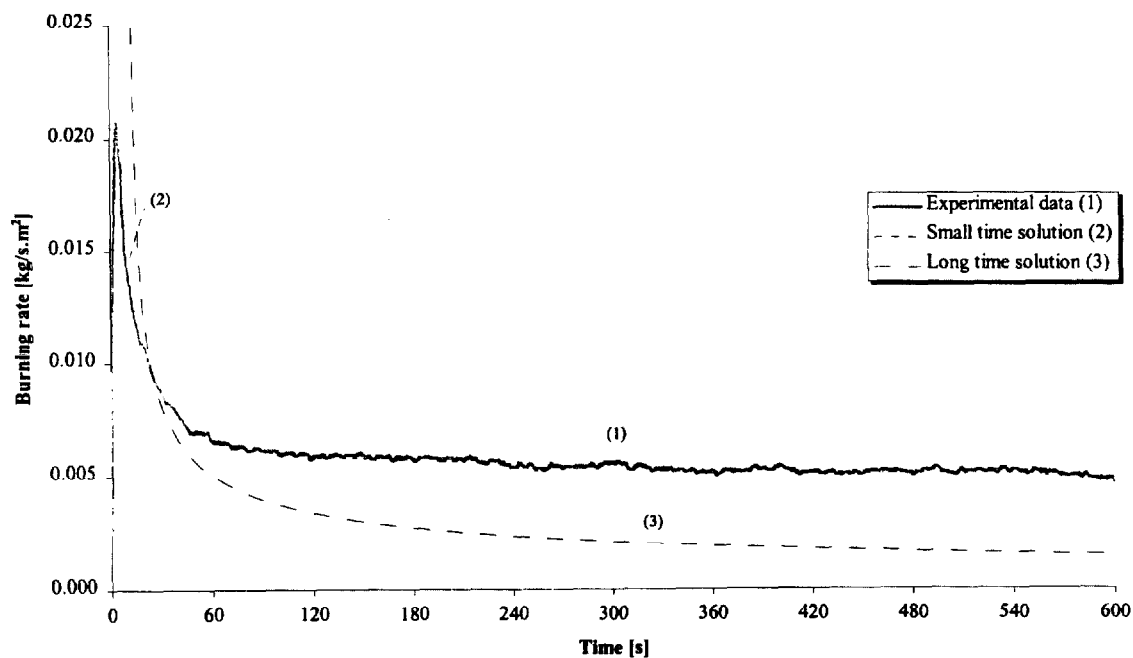

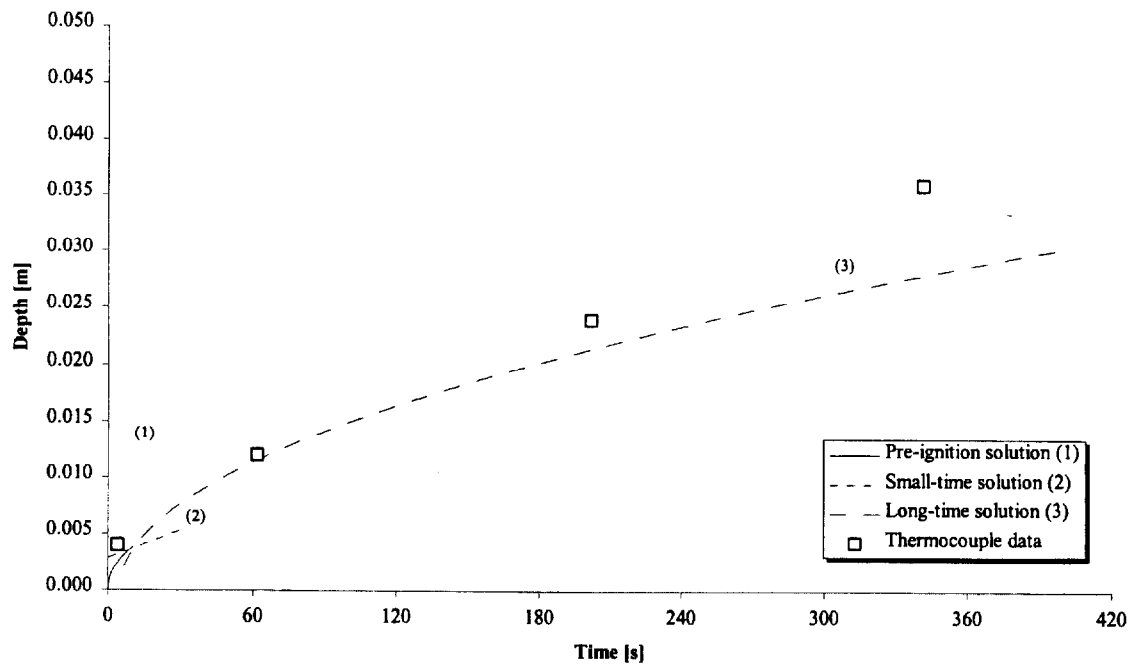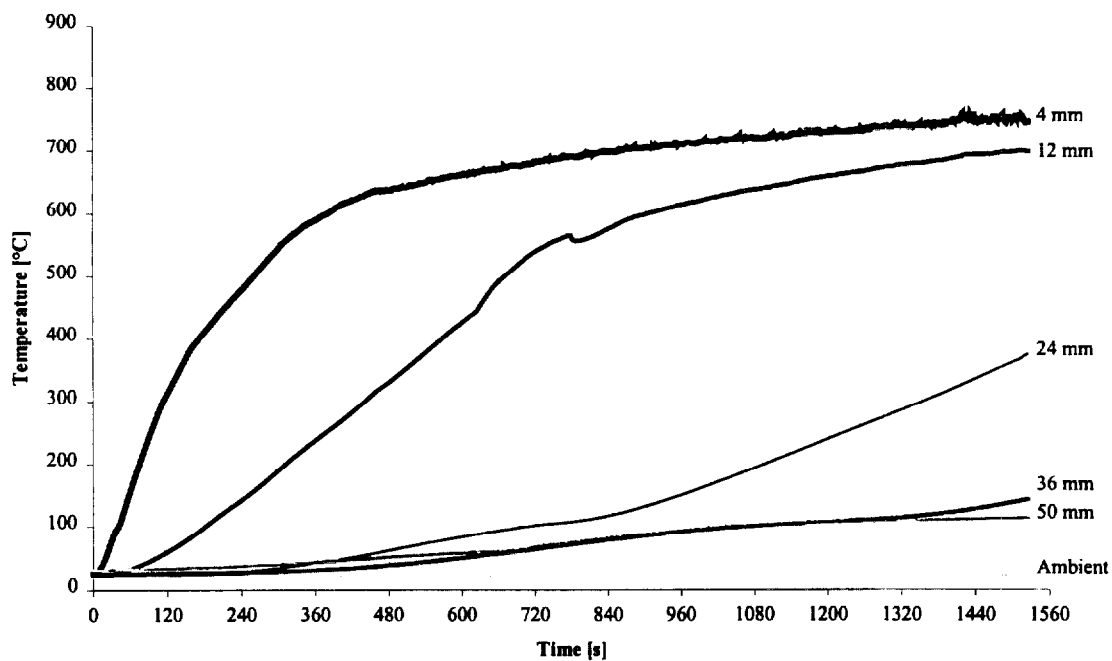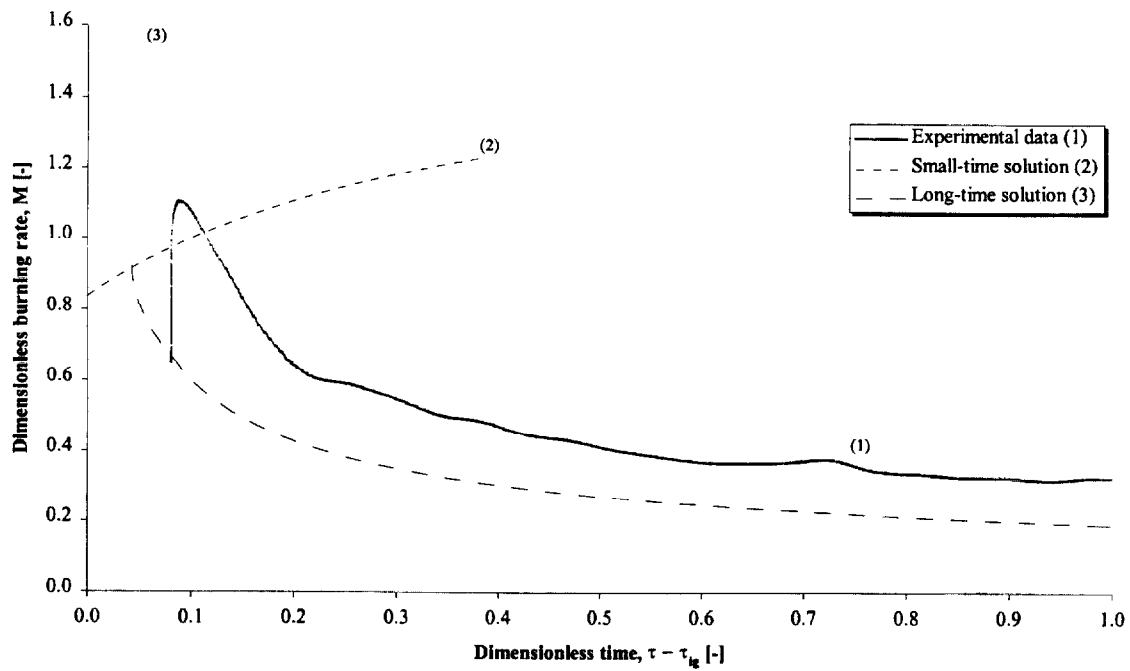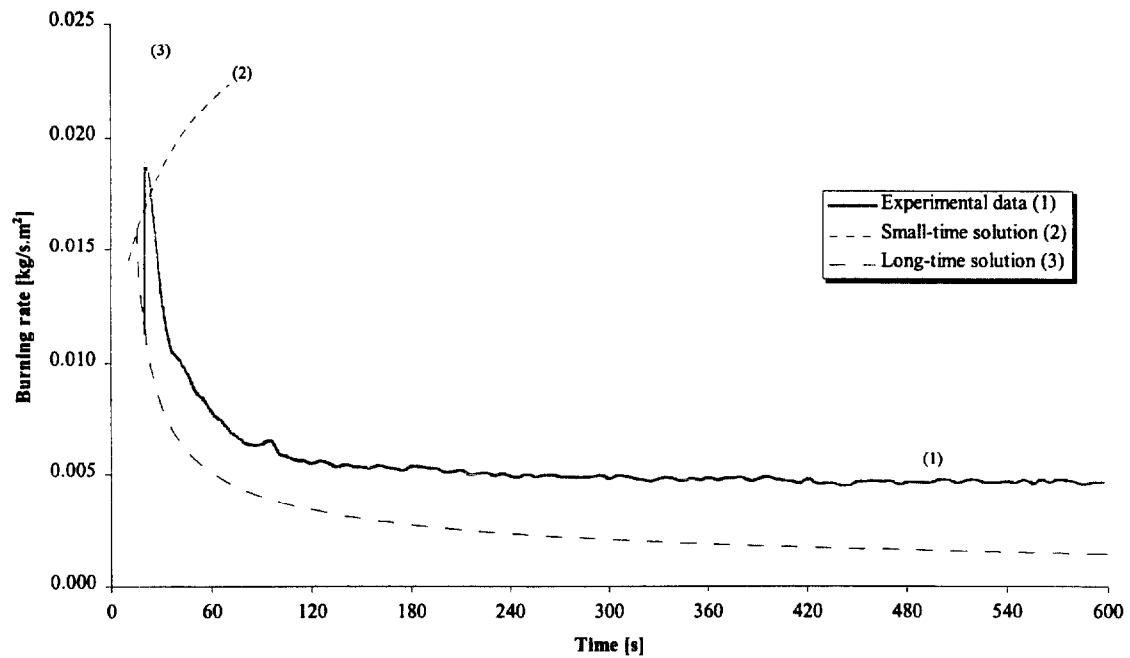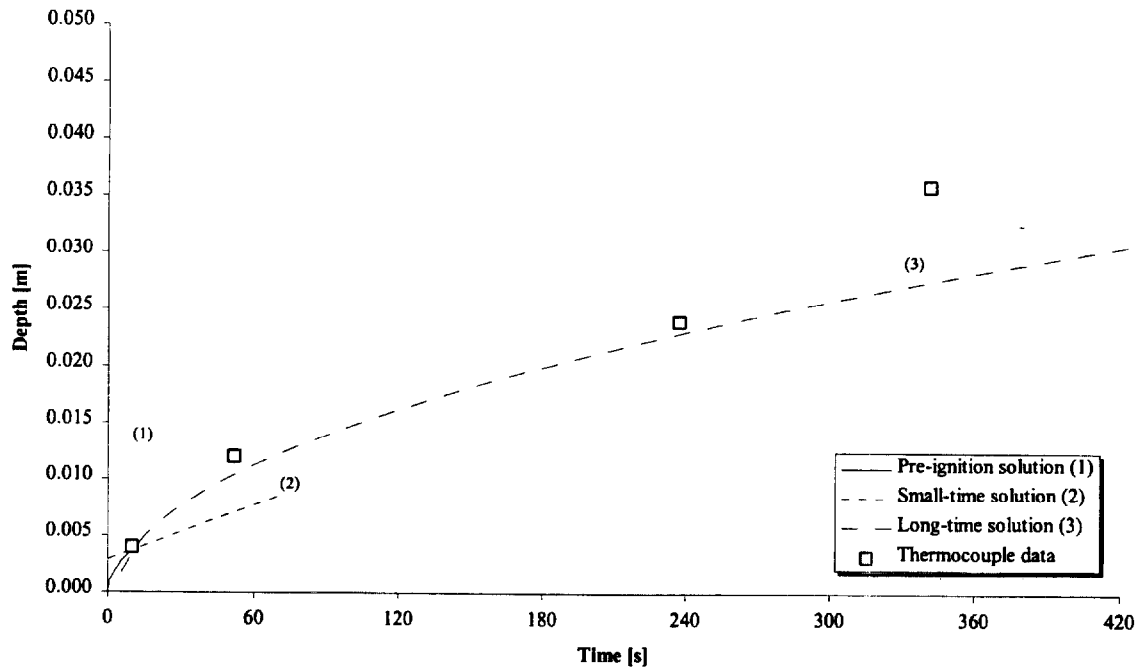**Figure 131.** Comparison of burning rate using derived properties for species and orientation (1DFL1).

230
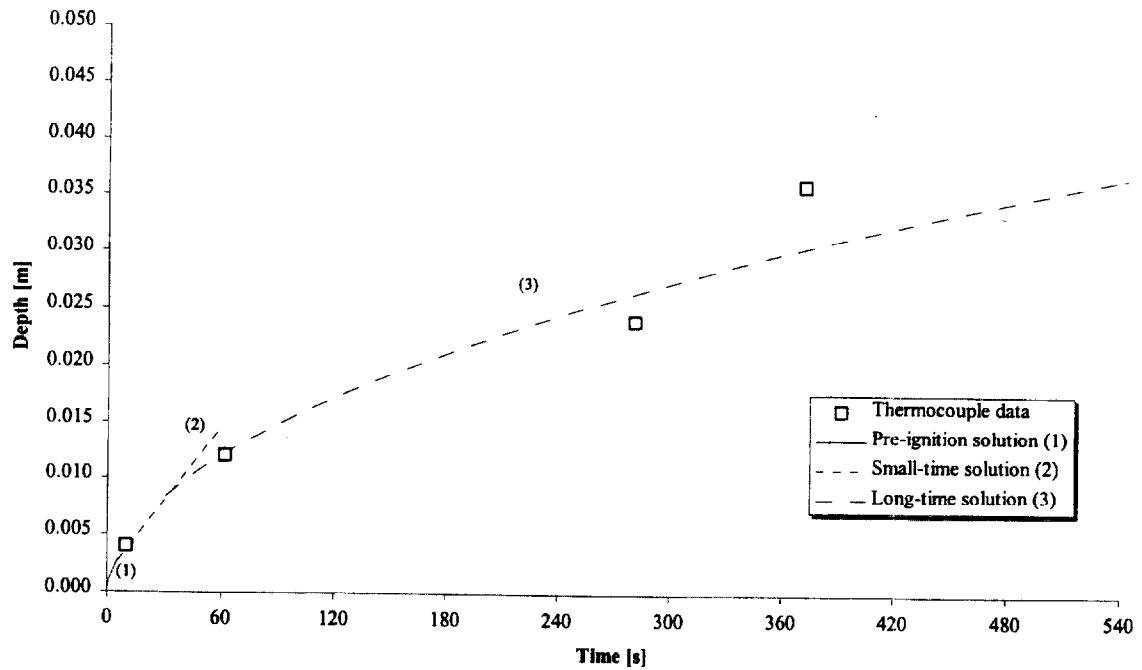
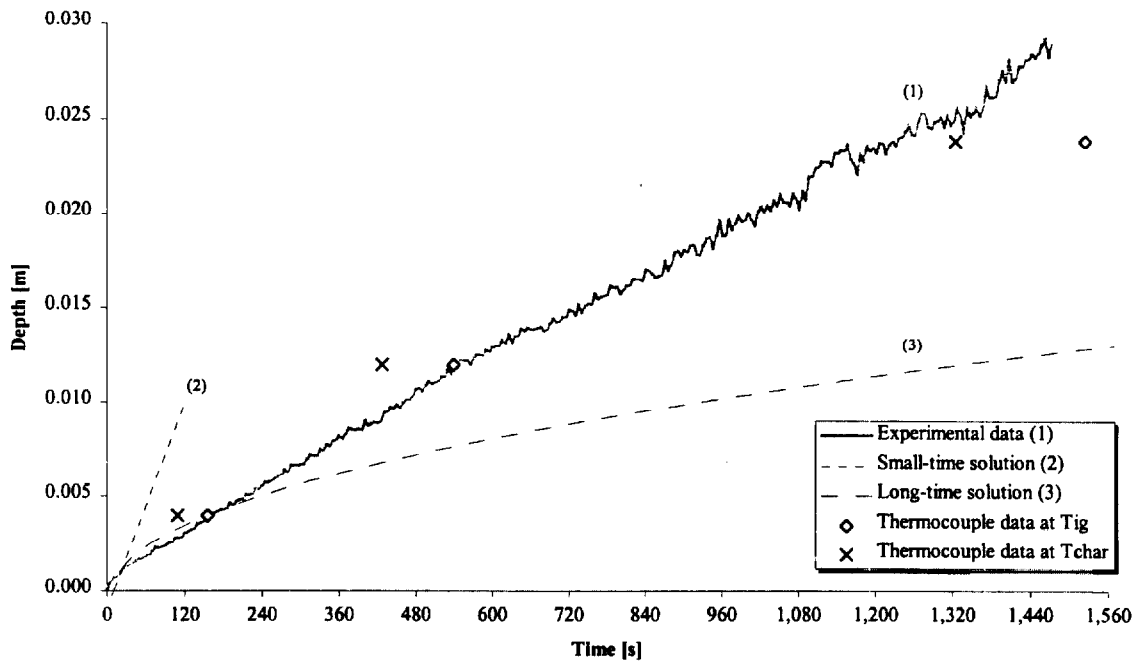**Figure 132.** Comparison of measured and calculated thermal penetration depth (1DFL1).
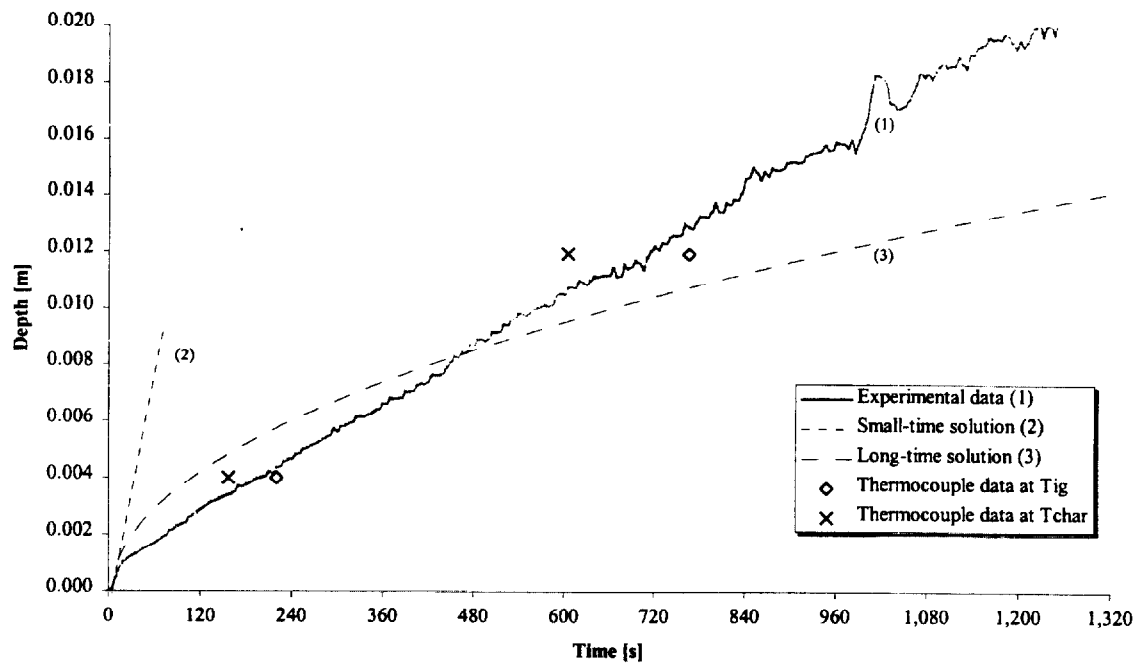
Figure 133. Comparison of estimated char depth from experimental data and the
calculated char depth (1DFL1).

231

Test (1DFL2), Douglas Fir, along grain at 75 kW/m² for 25 minutes.
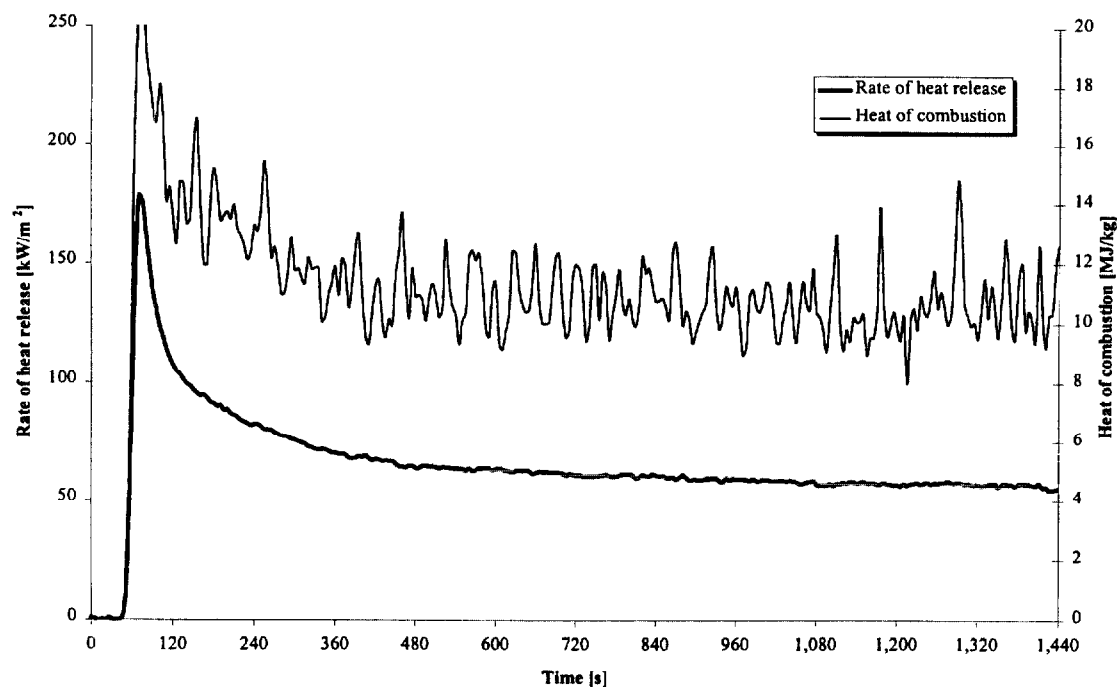
Figure 134. Rate of heat release and heat of combustion (1DFL2).
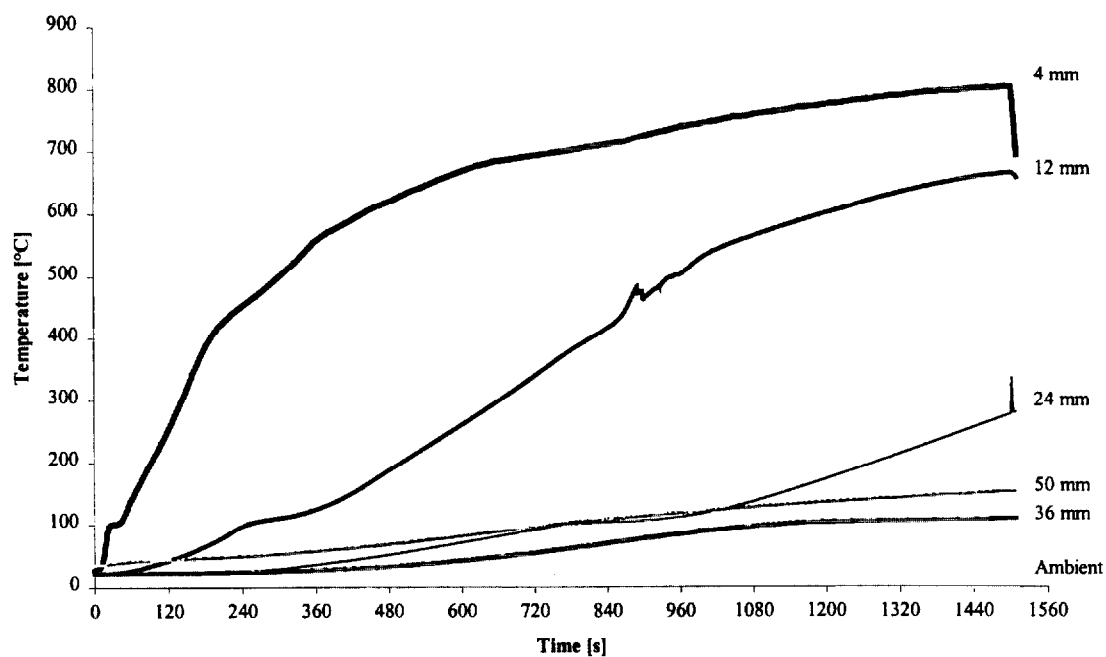
Figure 135. Temperatures measured in sample (1DFL2).
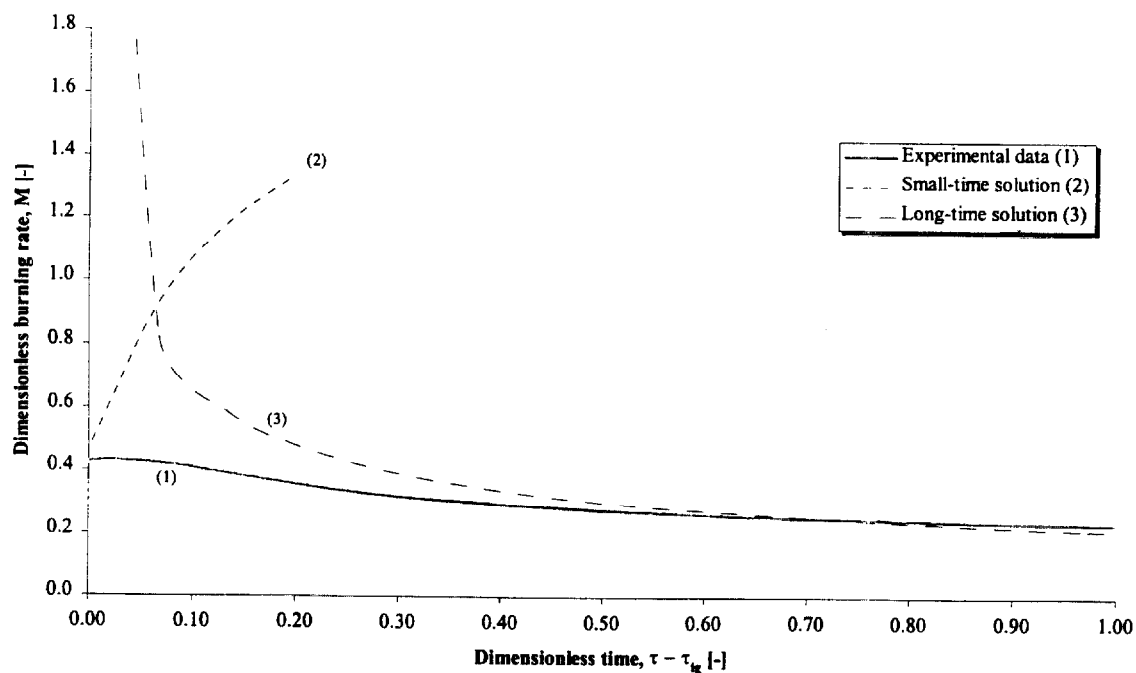
Figure 136. Comparison of dimensionless burning rate using derived properties for species and orientation (1DFL2).
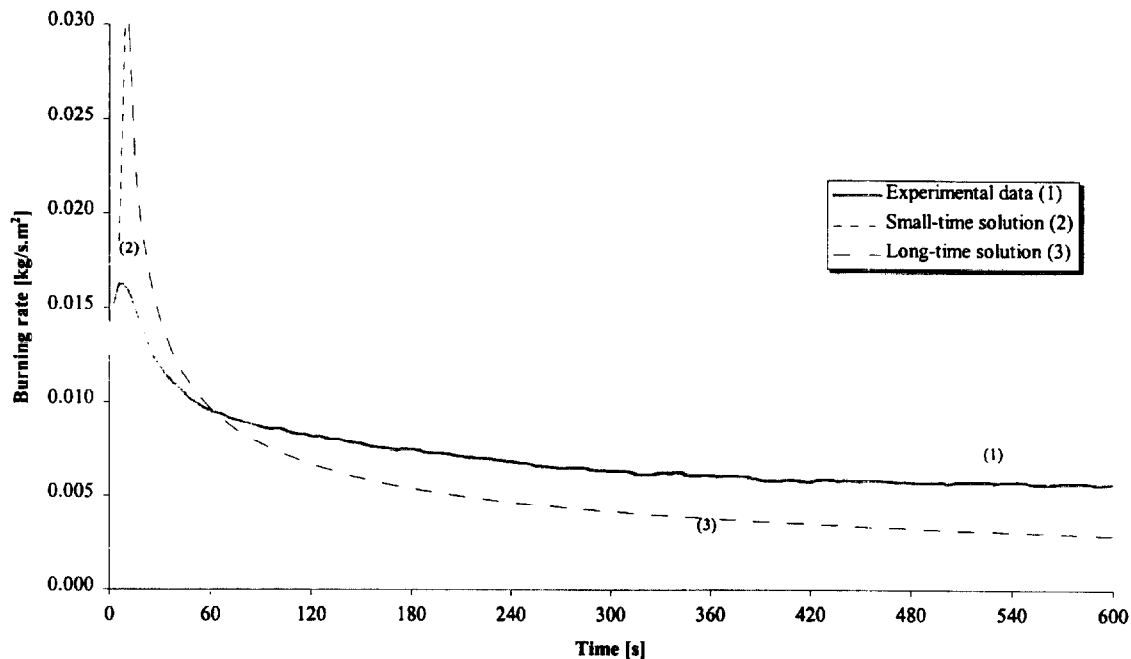
Figure 137. Comparison of burning rate using derived properties for species and orientation (1DFL2).
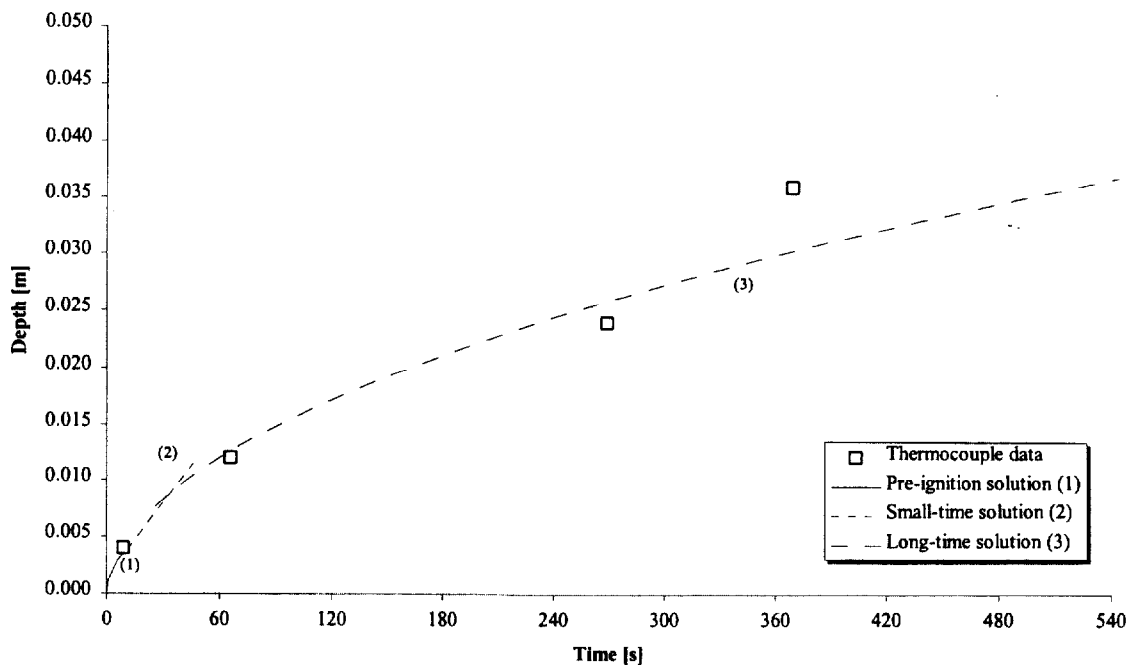
Figure 138. Comparison of measured and calculated thermal penetration depth (1DFL2).
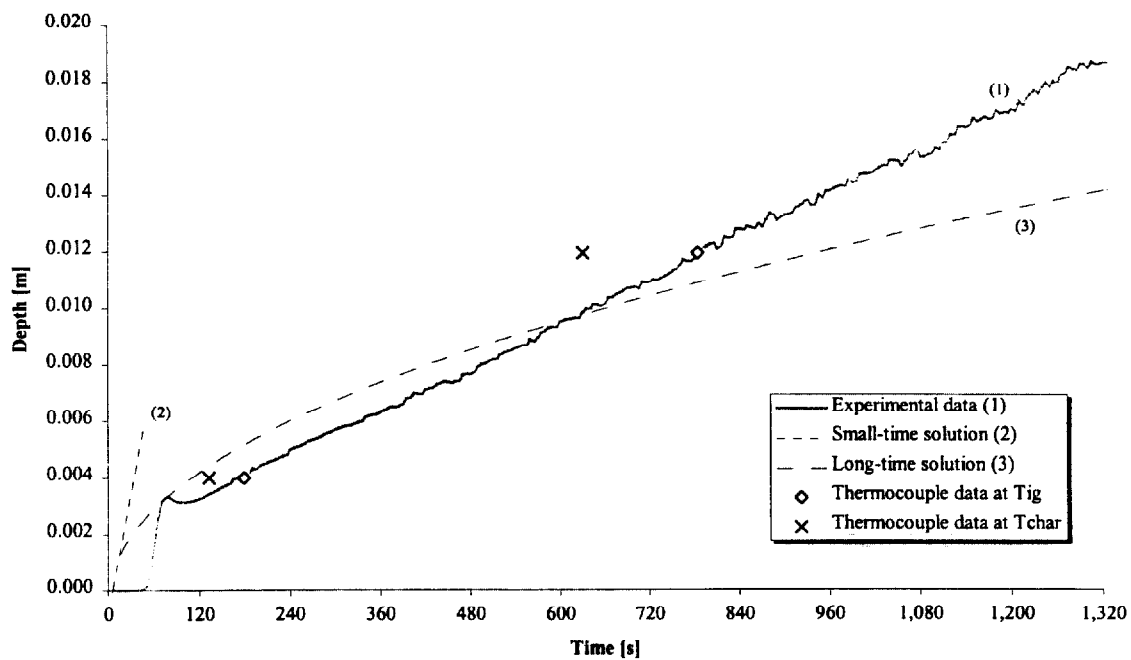
Figure 139. Comparison of estimated char depth from experimental data and the calculated char depth (1DFL2).

234

Test (1DFL3), Douglas Fir, along grain at 25 kW/m^2 for 25 minutes.
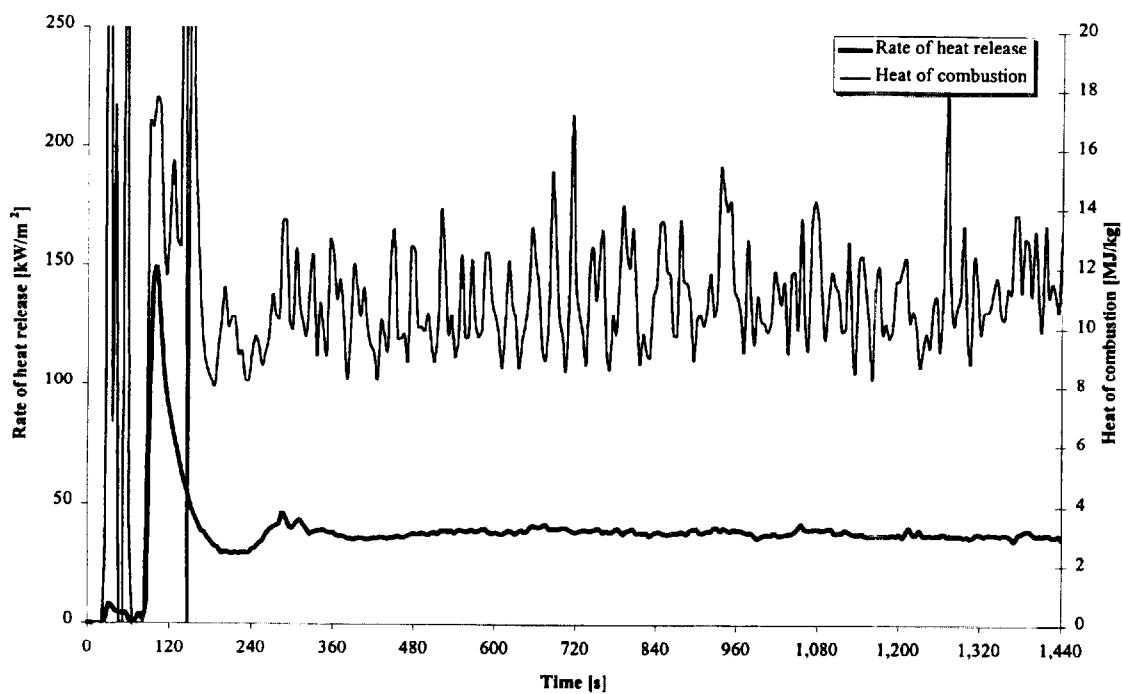
Figure 140. Rate of heat release and heat of combustion (1DFL3).
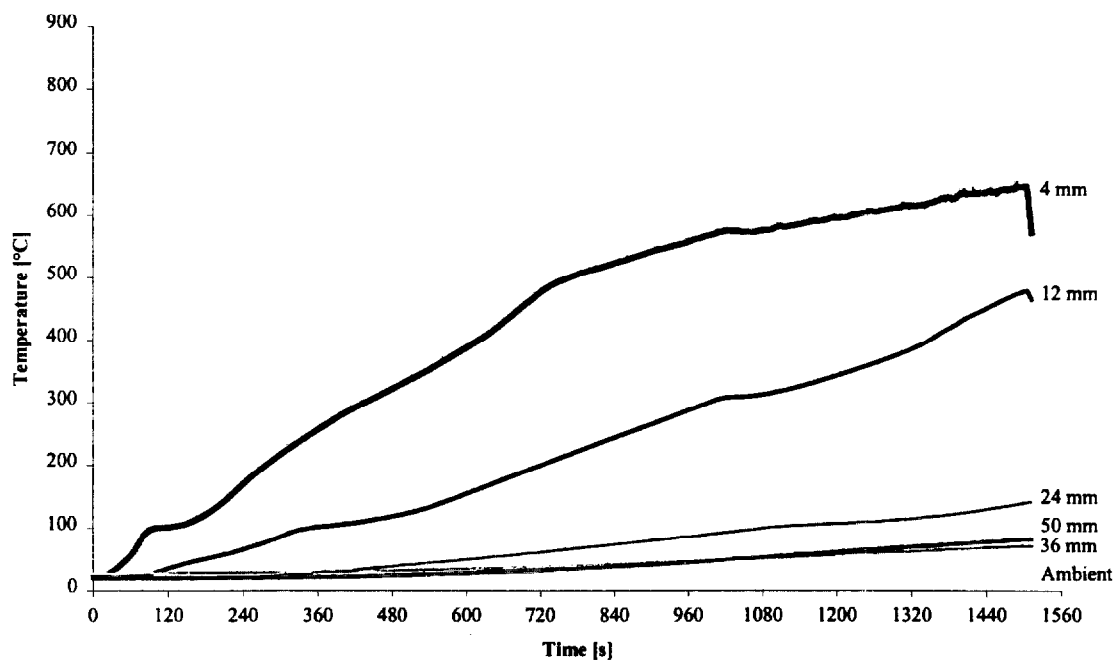
Figure 141. Temperatures measured in sample (1DFL3).
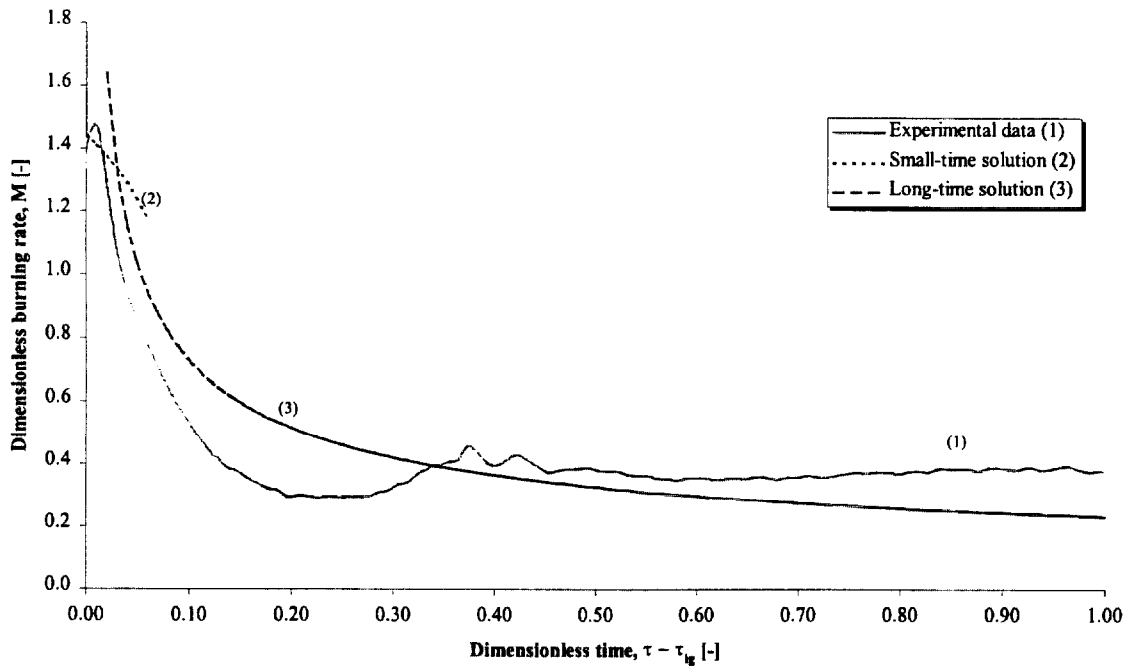
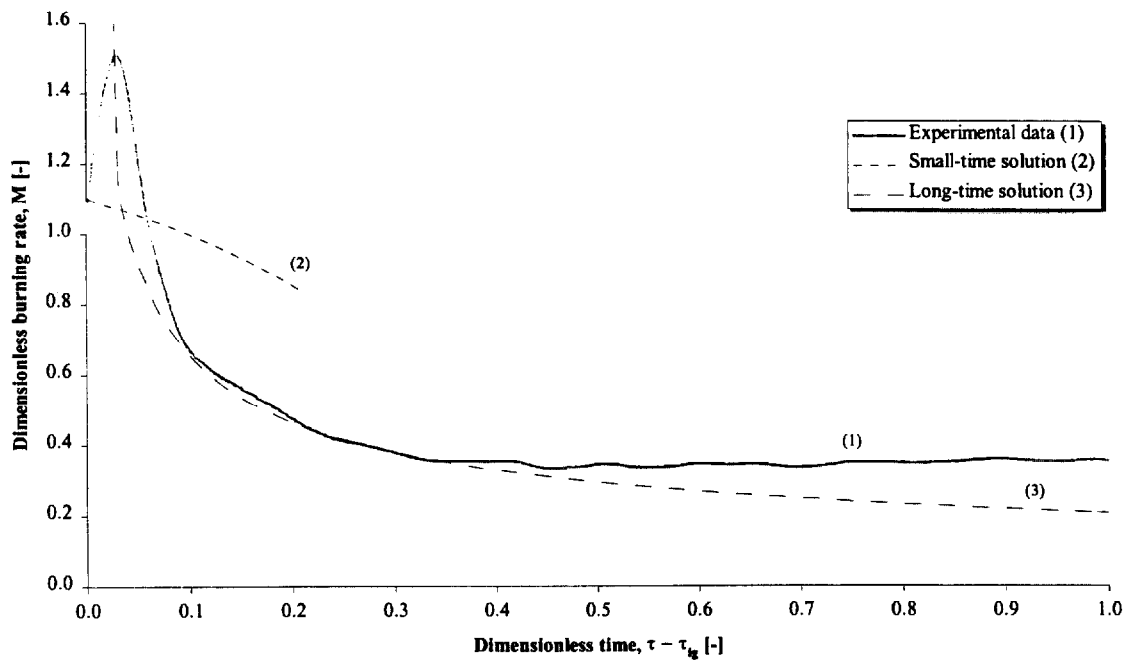**Figure 142.** Comparison of dimensionless burning rate using derived properties for species and orientation (1DFL3).
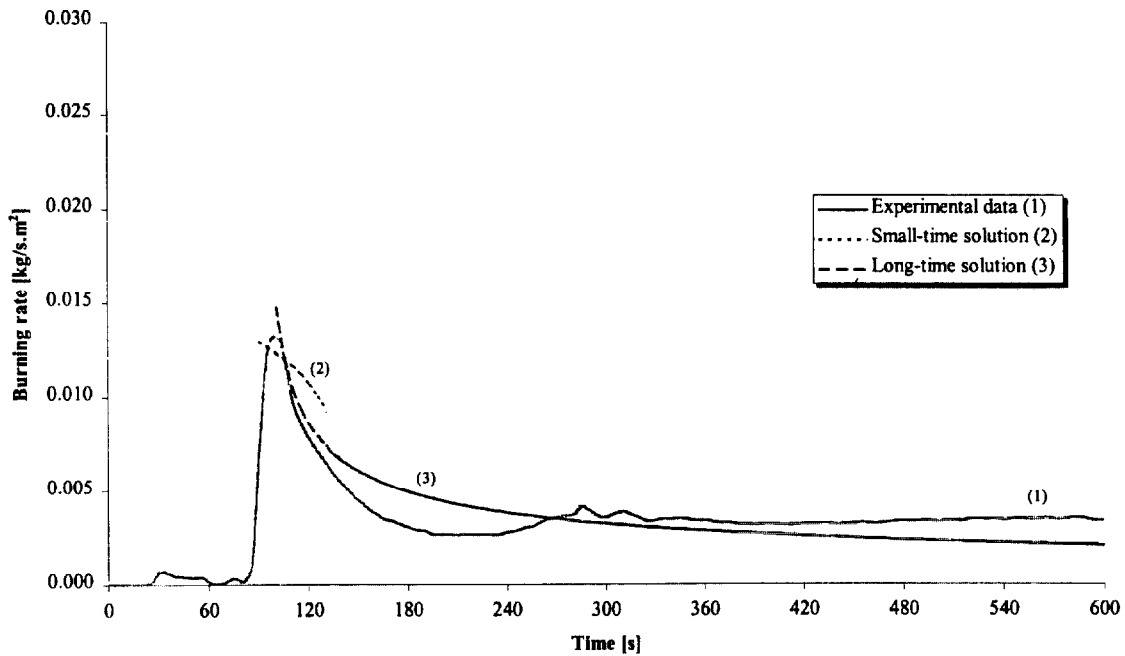
Figure 143. Comparison of burning rate using derived properties for species and orientation (1DFL3).
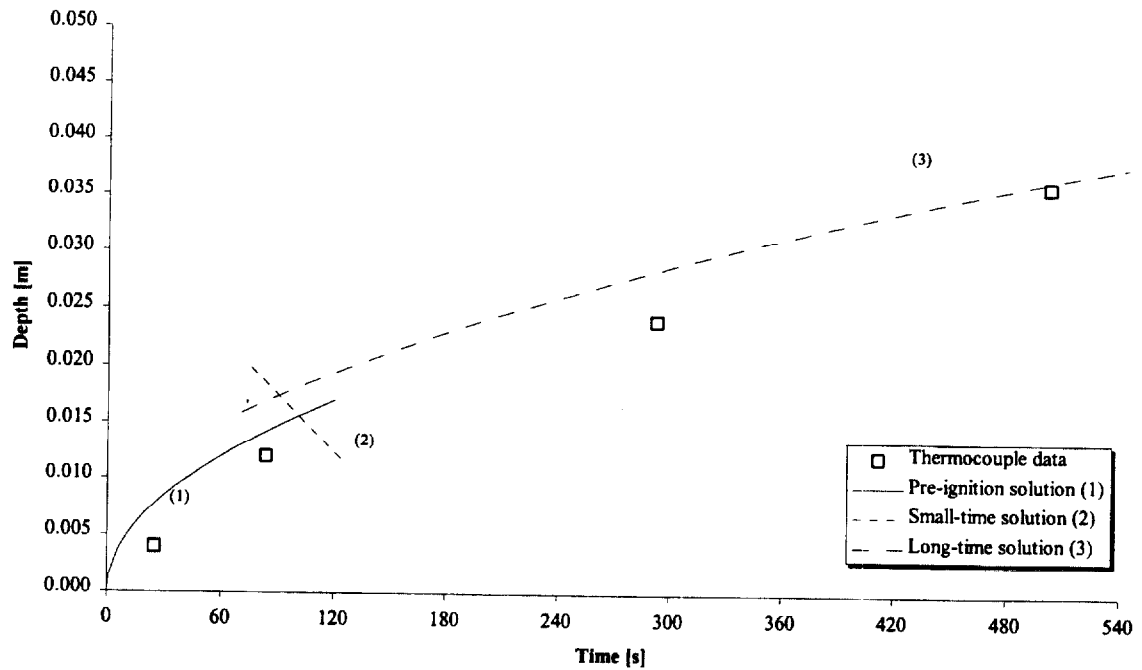
Figure 144. Comparison of measured and calculated thermal penetration depth (1DFL3).
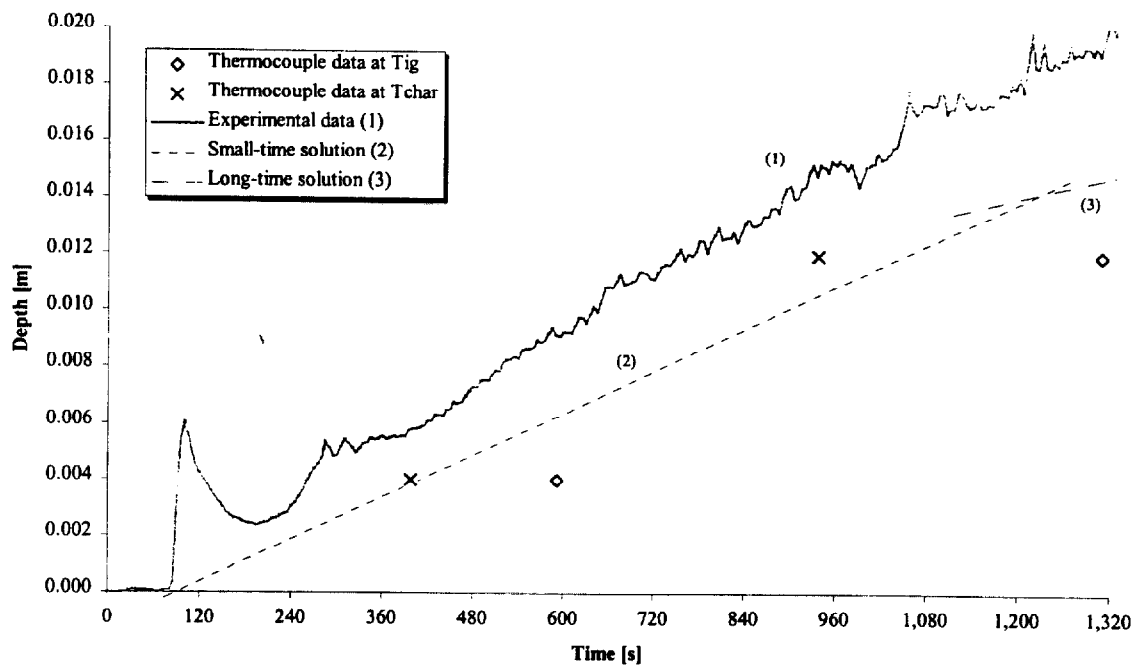
Figure 145. Comparison of estimated char depth from experimental data and the calculated char depth (1DFL3).

237

Test (1DFL4), Douglas Fir, along grain at 75 kW/m^2 for 25 minutes.
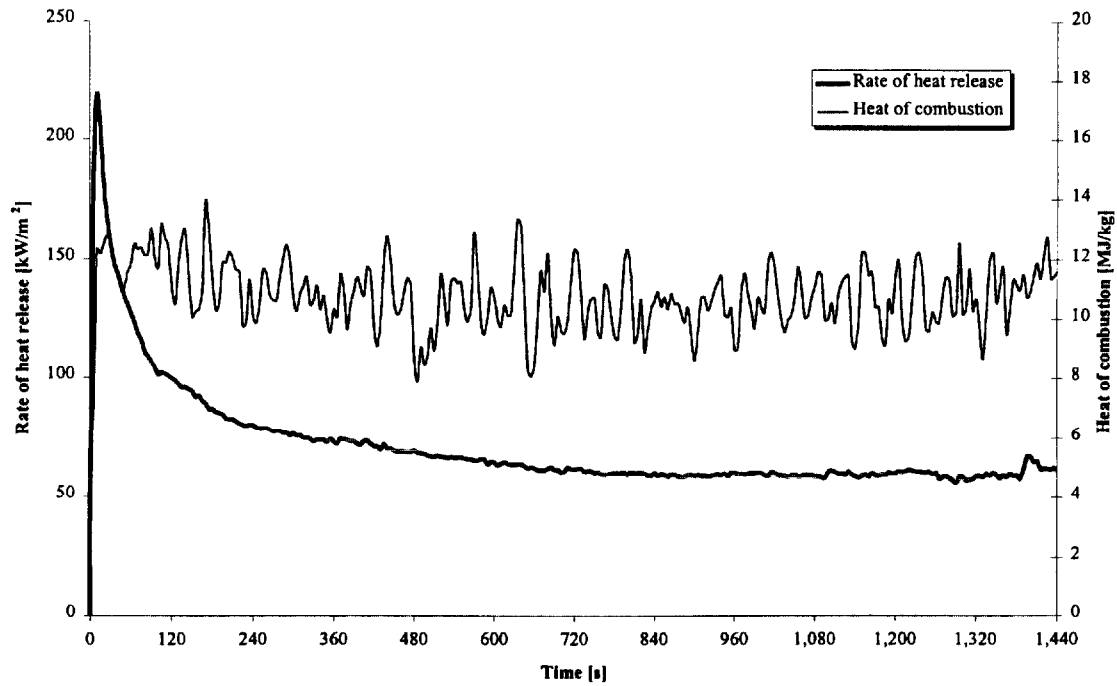
Figure 146. Rate of heat release and heat of combustion (1DFL4).
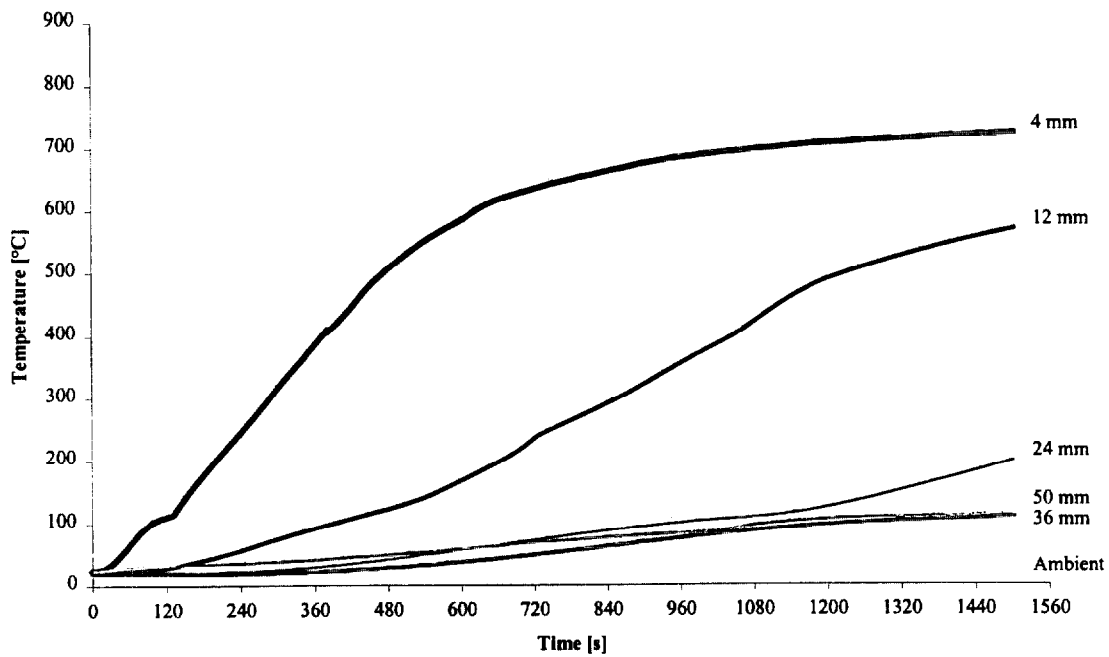
Figure 147. Temperatures measured in sample (1DFL4).
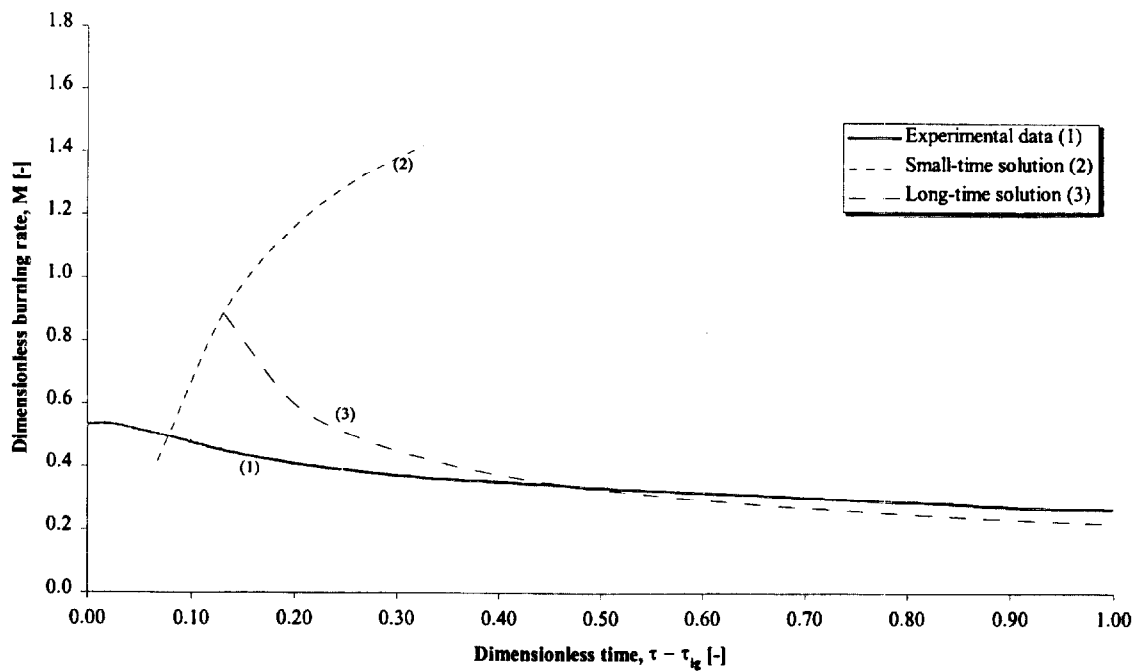
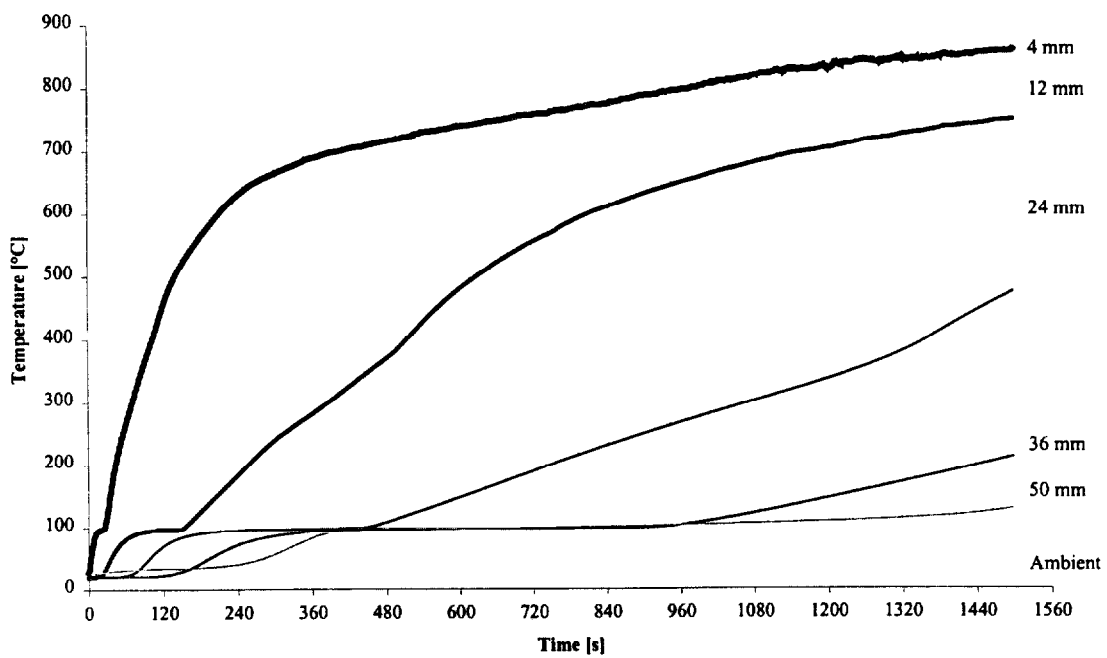**Figure 148.** Comparison of dimensionless burning rate using derived properties for species and orientation (1DFL4).
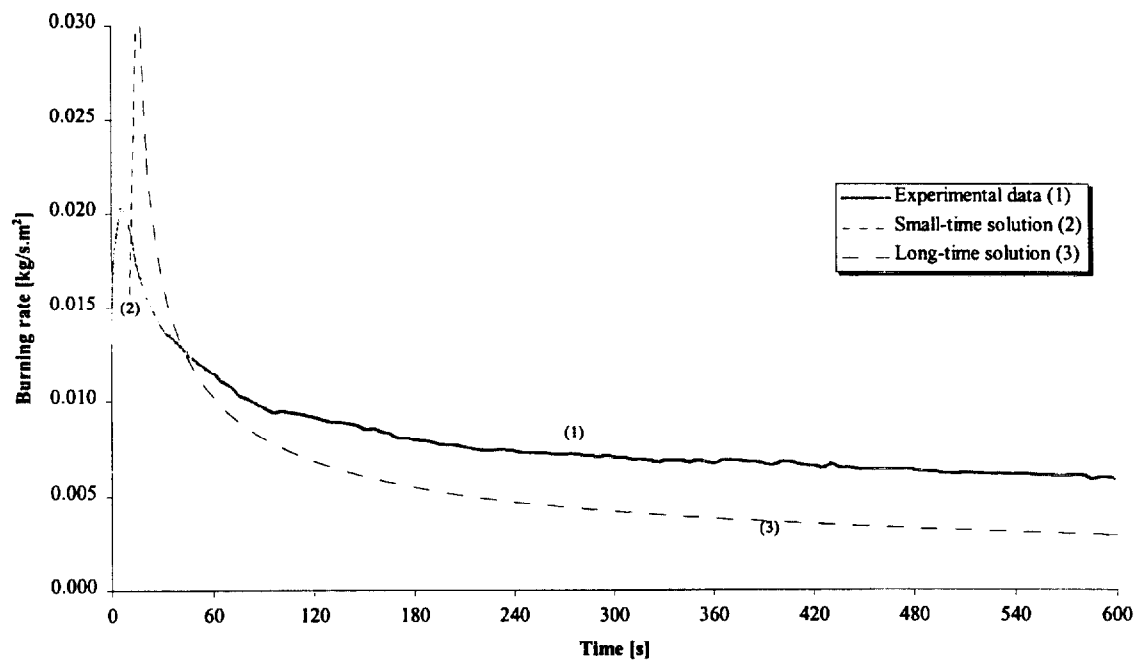
Figure 149. Comparison of burning rate using derived properties for species and orientation (1DFL4).

239
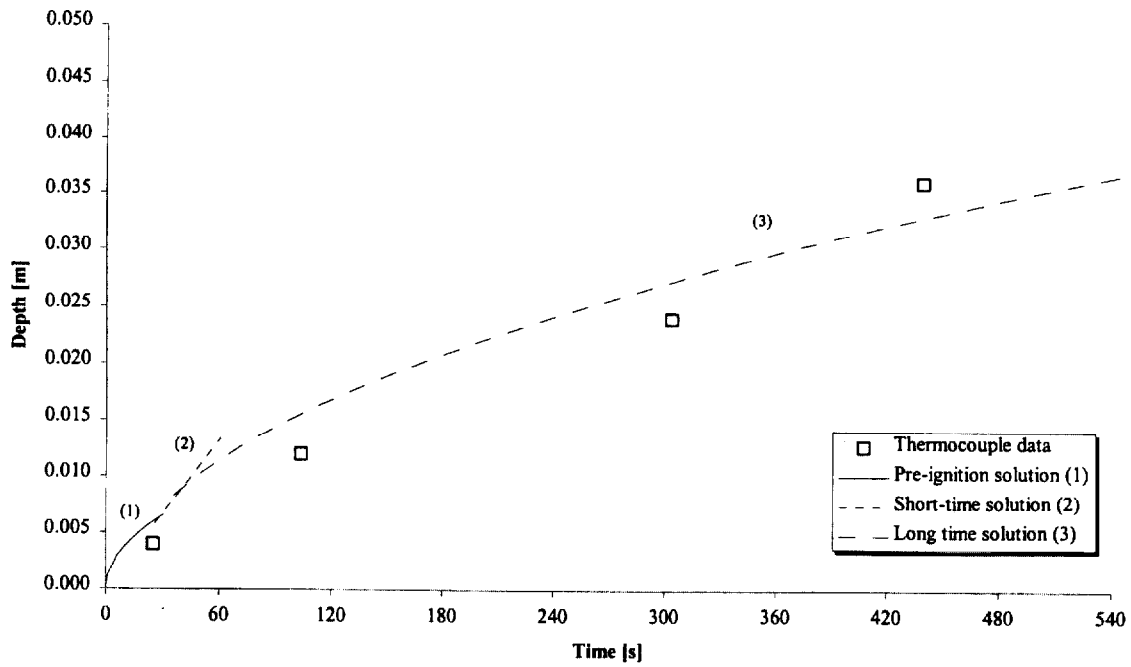
Figure 150. Comparison of measured and calculated thermal penetration depth (1DFL4).
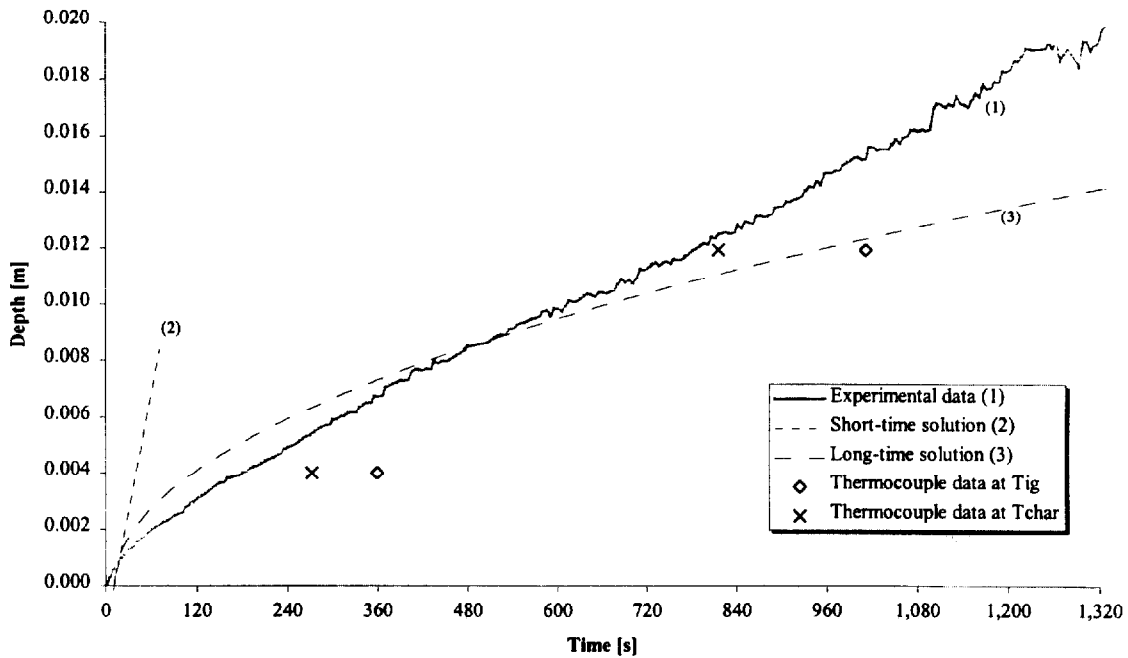
Figure 151. Comparison of estimated char depth from experimental data and the calculated char depth (1DFL4).

240

Test (1DFL6), Douglas Fir, along grain at 50 kW/m^2 for 25 minutes.
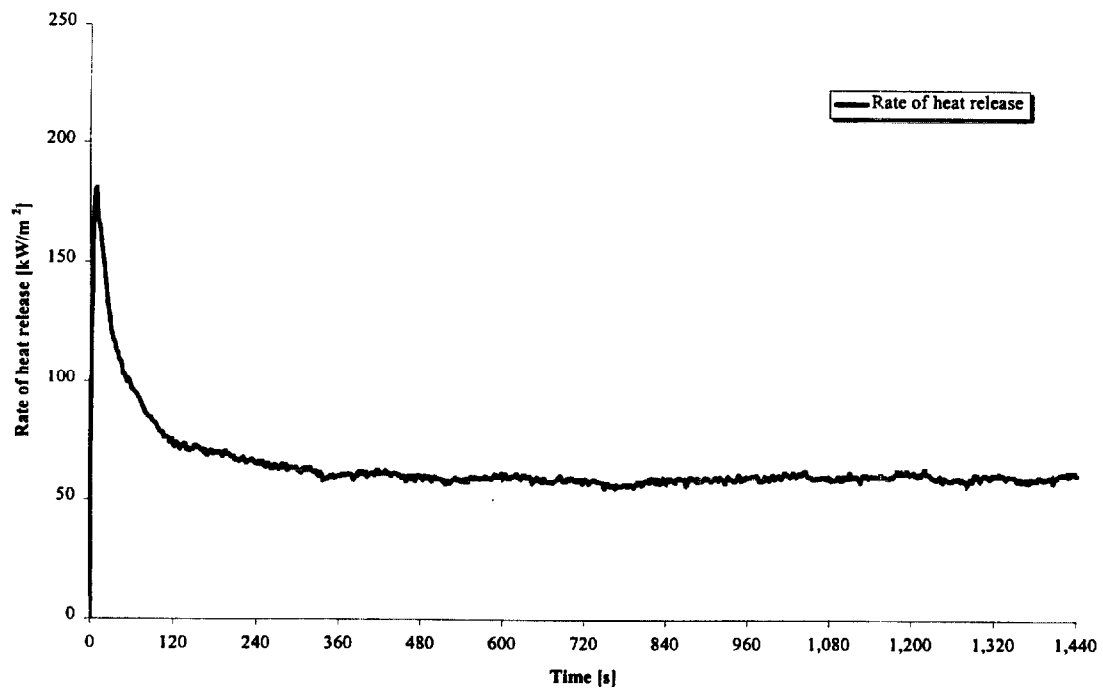
Figure 152. Rate of heat release (1DFL6).
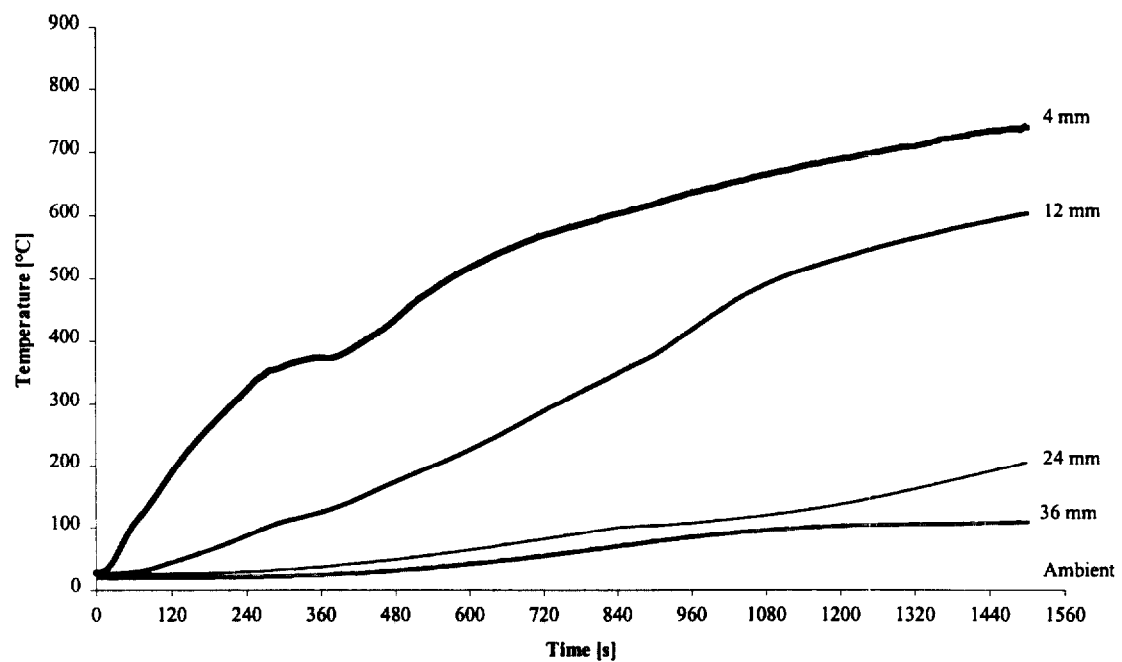
Figure 153. Temperatures measured in sample (1DFL6).

241
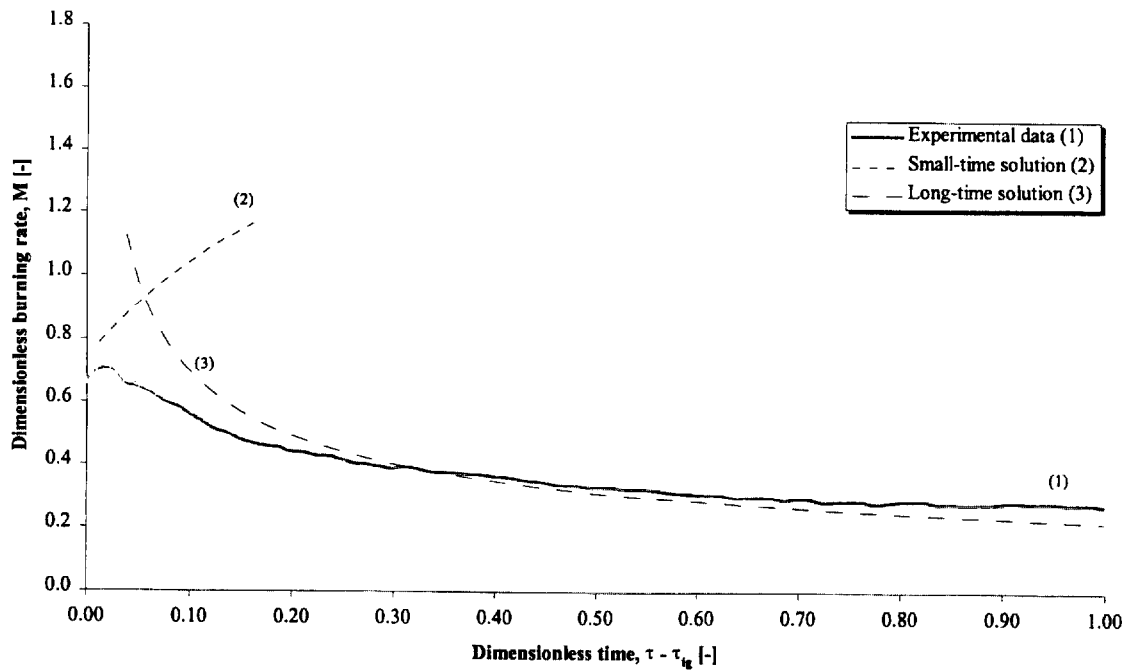
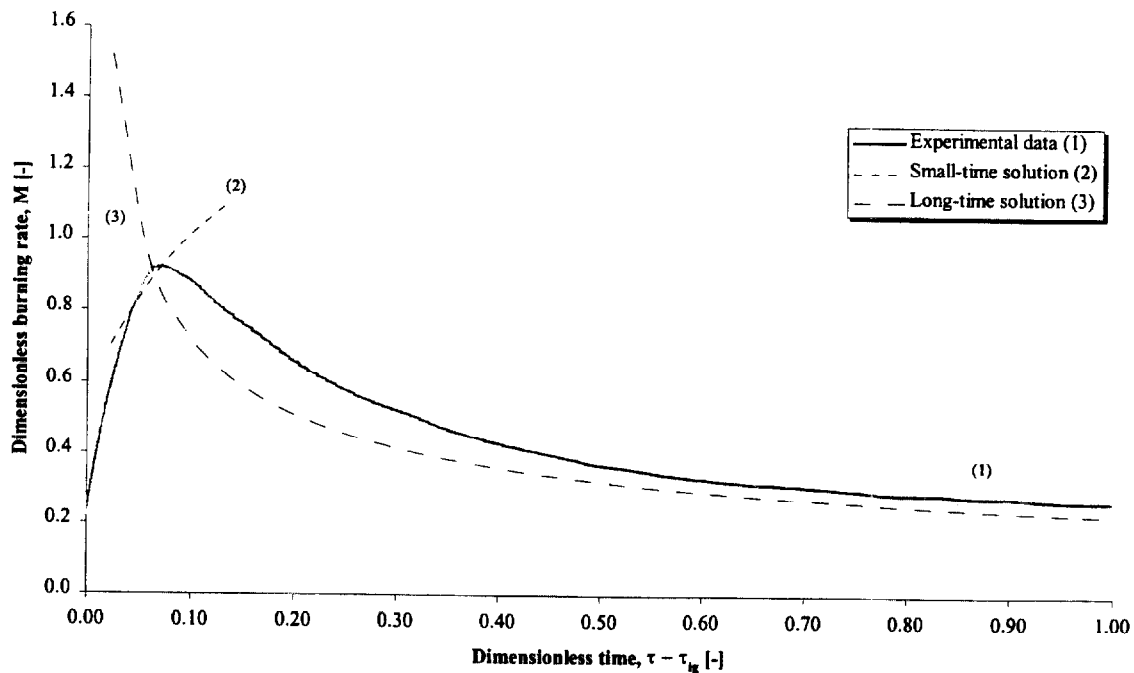**Figure 154.** Comparison of dimensionless burning rate using derived properties for species and orientation (1DFL6).
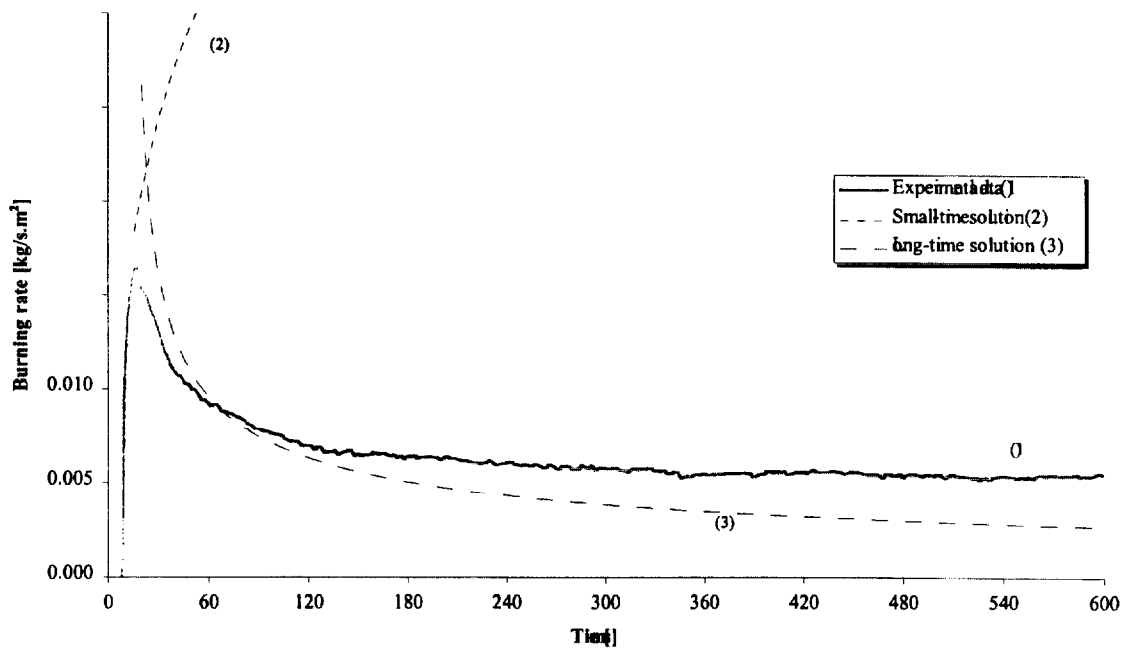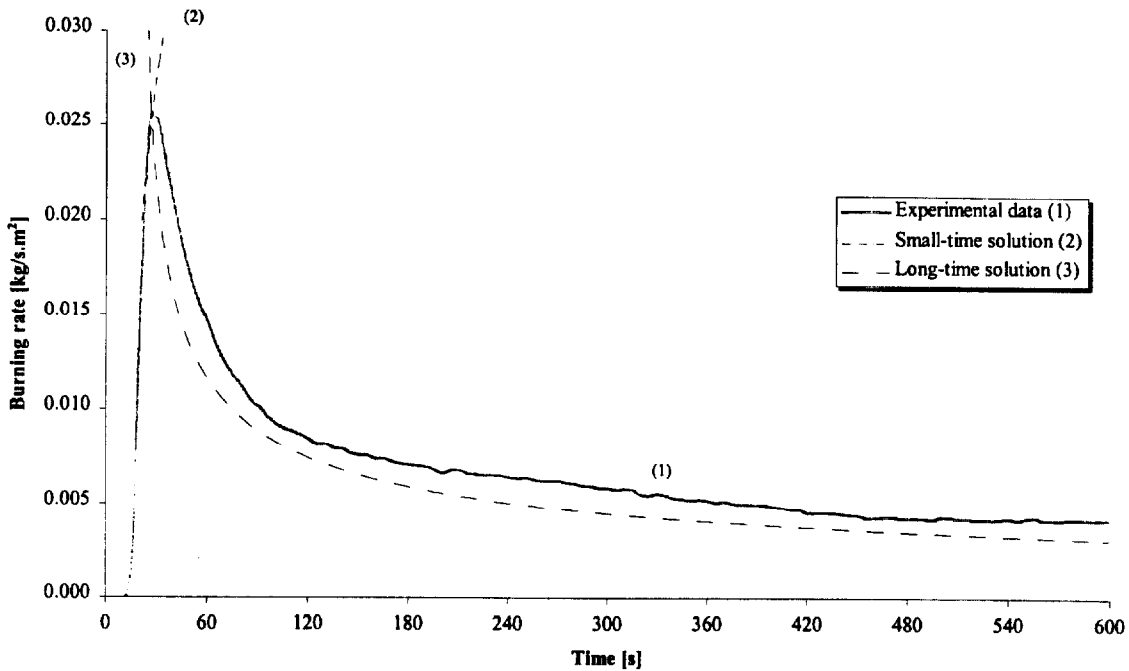

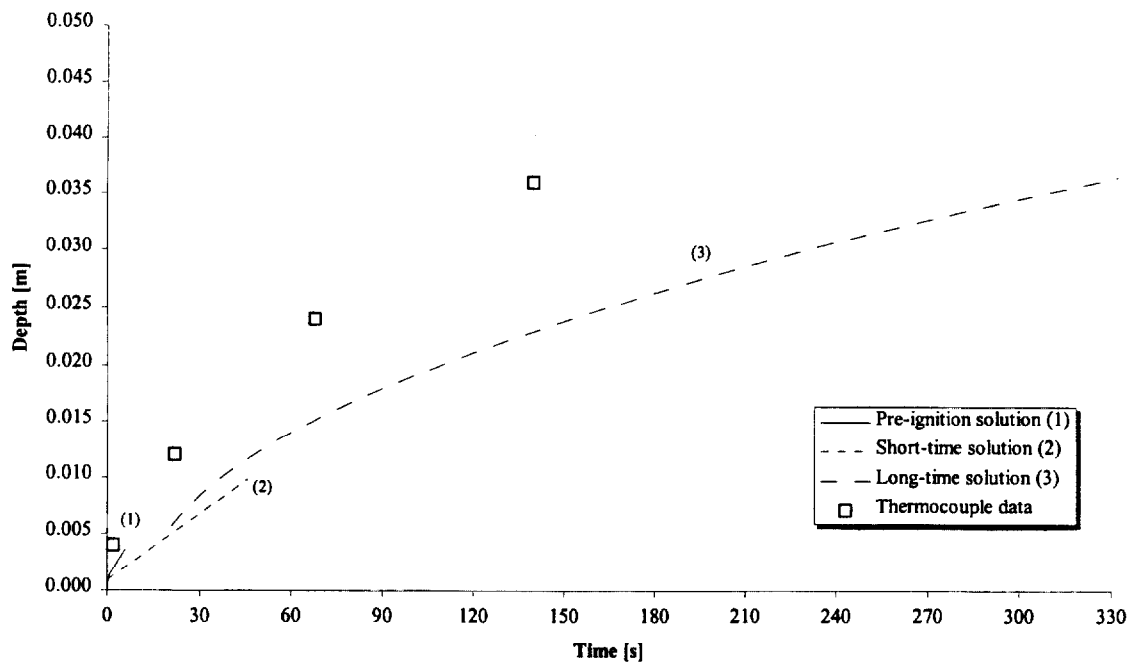**Figure 155.** Comparison of burning rate using derived properties for species and orientation (1DFL6).
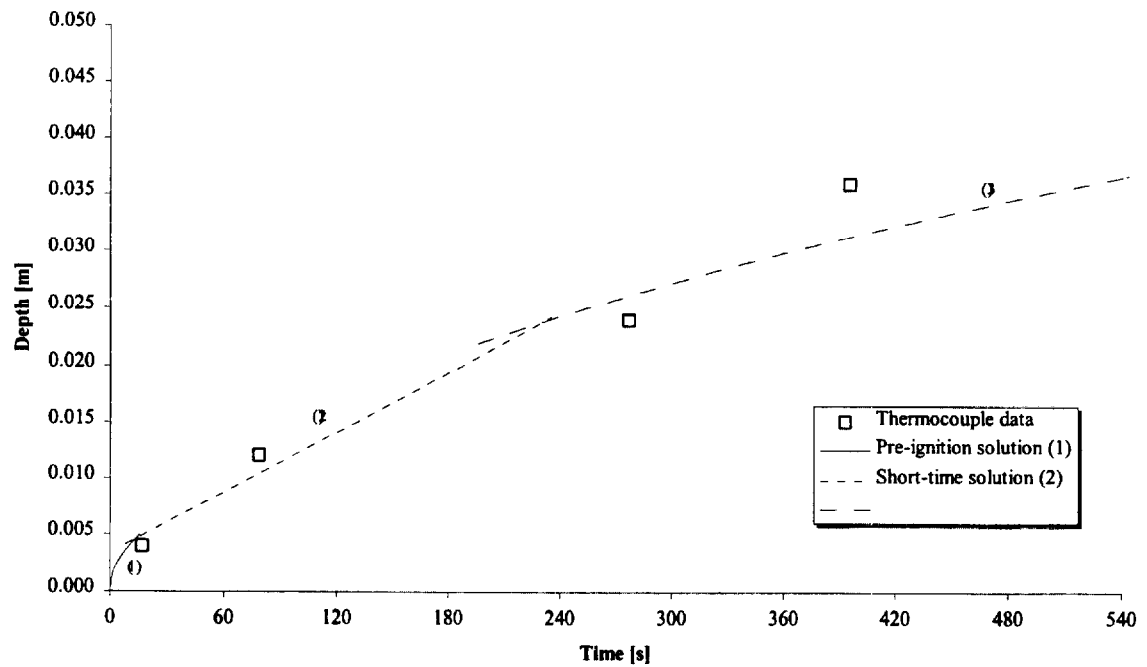
Figure 156. Comparison of measured and calculated thermal penetration depth (1DFL6).
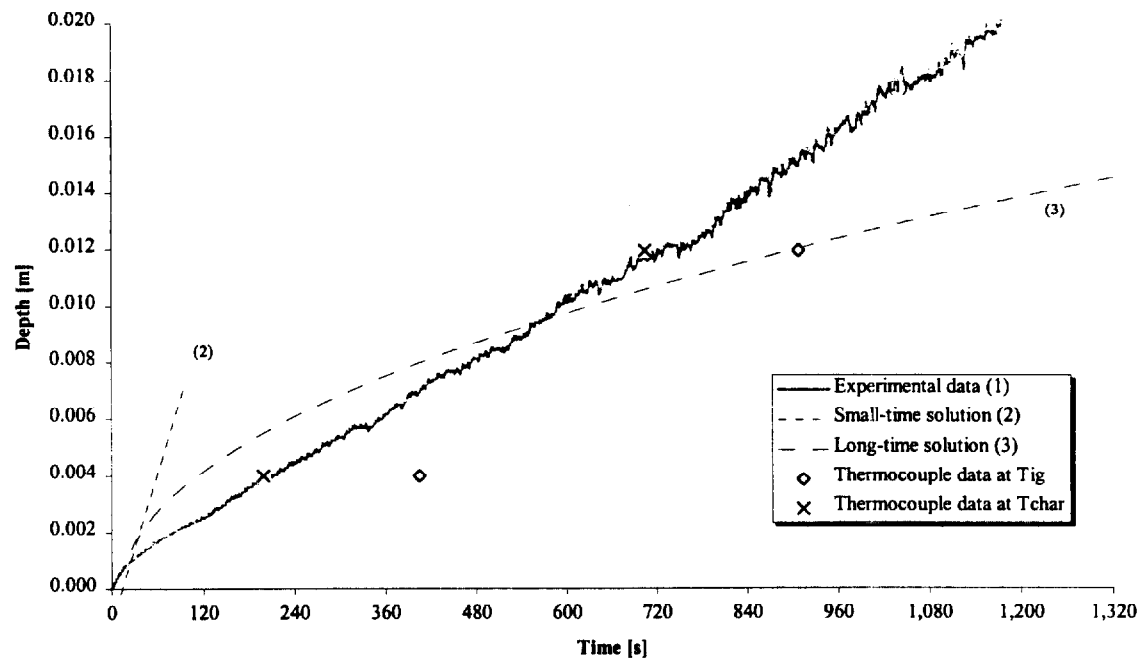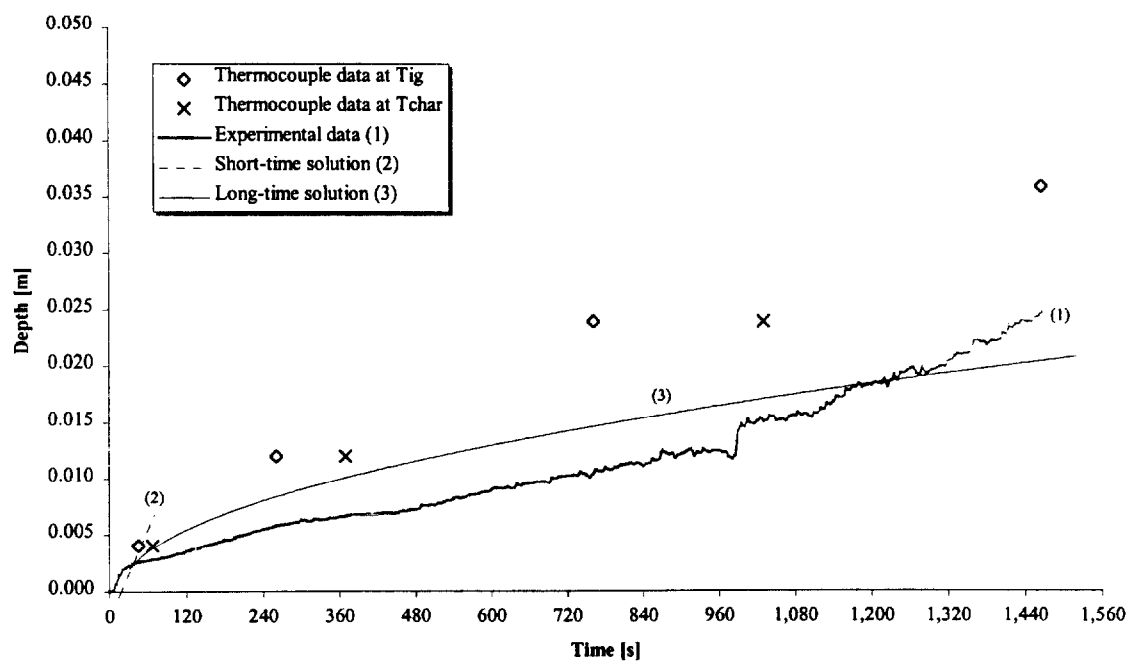

Figure 157. Comparison of estimated char depth from experimental data and the calculated char depth (1DFL6).

243

Test (1DFL7), Douglas Fir, along grain at 50 kW/m² for 25 minutes.
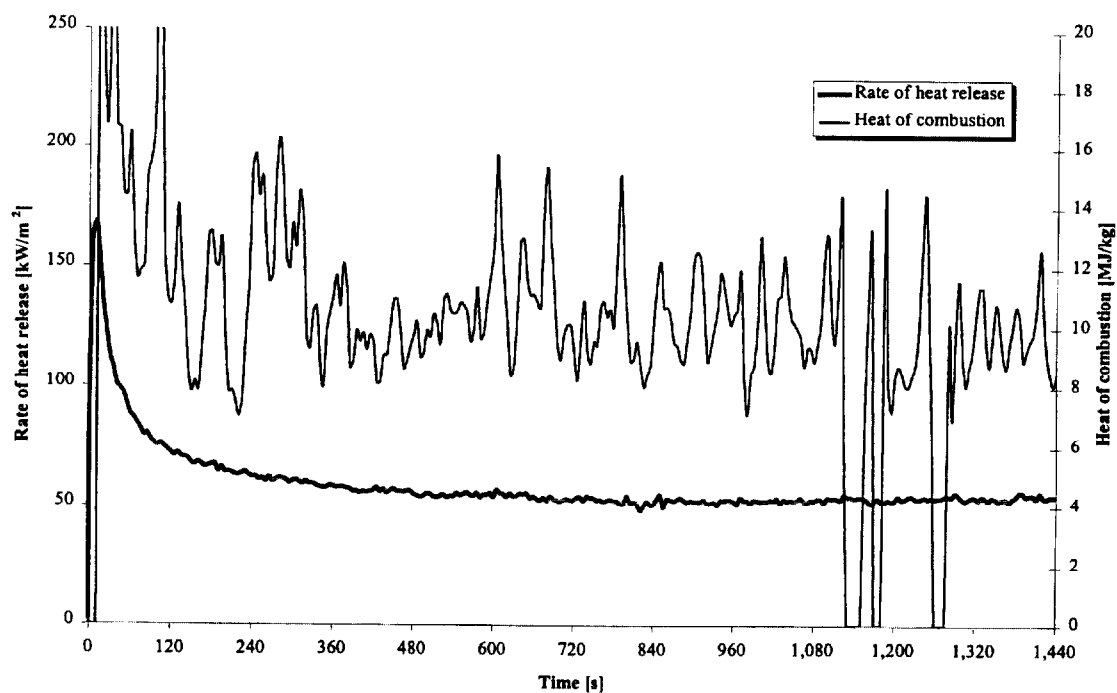
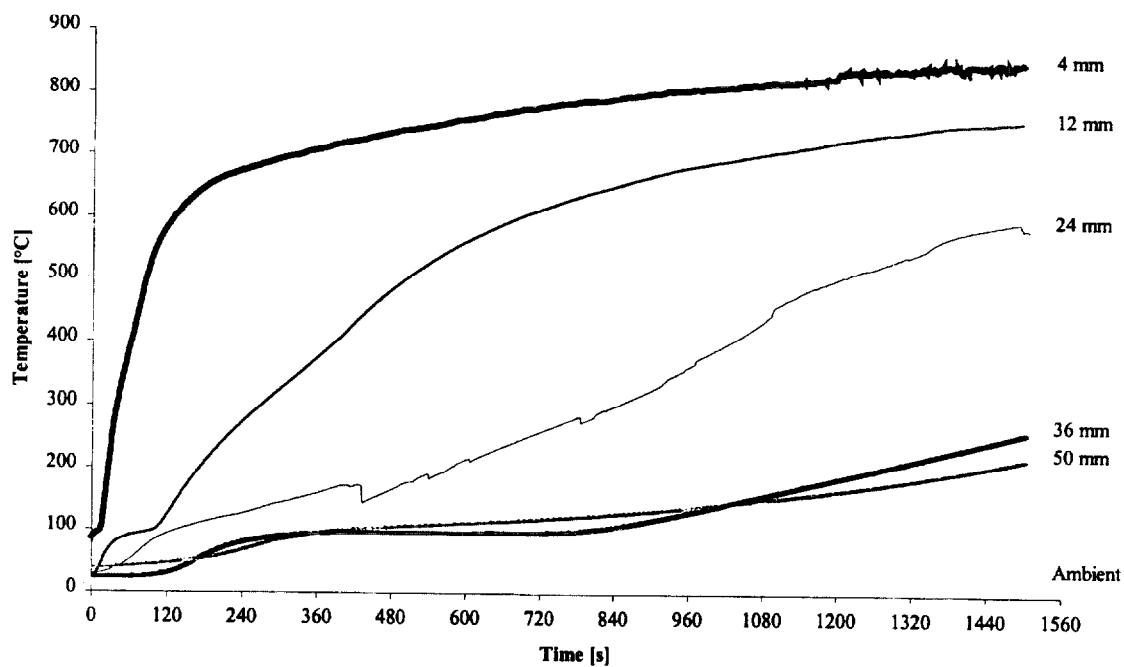**Figure 158.** Rate of heat release and heat of combustion (1DFL7).
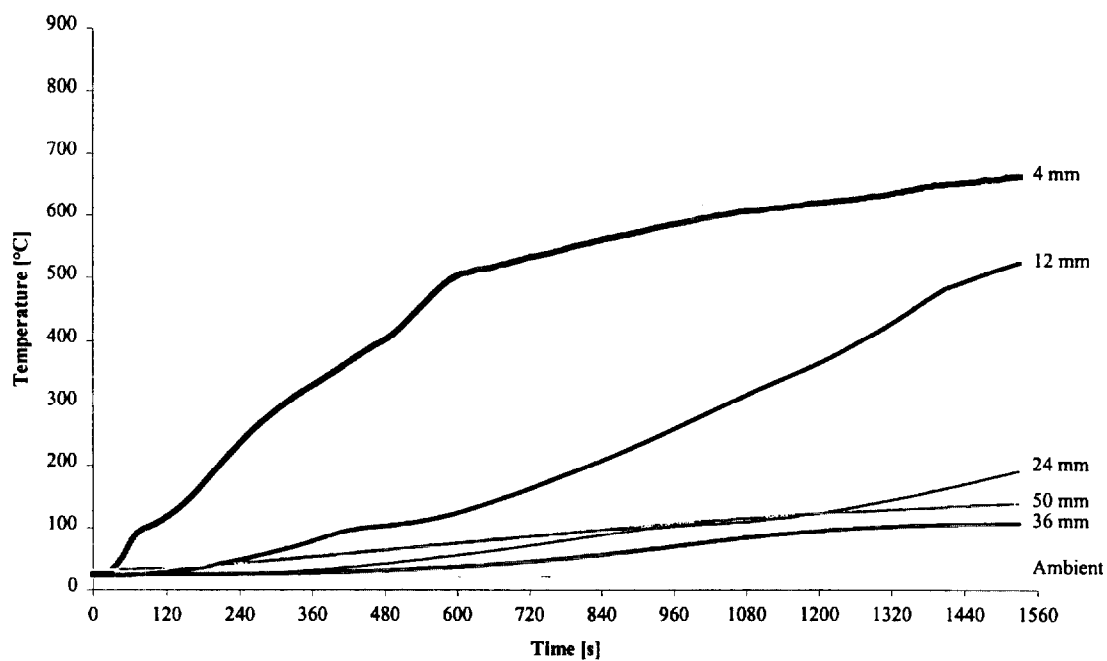
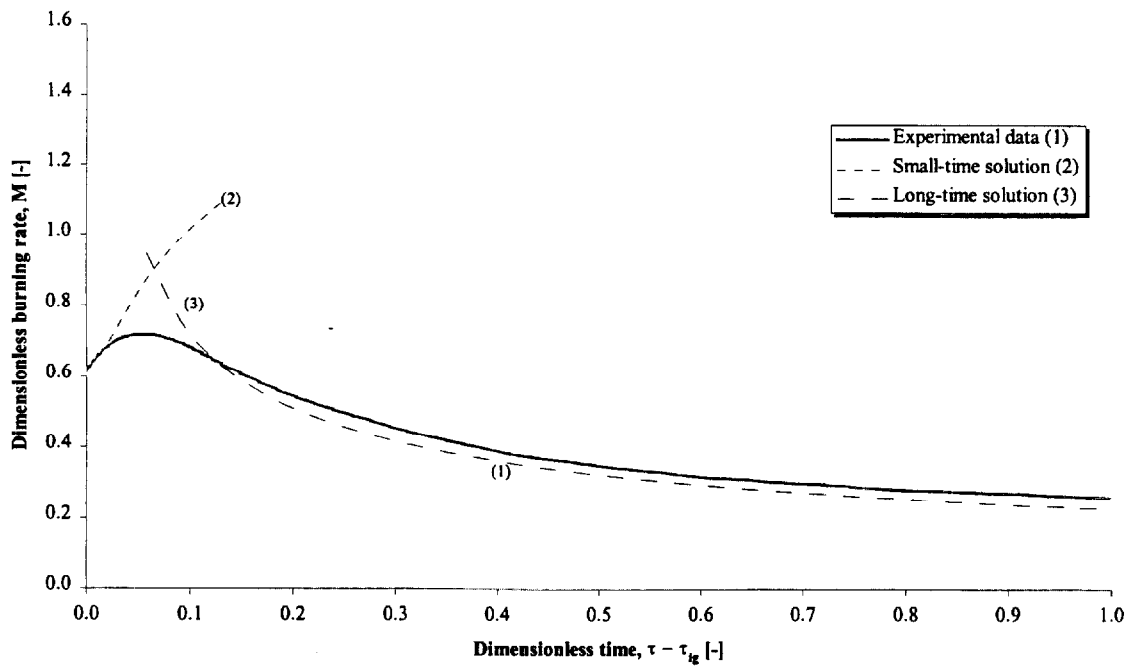**Figure 159.** Temperatures measured in sample (1DFL7).
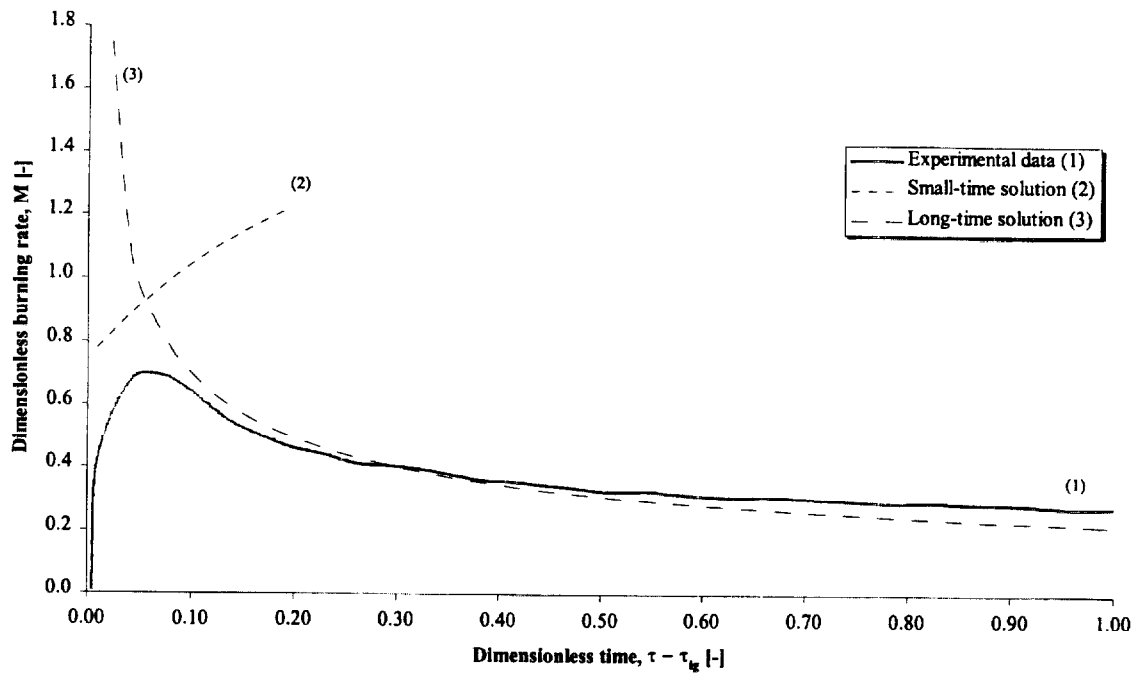
Figure 160. Comparison of dimensionless burning rate using derived properties for species and orientation (1DFL7).
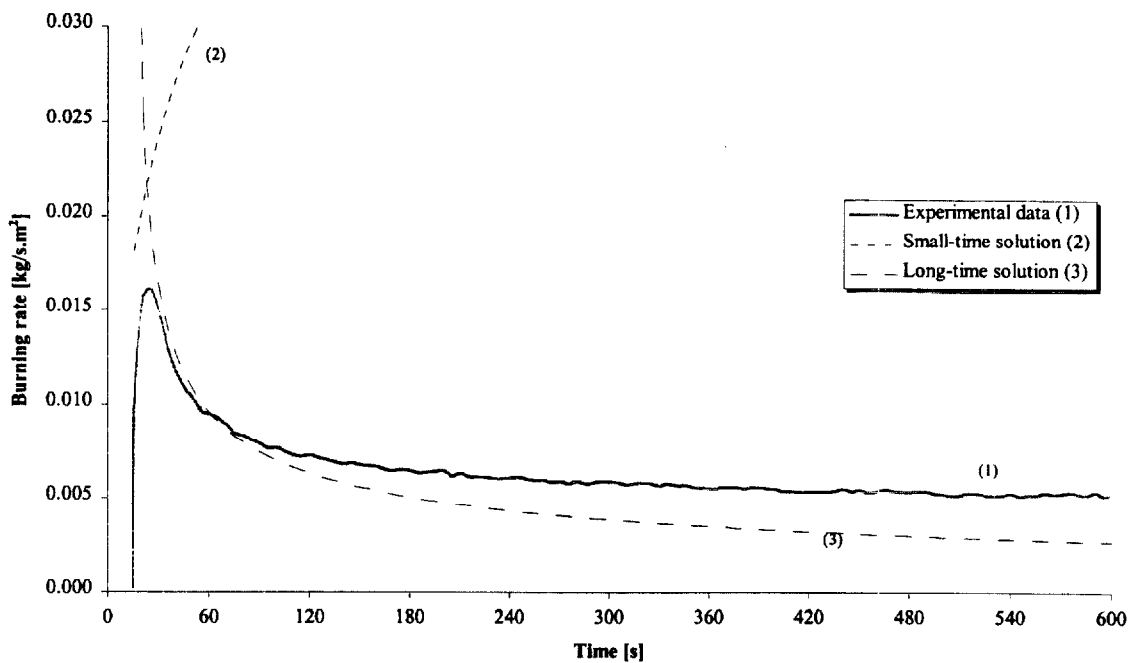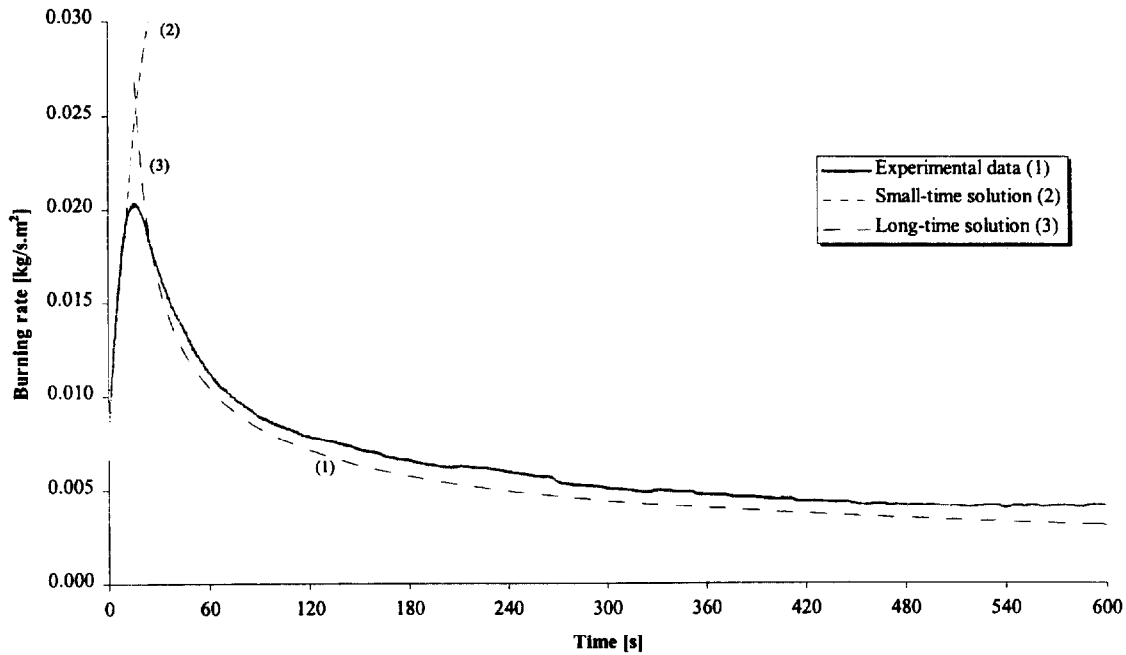

Figure 161. Comparison of burning rate using derived properties for species and orientation (1DFL7).

245
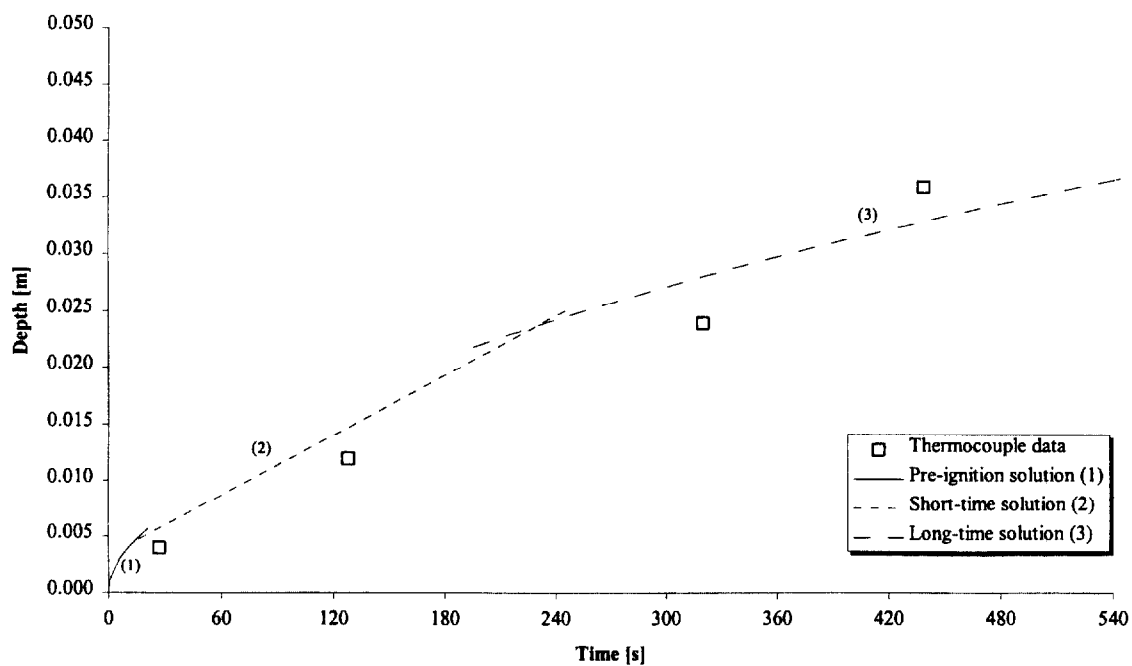
Figure 162. Comparison of measured and calculated thermal penetration depth (1DFL7).
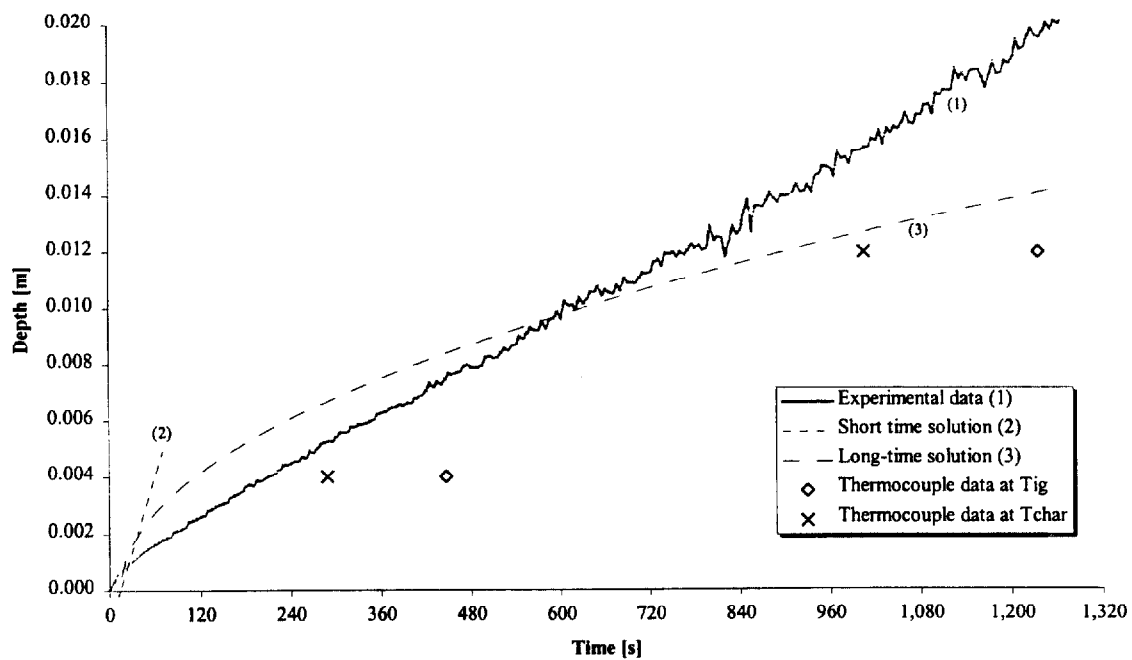
Figure 163. Comparison of estimated char depth from experimental data and the calculated char depth (1DFL7).

246

Test (1DFL8), Douglas Fir, along grain at 50 kW/m^2 for 25 minutes.
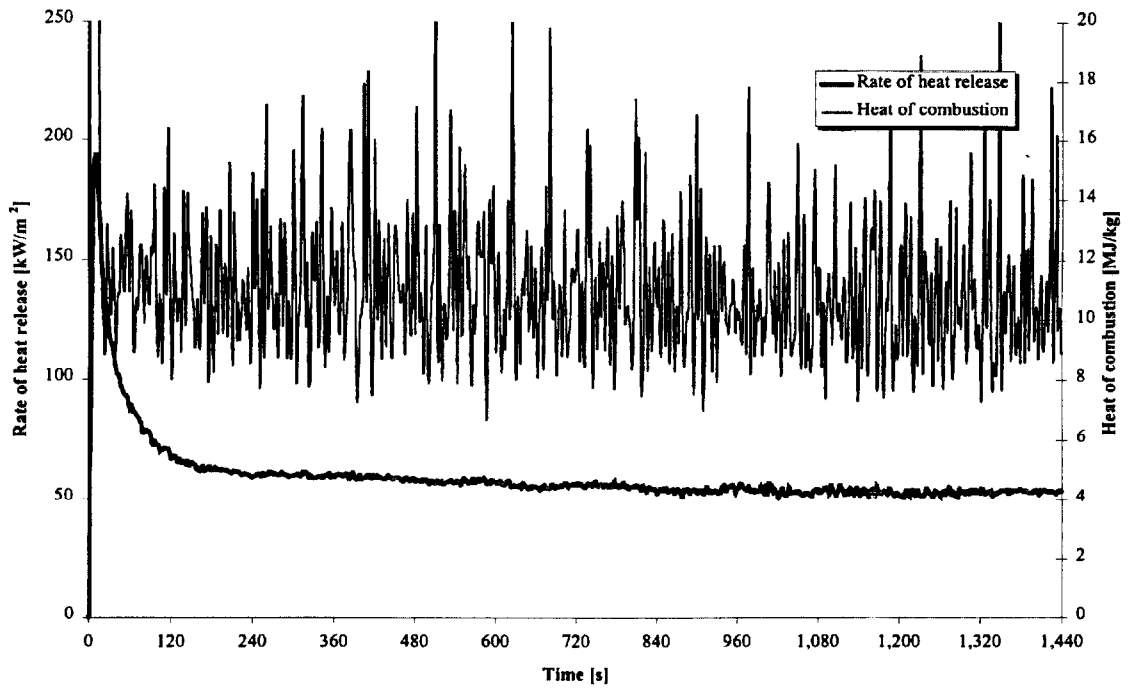
Figure 164. Rate of heat release and heat of combustion (1DFL8).
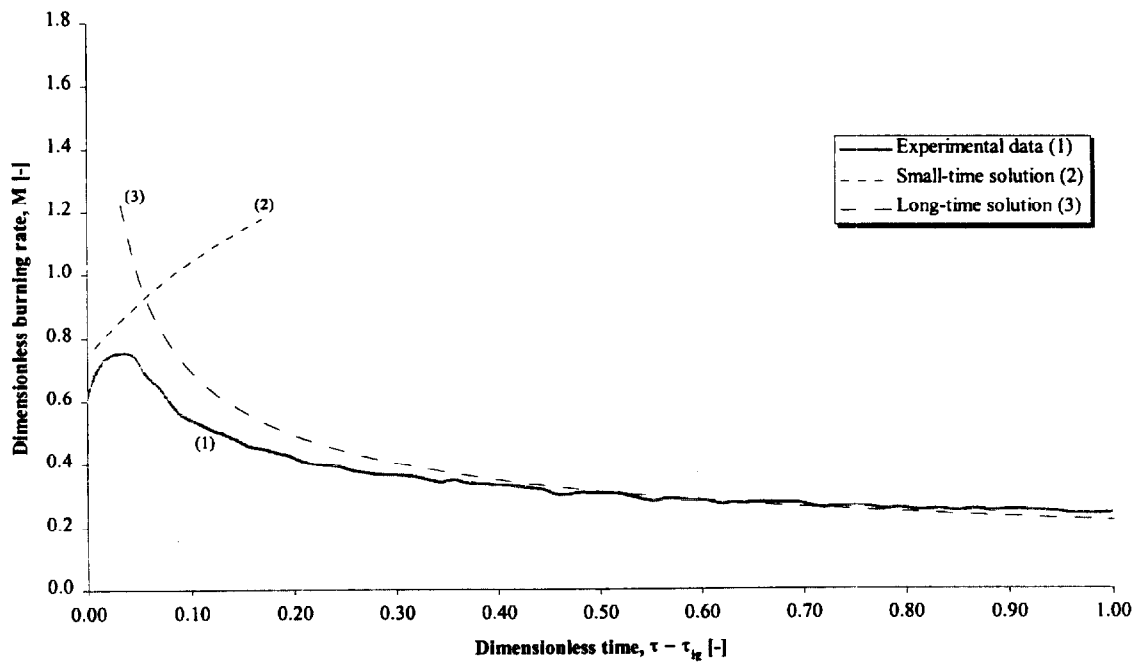
Figure 165. Comparison of dimensionless burning rate using derived properties for species and orientation (1DFL8).
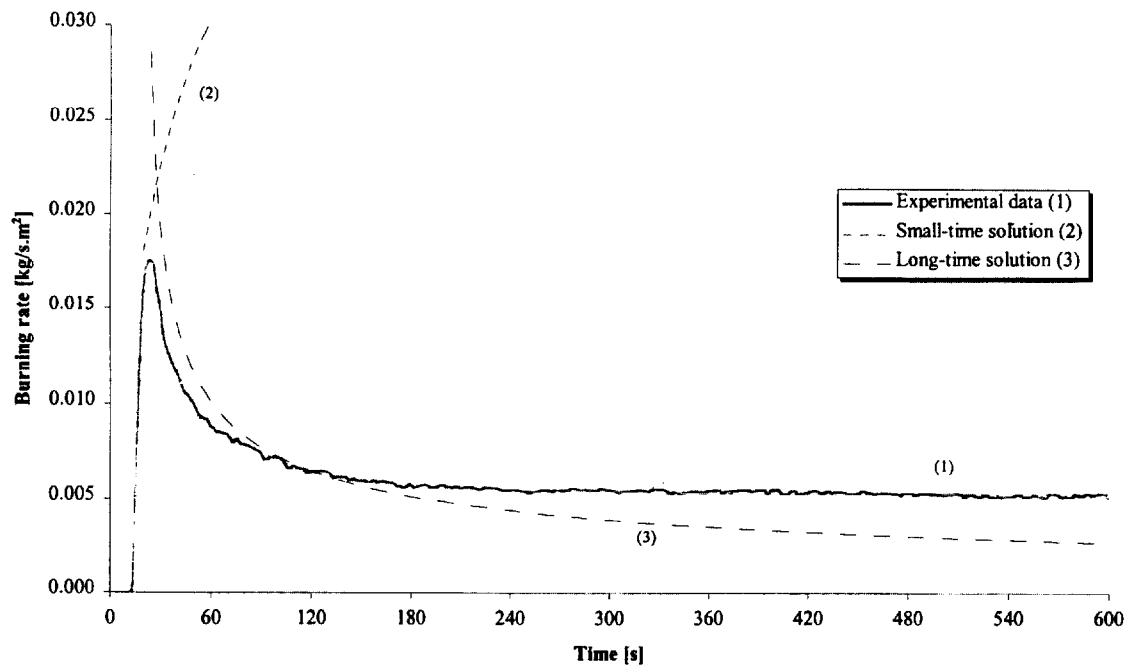
Figure 166. Comparison of burning rate using derived properties for species and orientation (1DFL8).
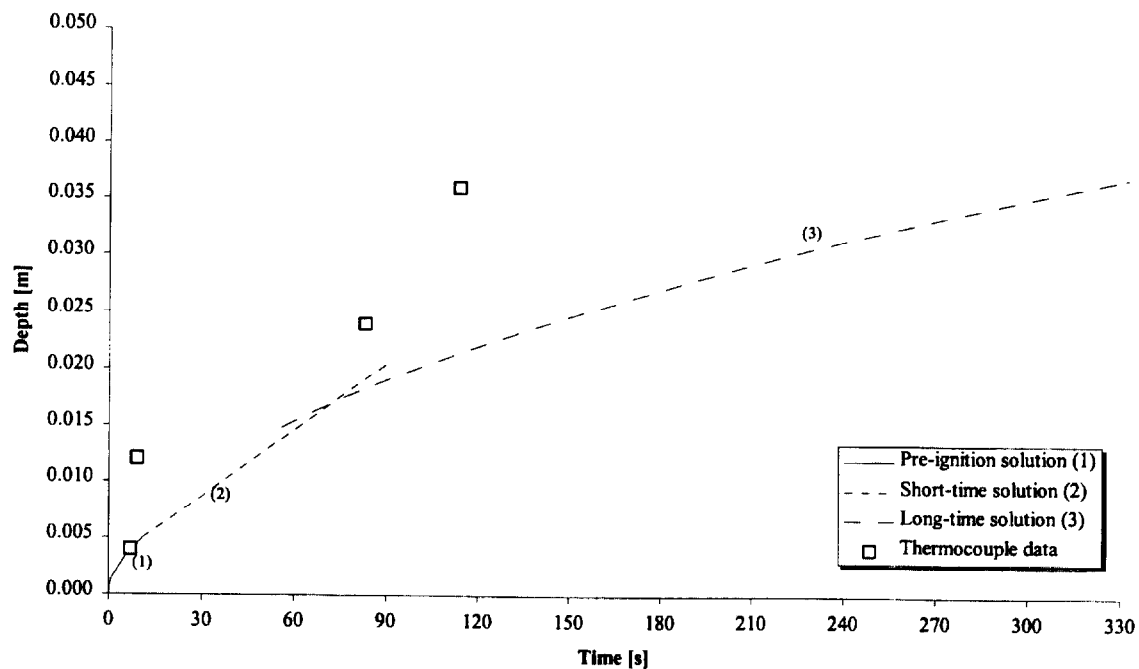
Test (1DFL9), Douglas Fir, along grain at 35 kW/m² for 25 minutes.
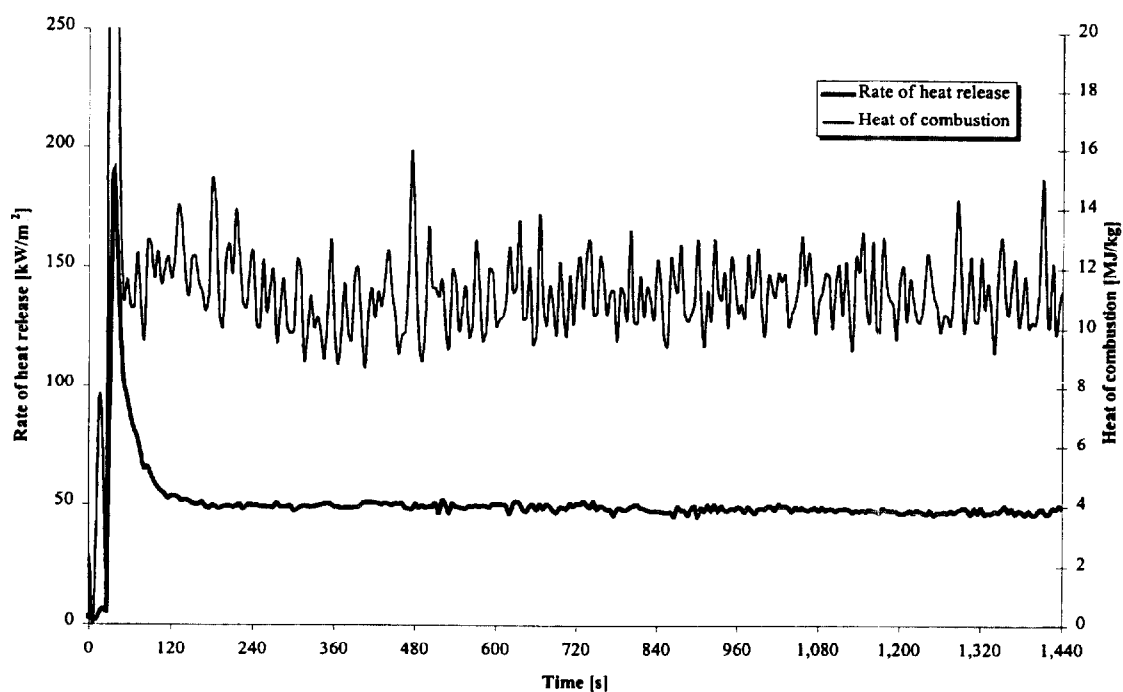
Figure 167. Rate of heat release and heat of combustion (1DFL9).
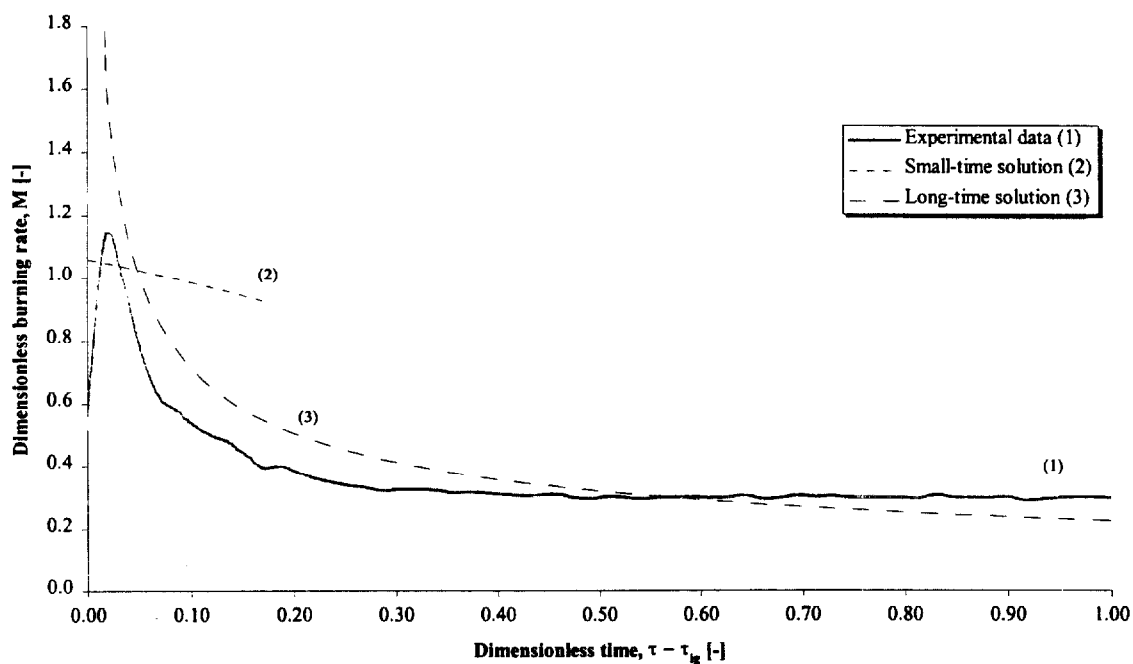
Figure 168. Comparison of dimensionless burning rate using derived properties for species and orientation (1DFL9).

249
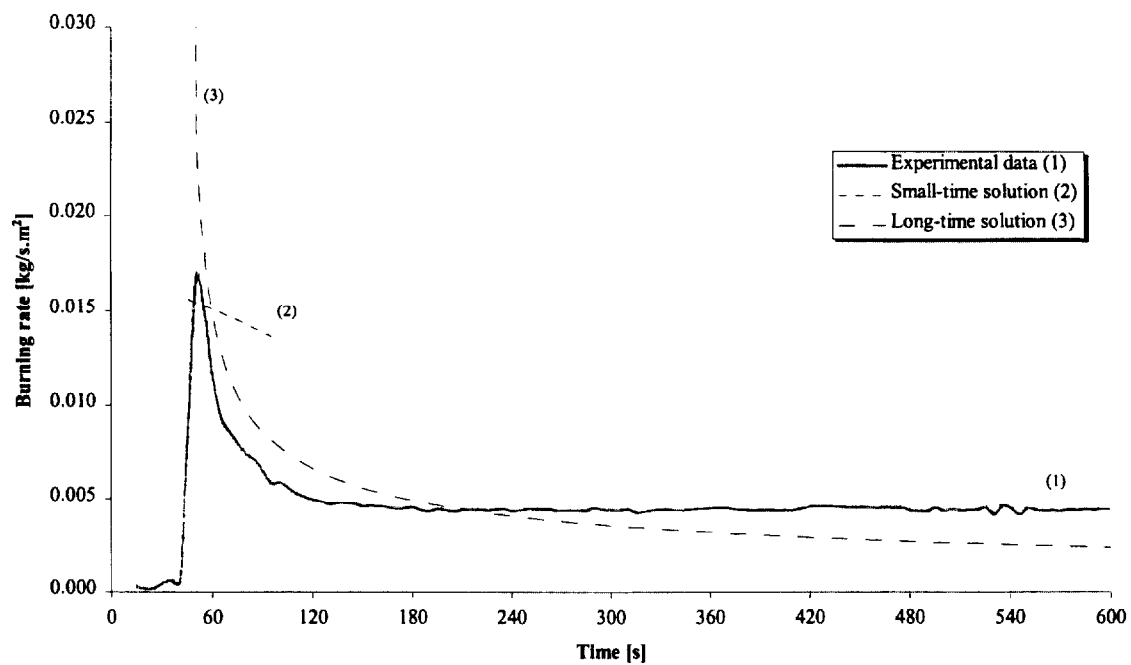
Figure 169. Comparison of burning rate using derived properties for species and orientation (1DFL9).

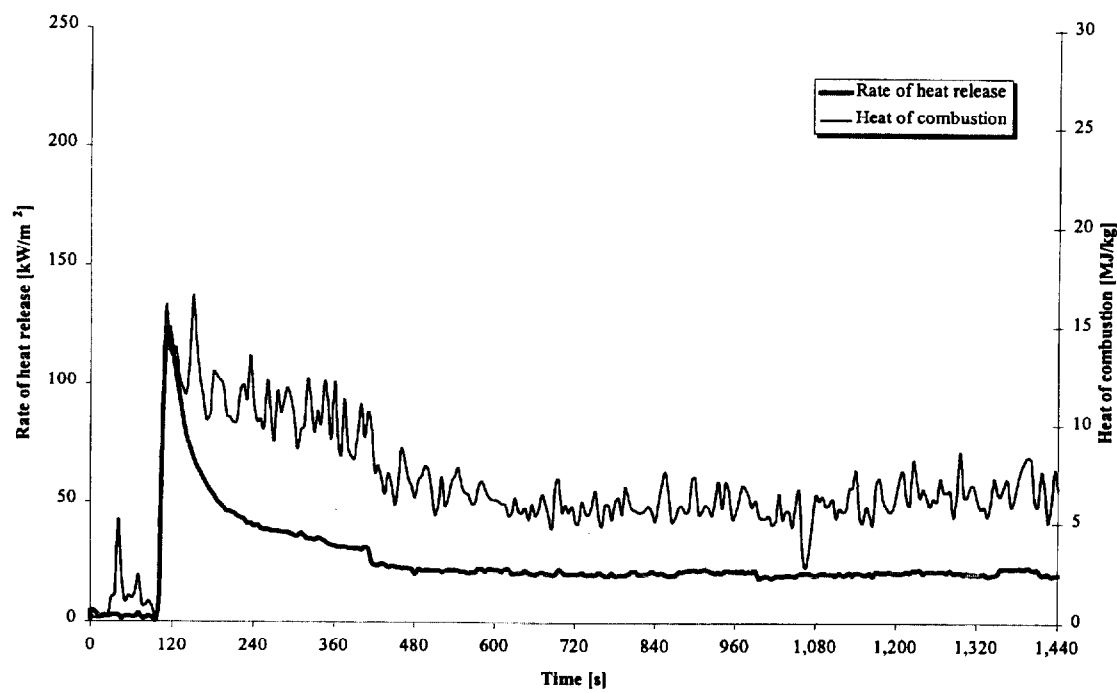Test (1DFX1), Douglas Fir, across grain at 75 kW/m^2 for 25 minutes.
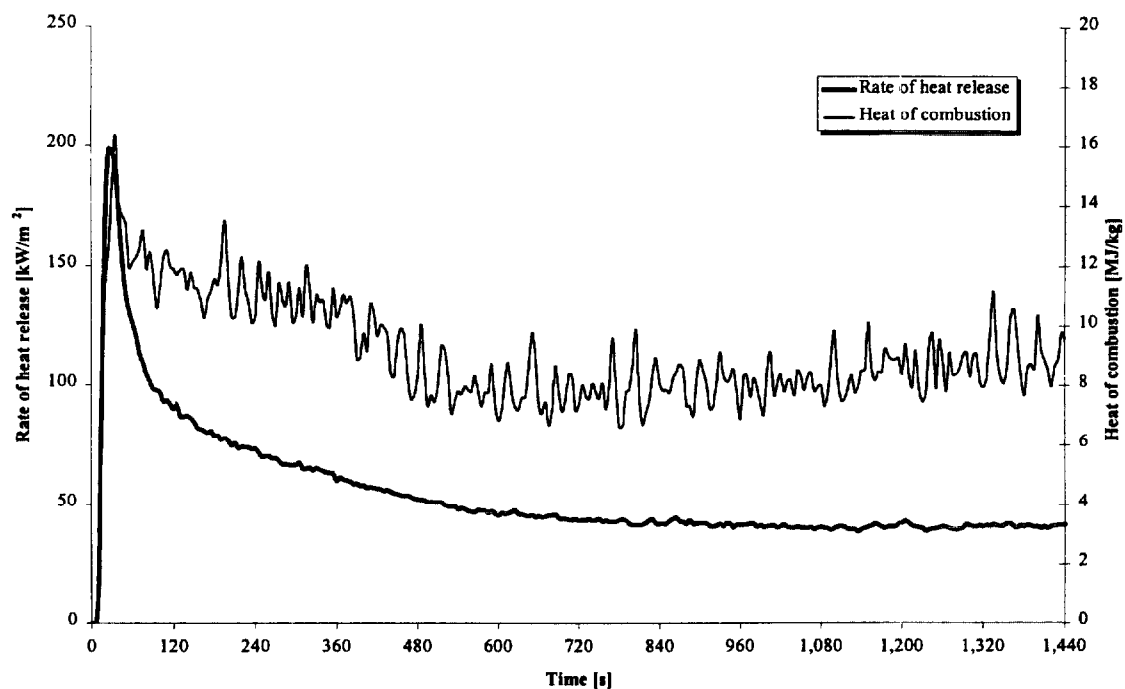
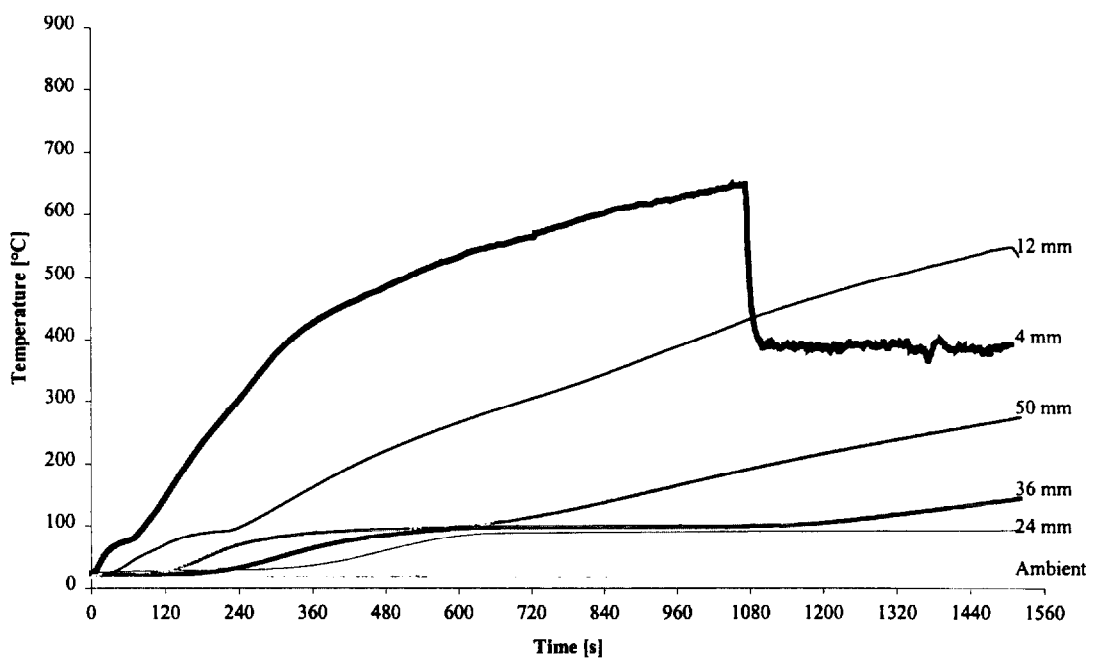**Figure 170.** Rate of heat release and heat of combustion (1DFX1).
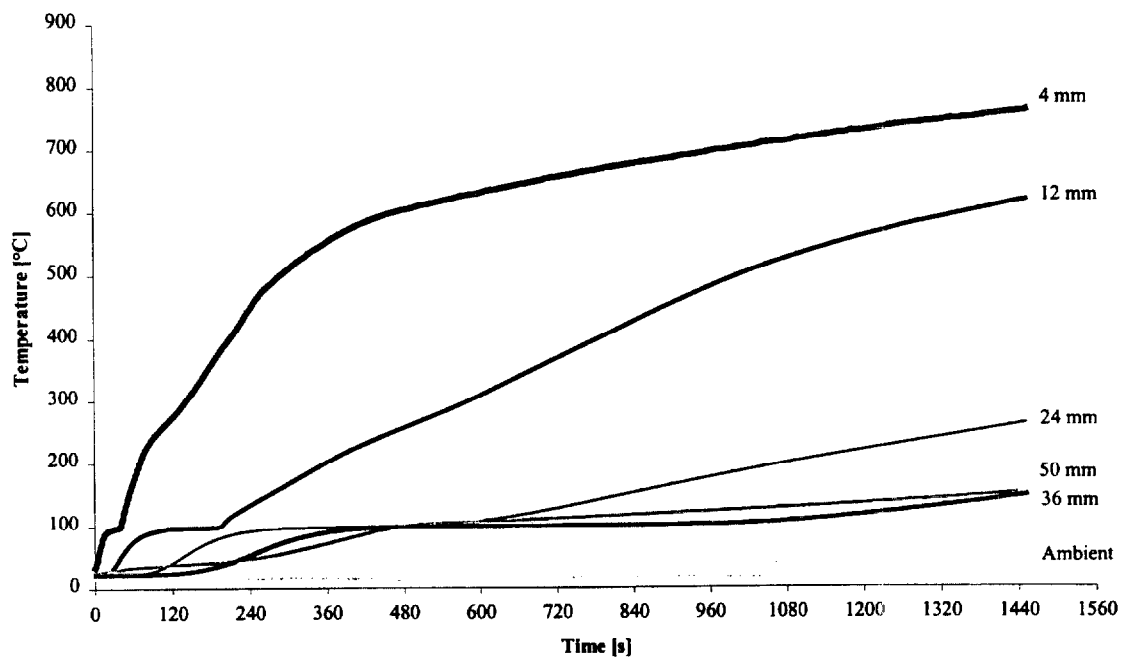
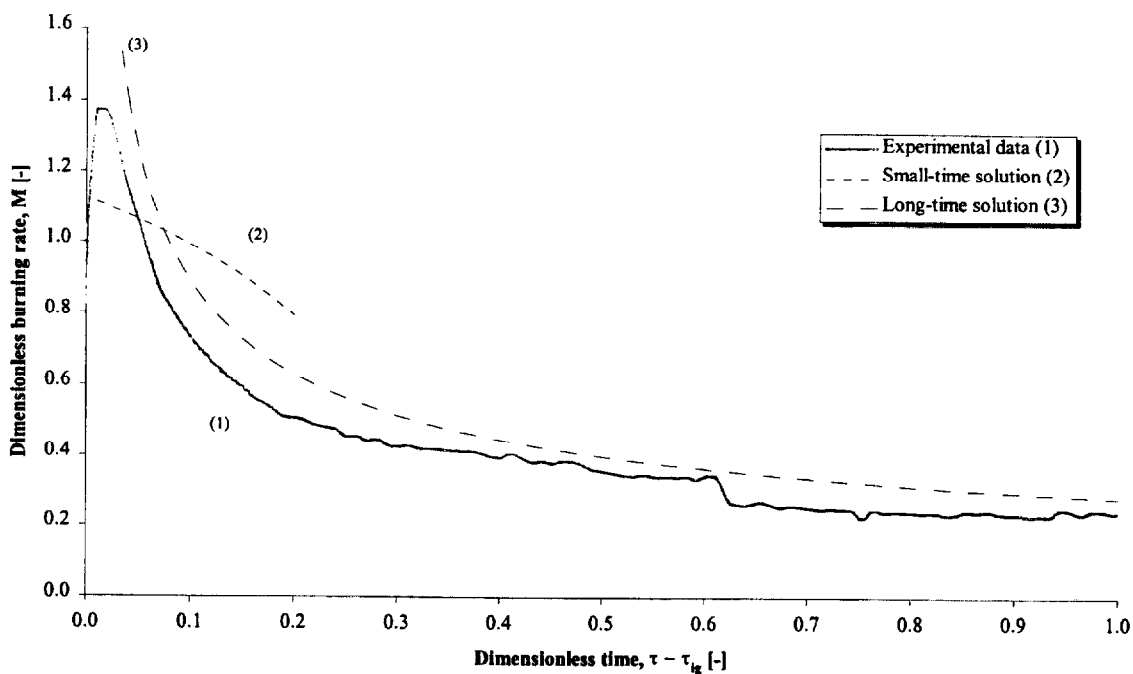**Figure 171.** Temperatures measured in sample (1DFX1).
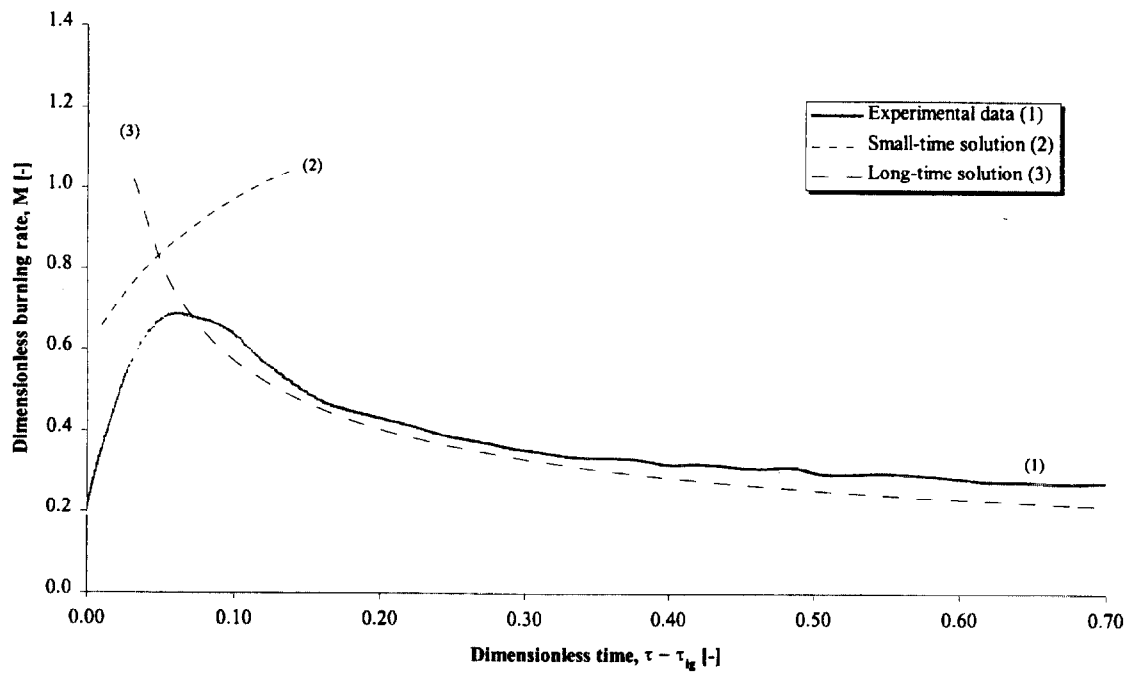
Figure 172. Comparison of dimensionless burning rate using derived properties for species and orientation (1DFX1).
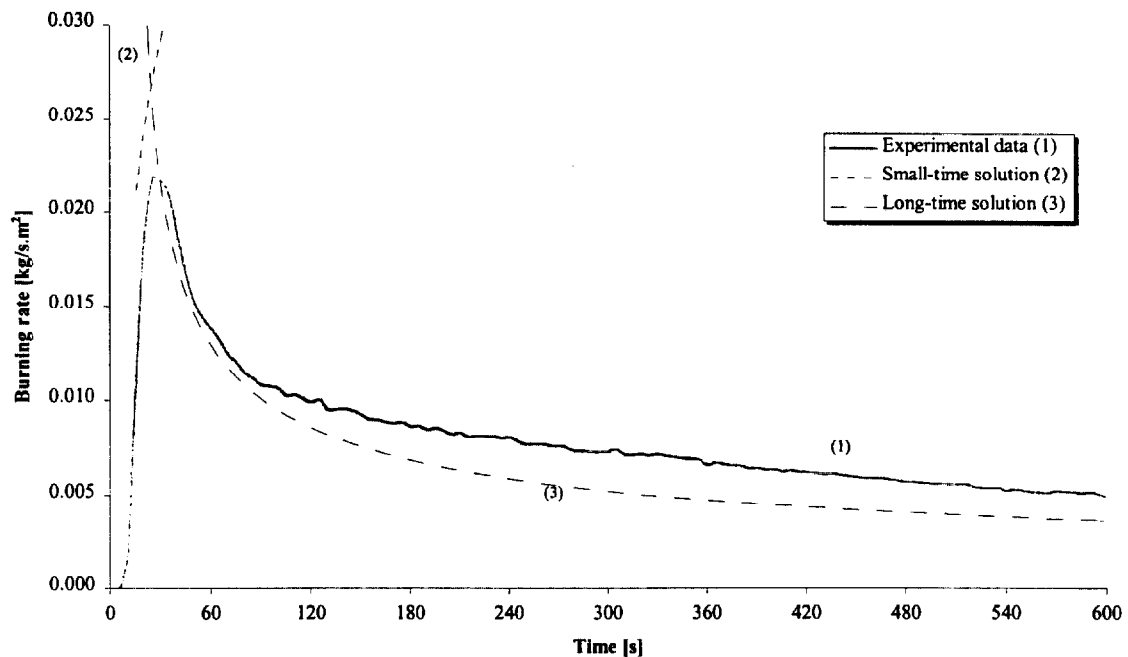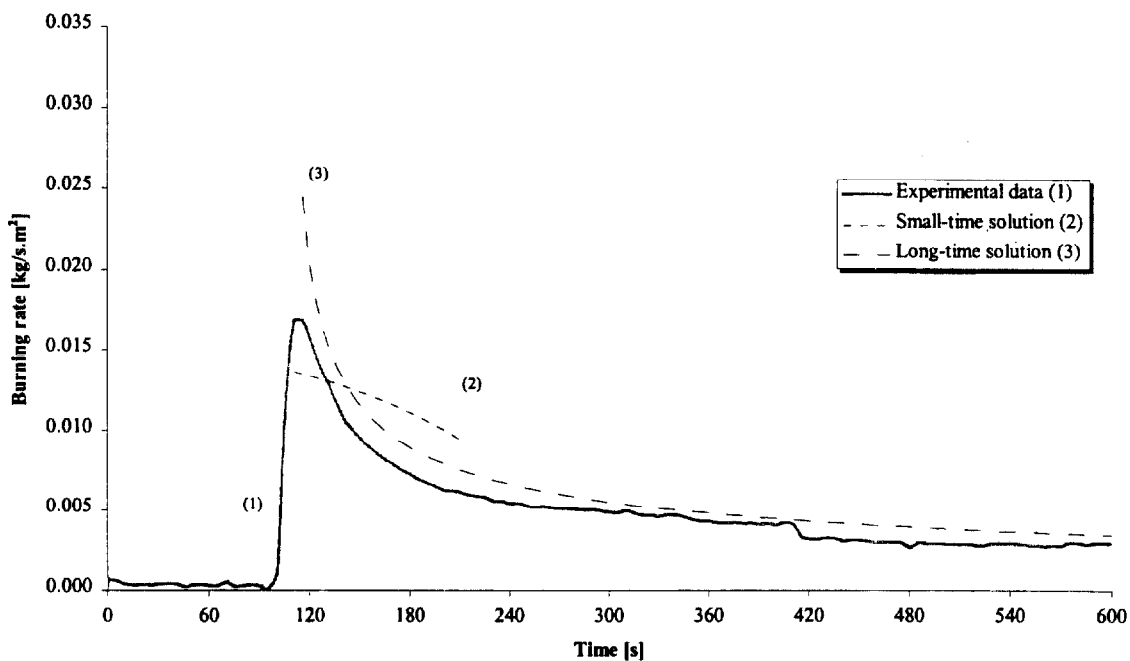

Figure 173. Comparison of burning rate using derived properties for species and orientation (1DFX1).

252
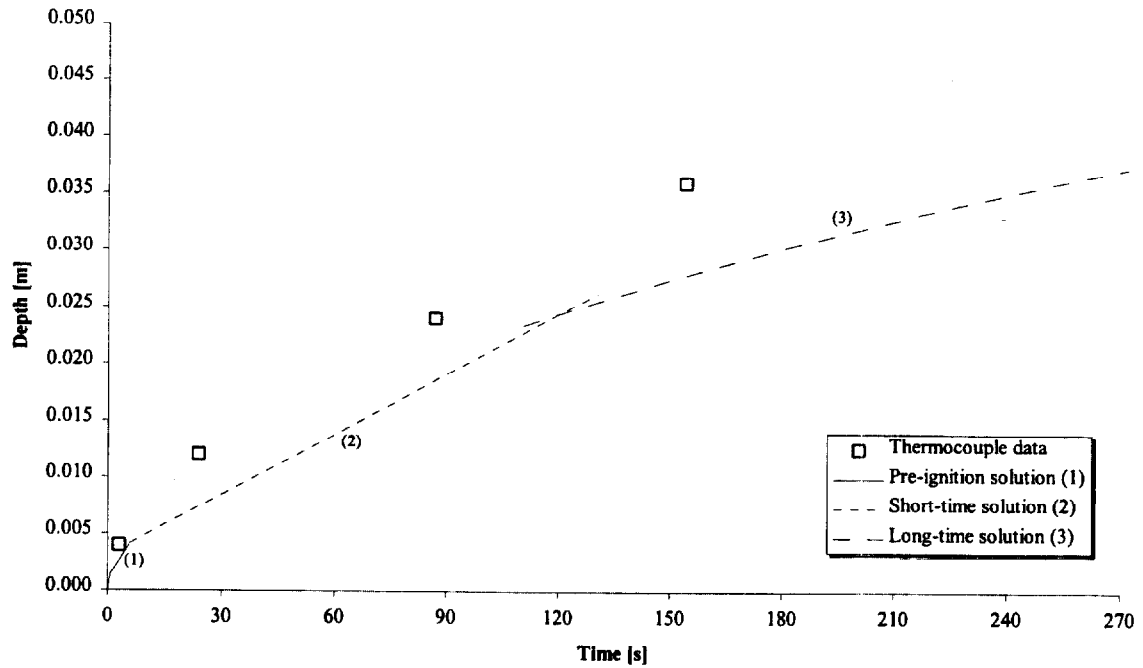
Figure 174. Comparison of measured and calculated thermal penetration depth (1DFX1).
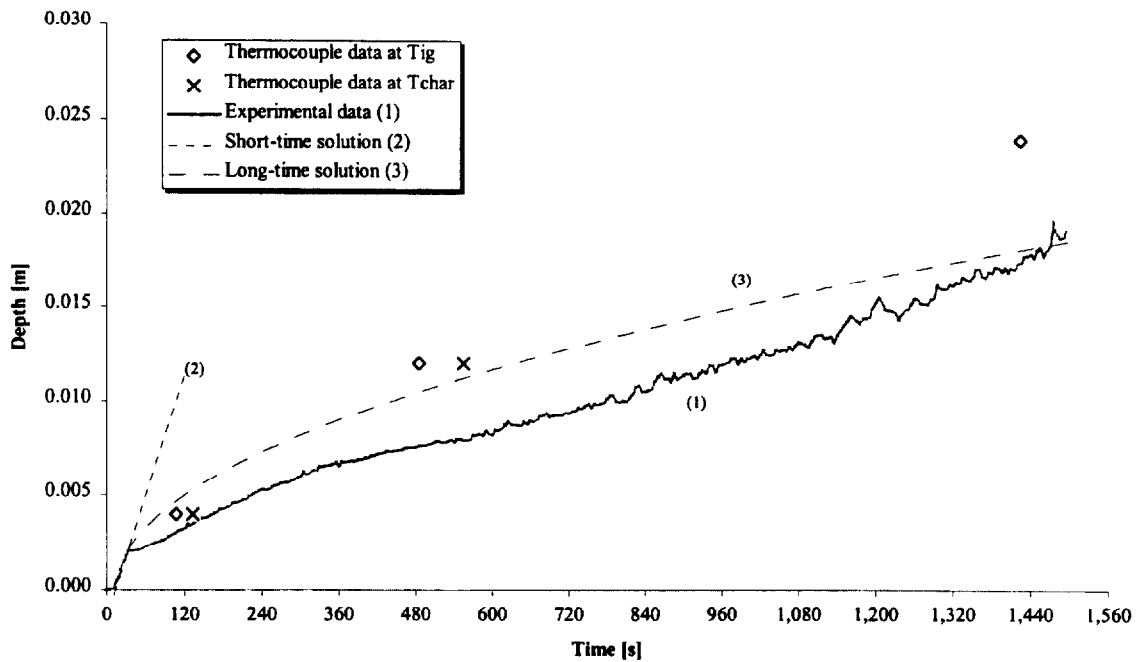
Figure 175. Comparison of estimated char depth from experimental data and the calculated char depth (1DFX1).

253

Test (1DFX2), Douglas Fir, across grain at 75 kW/m² for 25 minutes.
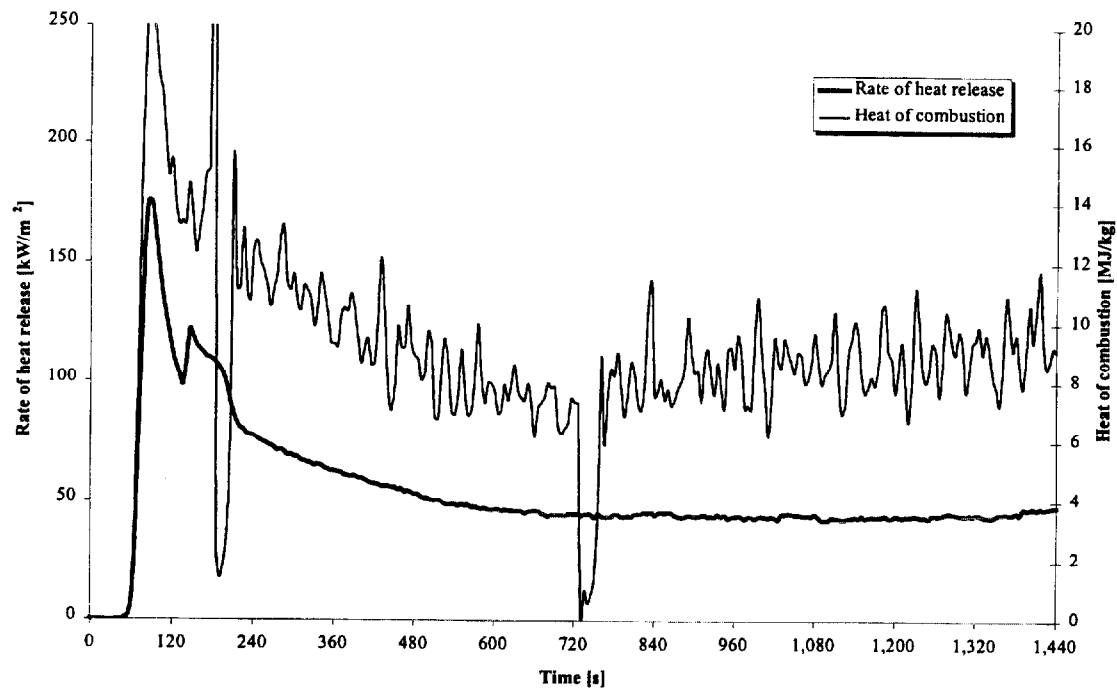
Figure 176. Rate of heat release and heat of combustion (1DFX2).
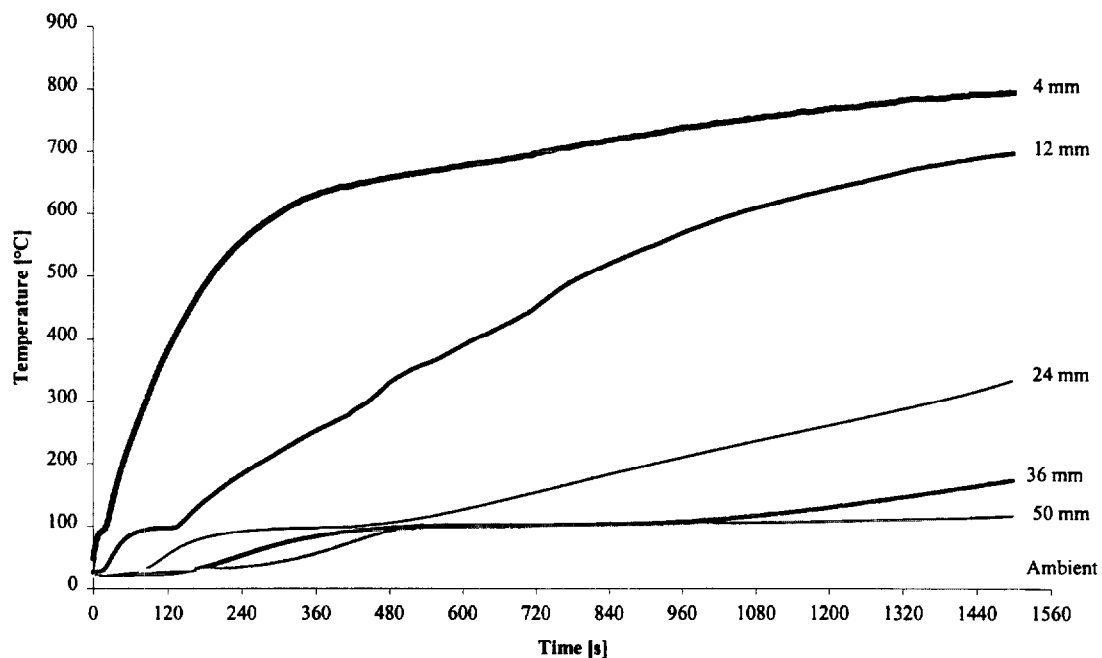
Figure 177. Temperatures measured in sample (1DFX2).

254
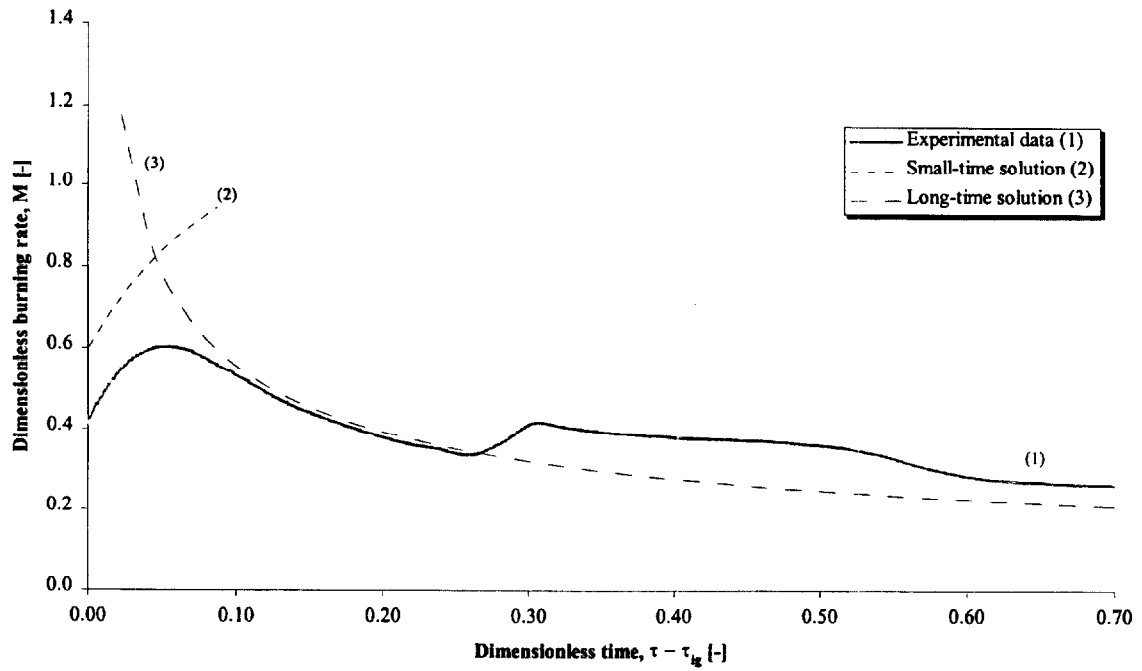
Figure 178. Comparison of dimensionless burning rate using derived properties for species and orientation (1DFX2).
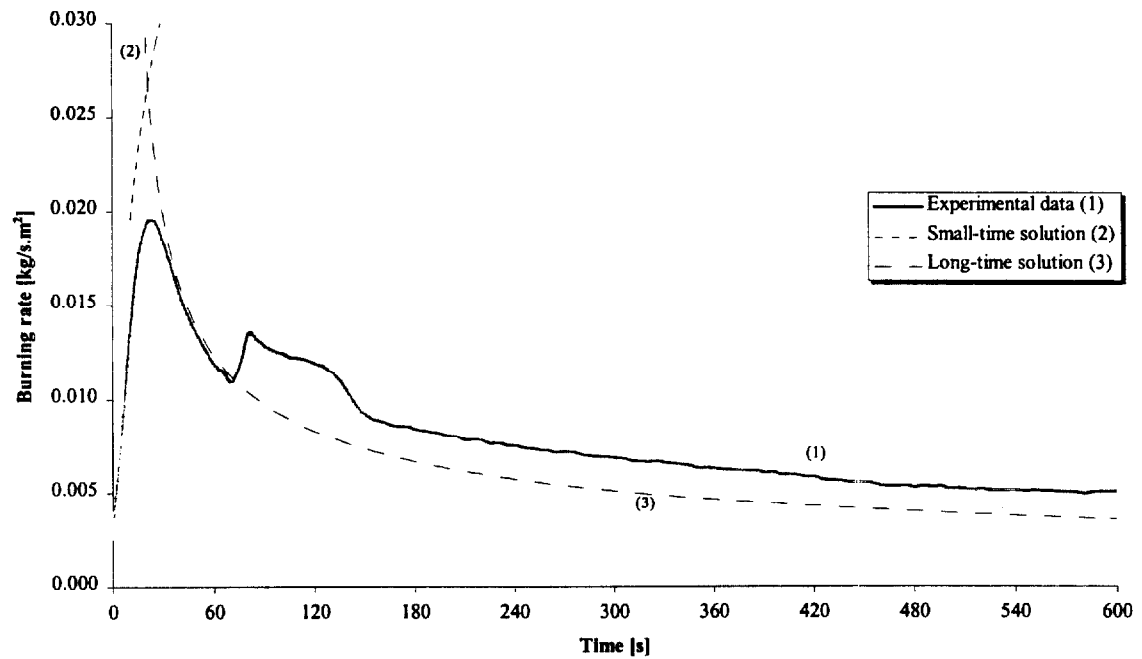
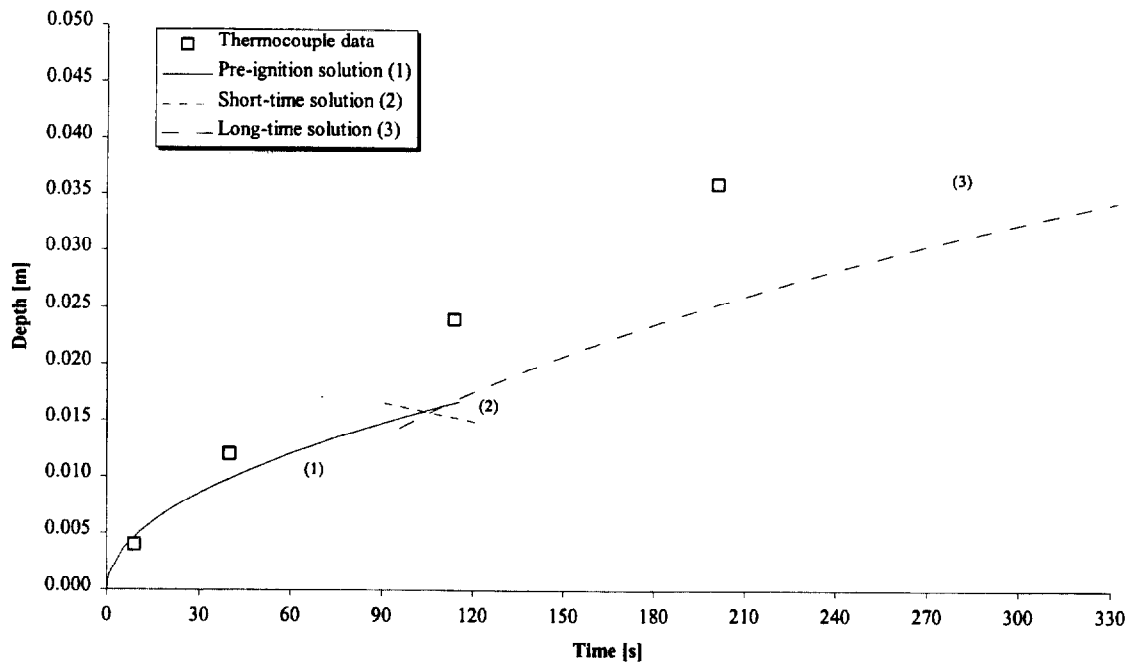**Figure 179.** Comparison of burning rate using derived properties for species and orientation (1DFX2).
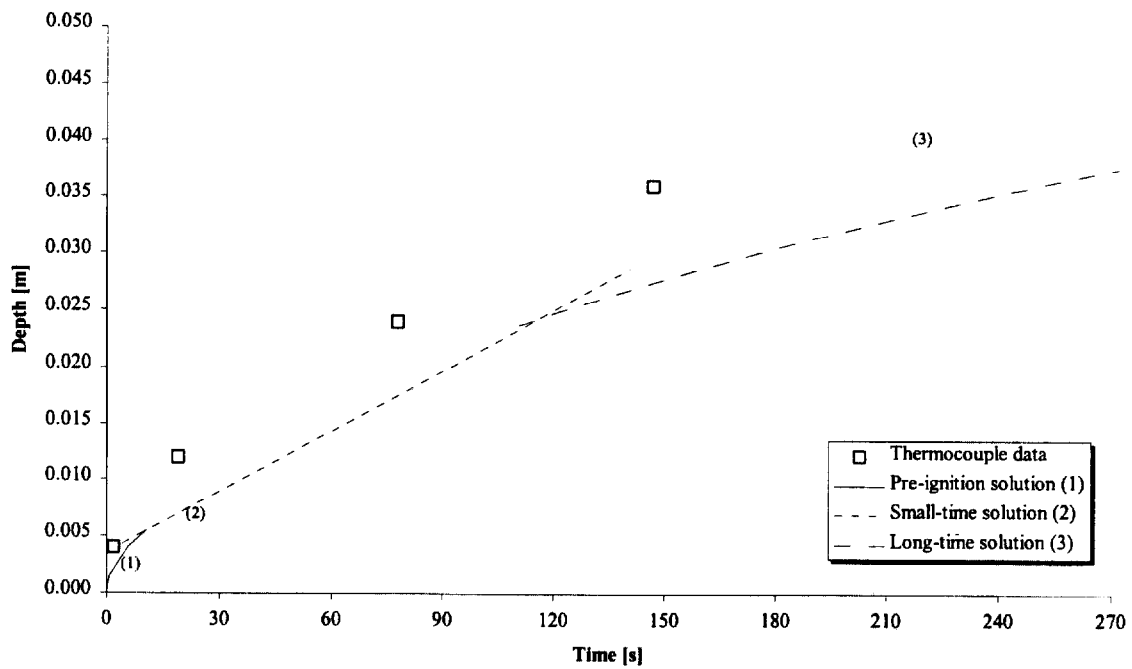
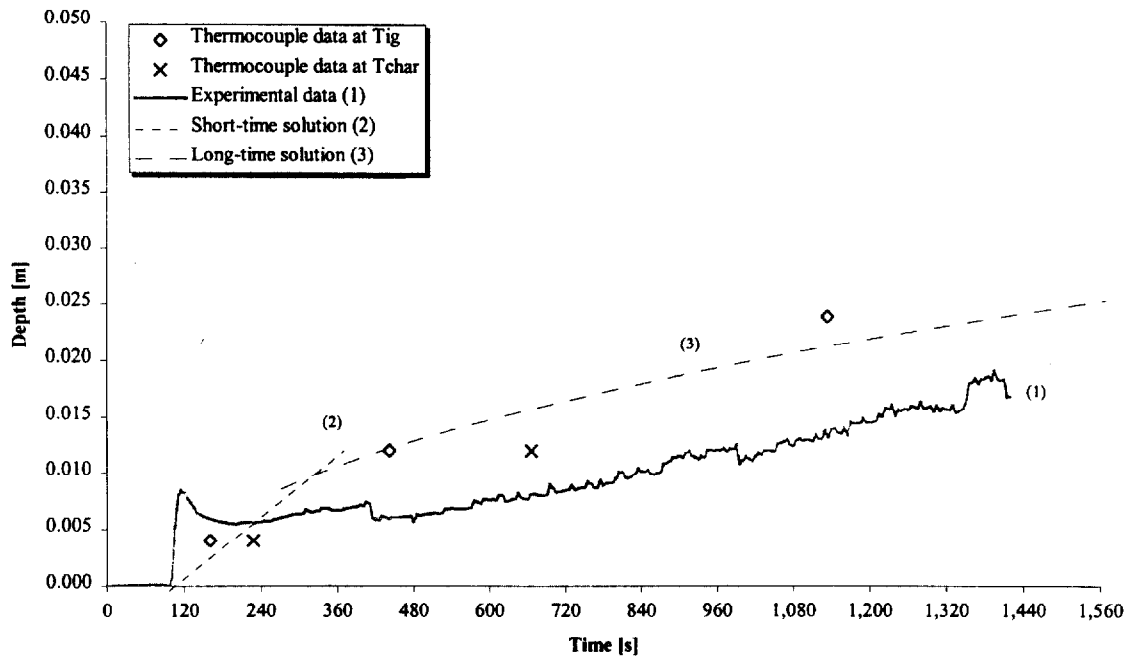**Figure 180.** Comparison of measured and calculated thermal penetration depth (1DFX2).
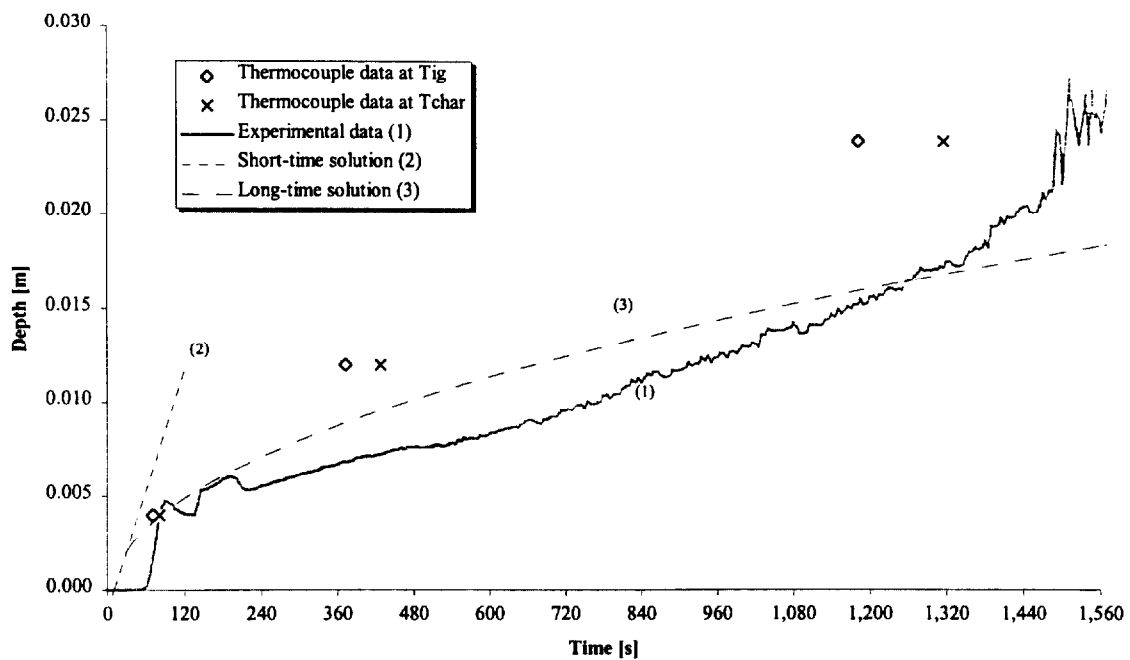
Figure 181. Comparison of estimated char depth from experimental data and the calculated char depth (1DFX2).

256

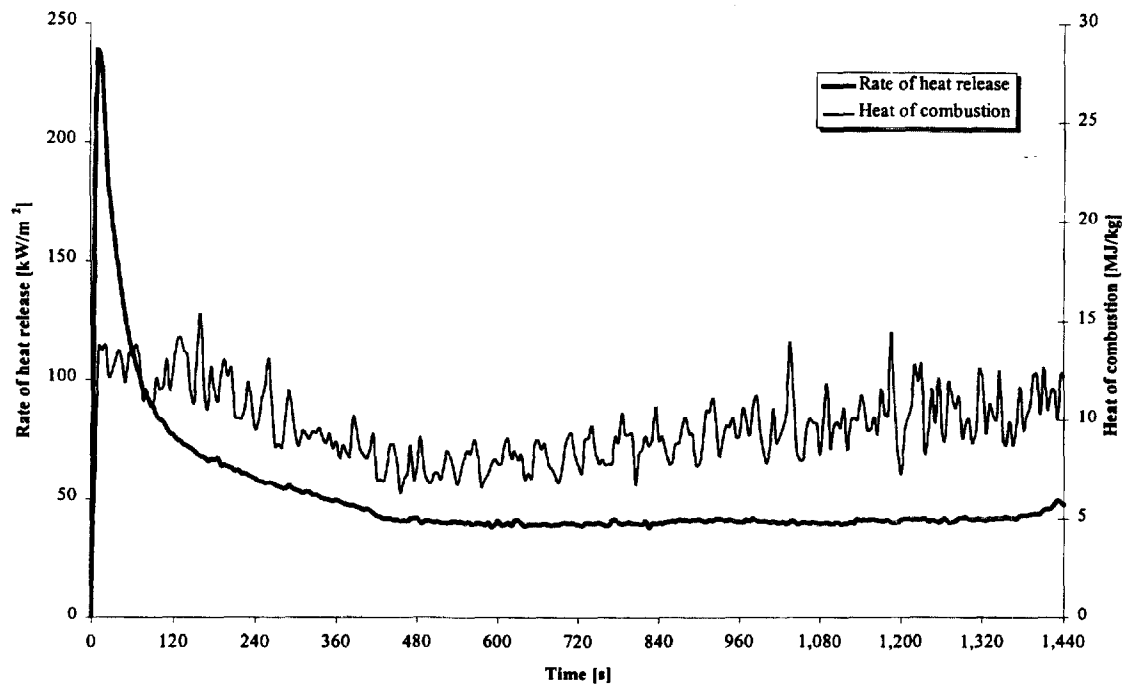Test (1DFX3), Douglas Fir, across grain at 75 kW/m² for 75 minutes.
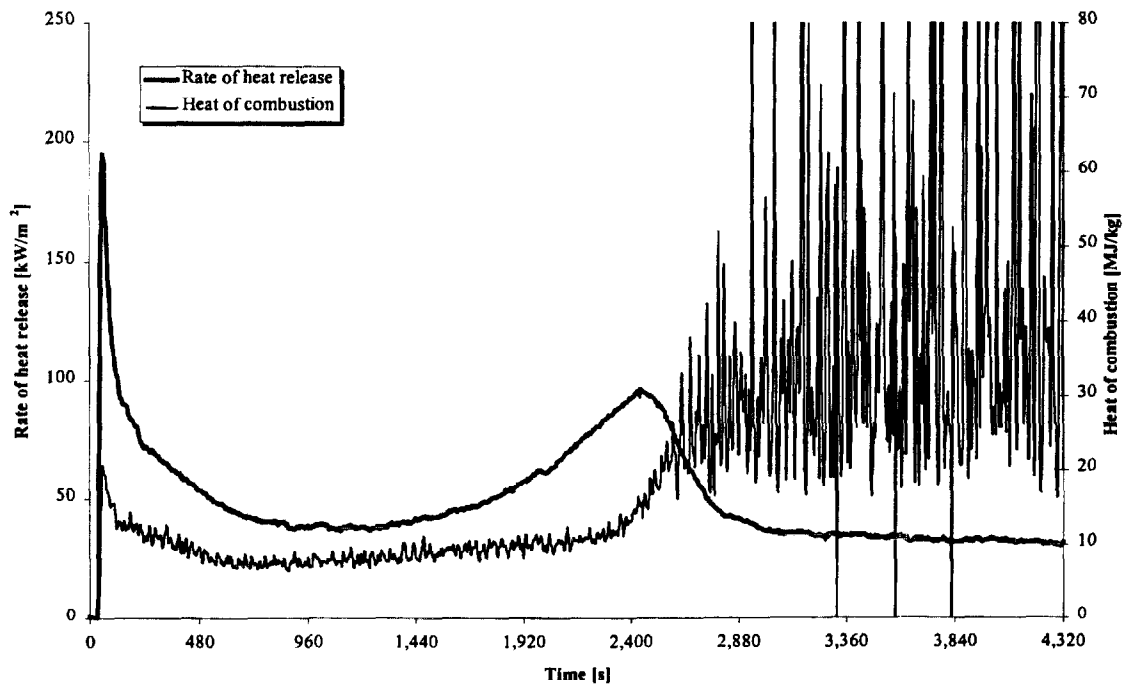
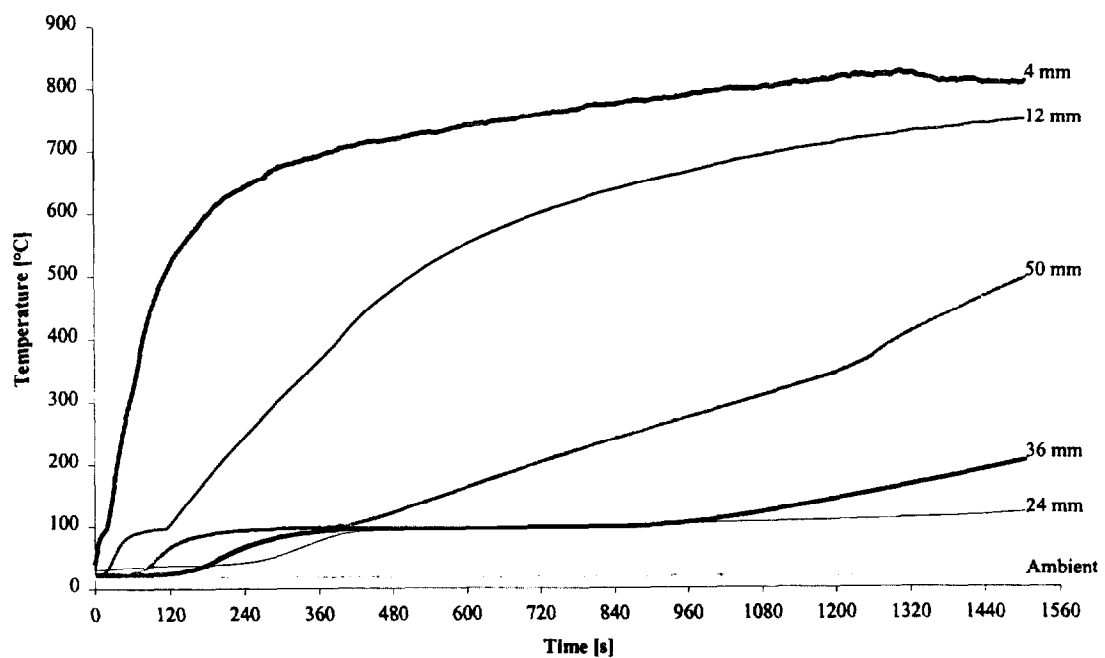**Figure 182.** Rate of heat release and heat of combustion (1DFX3).
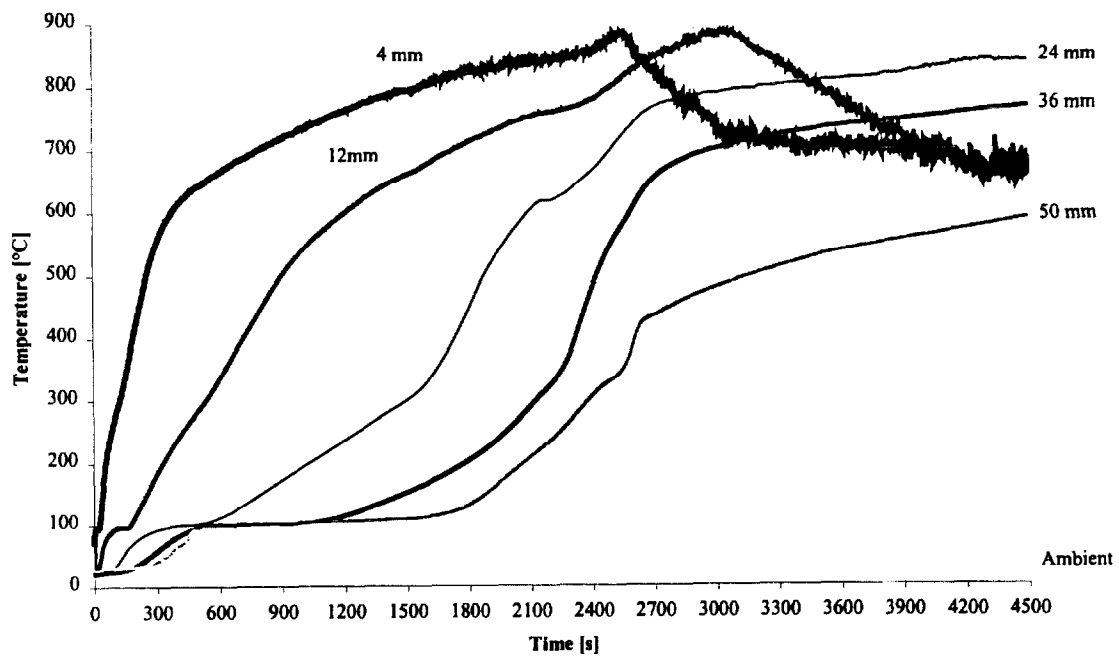
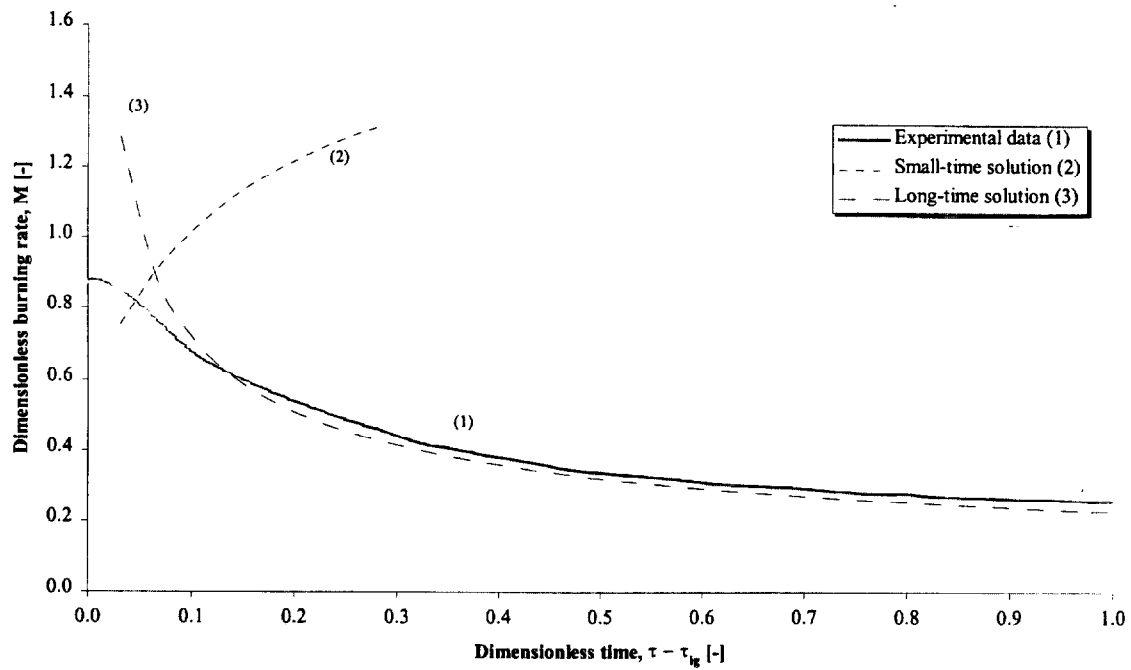**Figure 183.** Temperatures measured in sample (1DFX3).
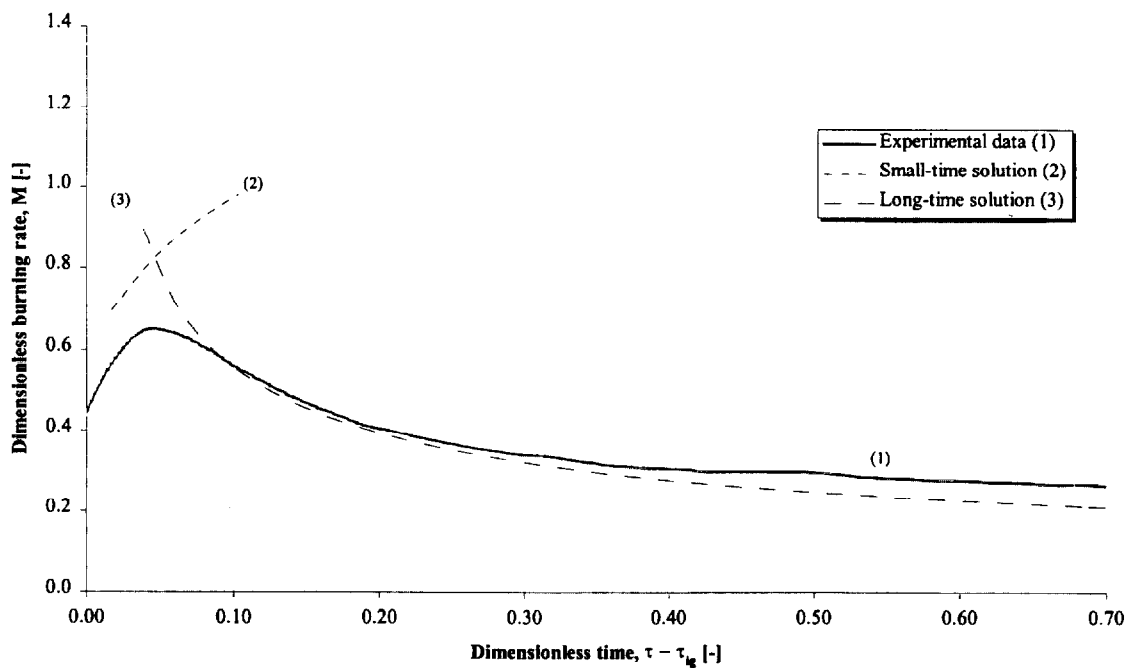
Figure 184. Comparison of dimensionless burning rate using derived properties for species and orientation (1DFX3).
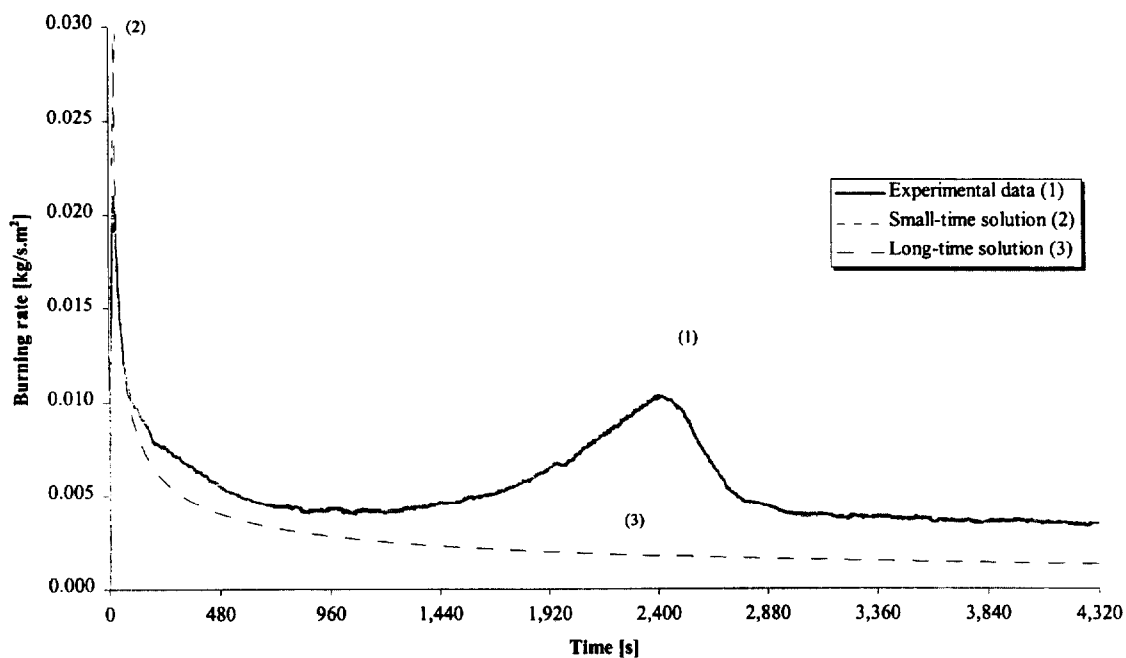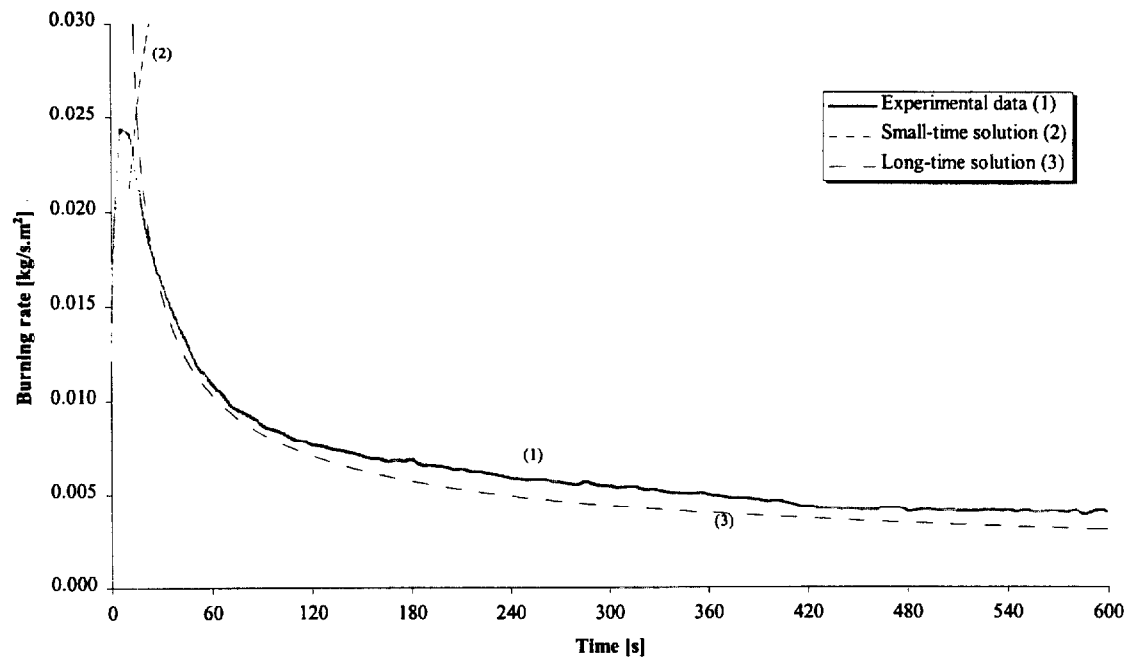

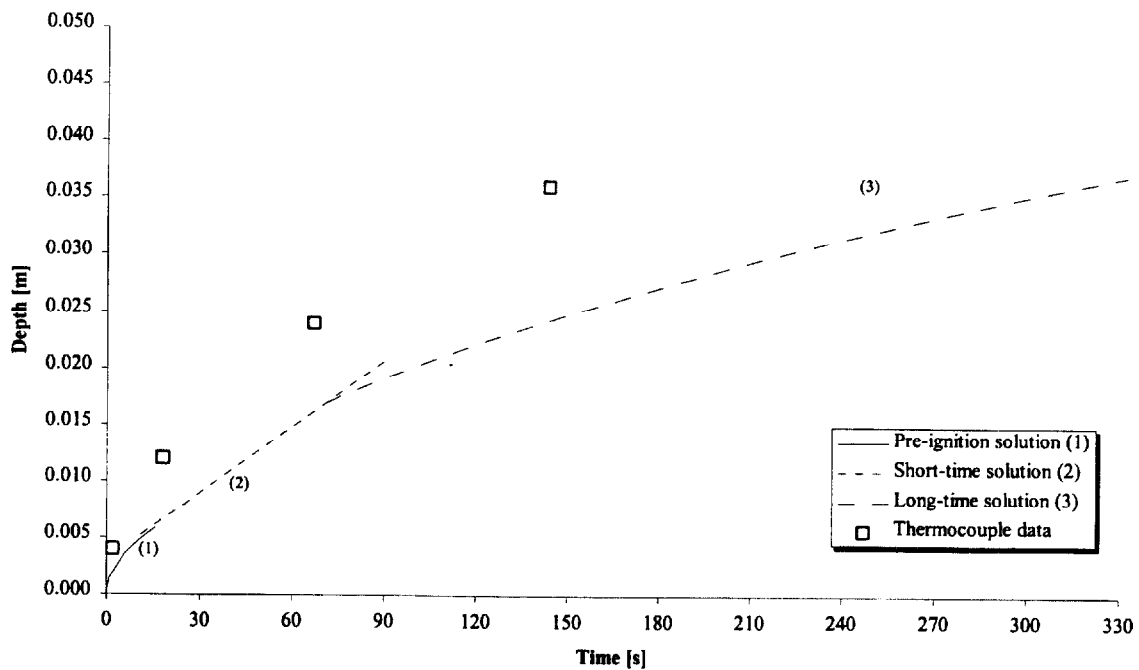**Figure 185.** Comparison of burning rate using derived properties for species and orientation (1DFX3).

258
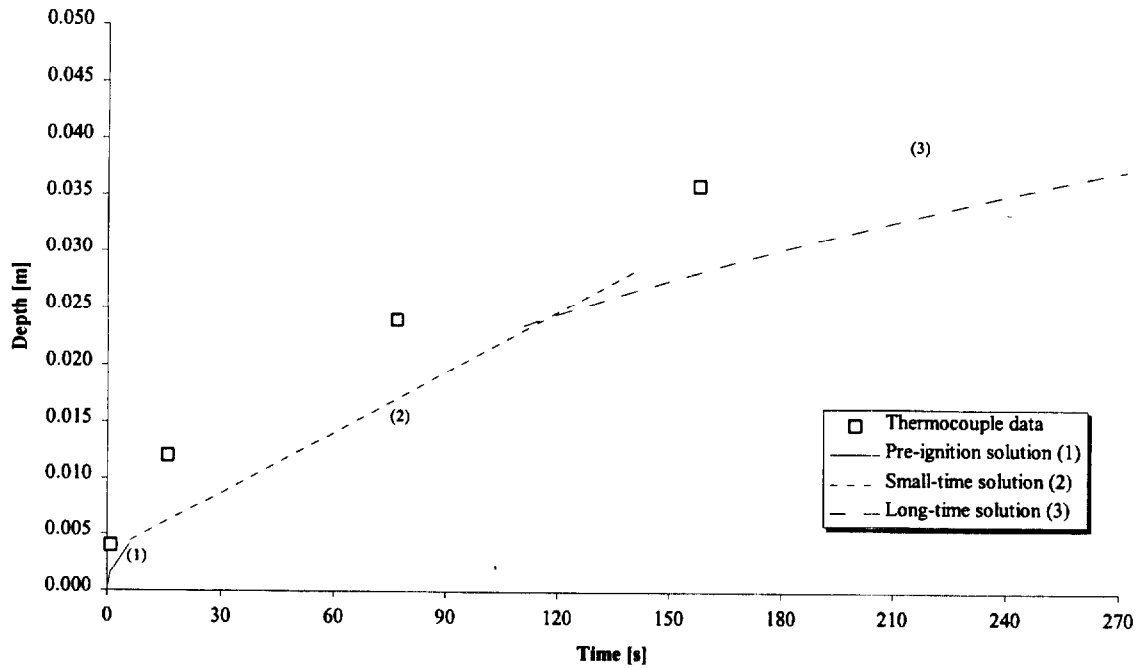
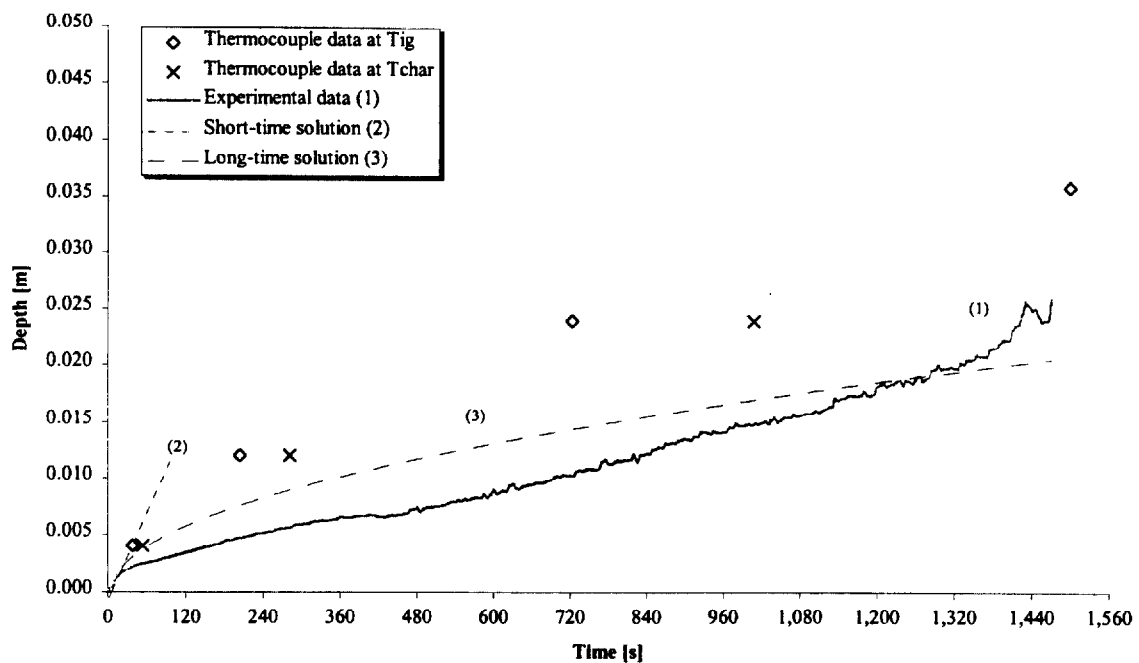**Figure 186.** Comparison of measured and calculated thermal penetration depth (1DFX3).
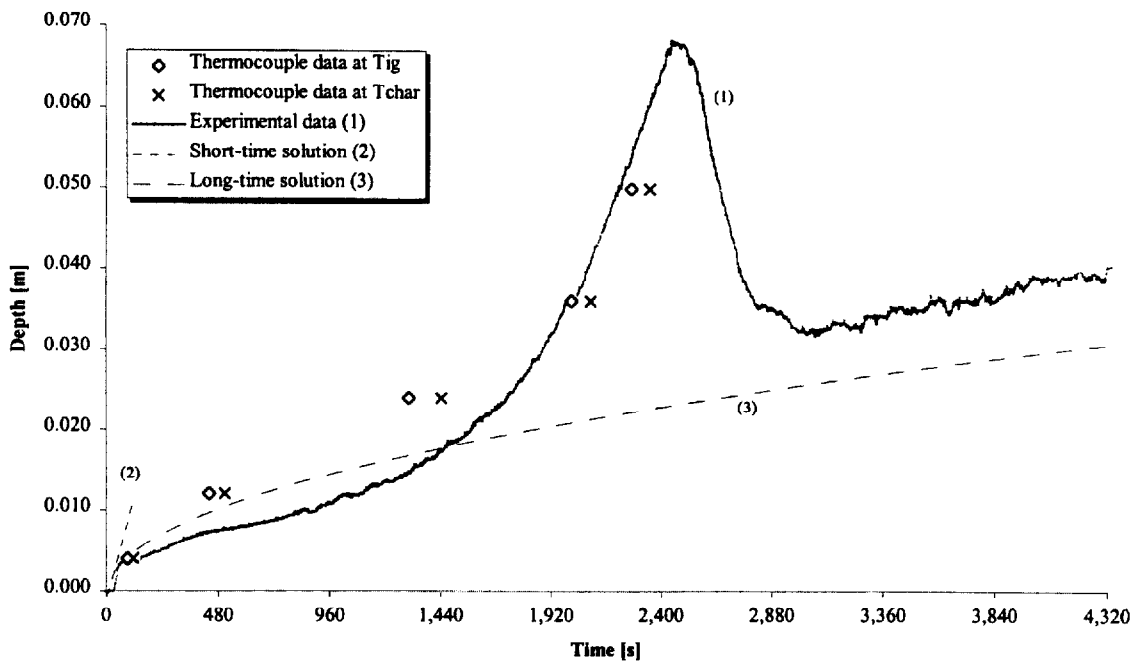
Figure 187. Comparison of estimated char depth from experimental data and the calculated char depth (1DFX3).

259

Test (1DFX4), Douglas Fir, across grain at 25 kW/m^2 for 25 minutes.
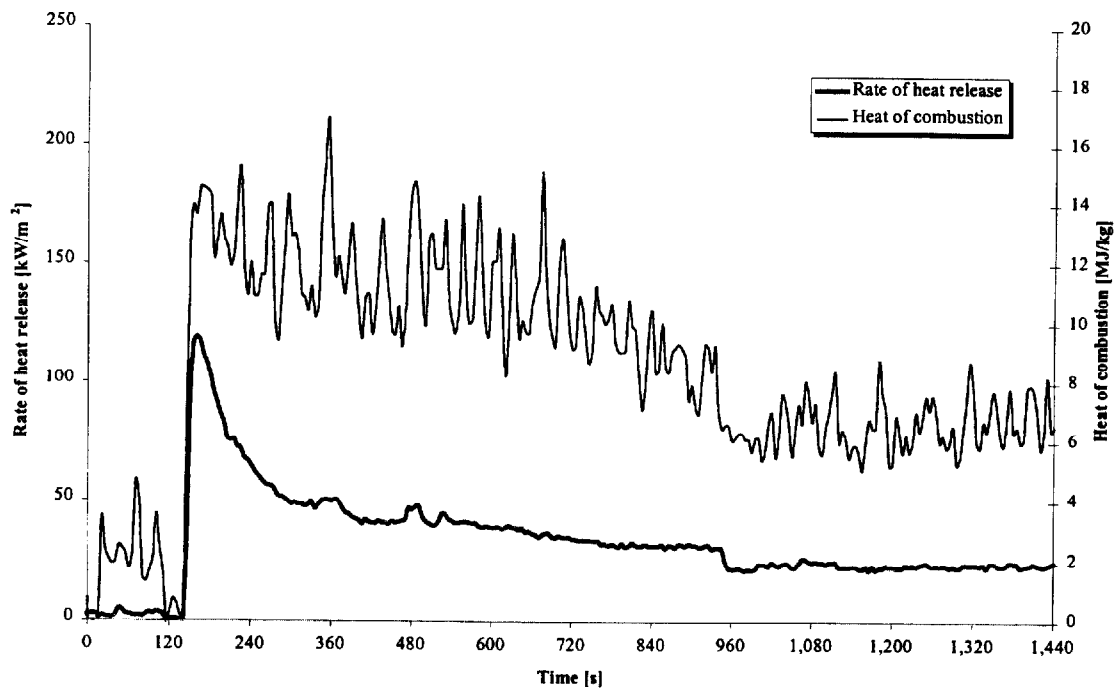
Figure 188. Rate of heat release and heat of combustion (1DFX4).
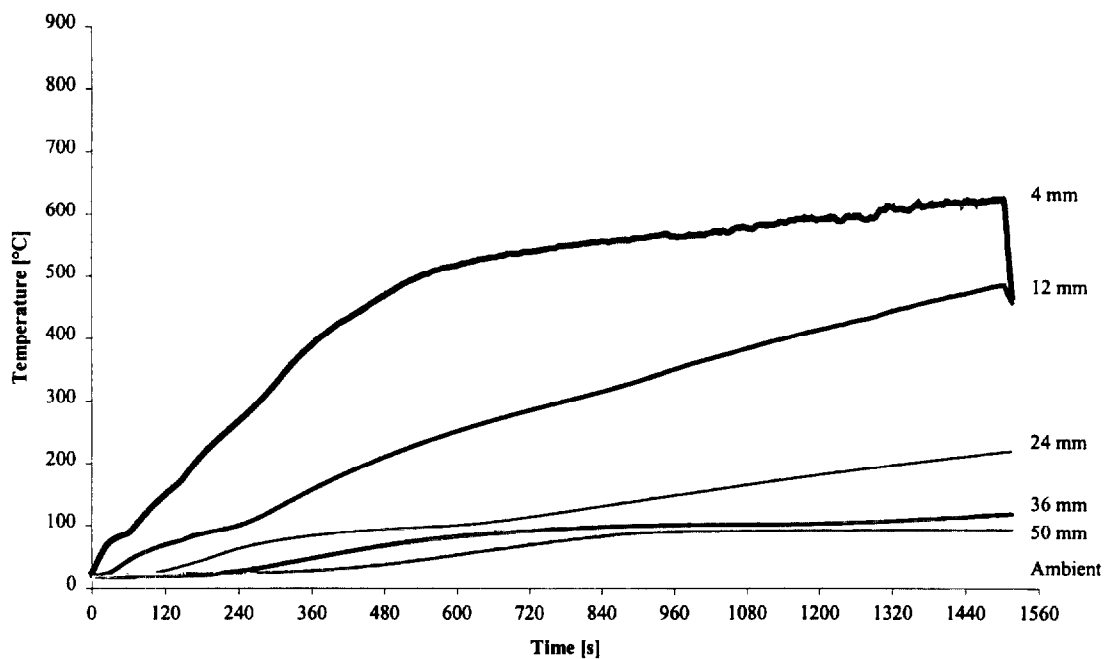
Figure 189. Temperatures measured in sample (1DFX4).
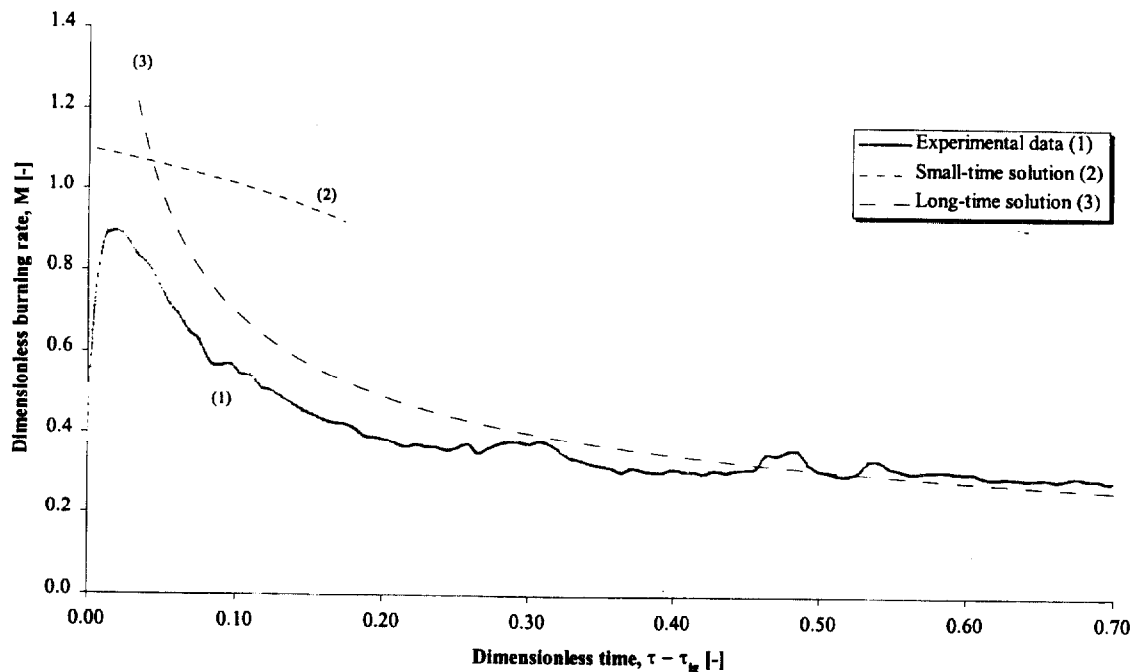
Figure 190. Comparison of dimensionless burning rate using derived properties for species and orientation (1DFX4).
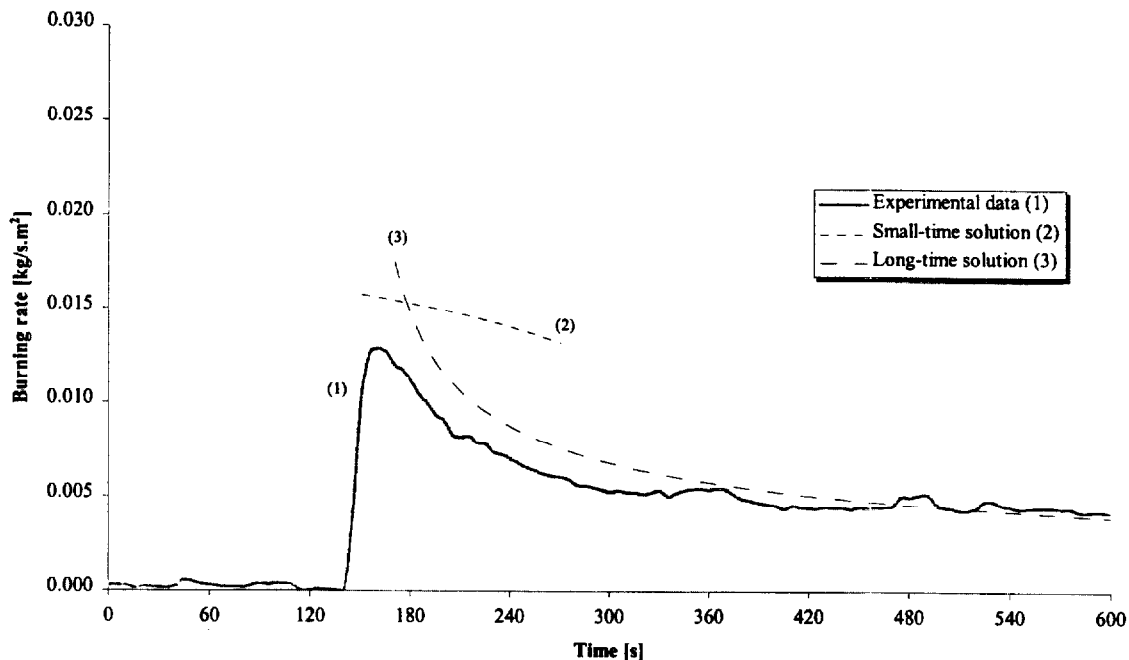
Figure 191. Comparison of burning rate using derived properties for species and orientation (1DFX4).
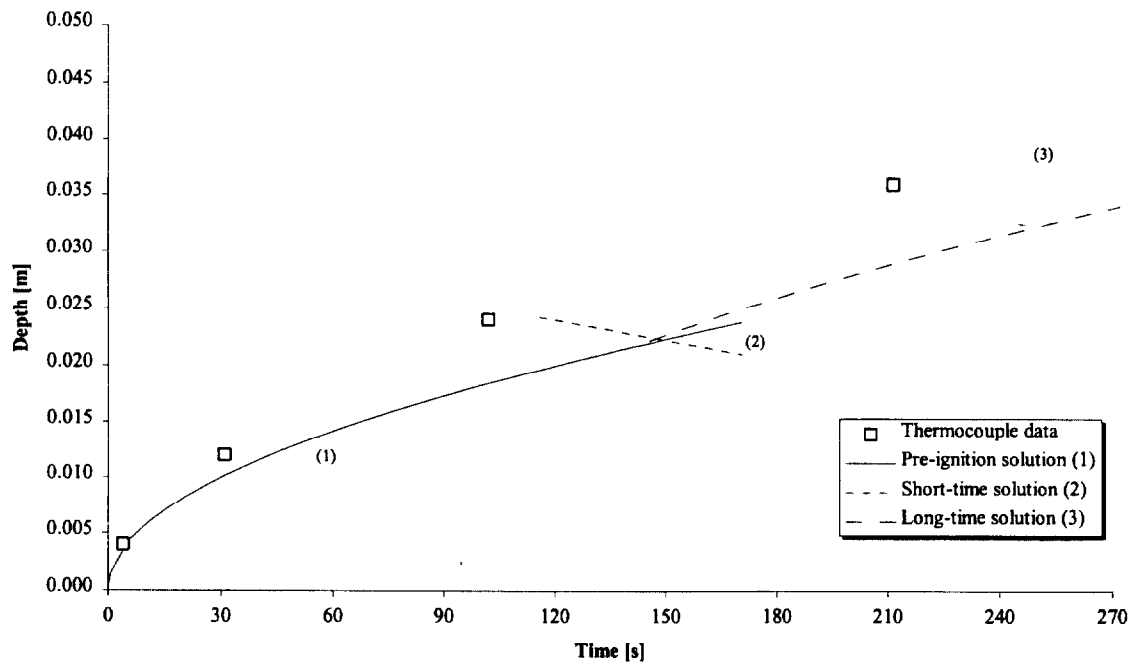
Figure 192. Comparison of measured and calculated thermal penetration depth (1DFX4).
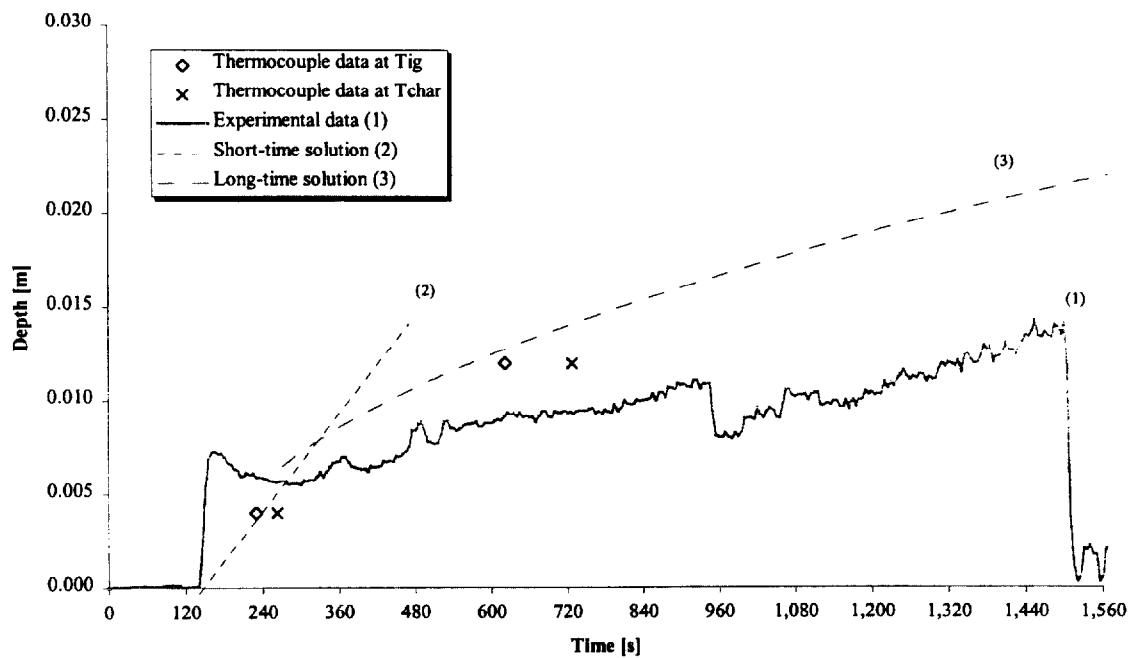
Figure 193. Comparison of estimated char depth from experimental data and the calculated char depth (1DFX4).

Test (1DFX5), Douglas Fir, across grain at 75 kW/m^2 for 25 minutes.
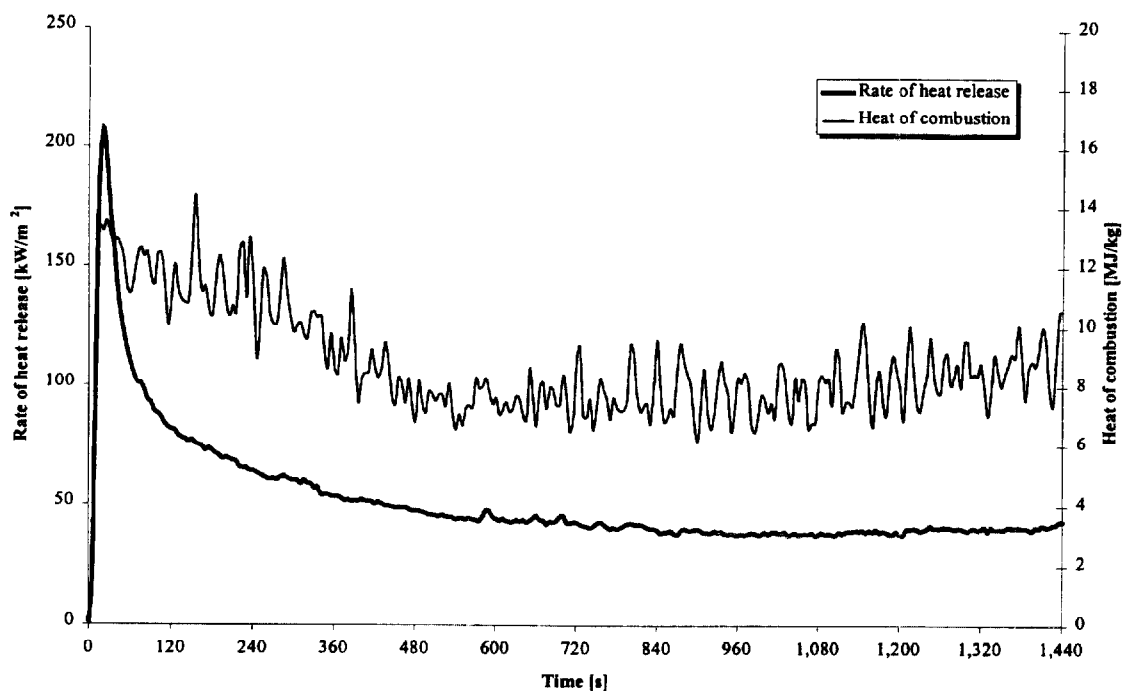
Figure 194. Rate of heat release and heat of combustion (1DFX5).
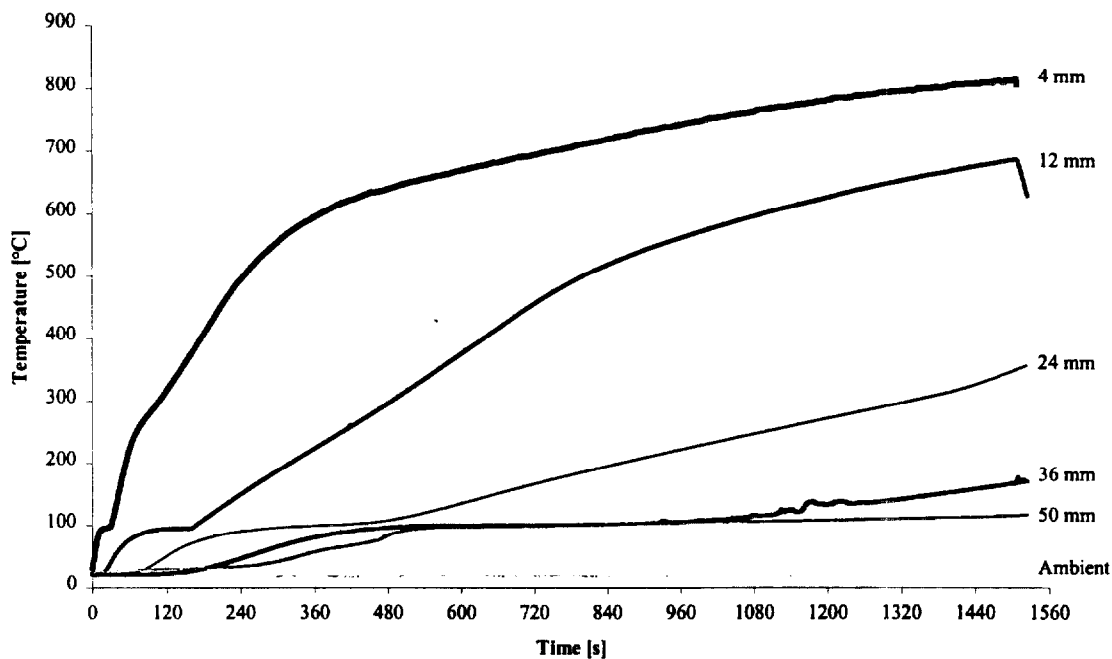
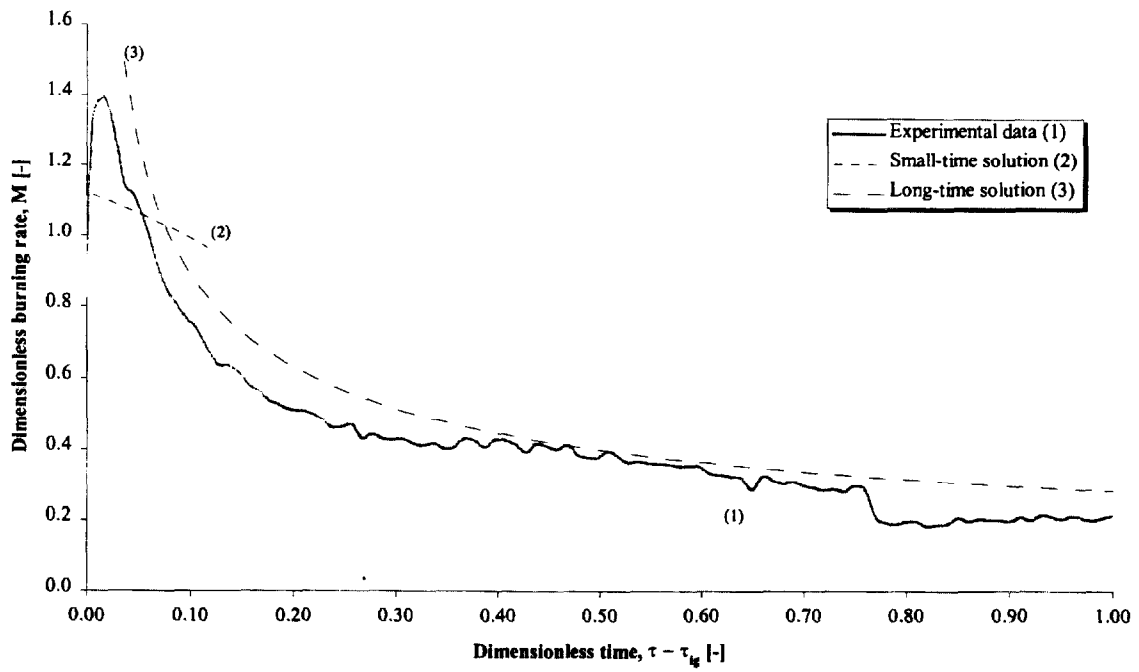**Figure 195.** Temperatures measured in sample (1DFX5).

263
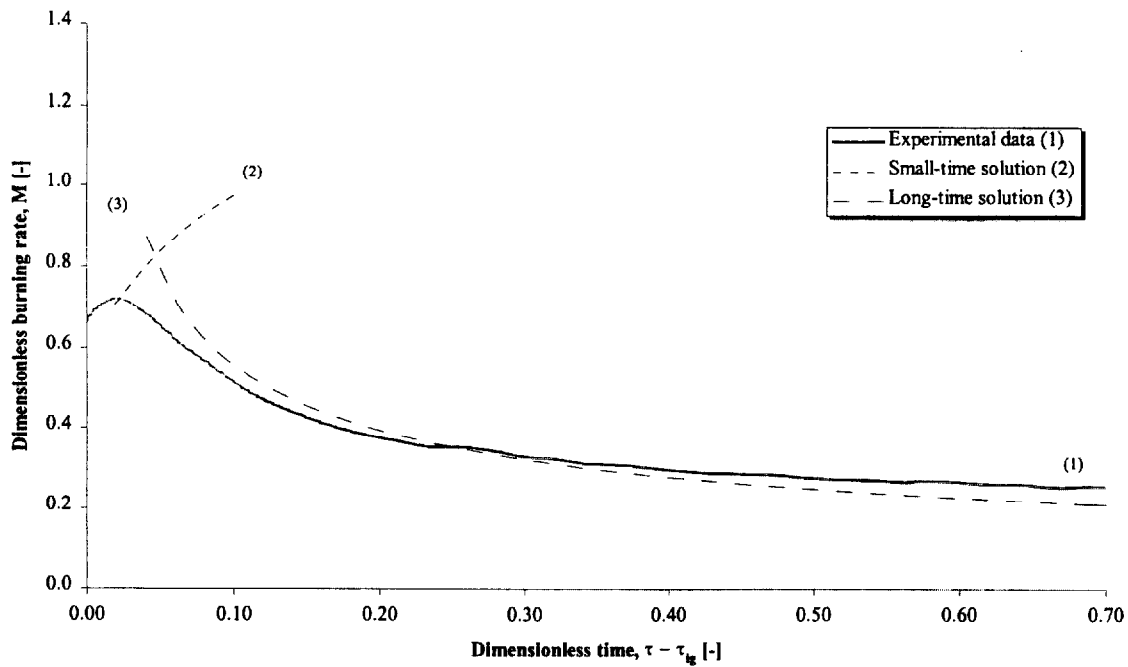
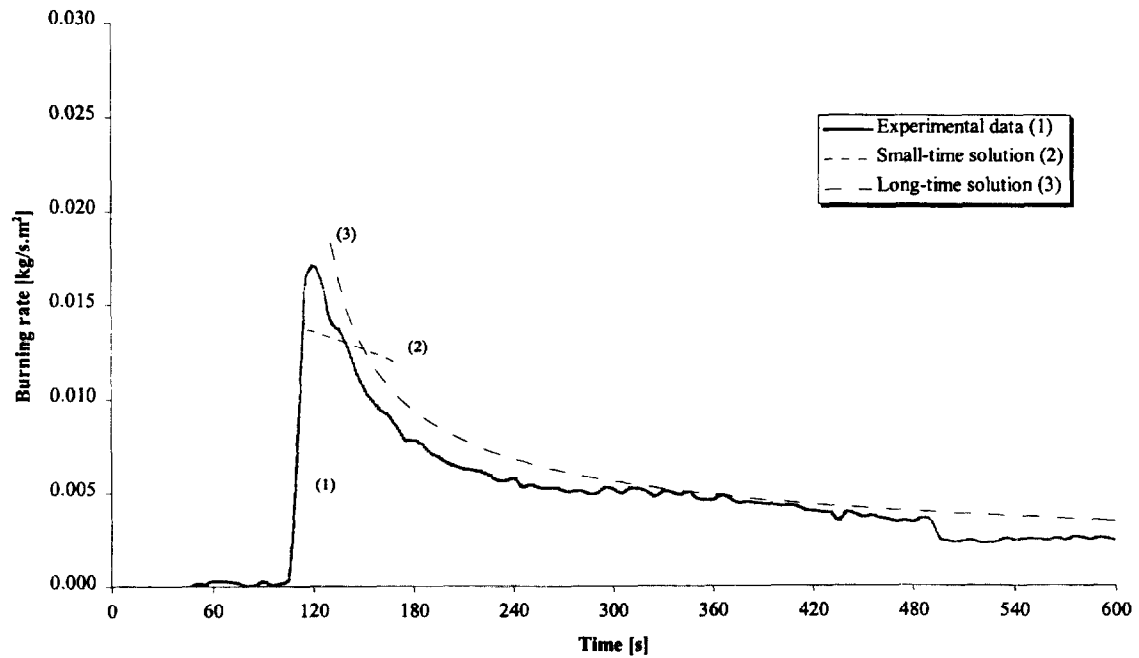**Figure 196.** Comparison of dimensionless burning rate using derived properties for species and orientation (1DFX5).
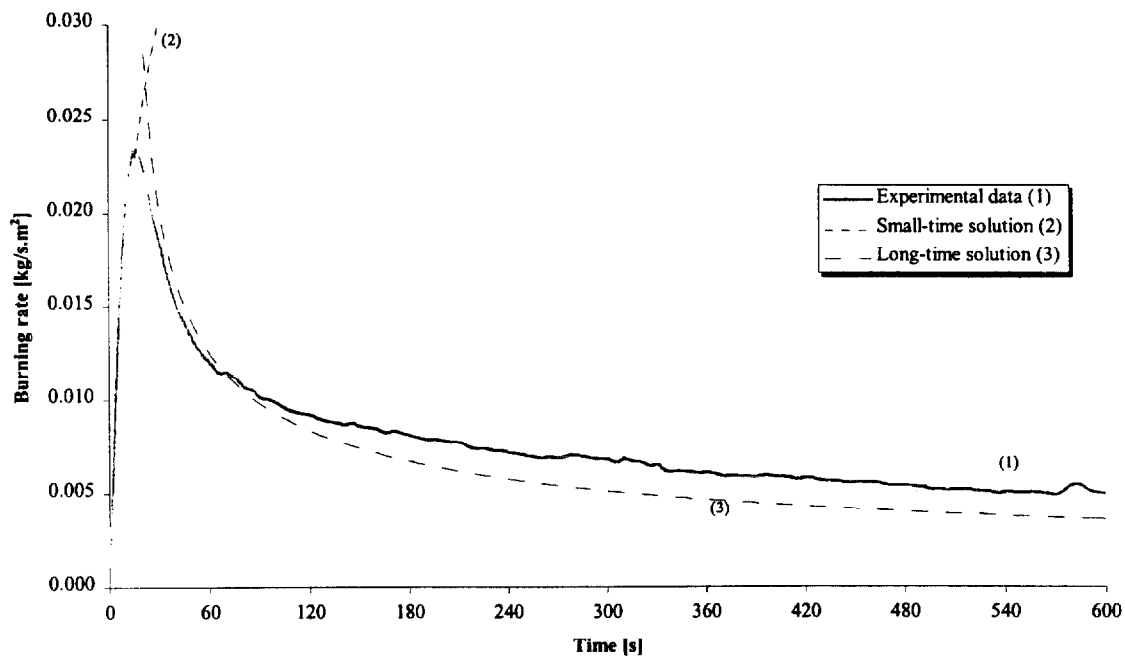
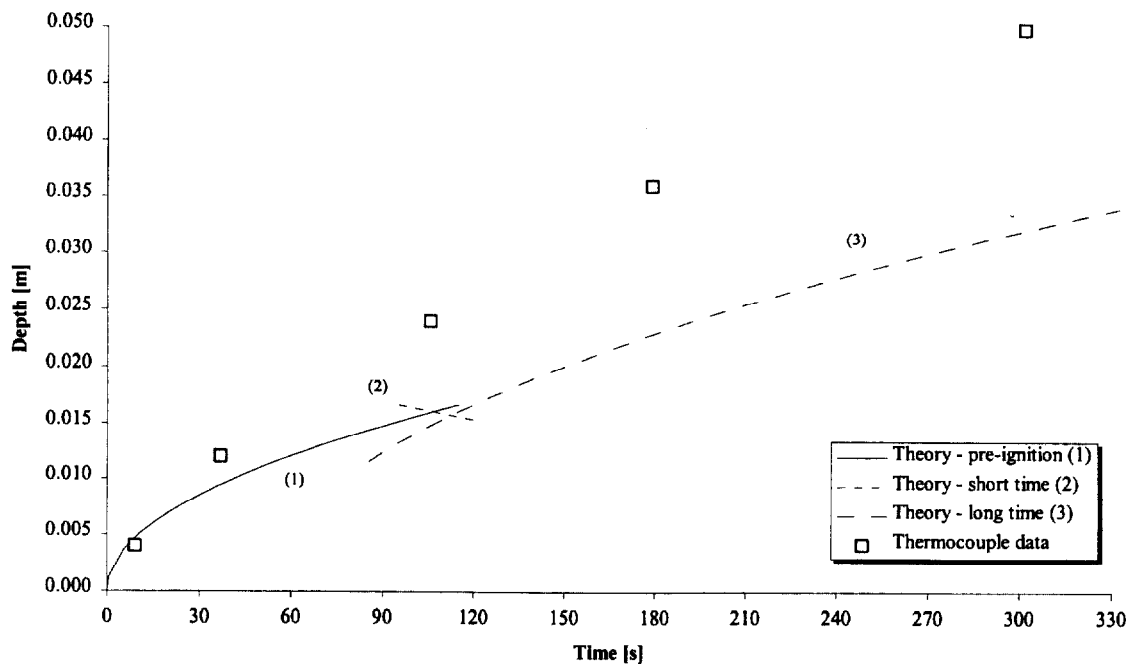**Figure 197.** Comparison of burning rate using derived properties for species and orientation (1DFX5).

264
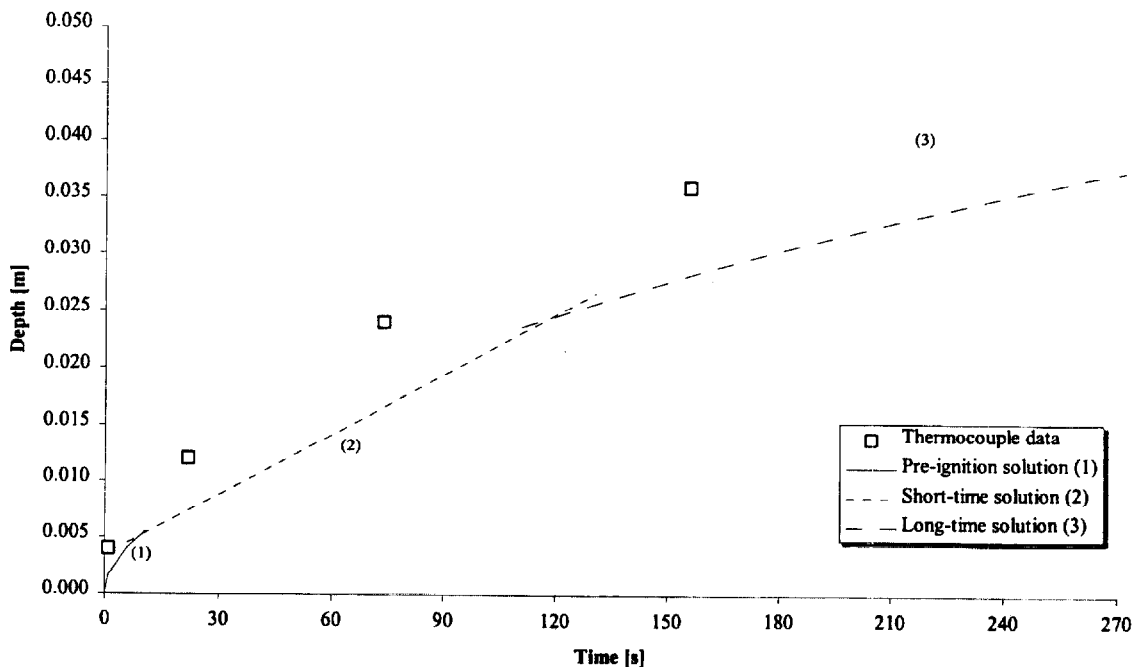
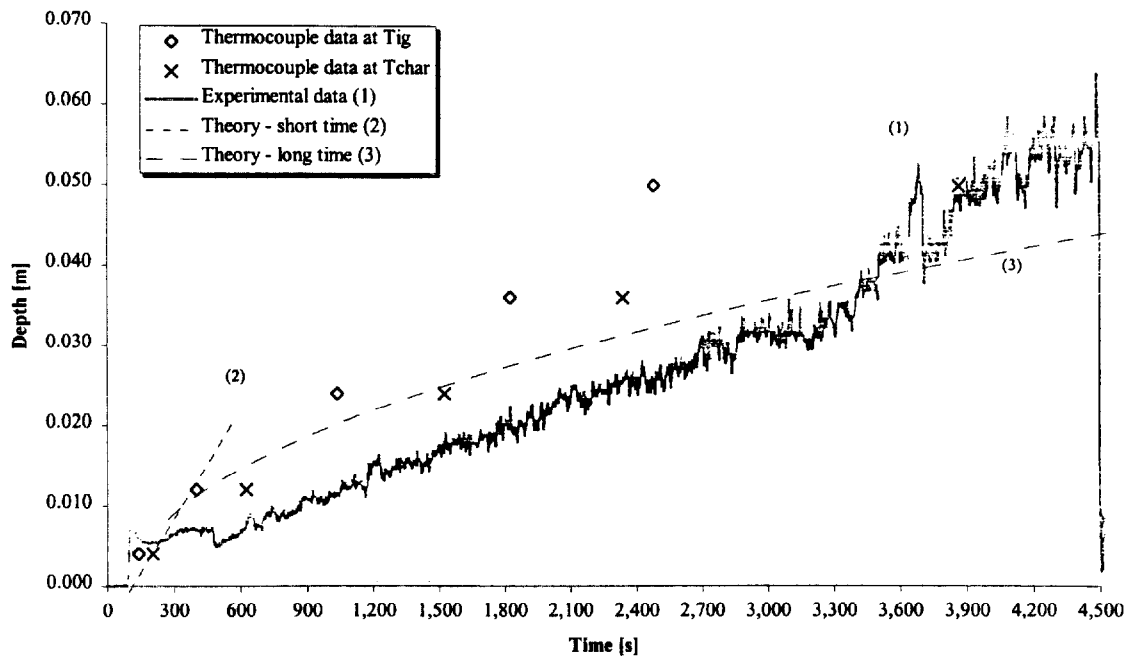**Figure 198.** Comparison of measured and calculated thermal penetration depth (1DFX5).
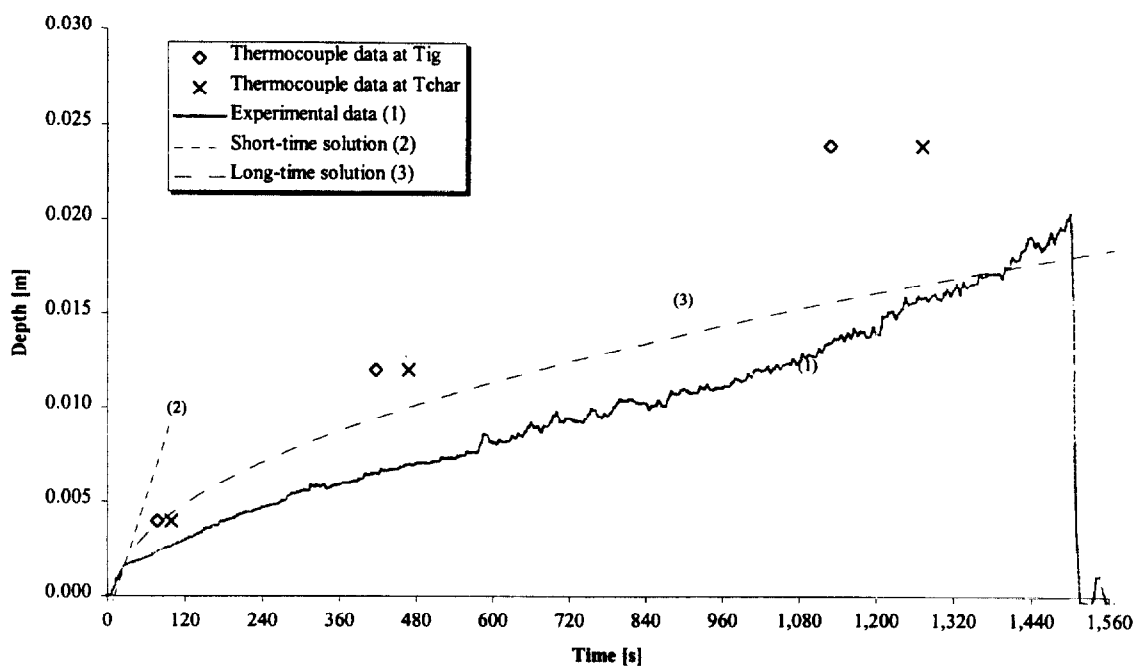
Figure 199. Comparison of estimated char depth from experimental data and the calculated char depth (1DFX5).

265

Test (1DFX6), Douglas Fir, across grain at 50 kW/m^2 for 25 minutes.
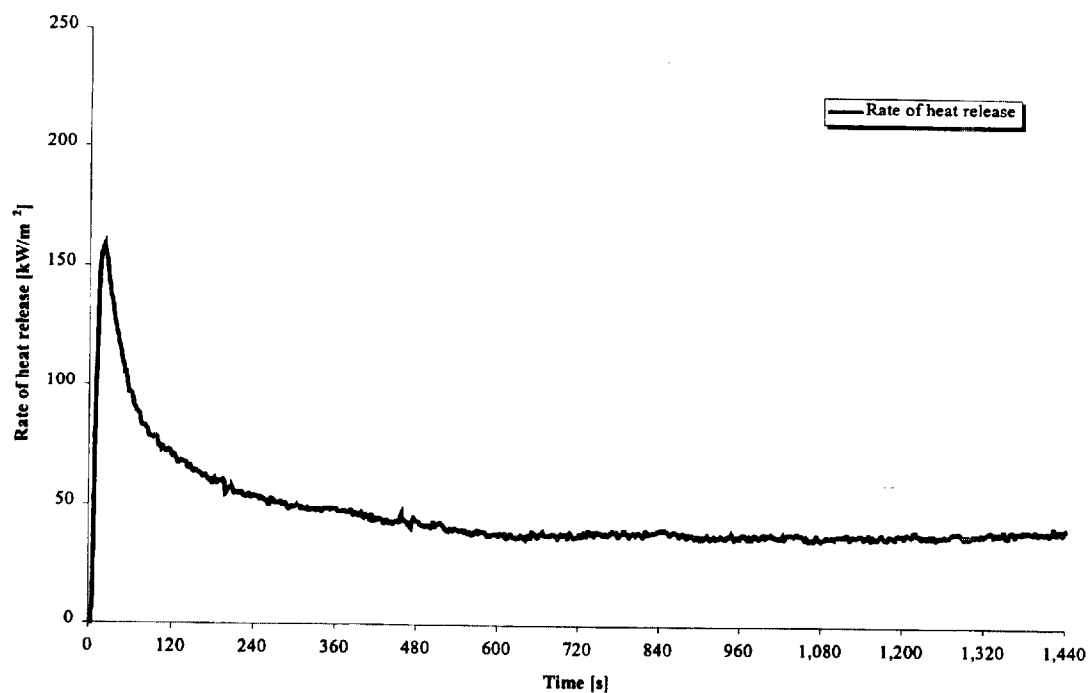
Figure 200. Rate of heat release (1DFX6).
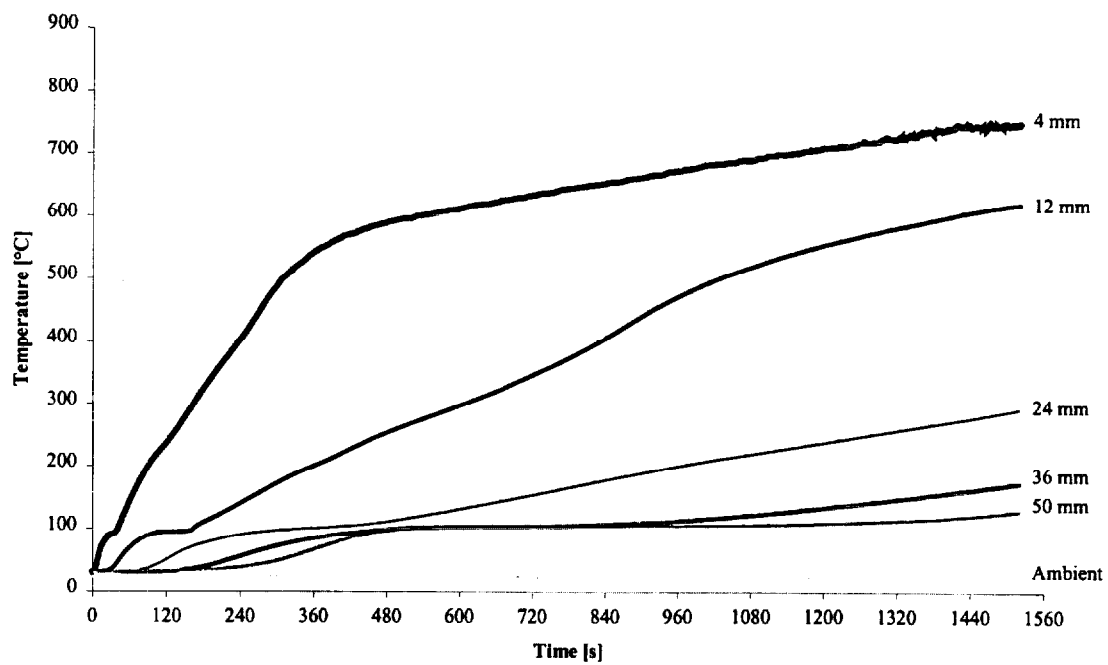
Figure 201. Temperatures measured in sample (1DFX6).

266
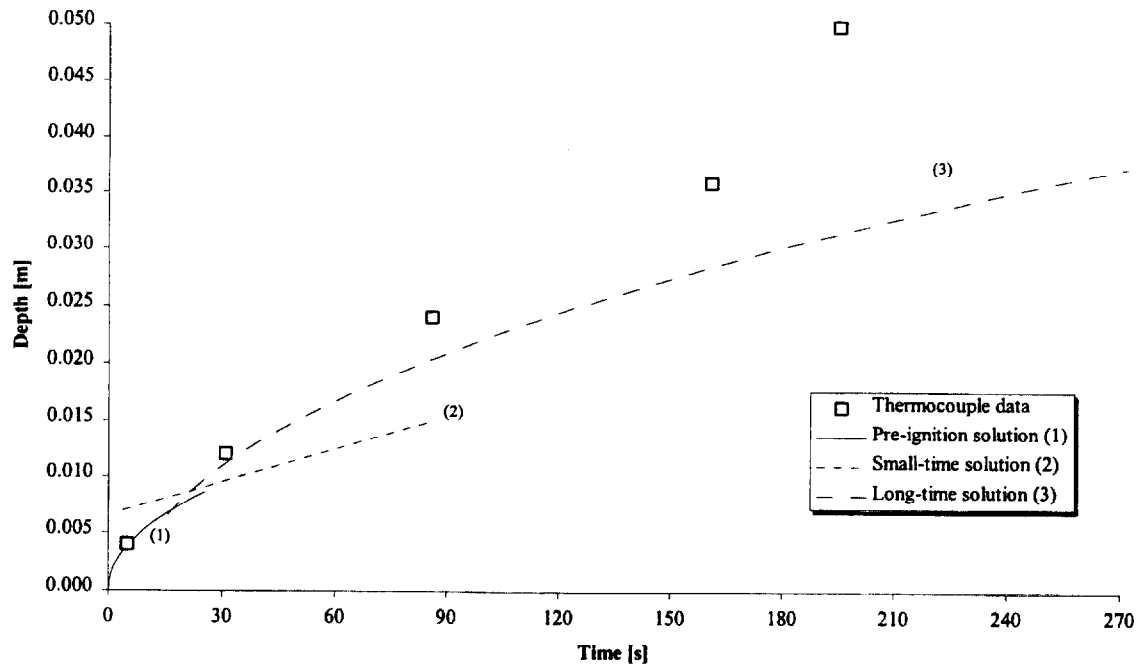
Figure 204. Comparison of measured and calculated thermal penetration depth (1DFX6).
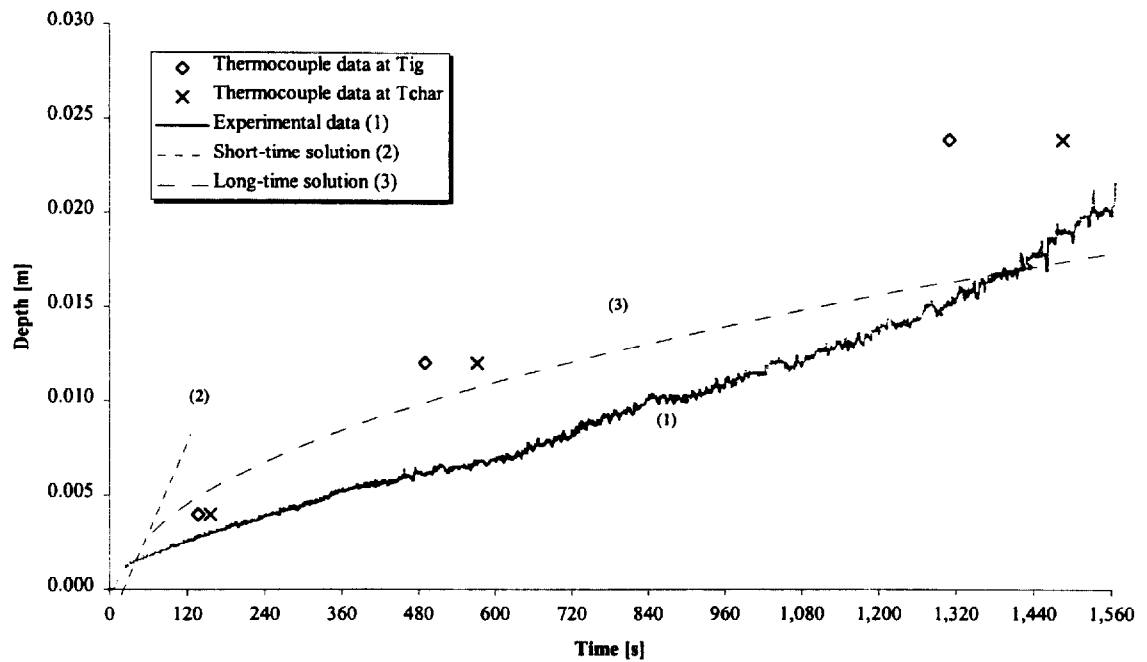
Figure 205. Comparison of estimated char depth from experimental data and the
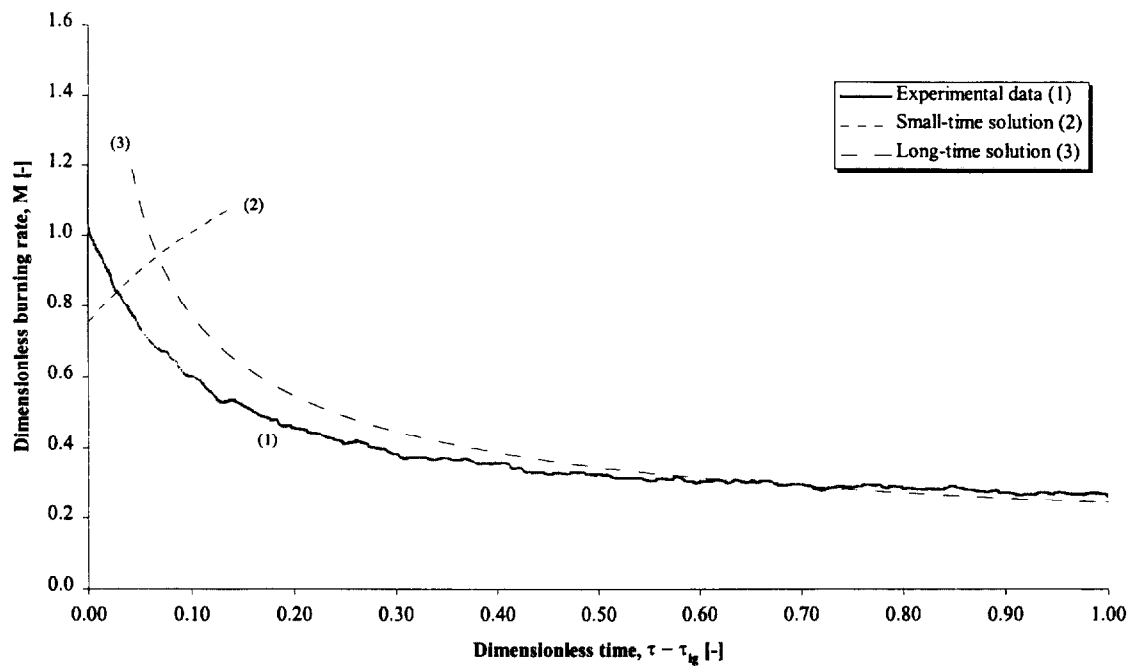calculated char depth (1DFX6).

268
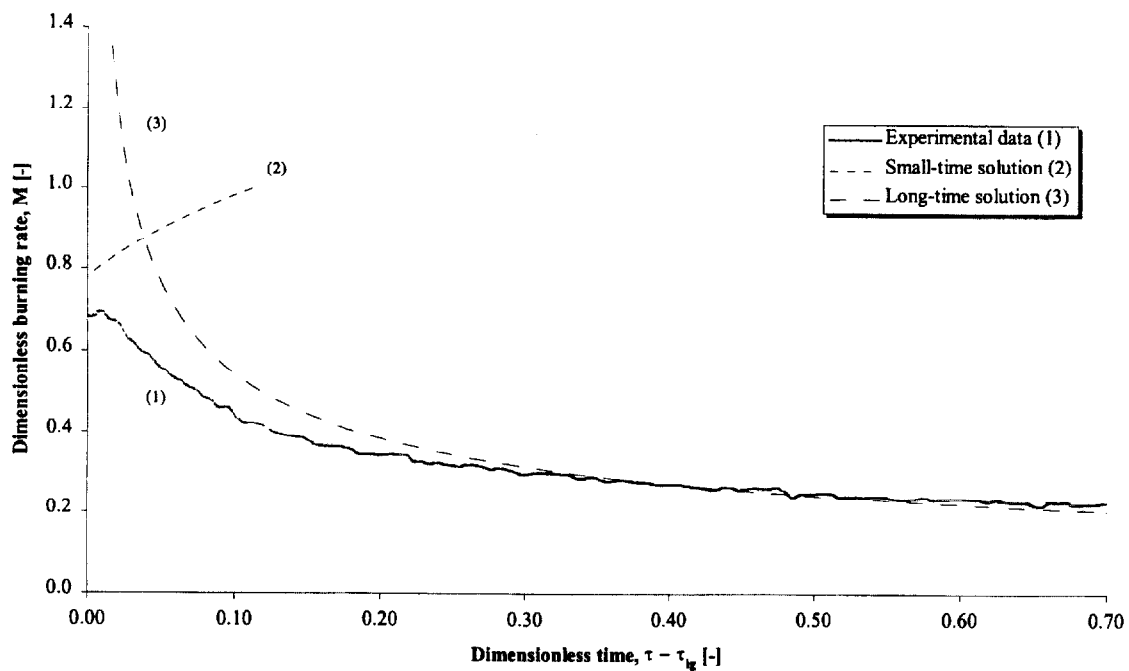
Figure 202. Comparison of dimensionless burning rate using derived properties for species and orientation (1DFX6).
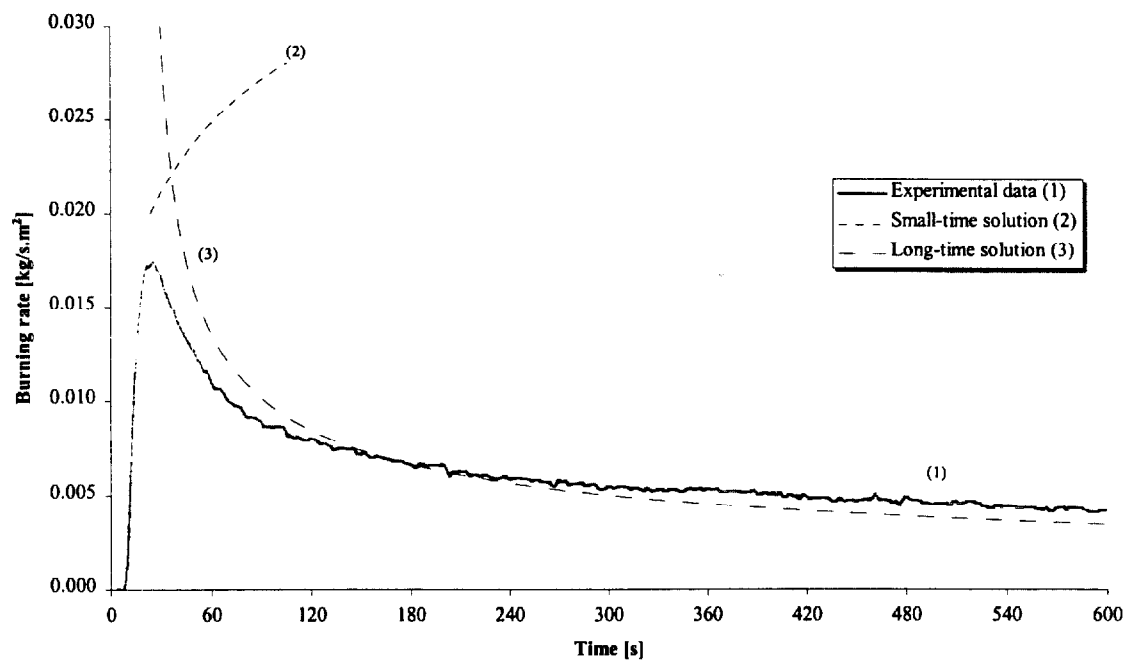
Figure 203. Comparison of burning rate using derived properties for species and orientation (1DFX6).

267

Test (1DFX7), Douglas Fir, across grain at 50 kW/m² for 25 minutes.
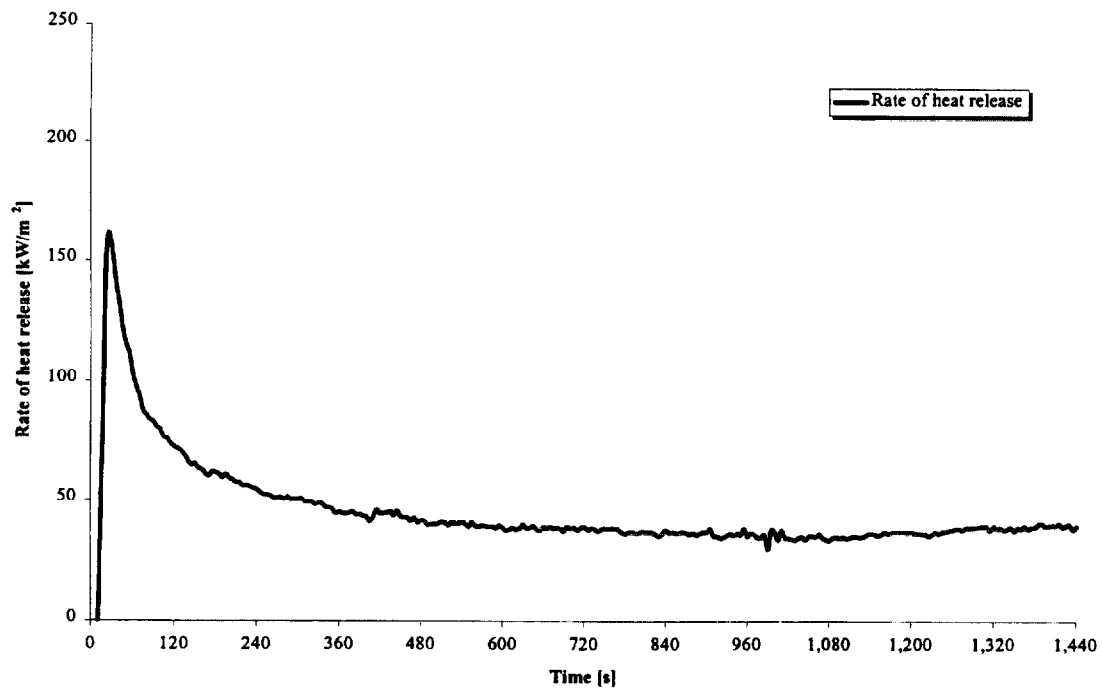
Figure 206. Rate of heat release (1DFX7).
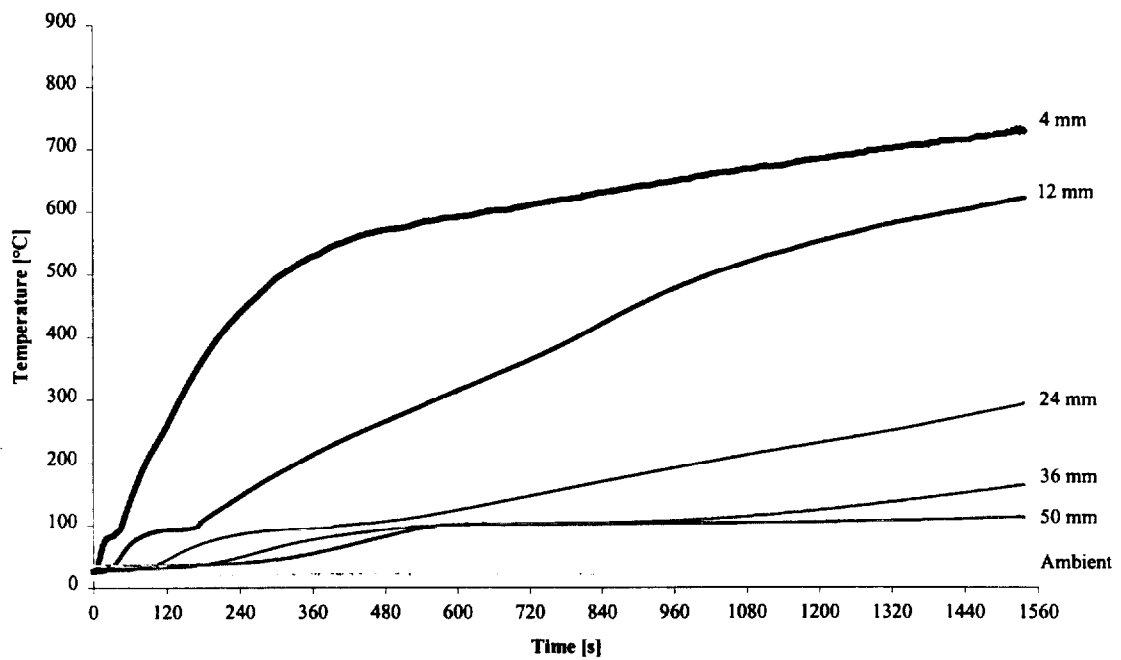
Figure 207. Temperatures measured in sample (1DFX7).
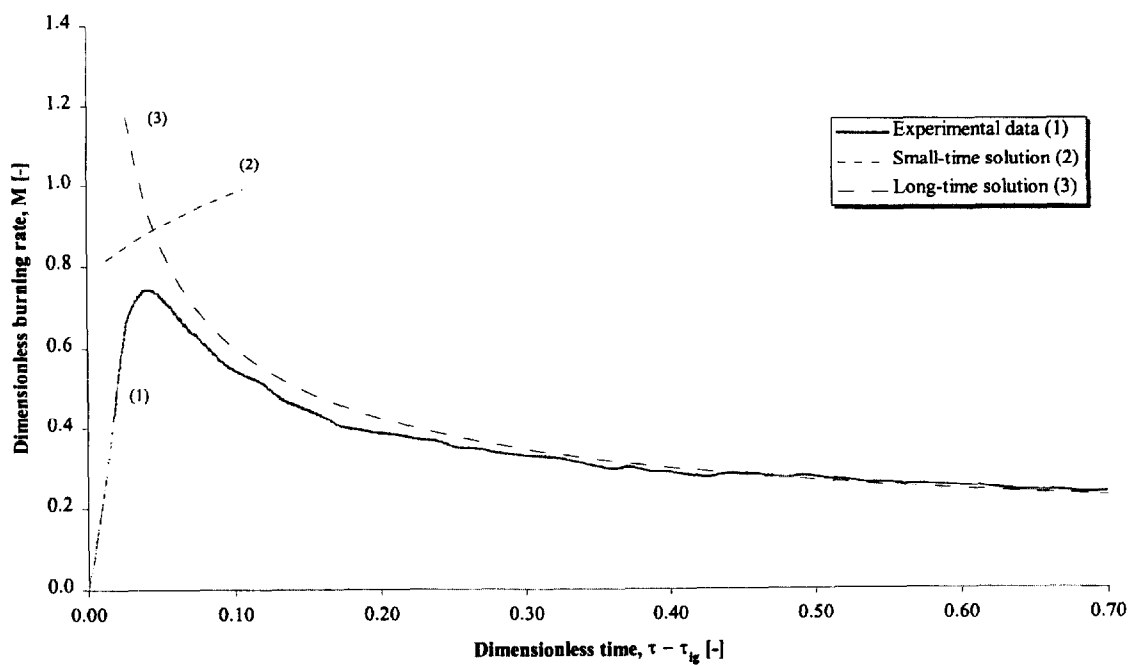
Figure 208. Comparison of dimensionless burning rate using derived properties for species and orientation (1DFX7).
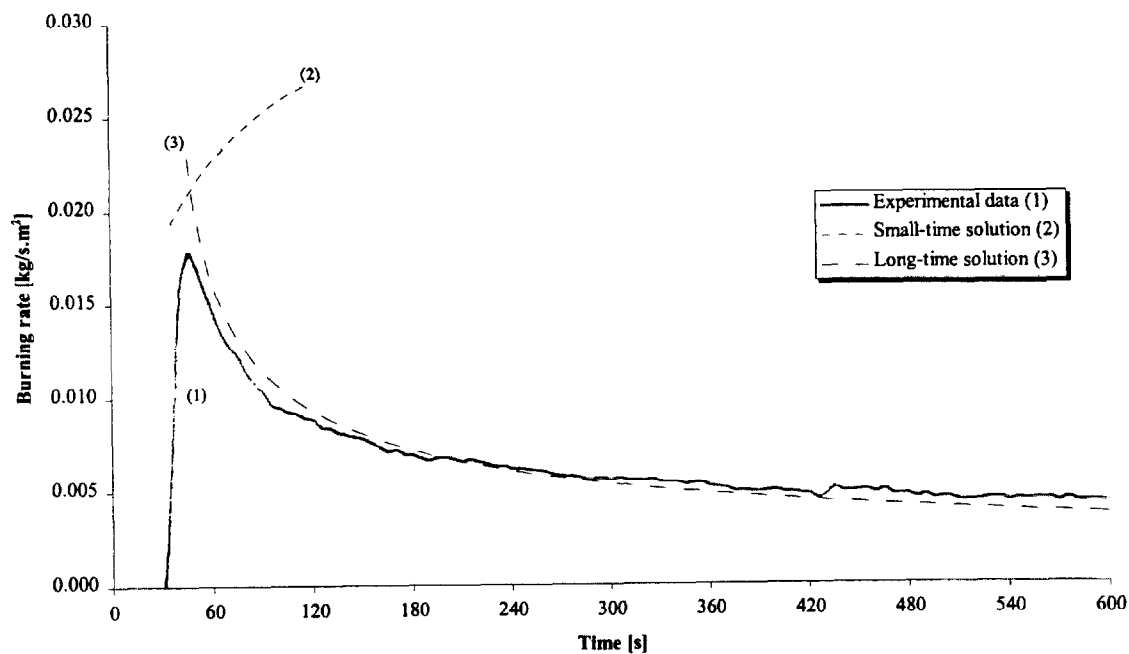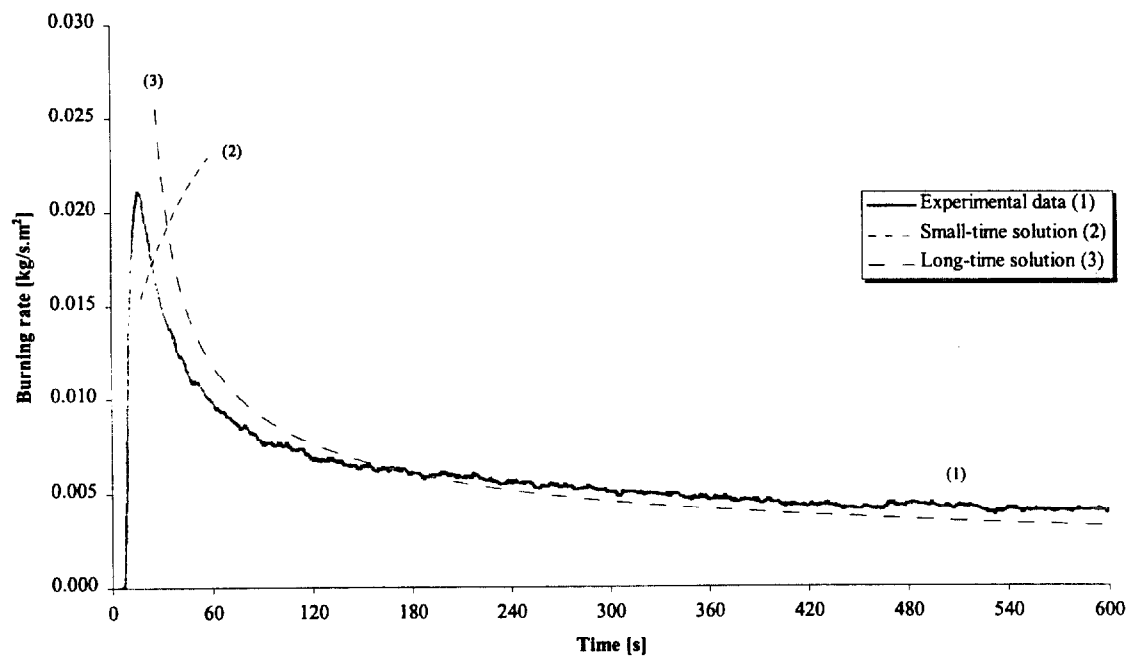

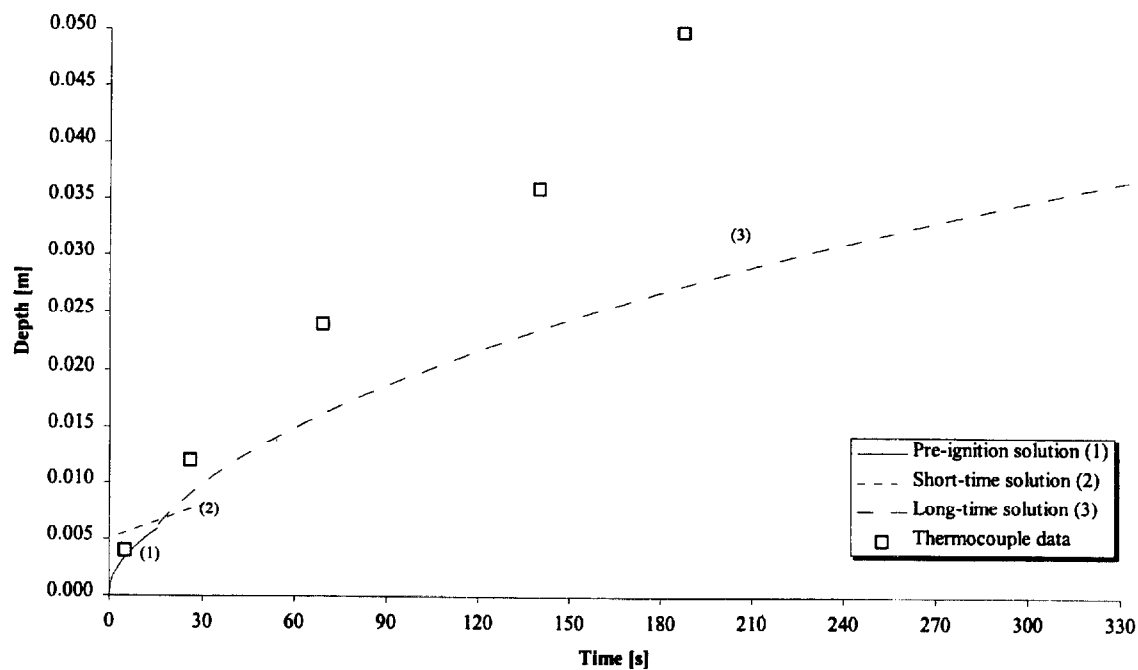**Figure 209.** Comparison of burning rate using derived properties for species and orientation (1DFX7).

270
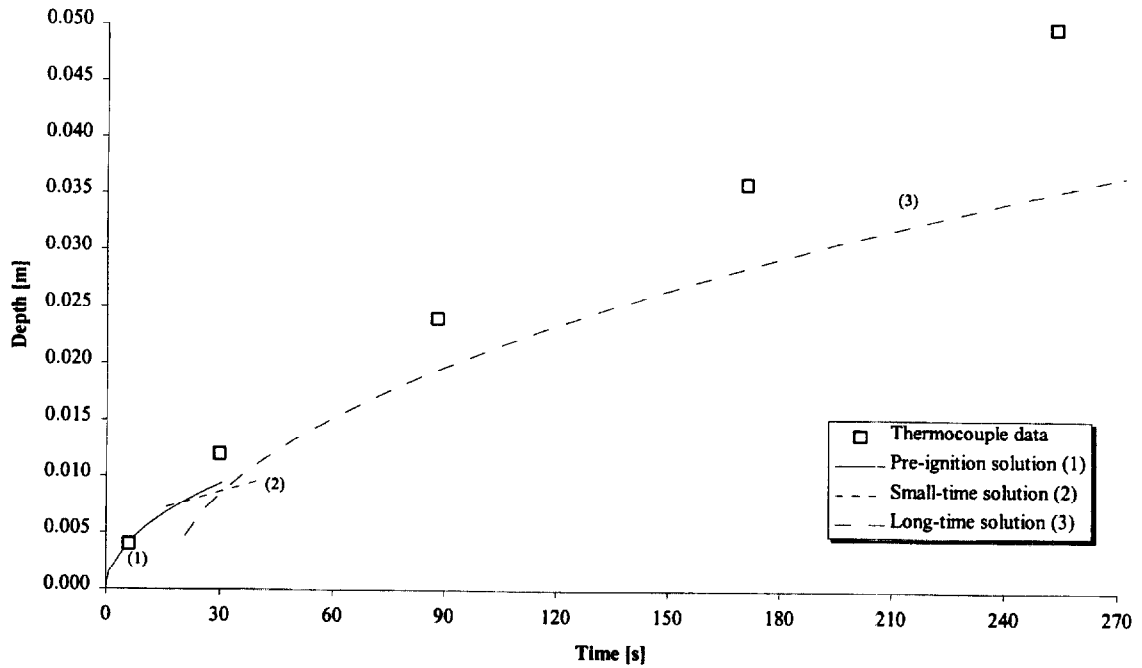
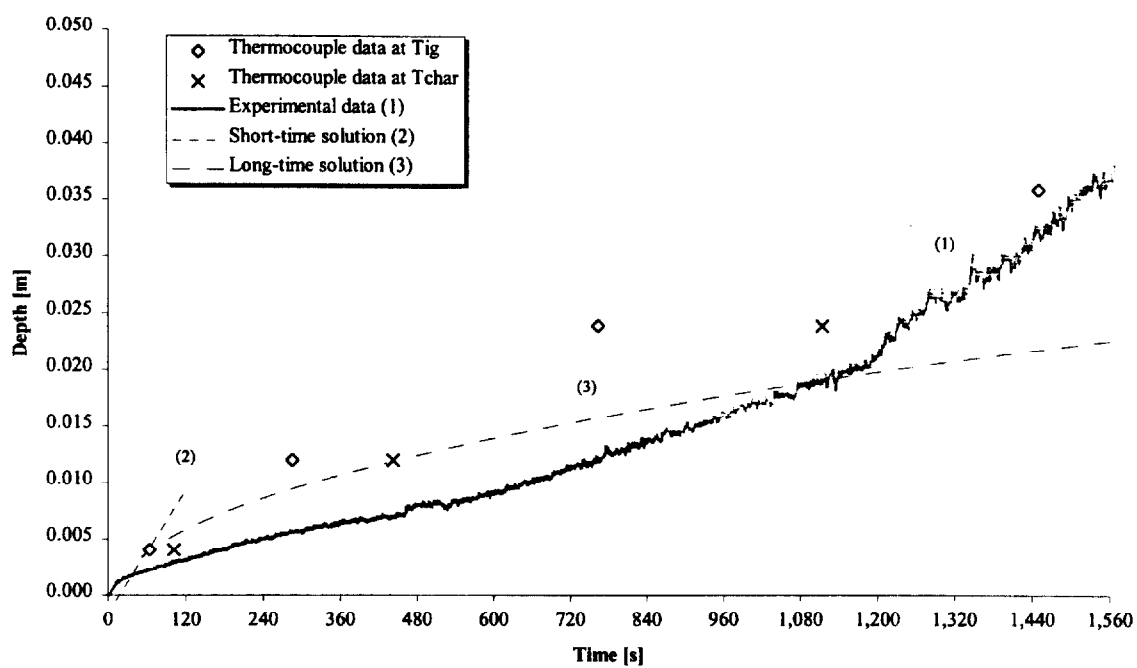**Figure 210.** Comparison of measured and calculated thermal penetration depth (1DFX7).
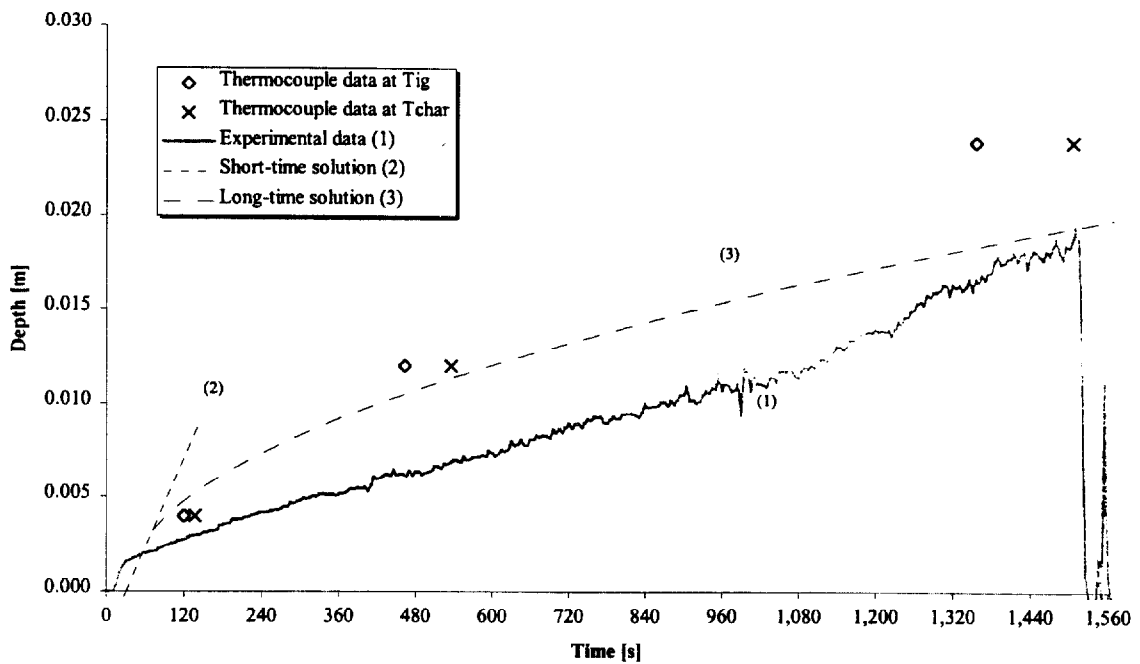
Figure 211. Comparison of estimated char depth from experimental data and the calculated char depth (1DFX7).

271

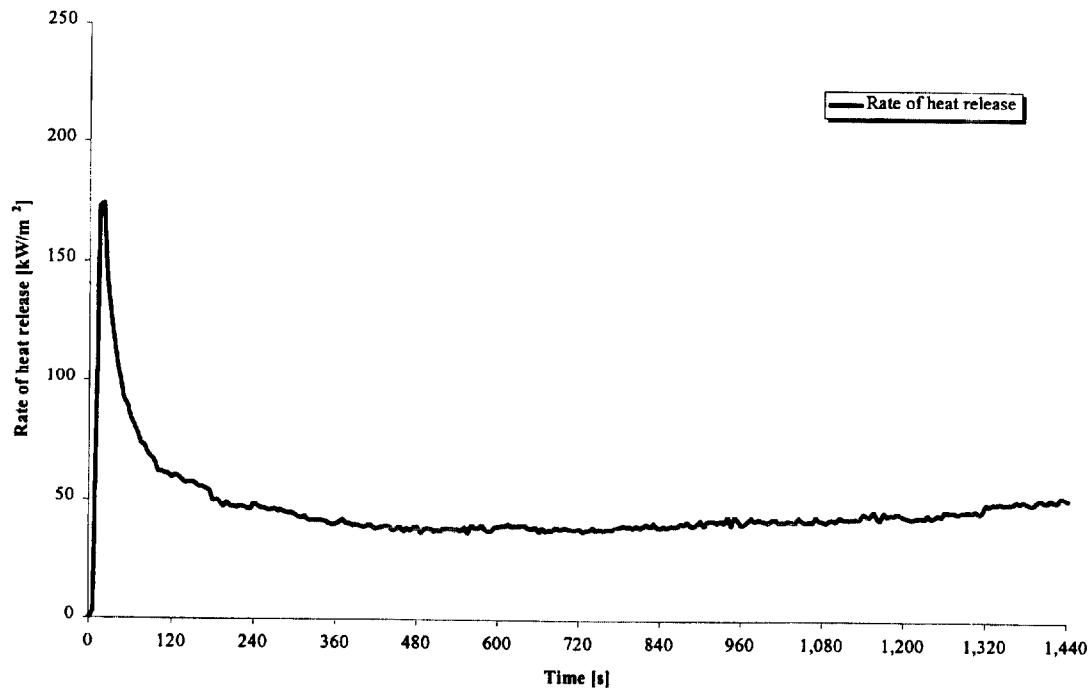Test (1RL1), Redwood, along grain at 75 kW/m² for 25 minutes.
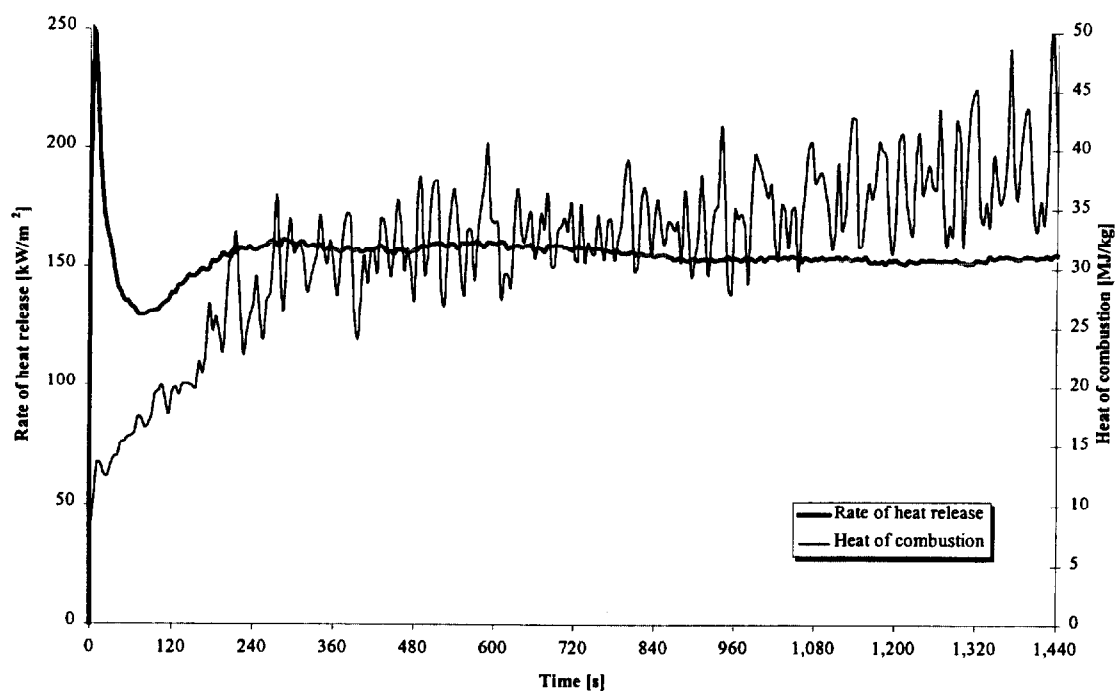
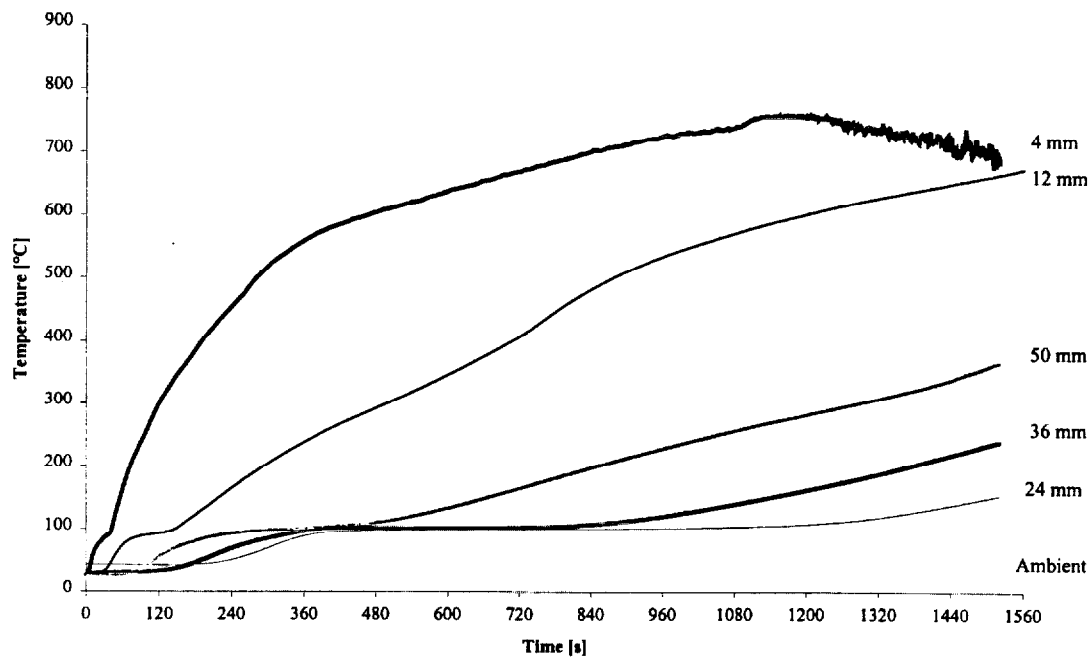**Figure 212.** Rate of heat release and heat of combustion (1RL1).
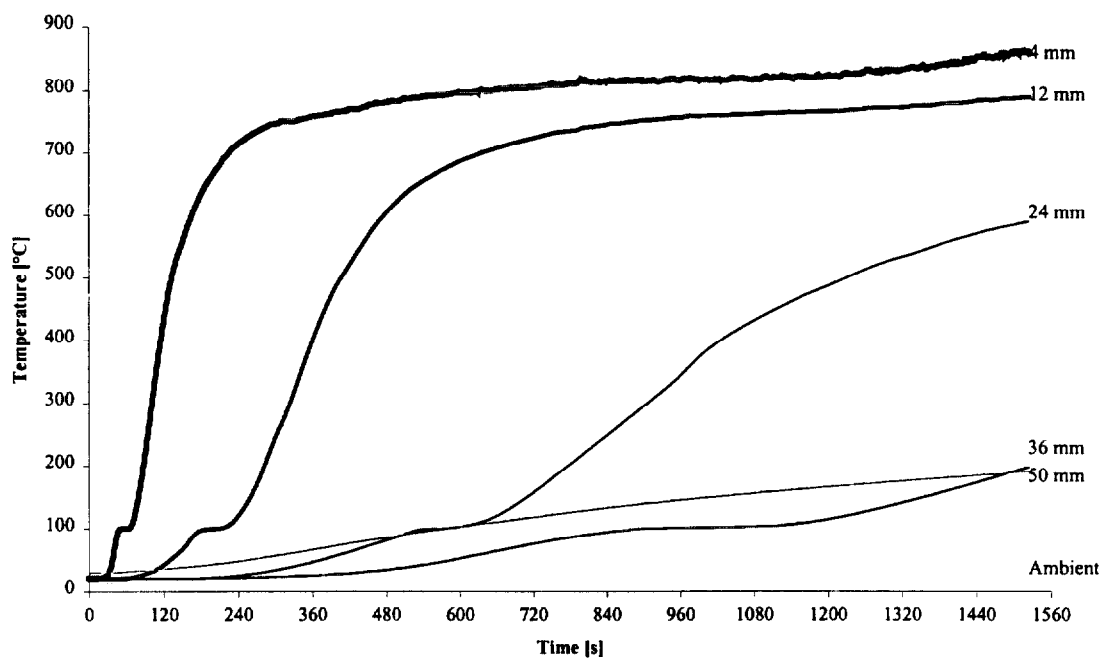
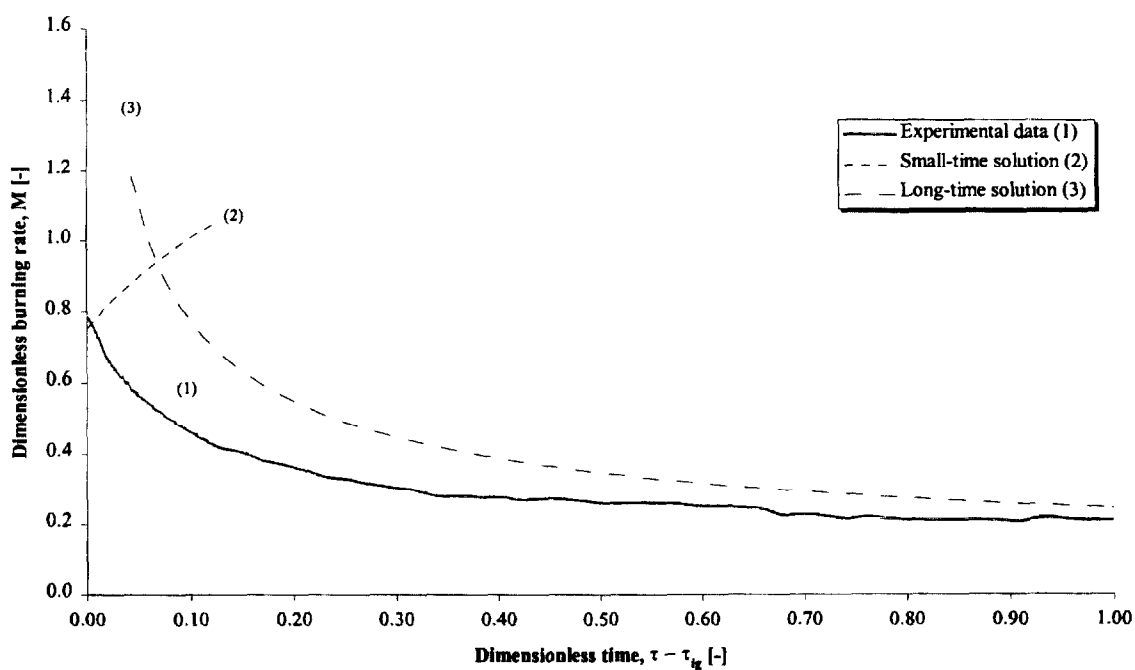**Figure 213.** Temperatures measured in sample (1RL1).

272
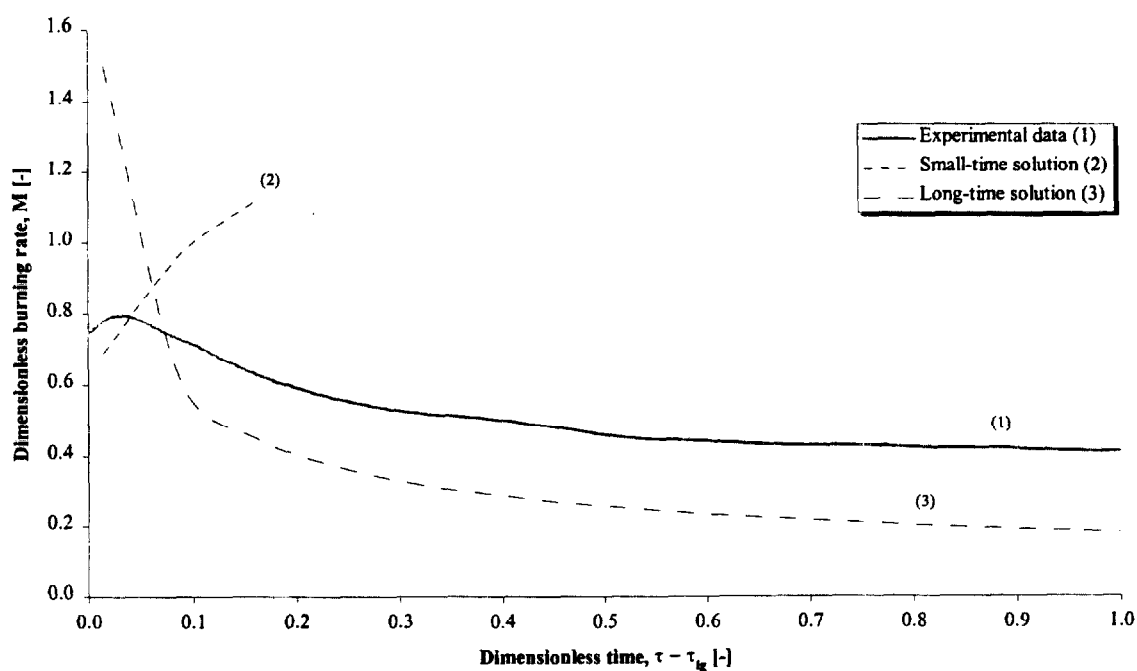
Figure 214. Comparison of dimensionless burning rate using derived properties for species and orientation (1RL1).
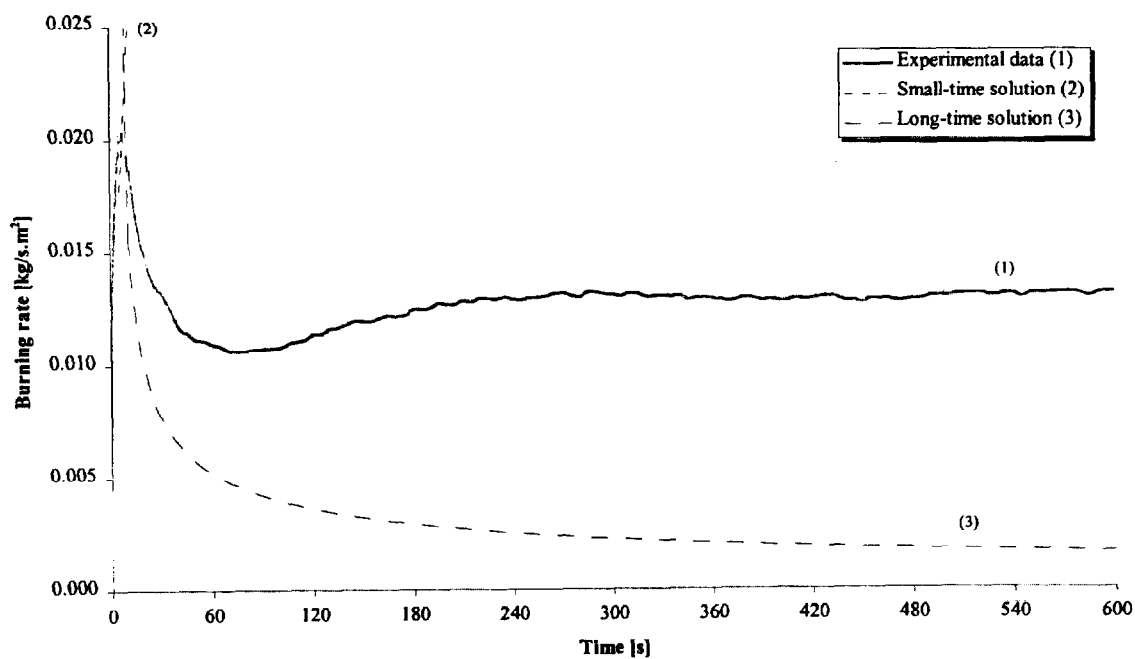
Figure 215. Comparison of burning rate using derived properties for species and orientation (1RL1).

273
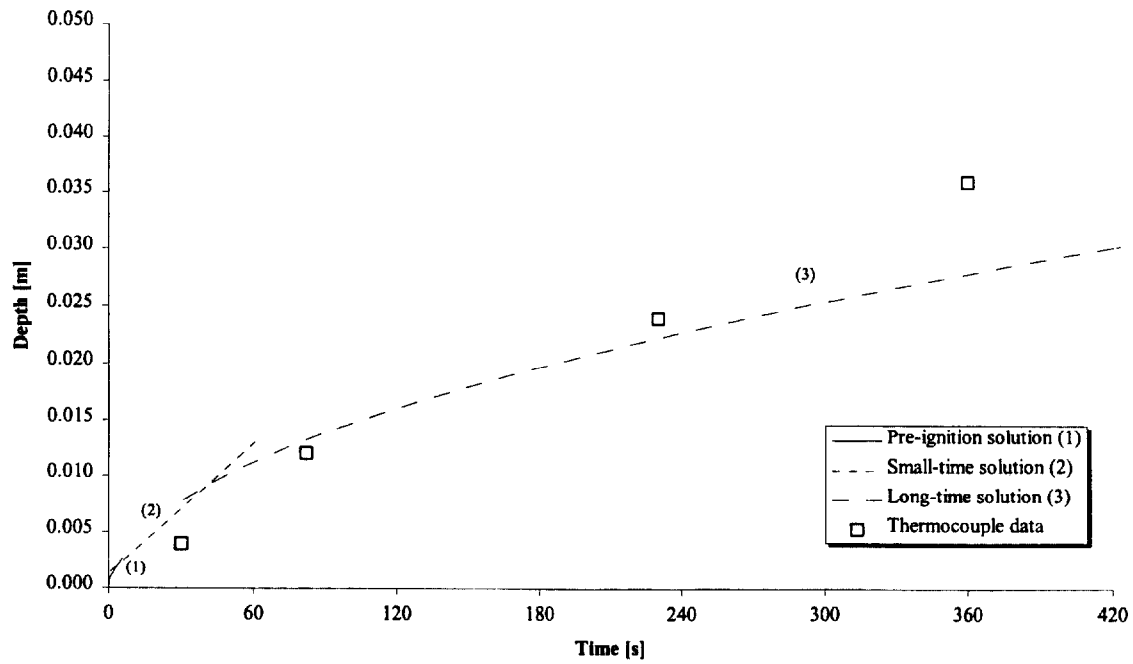
Figure 216. Comparison of measured and calculated thermal penetration depth (1RL1).
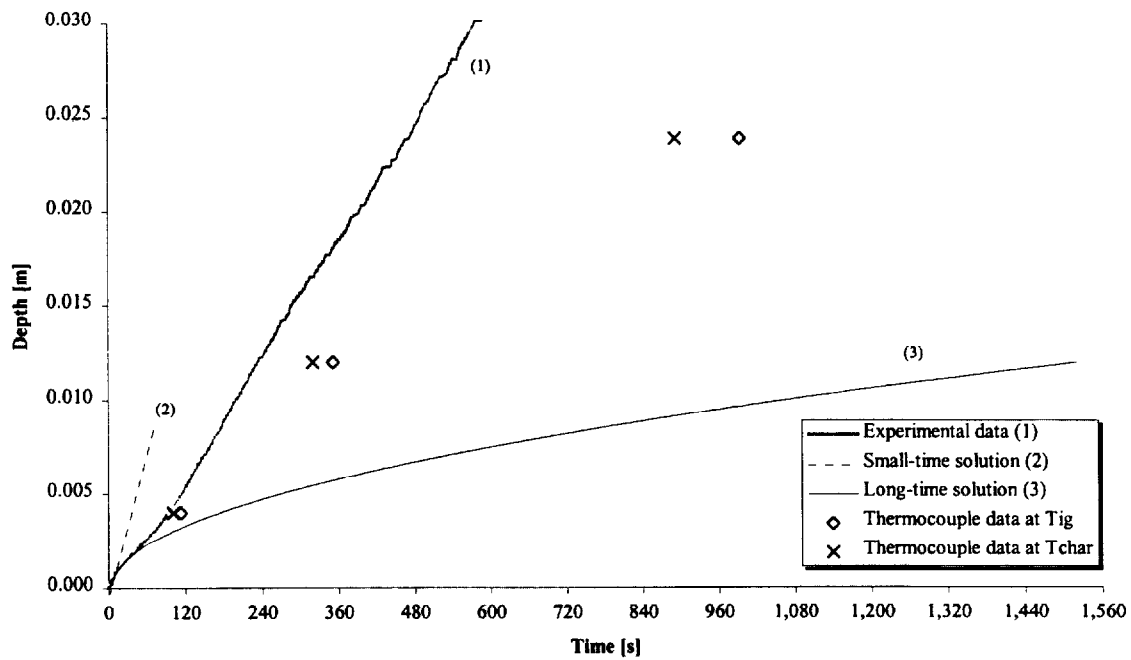
Figure 217. Comparison of estimated char depth from experimental data and the calculated char depth (1RL1).

274

Test (1RL2), Redwood, along grain at 75 kW/m² for 25 minutes.
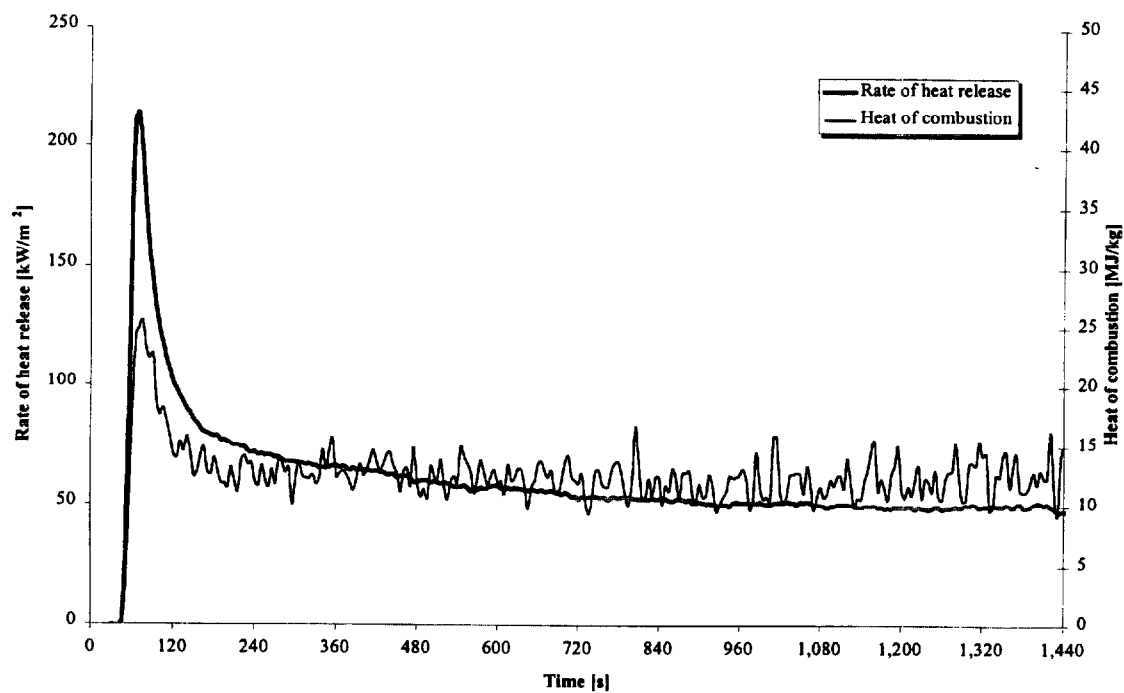
Figure 218. Rate of heat release and heat of combustion (1RL2).
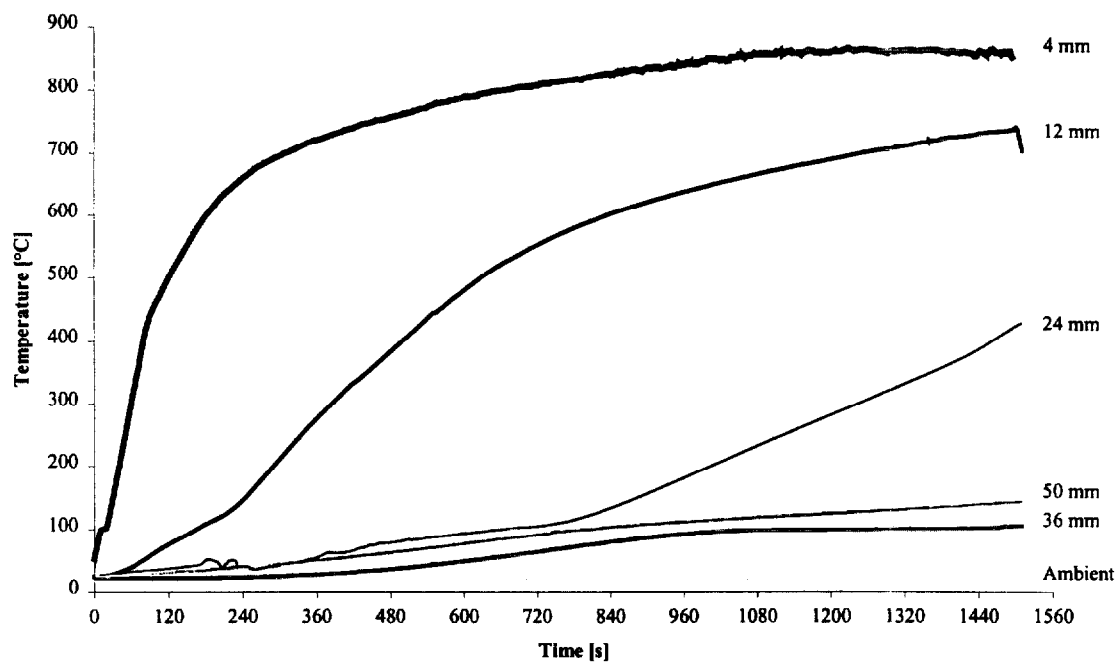
Figure 219. Temperatures measured in sample (1RL2).
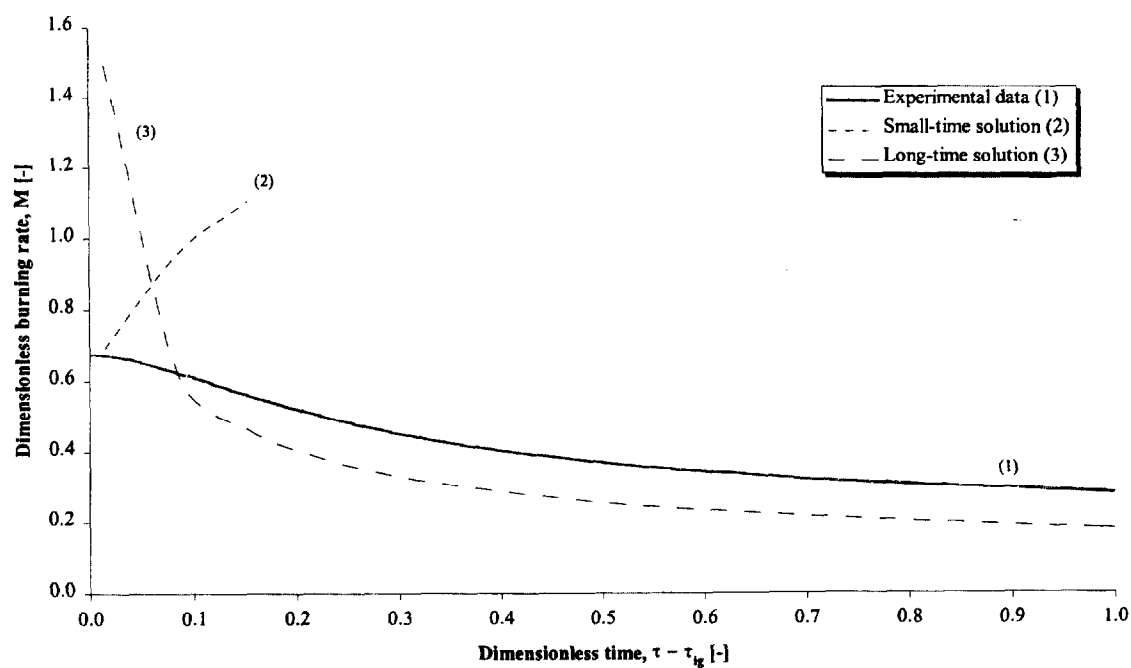
Figure 220. Comparison of dimensionless burning rate using derived properties for species and orientation (1RL2).
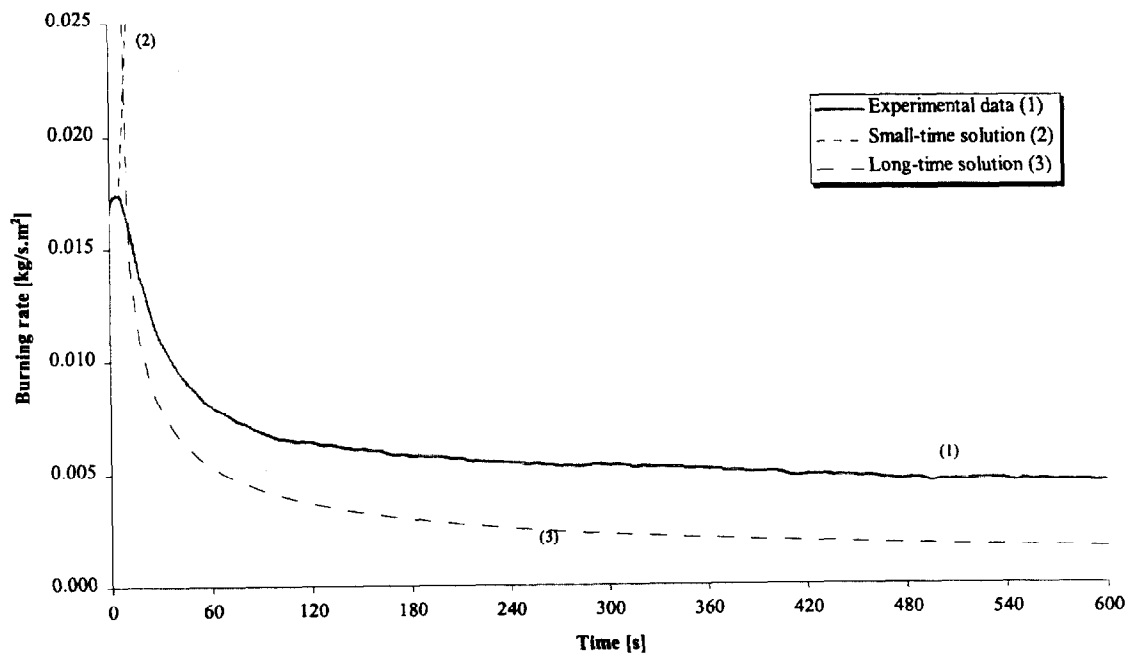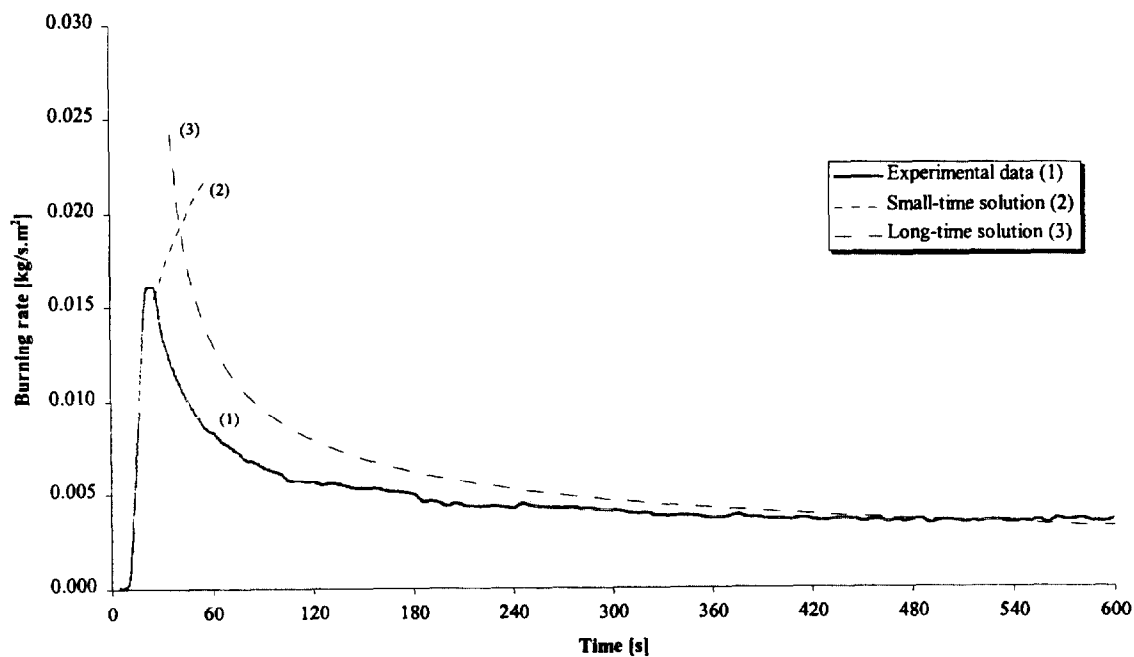

Figure 221. Comparison of burning rate using derived properties for species and orientation (1RL2).
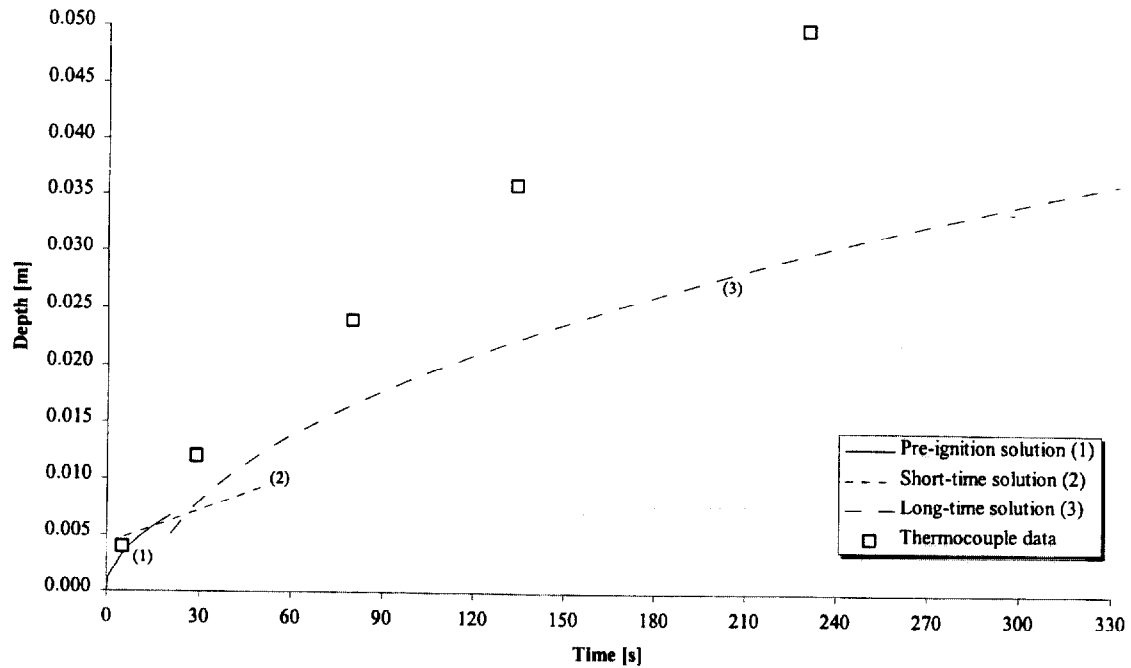
276
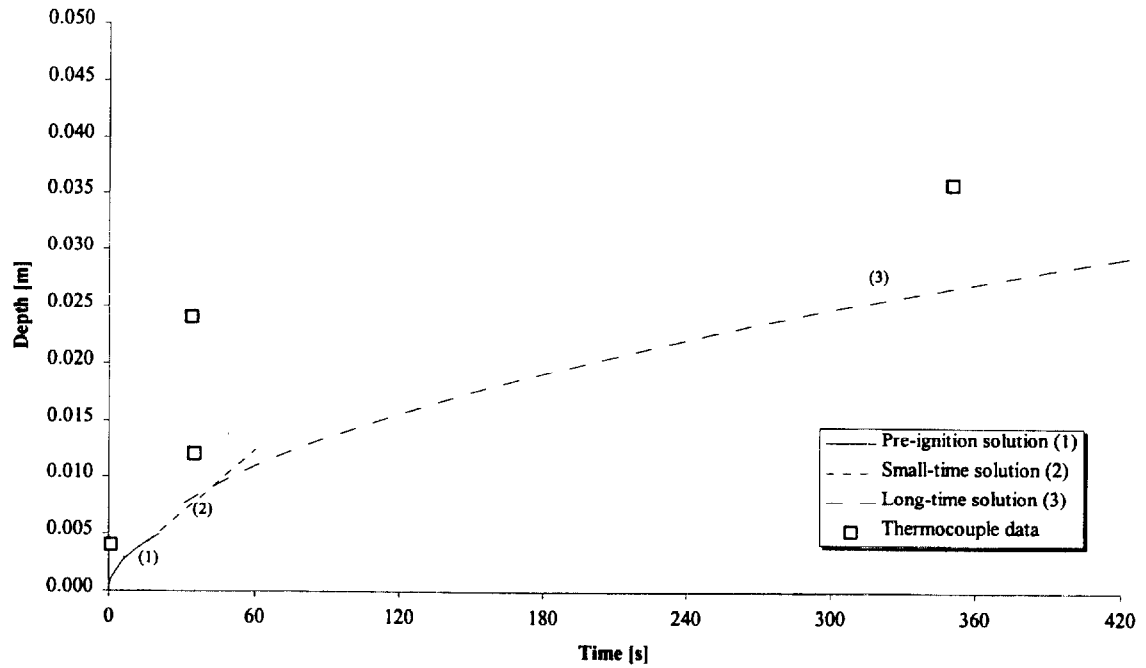
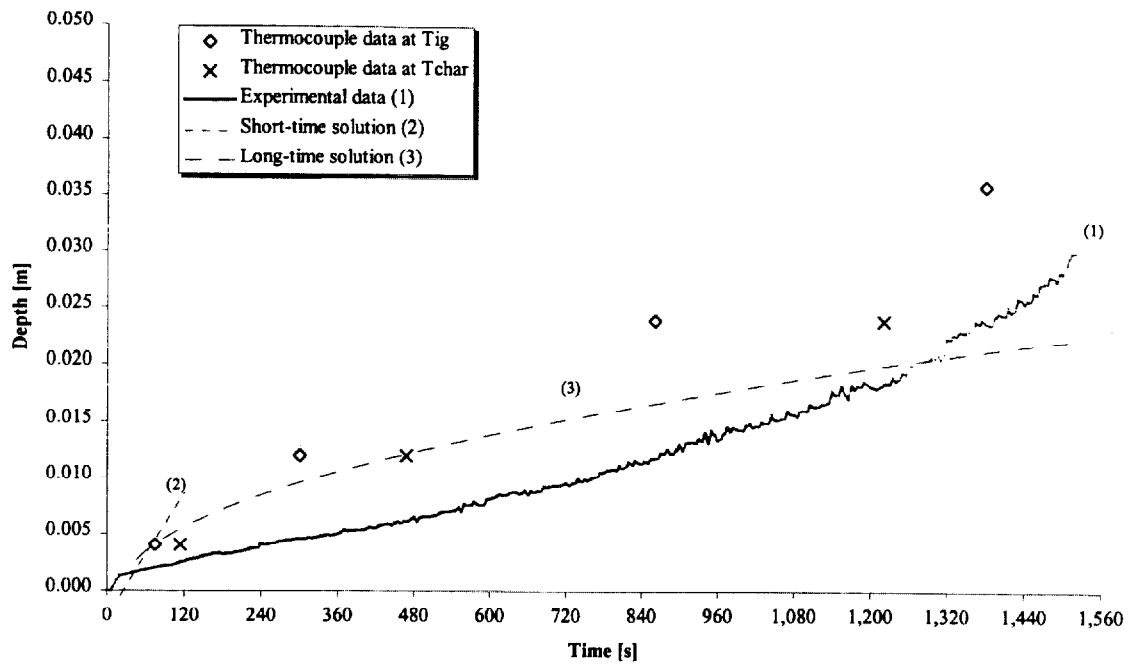**Figure 222.** Comparison of measured and calculated thermal penetration depth (1RL2).
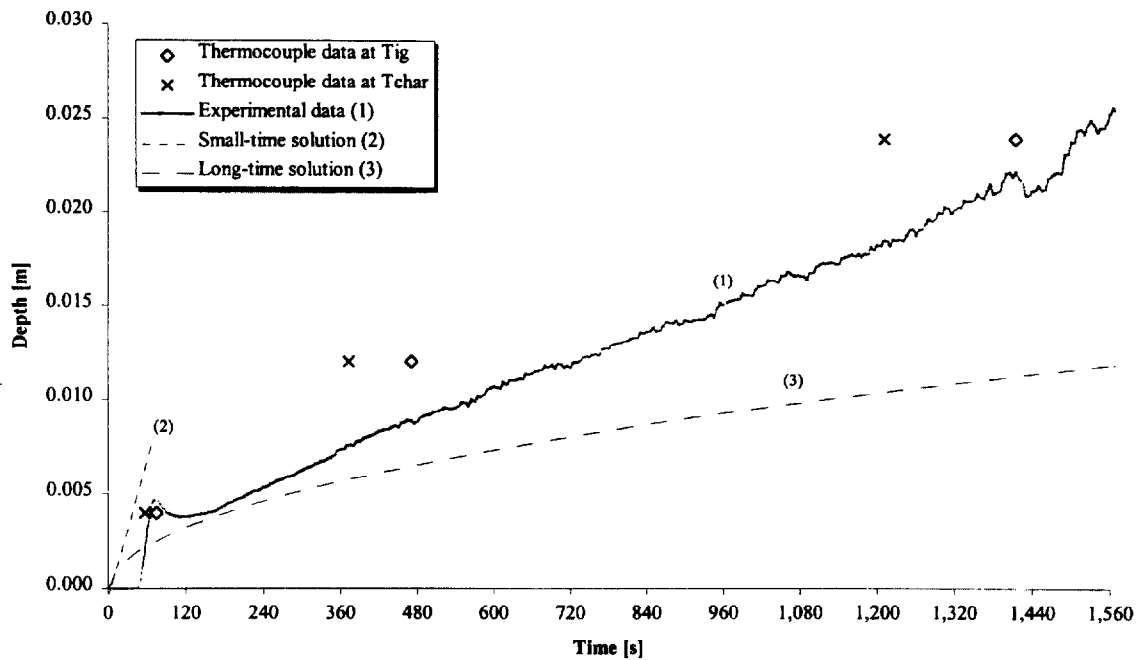
Figure 223. Comparison of estimated char depth from experimental data and the calculated char depth (1RL2).

277

Test (1RL3), Redwood, along grain at 25 kW/m^2 for 25 minutes.
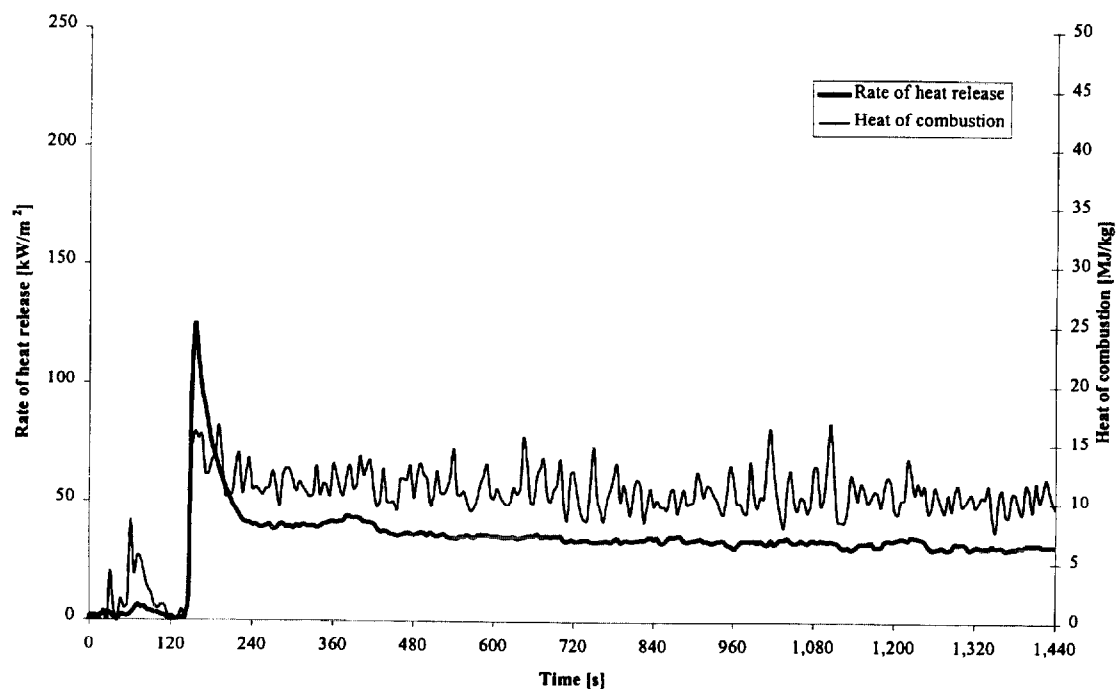
Figure 224. Rate of heat release and heat of combustion (1RL3).
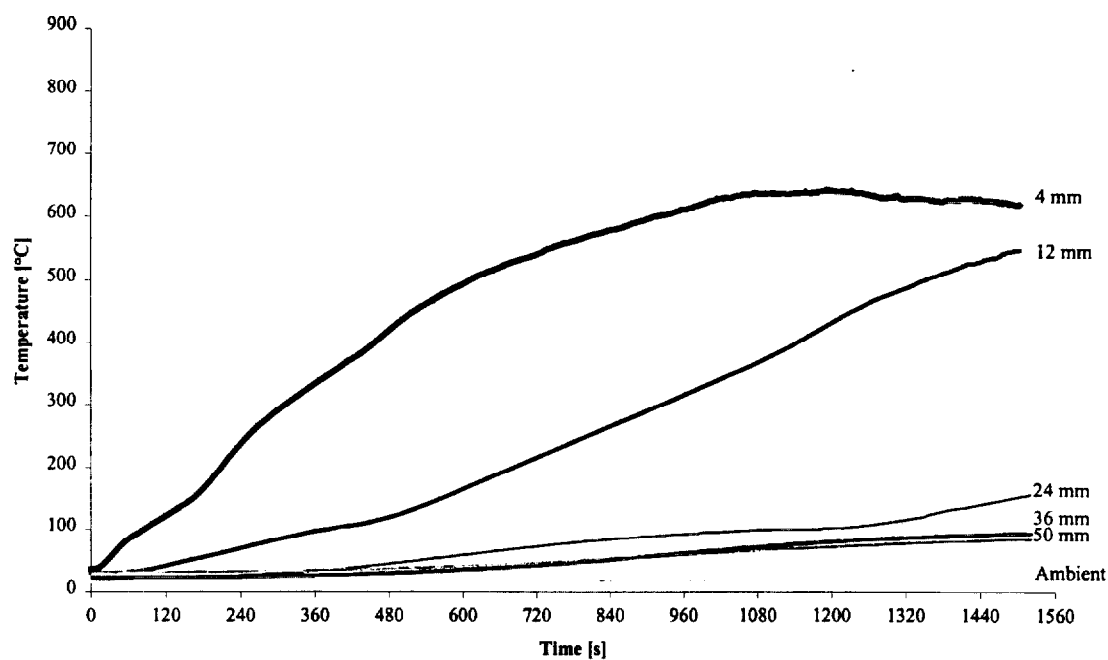
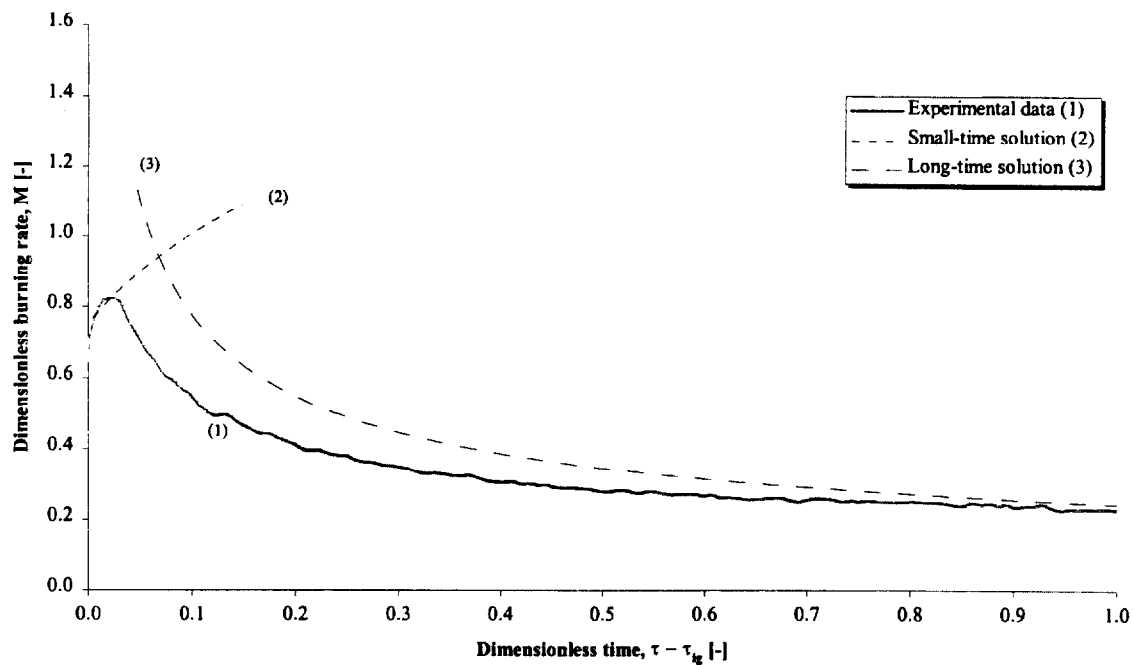**Figure 225.** Temperatures measured in sample (1RL3).
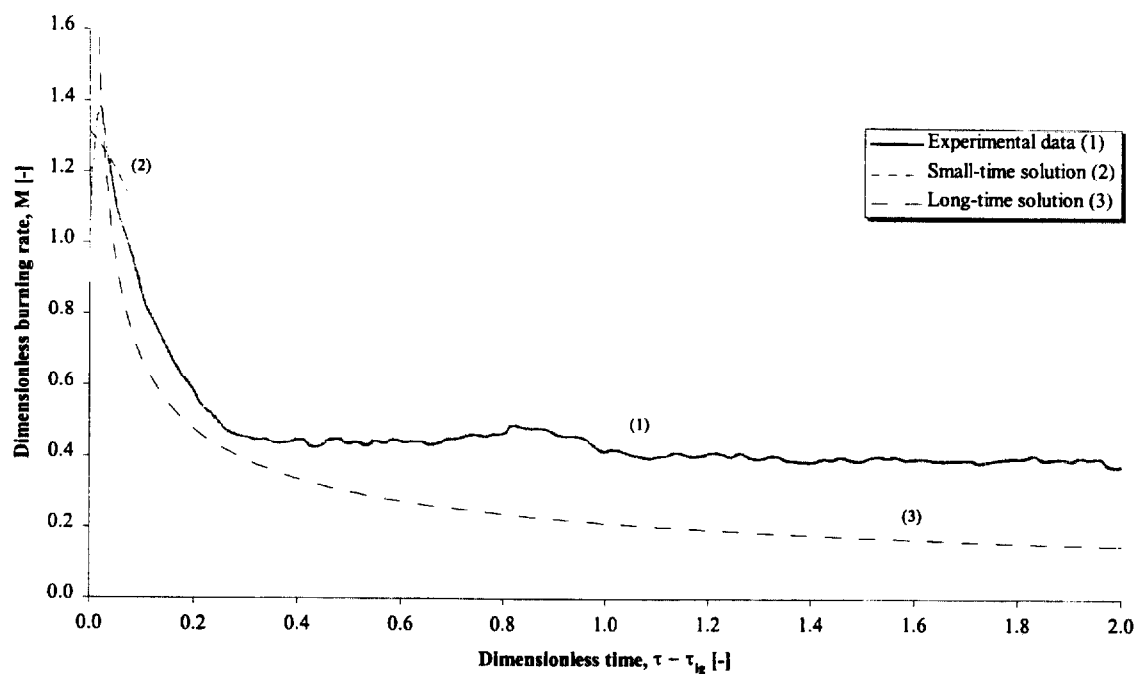
Figure 226. Comparison of dimensionless burning rate using derived properties for species and orientation (1RL3).
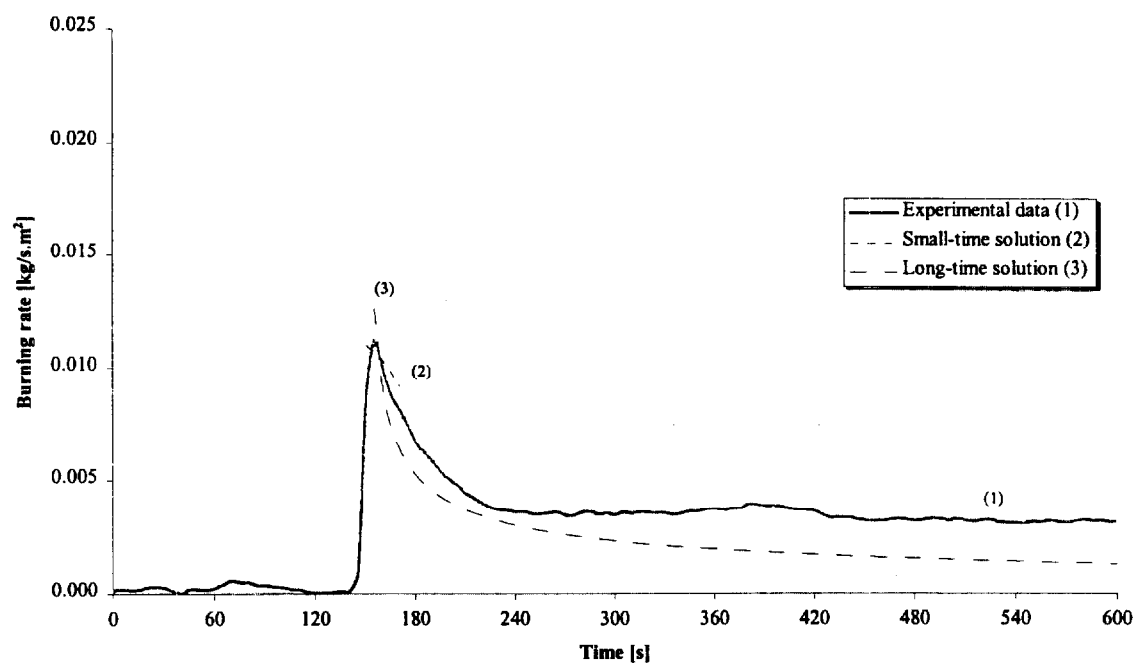
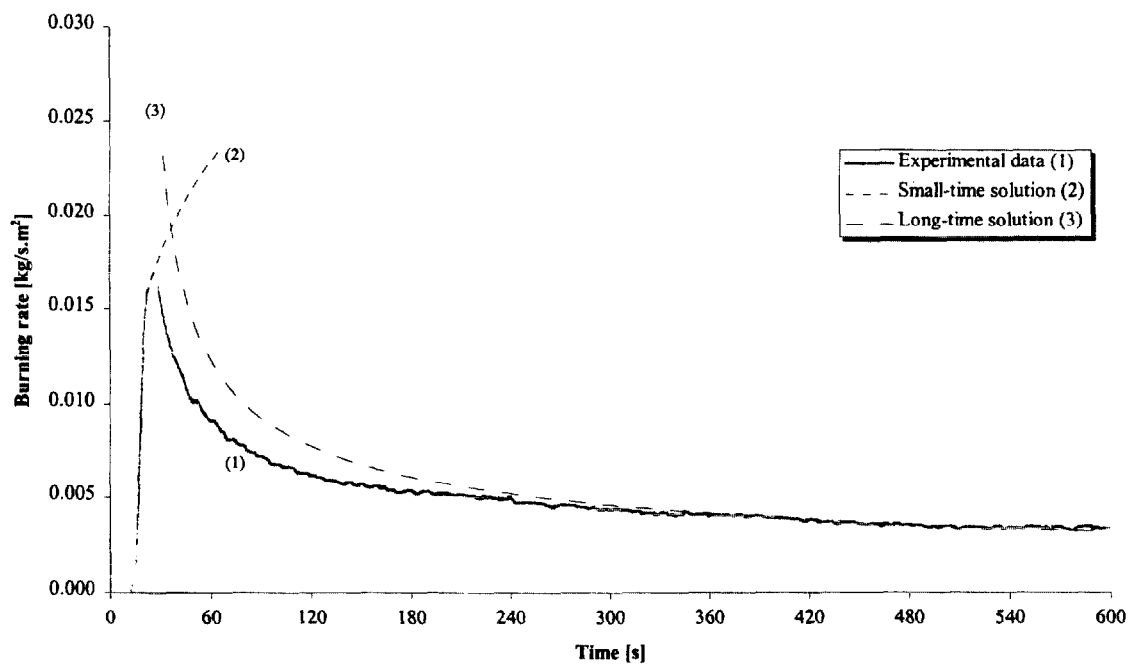**Figure 227.** Comparison of burning rate using derived properties for species and orientation (1RL3).
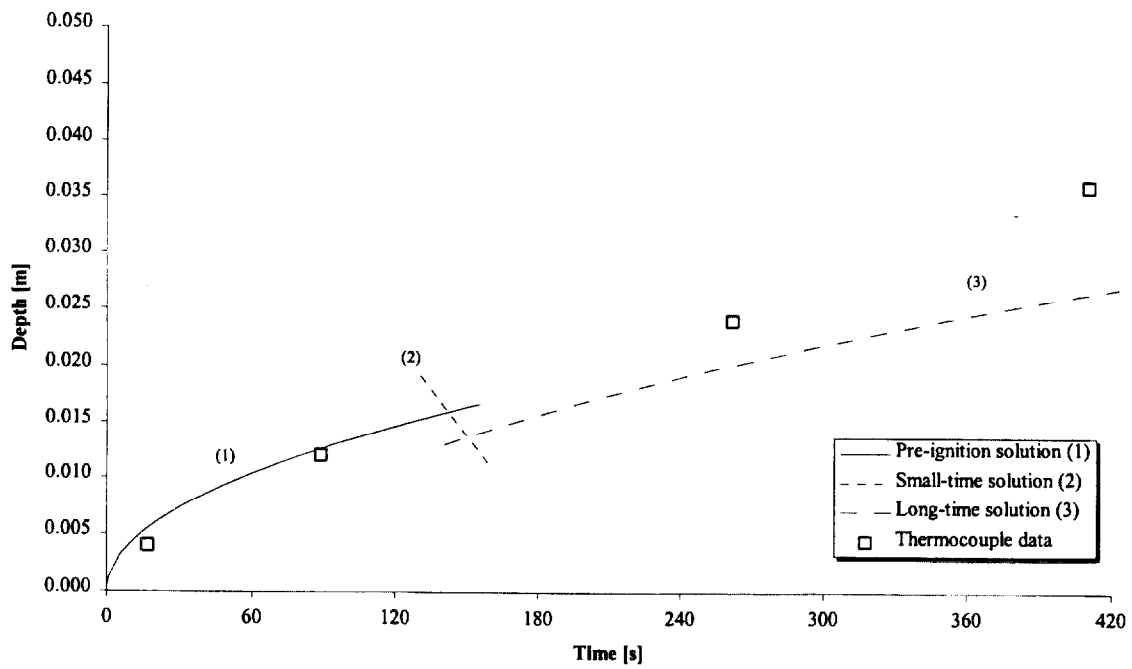
Figure 228. Comparison of measured and calculated thermal penetration depth (1RL3).
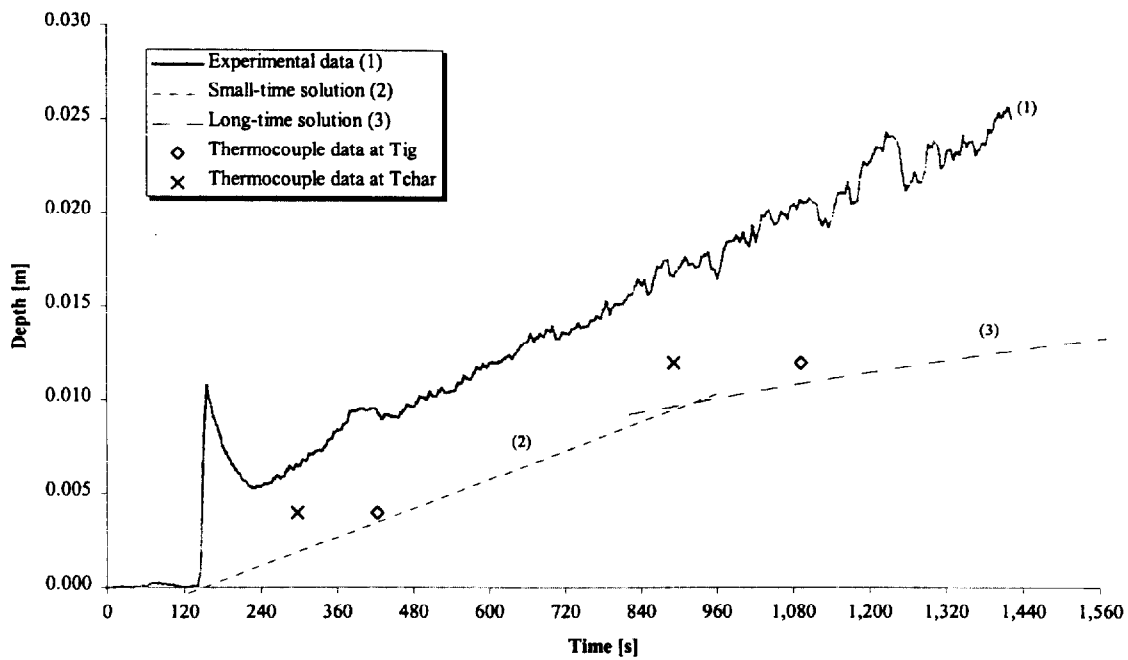
Figure 229. Comparison of estimated char depth from experimental data and the calculated char depth (1RL3).

280

Test (1RL4), Redwood, along grain at 75 kW/m^2 for 25 minutes.
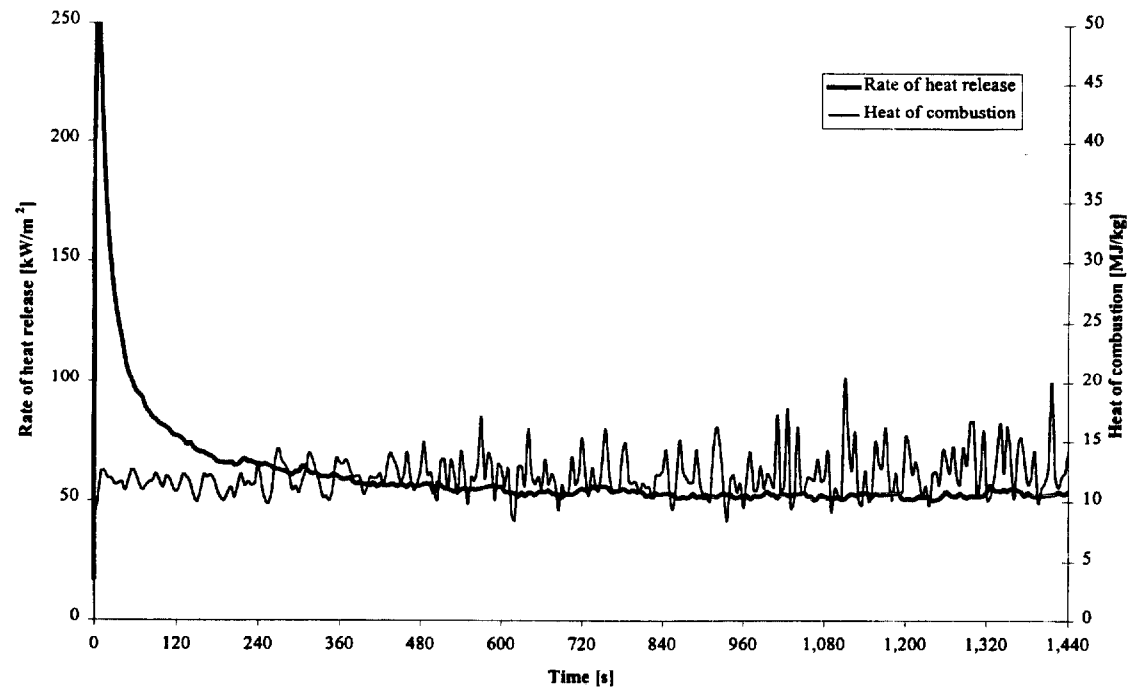
Figure 230. Rate of heat release and heat of combustion (1RL4).
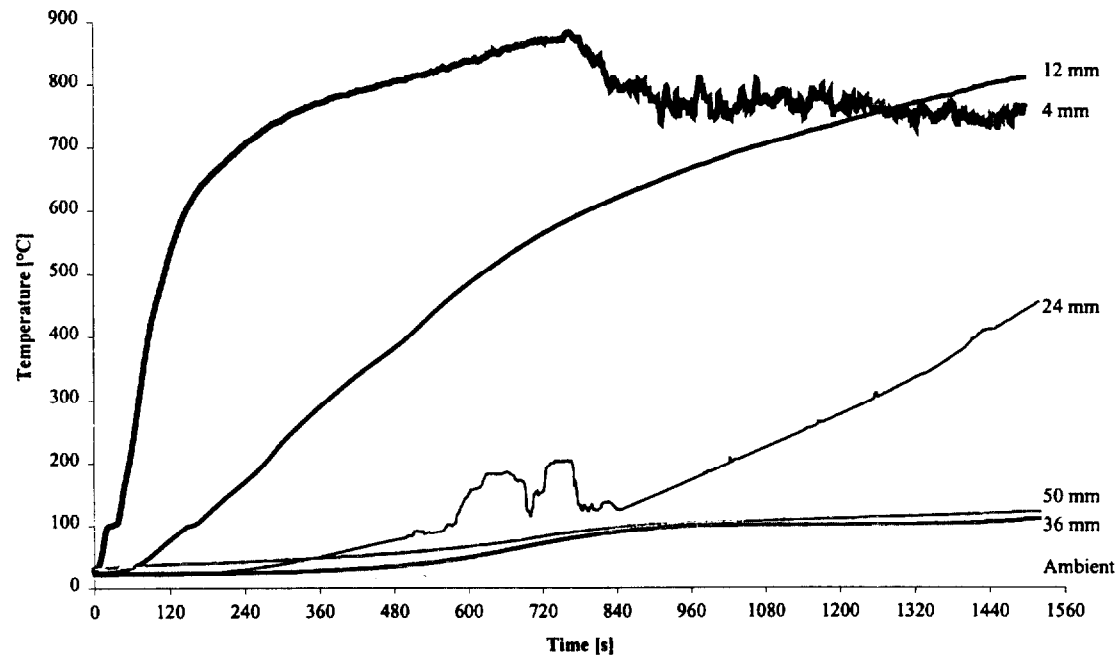
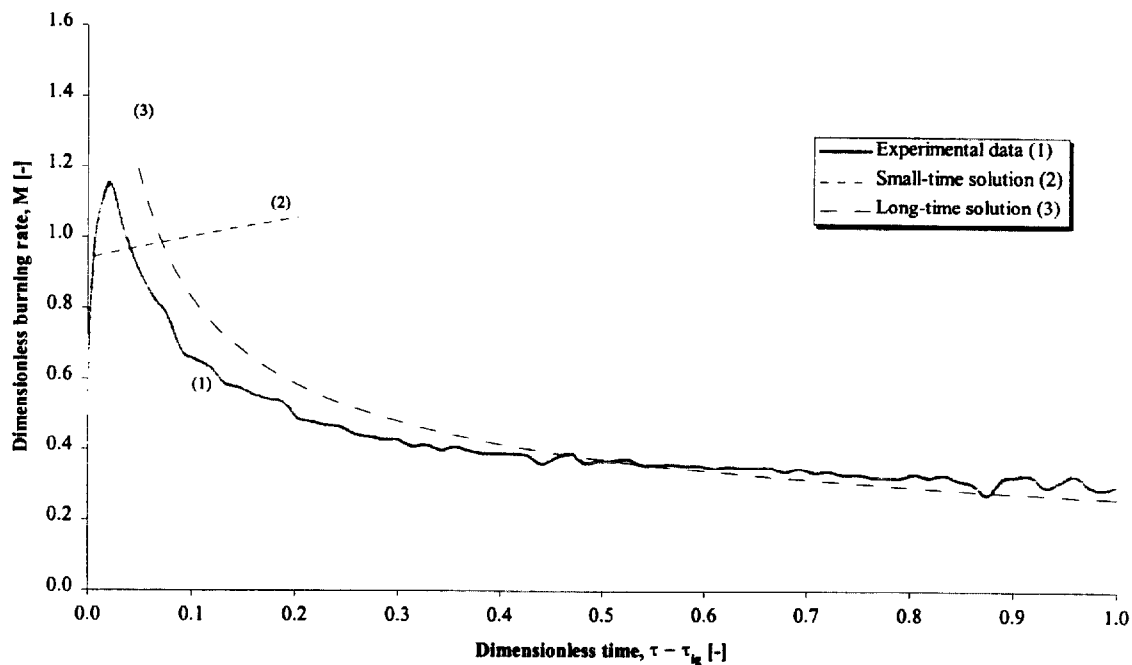**Figure 231.** Temperatures measured in sample (1RL4).
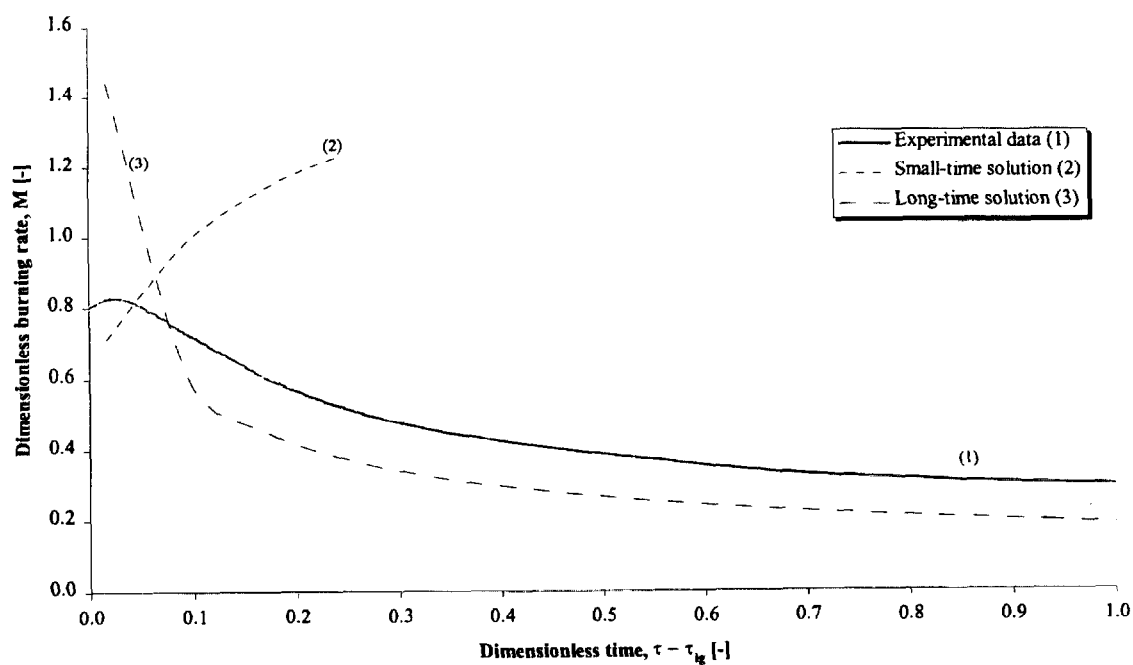
Figure 232. Comparison of dimensionless burning rate using derived properties for species and orientation (1RL4).
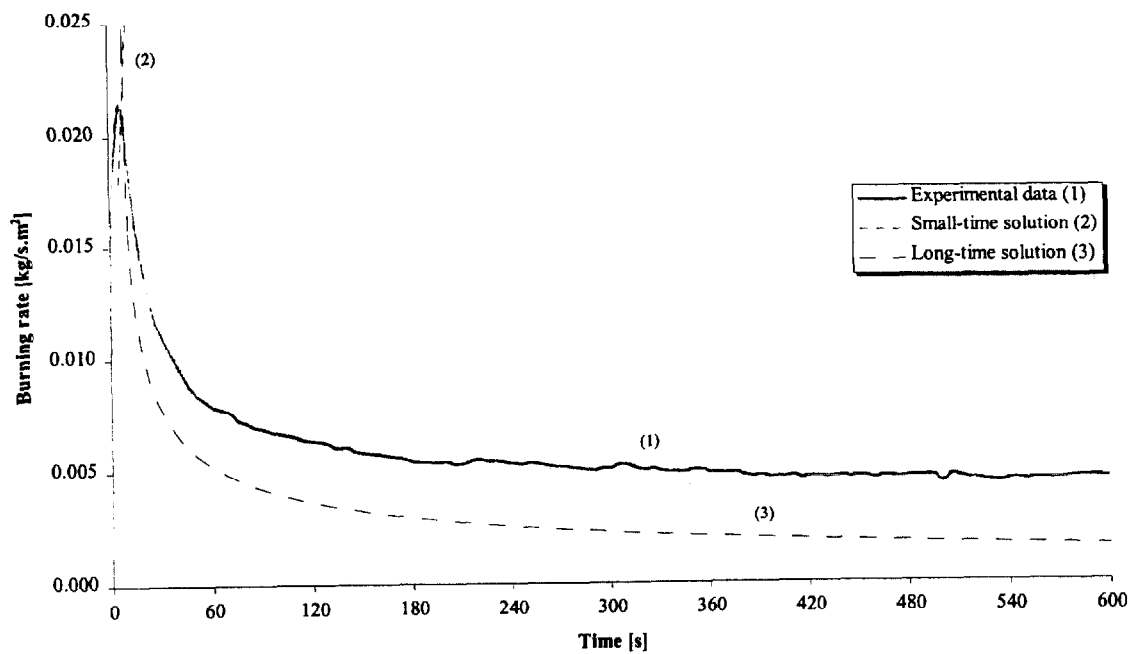
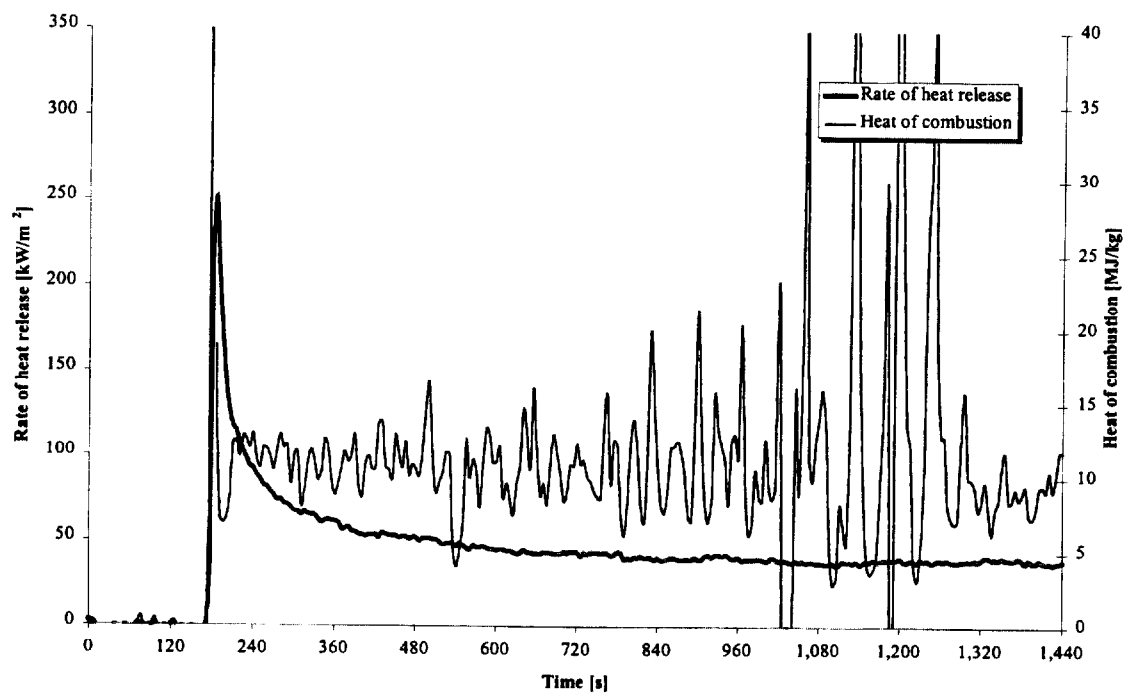**Figure 233.** Comparison of burning rate using derived properties for species and orientation (1RL4).

282
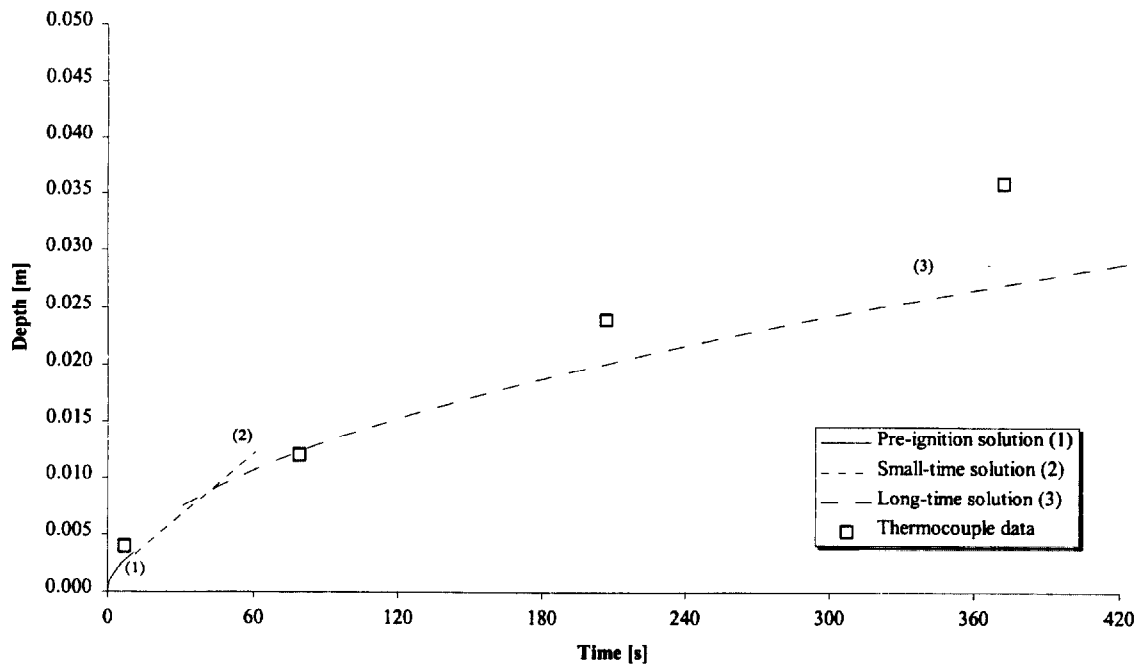
Figure 234. Comparison of measured and calculated thermal penetration depth (1RL4).
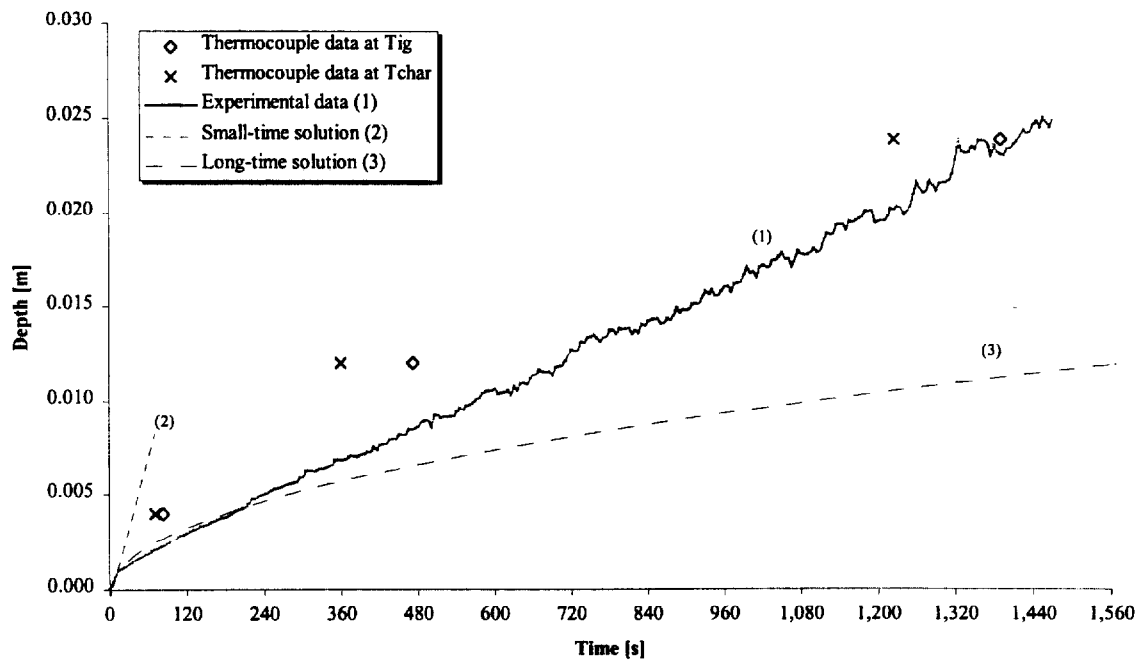
Figure 235. Comparison of estimated char depth from experimental data and the calculated char depth (1RL4).

Test (1RL6), Redwood, along grain at 50 kW/m^2 for 25 minutes.
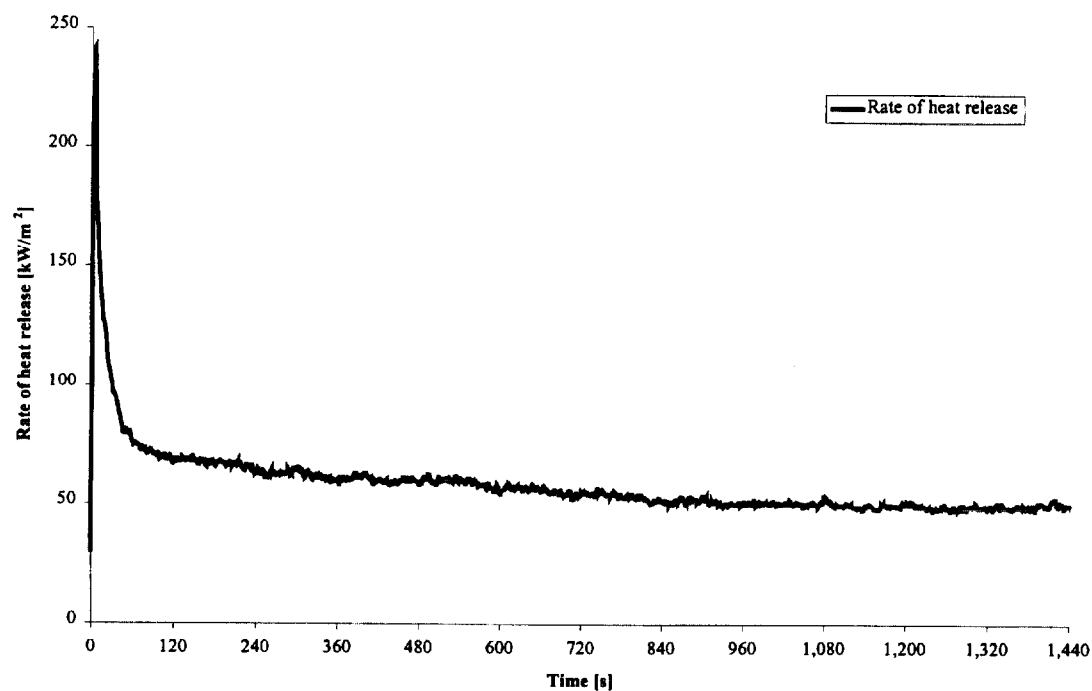
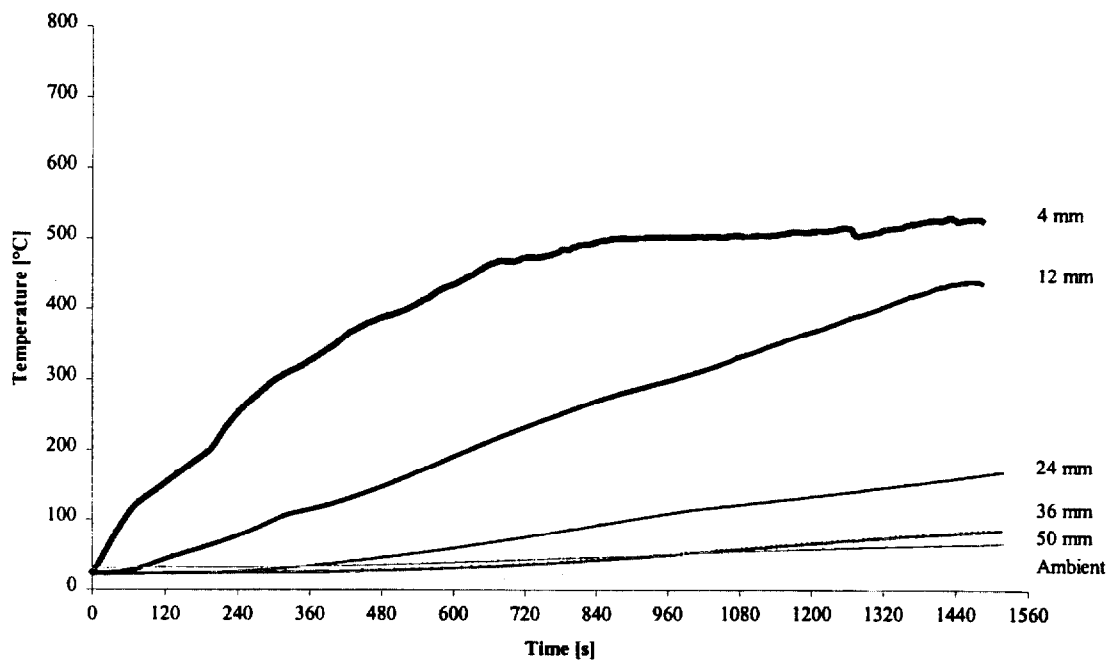

Figure 236. Rate of heat release (1RL6).
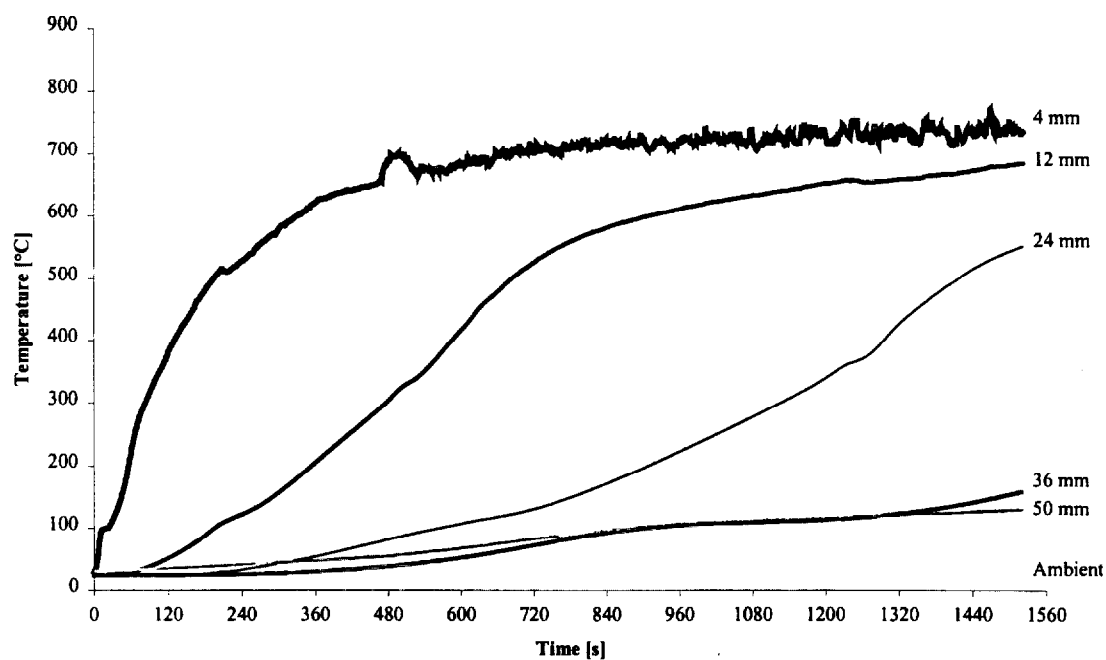
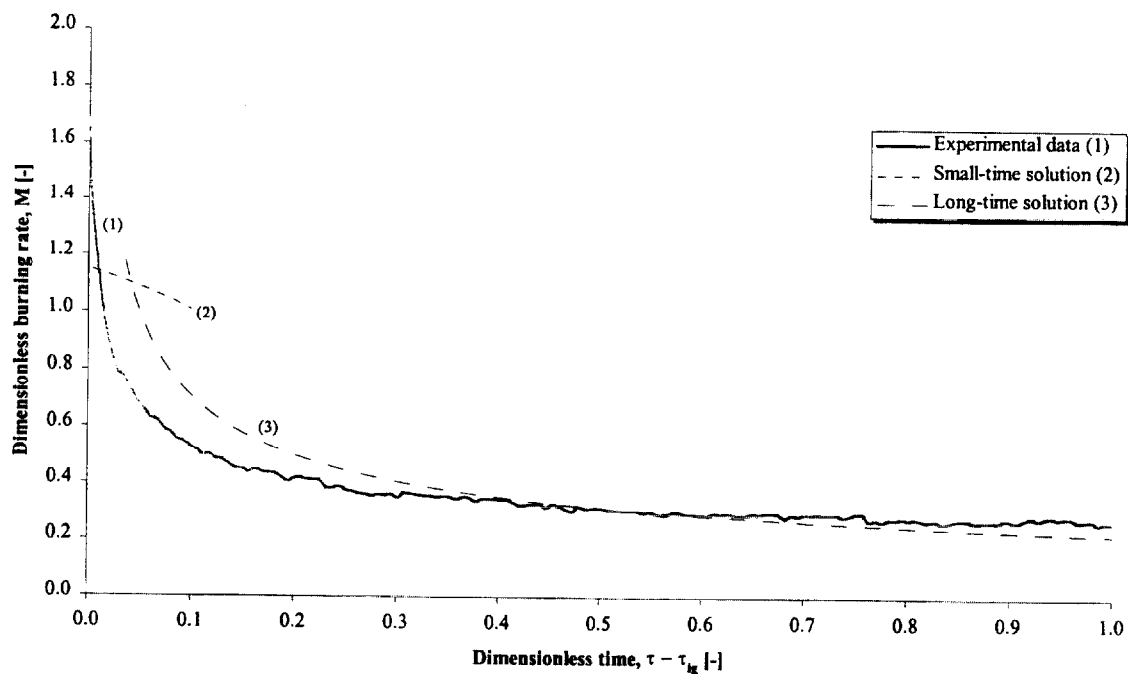**Figure 237.** Temperatures measured in sample (1RL6).
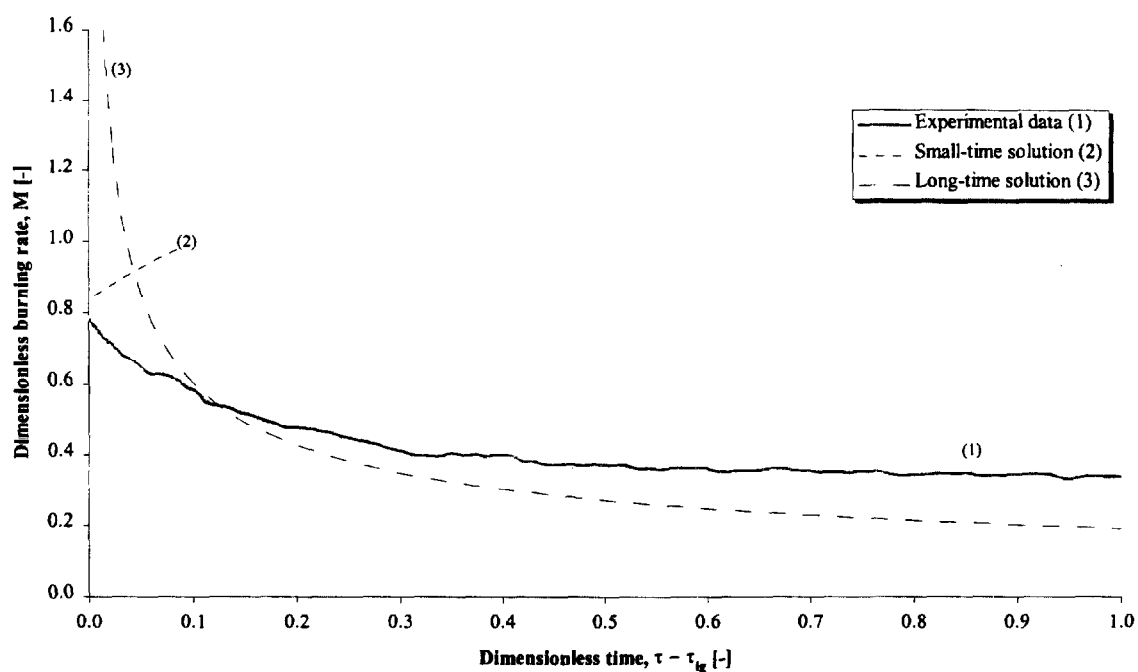
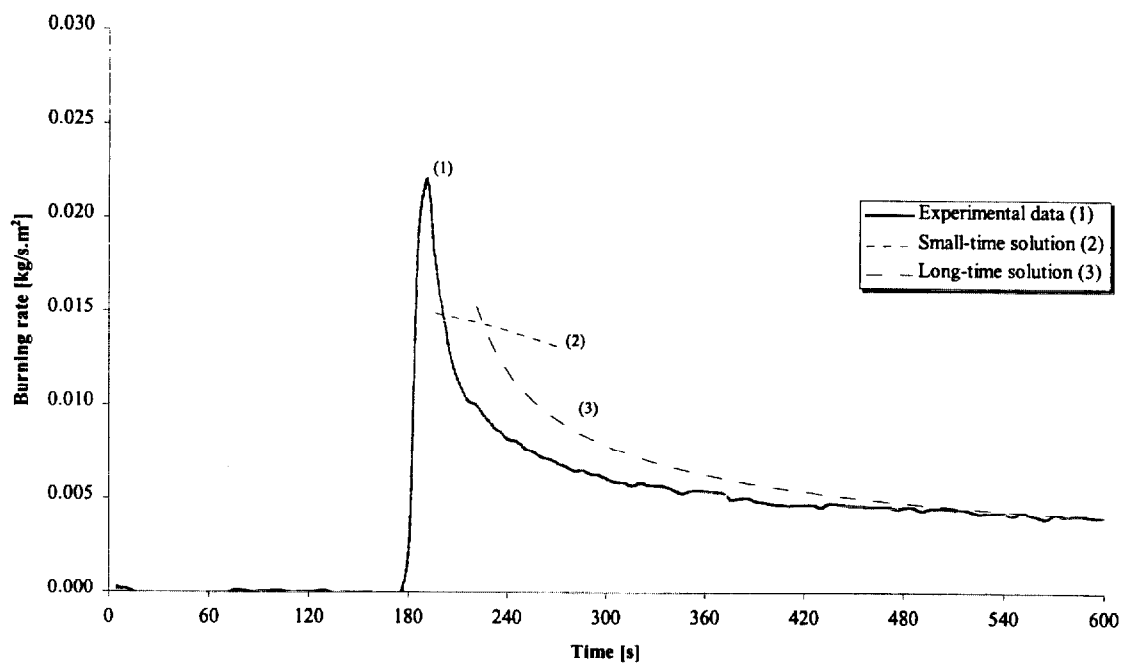**Figure 238.** Comparison of dimensionless burning rate using derived properties for species and orientation (1RL6).

Figure 239. Comparison of burning rate using derived properties for species and orientation (1RL6).

Figure 240. Comparison of measured and calculated thermal penetration depth (1RL6).
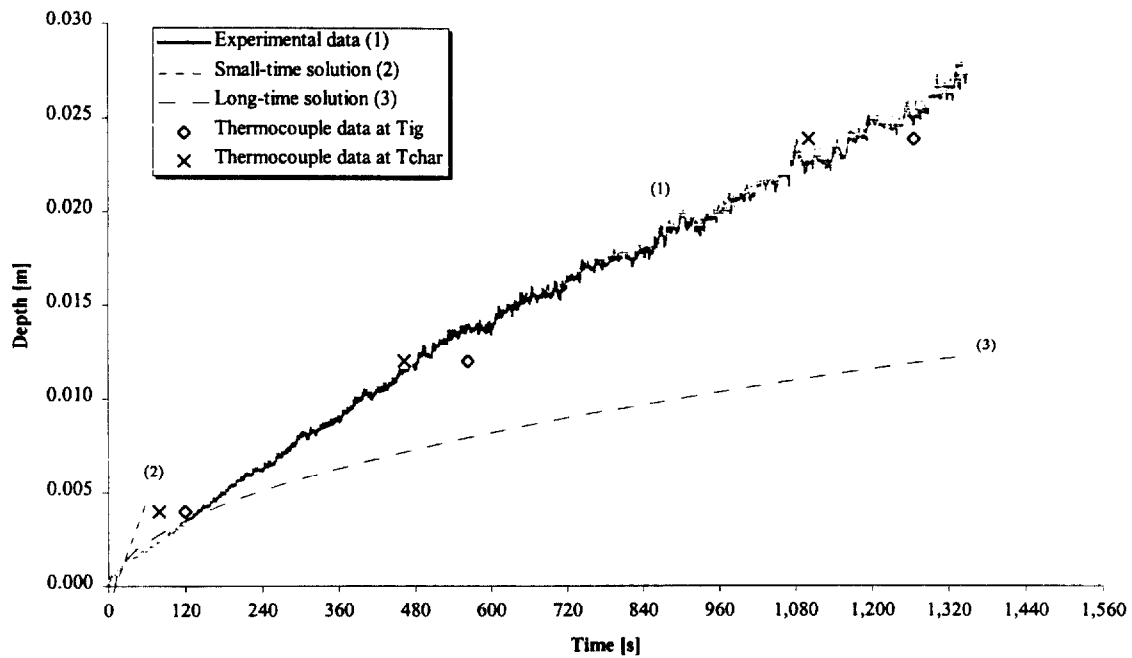
Figure 241. Comparison of estimated char depth from experimental data and the calculated char depth (1RL6).

286

Test (1RL7), Redwood, along grain at 50 kW/m² for 25 minutes.
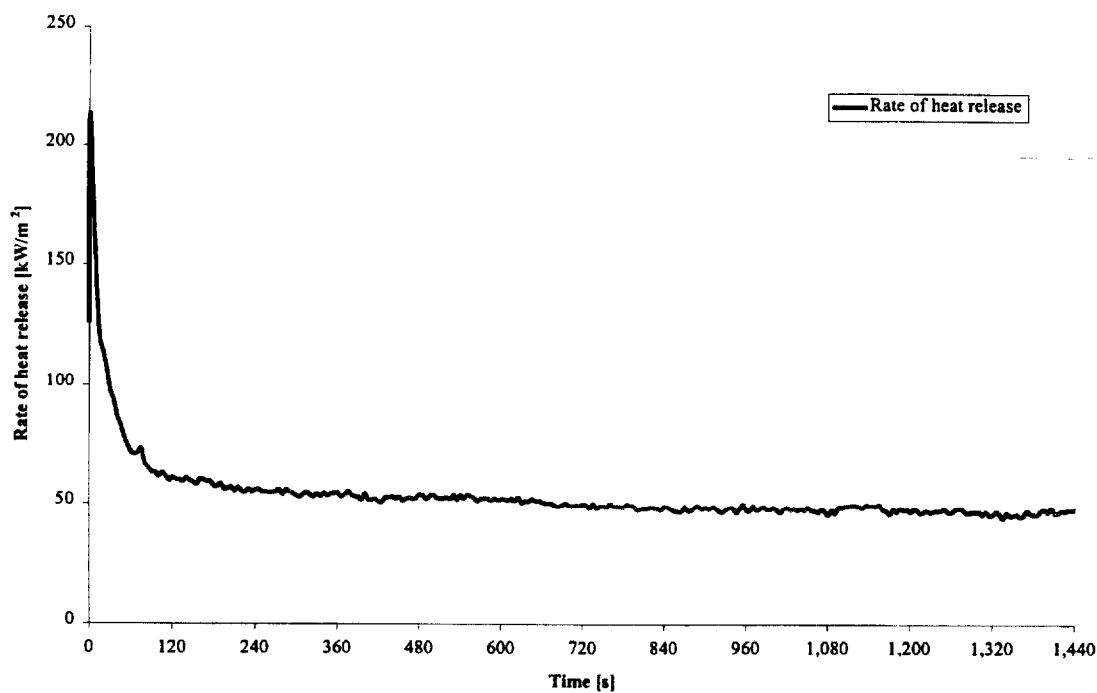
Figure 242. Rate of heat release (1RL7).

Figure 243. Temperatures measured in sample (1RL7).

287

Figure 244. Comparison of dimensionless burning rate using derived properties for species and orientation (1RL7).

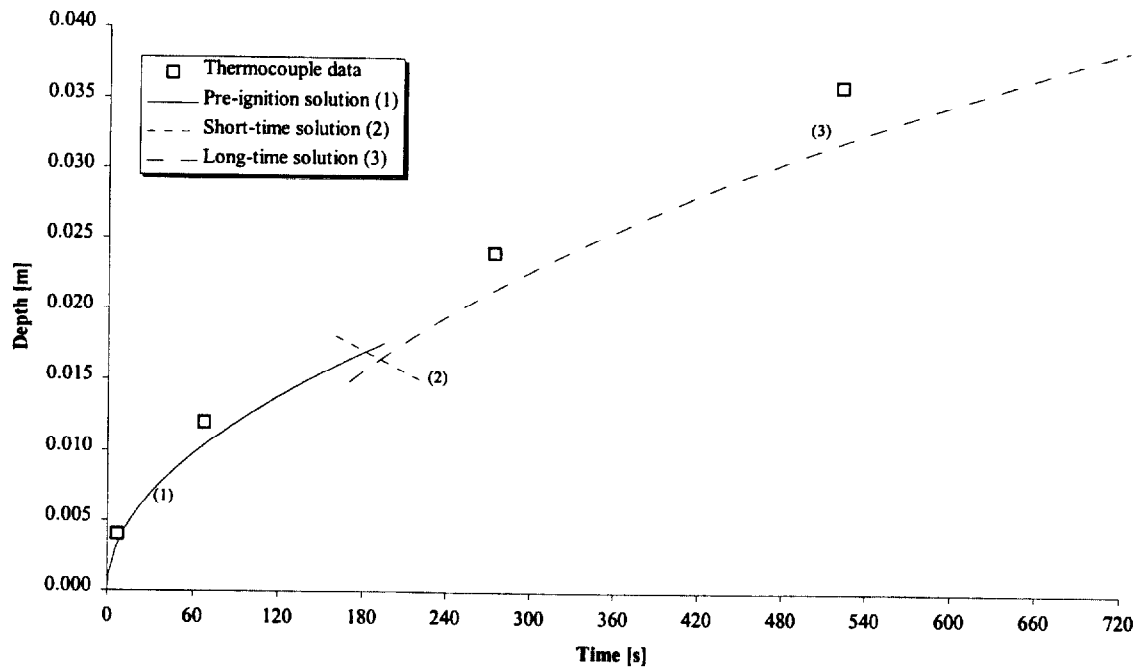**Figure 245.** Comparison of burning rate using derived properties for species and orientation (1RL7).

288

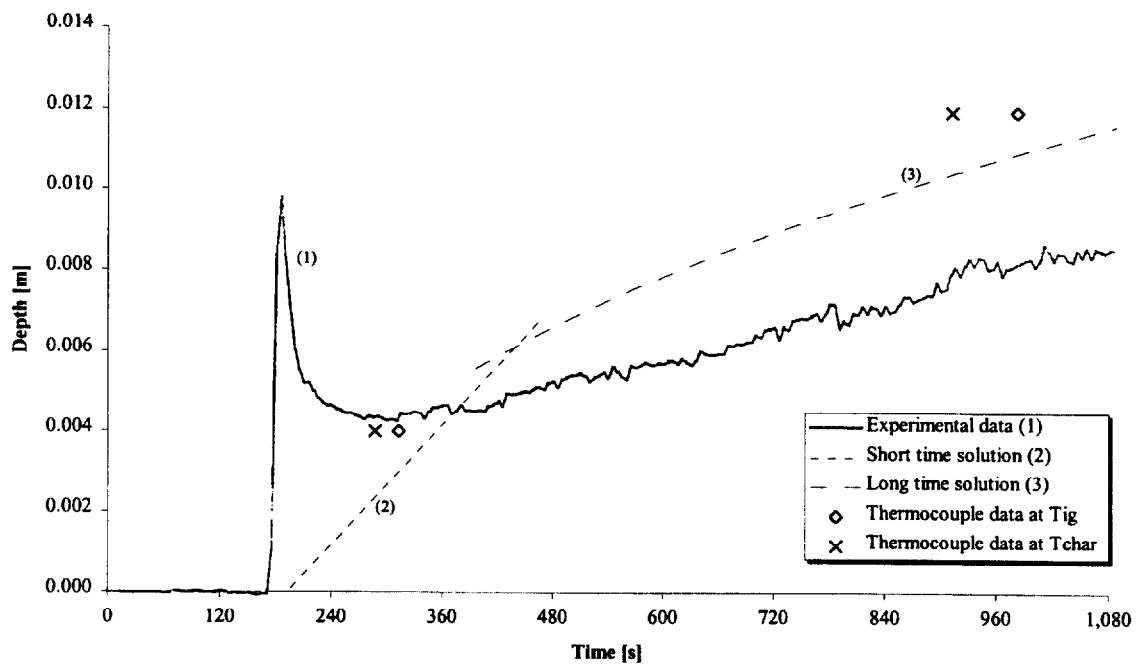**Figure 246.** Comparison of measured and calculated thermal penetration depth (1RL7).

Figure 247. Comparison of estimated char depth from experimental data and the calculated char depth (1RL7).

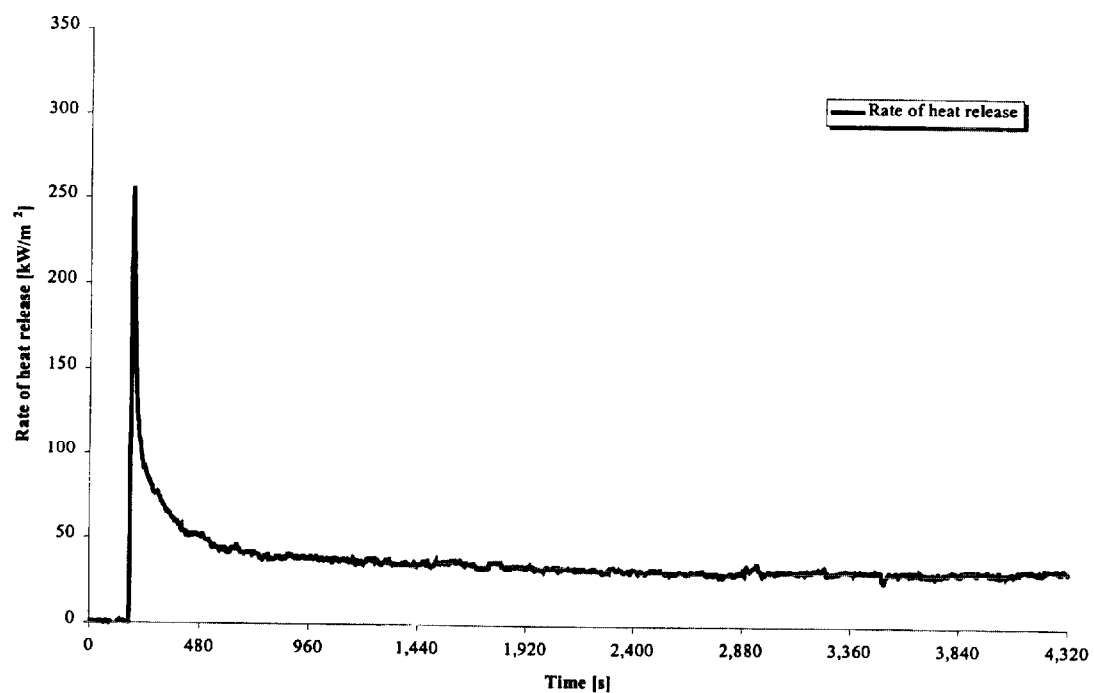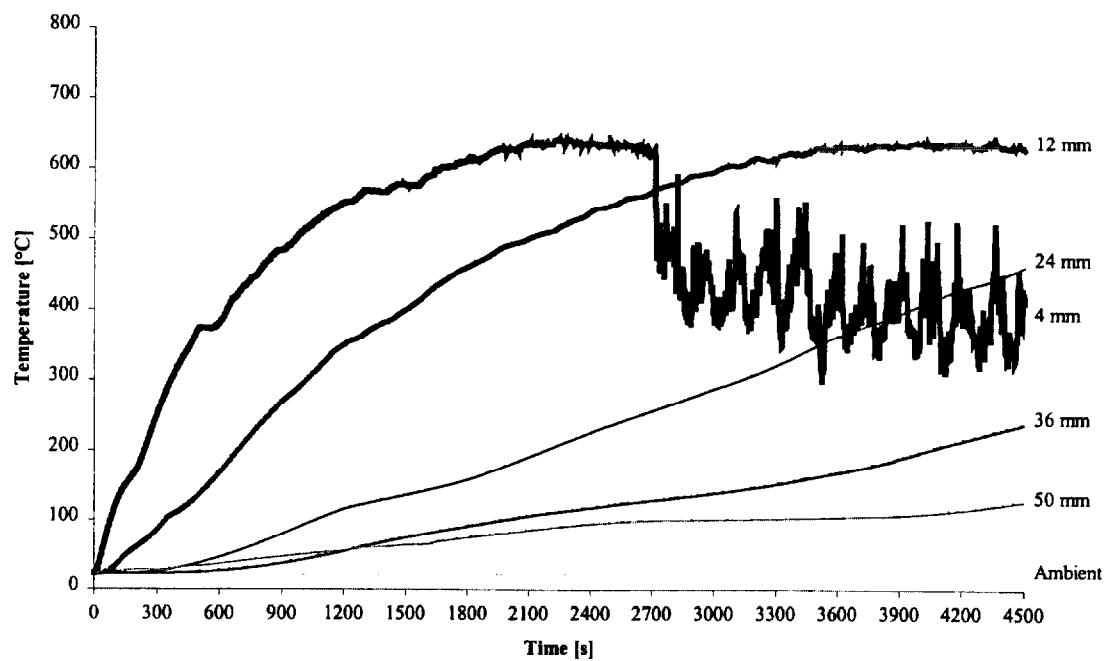Test (1RL8), Redwood, along grain at 50 kW/m^2 for 25 minutes.
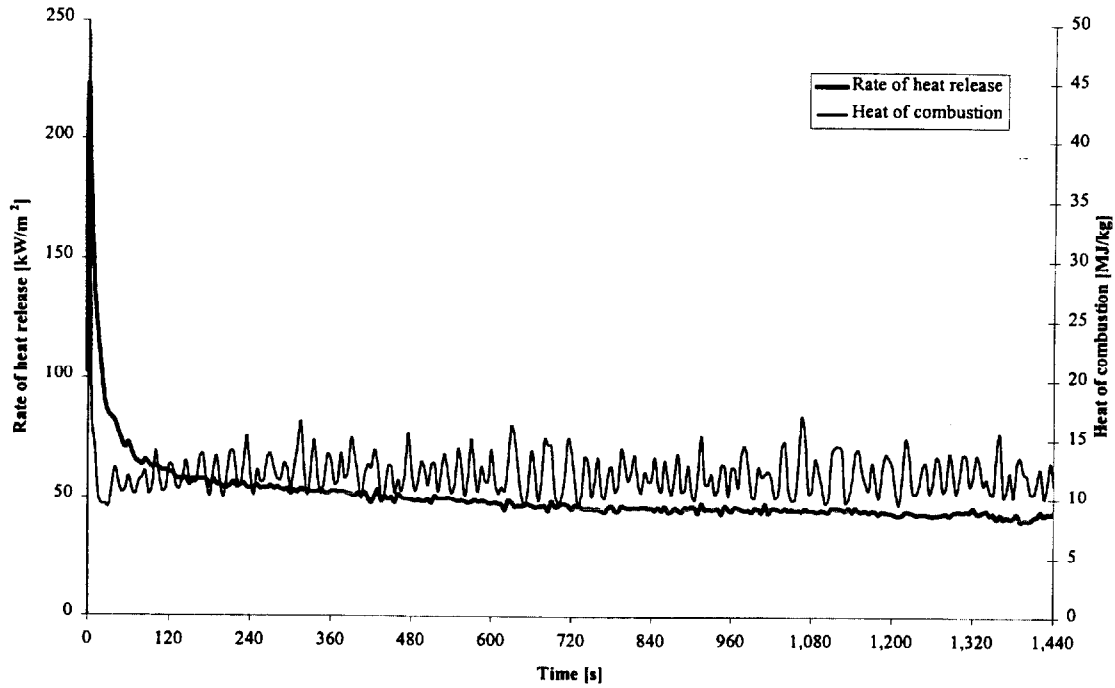
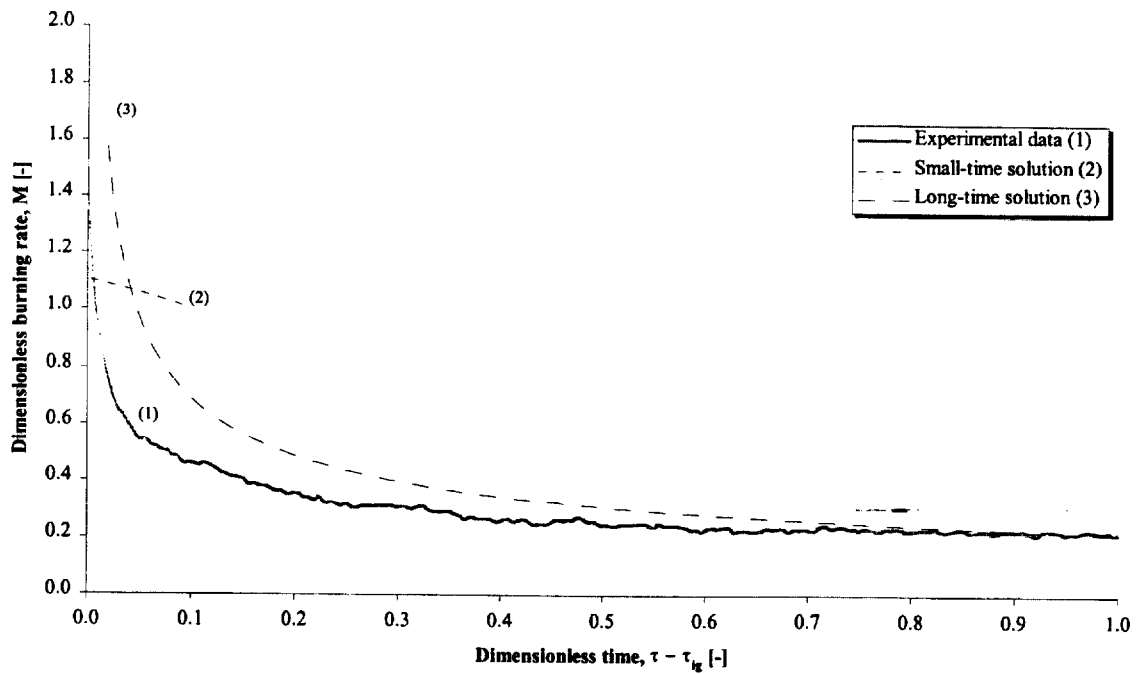**Figure 248.** Rate of heat release and heat of combustion (1RL8).
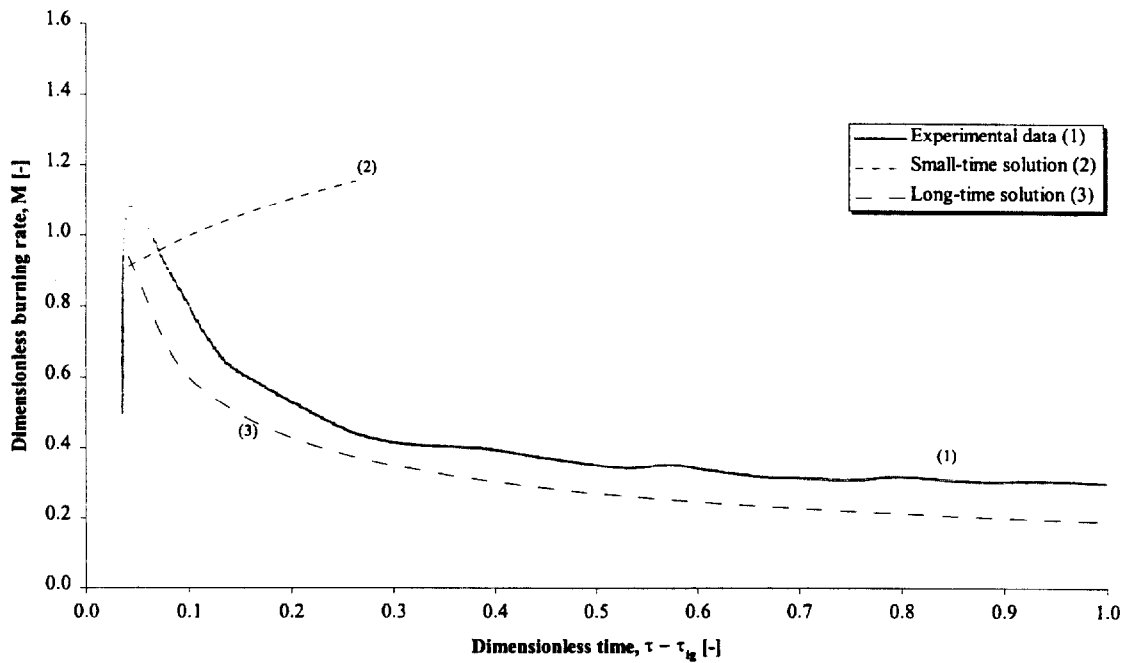
Figure 249. Comparison of dimensionless burning rate using derived properties for species and orientation (1RL8).
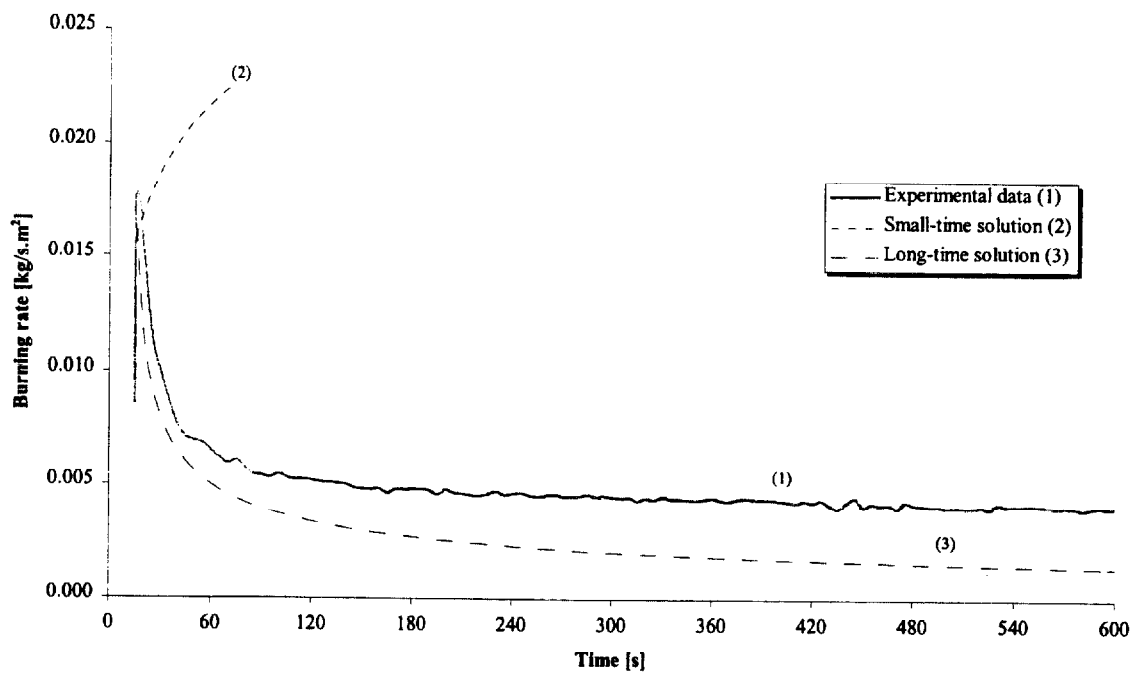
Figure 250. Comparison of burning rate using derived properties for species and orientation (1RL8).

Test (1RL9), Redwood, along grain at 35 kW/m^2 for 25 minutes.
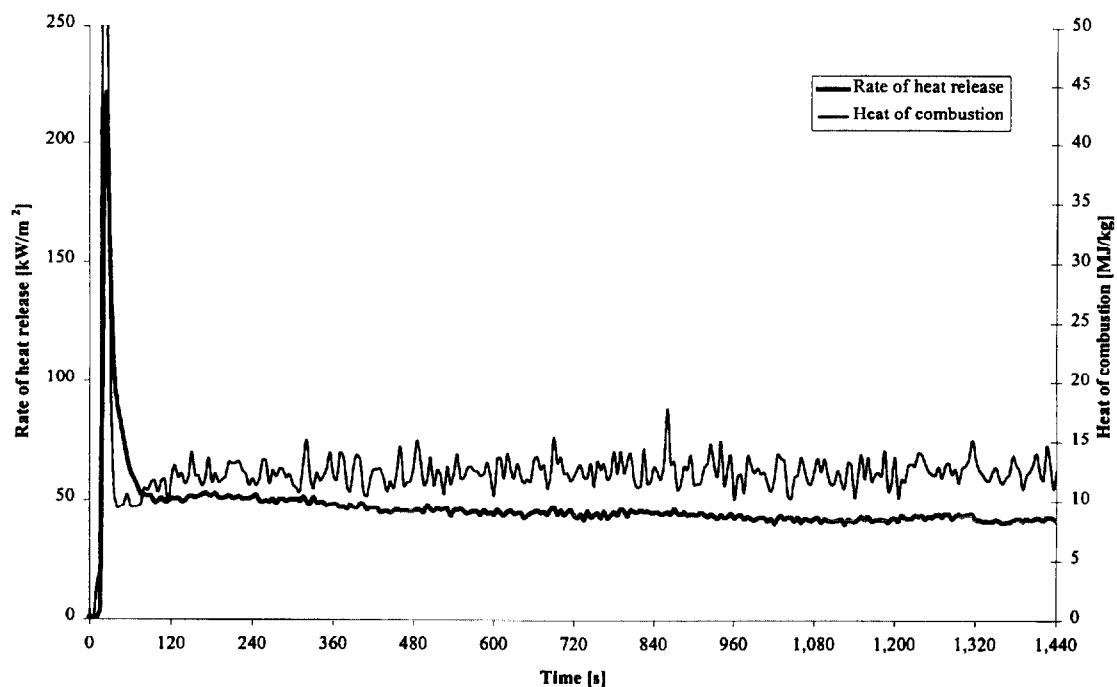
Figure 251. Rate of heat release and heat of combustion (1RL9).

Figure 252. Comparison of dimensionless burning rate using derived properties for species and orientation (1RL9).

292
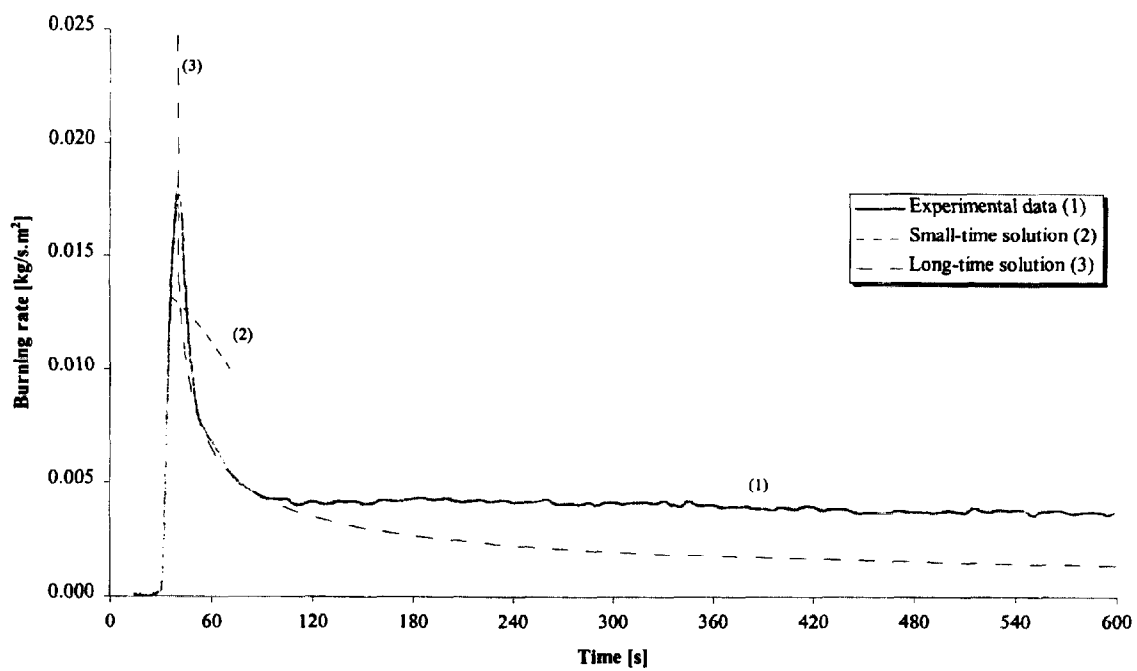
Figure 253. Comparison of burning rate using derived properties for species and orientation (1RL9).
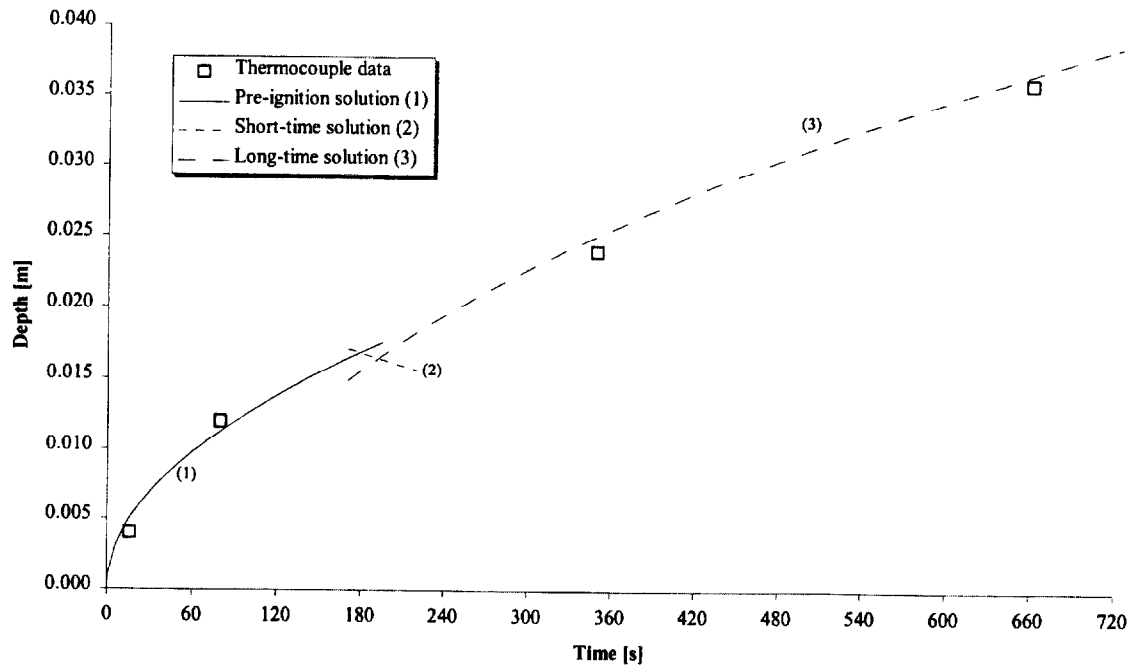
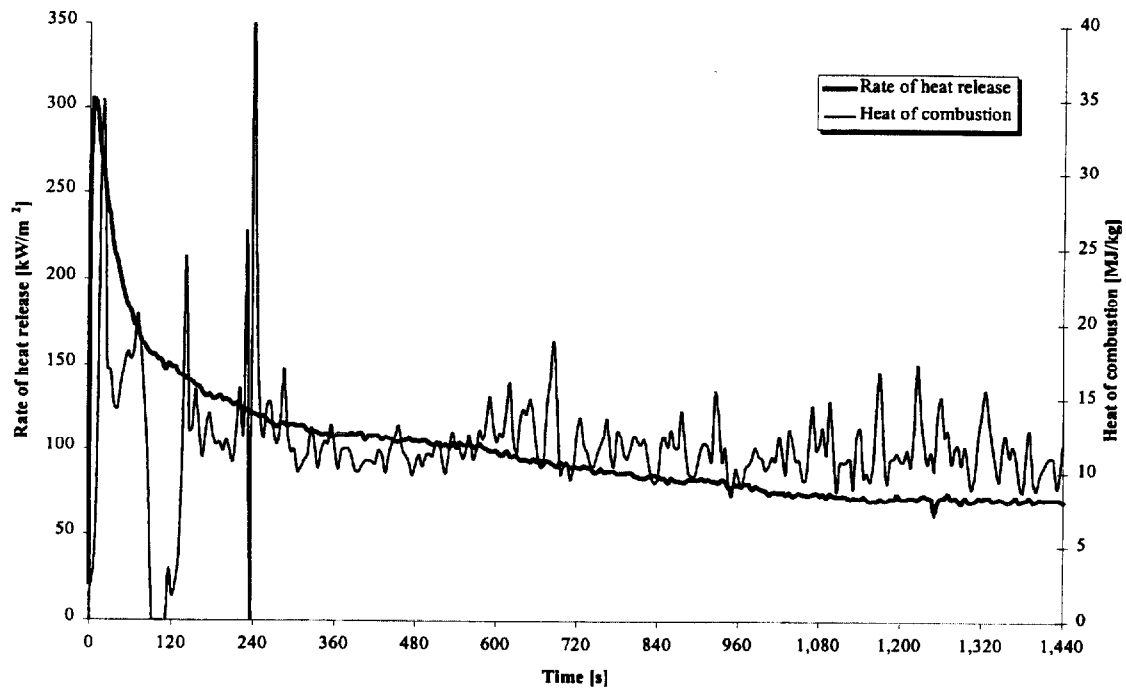Test (1RX1), Redwood, across grain at 75 kW/m² for 25 minutes.
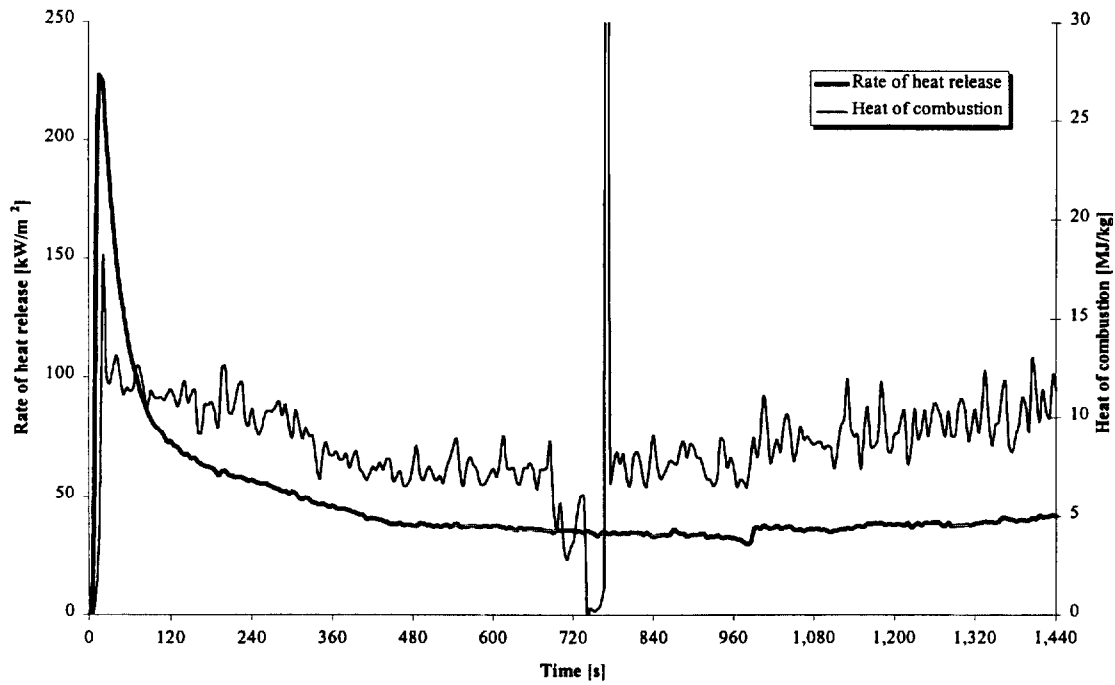
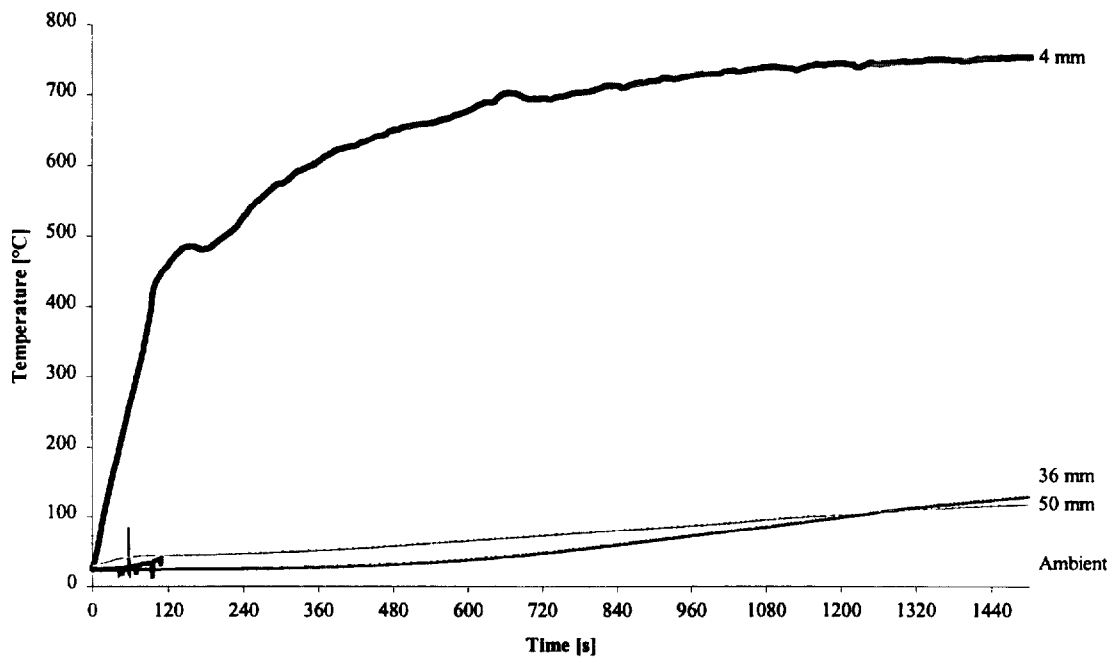**Figure 254.** Rate of heat release and heat of combustion (1RX1).

Figure 255. Temperatures measured in sample (1RX1).

Figure 256. Comparison of dimensionless burning rate using derived properties for species and orientation (1RX1).

Figure 257. Comparison of burning rate using derived properties for species and orientation (1RX1).

Figure 258. Comparison of measured and calculated thermal penetration depth (1RX1).

Figure 259. Comparison of estimated char depth from experimental data and the calculated char depth (1RX1).

Test (1RX2), Redwood, across grain at 75 kW/m^2 for 25 minutes.
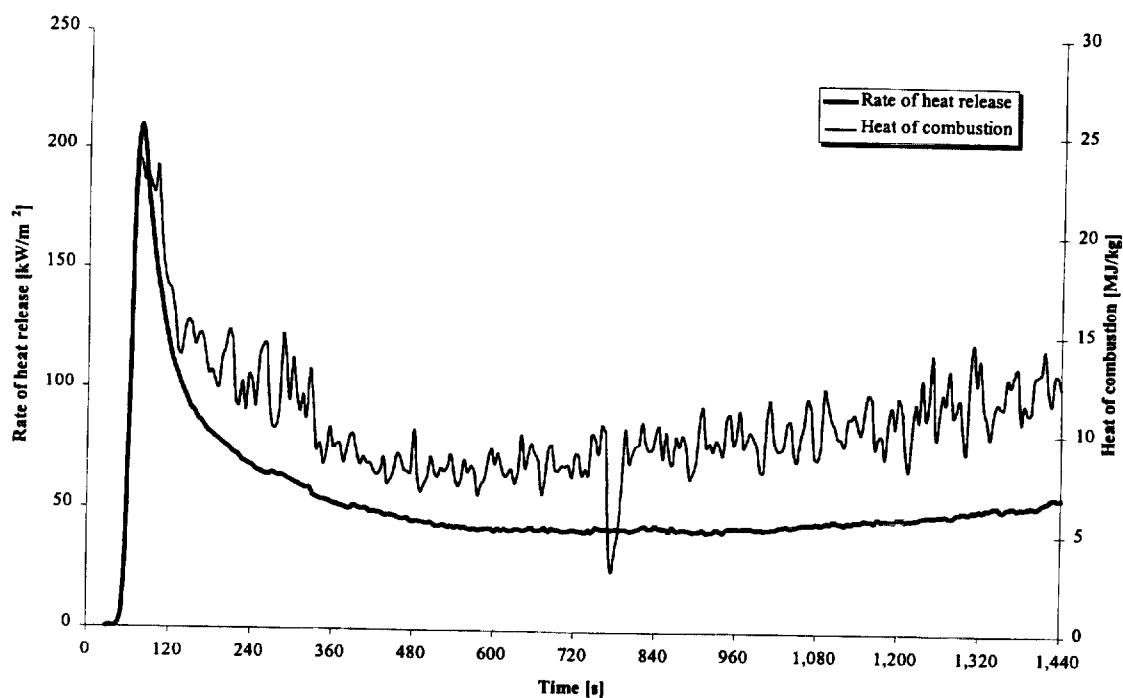
Figure 260. Rate of heat release and heat of combustion (1RX2).

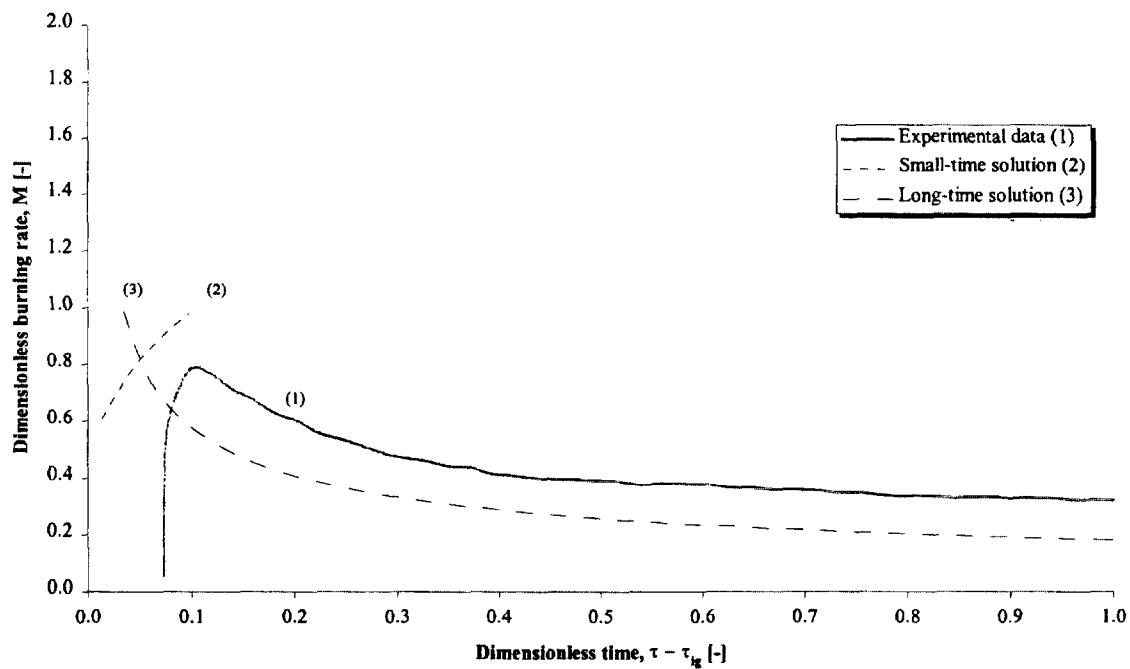**Figure 261.** Temperatures measured in sample (1RX2).

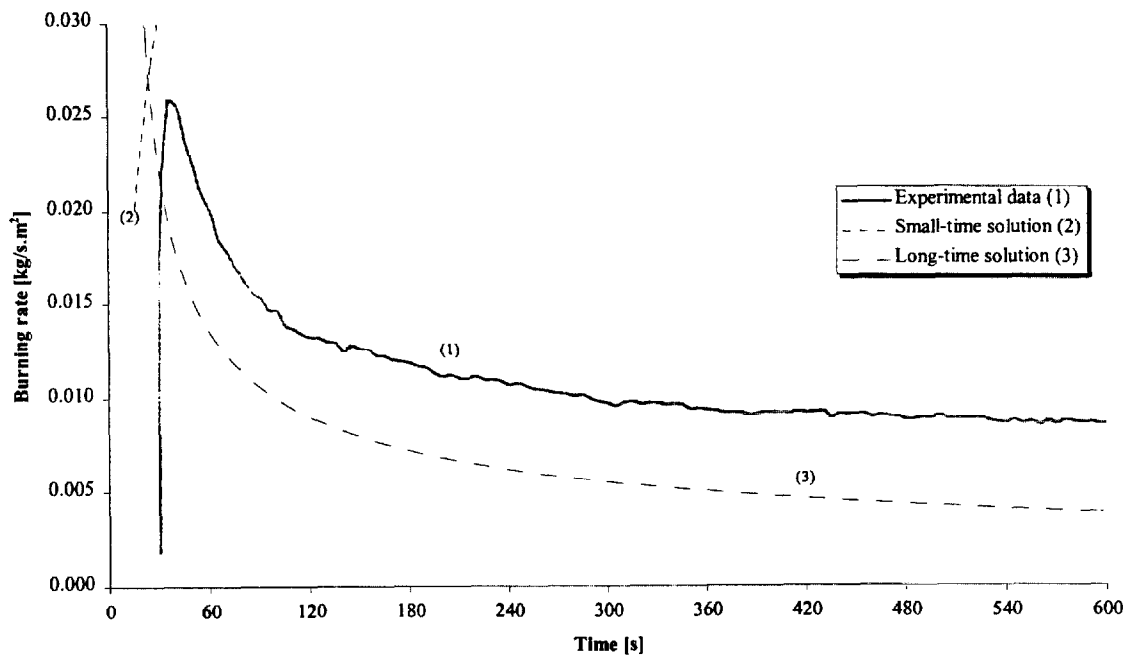**Figure 262.** Comparison of dimensionless burning rate using derived properties for species and orientation (1RX2).

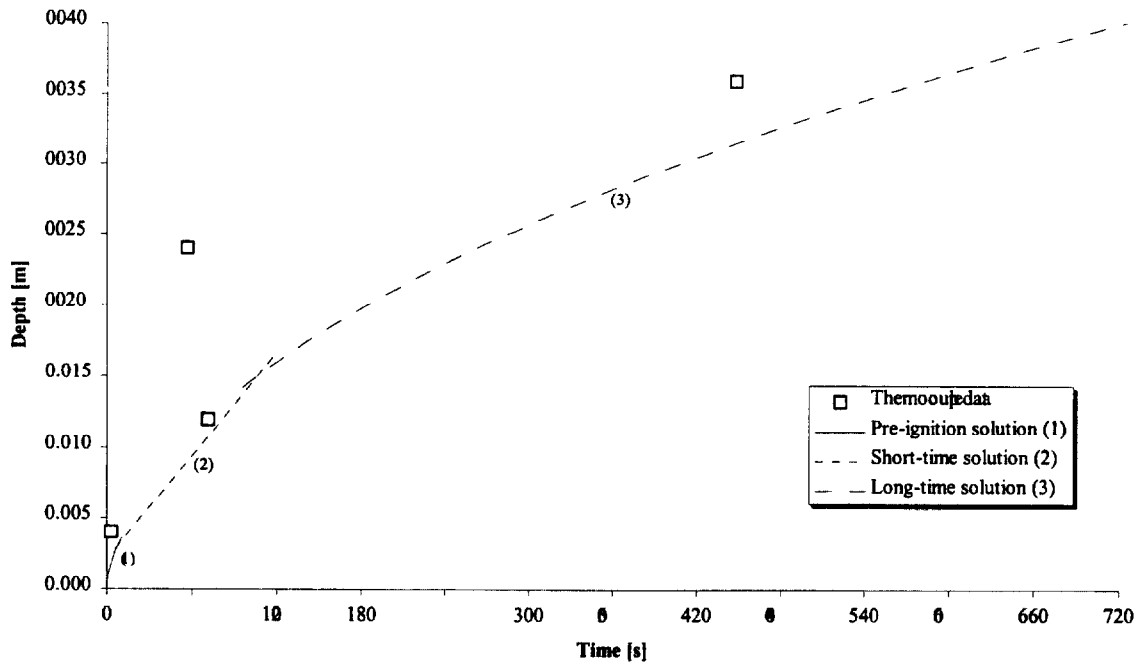**Figure 263.** Comparison of burning rate using derived properties for species and orientation (1RX2).

298

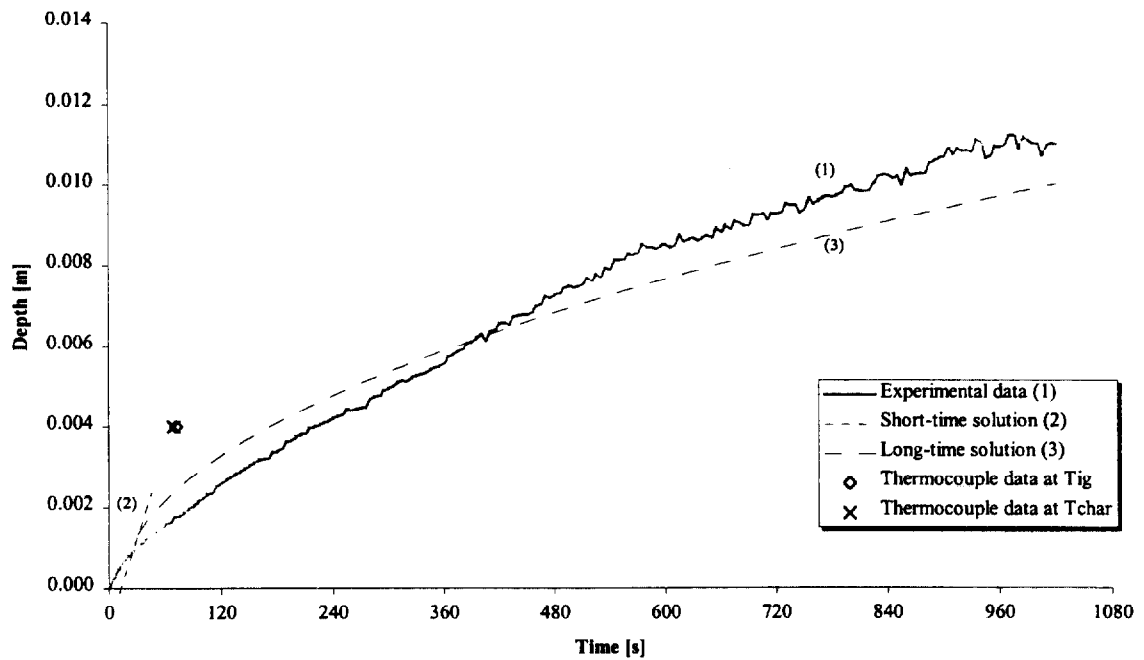**Figure 264.** Comparison of measured and calculated thermal penetration depth (1RX2).
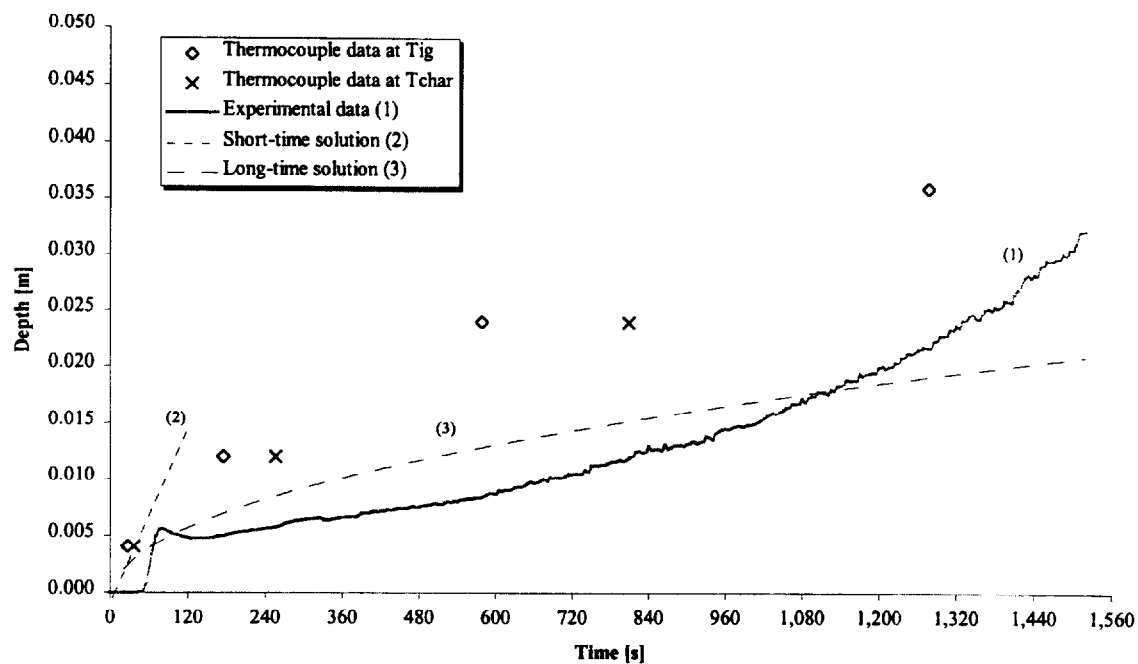
Figure 265. Comparison of estimated char depth from experimental data and the calculated char depth (1RX2).

299

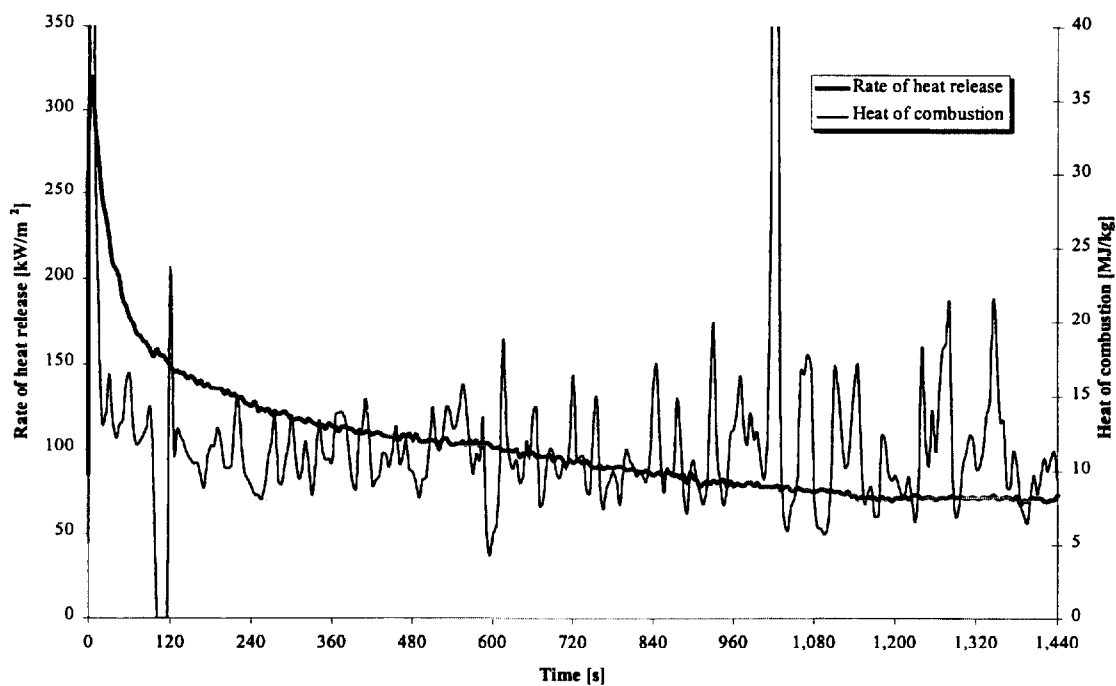Test (1RX3), Redwood, across grain at 25 kW/m^2 for 25 minutes.

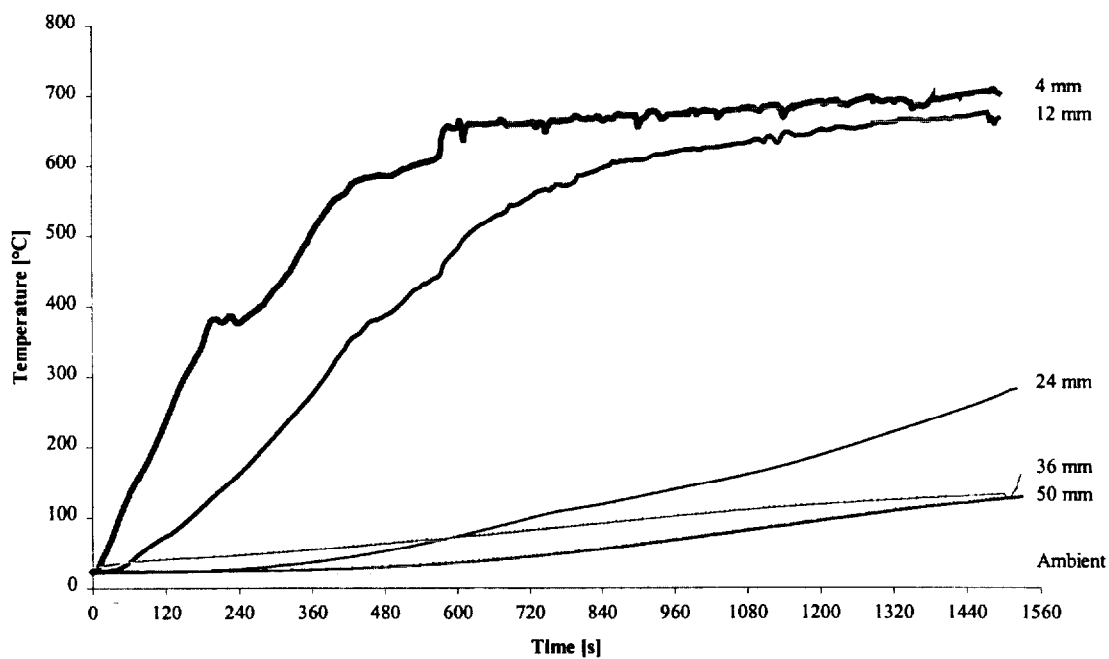**Figure 266.** Rate of heat release and heat of combustion (1RX3).

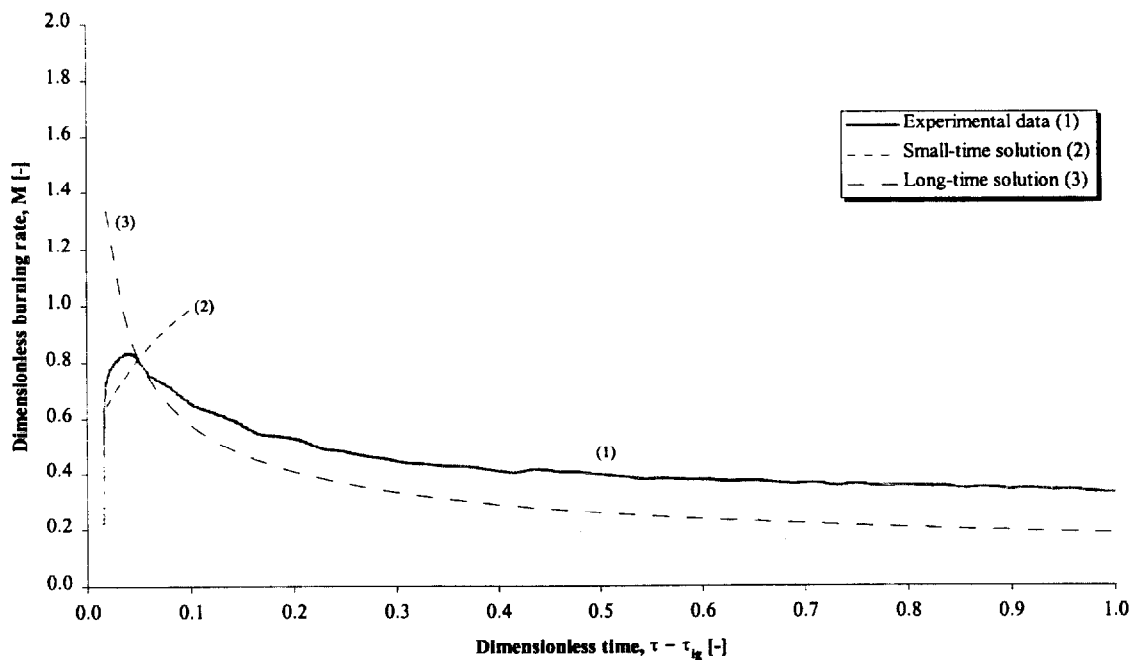**Figure 267.** Temperatures measured in sample (1RX3).

300

Figure 268. Comparison of dimensionless burning rate using derived properties for species and orientation (1RX3).

Figure 269. Comparison of burning rate using derived properties for species and orientation (1RX3).

301

Figure 270. Comparison of measured and calculated thermal penetration depth (1RX3).

Figure 271. Comparison of estimated char depth from experimental data and the calculated char depth (1RX3).

302

Test (1RX4), Redwood, across grain at 25 kW/m^2 for 25 minutes.

Figure 272. Rate of heat release and heat of combustion (1RX4).

Figure 273. Temperatures measured in sample (1RX4).

303

Figure 274. Comparison of dimensionless burning rate using derived properties for species and orientation (1RX4).
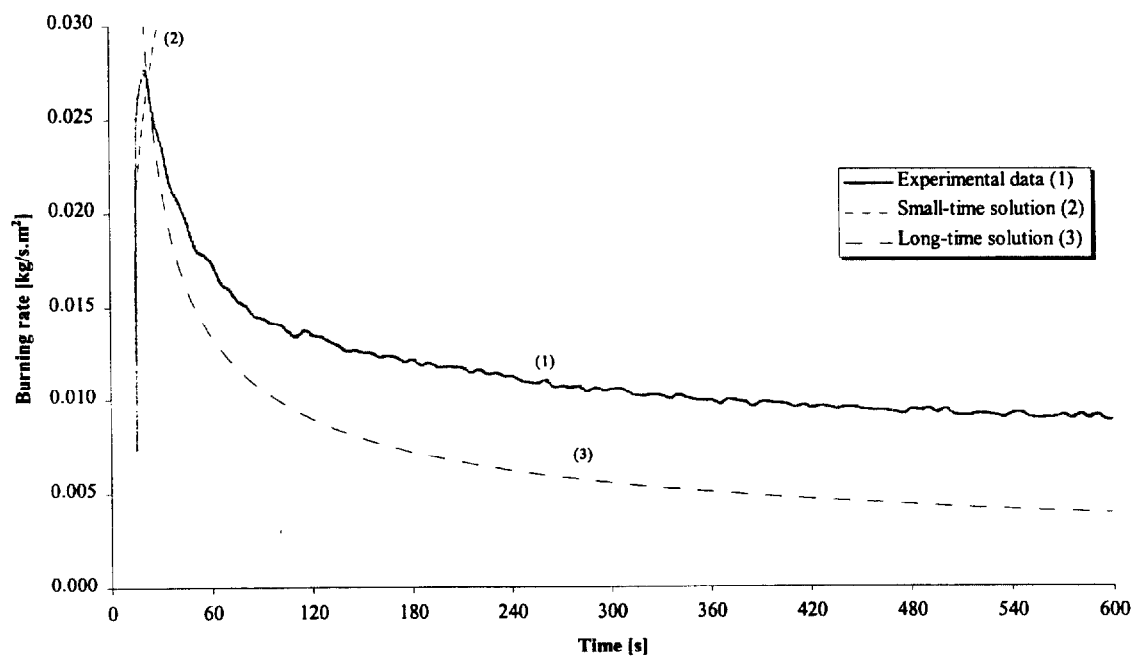

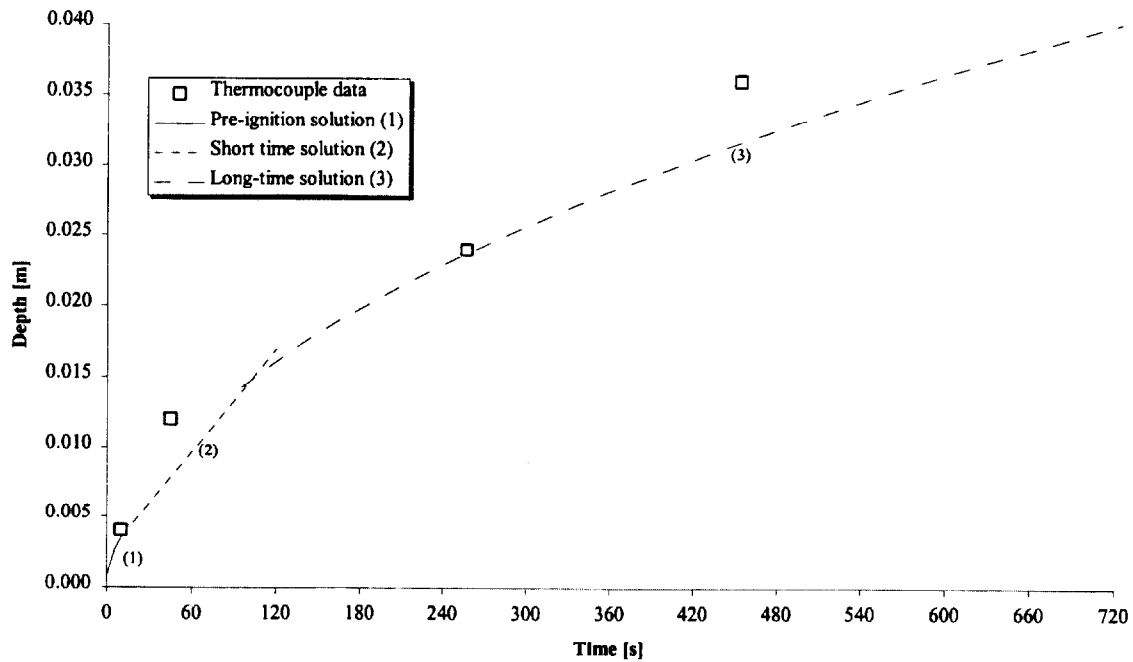**Figure 275.** Comparison of burning rate using derived properties for species and orientation (1RX4).

304

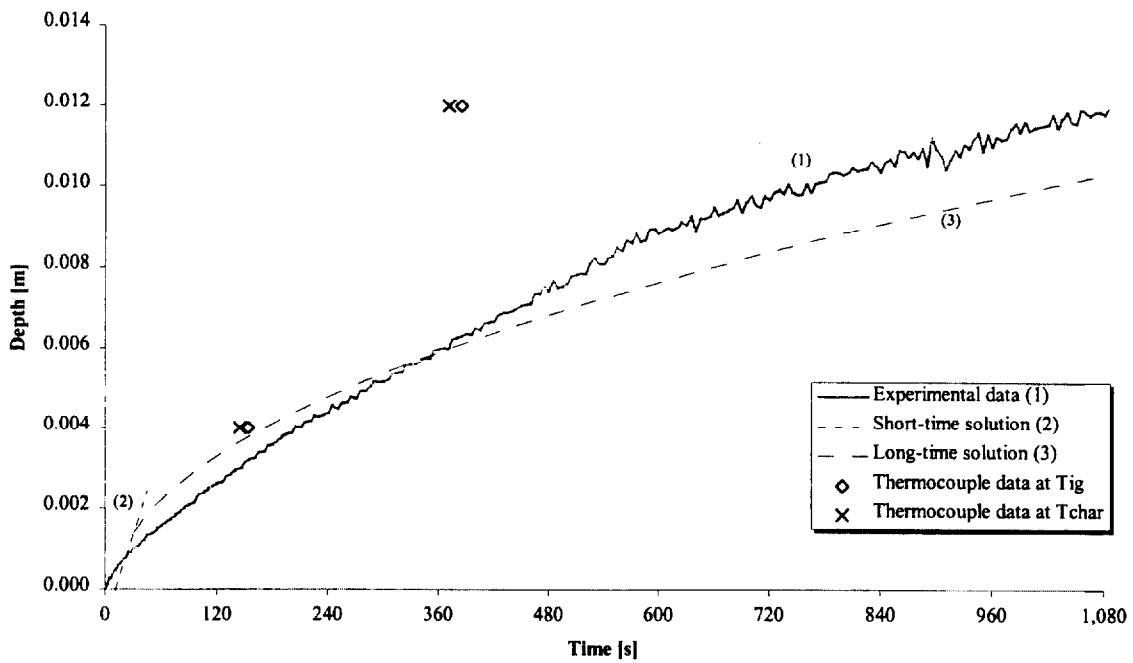**Figure 276.** Comparison of measured and calculated thermal penetration depth (1RX4).

Figure 277. Comparison of estimated char depth from experimental data and the calculated char depth (1RX4).

Test (1RX6), Redwood, across grain at 25 kW/m² for 75 minutes.
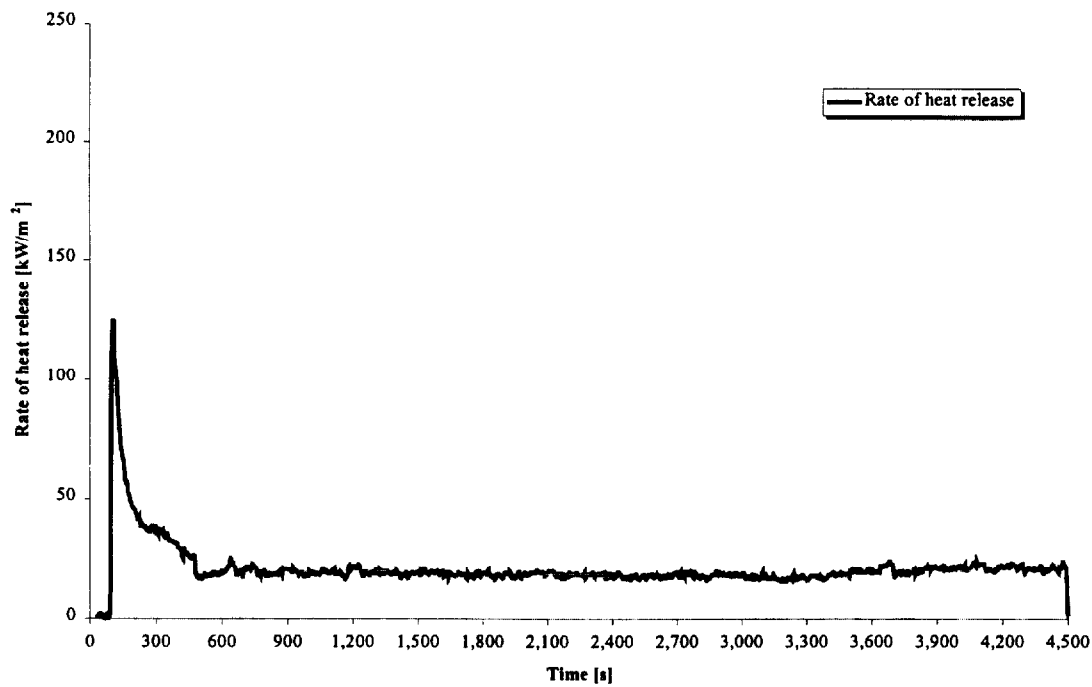
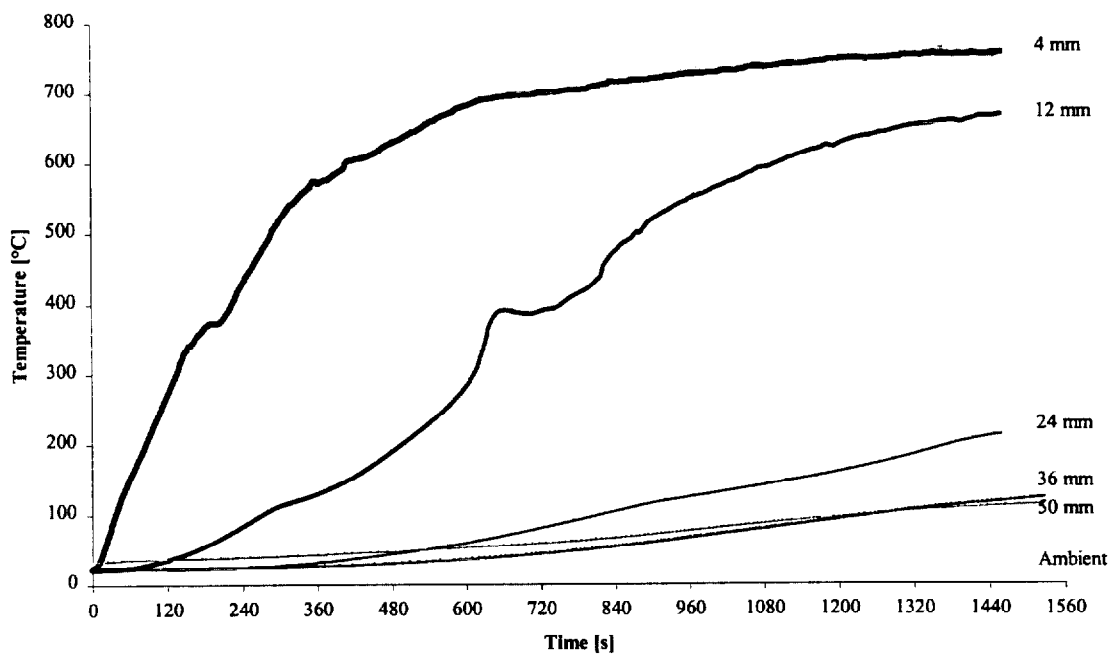**Figure 278.** Rate of heat release (1RX6).
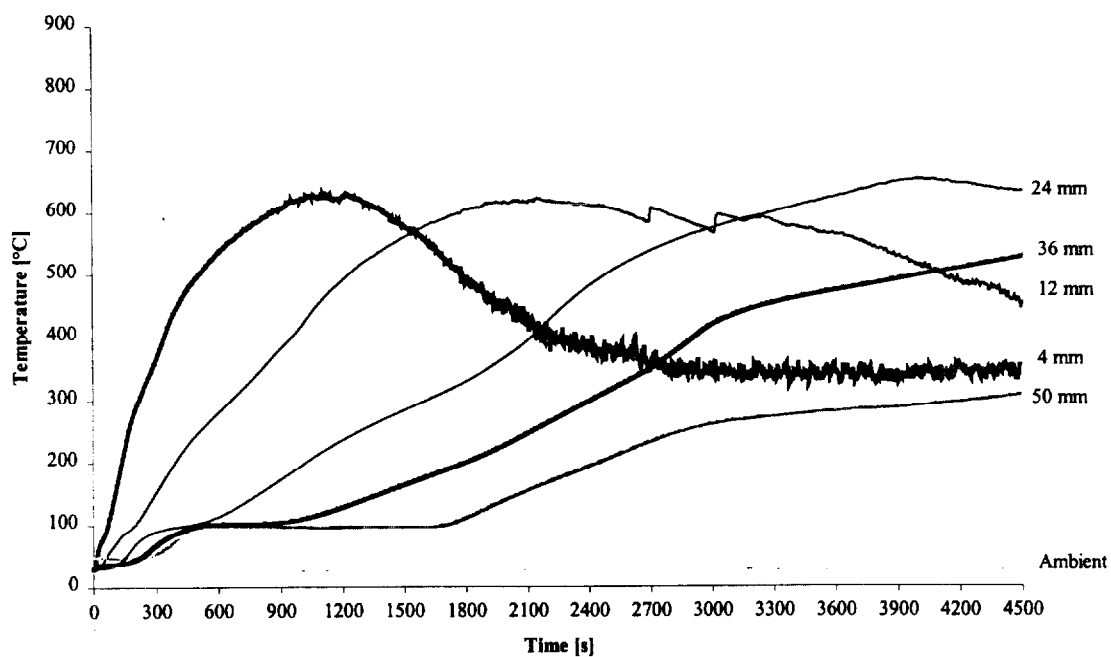
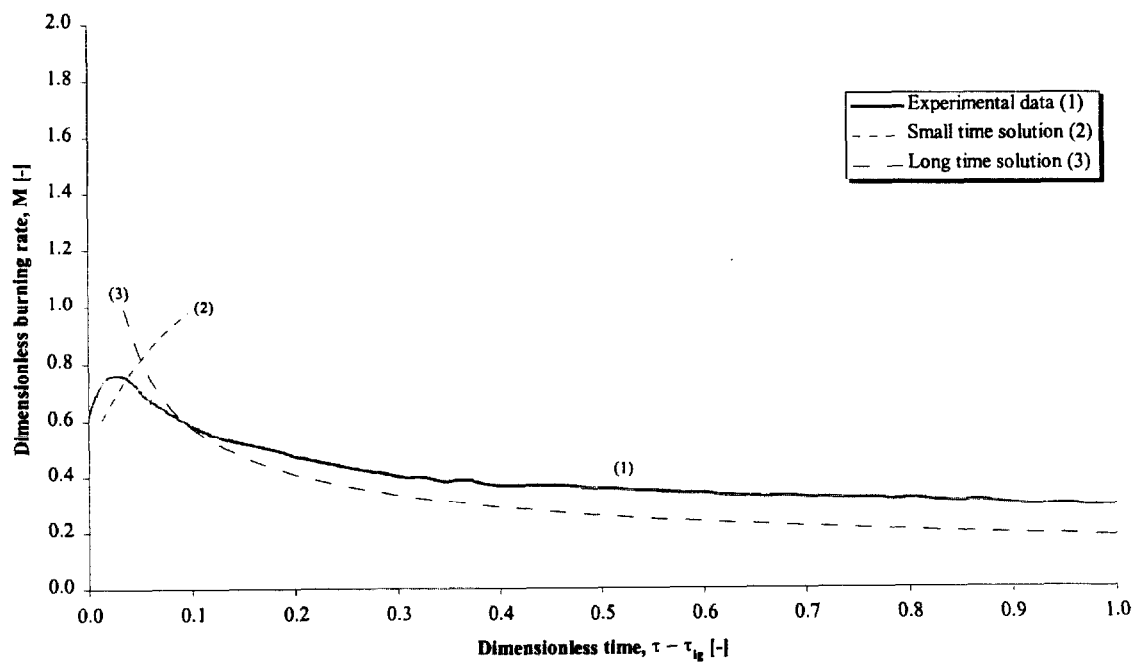**Figure 279.** Temperatures measured in sample (1RX6).

306

Figure 280. Comparison of dimensionless burning rate using derived properties for species and orientation (1RX6).

Figure 281. Comparison of burning rate using derived properties for species and orientation (1RX6).

307

Figure 282. Comparison of measured and calculated thermal penetration depth (1RX6).

Figure 283. Comparison of estimated char depth from experimental data and the calculated char depth (1RX6).

308

Test (1RX7), Redwood, across grain at 50 kW/m^2 for 25 minutes.
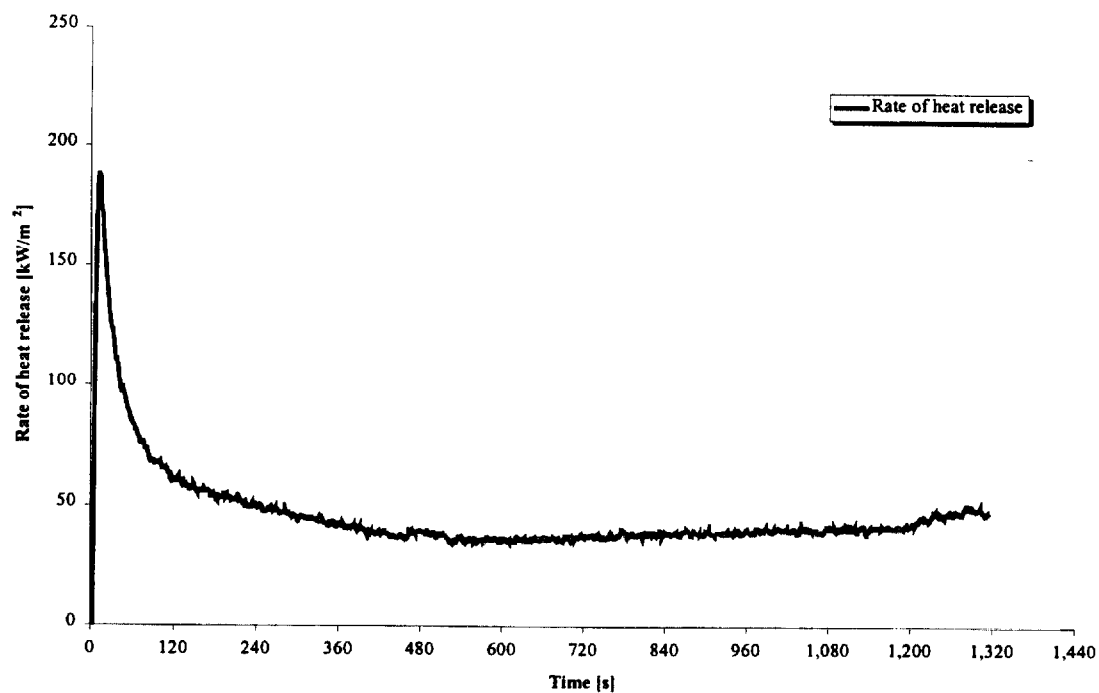
Figure 284. Rate of heat release (1RX7).
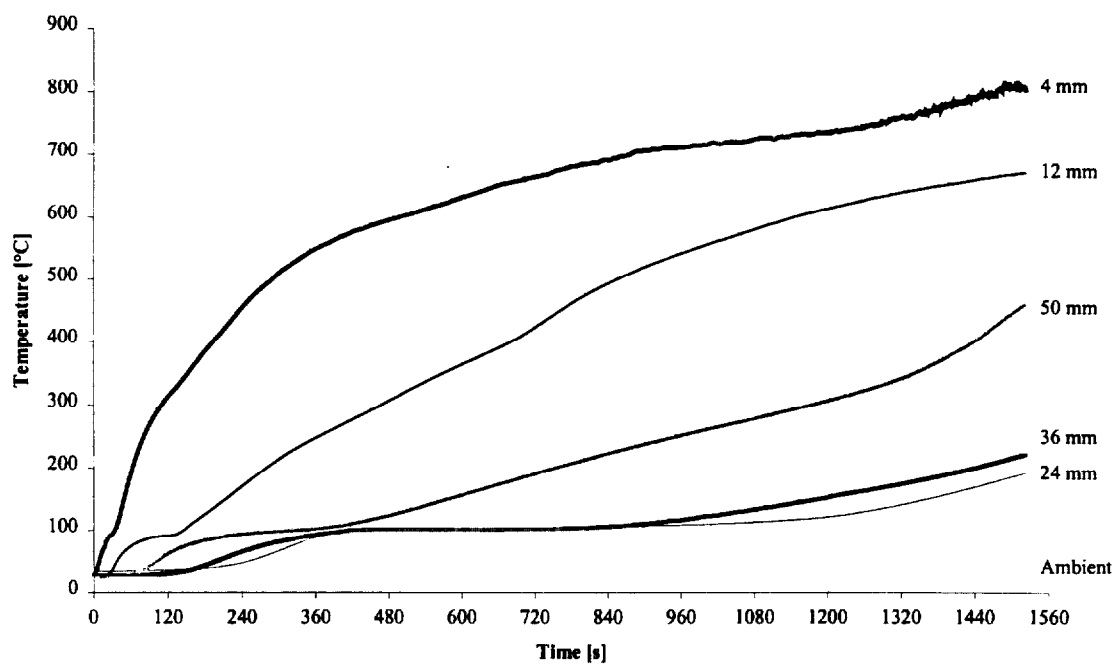
Figure 285. Temperatures measured in sample (1RX7).

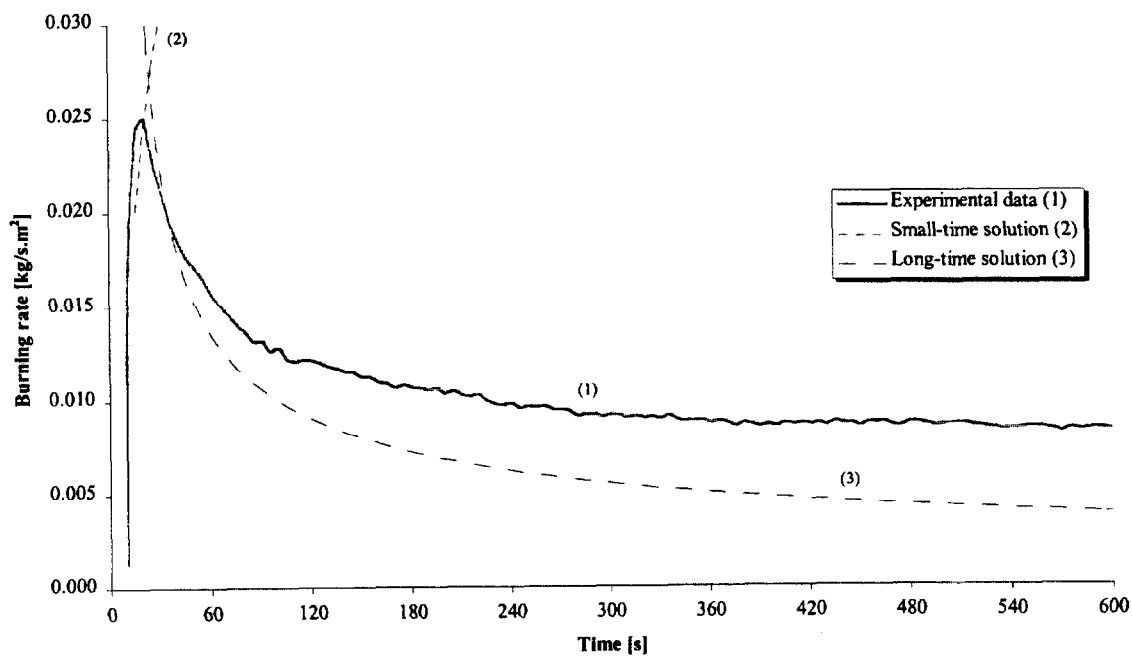**Figure 286.** Comparison of dimensionless burning rate using derived properties for species and orientation (1RX7).

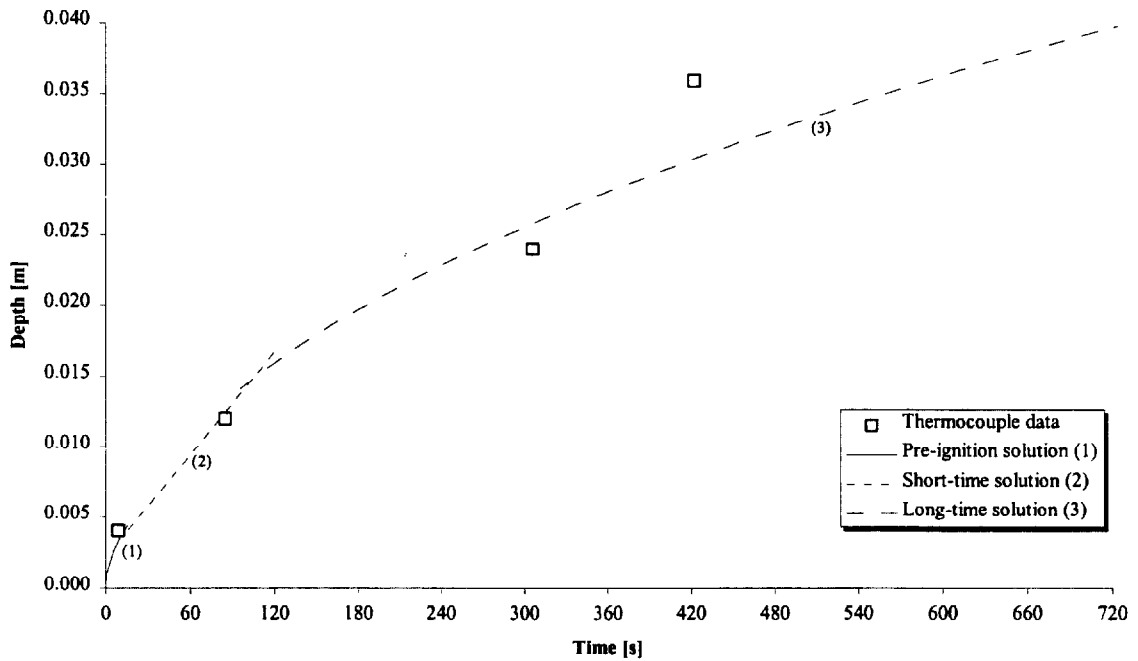**Figure 287.** Comparison of burning rate using derived properties for species and orientation (1RX7).

310

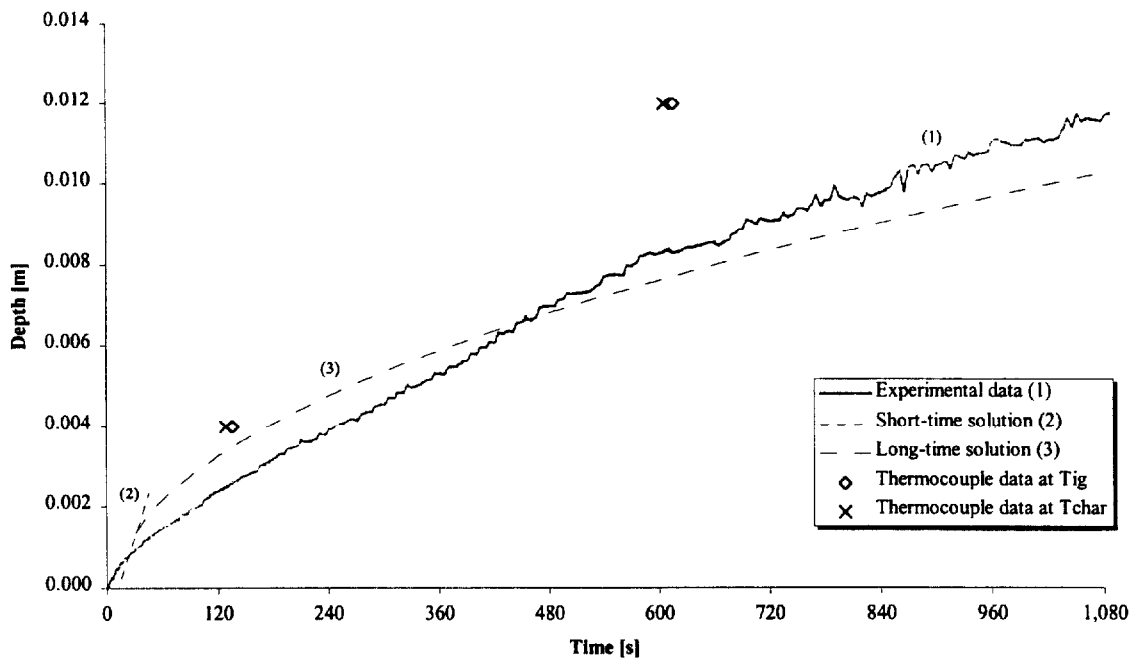**Figure 288.** Comparison of measured and calculated thermal penetration depth (1RX7).

Figure 289. Comparison of estimated char depth from experimental data and the calculated char depth (1RX7).

311

Test (1RX8), Redwood, across grain at 50 kW/m² for 25 minutes.

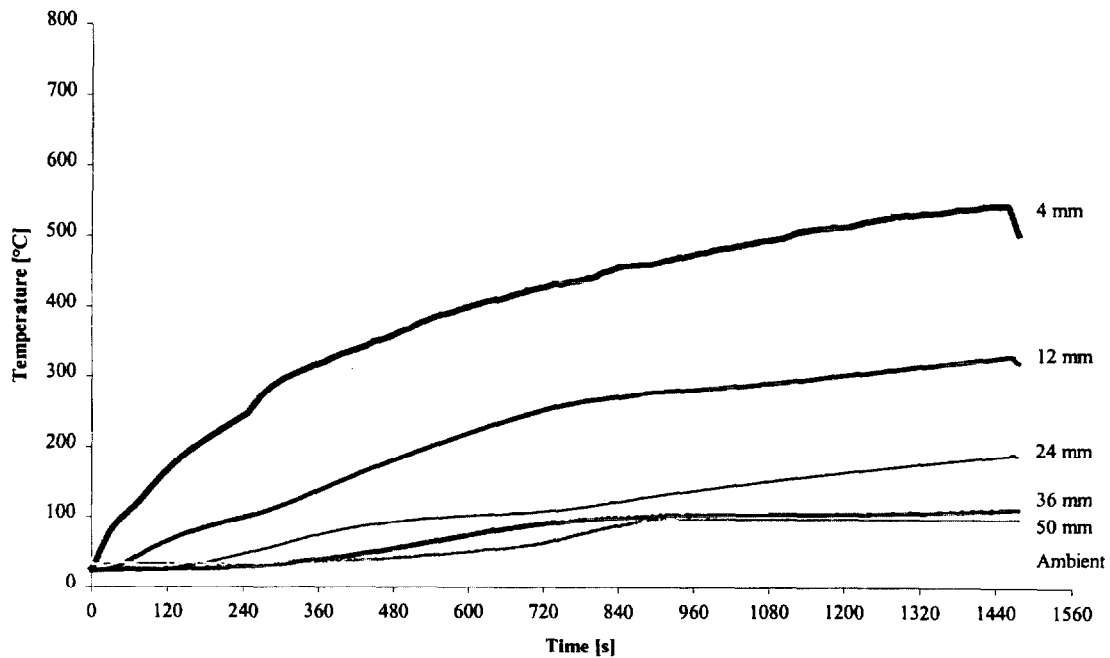**Figure 290.** Rate of heat release (1RX8).

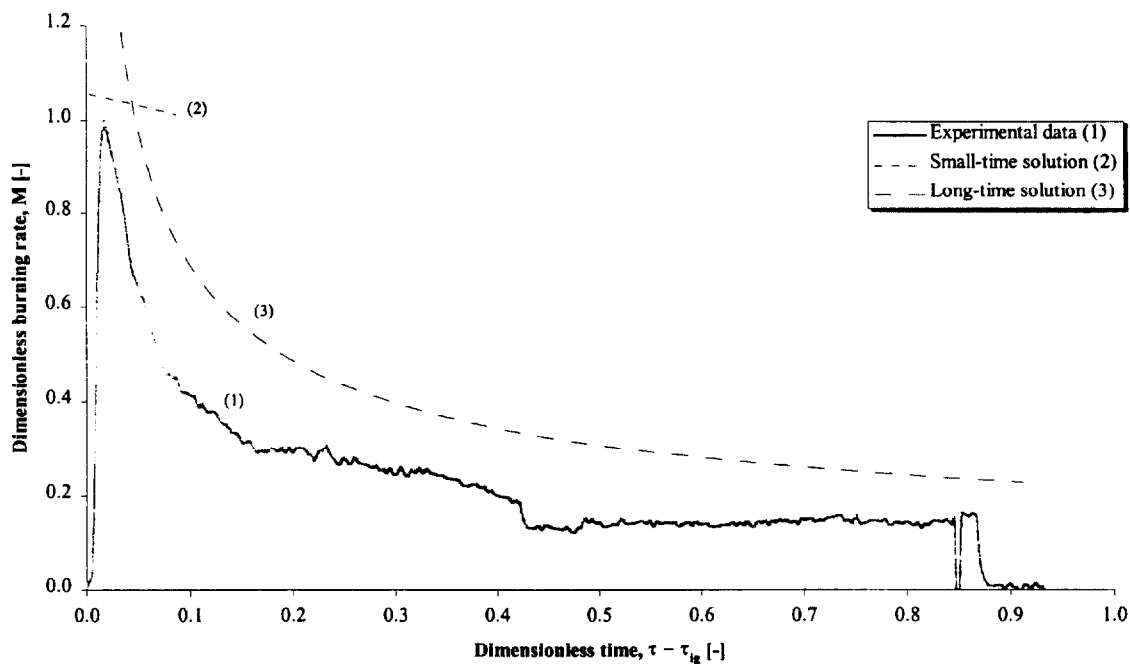**Figure 291.** Temperatures measured in sample (1RX8).

312

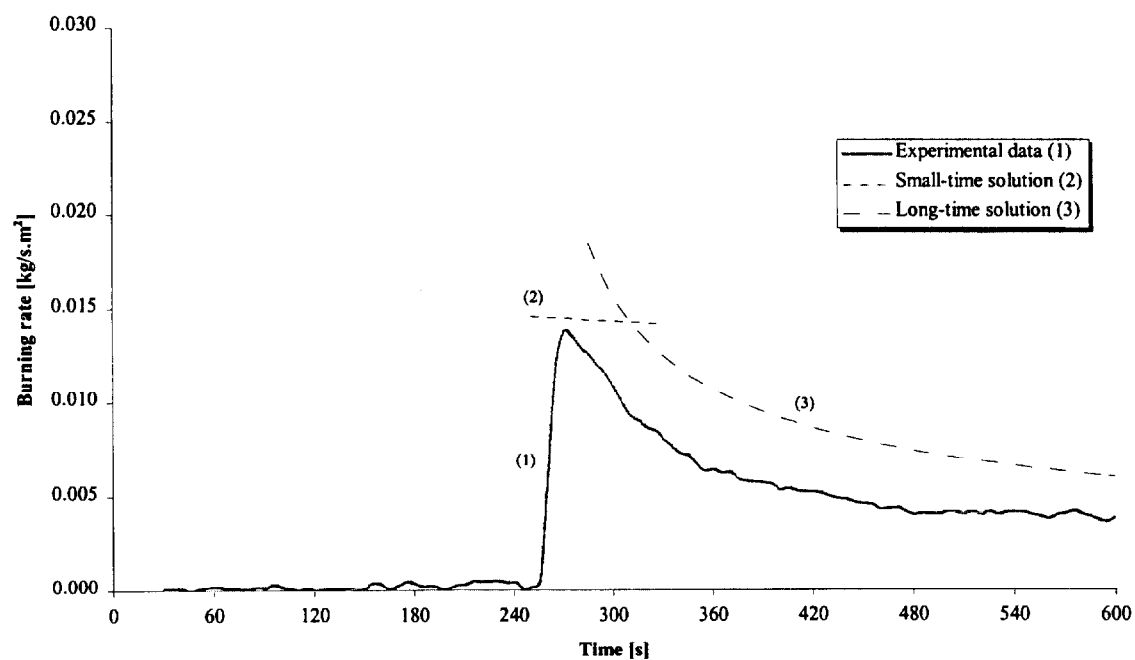**Figure 292.** Comparison of dimensionless burning rate using derived properties for species and orientation (1RX8).

Figure 293. Comparison of burning rate using derived properties for species and orientation (1RX8).

313

Figure 294. Comparison of measured and calculated thermal penetration depth (1RX8).

Figure 295. Comparison of estimated char depth from experimental data and the calculated char depth (1RX8).

314

Test (1RX9), Redwood, across grain at 50 kW/m² for 25 minutes.
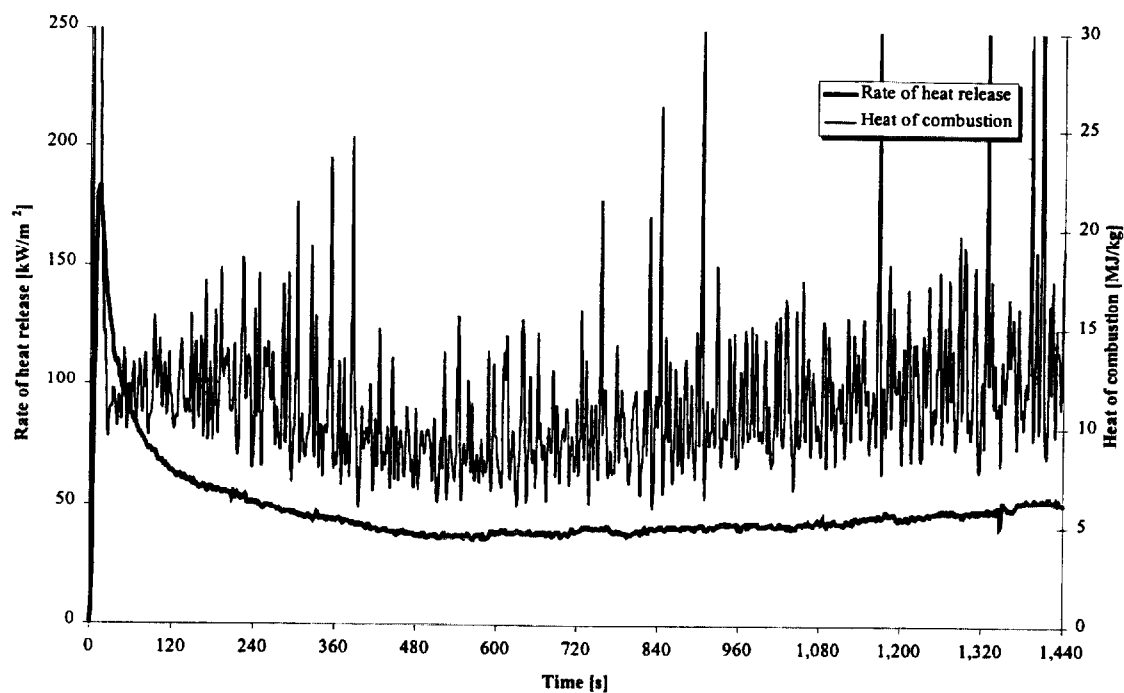
Figure 296. Rate of heat release and heat of combustion (1RX9).

Figure 297. Comparison of dimensionless burning rate using derived properties for species and orientation (1RX9).

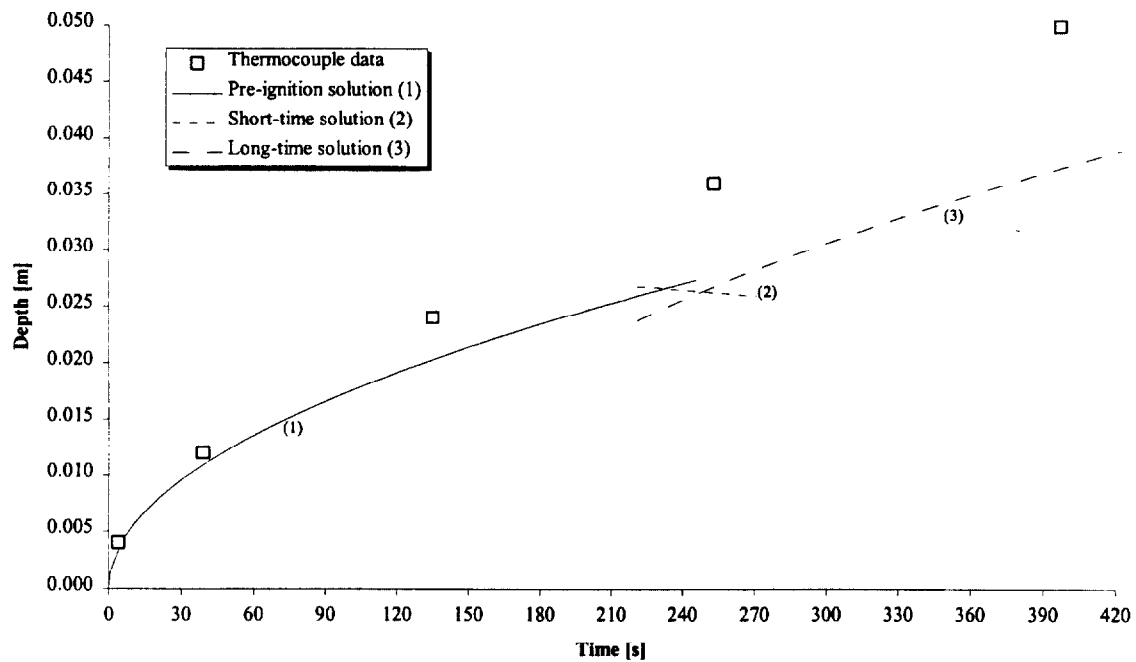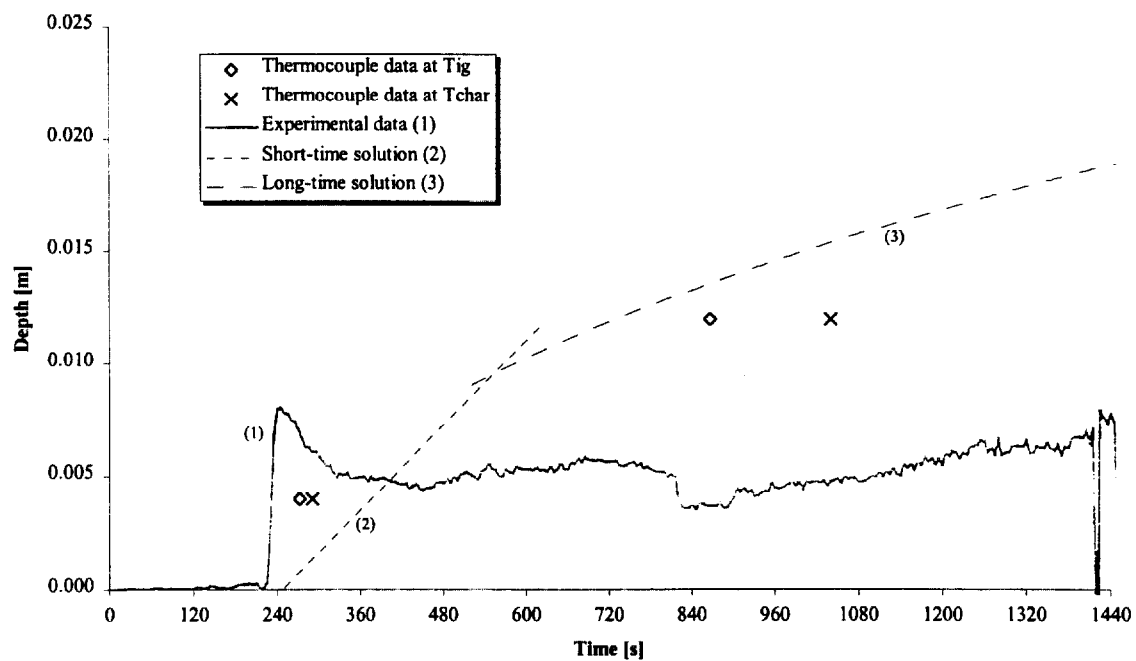**Figure 298.** Comparison of burning rate using derived properties for species and orientation (1RX9).

Test (1RX10), Redwood, across grain at 35 kW/m^2 for 25 minutes.
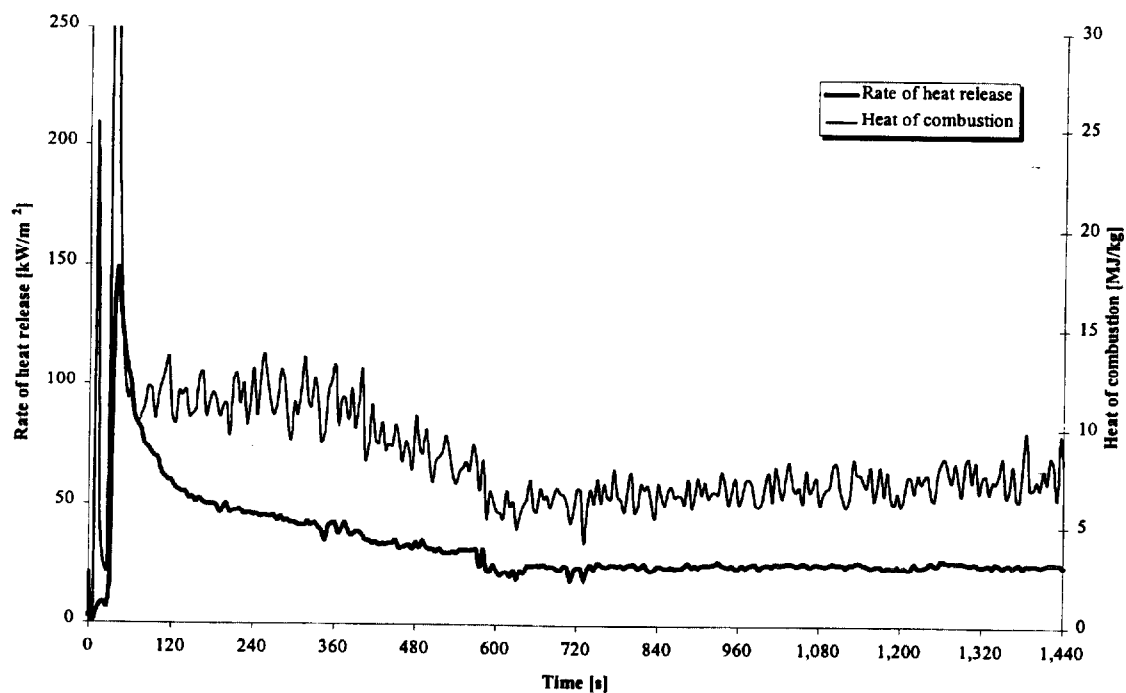
Figure 299. Rate of heat release and heat of combustion (1RX10).

Figure 300. Comparison of dimensionless burning rate using derived properties for species and orientation (1RX10).

317
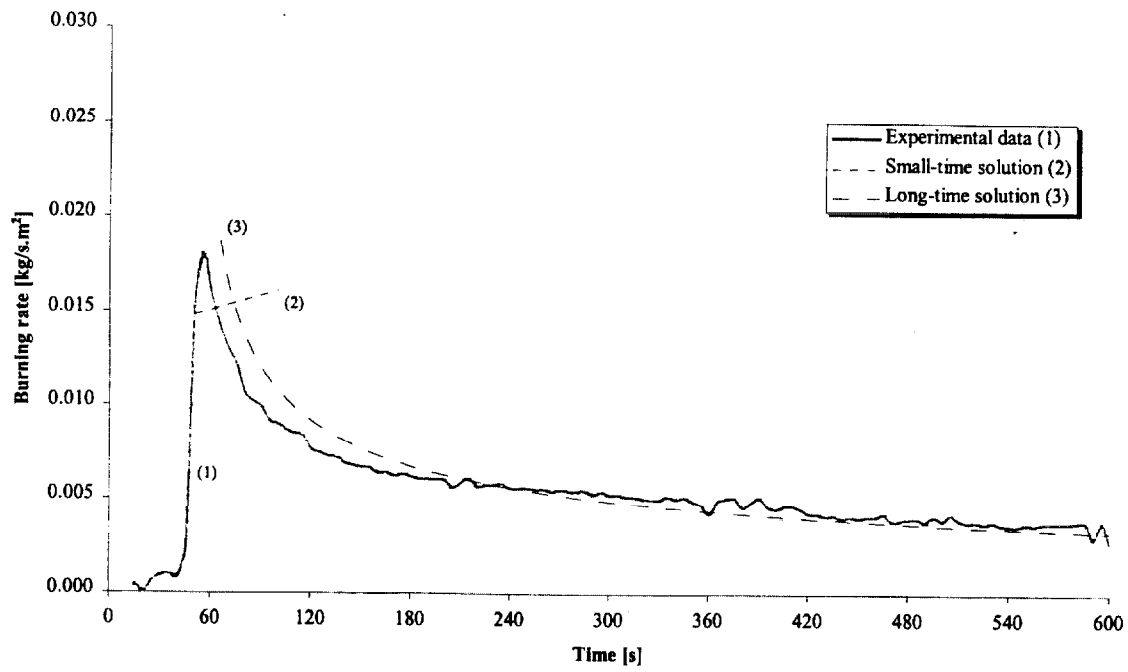
Figure 301. Comparison of burning rate using derived properties for species and
orientation (1RX10).

Test (1OL1), Red oak, along grain at 25 kW/m² for 25 minutes.

Figure 302. Rate of heat release and heat of combustion (1OL1).
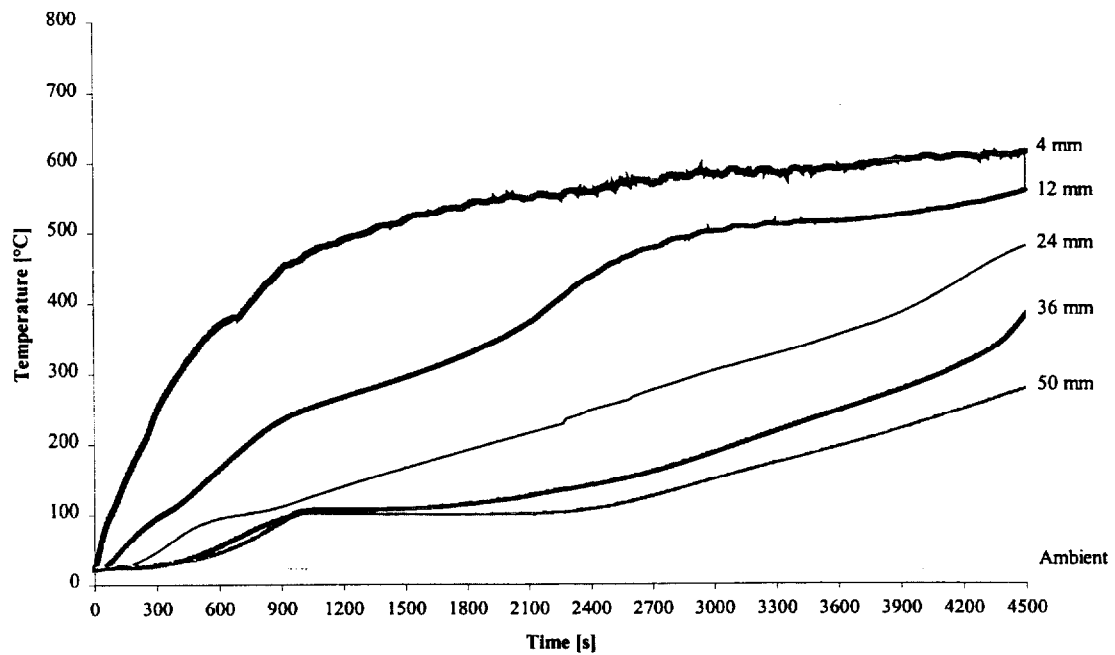

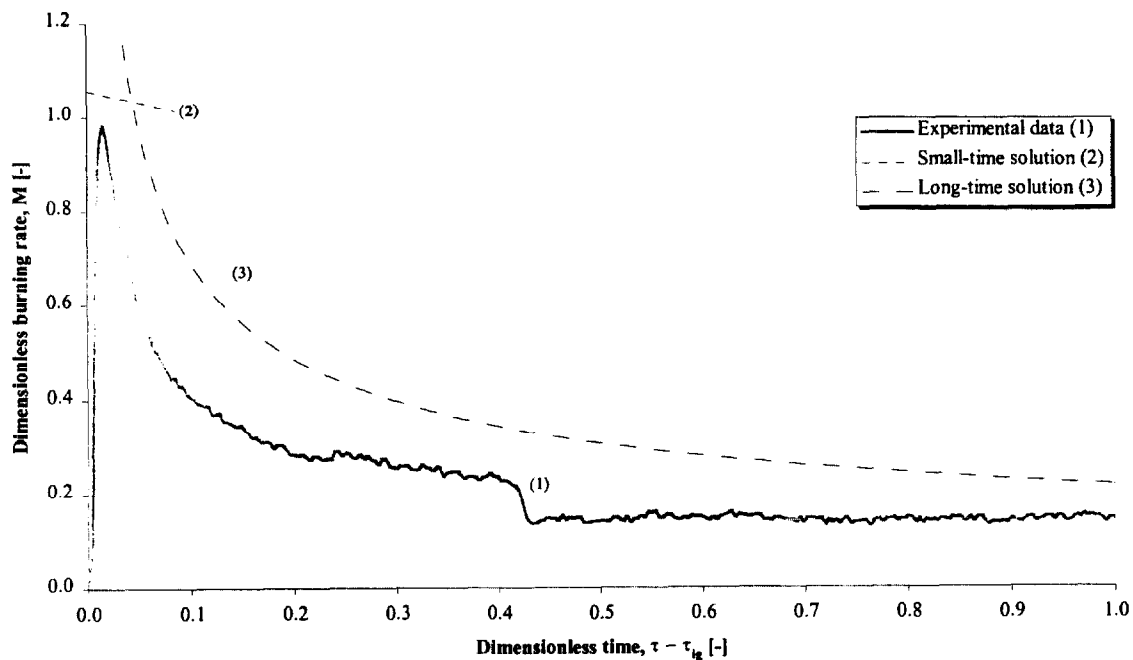**Figure 303.** Temperatures measured in sample (1OL1).

319

Figure 304. Comparison of dimensionless burning rate using derived properties for species and orientation (1OL1).
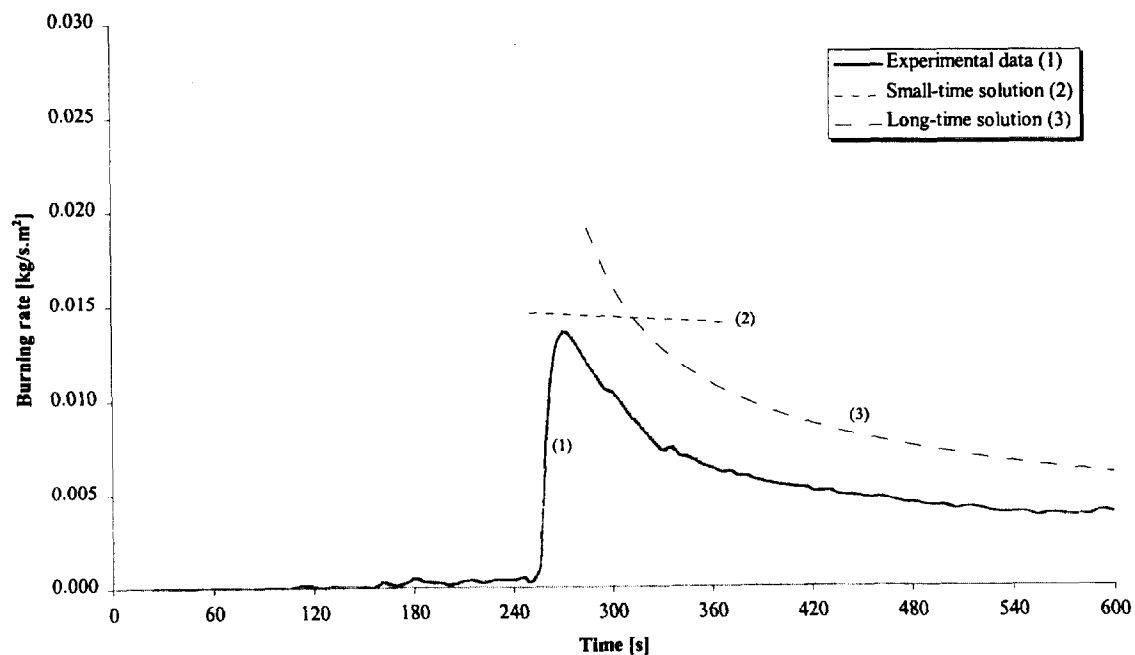

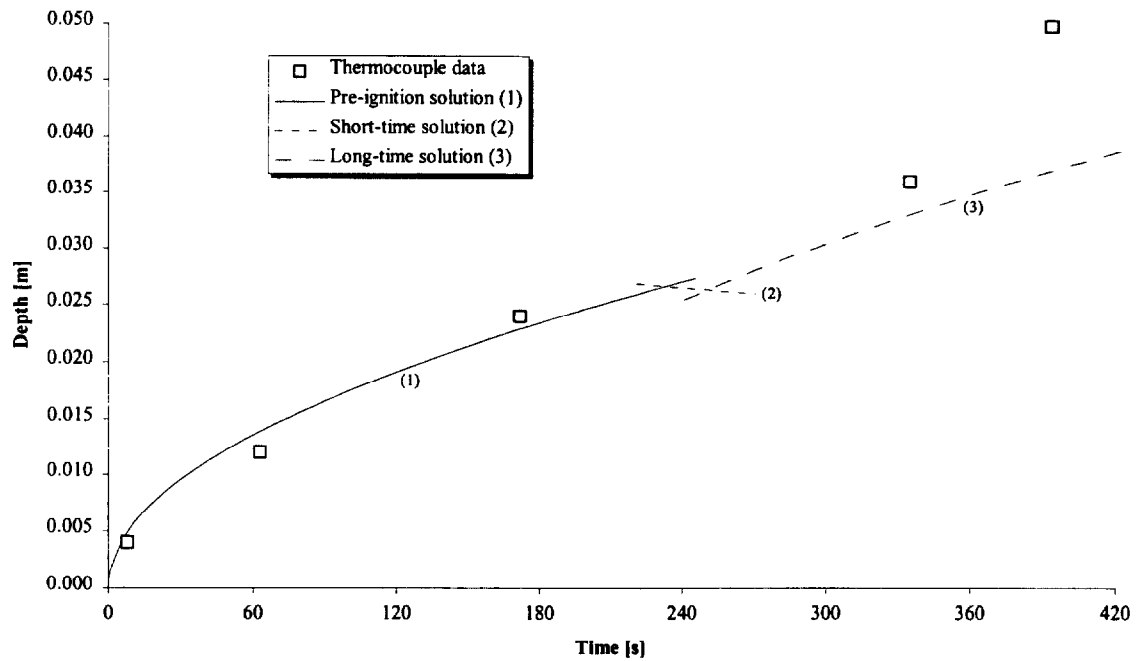**Figure 305.** Comparison of burning rate using derived properties for species and orientation (1OL1).

320

Figure 306. Comparison of measured and calculated thermal penetration depth (1OL1).
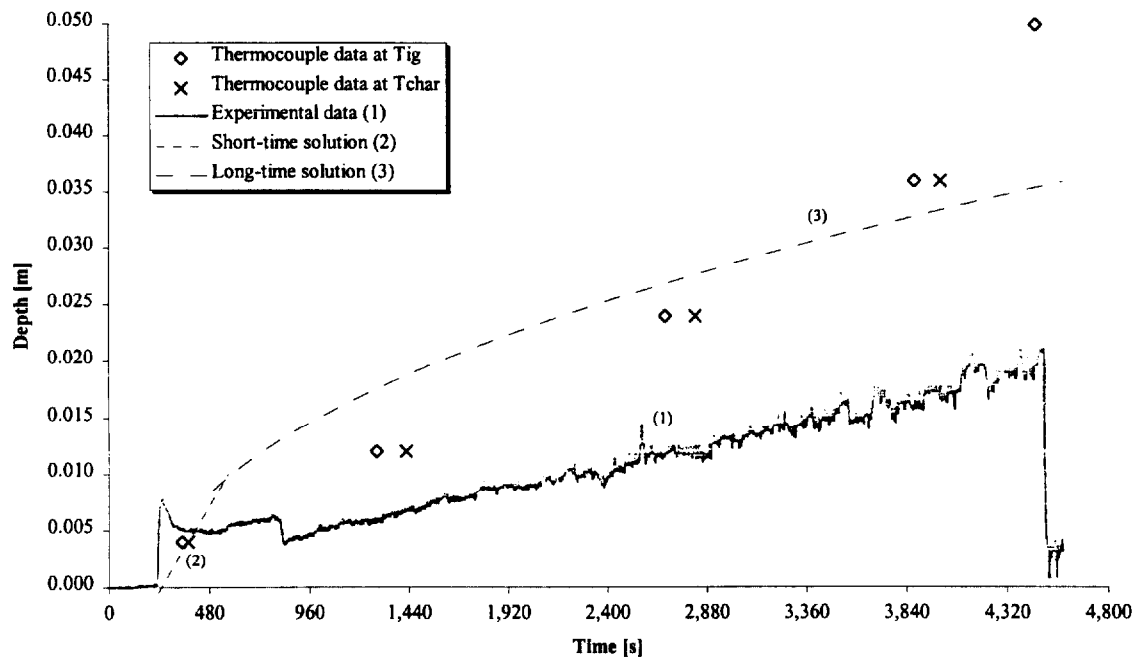

Figure 307. Comparison of estimated char depth from experimental data and the calculated char depth (1OL1).

321

Test (1OL2), Red oak, along grain at 25 kW/m² for 75 minutes.

Figure 308. Rate of heat release (1OL2).

Figure 309. Temperatures measured in sample (1OL2).

322

Figure 310. Comparison of dimensionless burning rate using derived properties for species and orientation (1OL2).
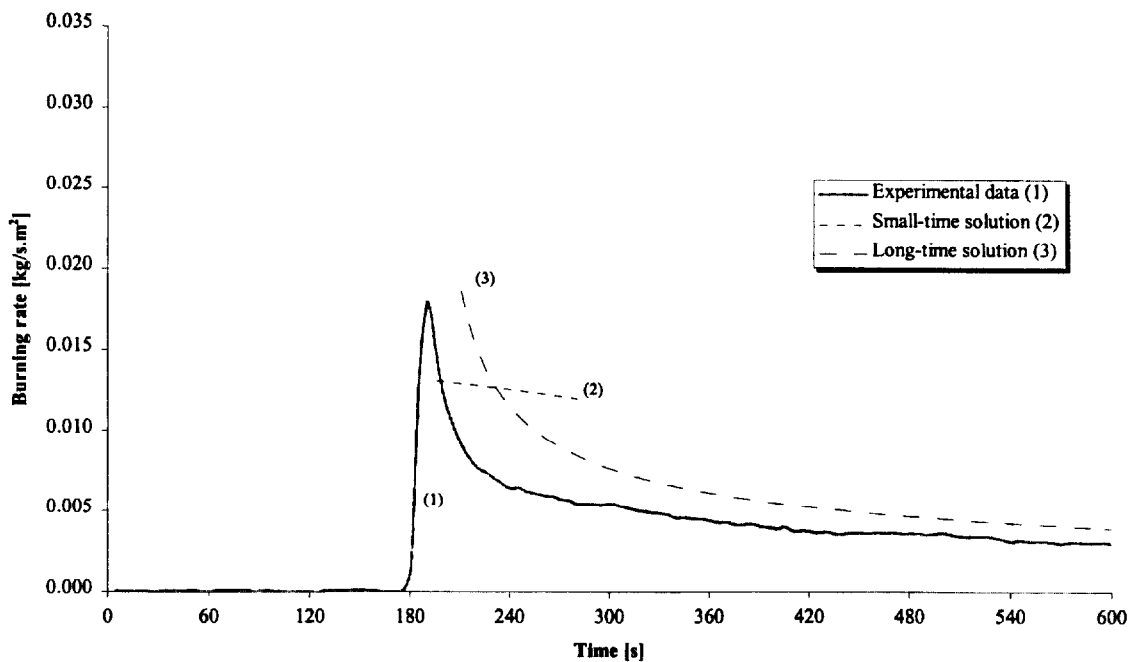
Figure 311. Comparison of burning rate using derived properties for species and orientation (1OL2).

Figure 312. Comparison of measured and calculated thermal penetration depth (1OL2).
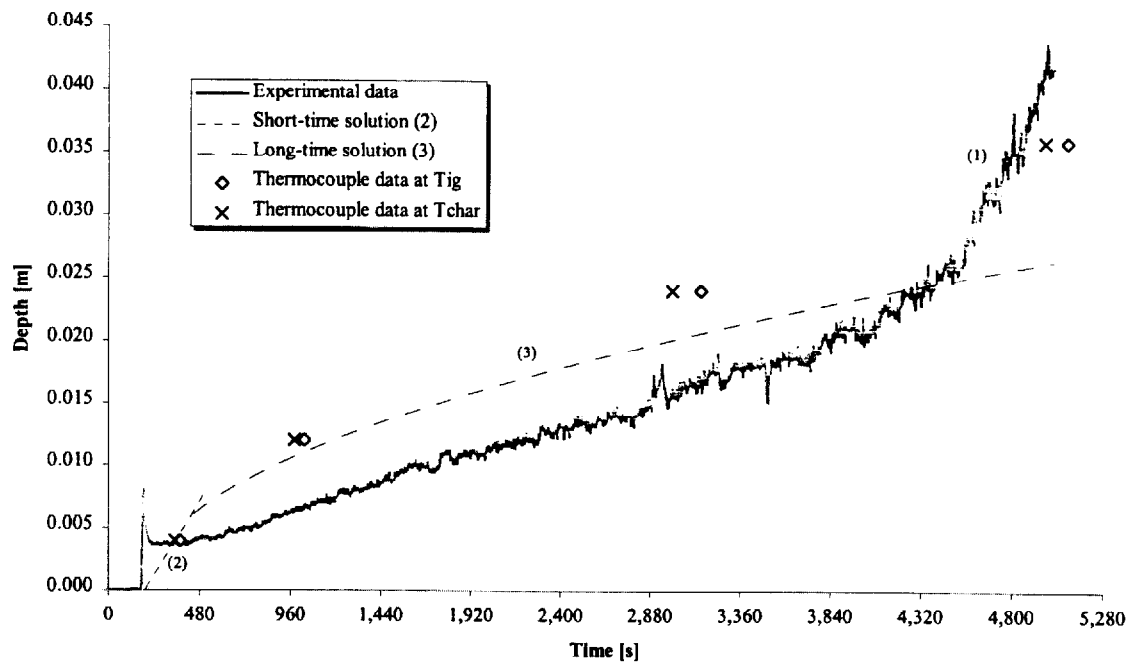
Figure 313. Comparison of estimated char depth from experimental data and the calculated char depth (1OL2).

324

Test (1OL3), Red oak, along grain at 75 kW/m^2 for 25 minutes.

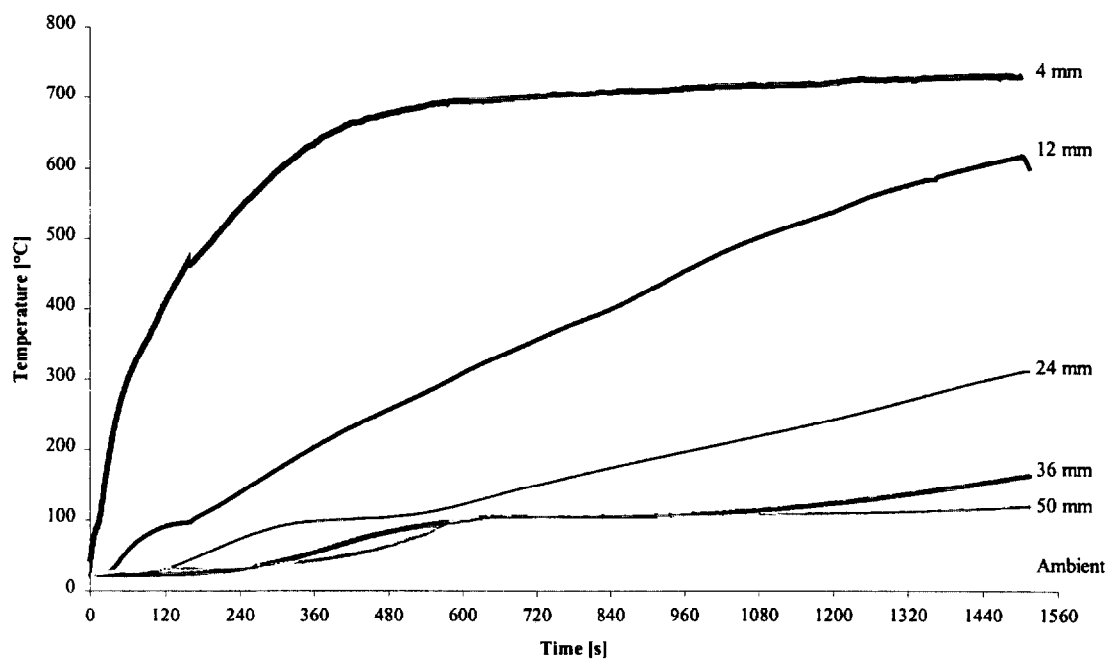

Figure 314. Rate of heat release and heat of combustion (1OL3).

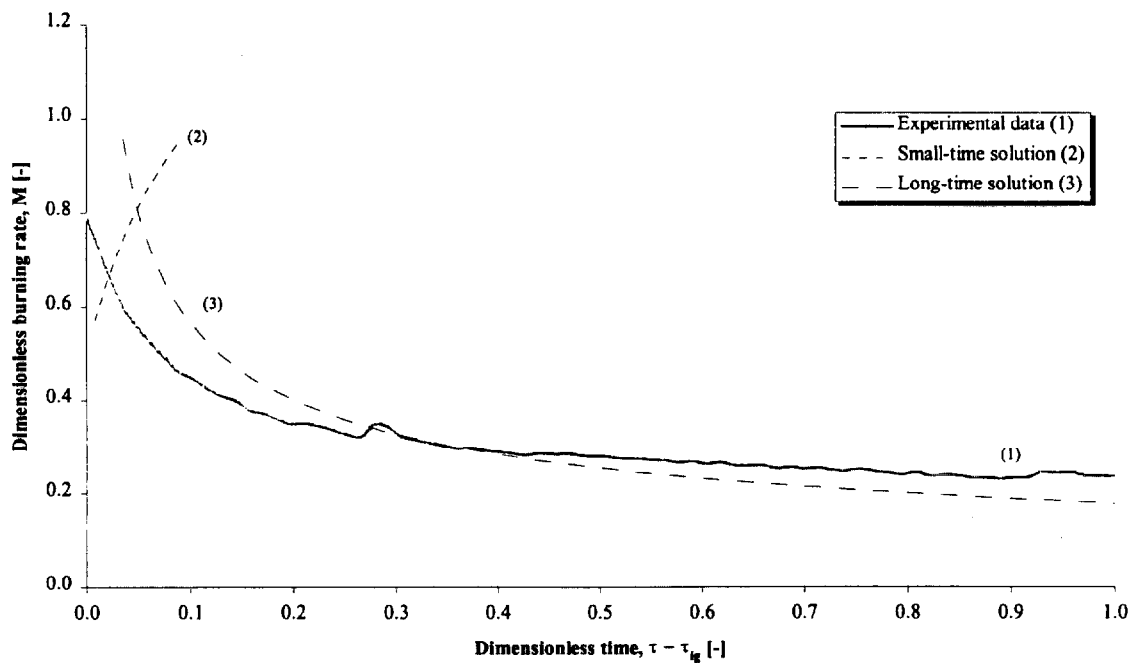**Figure 315.** Temperatures measured in sample (1OL3).

Figure 316. Comparison of dimensionless burning rate using derived properties for species and orientation (1OL3).
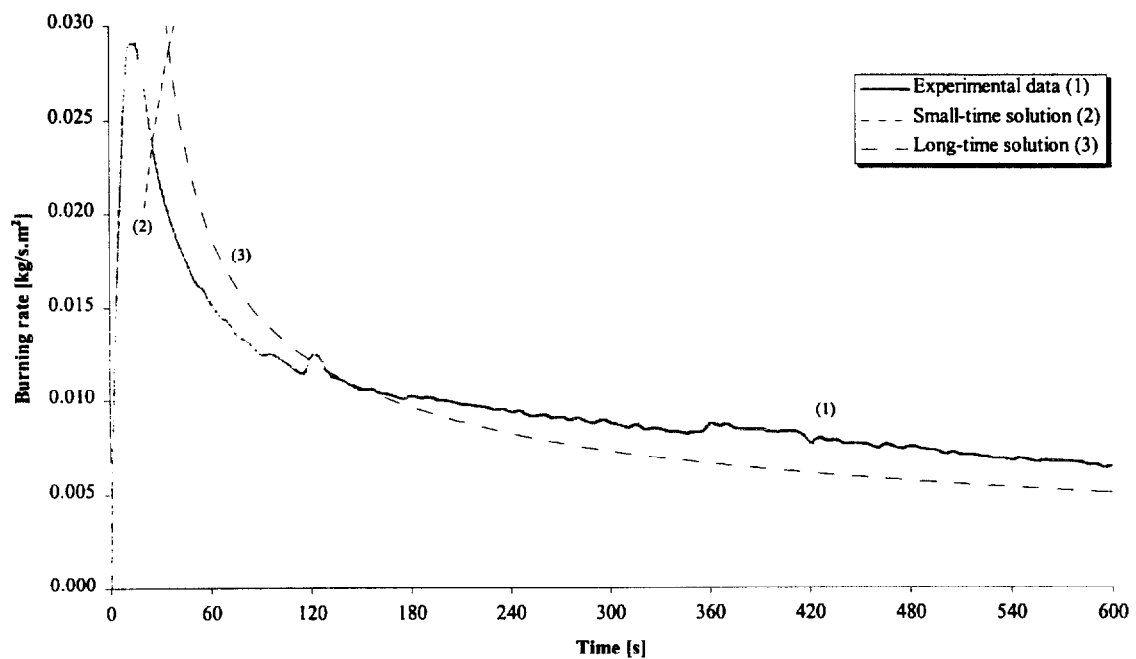

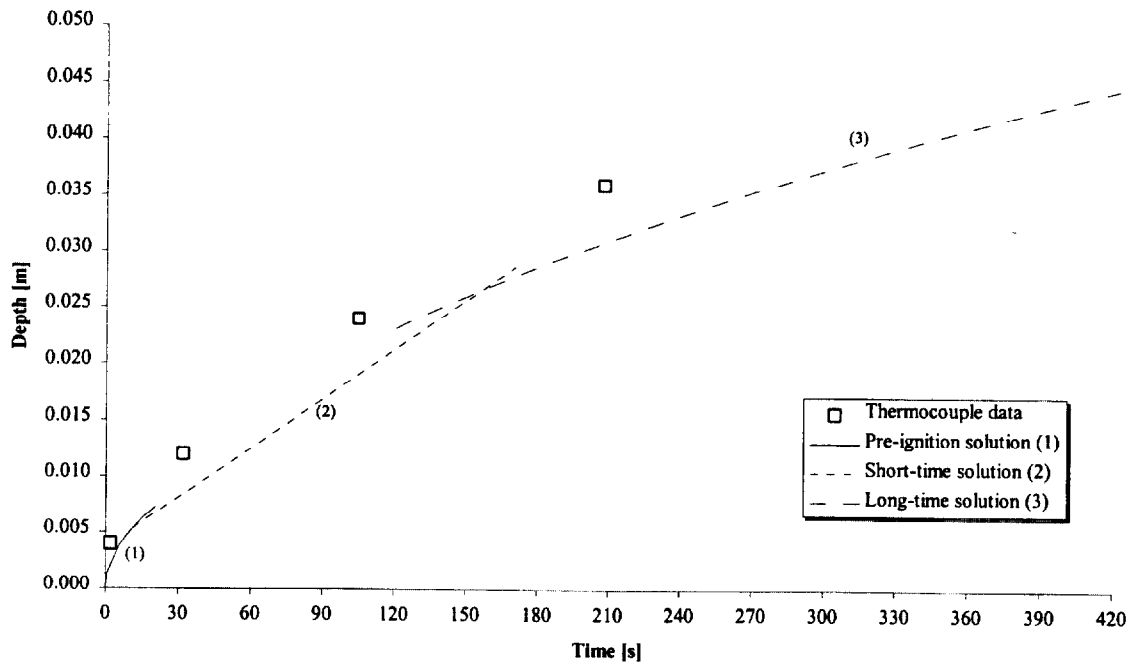**Figure 317.** Comparison of burning rate using derived properties for species and orientation (1OL3).

326

Figure 318. Comparison of measured and calculated thermal penetration depth (1OL3).
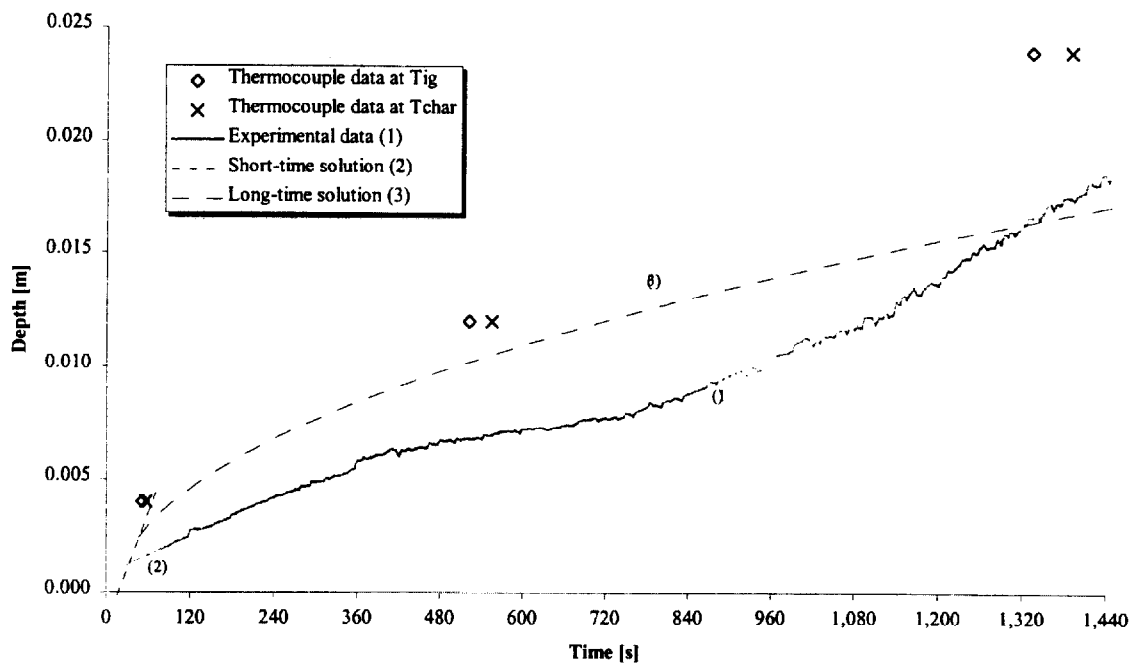

Figure 319. Comparison of estimated char depth from experimental data and the calculated char depth (1OL3).

327

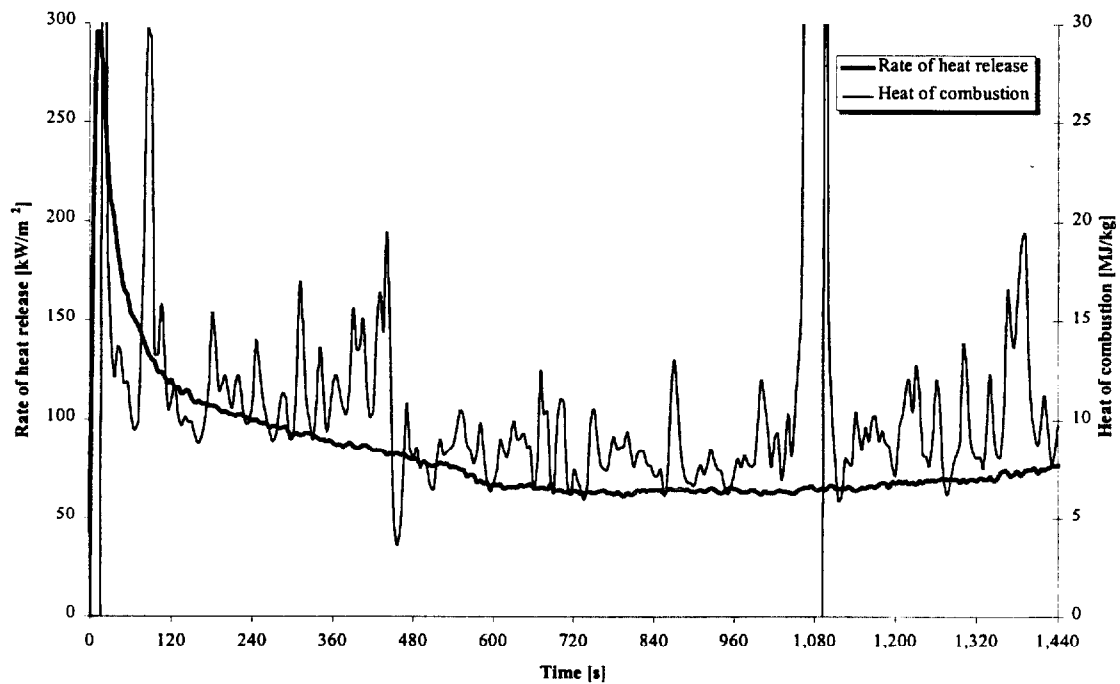Test (1OL4), Red oak, along grain at 75 kW/m^2 for 25 minutes.

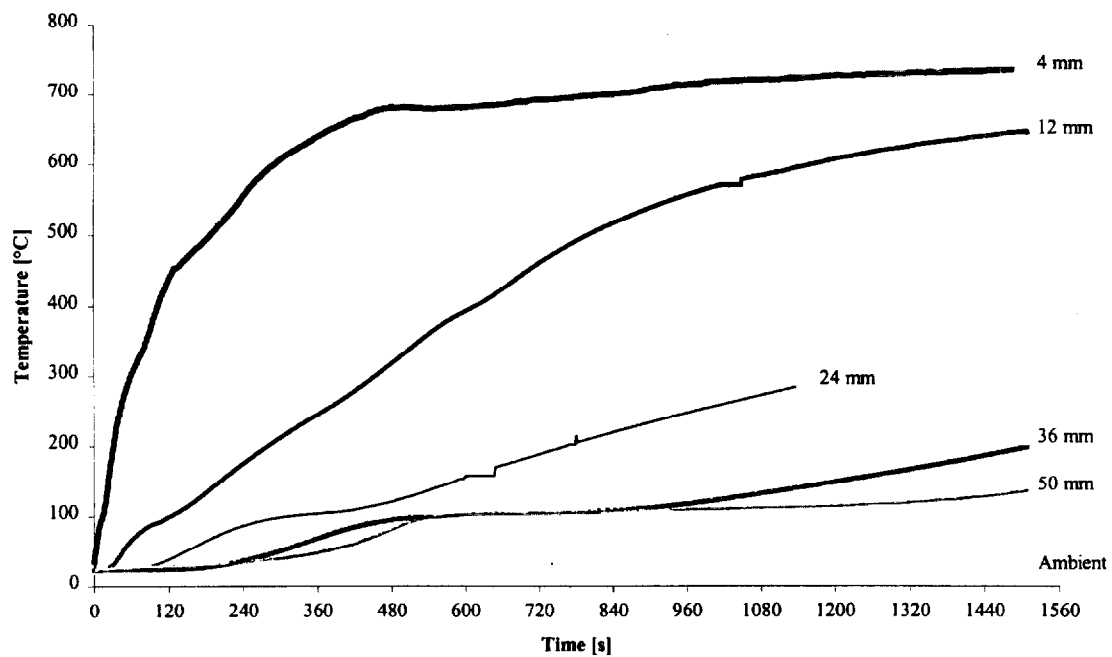**Figure 320.** Rate of heat release and heat of combustion (1OL4).

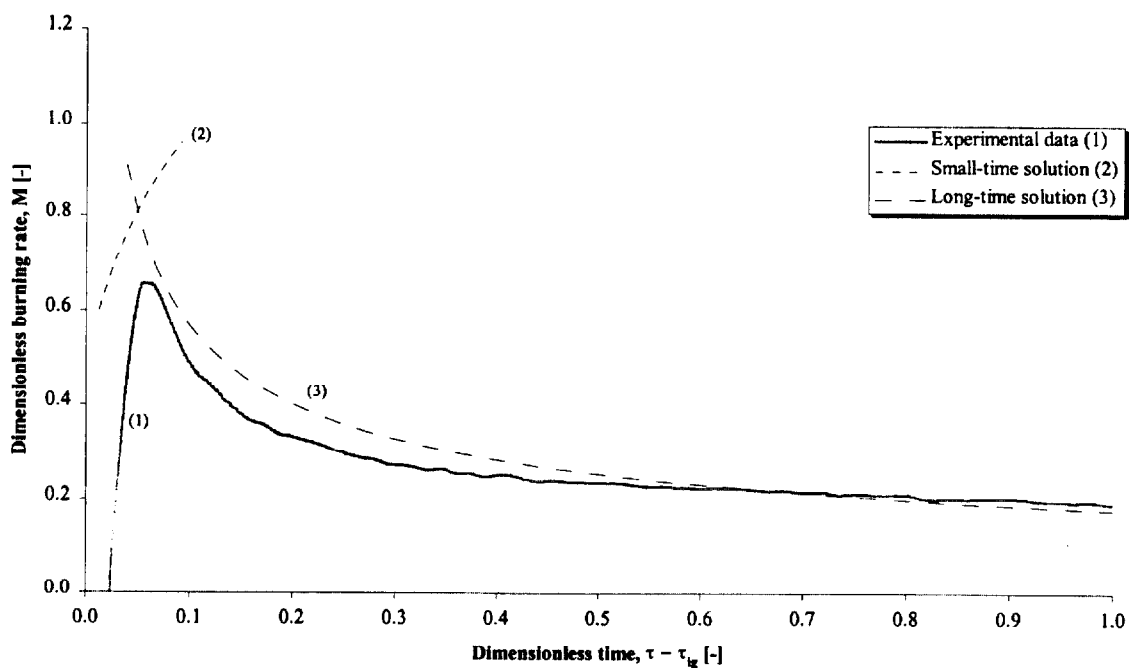**Figure 321.** Temperatures measured in sample (1OL4).

Figure 322. Comparison of dimensionless burning rate using derived properties for species and orientation (1OL4).

Figure 323. Comparison of burning rate using derived properties for species and orientation (1OL4).

329

Figure 324. Comparison of measured and calculated thermal penetration depth (1OL4).

Figure 325. Comparison of estimated char depth from experimental data and the calculated char depth (1OL4).

330

Test (1OL5), Red oak, along grain at 75 kW/m² for 25 minutes.
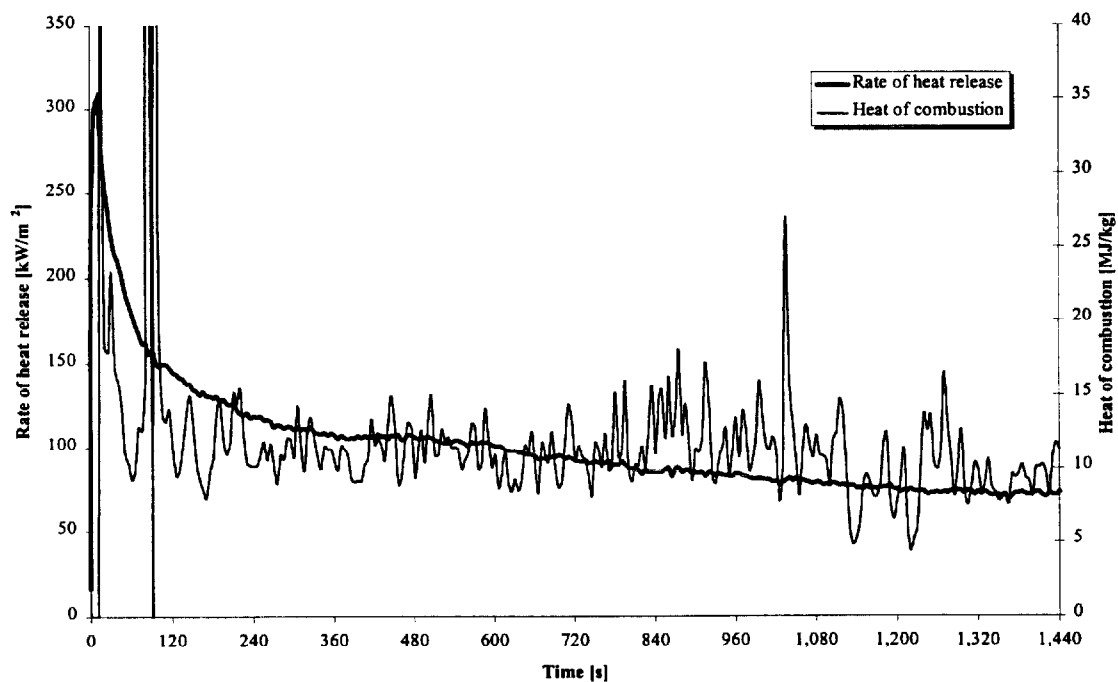
Figure 326. Rate of heat release and heat of combustion (1OL5).

Figure 327. Temperatures measured in sample (1OL5).

331

Figure 328. Comparison of dimensionless burning rate using derived properties for species and orientation (1OL5).
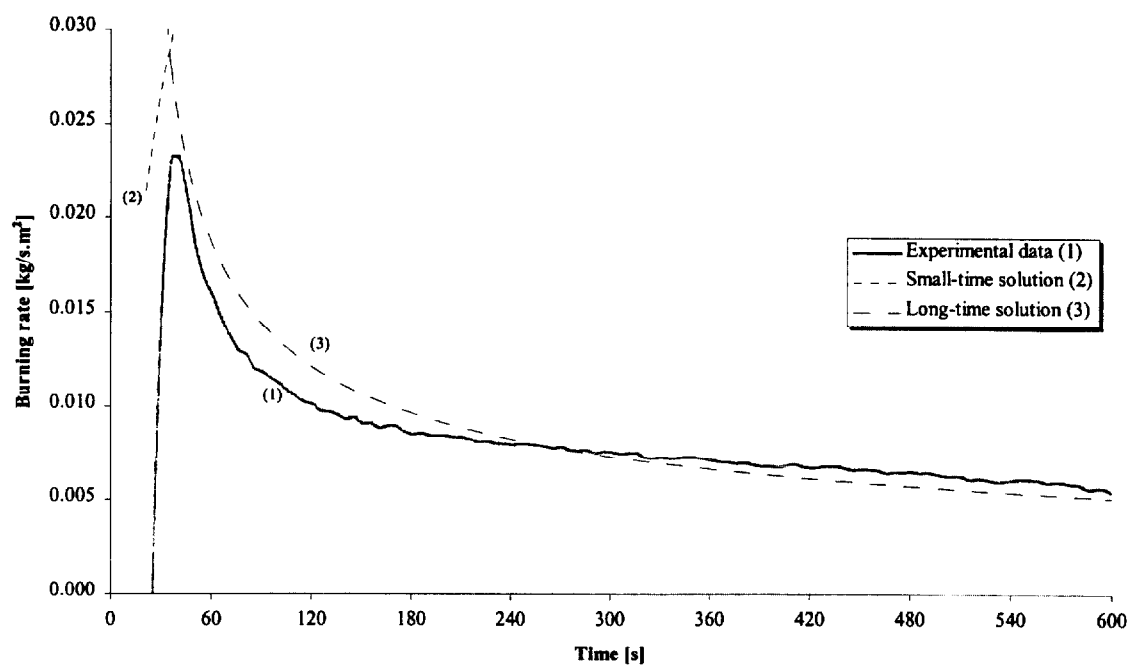

Figure 329. Comparison of burning rate using derived properties for species and orientation (1OL5).
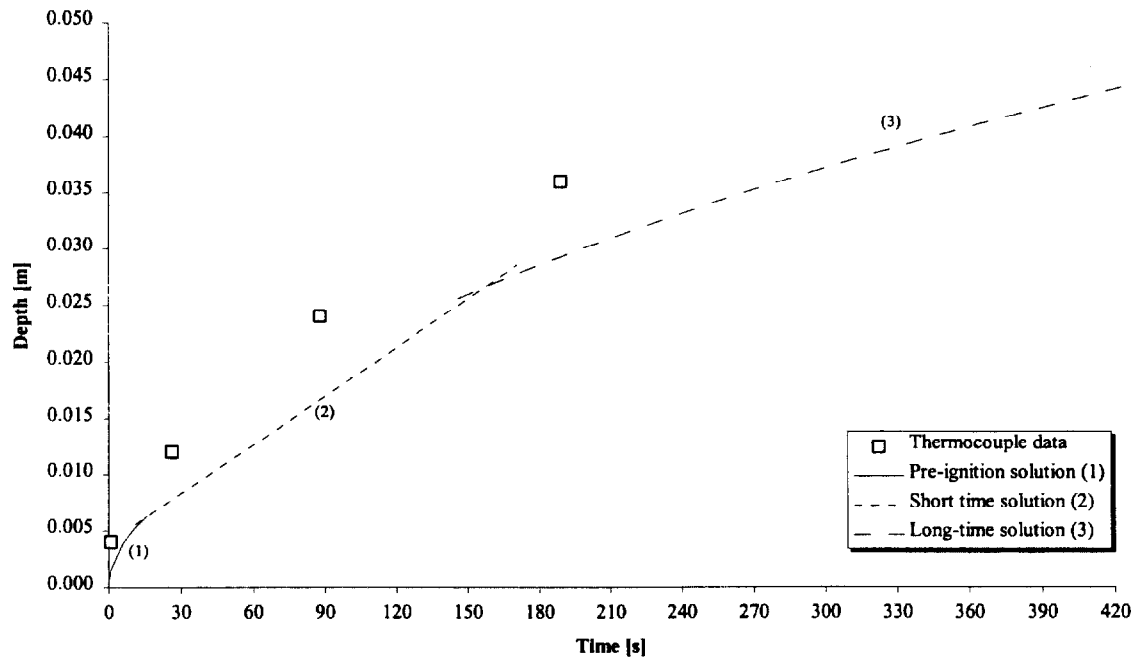
332

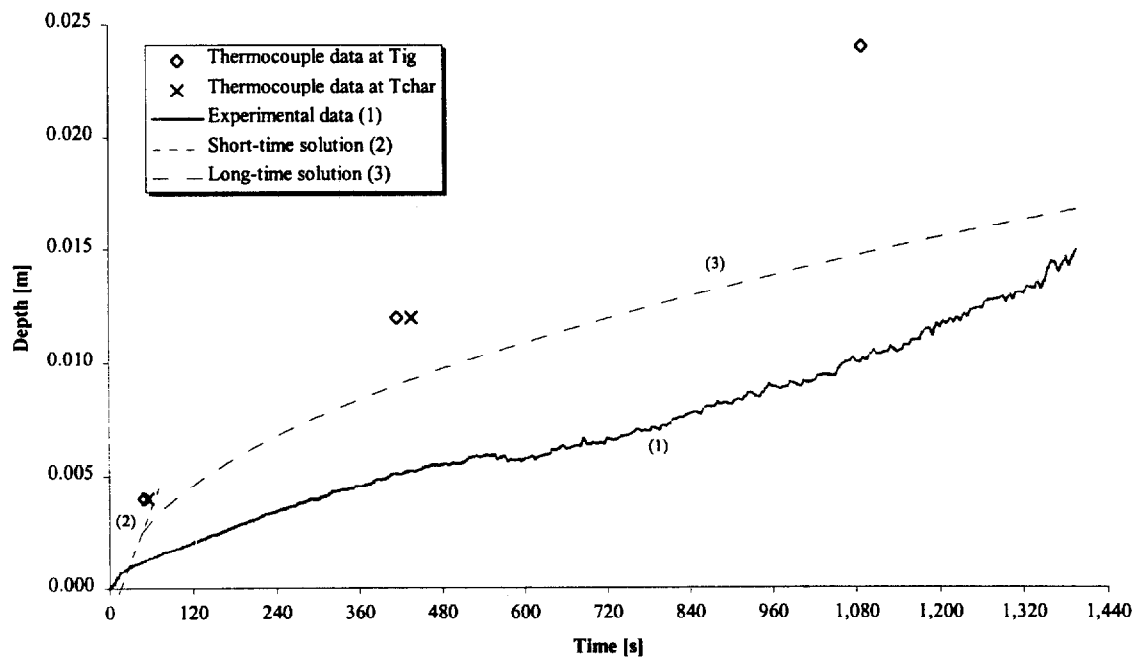**Figure 330.** Comparison of measured and calculated thermal penetration depth (1OL5).

Figure 331. Comparison of estimated char depth from experimental data and the calculated char depth (1OL5).

333

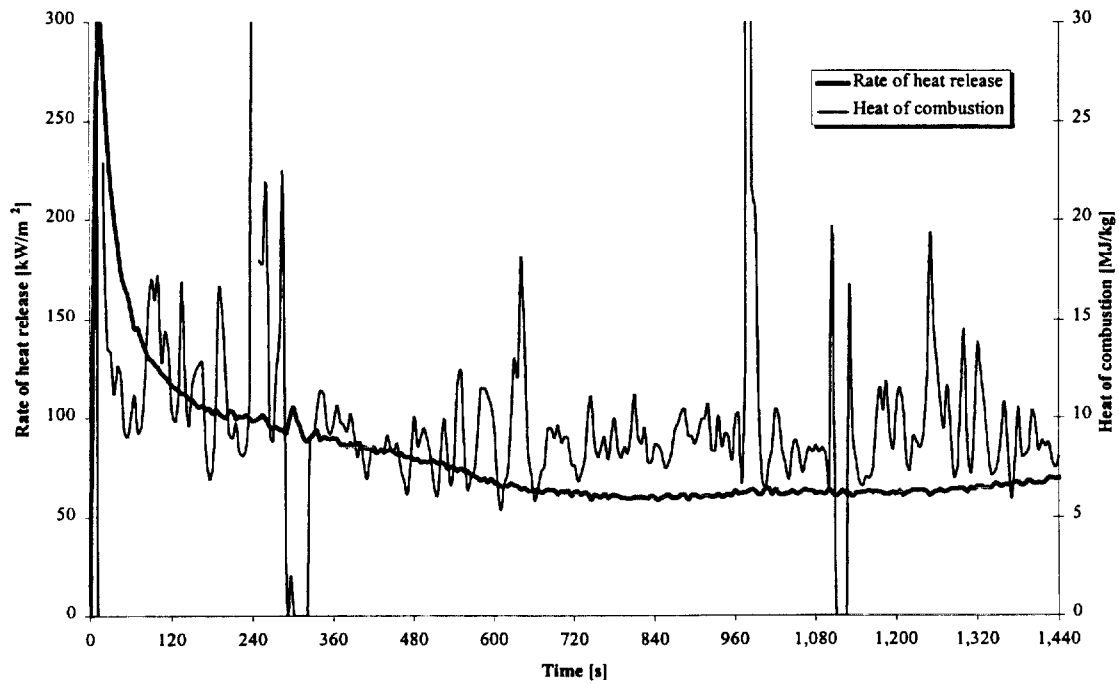Test (1OX1), Red oak, along grain at 25 kW/m^2 for 25 minutes.
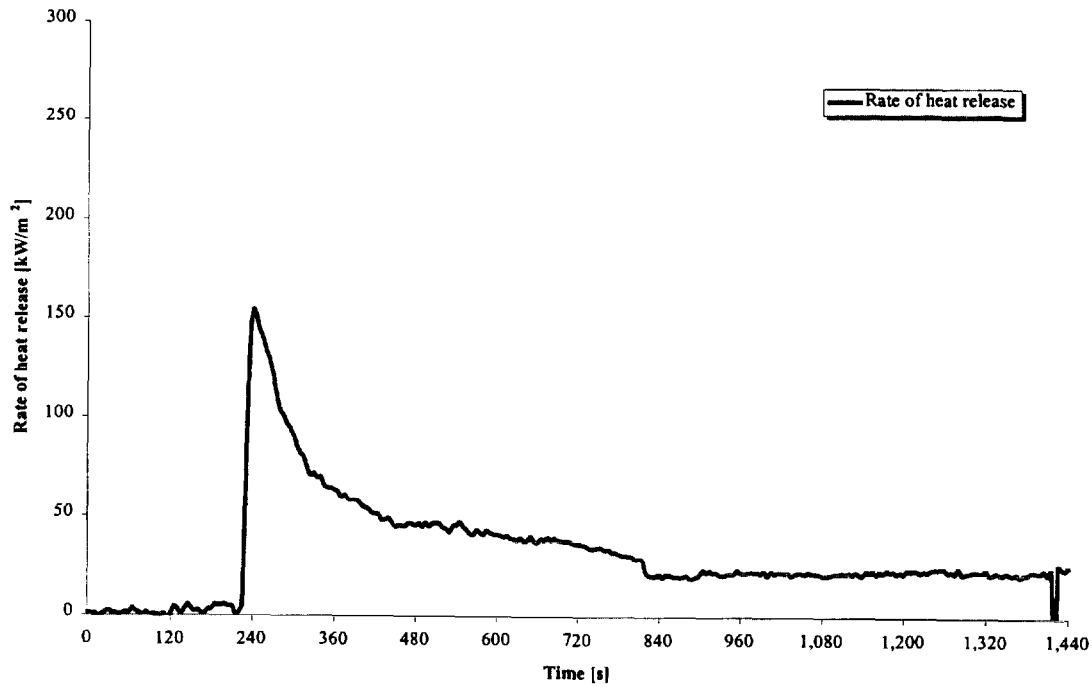
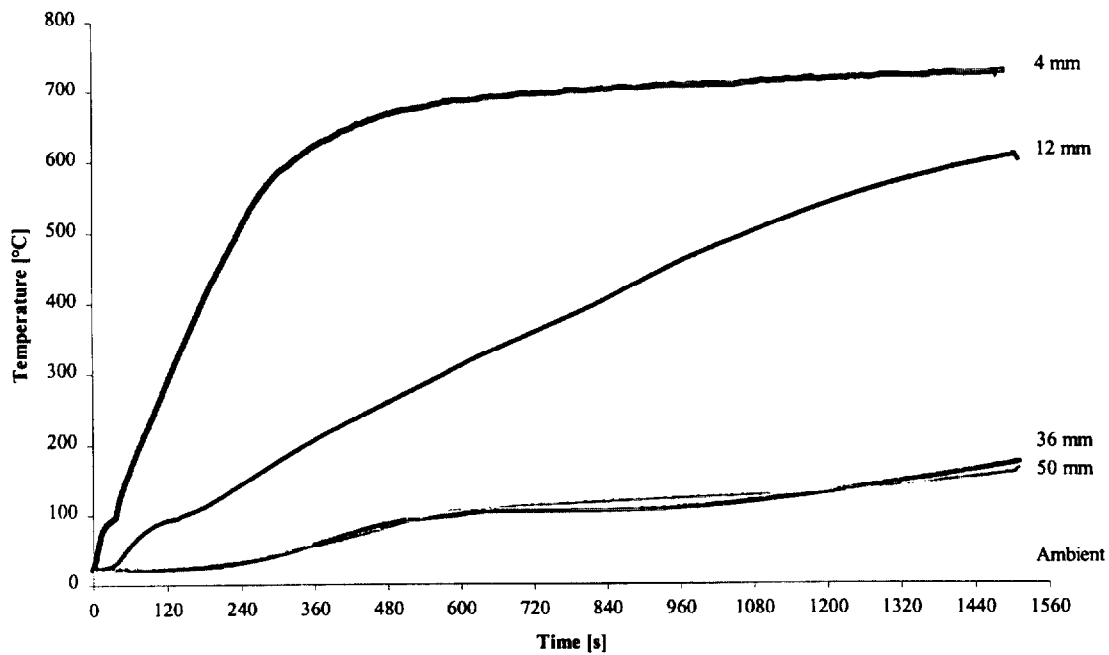

Figure 332. Rate of heat release (1OX1).

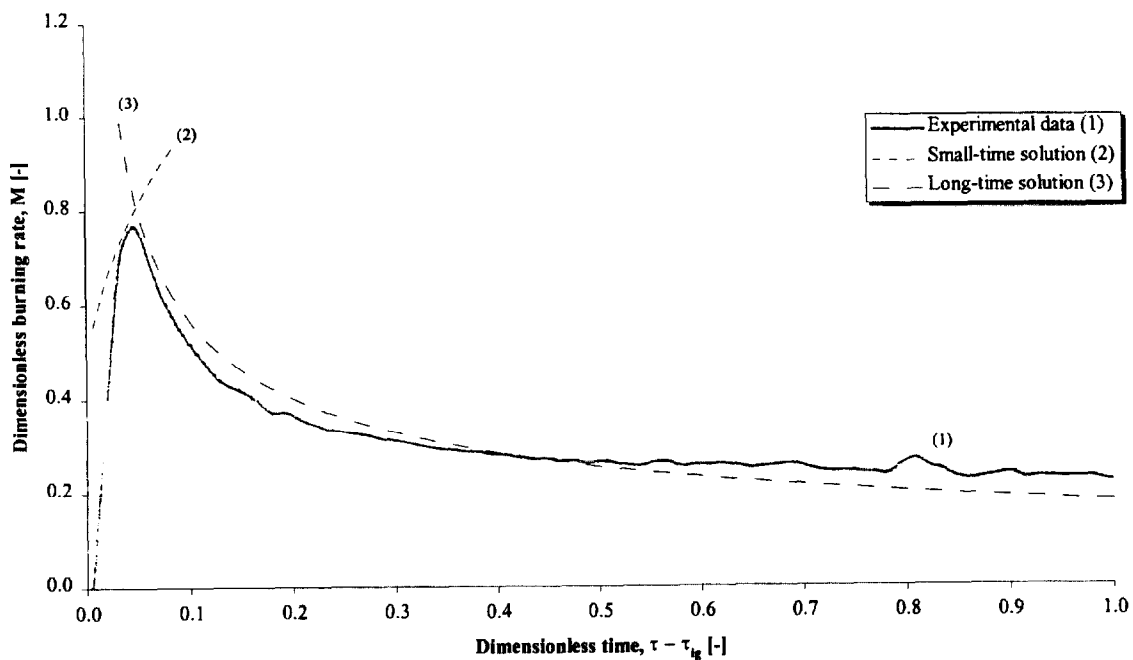**Figure 333.** Temperatures measured in sample (1OX1).

Figure 334. Comparison of dimensionless burning rate using derived properties for species and orientation (1OX1).

Figure 335. Comparison of burning rate using derived properties for species and orientation (1OX1).

335

Figure 336. Comparison of measured and calculated thermal penetration depth (1OX1).

Figure 337. Comparison of estimated char depth from experimental data and the calculated char depth (1OX1).

336

Test (1OX2), Red oak, along grain at 25 kW/m^2 for 75 minutes.
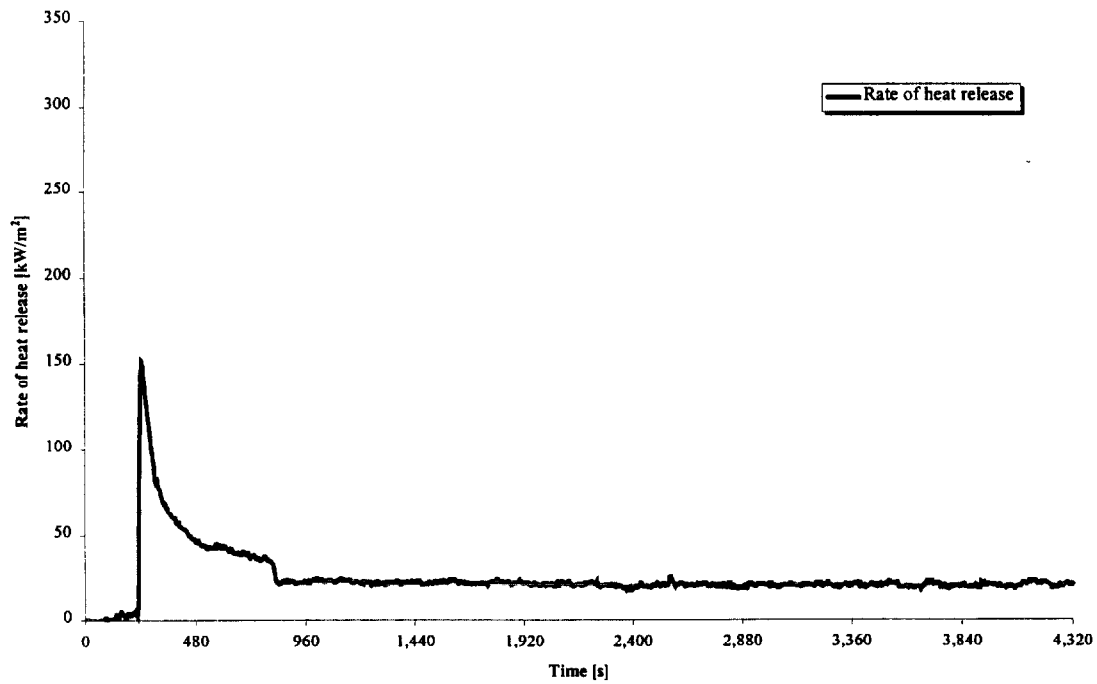
Figure 338. Rate of heat release (1OX2).

Figure 339. Temperatures measured in sample (1OX2).

337

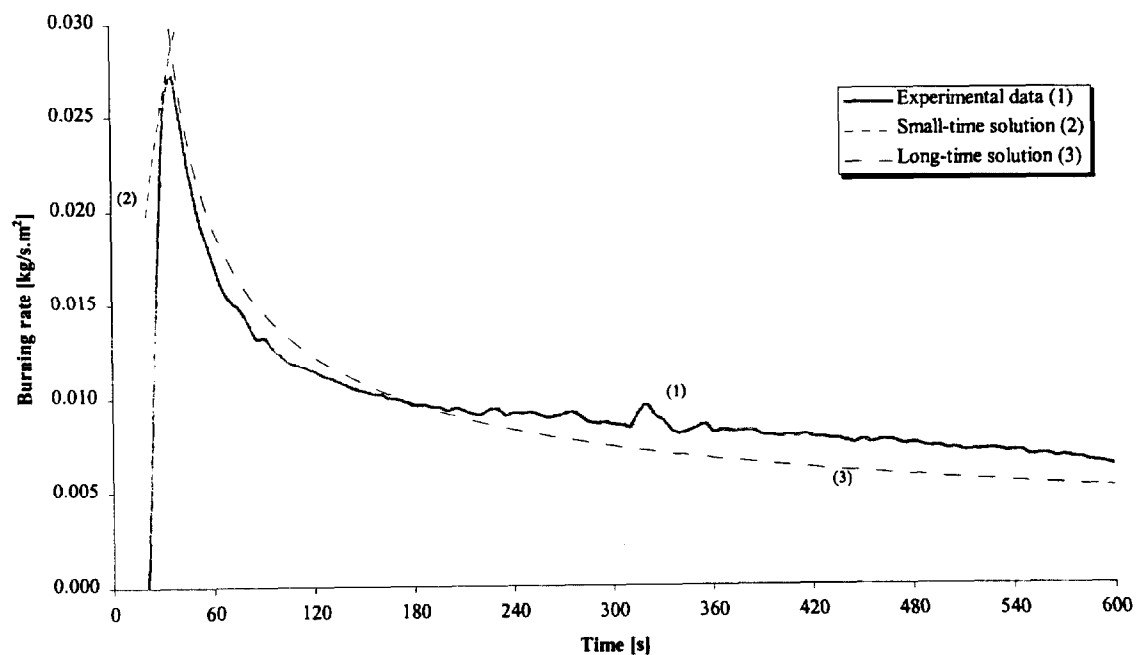**Figure 340.** Comparison of dimensionless burning rate using derived properties for species and orientation (1OX2).

Figure 341. Comparison of burning rate using derived properties for species and orientation (1OX2).
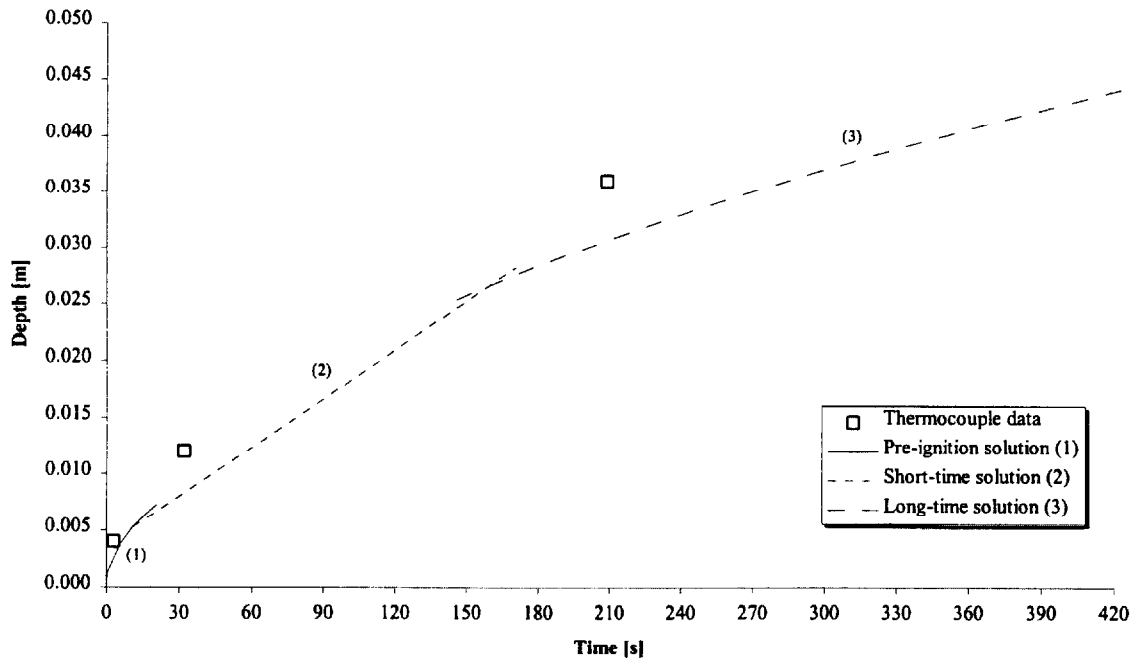
338

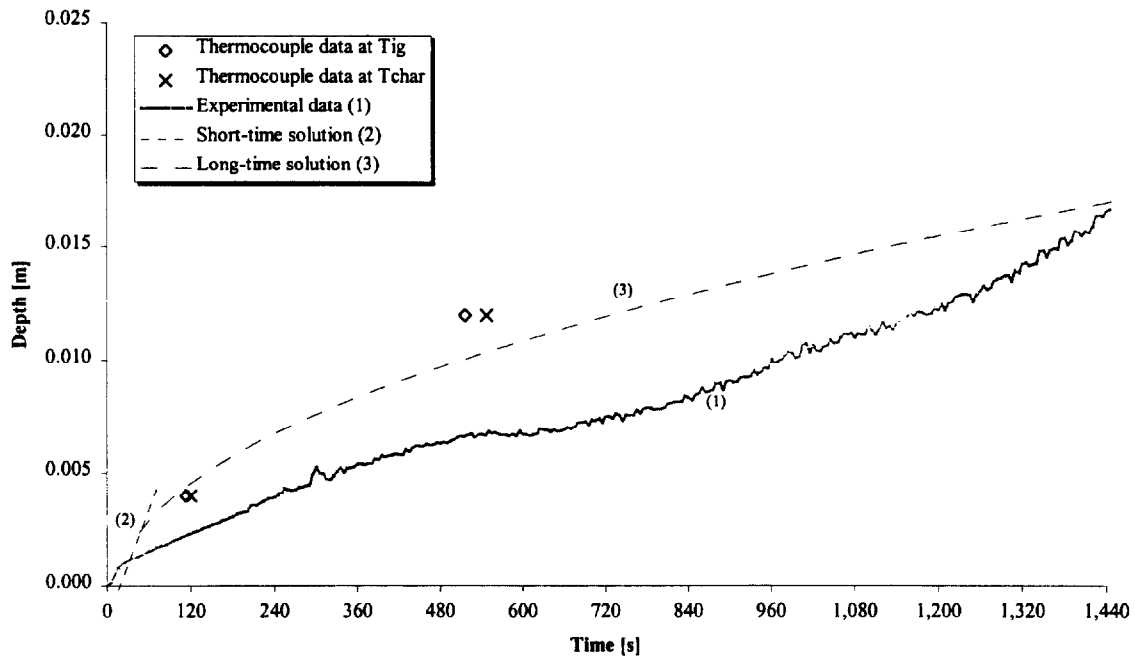**Figure 342.** Comparison of measured and calculated thermal penetration depth (1OX2).

Figure 343. Comparison of estimated char depth from experimental data and the calculated char depth (1OX2).

339

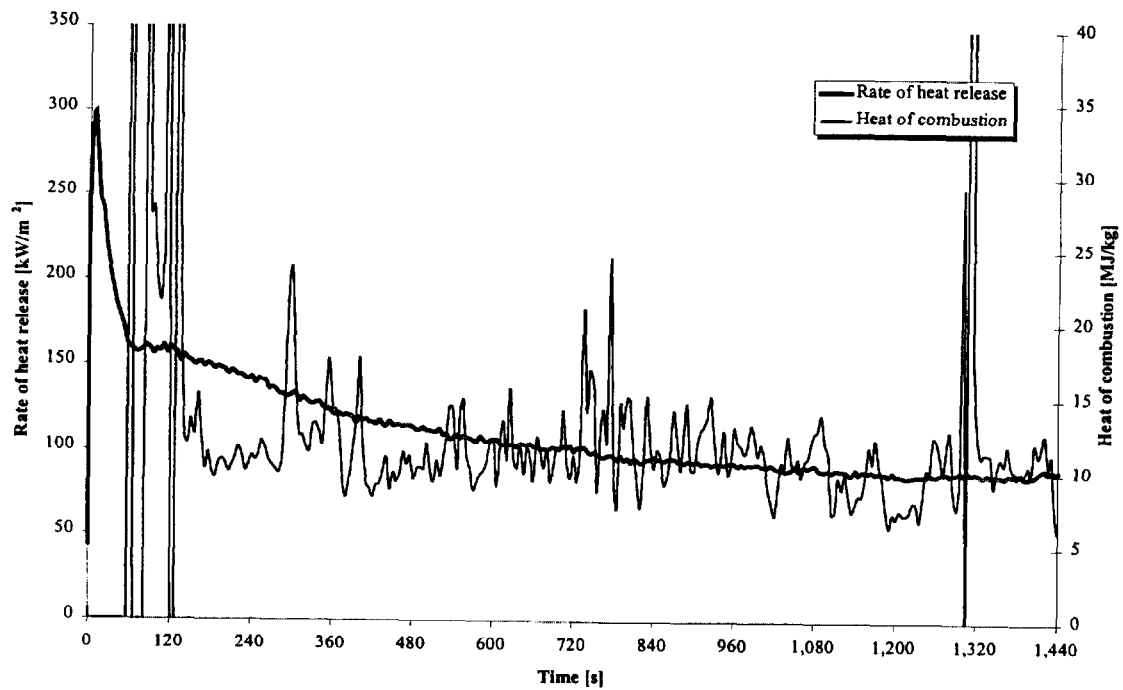Test (1OX3), Red oak, along grain at 75 kW/m^2 for 25 minutes.
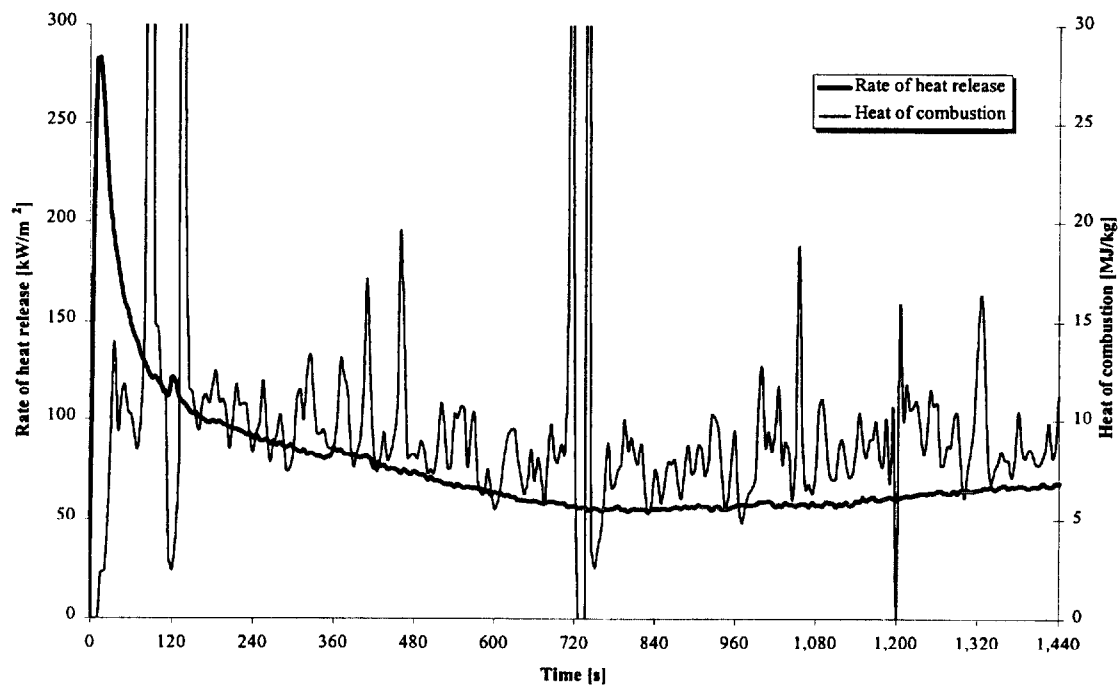
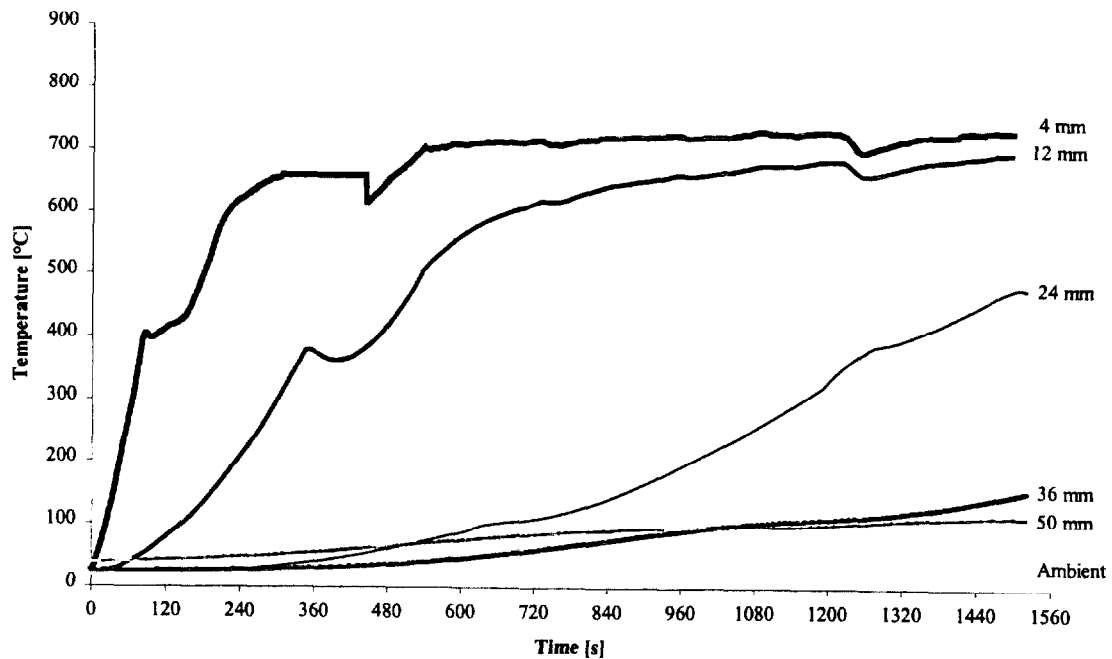**Figure 344.** Rate of heat release and heat of combustion (1OX3).

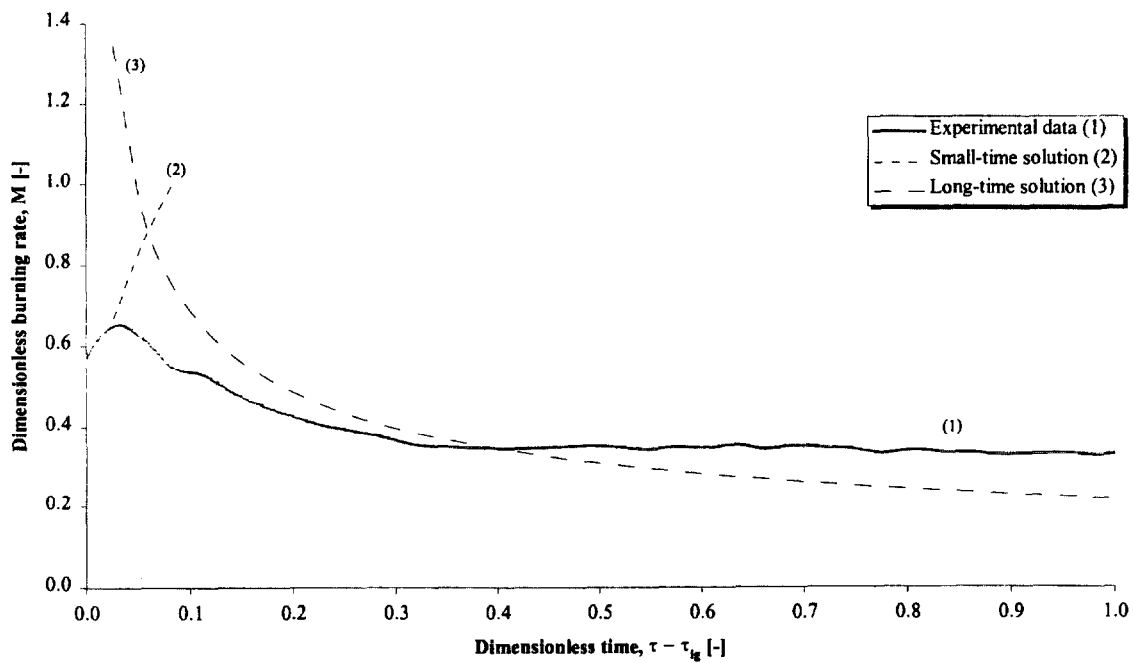**Figure 345.** Temperatures measured in sample (1OX3).

340

Figure 346. Comparison of dimensionless burning rate using derived properties for species and orientation (1OX3).
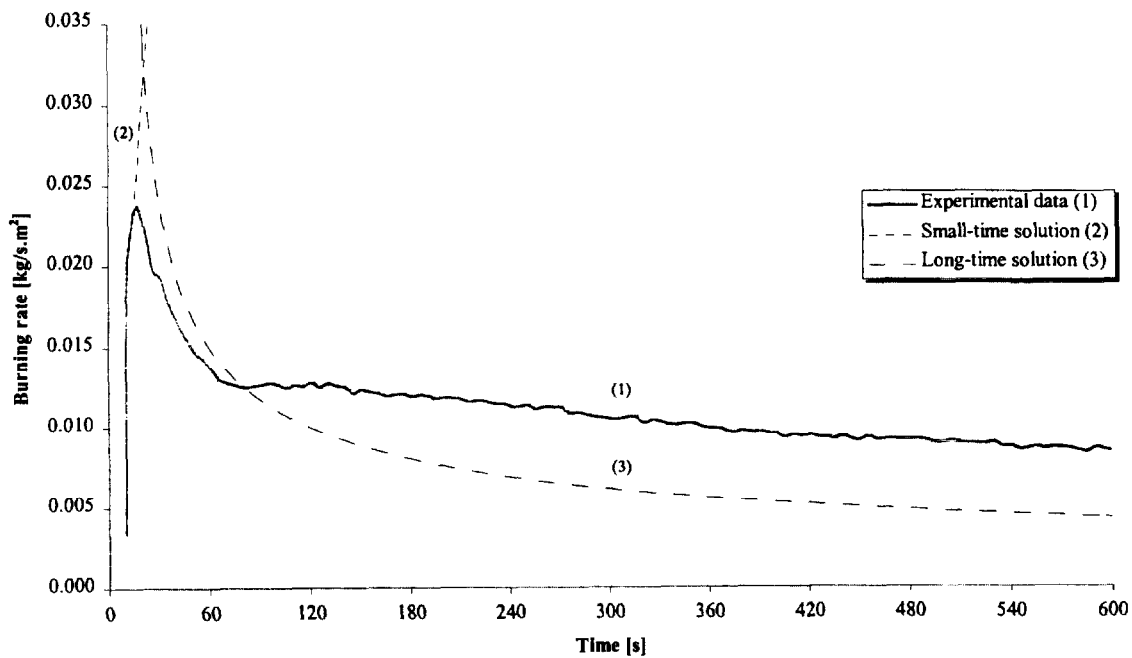

Figure 347. Comparison of burning rate using derived properties for species and orientation (1OX3).

Figure 348. Comparison of measured and calculated thermal penetration depth (1OX3).

Figure 349. Comparison of estimated char depth from experimental data and the calculated char depth (1OX3).

Test (1OX4) : Red oak, along grain at 75 kW/m^2 for 25 minutes.

Figure 350. Rate of heat release and heat of combustion (1OX4).

Figure 351. Temperatures measured in sample (1OX4).

343

Figure 352. Comparison of dimensionless burning rate using derived properties for species and orientation (1OX4).

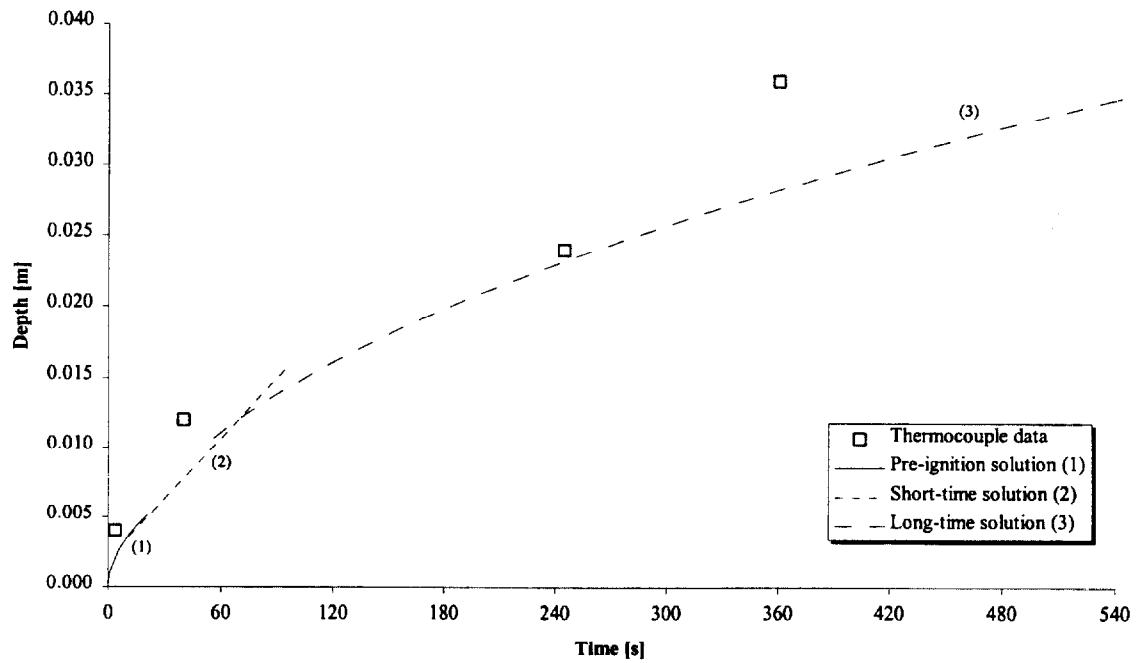**Figure 353.** Comparison of burning rate using derived properties for species and orientation (1OX4).

344

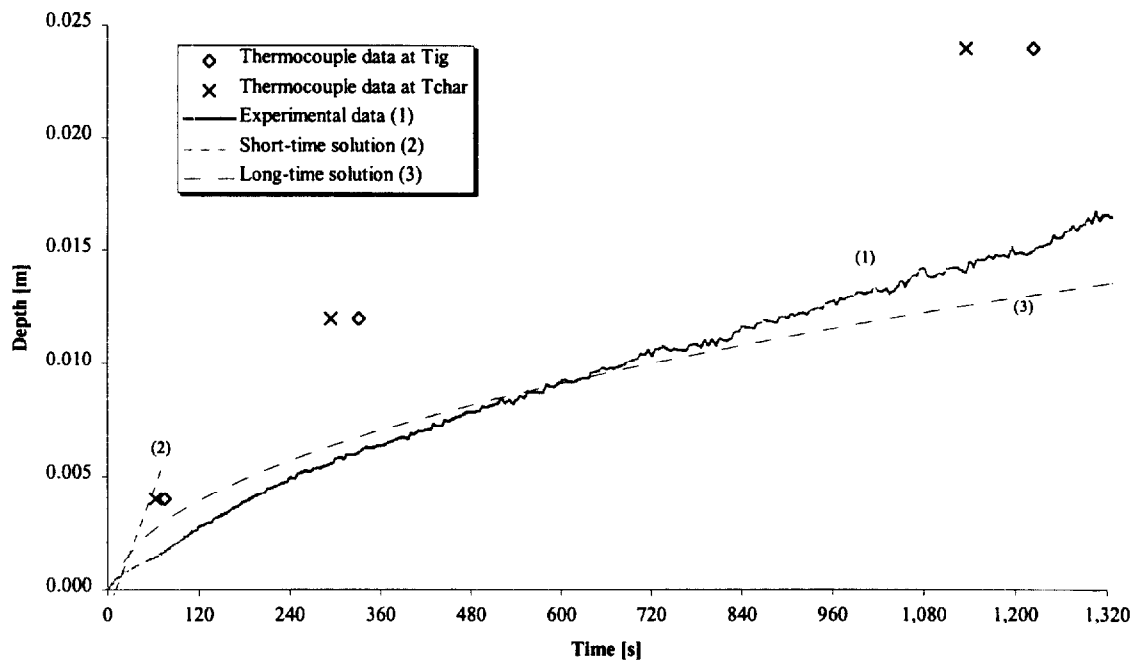**Figure 354.** Comparison of measured and calculated thermal penetration depth (1OX4).

Figure 355. Comparison of estimated char depth from experimental data and the calculated char depth (1OX4).

345

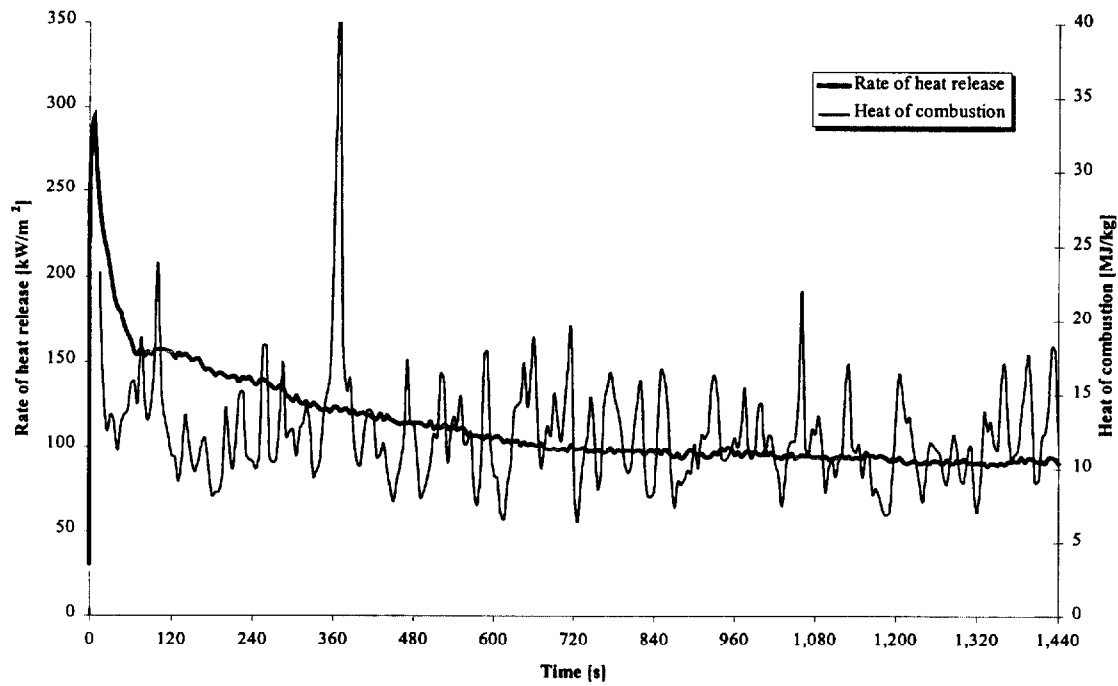Test 1OX5 : Red oak, along grain at 75 kW/m² for 25 minutes.

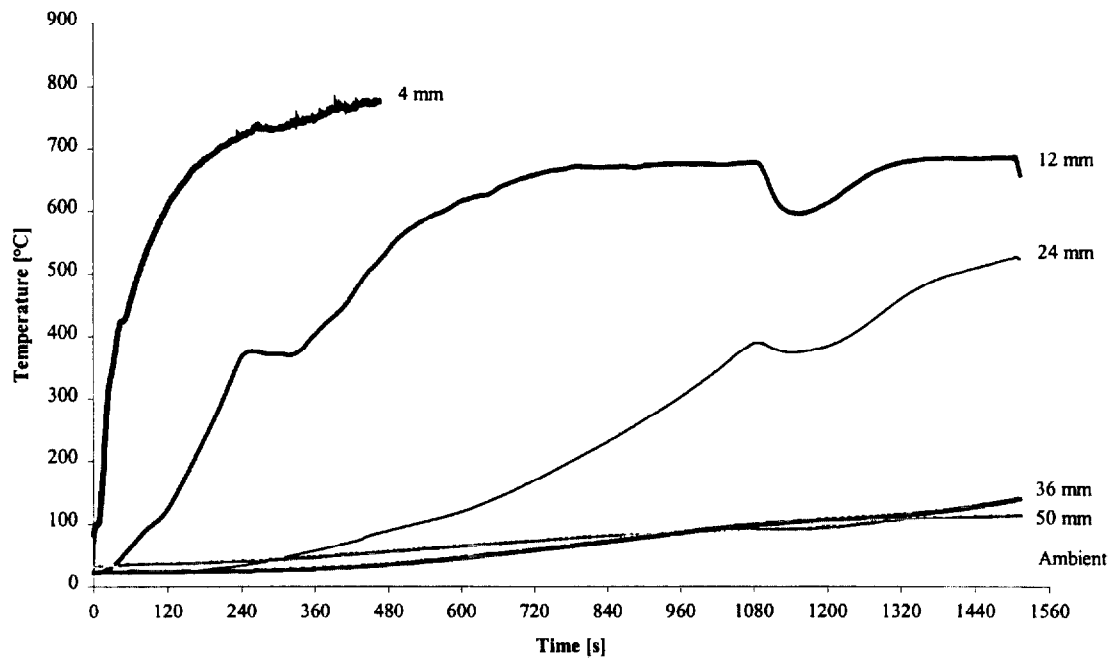**Figure 356.** Rate of heat release and heat of combustion (1OX5).

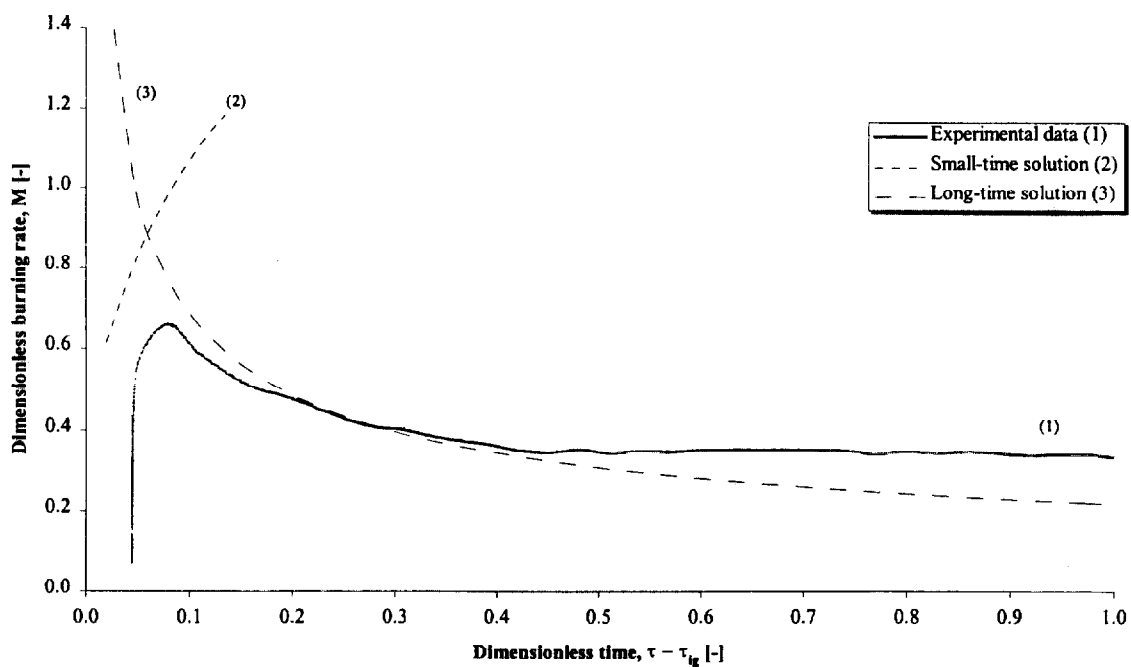**Figure 357.** Temperatures measured in sample (1OX5).

346

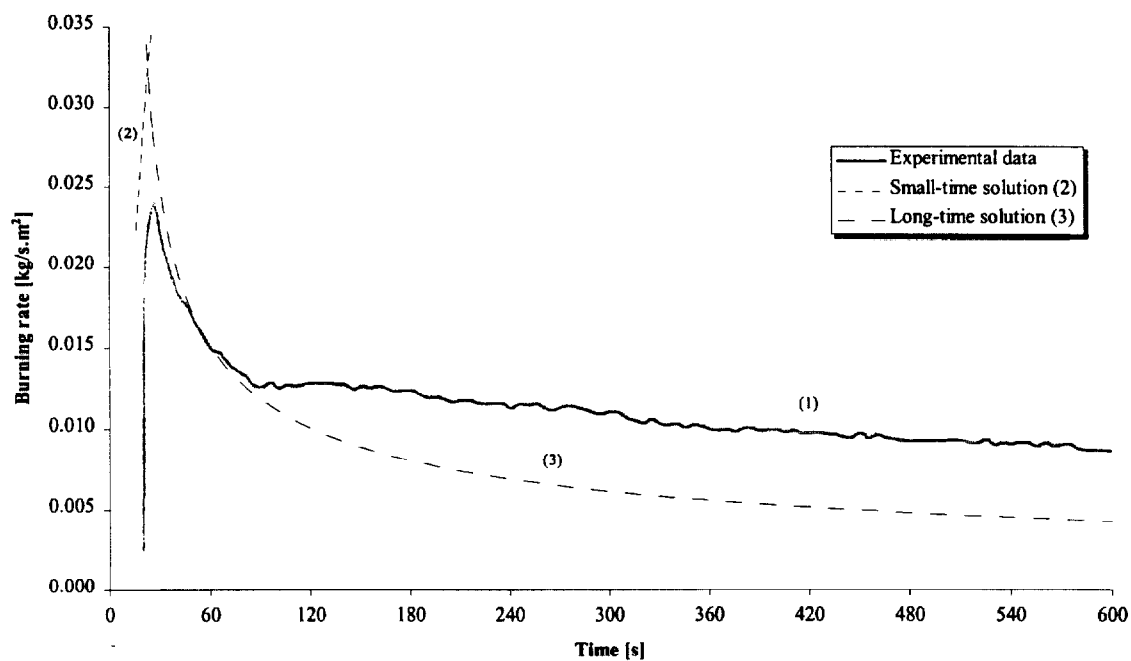**Figure 358.** Comparison of dimensionless burning rate using derived properties for species and orientation (1OX5).

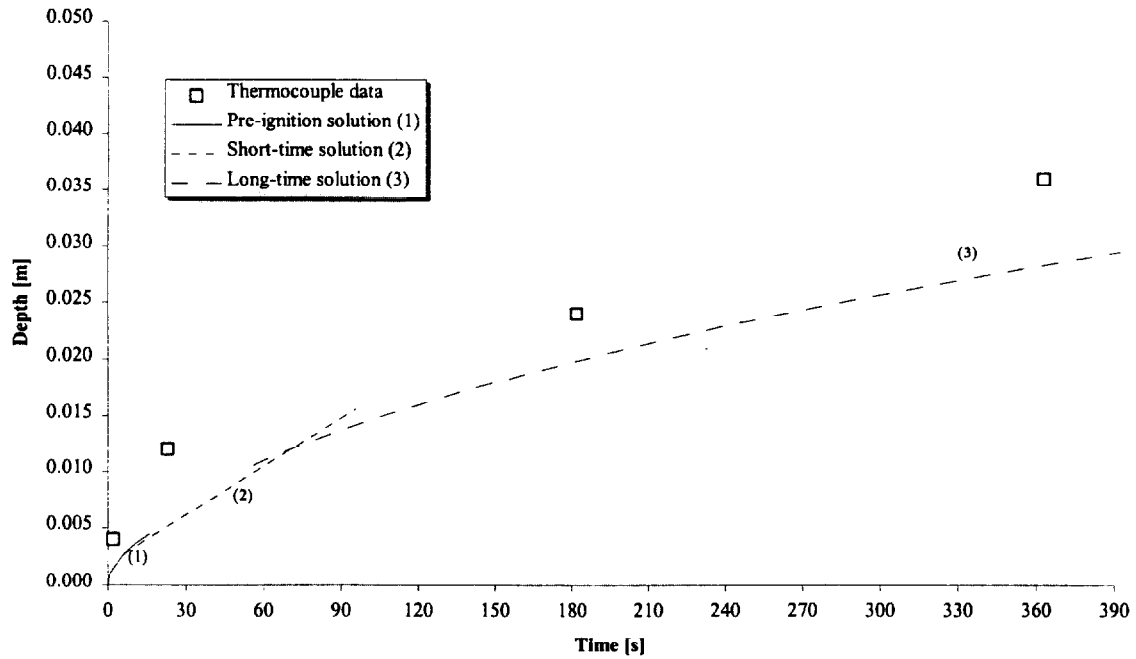**Figure 359.** Comparison of burning rate using derived properties for species and orientation (1OX5).

347

Figure 360. Comparison of measured and calculated thermal penetration depth (1OX5).

Figure 361. Comparison of estimated char depth from experimental data and the calculated char depth (1OX5).

348

Test (1ML1), Maple, along grain at 75 kW/m² for 25 minutes.

Figure 362. Rate of heat release and heat of combustion (1ML1).

Figure 363. Temperatures measured in sample (1ML1).

Figure 364. Comparison of dimensionless burning rate using derived properties for species and orientation (1ML1).

Figure 365. Comparison of burning rate using derived properties for species and orientation (1ML1).

350

Figure 366. Comparison of measured and calculated thermal penetration depth (1ML1).
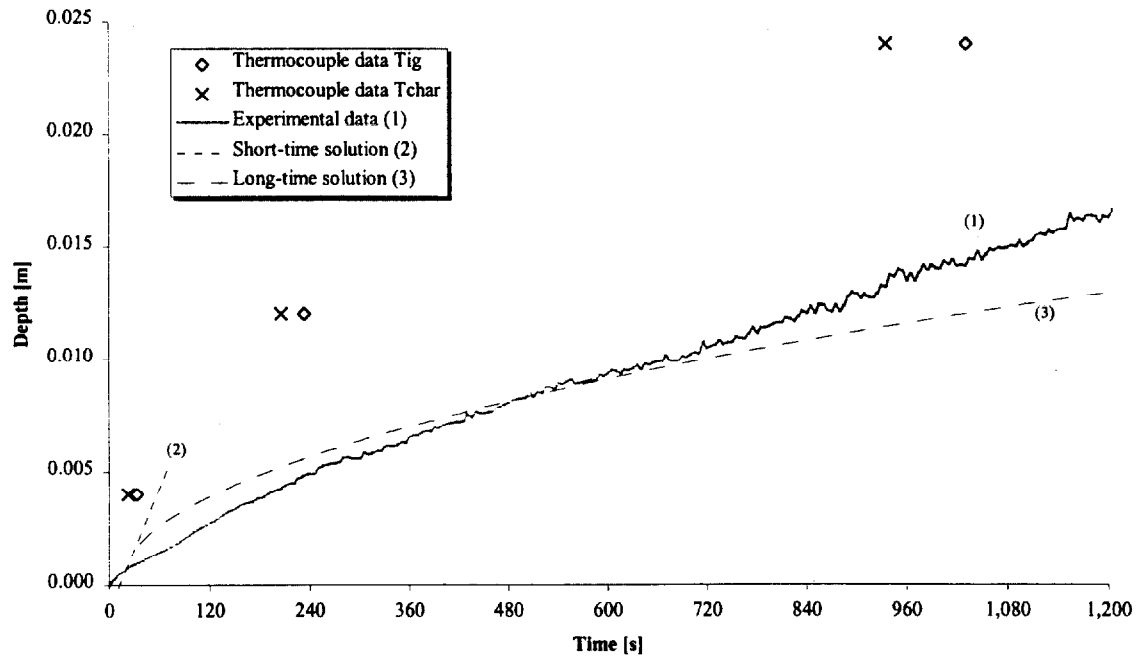

Figure 367. Comparison of estimated char depth from experimental data and the calculated char depth (1ML1).

351

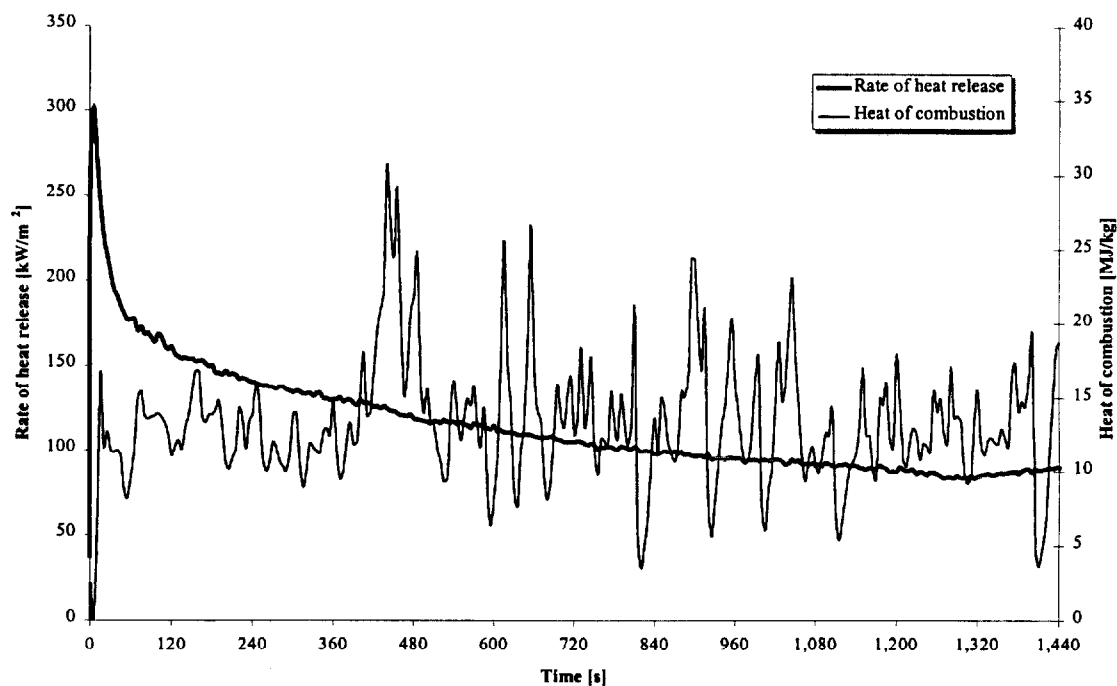Test (1ML2), Maple, along grain at 75 kW/m² for 25 minutes.

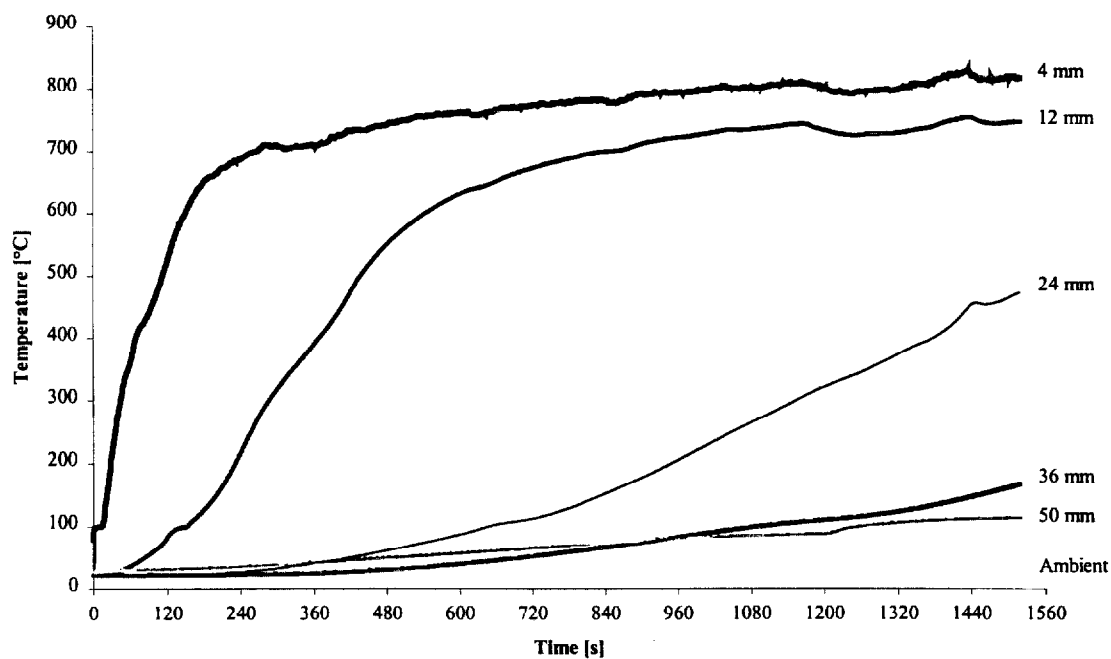**Figure 368.** Rate of heat release and heat of combustion (1ML2).

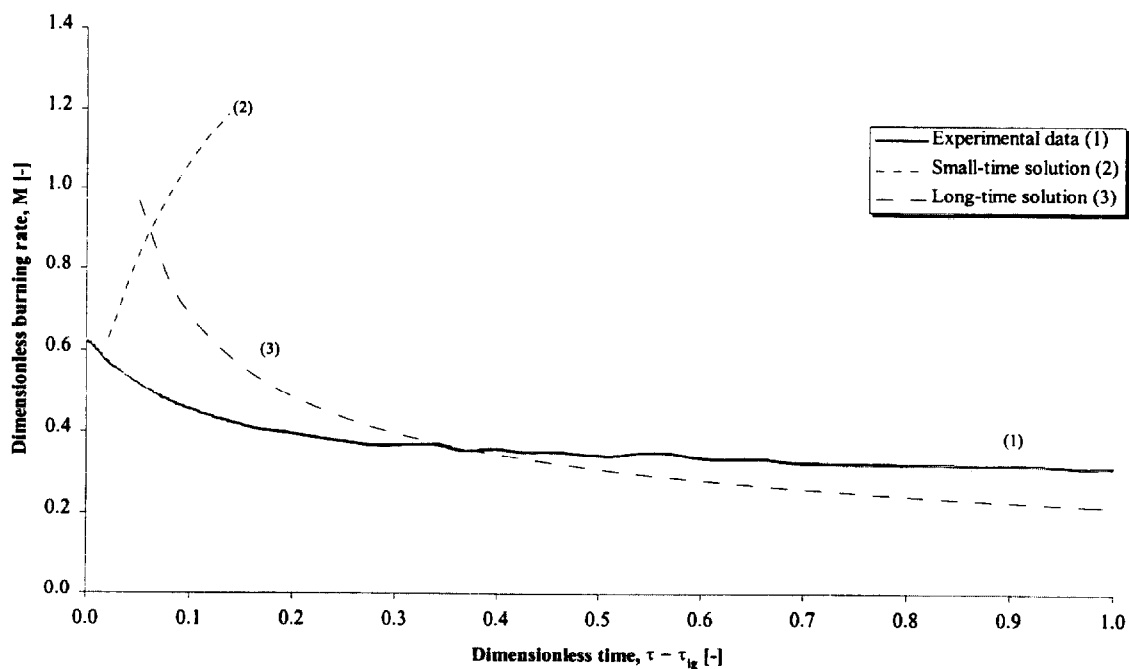**Figure 369.** Temperatures measured in sample (1ML2).

Figure 370. Comparison of dimensionless burning rate using derived properties for species and orientation (1ML2).
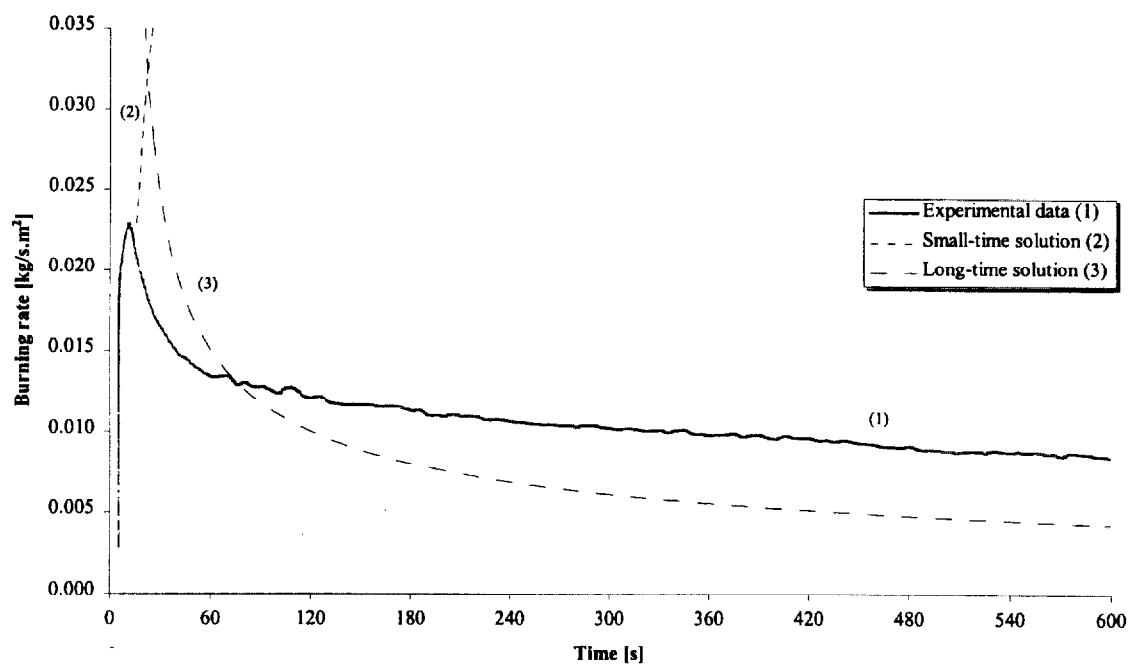

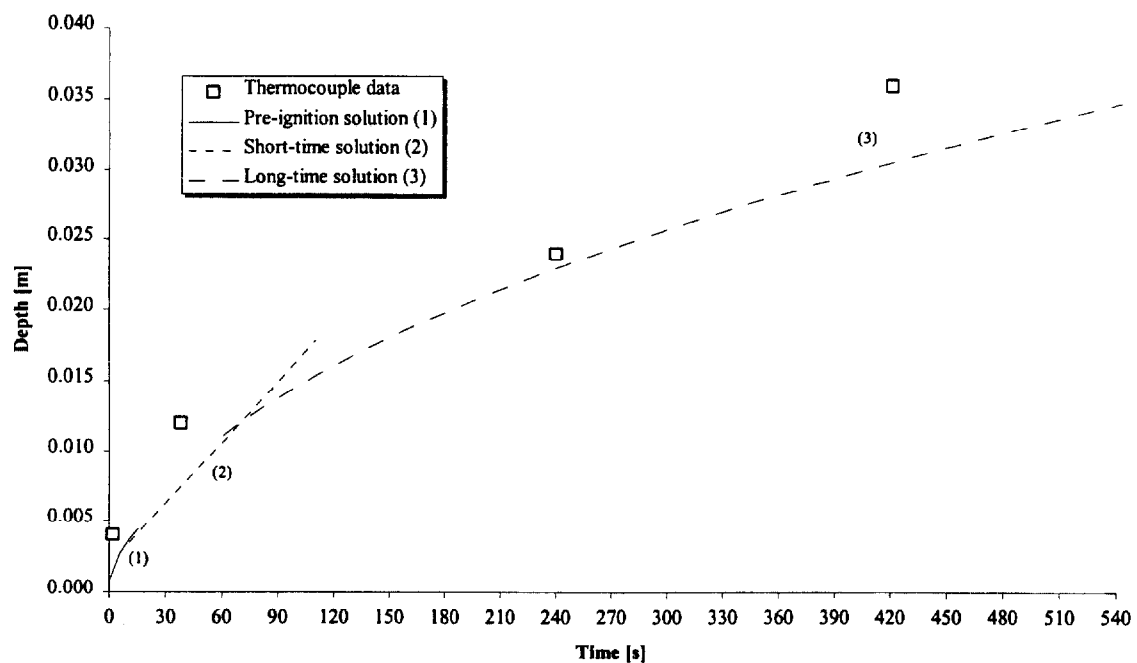**Figure 371.** Comparison of burning rate using derived properties for species and orientation (1ML2).

353

Figure 372. Comparison of measured and calculated thermal penetration depth (1ML2).
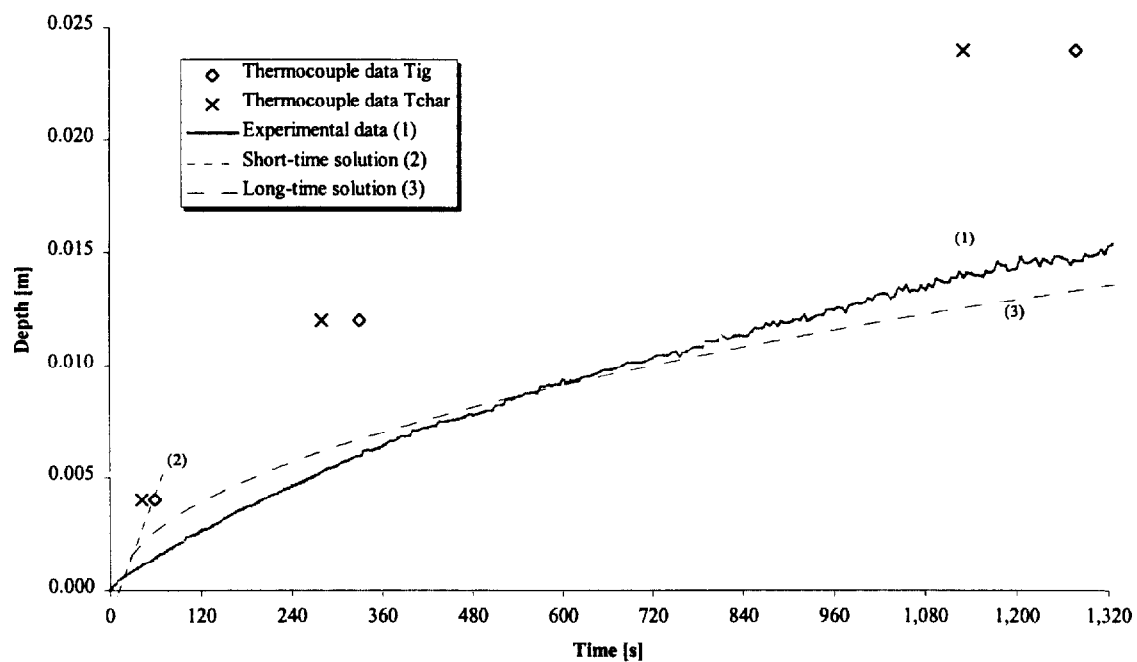

Figure 373. Comparison of estimated char depth from experimental data and the calculated char depth (1ML2).

354

Test (1ML3), Maple, along grain at 75 kW/m^2 for 25 minutes.

Figure 374. Rate of heat release and heat of combustion (1ML3).

Figure 375. Temperatures measured in sample (1ML3).

355

Figure 376. Comparison of dimensionless burning rate using derived properties for species and orientation (1ML3).

Figure 377. Comparison of burning rate using derived properties for species and orientation (1ML3).

356

Figure 378. Comparison of measured and calculated thermal penetration depth (1ML3).

Figure 379. Comparison of estimated char depth from experimental data and the calculated char depth (1ML3).

357

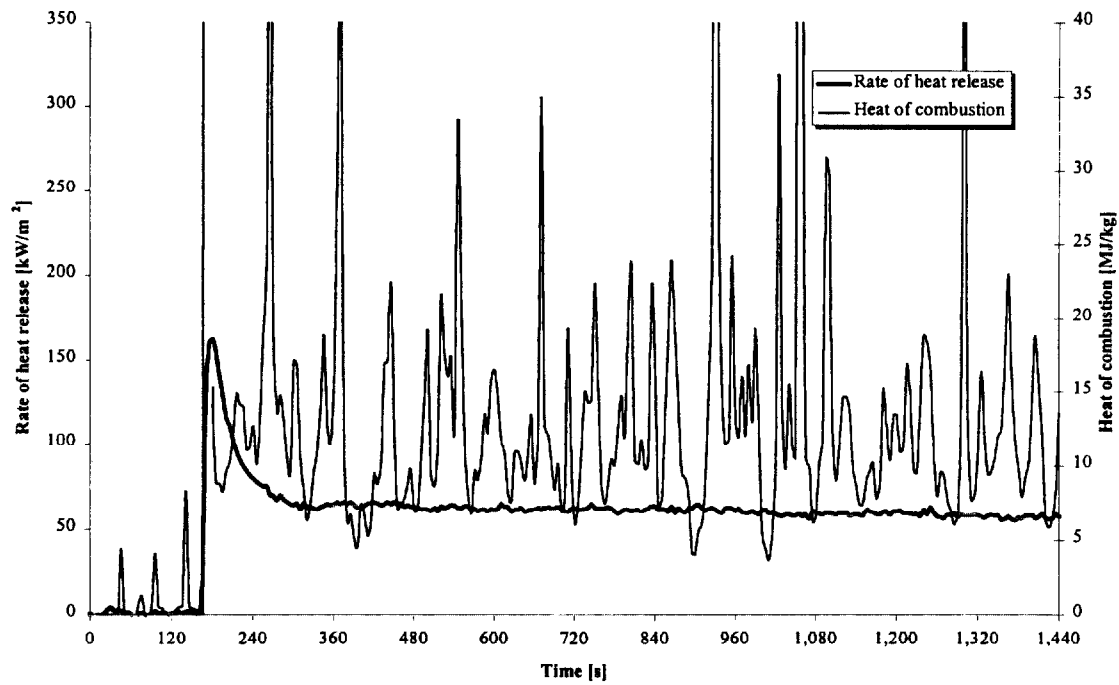Test (1ML4), Maple, along grain at 25 kW/m² for 25 minutes.

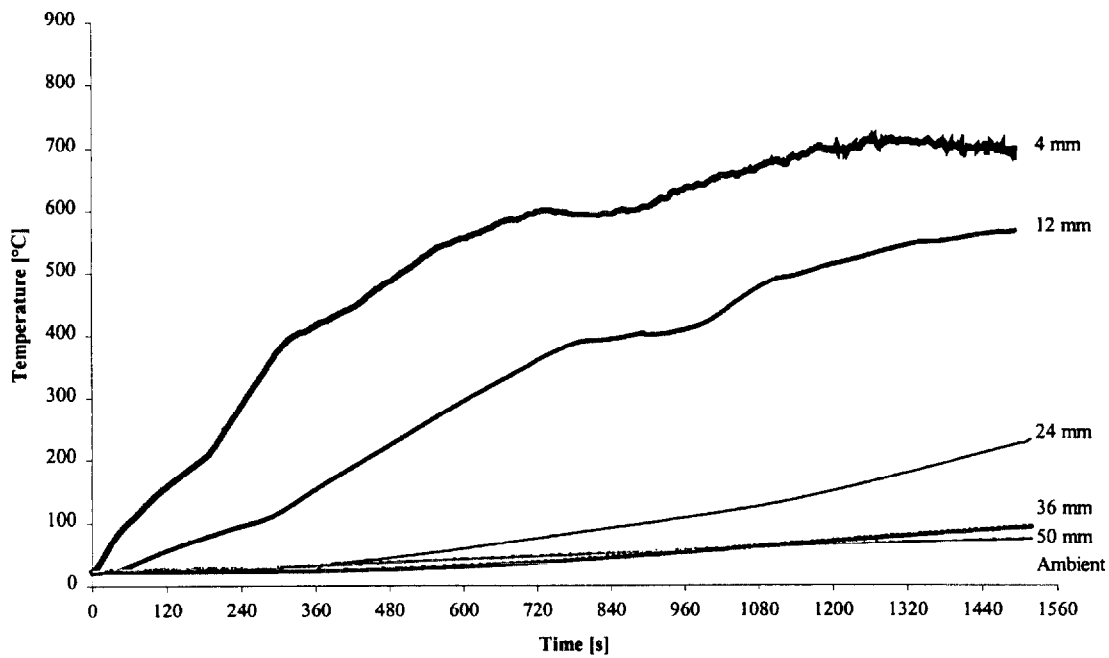**Figure 380.** Rate of heat release and heat of combustion (1ML4).

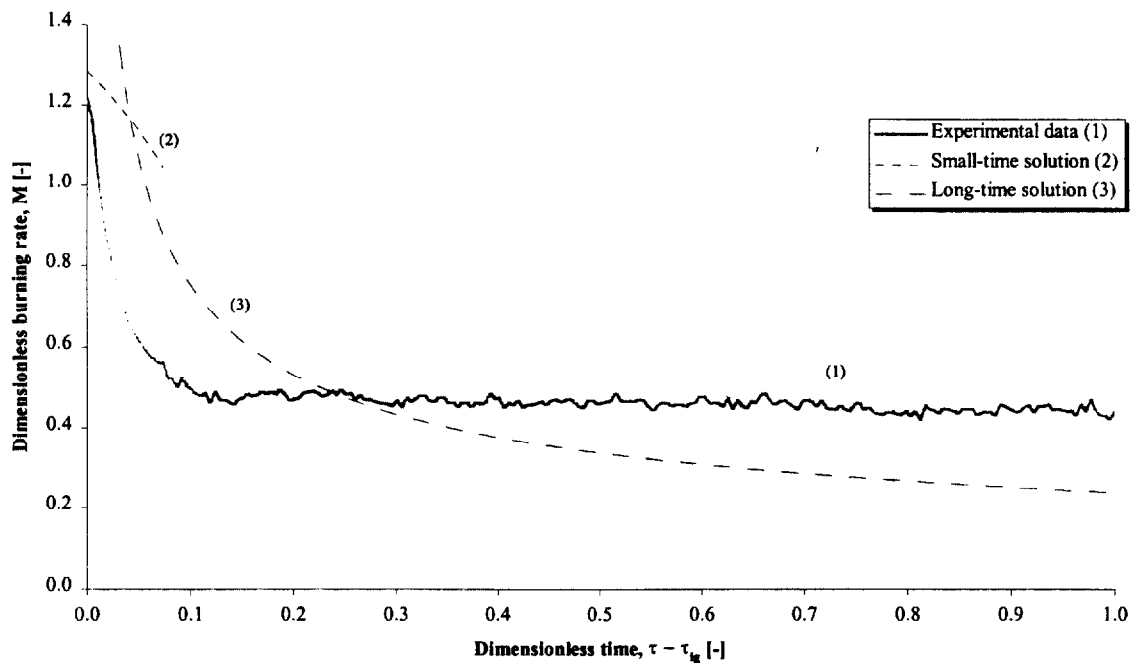**Figure 381.** Temperatures measured in sample (1ML4).

Figure 382. Comparison of dimensionless burning rate using derived properties for species and orientation (1ML4).
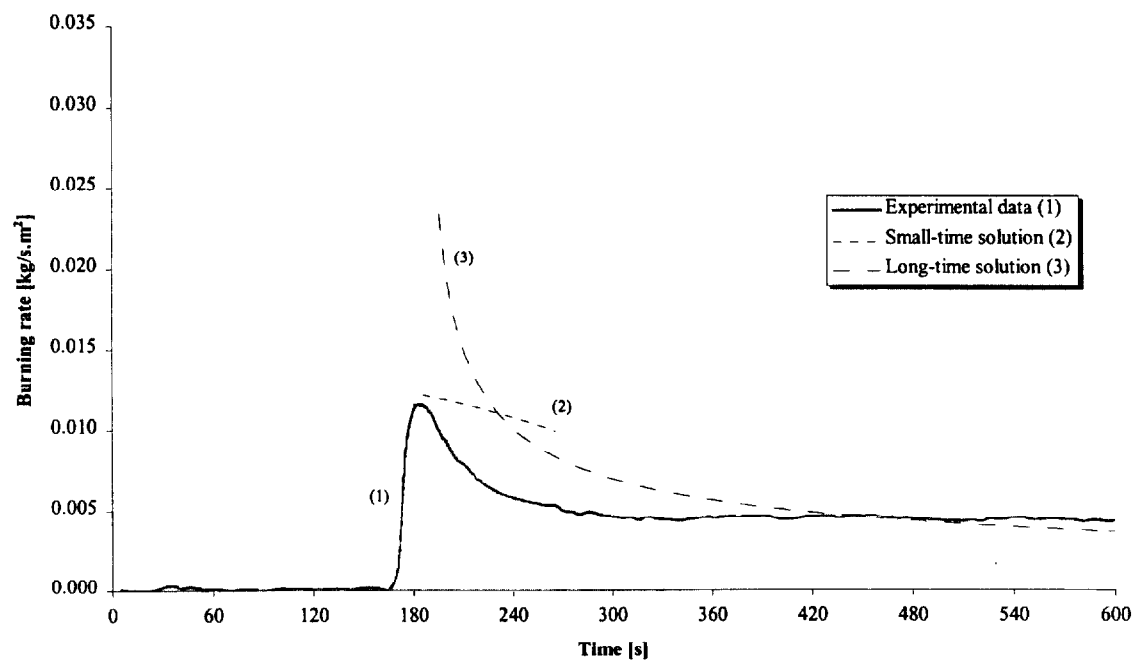

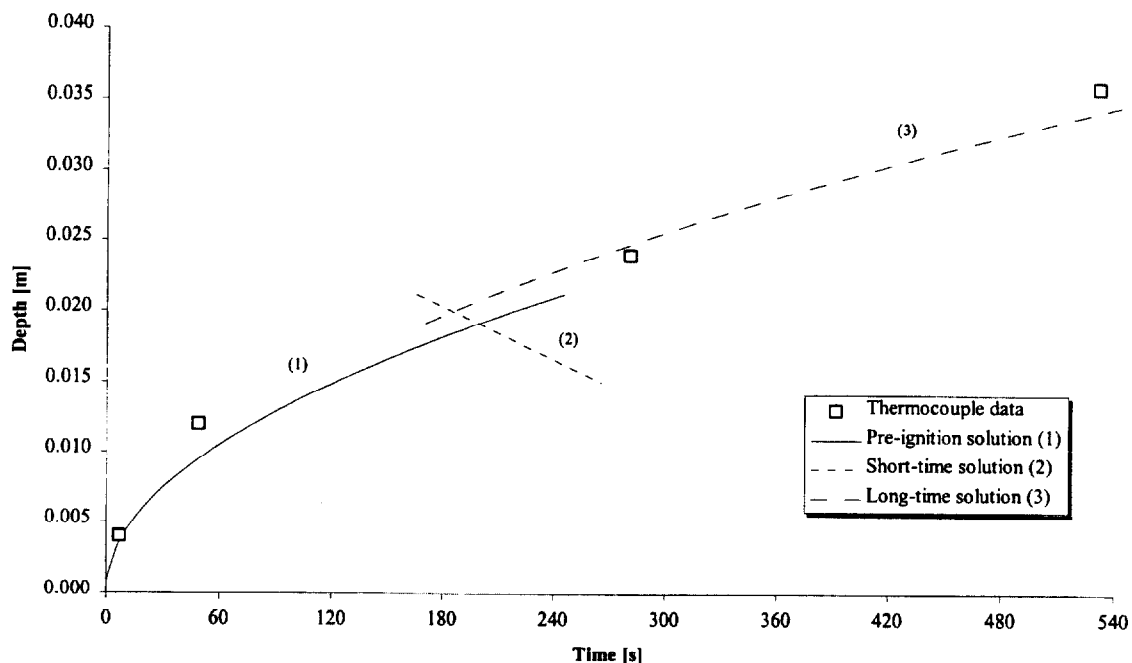**Figure 383.** Comparison of burning rate using derived properties for species and orientation (1ML4).

Figure 384. Comparison of measured and calculated thermal penetration depth (1ML4).
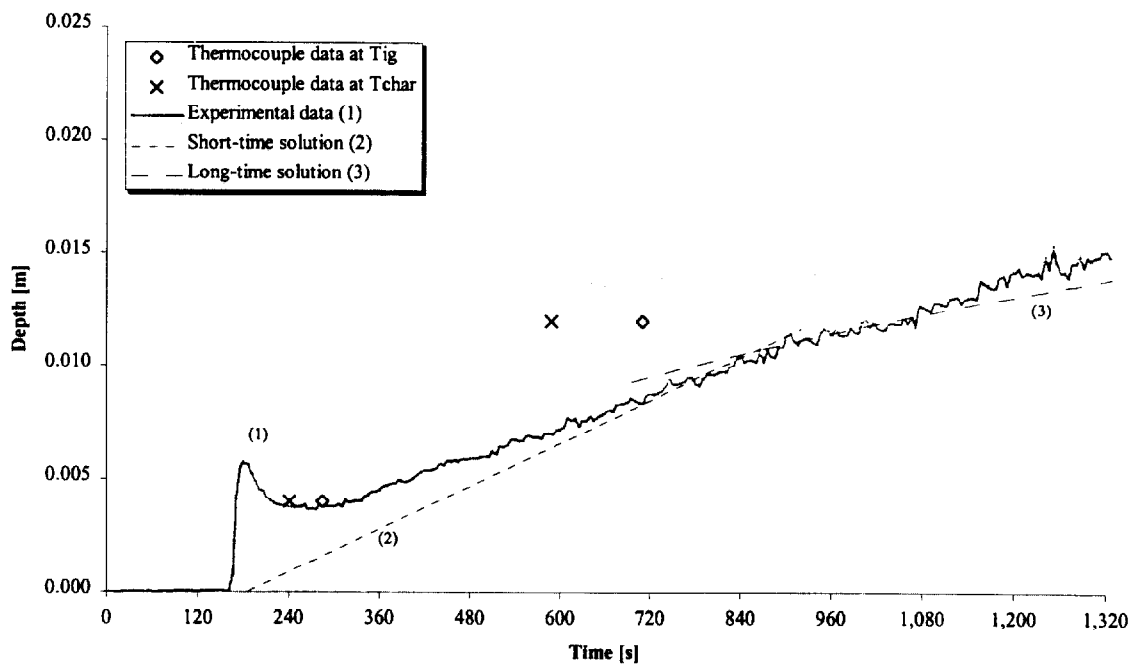

Figure 385. Comparison of estimated char depth from experimental data and the calculated char depth (1ML4).

360

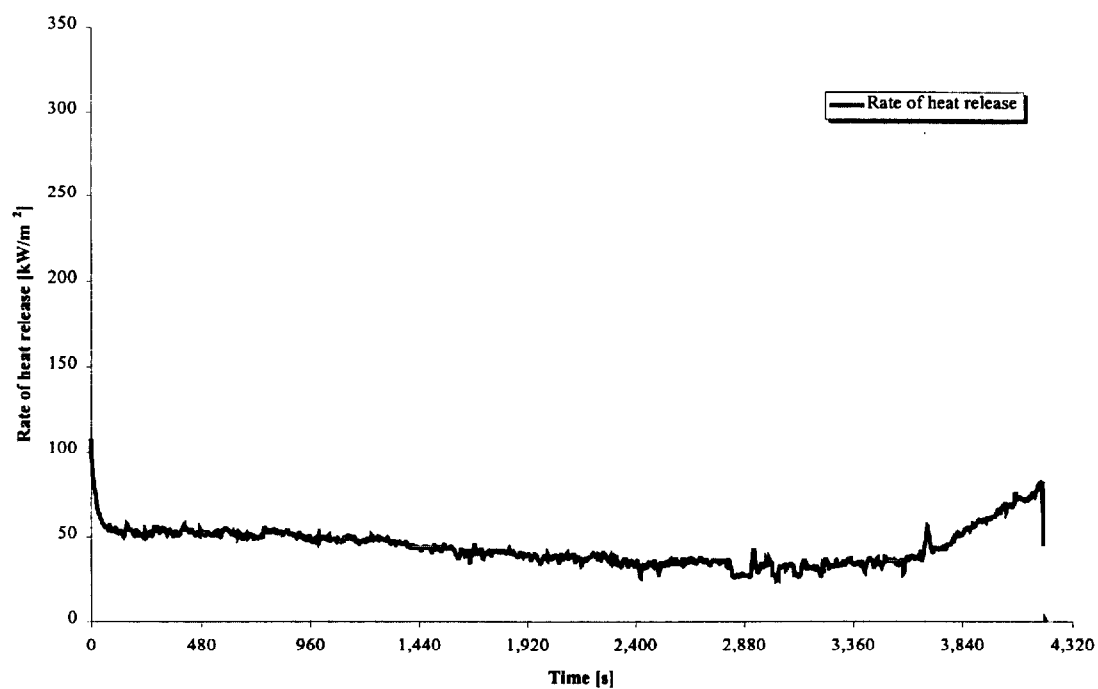Test (1ML5), Maple, along grain at 25 kW/m^2 for 75 minutes.

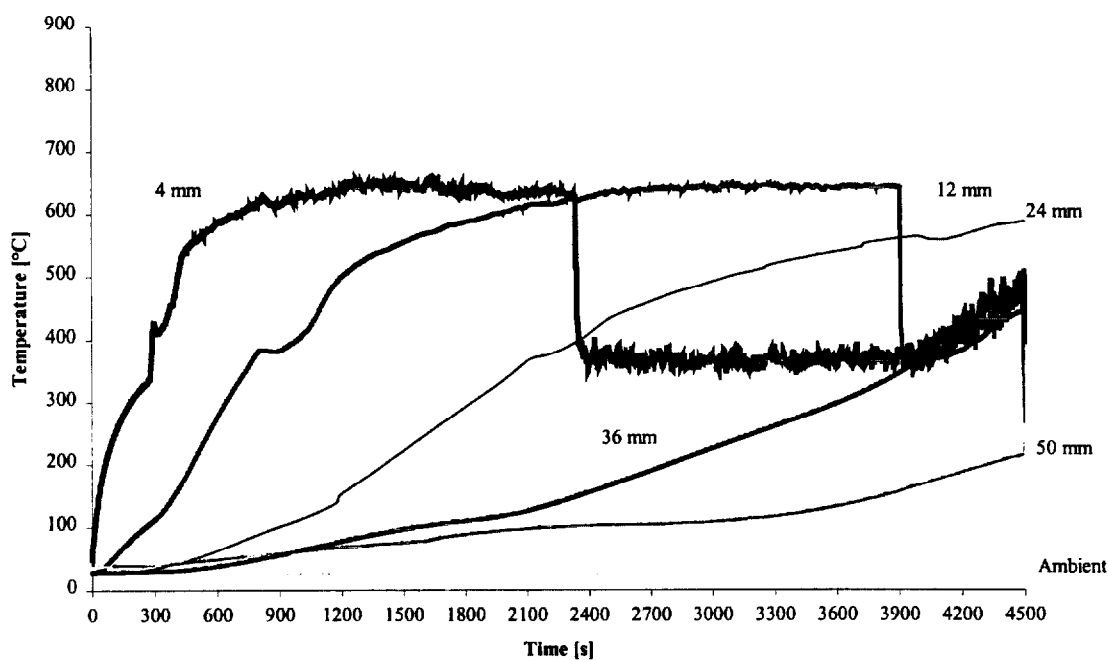**Figure 386.** Rate of heat release (1ML5).

Figure 387. Temperatures measured in sample (1ML5).

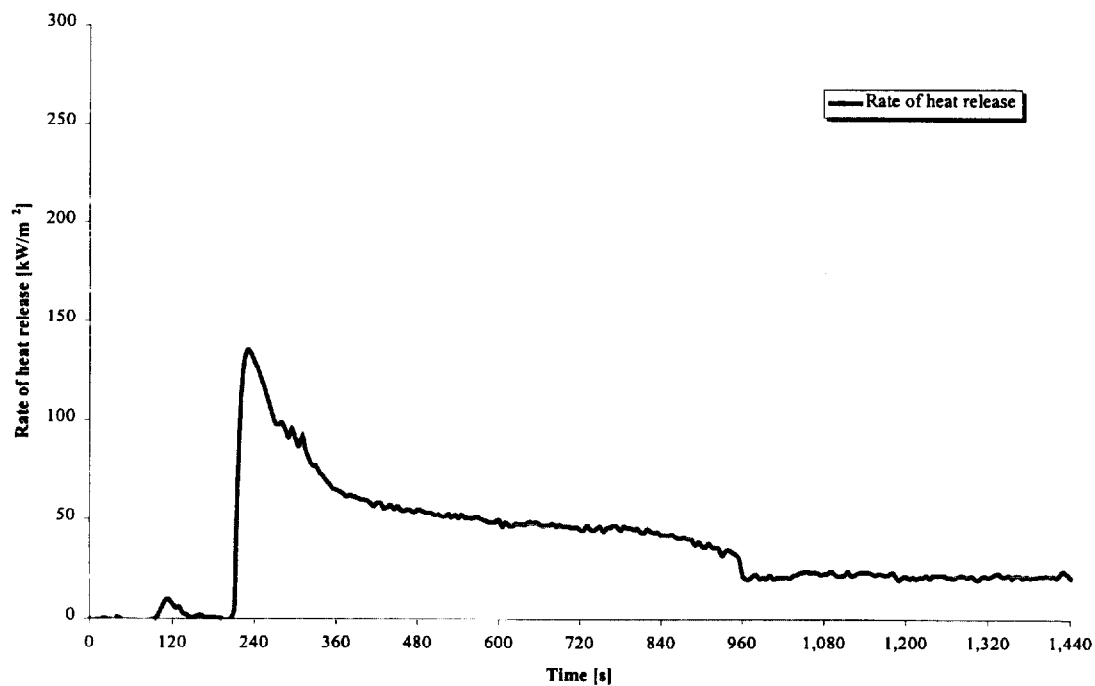Test (1MX1), Maple, across grain at 25 kW/m² for 25 minutes.

Figure 388. Rate of heat release (1MX1).

Figure 389. Temperatures measured in sample (1MX1).

Figure 390. Comparison of dimensionless burning rate using derived properties for species and orientation (1MX1).

Figure 391. Comparison of burning rate using derived properties for species and orientation (1MX1).

Figure 392. Comparison of measured and calculated thermal penetration depth (1MX1).

Figure 393. Comparison of estimated char depth from experimental data and the calculated char depth (1MX1).

Test (1MX2), Maple, across grain at 25 kW/m² for 75 minutes.

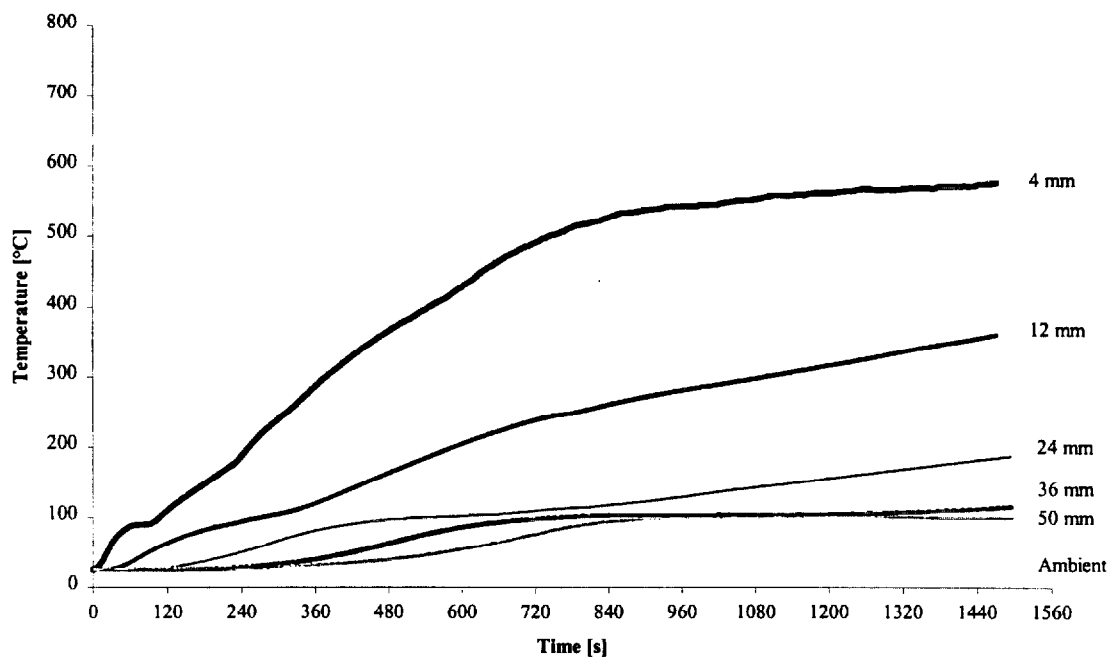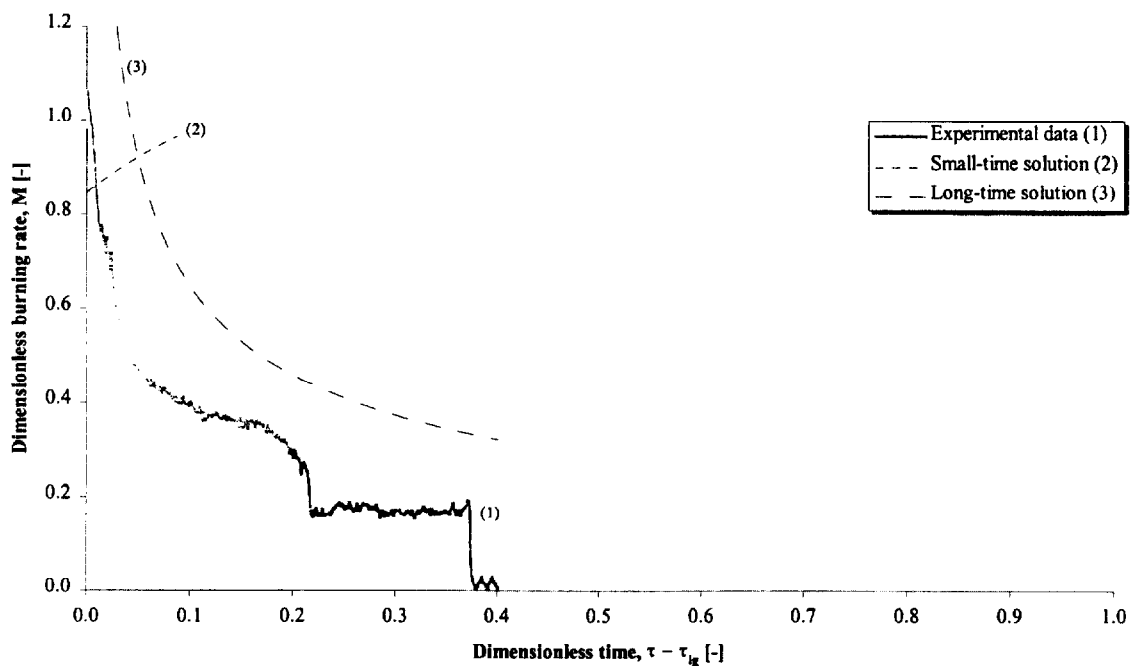**Figure 394.** Rate of heat release (1MX2).

Figure 395. Temperatures measured in sample (1MX2).

365

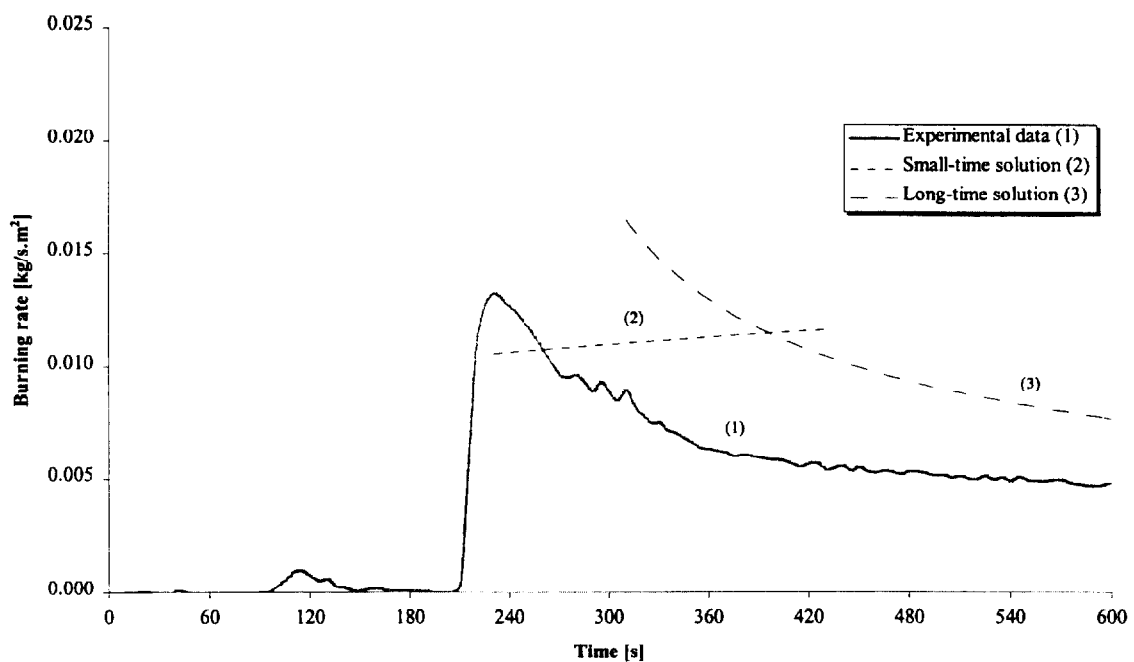**Figure 396.** Comparison of dimensionless burning rate using derived properties for species and orientation (1MX2).

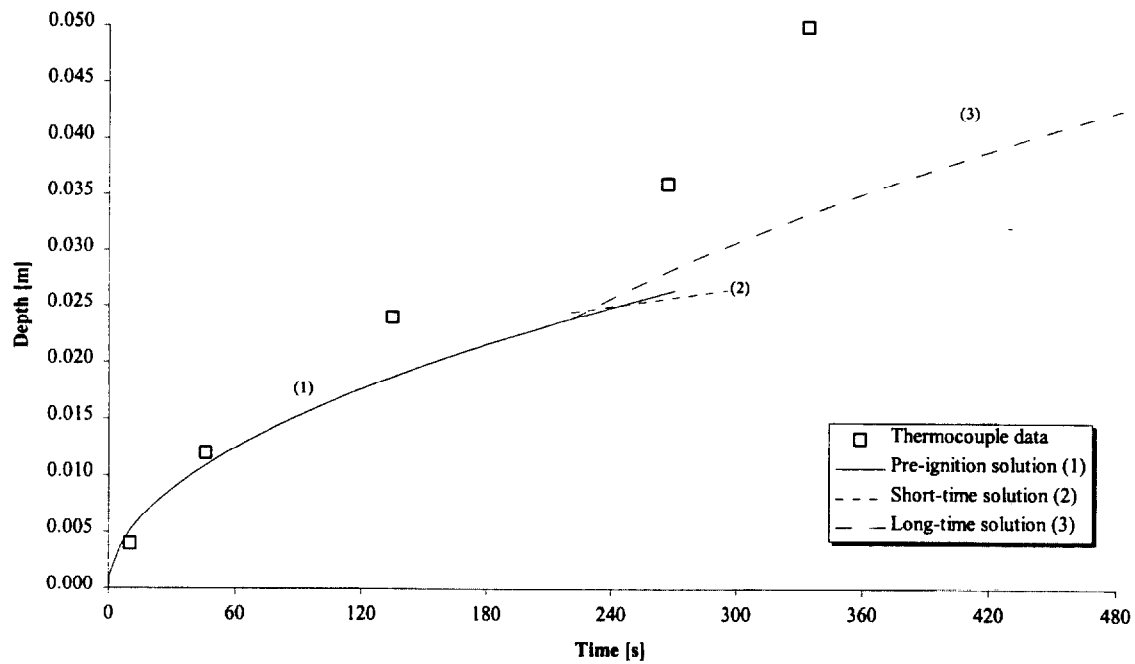**Figure 397.** Comparison of burning rate using derived properties for species and orientation (1MX2).

366

Figure 398. Comparison of measured and calculated thermal penetration depth (1MX2).
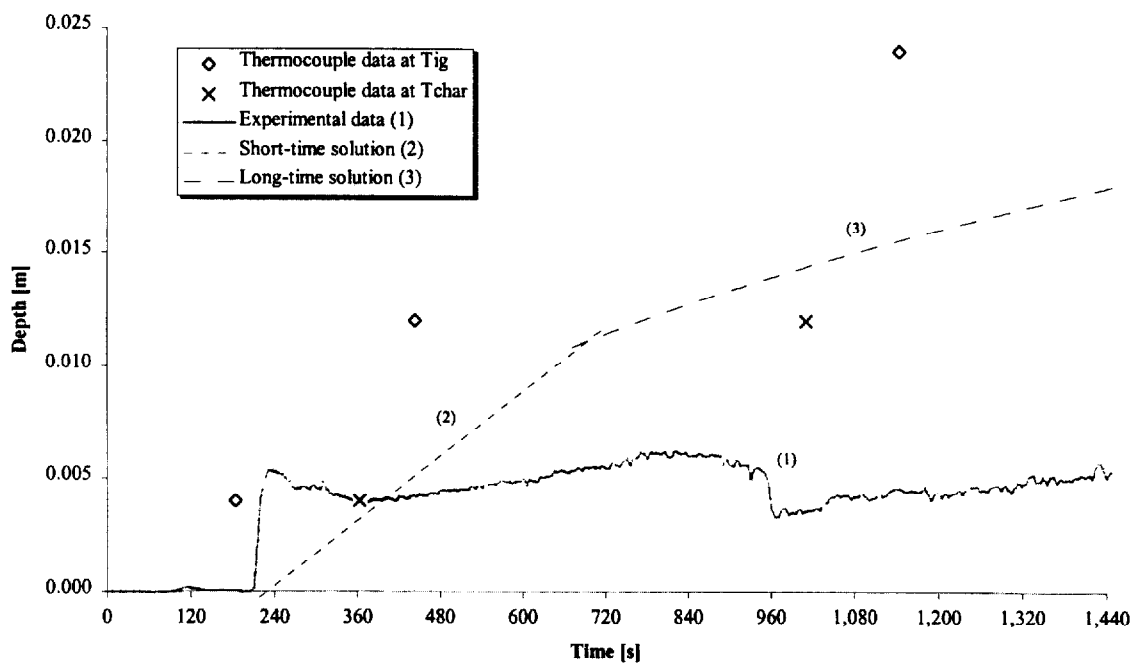

Figure 399. Comparison of estimated char depth from experimental data and the calculated char depth (1MX2).

367

Test (1MX3), Maple, across grain at 75 kW/m^2 for 25 minutes.

Figure 400. Rate of heat release and heat of combustion (1MX3).

Figure 401. Temperatures measured in sample (1MX3).

368

Figure 402. Comparison of dimensionless burning rate using derived properties for species and orientation (1MX3).

Figure 403. Comparison of burning rate using derived properties for species and orientation (1MX3).

369

Figure 404. Comparison of measured and calculated thermal penetration depth (1MX3).

Figure 405. Comparison of estimated char depth from experimental data and the calculated char depth (1MX3).

370

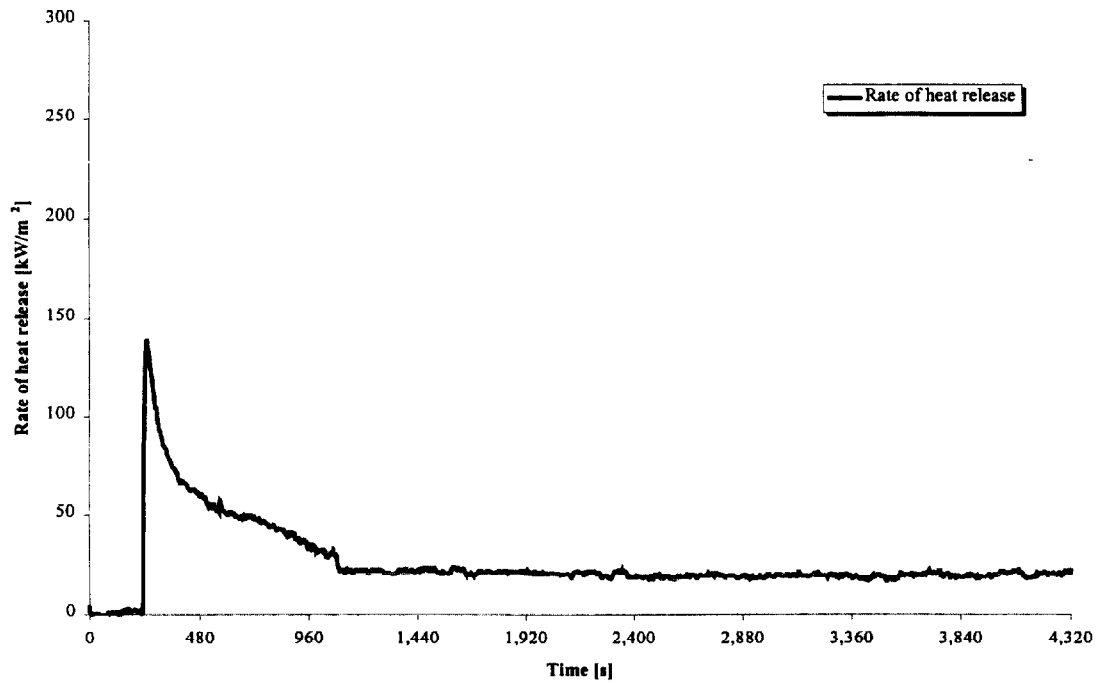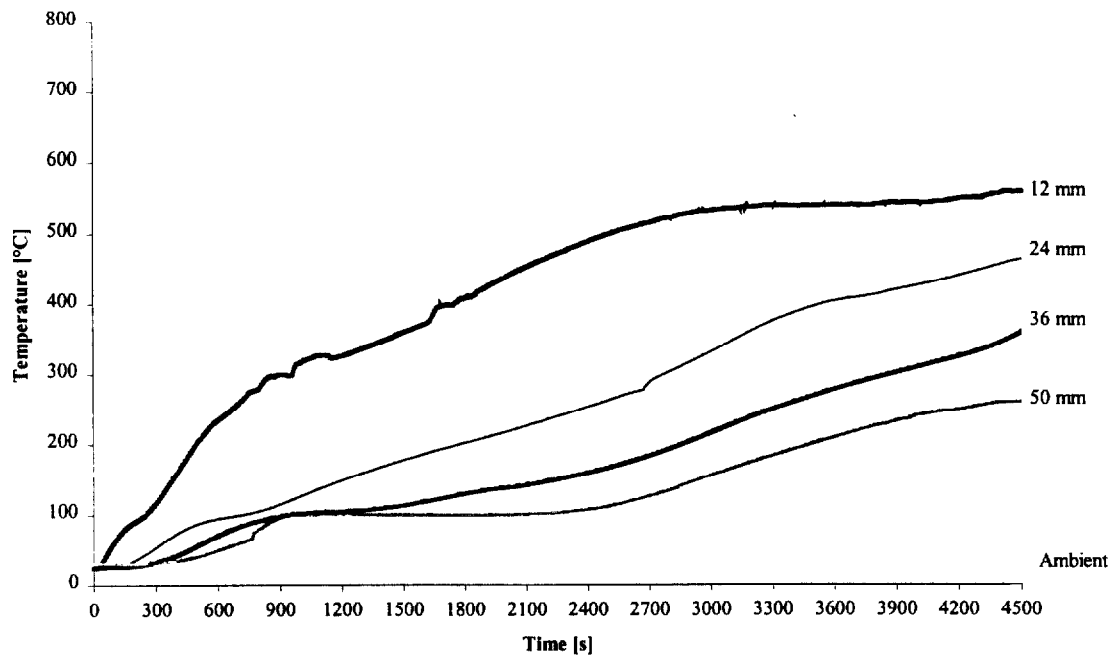Test (1MX4), Maple, across grain at 75 kW/m² for 25 minutes.
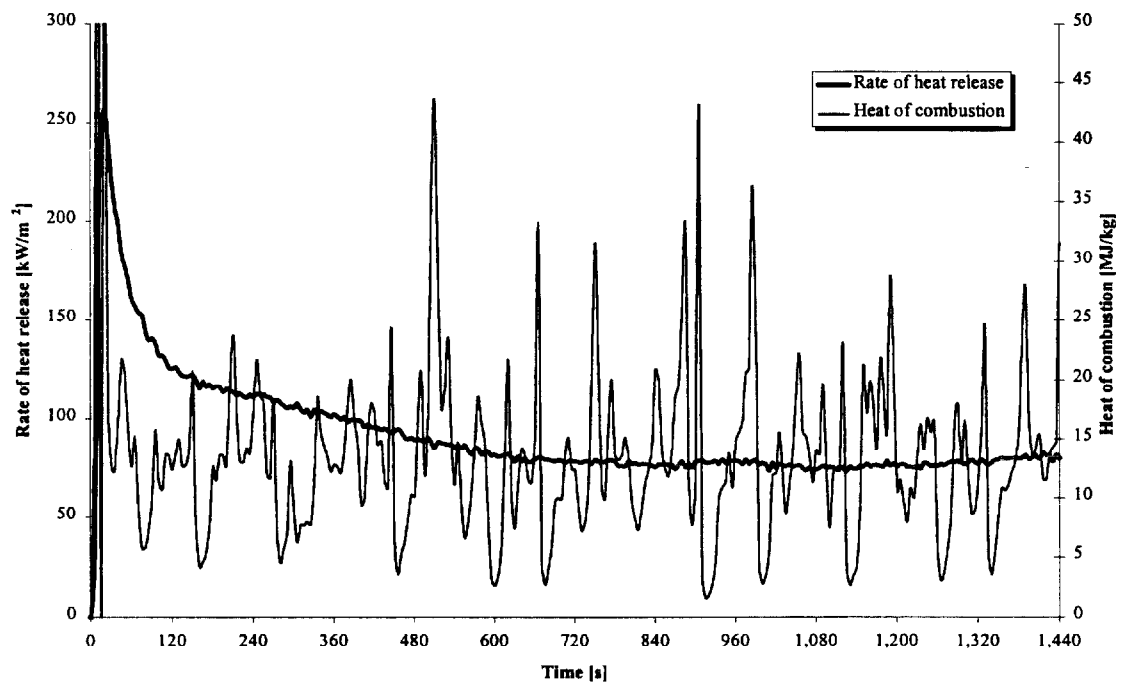
Figure 406. Rate of heat release and heat of combustion (1MX4).
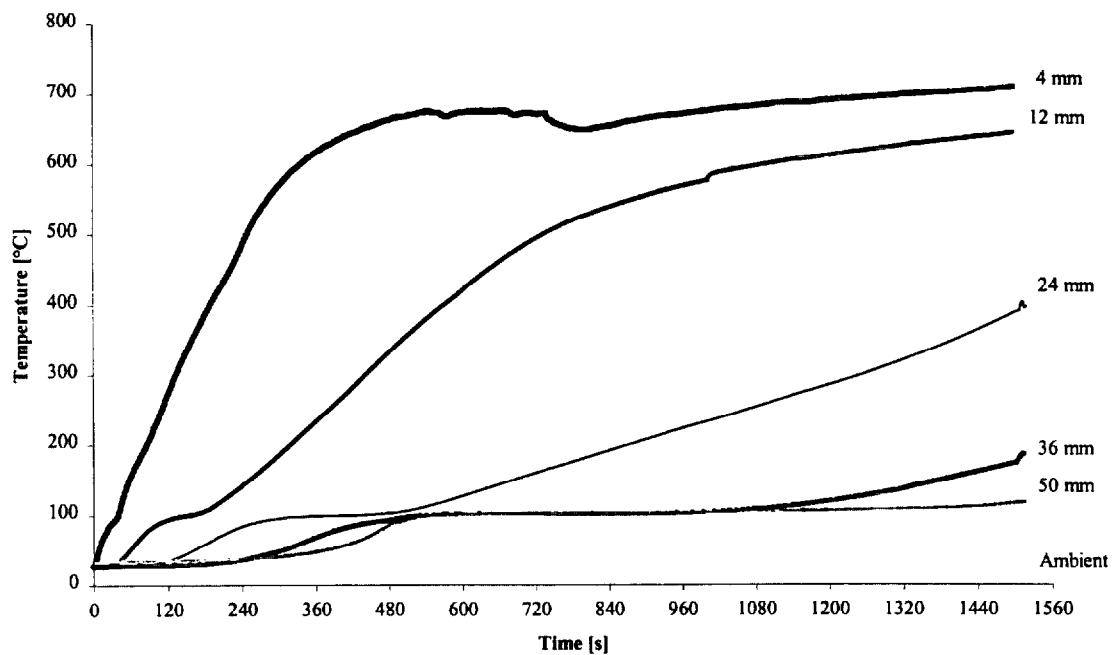
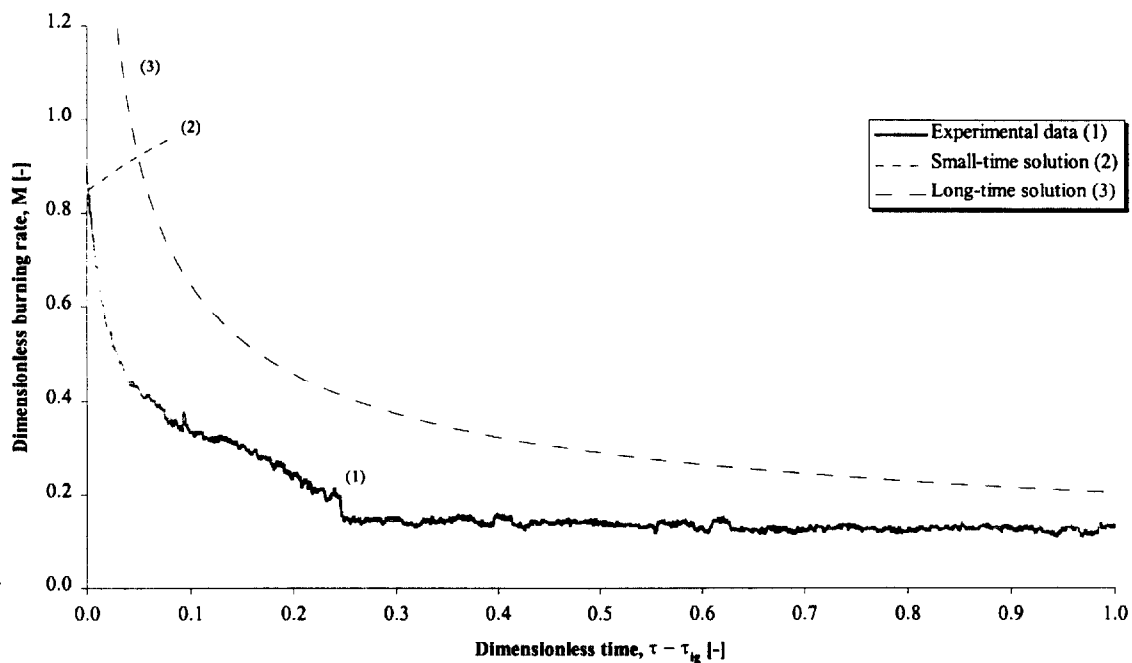**Figure 407.** Temperatures measured in sample (1MX4).

371
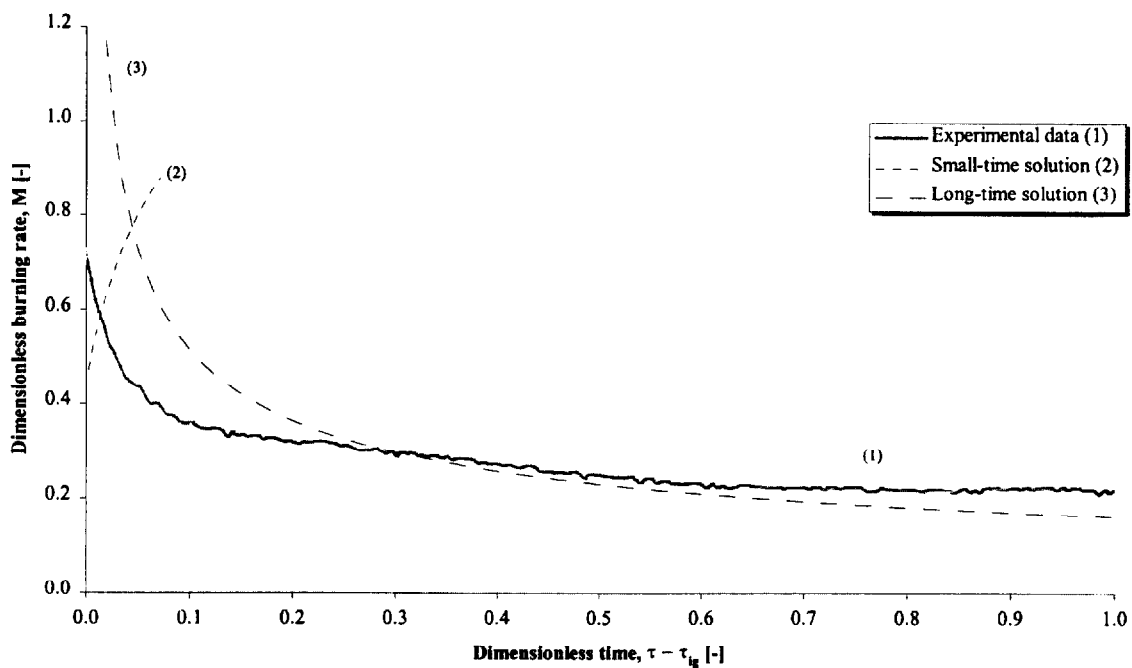
Figure 408. Comparison of dimensionless burning rate using derived properties for species and orientation (1MX4).
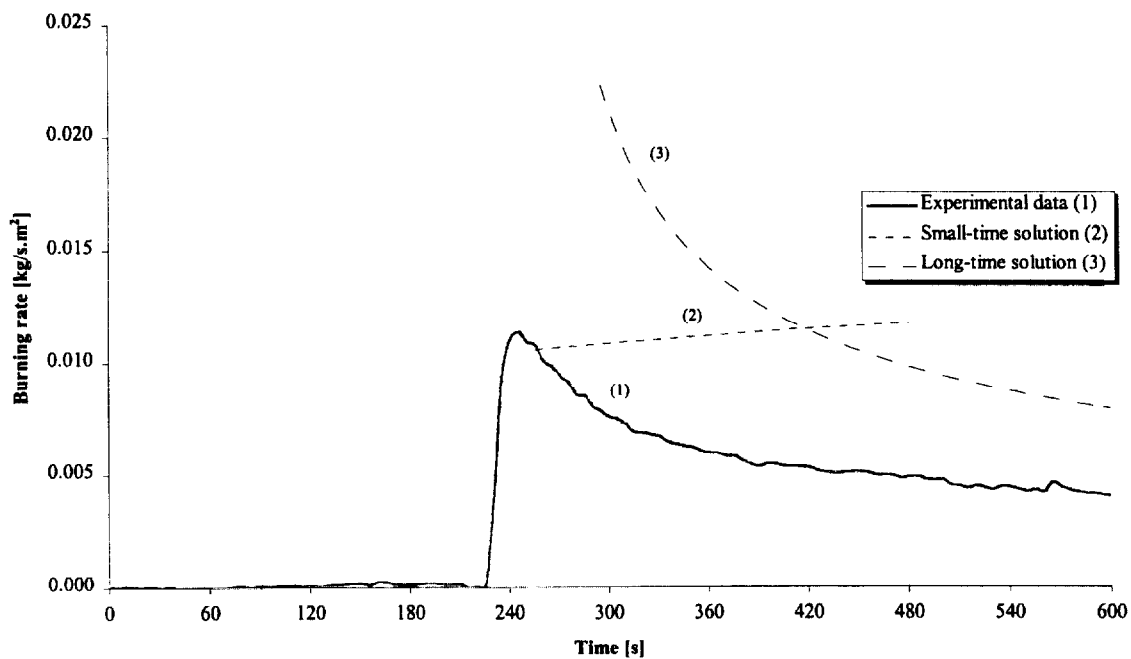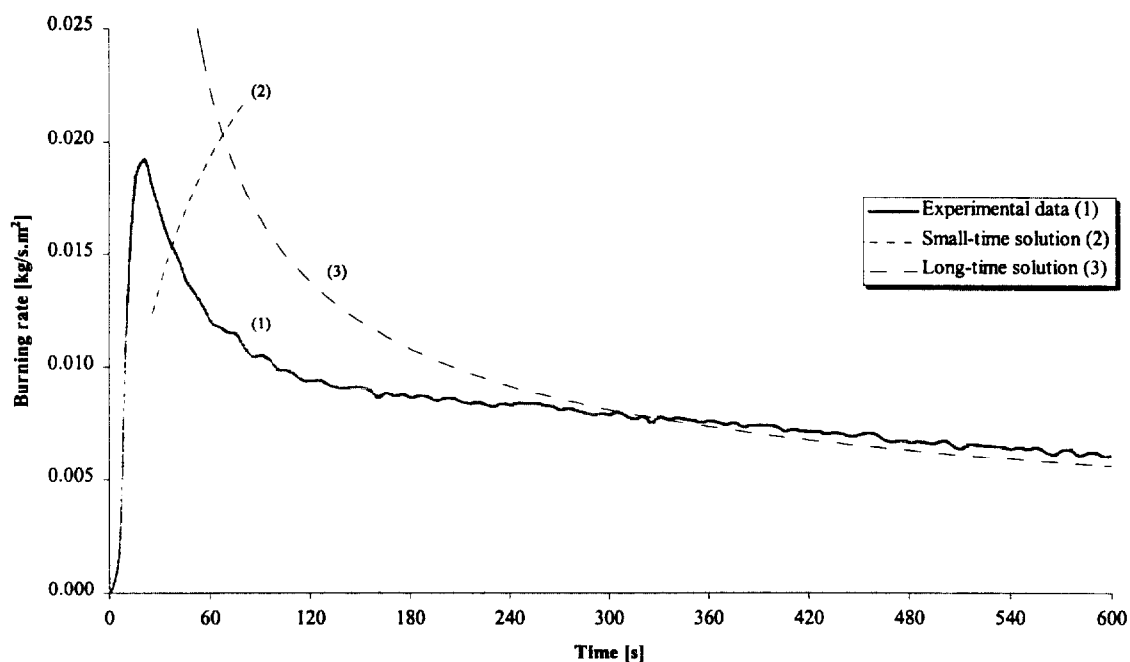

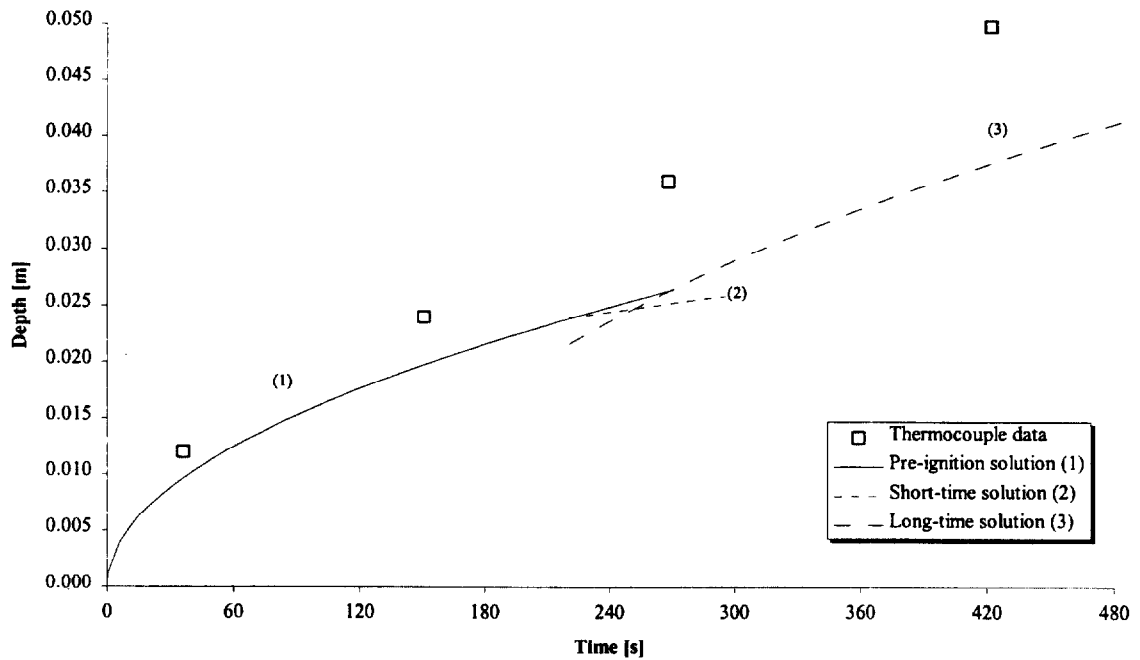**Figure 409.** Comparison of burning rate using derived properties for species and orientation (1MX4).

372
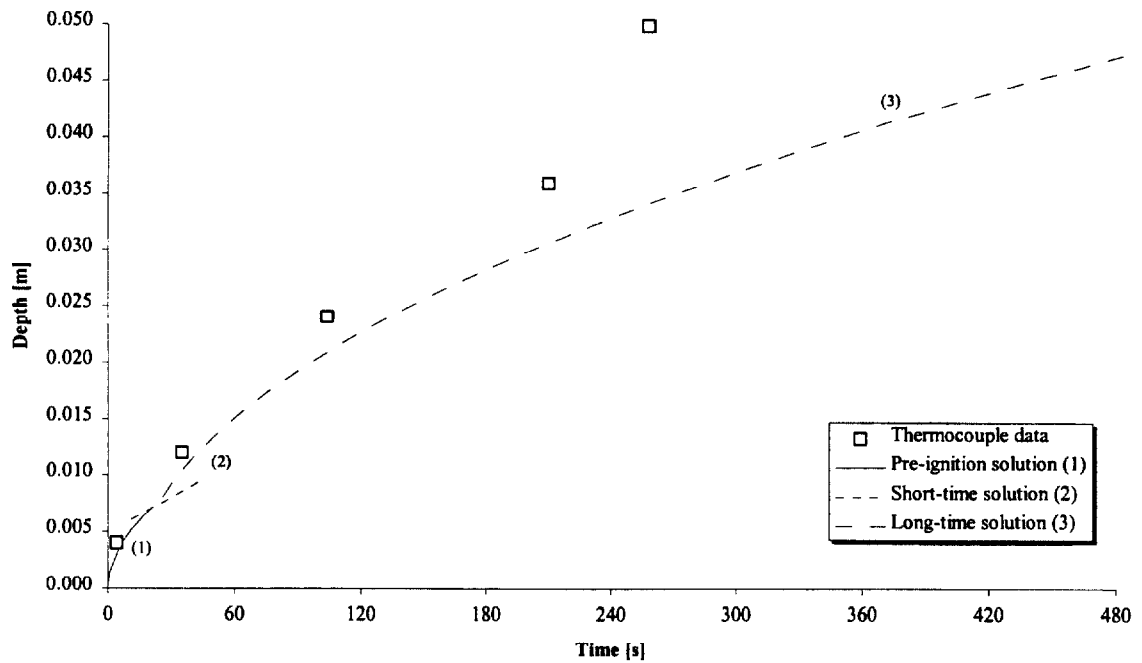
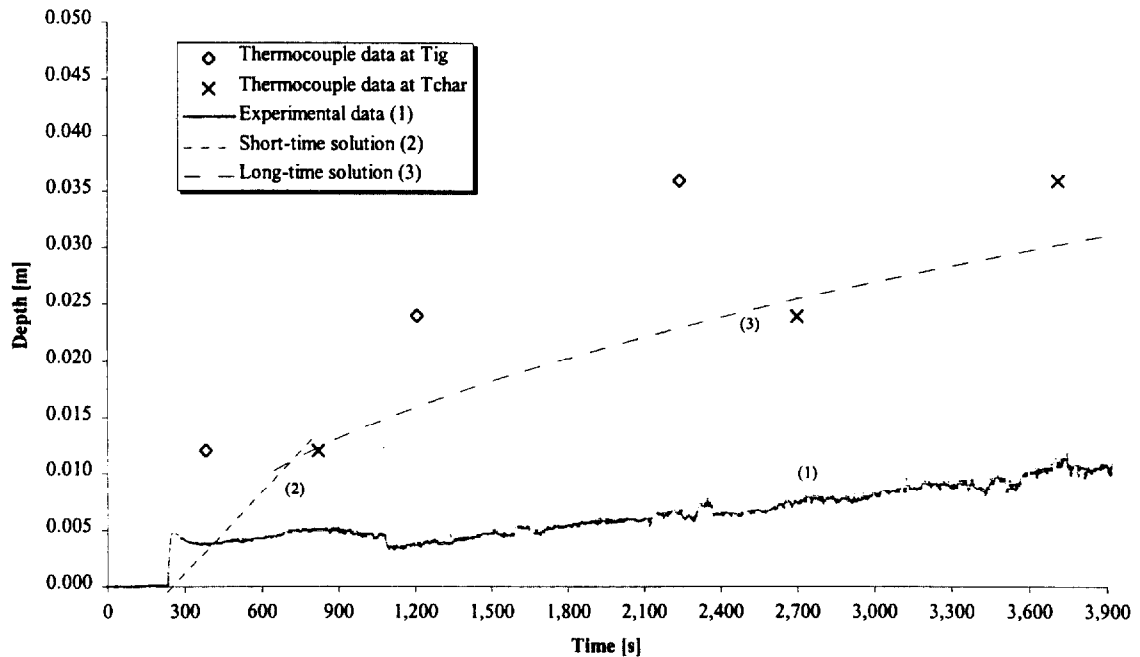**Figure 410.** Comparison of measured and calculated thermal penetration depth (1MX4).
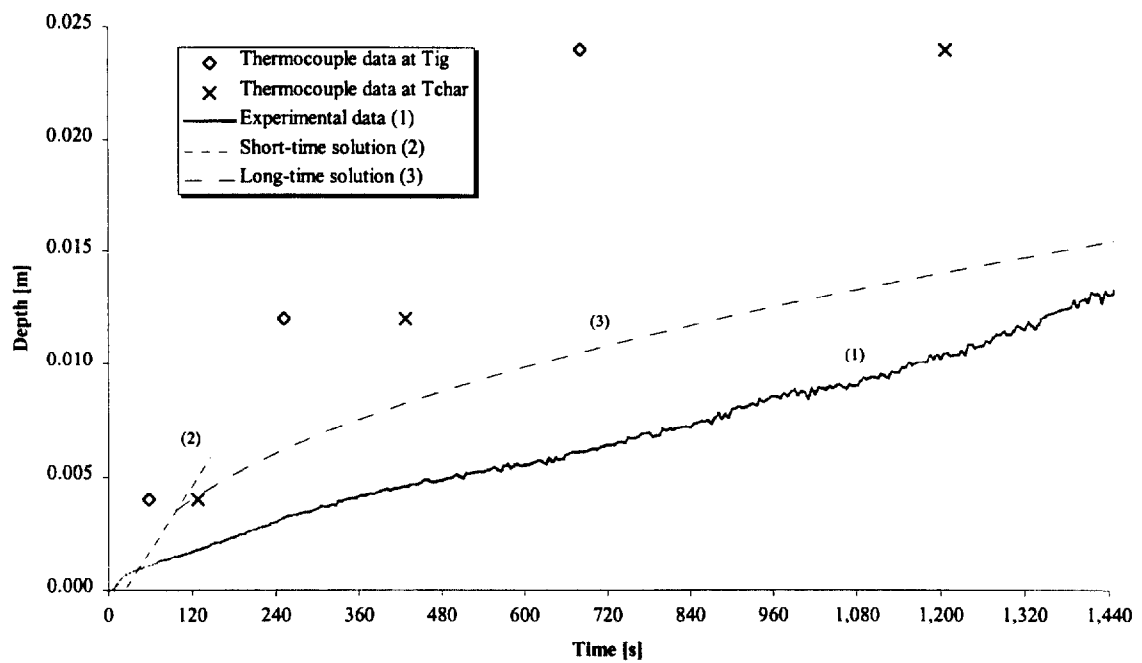
Figure 411. Comparison of estimated char depth from experimental data and the calculated char depth (1MX4).

373

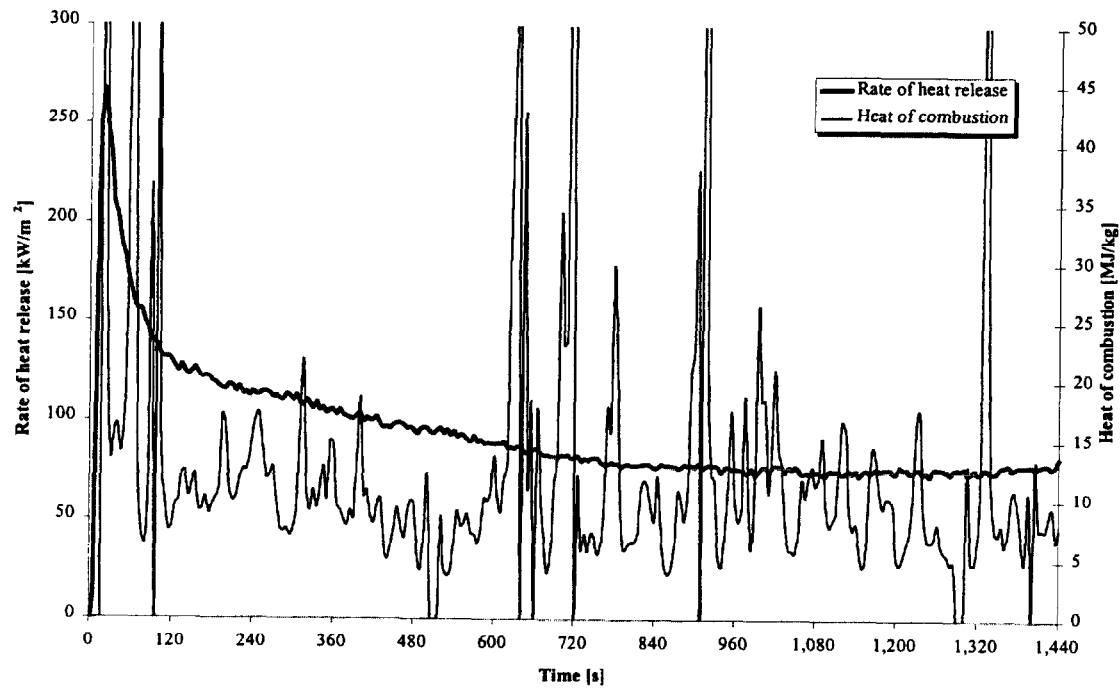Test (1MX5), Maple, across grain at 25 kW/m² for 75 minutes.
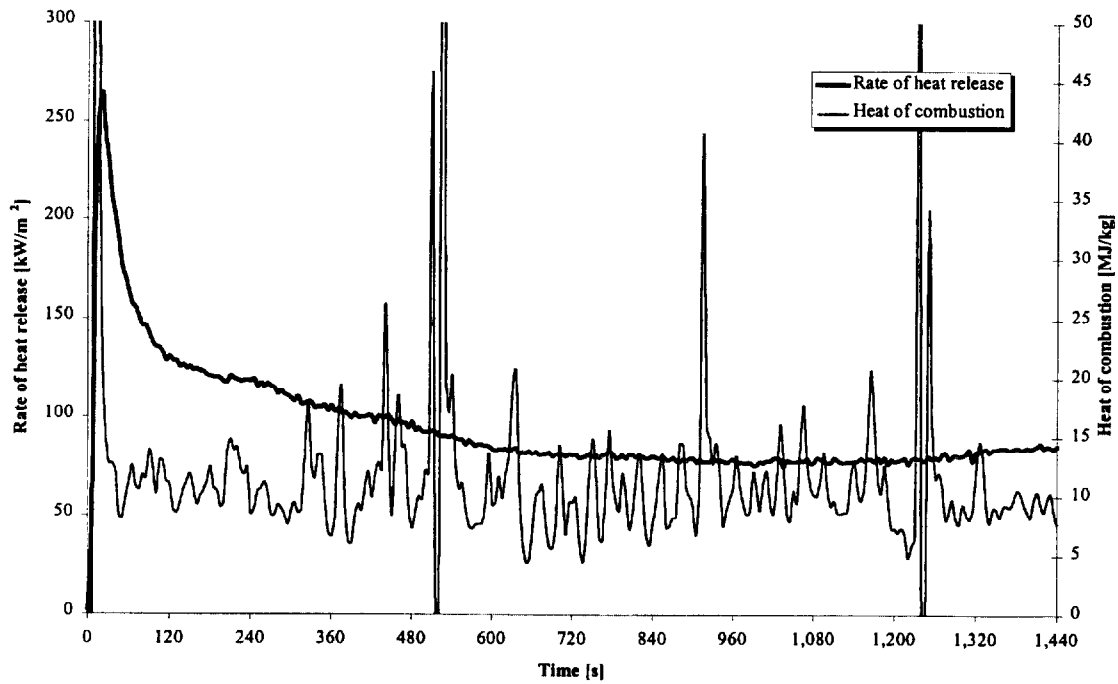
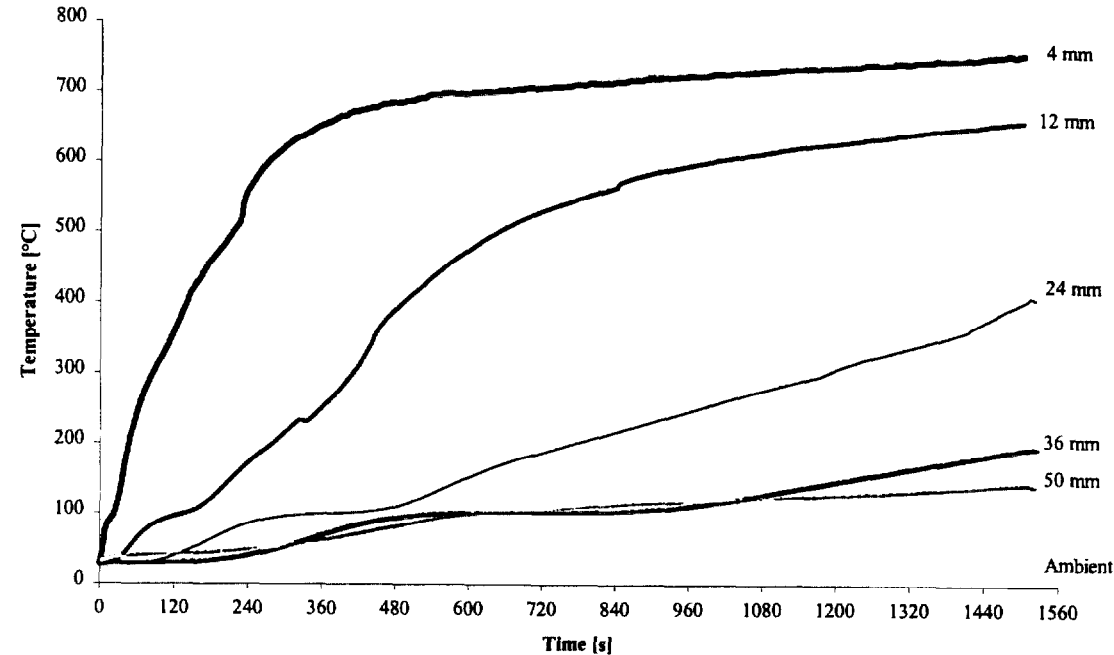**Figure 412.** Rate of heat release and heat of combustion (1MX5).
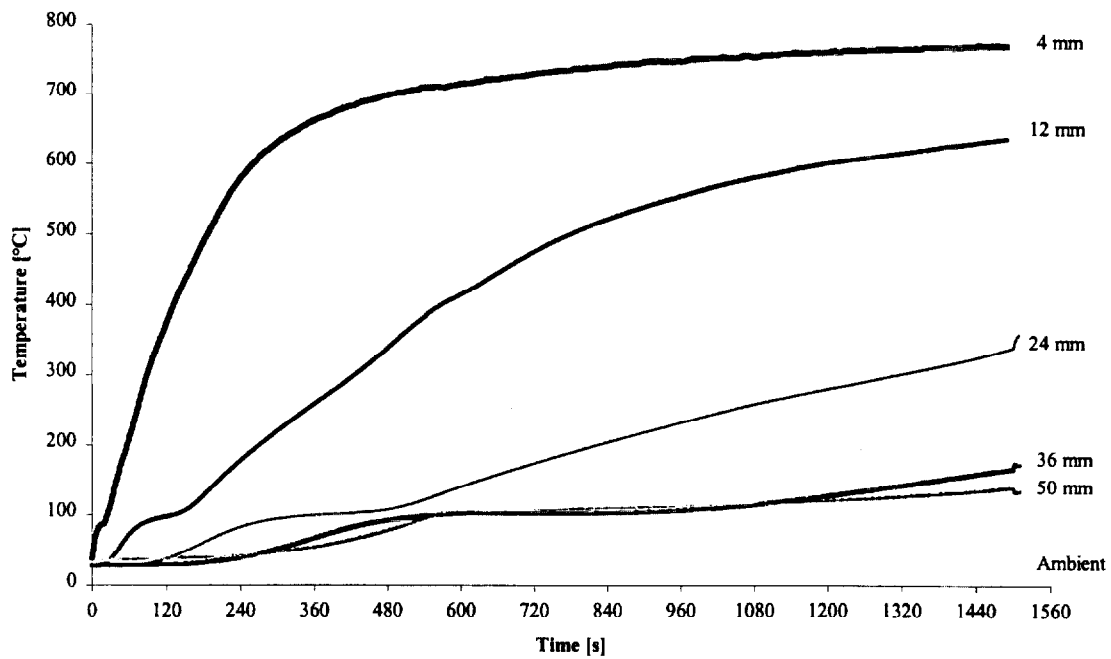
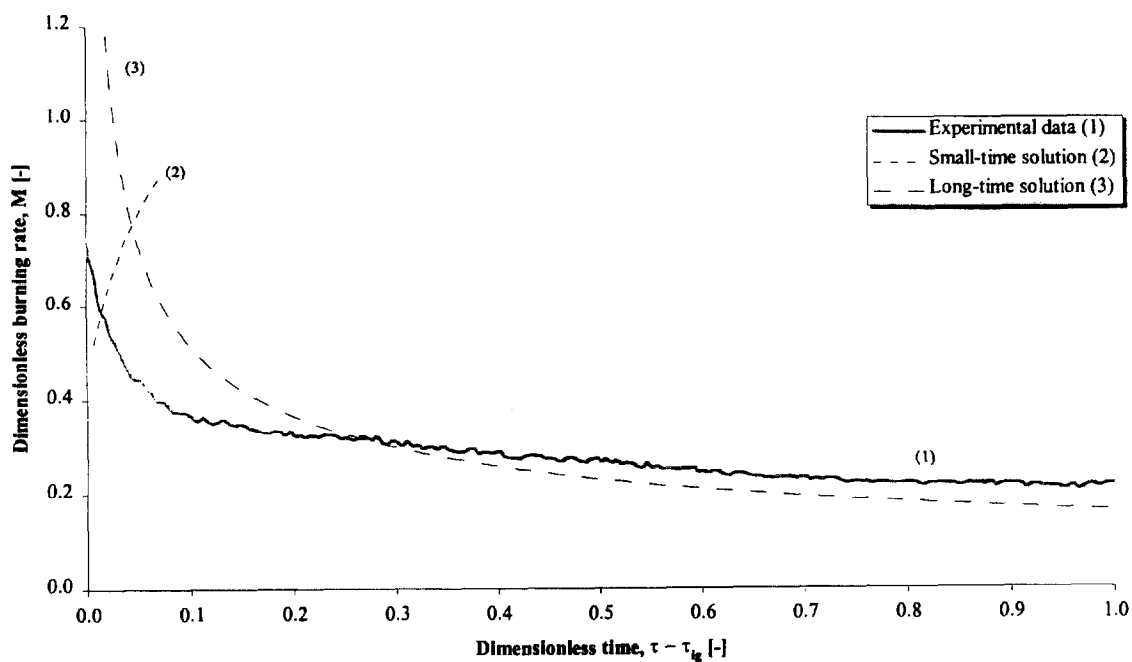**Figure 413.** Temperatures measured in sample (1MX5).

374
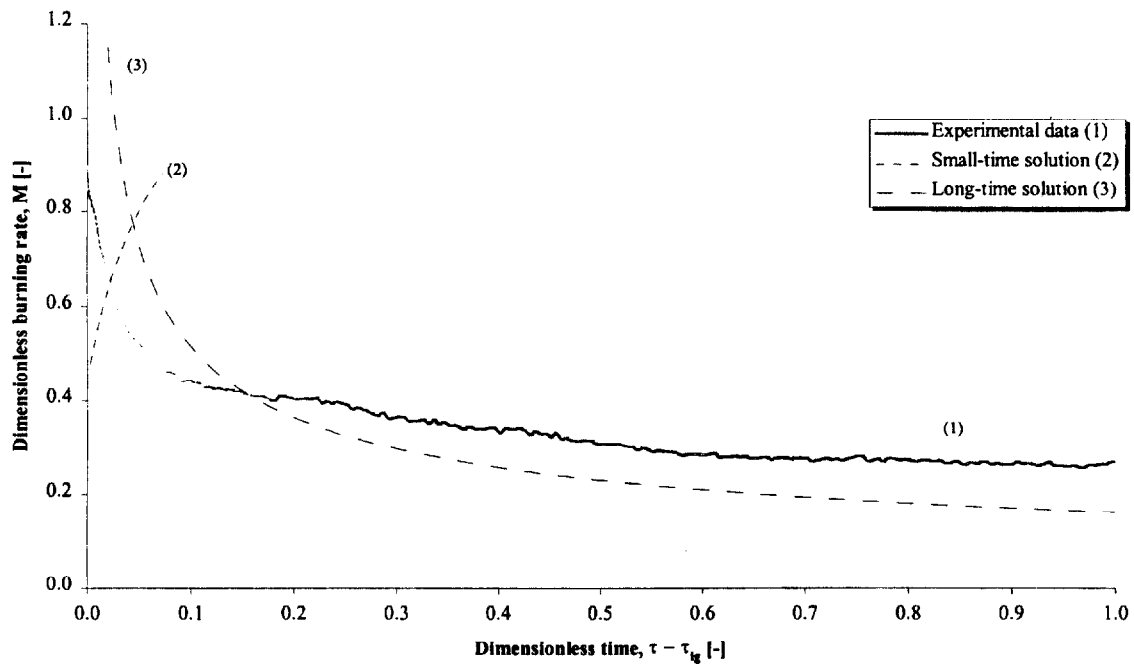
Figure 414. Comparison of dimensionless burning rate using derived properties for species and orientation (1MX5).
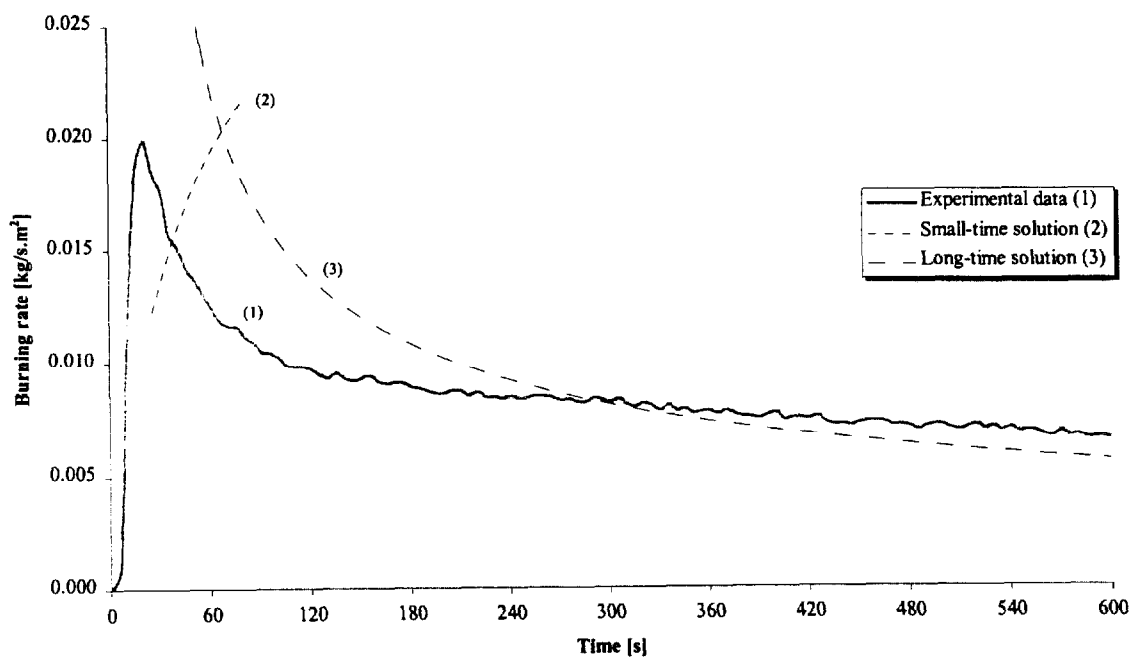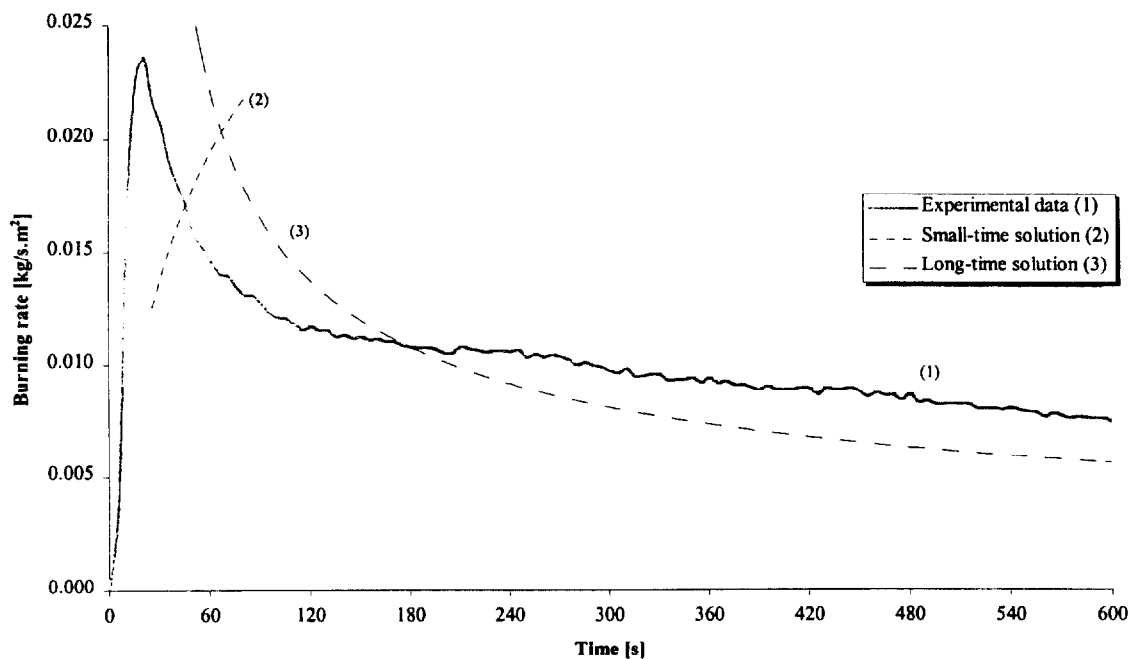

Figure 415. Comparison of burning rate using derived properties for species and orientation (1MX5).
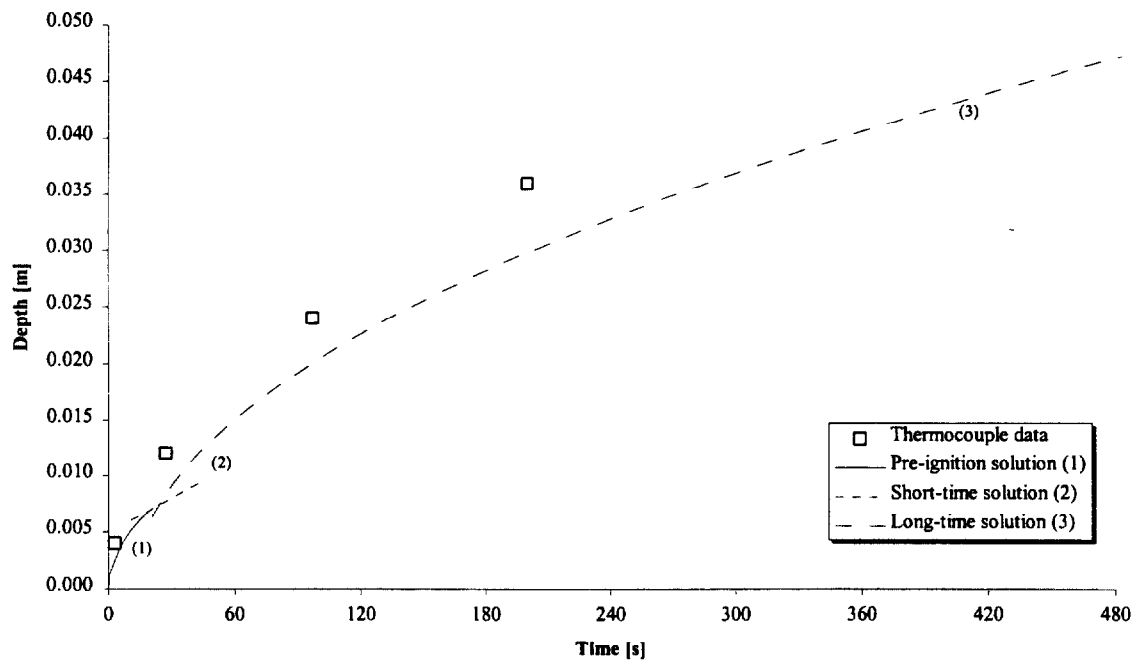
375
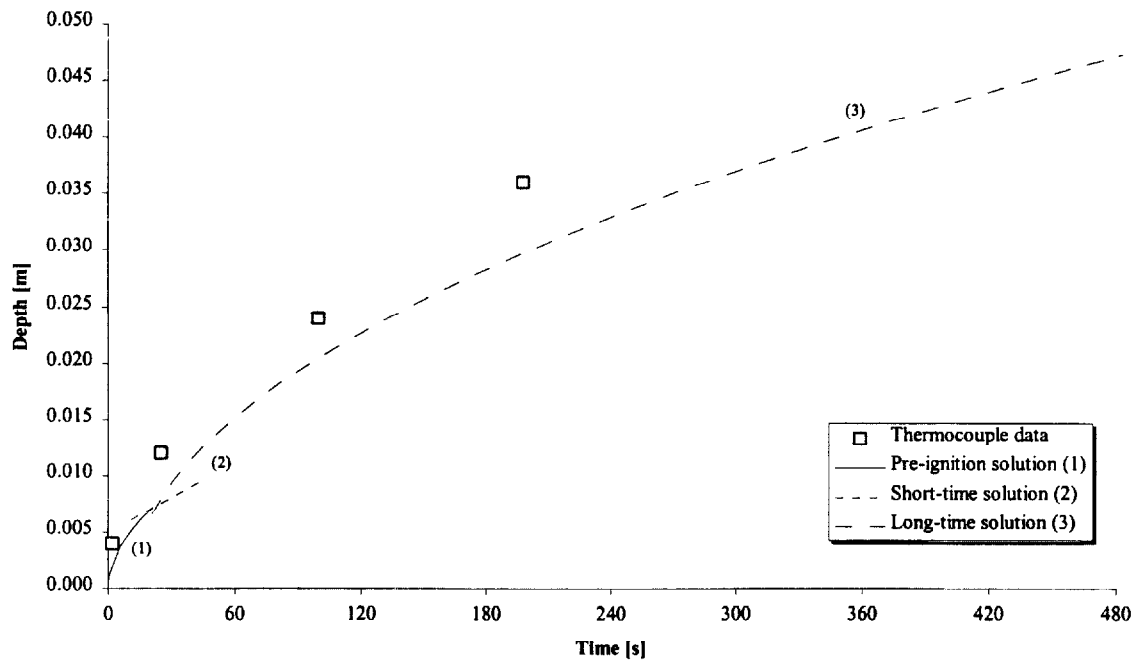
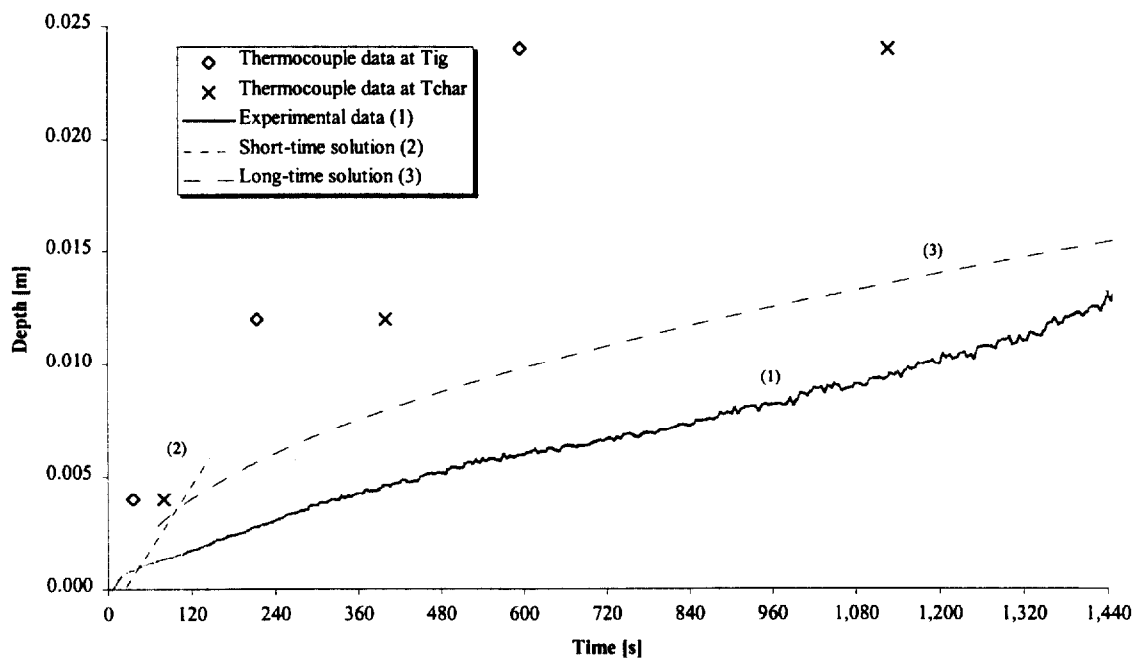**Figure 416.** Comparison of measured and calculated thermal penetration depth (1MX5).
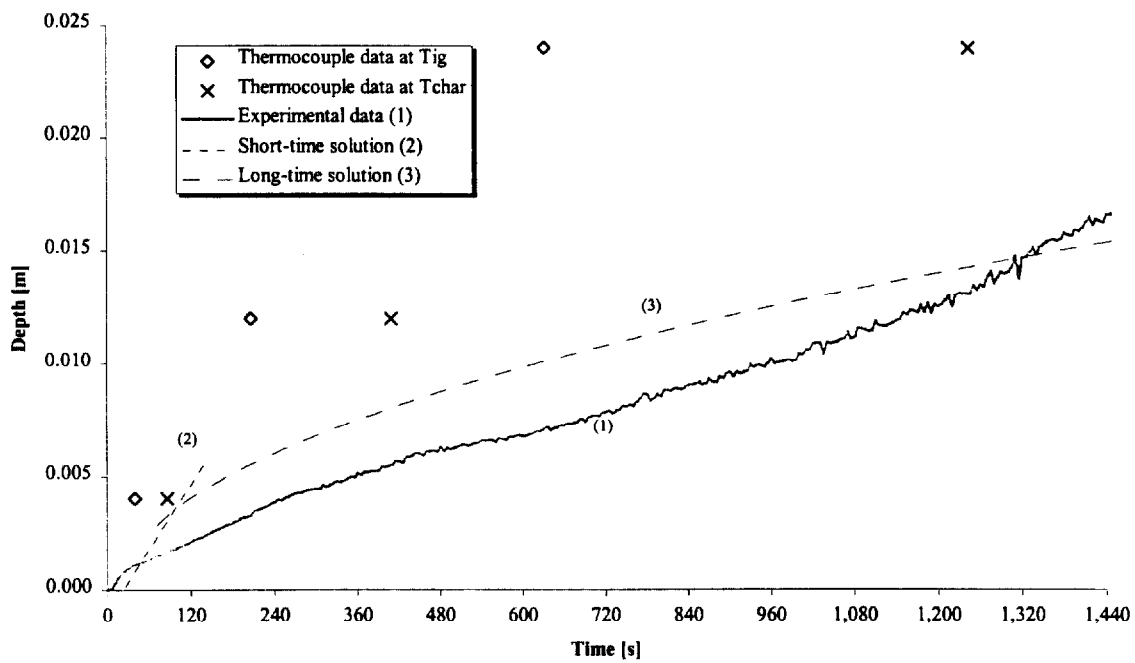
Figure 417. Comparison of estimated char depth from experimental data and the calculated char depth (1MX5).

376

8. REFERENCES

1. Janssens M., Fundamental thermophysical characteristics of wood and their role in enclosure fire growth. PhD thesis, 1991.

2. Drysdale D., An introduction to fire dynamics. John Wiley & Sons, 1996.

3. Cholin J. M., Wood and wood-based products. Section 4 Chapter 3. Fire Protection Handbook, 18th Edition, National Fire Protection Association, Quincy, MA, 1997.

4. Parker W. J., Prediction of the heat release rate of wood, Fire Safety Science - Proceedings of the First International Symposium, pp.207-216.

5. Babrauskas V., The Cone Calorimeter, A new tool for fire safety engineering. ASTM Standardization News, January 1990, pp.32-35.

6. Woodford T., A systematic operational guide for calibration and use of the Cone Calorimeter. Master of Science Graduate thesis, University of Maryland, 1996.

7. Anon. Standard test method for heat and visible smoke release rates for materials and products using an oxygen consumption calorimeter, NFPA 264, 1995. National Fire Protection Association, Quincy, MA.

8. Anon. Standard test method for heat and visible smoke release rates for materials and products using an oxygen consumption calorimeter. ASTM E1354-94. American Society for Testing and Materials, Philadelphia, PA.

9. Janssens M., Calorimetry. SFPE Handbook of Fire Protection Engineering, Second ed., Section 3/Chapter 2, pp.3-16 to 3-36, Society of Fire Protection Engineers, Boston, MA, 1995.

10. Schroeder R., The post fire analysis of construction materials, PhD thesis to be published. University of California, Berkley.

11. Anon. Standard test method for determining material ignition and flame spread properties. ASTM E1321-93. American Society for Testing and Materials, Philadelphia, PA.

12. Martin S. Diffusion-controlled ignition of cellulosic materials by intense radiant energy. Tenth Symposium (International) on Combustion, The Combustion Institute, 1965 pp.877-896.

13. Kanury A. M., Flaming ignition of solid fuels. SFPE Handbook of Fire Protection Engineering, Second ed., Section 2/Chapter 13, pp.2-190 to 2-204, Society of Fire Protection Engineers, Boston, MA, 1995.

14. Roberts A. F., A review of kinetics data for the pyrolysis of wood and related substances. Combustion and Flame, 14, 261-272 (1970).

15. Simms D. L., Damage to cellulosic solids by thermal radiation. Combustion and Flame, Vol. 6, December 1962 pp.303-318.

16. Kanury A. M., Rate of charring combustion in a fire. Proceedings of the Fourteenth Symposium (International) on Combustion, Pennsylvania State University, 1972.

17. Schaffer E. L., Charring rate of selected wood - transverse to the grain. Res. Paper FPL 69, USDA Forest Products Laboratory, 1967.

18. Atreya A., Pyrolysis, ignition and fire spread on horizontal surfaces of wood. PhD thesis, Harvard University, Cambridge, MA, 1983.

19. Tzeng L, Atreya A., Theoretical investigation of piloted ignition of wood. NIST-GCR-91-595, National Institute of Standards and Technology, 1991.

20. Abu-Zaid M., Atreya A. Effect of water on piloted ignition of cellulosic materials. Michigan State Univ., East Lansing National Institute of Standards and Technology, Gaithersburg, MD NIST GCR 89-561; 189 p. February 1989.

21. Atreya A., Carpentier C., Harkleroad M. Effect of sample orientation on piloted ignition and flame spread. Fire Safety Science - Proceedings of the First International Symposium, pp.97-109.

22. Suuberg E. M., Milosavljevic I., Lilly W. D., Behavior of charring materials in simulated fire environments. NIST-GCR-94-645, National Institute of Standards and Technology, Gaithersburg, MD, 1994.

23. Delichatsios M. A., de Ris L., An analytical model for the pyrolysis of charring materials. Factory Mutual Technical Report, 1983.

24. Chen Y., Delichatsios M. A., Motevalli V. Material pyrolysis properties, Part 1: An integral model for one-dimensional transient pyrolysis of charring and non-charring materials. Combustion Science and Technology, Vol. 88 pp.309-328 (1993).

25. Wichman I. S., Atreya A., A simplified model for the pyrolysis of charring materials. Combustion and Flame, Vol. 68, pp.231-247 (1987).

26. Yuen R., Casey R., De Vahl Davis G., Leonardi E., Yeoh G. H., Chandrasekaran V., Grubits S. J. Three dimensional mathematical model for the pyrolysis of wet wood. Fire Safety Science. Proceedings. Fifth International Symposium, Melbourne, Australia, Intl. Assoc. for Fire Safety Science, Boston, MA, Hasemi Y., Editor, 189-200 pp, 1997.

27. Quintiere J. G., A semi-quantitative model for the burning rate of solid materials. NISTIR 4840, National Institute of Standards and Technology, Gaithersburg, MD, 1992.

28. Quintiere J. G., Iqbal N. Approximate integral model for the burning rate of a thermoplastic-like material. Fire and Materials, Vol. 18, 89-98, 1994.

29. Anderson G. W., A burning rate model for charring materials. Master of Science Thesis, University of Maryland, College Park, MD, 1996.

30. Hopkins D., Predicting the ignition time and burning rate of thermoplastics in the Cone Calorimeter. NIST-GCR-95-677, National Institute of Standards and Technology, Gaithersburg, MD, 1995.

31. Moghtaderi B., Novozhilov V., Fletcher D., Kent J. H., An integral model for the transient pyrolysis of solid materials. Fire and Materials, Vol 21, 7-16 (1997).

32. Janssens M., Cone calorimeter measurements of the heat of gasification of wood. Interflam '93, pp549-555.

33. Janssens M., A thermal model for piloted ignition of wood including variable thermophysical properties. Fire Safety Science - Proc. Third International Symposium, pp.167-176.

34. Tran H. C., White R. H., Burning rate of solid wood measured in a heat release calorimeter. Fire and Materials, 16, 197-206 (1992).

35. Parker W. J., Prediction of the heat release rate of Douglas fir, Fire Safety Science - Proceedings of the Second International Symposium, pp.337-346.

36. Dietenberger M. A., Ignitability analysis using the cone calorimeter and LIFT apparatus. Proceedings of the International Conference on Fire Safety, Colombus, Ohio, USA, Product Safety Corporation, 1996, Vol. 22, pp.189-197.

37. Quintiere J. G., Anderson G. W., A burning rate model for charring materials - an integral solution. Unpublished paper, University of Maryland, College Park, MD.

38. Forest Products Laboratory, The wood engineering handbook. Second edition. Prentice Hall, New Jersey, 1990.

39. Fredlund B. A model for heat and mass transfer in timber structures during fire. Institute of Science and Technology, Department of Fire Safety Engineering, Lund University, Sweden, 1988.

40. Desch H. E., Dinwoodie J. M., Timber - Structure, properties, conversion and use. Seventh edition. Food Products Press, 1996.

41. Janssens M., Thermo-physical properties for wood pyrolysis models. Fire Technology.

42. Quintiere J. G., Comparison of approximate solutions for ignition, Private Communication, January 1999.

43. Delichatsios M. A., Panagiotou TH., Kiley F., The use of time to ignition data for characterizing the thermal inertia and the minimum (critical) heat flux for ignition or pyrolysis. Combustion and Flame 84 323-332 (1991).

44. Carslaw H. S., Jaeger J. C., Heat conduction in solids. Second Edition, Oxford University Press, London, 1959.

45. Spearpoint M. J., Measurement of the convective heat transfer in the Cone Calorimeter, Unpublished data, January 1999.

46. Rhodes B. T., Quintiere J. G., Burning rate and flame heat flux for PMMA in a Cone

    Calorimeter. Fire Safety Journal, 26 (1996) 221-240.

47. Siegel R., Howell J. R., Thermal radiation heat transfer. Second edition. Hemisphere

    Publishing Corp. 1981.

48. Anon, Annual Reports, Fire Research, Joint Fire Research Organisation,

    Borehamwood, p.14 (1963), p.12 (1959).

TITLE AND SUBTITLE (CITE IN FULL)

Predicting the Ignition and Burning Rate of Wood in the Cone Calorimeter Using an Integral Model

CONTRACT OR GRANT NUMBER	TYPE OF REPORT AND/OR PERIOD COVERED
60NANB2D1266	Thesis

AUTHOR(S) (LAST NAME, FIRST INITIAL, SECOND INITIAL

Spearpoint, M.J.

PERFORMING ORGANIZATION (CHECK (X) ONE BOX)

- NIST/GAITHERSBURG
- NIST/BOULDER
- NIST/JILA

LABORATORY AND DIVISION NAMES (FIRST NIST AUTHOR ONLY)

SPONSORING ORGANIZATION NAME AND COMPLETE ADDRESS (STREET, CITY, STATE, ZIP)

U.S. Department of Commerce

PROPOSED FOR NIST PUBLICATION

- JOURNAL OF RESEARCH (NIST JRES)
- J. PHYS. & CHEM. REF. DATA (JPCRD)
- HANDBOOK (NIST HB)
- SPECIAL PUBLICATION (NIST SP)
- TECHNICAL NOTE (TN)

- MONOGRAPH (NIST MN)
- NATL. STD. REF. DATA SERIES (NIST NSRDS)
- FEDERAL INFO. PROCESS. STDS. (NIST FIPS)
- LIST OF PUBLICATIONS (NIST LP)
- INTERAGENCY/INTERNAL REPORT (NISTIR)

- LETTER CIRCULAR
- BUILDING SCI. SERIES
- PRODUCT STANDARDS
- OTHER
- [X] NIST GCR—

PROPOSED FOR NON-NIST PUBLICATION (CITE FULLY): — U.S.   FOREIGN —

PUBLISHING MEDIUM:	PAPER	DISKETTE	CD-ROM	WWW	OTHER

SUPPLEMENTARY NOTES

ABSTRACT (A 2000-CHARACTER OR LESS FACTUAL SUMMARY OF MOST SIGNIFICANT INFORMATION. IF DOCUMENT INCLUDES A SIGNIFICANT BIBLIOGRAPHY OR LITERATURE SURVEY, CITE IT HERE. SPELL OUT ACRONYMS ON FIRST REFERENCE.) (CONTINUE ON SEPARATE PAGE, IF NECESSARY.)

This study compares ignition and burning rate measurements of wood in the Cone Calorimeter with a one-dimensional integral model that describes the transient pyrolysis of a semi-infinite charring solid subject to a constant radiant heat flux.

Four species of wood were exposed to a range of incident heat fluxes both with their grain parallel and perpendicular to the incident heat flux. The time to ignition and burning rate measurements obtained from the Cone Calorimeter were used to derive characteristic properties of the materials. These properties were used as input to the integral model to compare its predictions with the experimental data.

Thermocouples were embedded as various depths in the samples. Temperature measurements were used to determine the progress of the thermal penetration wave and char depth through the material. The measurements were compared to predictions from the integral model.

KEY WORDS (MAXIMUM OF 9; 28 CHARACTERS AND SPACES EACH; SEPARATE WITH SEMICOLONS; ALPHABETIC ORDER; CAPITALIZE ONLY PROPER NAMES)

burning rate; cone calorimeters; ignition; radiant flux; wood

AVAILABILITY:
[X] UNLIMITED   FOR OFFICIAL DISTRIBUTION - DO NOT RELEASE TO NTIS
    ORDER FROM SUPERINTENDENT OF DOCUMENTS, U.S. GPO, WASHINGTON, DC 20402
[X] ORDER FROM NTIS, SPRINGFIELD, VA 22161

NOTE TO AUTHOR(S): iF YOU DO NOT WISH THIS
MANUSCRIPT ANNOUNCED BEFORE PUBLICATION,
PLEASE CHECK HERE.